Age, origin and extent of the Newer Volcanic Province in the Melbourne region, Australia

Michael Anthony Heath

ORCID: 0000-0002-5184-4989

Doctor of Philosophy – Science

July 2019

School of Earth Sciences

The University of Melbourne

This thesis is submitted as complete fulfilment of the requirements of the degree of

Doctor of Philosophy - Science

Abstract

Intraplate basaltic volcanism is present on every continent, untethered to any specific tectonic setting. The ca. 4.6 Ma – 5 ka Newer Volcanic Province (NVP) in south-eastern Australia is a chemically and morphologically diverse intraplate basaltic province. Its diversity, preservation and accessibility make it an ideal natural laboratory for investigating the causes and evolution of intraplate magmatism worldwide. Previous studies in the NVP have put forward competing magmatic models, but their validity is dependent on a limited geochronological dataset. Furthermore, previous geochronology has seldom been supported by geochemical or geomorphological studies on the same volcanic products, such that there is often a disconnect between the absolute ages of NVP rocks and the extent and composition of their associated lava flows or eruption points.

This study utilised a holistic approach to lava flow mapping, with a focus on the diagnostic petrographic and geochemical features of individual basaltic lava flows selected for geochronology. The current study area of Melbourne, which is located at the eastern margin of the NVP, was selected for its age range and geochemical complexity, rivalling those of the entire NVP. Drill core was utilised to trace lava flows at depths of up to 80 m, thereby unravelling complex flow networks and facilitating the construction of a detailed lava flow map for the Melbourne area. Trace element geochemistry was utilised to distinguish between petrographically similar flows, and to investigate the eruption of three chemically distinct magma batches erupted consecutively from Mount Fraser. This mapping and geochemical work is complemented by new, high-precision ^{40}Ar/^{39}Ar age constraints, spanning ~7.9 Ma – 0.8 Ma.

The new geochronological constraints on Melbourne lava flows reveal that the earliest activity (~7.9 – 3.8 Ma) was dominated by small-volume eruptions that predominantly produced alkali basalts. From oldest to youngest, these included the Bald Hill, Mount Ridley, Tullamarine, Crowe Hill, Spring Hill, Summerhill Rd, Redstone Hill and Aitken Hill lava flows. After ~3.8 Ma, large-volume eruptions dominated, with Fenton Hill, Mount Kororoit, Tulloch Hill and Mount Fraser producing lavas generally of tholeiitic composition. This progression from alkali basalt to tholeiitic volcanism over time is contrary to the purported province-wide progression from tholeiitic to alkali-rich lavas, indicating either that geochemical evolution in Melbourne was distinct from that of the NVP, or that the conclusions of province-wide studies are based on an unrepresentative sample set.

An age of 7.931 ± 0.038 Ma for the Bald Hill Lava Flow far exceeds the generally accepted maximum age of NVP activity (ca. 4.6 Ma). This lava flow, along with those erupted from Pretty Sally, Green Hill and Mount Cooper, is also geochemically distinct from other Victorian NVP products, but is not dissimilar to lavas of the Cosgrove Leucitite suite, the purported products of a long-lived mantle plume. This raises the possibility that the ‘Cosgrove Plume’ traversed the latitude of Melbourne just after 7.9 Ma, casting doubt on its possible role in the initiation of NVP activity some 3.3 million years later.

11 of the 38 samples selected for ^{40}Ar/^{39}Ar dating produced concordant results, with the remainder exhibiting varying degrees of discordance. The underlying causes of this discordance and implications for accurate age determinations are examined and modelled in age spectra and inverse isochron space. A correlation is found between the proportion

of radiogenic ^{40}Ar (^{40}Ar*) released and the nature of discordance exhibited by a sample. ^{39}Ar recoil is suggested as the most likely cause of discordance in high-^{40}Ar* samples, whereas low-^{40}Ar* samples exhibit discordance consistent with the modelled effects of mass-dependent fractionation.

Based on modelling results, isochron rotation is the main impact of isotopic disturbance on an inverse isochron plot (^{39}Ar/^{40}Ar vs ^{36}Ar/^{40}Ar), leading to a negative correlation between ^{40}Ar/^{39}Ar ages and $(^{40}\mathrm{Ar}/^{36}\mathrm{Ar})_{i}$ values. A new framework for the treatment of ^{40}Ar/^{39}Ar data from basaltic rocks is submitted, optimising the interpretation of inverse isochrons and informing the allocation of age constraints. Finally, a new method of ^{40}Ar/^{39}Ar data treatment, here named the multi-isochron approach to ^{40}Ar/^{39}Ar dating, is introduced. A multi-isochron regression utilises the combined output of all possible inverse isochrons from data of a single aliquant to determine its ideal isochron and eruption age. This method has the potential of transforming ^{40}Ar/^{39}Ar data treatment, allowing eruption ages to be calculated even when isotopic disturbance is severe, and to be reported in cases where this was previously not possible.

Declarations

I, Michael Heath, hereby declare that:

i) The thesis comprises only my original work towards the degree of Doctor of Philosophy – Science, except where indicated in the preface;

ii) Due acknowledgement has been made in the text to all other material used; and

iii) The thesis word count is below the maximum word limit, exclusive of tables, maps, bibliographies and appendices.

x

Michael Heath

Preface

The work submitted as part of this thesis has not been submitted for any other qualification and was not undertaken prior to commencement of this degree. No external editorial assistance was provided in the completion of this thesis. This thesis includes published material, completed in collaboration with other scientists.

Chapters 1 – 4 are composed of unpublished material not submitted for publication and are the sole work of the author of this thesis.

Chapter 5 was published online in *Earth and Planetary Science Letters* on September 28th 2018:

Heath, M., Phillips, D., & Matchan, E. L. (2018). An evidence-based approach to accurate interpretation of ^{40}Ar/^{39}Ar ages from basaltic rocks. *Earth and Planetary Science Letters*, *498*, 65-76.

My PhD co-supervisors at University of Melbourne (Prof. David Phillips and Dr. Erin Matchan) were co-authors on the paper. Their contributions were typical of those expected from PhD supervisors (i.e. financial support, data interpretation and comments on written work). The remainder of the work for the paper was conducted by the author of this thesis.

The author accepted manuscript is presented in this thesis.

Chapter 6 is work currently submitted for publication in Journal of Volcanology and Geothermal Research.

My PhD co-supervisors at University of Melbourne (Prof. David Phillips and Dr. Erin Matchan) were co-authors on the paper. Their contributions were typical of those expected from PhD supervisors (i.e. financial support, data interpretation and comments on written work). The remainder of the work for the paper was conducted by the author of this thesis.

The submitted manuscript is included in this thesis.

Chapters 7 – 9 are composed of unpublished material not submitted for publication and are the sole work of the author of this thesis.

This work was made possible due to financial support provided by the Australian Postgraduate Award – 2015, Research Training Program Scholarship – 2017 and an Australian Research Council grant (DP130100517) to David Phillips.

Acknowledgements

All $^{40}Ar/^{39}Ar$ dating work was undertaken with the help of Stan Szczepanski. Graham Hutchinson supervised Scanning Electron Microscopy and Energy Dispersive Spectrometry for element mapping. Sample preparation and analysis for Inductively Coupled Plasma Mass Spectrometry was completed under the guidance and with the assistance of Dr Alan Greig. Prof. Jon Woodhead provided training for X-Ray Fluorescence work.

I am extremely grateful to the Geological Survey of Victoria for allowing access to hundreds of drill core samples and petrographic thin sections. I would also like to thank GHD, Golder Associates and Melbourne Museum for providing samples.

I would like to thank my co-supervisors, Prof. David Phillips and Dr. Erin Matchan, for their feedback and support over the six years I have been their student. I would also like to acknowledge (thank would be taking it a bit far) my fellow PhD and Masters students for their friendship and support over the journey. Angus and Hayden – thank you for the conversations, warm milk and unethically acquired medium cappuccinos. Ashton – thank you for putting up with my in-office bicycle, and for your constructive feedback whenever I have asked it of you.

Finally, and incomparably (sorry, not sorry), I would like to thank my beautiful, caring, supportive, courageous and loving wife, Jungyung. Thank you for your sacrifices and compromises. Thank you for always being proud of me. Thank you for giving me a reason to continue, and for never giving up. I am truly grateful for everything you have endured to carry me this far.

Table of Contents

Title page 1

Abstract 2

Author's declaration 5

Preface 6

Acknowledgements 8

Table of contents 9

List of figures 14

List of tables 18

List of all third-party copyright material included in this thesis 20

Chapter 1) Introduction, aims and approach 21

- 1.1 Introduction 21
- 1.2 Aims 26
- 1.3 Approach 27

Chapter 2) Previous work on the Newer Volcanic Province 29

- 2.1 Geomorphology and volcanology 29
- 2.2 Geochemistry 31
- 2.3 Geochronology 35
    - 2.3.1 K-Ar dating studies 36
    - 2.3.2 Previous $^{40}Ar/^{39}Ar$ studies 38
- 2.4 The cause(s) of NVP volcanism 41
- 2.5 NVP activity in the Melbourne area 43

Chapter 3) Sample collection and preparation 50

- 3.1 Sample collection 50
- 3.2 Sample preparation 54
    - 3.2.1 Petrography and scanning electron microscopy 54
    - 3.2.2 X-ray fluorescence (XRF) major element analysis 54
    - 3.2.3 Inductively coupled plasma mass spectrometry (ICP-MS) 54
    - 3.2.4 $^{40}Ar/^{39}Ar$ dating 54

Chapter 4) Analytical Methods 56

- 4.1 Lava flow mapping 56
    - 4.1.1 Petrography 56
    - 4.1.2 Major element geochemistry 56

4.1.2.1 Analytical methods for XRF 57

4.1.3 Trace element geochemistry 57

4.1.3.1 Analytical methods for ICP-MS 60

4.2 ^{40}Ar/^{39}Ar dating of basaltic rocks 61

4.2.1 The K-Ar decay scheme 61

4.2.2 The K-Ar dating method 62

4.2.3 The correction for atmospheric argon 63

4.2.4 Disadvantages of the K-Ar method 63

4.2.5 ^{40}Ar/^{39}Ar dating 65

4.2.5.1 Theory behind the ^{40}Ar/^{39}Ar method 65

4.2.5.2 Benefits of the ^{40}Ar/^{39}Ar dating method 66

4.2.5.2.1 Step-heating spectra 66

4.2.5.2.1.1 Plateau ages 67

4.2.5.2.1.2 Common types of age spectra 69

4.2.5.2.2 Inverse isochron diagrams 70

4.2.5.3 Complications of the ^{40}Ar/^{39}Ar dating method 72

4.2.5.3.1 ^{39}Ar and ^{37}Ar recoil 73

4.2.5.3.2 Interference reactions 74

4.2.5.3.3 Mass-dependent fractionation 74

4.2.6 Applicability to this project 74

4.2.7 ^{40}Ar/^{39}Ar analytical methods 75

4.3 Analytical methods for scanning electron microscopy 77

Chapter 5) An evidence-based approach to accurate interpretation of ^{40}Ar/^{39}Ar ages from basaltic rocks 78

Abstract 78

5.1 Introduction 79

5.2 Sample locations 82

5.3 Methods 84

5.3.1 Sample preparation 84

5.3.2 ^{40}Ar/^{39}Ar analyses 85

5.3.3 XRF major element geochemistry 87

5.4 Results 87

5.4.1 Petrography and major element geochemistry 87

5.4.2 ^{40}Ar/^{39}Ar results 90

5.4.2.1 Flow A 90

5.4.2.2 Flow B 92
5.4.3 Results from step-heating study of unirradiated sample MH70 96
5.5 Discussion 97
5.5.1 Timing of eruption events 97
5.5.1.1 Flow A 97
5.5.1.2 Flow B 98
5.5.2 Possible causes of discordant ^{40}Ar/^{39}Ar spectra 98
5.5.3 Insights from inverse isochron diagrams 102
5.5.4 Modelling possible causes of argon isotopic disturbance 103
5.5.4.1 Modelling results 104
5.5.5 Causes of ^{40}Ar*/^{39}Ar discordance for flows A and B 107
5.5.6 Total-gas ages 108
5.5.7 Interpretation of ^{40}Ar/^{39}Ar data for basaltic samples 110
5.6 Conclusions 111
5.7 Addendum: The cause of low ^{40}Ar* content in basaltic samples 112
Chapter 6) Basalt lava flows of the intraplate Newer Volcanic Province in south-east Australia (Melbourne region): ^{40}Ar/^{39}Ar geochronology reveals ~8 Ma of episodic activity 116
Abstract 116
6.1 Introduction 118
6.2 Geology of the Newer Volcanic Province (NVP) 119
6.2.1 NVP volcanism in the Melbourne area 123
6.3 Methods 125
6.3.1 Sample selection 125
6.3.2 Sample preparation 128
6.3.3 ^{40}Ar/^{39}Ar analyses 128
6.4 Results 129
6.4.1 Lava flow mapping 129
6.4.2 Major element geochemistry 134
6.4.3 ^{40}Ar/^{39}Ar dating results 138
6.5 Discussion 150
6.5.1 Interpretation of ^{40}Ar/^{39}Ar results 150
6.5.2 Lava flow map of the Melbourne area 154
6.5.3 Eruption chronology of the Melbourne area 154
6.5.4 A comparison with previous mapping and geochronology 158

6.5.5 Older eruption centres of the Melbourne area 159
6.5.6 Volcanic evolution of the NVP 161
6.6 Conclusions 162
Chapter 7) Trace element geochemistry of Melbourne basalt 164
7.1 Trace element geochemistry results 164
7.2 Lava flow mapping by trace elements: Mount Fraser vs Tulloch Hill 168
7.3 Mount Fraser magma mixing 170
7.3.1 Background 170
7.3.2 Mount Fraser flow units 170
Chapter 8) A preliminary multi-isochron model for constraining basalt ages from 'disturbed' ^{40}Ar/^{39}Ar results 178
8.1 Background 178
8.2 The multi-isochron regression 178
8.3 Preliminary results and discussion 183
Chapter 9) Conclusions 186
9.1 Addressing the aims of this study 186
9.2 Recommendations for future work 190
References 192
Appendix A.1: Flow A and Flow B micrographs, ^{40}Ar/^{39}Ar spectra and isochrons 203
Appendix A.2: Micrographs, ^{40}Ar/^{39}Ar spectra and isochrons of all other flows 246
Appendix A.3: ^{40}Ar/^{39}Ar data for Mount Fraser Flow samples 280
Appendix A.4: ^{40}Ar/^{39}Ar data for Tulloch Hill Flow samples 292
Appendix A.5: ^{40}Ar/^{39}Ar data for Aitken Hill Flow samples 300
Appendix A.6: ^{40}Ar/^{39}Ar data for Bald Hill Flow samples 301
Appendix A.7: ^{40}Ar/^{39}Ar data for Crowe Hill Flow samples 303
Appendix A.8: ^{40}Ar/^{39}Ar data for Fenton Hill Flow samples 305
Appendix A.9: ^{40}Ar/^{39}Ar data for Mount Kororoit Flow samples 306
Appendix A.10: ^{40}Ar/^{39}Ar data for Mount Ridley Flow samples 313
Appendix A.11: ^{40}Ar/^{39}Ar data for Redstone Hill Flow samples 315
Appendix A.12: ^{40}Ar/^{39}Ar data for Springs Hill Flow samples 317
Appendix A.13: ^{40}Ar/^{39}Ar data for Summerhill Rd Flow samples 319
Appendix A.14: ^{40}Ar/^{39}Ar data for Tullamarine Flow samples 321
Appendix A.15: ^{40}Ar/^{39}Ar data for unirradiated sample MH70 322

Appendix A.16: Major element results for Chapter 5 ^{40}Ar/^{39}Ar samples 323

Appendix A.17: Chapter 5 modelling details 324

Appendix A.18: Major element results for all samples 327

Appendix A.19: ^{40}Ar/^{39}Ar analytical details for Chapter 6 330

Appendix A.20: ICP-MS trace element concentrations for selected samples 331

Appendix A.21: Irradiation Dates 332

List of figures

Chapter 1

Figure 1.1: Eruption points and erupted products of the NVP in Victoria and South Australia.

Chapter 2

Figure 2.1: The ages and characteristics of the regolith landform units of the NVP.

Figure 2.2: The $^{87}Sr/^{86}Sr$ domains of Gray and McDougall (2009).

Figure 2.3: Total alkalis vs silica of Melbourne basalt - literature values.

Figure 2.4: Eruption centres proposed as being the sources of Melbourne basalt.

Figure 2.5: K-Ar and $^{40}Ar/^{39}Ar$ ages from previous work within the Melbourne area.

Chapter 3

Figure 3.1: Sample locations across the Melbourne area.

Figure 3.2: Field samples collected from road cuttings, disused quarries and natural cliffs.

Figure 3.3: Samples collected from eruption points.

Figure 3.4: Borehole samples.

Chapter 4

Figure 4.1: The dual decay of ^{40}K.

Figure 4.2: Common patterns in age spectra.

Figure 4.3: The inverse isochron diagram.

Chapter 5

Figure 5.1: Location of the Newer Volcanic Province in southeast Australia and lava flows A and B in the Melbourne area.

Figure 5.2: Plane-polarised images of samples YY3C, MH70, MH52 and MH69.

Figure 5.3: Total alkalis versus silica diagram for ^{40}Ar/^{39}Ar samples.

Figure 5.4: Age spectra and inverse isochron results for Flow A and B samples.

Figure 5.5. ^{38}Ar/^{36}Ar step-heating results of an unirradiated sample.

Figure 5.6: Modelled step-heating spectrum and inverse isochrons for a ^{39}Ar recoil-affected sample.

Figure 5.7: Modelled ^{40}Ar* loss and mass fractionation effects shown for a low-^{40}Ar* sample.

Figure 5.8: Plane-polarised images of samples MH69, MH75C, BH269 and MH24.

Figure 5.9. Back-scattered electron SEM images, K elemental maps and Ca-Fe composite elemental maps of samples YY6, MO43B, MH70 and MH66.

Chapter 6

Figure 6.1: The extent of the NVP in Victoria and South Australia.

Figure 6.2: Schematic representation of the edge-driven convection model applied to south eastern Australia

Figure 6.3: Initial ^{87}Sr/^{86}Sr domains, K-Ar ages and eruption chronology from previous work within the study area.

Figure 6.4: Field and borehole sample locations.

Figure 6.5: Sample locations distant and proximal to their source.

Figure 6.6: Plane-polarised and cross-polarised photomicrographs of samples from two flows with internally consistent petrographic features.

Figure 6.7: NVP lava flow map and ^{40}Ar/^{39}Ar geochronology of the Melbourne area.

Figure 6.8: XRF major element geochemistry of samples from NVP lava flows in the Melbourne area.

Figure 6.9: ^{40}Ar/^{39}Ar results for Springs Hill and Bald Hill flow samples.

Figure 6.10: ^{40}Ar/^{39}Ar results for Tullamarine and Fenton Hill flow samples

Figure 6.11: ^{40}Ar/^{39}Ar results for Redstone Hill and Mount Kororoit flow samples.

Figure 6.12: Representative ^{40}Ar/^{39}Ar results for aliquants of the Aitken Hill, Crowe Hill, Mount Ridley and Summerhill Road flows.

Chapter 7

Figure 7.1: REE patterns of selected samples normalised to C1 chondrite.

Figure 7.2: Mount Fraser A vs Tulluch Hill A trace elements.

Figure 7.3: Plane-polarised and cross-polarised photomicrographs of typical samples from the Mount Kororoit Flow.

Figure 7.4: Satellite image showing the areal extent of the three flow units erupted from Mount Fraser and plane-polarised images of samples from each flow unit.

Figure 7.5: Geochemical evolution of the Mount Fraser Flow.

Chapter 8

Figure 8.1: Schematic illustration of the effects of clockwise and anti-clockwise isochron rotation.

Figure 8.2: Inverse isochron results for aliquots of the Mount Fraser lava flow.

Figure 8.3: Schematic illustration of a multi-isochron regression using modelled data.

Figure 8.4: Age spectra and basic multi-isochron regressions for aliquants MH70-1 and KA13B-1.

List of tables

Chapter 2

Table 2.1: Summary of previous K-Ar work on NVP basalts.

Table 2.2: Initial ^{87}Sr/^{86}Sr zones of the Melbourne area.

Chapter 4

Table 4.1: Zr abundances in samples from three different batches of magma from Mount Rouse.

Chapter 5

Table 5.1. ^{40}Ar/^{39}Ar results for two concordant samples from Flow A.

Table 5.2. Summary of ^{40}Ar/^{39}Ar inverse isochron results for Flow A and B samples.

Table 5.3. Summary of preferred isochron ages and (^{40}Ar/^{36}Ar)$_i$ values for high ^{40}Ar* samples from Flow B.

Chapter 6

Table 6.1: Diagnostic features of each flow and flow unit.

Table 6.2: Preferred ^{40}Ar/^{39}Ar age constraints, radiogenic argon content and inferred dominant cause of isotopic disturbance in groundmass and anorthoclase samples.

Chapter 7

Table 7.1: Average major and trace element abundance for each of the lava flows of the Melbourne area.

List of all third-party copyright material included in this thesis

Chapter 5 was published online in *Earth and Planetary Science Letters* on 28/09/2018. Due to their "Green Open Access policy", it has only been possible to reproduce the author accepted manuscript version in this thesis.

Chapter 1) Introduction, aims and approach

1.1 Introduction

The Newer Volcanic Province (NVP) is located on the southern margin of continental Australia, between Melbourne in the east and Mount Gambier to the west (**Fig. 1.1**). It comprises over 416 eruption centres (Boyce, 2013), with volcanic products covering an area of approximately 23,000 km^2 (van den Hove et al., 2017b). The NVP is the most recent expression of volcanic activity in south-eastern Australia (Wellman and McDougall, 1974), and on the basis of existing K-Ar age constraints, began forming at least 4.6 million years ago (Gray and McDougall, 2009).

Three distinct regions are generally recognised within the NVP, referred to as the Central Highlands (sometimes Central Uplands), Western Plains, and Mount Gambier sub-provinces (**Fig. 1.1**; e.g., Joyce, 2004). The Central Highlands and Western Plains are located adjacent to one another in Victoria, and the Mount Gambier sub-province is located in South Australia, approximately 50 km from the western margin of the Western Plains. The three sub-provinces are distinguished by the nature and volume of volcanic products they are associated with, as well as their underlying lithologies and geographical locations (Joyce, 1975; Price et al., 1997; Joyce, 1999; McBride et al., 2001; Price et al., 2003; Joyce, 2004; Hare and Cas, 2005; Paul et al., 2005; Demidjuk et al., 2007; Gray and McDougall, 2009; Matchan and Phillips, 2011; Boyce, 2013; Boyce et al., 2015; Oostingh et al., 2016).

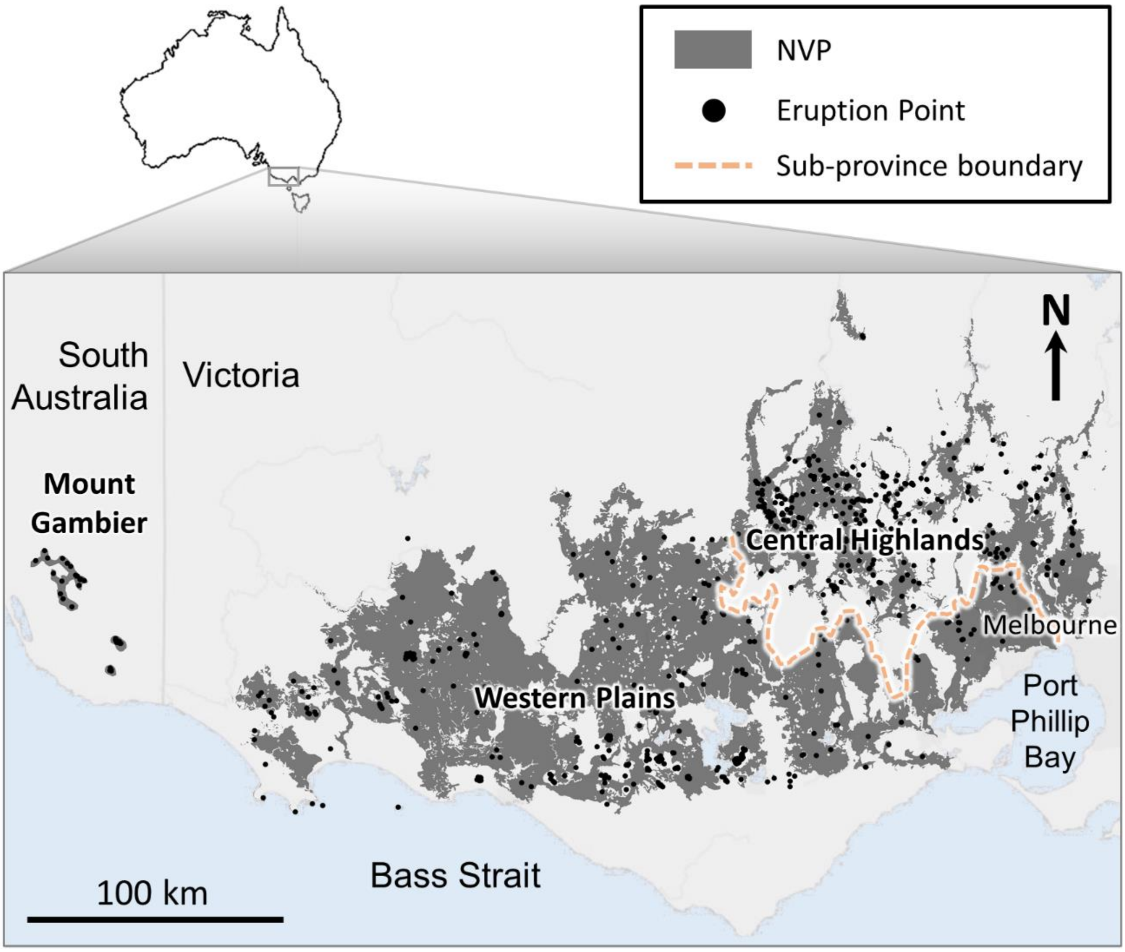

Figure 1.1: Eruption points and erupted products of the NVP in Victoria and South Australia. The Western Plains and Central Highlands sub-provinces are located adjacent to one another in southern Victoria, whereas the Mount Gambier sub-province is in South Australia.

The NVP overlies Paleozoic metasedimentary sequences and intrusive rocks in the Central Highlands, and Late Cretaceous to Holocene basin sediments in the Western Plains and Mount Gambier sub-provinces (e.g., Lesti et al., 2008). The Central Highlands sub-province has its eastern margin in line with the city of Melbourne (**Fig. 1.1**). It extends northwards almost 150 km from Melbourne, and east across the Paleozoic meta-sediments of the Lachlan fold belt. The greatest concentration of eruption points exists in this sub-province, with over 250 recognised (Boyce, 2013). The Western Plains sub-province begins on the western bank of the Maribyrnong River, in western Melbourne, and extends over 300 km to the west, overlying the Jurassic to Cenozoic sediments of the Otway Basin (e.g., Price et al., 1997). The Western Plains sub-province covers the largest area of the three sub-provinces and contains a wide variety of different types of eruption points. The Mount Gambier sub-province comprises over 40 eruption points (e.g., Boyce, 2013), distributed over a relatively small area (Fig 1.1).

A range of volcanic products, including lava, ash and scoria, have been recognised across the NVP. Lavas are the most volumetrically important product, with compositions ranging from basaltic icelandite to tholeiite (Price et al., 2003). These lavas, largely the product of low-profile lava shields, commonly flowed along river valleys and down sloping plains before crystallising and forming the basalt that covers much of southern and western Victoria. In the Mount Gambier and Western Plains sub-provinces, and less commonly in the Central Uplands, complex volcanic centres produced relatively small volumes of ash and scoria in the formation of maars and cones (Cas et al., 2017).

The Central Highlands sub-province is characterised by low-profile lava shields that produced long flows, filling paleovalleys and covering basement rocks with thicknesses typically exceeding 100m (Joyce, 2004). A number of scoria cones and rare maars and tuff rings also produced small volumes of scoria and ash (Lesti et al., 2008). In the Western Plains and Mount Gambier sub-provinces, complex volcanic centres and phreatomagmatic eruptive products are more common (Cas et al., 2017). Similar to the Central Highlands, long lava flows are common in the Western Plains, dominating much of the modern-day surface. In the Mount Gambier sub-province lava flows are rare and cover a much smaller area (Joyce, 2004).

The mechanism(s) behind the formation of the NVP has been the subject of extensive debate, and several competing theories have been put forward by various authors over the years (e.g., Wellman and McDougall, 1974; Lesti et al., 2008; Davies et al., 2015). Some of the earliest work invoked an asthenospheric hot spot migrating southwards along Australia's east coast as the continent was propelled northwards by rifting in the Southern Ocean (Wellman, 1983). It is evident, however, that the classic hotspot model has shortcomings with respect to the age range of NVP activity and its dispersion in an E-W direction, orthogonal to expected plate motion (Price et al., 1997). Most recently, edge-driven convection (EDC) has been suggested as the underlying cause of NVP volcanism, involving the formation of a convective cell due to a topographic step in the base of the lithosphere (Demidjuk et al., 2007; Davies and Rawlinson, 2014; Davies et al., 2015; Rawlinson et al., 2016; Cas et al., 2017). Reconstructions of the position of the east Australian ('Cosgrove Track') hotspot now suggest that it was likely to have been located under Victoria immediately before the beginning of NVP activity (Davies et al., 2015). As speculated by Davies et al. (2015), entrainment of this mantle plume in the edge-driven convective cell could explain the initiation of volcanism at ~5 Ma.

Elucidating the underlying controls on magma supply and the timing of eruptions has been a focus of several recent studies. A tectonic control on volcanism has been inferred from the spatial arrangement of eruption points (Lesti et al., 2008; van den Hove et al., 2017a) and the volume of erupted products (Cas et al., 2017; van den Hove et al., 2017b). However, it is difficult to reconcile such an interpretation with evidence for the southeast

Australian lithosphere having been under compression since at least 5 Ma (e.g., Sandiford et al., 2004).

A concise magmatic model for volcanism within the NVP requires a detailed understanding of both the age and nature of erupted products. Despite extensive work constraining the age of NVP volcanism (McDougall et al., 1966; Aziz-ur-Rahman and McDougall, 1972; Bowen, 1975; McDougall and Gill, 1975; Ollier, 1985; Edwards, 2004; Hare et al., 2005; Baker, 2008; Gray and McDougall, 2009; Ismail, 2010; Matchan and Phillips, 2011; Matchan, 2012; Traine, 2012; Ismail et al., 2013; Chang, 2014; Heath, 2014; Matchan and Phillips, 2014; Matchan et al., 2016; Che, 2017; Oostingh et al., 2017; Matchan et al., 2018), only 26 eruption centres have been dated from a total of at least 416 centres (Boyce, 2013), and only a minute proportion of the NVP has been geochronologically mapped in any detail (Hare et al., 2005; Boyce et al., 2014b; Matchan et al., 2016).

The Melbourne area records a long and complex volcanic history, with an age range rivalling that of the entire NVP (~4.6 to ~0.8 Ma; McDougall et al., 1966; Gray and McDougall, 2009; Ismail et al., 2013; Heath, 2014). The area also hosts a chemically diverse spectrum of lava flows, ranging from basanite to basaltic andesite (see **Fig. 2.3**; Edwards, 1938; Mitchell, 1990; Gray and McDougall, 2009) and intricate flow geometries (Hanks, 1955; Stewart, 1975; Stewart, 1977; Croker, 1984), making it an ideal microcosm for studying the evolution of the entire NVP, and evaluating the effectiveness of a holistic approach to volcanic chronology.

The ^{40}Ar/^{39}Ar dating technique is uniquely suited to producing robust age constraints for basaltic eruption events (e.g., Renne et al., 1992; Lanphere, 2000; Baksi, 2014; Singer et al., 2014) and its applicability to NVP basalts has been confirmed in several recent studies (e.g., Hare et al., 2005; Matchan and Phillips, 2011; Matchan and Phillips, 2014; Oostingh et al., 2017). With the advent of multi-collector mass spectrometry and the refinement of sample preparation procedures, ^{40}Ar/^{39}Ar dating is capable of obtaining precise and accurate results across almost the entire age range of the NVP (e.g., Matchan and Phillips, 2014). However, with this increased precision, subtle disturbances to argon isotope ratios are now resolvable, such that perfectly concordant ^{40}Ar/^{39}Ar analyses from basaltic rocks are rare (e.g., Chang, 2014; Heath, 2014; Che, 2017; Oostingh et al., 2017). The causes of discordance, however, remain poorly understood, and there are no succinct guidelines for the interpretation of disturbed ^{40}Ar/^{39}Ar data. This shortfall must be addressed in order improve the utility of such ^{40}Ar/^{39}Ar data, so that the maximum information can be extracted, even where discordance is resolvable.

1.2 Aims

Although the young lava flows of the Melbourne area have not been entirely overlooked by previous studies (e.g., Hanks, 1955; Stewart, 1975; Croker, 1984; Price et al., 1988; Gray and McDougall, 2009) the volcanic history of the area remains poorly understood. Lava flow mapping has been attempted using geomorphology, land systems approaches, borehole stratigraphy and ^{87}Sr/^{86}Sr isotopic domains, but no two studies have produced results consistent with one another. Geochronological work has focused on surface samples, and although basalt from 51 locations has been assigned age constraints, the context of these ages in relation to eruption events remains unknown. Multi-collector mass spectrometry is producing ever-increasing precision in ^{40}Ar/^{39}Ar ages for basaltic rocks. However, this increased resolution in ^{40}Ar/^{39}Ar spectra means that even small disturbances in isotopic ratios lead to discordant results. The aims of this study were as follows:

1) To map the NVP lava flows of the Melbourne area based on geomorphology, petrography and geochemistry, and determine which of these characteristics are the most useful discriminators.
2) To constrain the ages and defining characteristics of each lava flow within the Melbourne area.
3) To investigate the common causes of disturbance in ^{40}Ar/^{39}Ar data from basaltic samples and determine how each of their effects can be recognised.
4) To improve upon data treatment methods and the calculation of robust age constraints from disturbed ^{40}Ar/^{39}Ar data.

1.3 Approach

In order to address the aims of this study, the following approach was undertaken:

1) The generation of a detailed lava flow map of the Melbourne area was supported by high-resolution sampling of basalt from across the Melbourne area, both at the surface and underground. Petrographic sections of 388 field and borehole samples were created, and an additional 283 sections were provided by the Geological Survey of Victoria. A total of 140 samples were selected for major element analysis by x-ray fluorescence and 27 of these were selected for trace element analysis by inductively coupled plasma mass spectrometry.

2) A lava flow map of the Melbourne area was generated based on petrographic and geochemical markers characteristic of each flow, while ensuring an adherence to geomorphological and stratigraphic considerations.
3) An eruption chronology for the Melbourne area was constructed by placing new $^{40}Ar/^{39}Ar$ age constraints on 12 lava flows.
4) By comparing disturbed $^{40}Ar/^{39}Ar$ data with concordant $^{40}Ar/^{39}Ar$ data for samples of the same flow, the common causes of disturbance were investigated and an evidence-based approach to obtaining accurate $^{40}Ar/^{39}Ar$ ages of basaltic rocks put forward. This new approach utilises inverse isochron analysis to inform the objective allocation of age constraints, circumventing the need for assumptions around the causes of extraneous argon or argon loss.

Chapter 2) Previous work on the Newer Volcanic Province

Previous work within the NVP has included geomorphological (Skeats and James, 1937; Hanks, 1955; Joyce, 1999; Sutalo and Joyce, 2004), geochemical (Frey and Green, 1974; Frey et al., 1978; Price et al., 1991; Price et al., 1997; McBride et al., 2001; Boyce et al., 2015; Oostingh et al., 2016) and geochronological (McDougall et al., 1966; Aziz-ur-Rahman and McDougall, 1972; Gray and McDougall, 2009; Matchan and Phillips, 2011; Matchan and Phillips, 2014; Matchan et al., 2016; Oostingh et al., 2017; Matchan et al., 2018) studies on various eruptive products. Other studies have focused on geophysical interpretation of subsurface structures (Graeber et al., 2002; Bishop, 2007; Ford et al., 2010; Rawlinson and Fishwick, 2012; Davies and Rawlinson, 2014) and volcanological investigations of individual eruption centres (van Otterloo et al., 2014; Blaikie et al., 2015; Jordan et al., 2015). Previous investigations have used the above information to understand the triggers of volcanism in the NVP and the underlying processes behind magma generation (Frey et al., 1978; Price et al., 1997; Demidjuk et al., 2007; Davies and Rawlinson, 2014) with several competing models proposed for the genesis of the NVP and the controls on continuing volcanism (Sutherland, 1981; McBride et al., 2001; Price et al., 2003; Demidjuk et al., 2007; Lesti et al., 2008; Davies and Rawlinson, 2014; Cas et al., 2017; Oostingh et al., 2017).

2.1 Geomorphology and Volcanology

Geomorphology was employed by early workers to provide an understanding of volcanic landforms and eruption centres (Hart, 1894; Hall, 1908; Skeats and James, 1937; Hanks, 1955), and continues to be an important tool in the mapping of individual flows, constraining the relative ages of lavas, and delineating individual eruption points (Sutalo and Joyce, 2004; Boyce et al., 2014b; Matchan et al., 2016). An important concept introduced by Jackson et al. (1972) and built upon by Joyce (1983) was the implementation of ‘land systems’ to regolith landform units in the NVP (**Fig. 2.1**). This approach utilised differences in the chemistry, colour and texture of overlying soil to estimate the age of underlying lava flows. This ‘land systems’ approach has been employed in subsequent flow mapping studies to delineate flows and estimate approximate eruption ages (Croker, 1984; Ollier, 1985; Matchan et al., 2016).

Volcanological and geophysical work on individual eruption centres of the NVP has revealed a wide range of volcanic facies, including ash-lapilli, scoria and phreatomagmatic base-surge deposits, along with common lava flows. Individual centres are often geomorphologically complex, formed over numerous eruption sequences. Recent contributions have focused on eruption volumes (van Otterloo and Cas, 2013; Blaikie et al., 2015), mechanisms behind diatreme formation (Jordan, 2013; Blaikie et al., 2014) and the geochemical and morphological evolution of erupted products (van Otterloo et al., 2013; Jordan et al., 2015). Such studies have revealed that despite their purported monogenetic nature, eruption centres of the NVP are generally not formed in a single event, but by numerous eruptions over a short time span (e.g., van Otterloo et al., 2013), reflecting evolving interactions between upwelling basaltic magma, crust and hydrosphere (Cas et al., 2017). These studies indicate that eruption styles are controlled by numerous factors, including magma ascent rate, magma chemistry and groundwater availability (van Otterloo and Cas, 2013; Jordan et al., 2015; Cas et al., 2017).

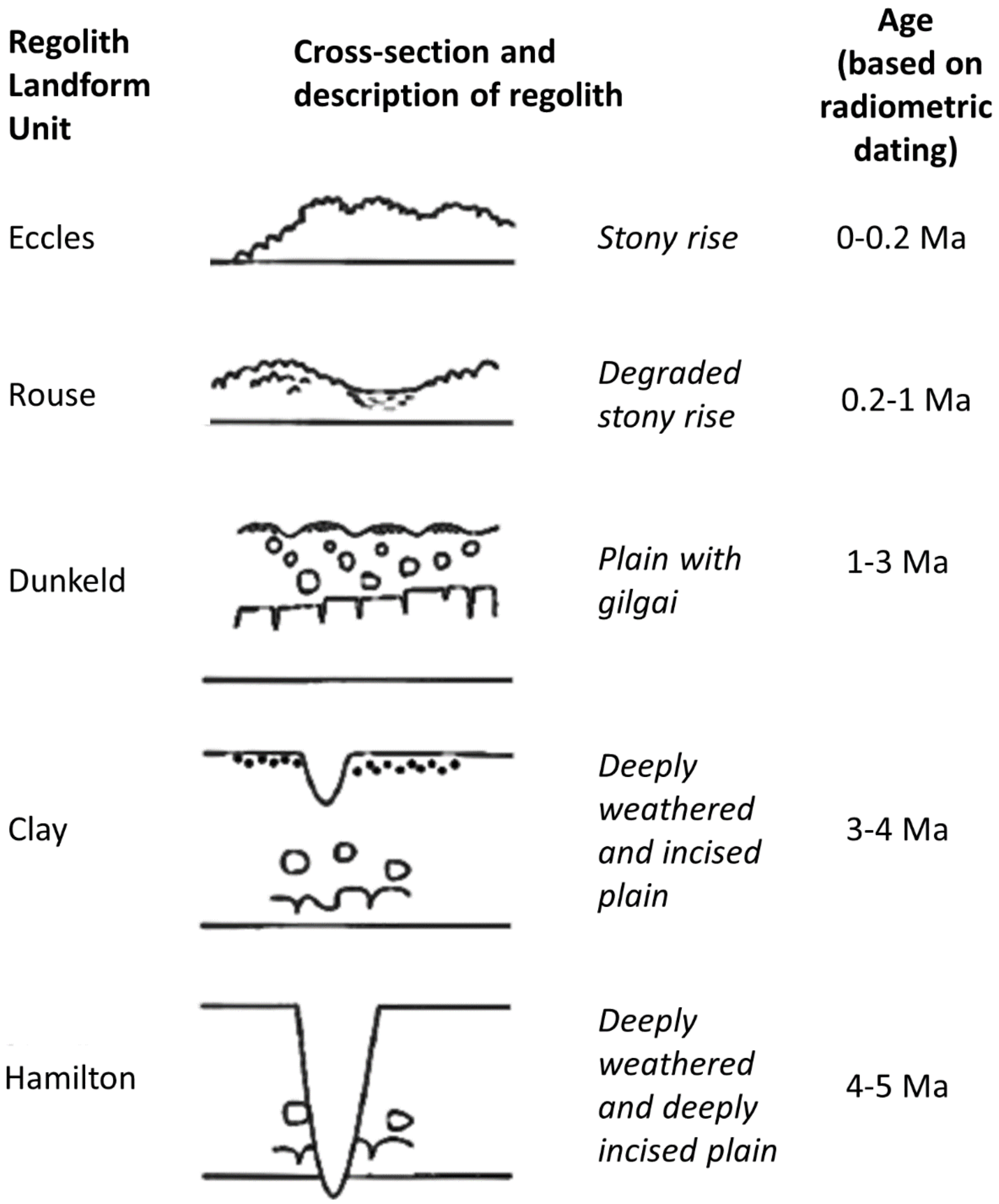

Regolith Landform Unit	Cross-section and description of regolith	Age (based on radiometric dating)
Eccles	*Stony rise*	0-0.2 Ma
Rouse	*Degraded stony rise*	0.2-1 Ma
Dunkeld	*Plain with gilgai*	1-3 Ma
Clay	*Deeply weathered and incised plain*	3-4 Ma
Hamilton	*Deeply weathered and deeply incised plain*	4-5 Ma

Figure 2.1: The ages and characteristics of the regolith landform units of the NVP (modified from Joyce, 1999).

2.2 Geochemistry

Early geochemical studies focused on major element compositions and rock type classifications, providing a broad understanding of the nature of NVP products (e.g., Edwards, 1938; Bahat, 1967; Irving and Green, 1976). Several early studies investigated individual volcanic centres (e.g., Ferguson, 1971; Elias, 1973; Evans, 1980; Nosiara, 1981; Tunjc, 1988), commonly finding them to have formed by the eruption of several geochemically distinct batches of melt, challenging the supposedly monogenetic nature of volcanism. Other work was at a larger scale, investigating the regional and province-wide geochemistry of NVP products (e.g., Bahat, 1967; O'Hanlon, 1975; Gawith, 1977; Evans, 1980; Murphy, 1983). Edwards (1938) conducted major element analysis of more than 50 samples from across the NVP. In conjunction with petrography, major element concentrations were used to classify volcanic products into different rock types, and investigate any observable chemical trends across the province. The classification scheme utilised by Edwards divided NVP samples into 13 groupings, from the most basic ("limburgites") to the most acidic ("sölvsbergites") and suggested a progression from more acidic to basic compositions over time in various localities. In another province-wide study, Irving and Green (1976) analysed the major element contents of around 100 samples from the NVP and concluded that although different magma types appear to be spatially restricted, there is no discernible geochemical progression with time.

Later studies incorporated trace element geochemistry and isotope ratio systematics (e.g., ^{87}Sr/^{86}Sr; ^{143}Nd/^{144}Nd) to investigate a range of issues including temporal changes in geochemistry, the underlying cause of NVP volcanism, the evolution of the sub-continental lithosphere, source composition, and the effects of alteration on basalt geochemistry (Frey et al., 1978; McDonough et al., 1985; Price et al., 1988; Price et al., 1991; Price et al., 1997; Vogel and Keays, 1997; Yaxley et al., 1998; McBride et al., 2001; Demidjuk et al., 2007; van Otterloo et al., 2014; Boyce et al., 2015; Oostingh et al., 2016). An extensive study begun by Price et al. (1988) and continued by later workers (Price et al., 1997; Price et al., 2003; Gray and McDougall, 2009), generated initial ^{87}Sr/^{86}Sr

($^{87}Sr/^{86}Sr)_i$ ratios for a large number of samples from across the Central Highlands and Western Plains sub-provinces in an attempt to distinguish individual flows and lava packages. Price et al. (1997) analysed ($^{87}Sr/^{86}Sr)_i$ ratio systematics, along with major and trace elements, for nearly 500 samples taken from what was defined as the 'Plains' sub-province of the NVP (essentially the area south of the Great Dividing Range between Melbourne and Portland). In a continuation of the ($^{87}Sr/^{86}Sr)_i$ work undertaken by Price et al. (1988), this study divided the NVP into 29 domains, intended to represent individual flows and groups of flows, based on strontium isotopic signature, major element geochemistry, flow mapping and any age data that was available (**Fig. 2.2**). A difference in $^{87}Sr/^{86}Sr$ ratios for areas to the east (0.7037 - 0.7058) and to the west (0.7037 - 0.7046) of the town of Mortlake was attributed to heterogeneity in basement lithologies and underlying lithosphere across an inferred boundary termed the 'Mortlake discontinuity' (**Fig 2.2**). Further work by Gray and McDougall (2009), using the same ($^{87}Sr/^{86}Sr)_i$ data, included further K-Ar dating work (see **section 2.3.1**) and highlighted a decrease in ($^{87}Sr/^{86}Sr)_i$ ratios over time, matched by an apparent progression from tholeiitic to alkalic type eruptions. This has led to a separation in much of the literature between an older 'plains' series and younger 'cones' series of NVP products. This proposed progression from predominantly tholeiitic to alkalic lavas over time has found support in subsequent dating work (Oostingh et al., 2017).

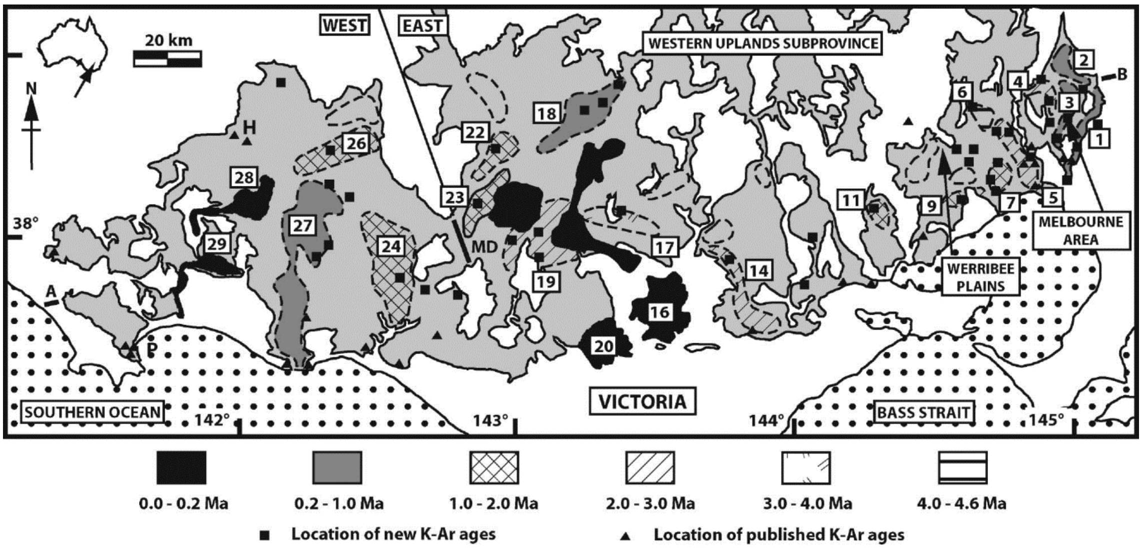

Figure 2.2: The 29 ^{87}Sr/^{86}Sr domains of Gray and McDougall (2009), adapted from Price et al. (1988) and Price et al. (1997), and intended to represent individual flows or groups of flows. MD = Mortlake Discontinuity.

On a more local-scale, the trace element geochemistry of NVP eruptive products has also been considered in a number of detailed studies focusing on specific eruption centres or groups of centres (Ferguson, 1971; Nosiara, 1981; Scutter, 1993; Boyce et al., 2015; Jordan et al., 2015). For example, Boyce et al. (2015) studied the trace element geochemistry, rare earth element (REE) patterns and Sr, Nd and Pb isotope systematics of the products of several different eruption points of a single eruption centre (Mount Rouse, Western Plains sub-province; see **section 3.2.3**). These authors concluded that separate batches of melt, extruded from different eruption points, could be distinguished by both their trace element and REE signatures. Similar studies at other individual centres have concluded the involvement of multiple batches of melt (e.g., Tunjc, 1988; van Otterloo et al., 2014), sometimes also invoking multiple sources (Jordan et al., 2015).

2.3 Geochronology

The eruptive history of the NVP has been examined in various studies involving a range of geochronological techniques targeted to specific rock types, improving the understanding of the eruption history of the NVP over the last ~50 years. Since the advent of K-Ar dating (Smits and Gentner, 1950), analysis of the absolute ages of NVP lavas has been possible. Extensive K-Ar dating work has been undertaken on NVP whole-rock samples, providing age constraints for more than 70 localities across the province (McDougall et al., 1966; Aziz-ur-Rahman and McDougall, 1972; Bowen, 1975; McDougall and Gill, 1975; Singleton et al., 1976; Gill, 1981; Ollier, 1985; Henley and Webb, 1990; Cayley et al., 1995; Edwards, 2004; Gray and McDougall, 2009). This work indicates an apparent maximum age of 4.6 Ma for the NVP, which has withstood more recent dating efforts. The most extensive K-Ar study, carried out by Gray and McDougall (2009), determined 51 new ages for NVP products across a wide area, and included a summary of previous K-Ar dating efforts.

More recently, ^{40}Ar/^{39}Ar dating has been used to generate high-precision ages for lava flows via step-heating analysis of whole rock/groundmass basaltic samples and plagioclase separates (Hare et al., 2005; Matchan and Phillips, 2011; Ismail et al., 2013; Matchan and Phillips, 2014; Matchan et al., 2016; Oostingh et al., 2017; Matchan et al., 2018). The greater precision afforded by recent improvements in noble gas mass spectrometer technology, together with improved accuracy from refined sample preparation techniques and the ability of ^{40}Ar/^{39}Ar age spectra to reveal more detail than a single K-Ar age, has allowed for the eruption history of the NVP to be considered in greater detail, and for previous K-Ar dates to be re-evaluated (Hare et al., 2005; Baker, 2008; Ismail, 2010; Matchan and Phillips, 2011; Traine, 2012; Ismail et al., 2013; Chang, 2014; Heath, 2014; Matchan and Phillips, 2014; Matchan et al., 2016; Che, 2017; Oostingh et al., 2017; Matchan et al., 2018).

Other dating techniques such as ^{14}C, thermoluminescence/optically-stimulated luminescence and cosmogenic exposure dating studies, have been used to constrain the age of some of the younger (<0.1 Ma) eruptive centres (Blackburn, 1982; Smith and Prescott, 1987; Robertson et al., 1996; Stone et al., 1997; Gillen et al., 2010; Gouramanis et al., 2010; Matchan, 2012) for which it has historically been challenging to resolve the radiogenic argon component. The youngest known eruptive centres in the NVP are considered to be Mount Gambier and Mount Schank, in the Mount Gambier sub-province, at ~5000 years old (Blackburn, 1982; Smith and Prescott, 1987; Gouramanis et al., 2010). The recent history of volcanism, along with mantle-derived $\delta^{13}C$ values in spring and ground waters (Chivas et al., 1987; Cartwright et al., 2002) and the existence of partial melts at depth (e.g., Graeber et al., 2002; Aivazpourporgou et al., 2015) have led authors to conclude that the NVP should be considered active, and that future eruptions are likely (Joyce, 2004; Boyce et al., 2014a; Cas et al., 2017).

2.3.1 K-Ar dating studies

The first K-Ar ages for lavas of the NVP were reported by McDougall et al. (1966) and Aziz-ur-Rahman and McDougall (1972). Whole-rock basalt samples from a combined total of 22 localities were dated in these studies (**Table 2.1**), resulting in an apparent age range for the NVP of 4.5 to 0.57 Ma, with younger NVP flows unable to be analysed by this method due to excessive atmospheric argon proportions (as discussed in **section 3.1.1.3**). The chosen samples were described as “olivine basalts,” believed to be essentially holocrystalline (glass-free) and free of significant alteration. Where multiple aliquots of the same sample were dated, ages were generally found to be in agreement, and this was used as a basis for inferring that little or no Ar-loss had occurred (see **section 3.1.1.4** for an explanation of Ar loss).

In a continuation of this work, Gray and McDougall (2009) published 51 new K-Ar ages for NVP lava flows (**Table 2.1**). This work included a compilation of previously published K-Ar ages, and divided the NVP into 29 age zones; a revision of the Price et al. (1988) $^{87}Sr/^{86}Sr$ zones (see **section 2.2**). These province-wide studies, together with numerous K-Ar studies focusing on specific areas, eruption points and flows (e.g., McDougall and Gill, 1975; Gill, 1981; Ollier, 1985) generated an apparent age range for the NVP of 4.6 Ma to ≤0.33 Ma, with an apparent peak of activity between 3.0 and 1.8 Ma (Gray and McDougall, 2009). Some studies on older flows of the NVP suggest that activity may have commenced as early as ~8 Ma (Cayley et al., 1995; Edwards, 2004). Cayley et al. (1995) suggested that sampling bias was to blame for only the youngest basalts in each area being dated, noting that K-Ar samples are often collected from the top of thick sequences of lava flows. If this is in fact the case, the initiation of activity within the NVP could have been earlier than has been suggested by many authors (Price et al., 1997; Hare et al., 2005; Gray and McDougall, 2009). Paul et al. (2005) noted that volcanism in southeast Australia has been somewhat continuous since the late Mesozoic, and argued for discontinuation of the ‘Newer Volcanic Province’ definition, in preference for ‘pre-10 Ma’ and ’10-5 Ma’ and ‘post-5 Ma’ age groupings. However, the NVP term remains in current use.

Table 2.1: A summary of previous K-Ar work on NVP basalts.

Paper	Number of samples dated
McDougall et al., (1966)	12
Aziz-ur-Rahman & McDougall (1972)	14
McDougall & Gill (1975)	5
Singleton et al., (1976)	7
Gill (1981)	1
Ollier (1985)	1
Henley & Webb (1990, unpublished)	10
Cayley et al., (1995, unpublished)	2
Edwards et al., (2004)	2
Gray & McDougall (2009)	51

2.3.2 Previous $^{40}Ar/^{39}Ar$ studies

The major advantage of the $^{40}Ar/^{39}Ar$ dating method over the K-Ar dating method is that it allows for evaluation of Ar isotope ratios over multiple heating steps and assessment of any disturbance that has occurred (see **section 3.1.2.2** for further discussion). The first $^{40}Ar/^{39}Ar$ study conducted within the NVP was by Hare et al. (2005), providing an age of 4.19 ± 0.18 Ma (2σ) for plagioclase separated from a basalt flow north of Werribee. Since publication of that study, there have been several $^{40}Ar/^{39}Ar$ dating studies involving both basaltic groundmass, plagioclase separates and feldspar megacrysts (e.g., Baker, 2008; Matchan and Phillips, 2011; Heath, 2014). New generation multi-collector mass spectrometers have been used in more recent work, providing unprecedented precision (Matchan and Phillips, 2014; Matchan et al., 2016; Oostingh et al., 2017; Matchan et al., 2018).

Groundmass basalt from two eruption centres in the Warrnambool – Port Fairy area (Mount Warrnambool and Mount Rouse), were dated using the furnace step-heating method by Matchan and Phillips (2011). The reported eruption ages were 542 ± 17 ka (95% CI) and 303 ± 13 ka (95% CI) respectively, with some samples excluded from calculations due to disturbed age spectra. This disturbance was attributed to extraneous argon contamination (see **section 3.1.1.4** for an explanation of extraneous argon). The age of Mount Rouse was revisited in a subsequent $^{40}Ar/^{39}Ar$ study by Matchan and Phillips (2014) on the then recently commissioned multi-collector ARGUSVI mass spectrometer at the University of Melbourne. An age of 284 ± 1.8 ka (95% CI) was determined for Mount Rouse, illustrating the vast improvement in precision provided by the advent of multi-collector mass spectrometry. $^{40}Ar/^{39}Ar$ dating of younger flows from Mount Eccles and Mount Porndon was also attempted by Matchan (2012), using the ARGUSVI. Although some difficulty was encountered due to very small amounts of radiogenic ^{40}Ar being present, unpublished $^{40}Ar/^{39}Ar$ age estimates of 92 ± 8 ka (2σ), and 105 ± 22 ka (2σ) were determined for Eccles and Porndon, respectively (Matchan, 2012).

Alkali-feldspar megacrysts from several NVP scoria cones, maars and flows were dated by the $^{40}Ar/^{39}Ar$ laser step-heating method in separate studies by Traine (2012), Ismail et al. (2013) and Matchan et al. (2018). A total of 13 new $^{40}Ar/^{39}Ar$ age constraints were found for 10 separate eruption centres, with varying levels of precision. Analytical errors were generally lower in the results from Traine (2012) and Matchan et al. (2018), where the ARGUSVI multi-collector mass spectrometer was employed. Specific issues related to dating megacrysts as compared to groundmass samples were noted by Traine (2012), including assessing whether the argon isotope systematics are "reset" upon eruption and assessing whether concordant ages are actually dating the eruption or some previous crystallisation event. Matchan et al. (2018) found that anorthoclase megacryst ages from two eruption centres (Mount Shadwell and Mount Leura) were almost indistinguishable (within a few thousand years) from groundmass basalt ages for the same eruption centres.

Chang (2014) and Heath (2014) performed ^{40}Ar/^{39}Ar laser step-heating on a total of 18 NVP basalt samples, mostly from the Central Highlands sub-province. A total of 33 groundmass aliquots and 3 plagioclase separates were analysed, and a total of 19 new ^{40}Ar/^{39}Ar age constraints were reported (unpublished data). The plagioclase separates all gave discordant age spectra, partially attributed by Heath (2014) to the small grain size and ^{39}Ar recoil effects. Both studies utilised the ARGUSVI, and achieved extremely high precision (0.3% to <2% errors (2σ)), although many of these ages were calculated using total gas data rather than age plateaux due to discordance in age spectra, and were hence essentially equivalent to high-precision K-Ar ages (see **section 3.1.1.2**). The dating results of Heath (2014), from the Melbourne area, are discussed further in **section 2.5**.

The most extensive ^{40}Ar/^{39}Ar study on NVP rocks was that of Oostingh et al. (2017), focusing on the Western Plains sub-province. Ages for a total of 23 lava flows and eruption points fell within an age range of 4.38 ± 0.02 Ma to 41.1 ± 2.2 ka, including the first three published ^{40}Ar/^{39}Ar eruption ages for any flows younger than 50 ka in the NVP. This study found an apparent evolution from tholeiitic to alkalic compositions over time within the NVP and suggested that a change in the mechanism behind volcanism was responsible (Oostingh et al., 2017).

The difficulties encountered in performing high-precision ^{40}Ar/^{39}Ar step-heating analyses using the ARGUSVI on even slightly altered or marginally non-holocrystalline samples have been discussed by Matchan and Phillips (2014) and Heath (2014). Any minor discordance in ^{40}Ar/^{39}Ar age spectra that may have been previously been masked by relatively large analytical uncertainties when employing older generation mass spectrometers is now resolvable, and commonly precludes satisfaction of age plateau criteria (see **section 3.1.2.2.1** for an explanation of age plateaux). Such discordance is evident even in holocrystalline samples lacking any visible alteration (Heath, 2014).

2.4 The cause(s) of NVP volcanism

A number of authors have put forward models to explain the genesis of the NVP. Early workers suggested that a stationary mantle hotspot was responsible, with the Australian plate slowly migrating northwards (Sutherland, 1981; Wellman, 1983). The hotspot model was supported by the extensive volcanism along Australia's east coast, and the fact that the products of the Older Volcanics (42-57 Ma) are mostly located to the north of those of the NVP (5-0 Ma) is broadly consistent with the Australian Plate's northward movement. Price et al. (1997) summarised the shortcomings of a hotspot model for the NVP, noting the absence of a linear chain of volcanoes, the continued volcanism at similar latitudes since the Tertiary, and the lack of a central volcano.

More recently, some authors have favoured mantle upwelling due to lithospheric extension resulting from Australia's separation from Antarctica (Price et al., 1997; Lesti et al., 2008). A model put forward by Price et al. (1997) invoked mantle plumes, or diapirs, upwelling from great depths and only reaching the solidus after 20 to 100 million years. This model accounted for the large gap in time between the initiation of seafloor spreading and beginning of volcanic activity in the NVP. Lesti et al. (2008) built on this model, suggesting that crustal controls on volcanism explained the lack of activity in other parts of Australia's south coast, which also should have experienced lithospheric thinning as they separated from Antarctica. However, southeast Australia has been under compression since the beginning of NVP magmatism (Sandiford et al., 2004), and upwelling rates derived from ^{238}U–^{230}Th disequilibria are too slow for an upwelling plume (Demidjuk et al., 2007).

Demidjuk et al. (2007) proposed an alternative model for NVP genesis. They suggested that topographical differences at the base of the Australian lithosphere could have led to the formation of a convective cell in a process termed “edge-driven convection.” Demidjuk et al. (2007) argued against upwelling mantle plumes, citing an apparent lack of crustal extension or other convincing evidence, and instead favoured localised convection leading to melting of a heterogeneous, complex mantle beneath the Australian continent. They proposed that NVP eruptive products could be generated by the mixing of upwelling asthenospheric melts with partial melts of amphibole ± phlogopite peridotite in the lithospheric mantle.

Seismic tomography and geodynamic modelling of the lithosphere under southeast Australia were utilised by Davies and Rawlinson (2014) to support the edge-driven convection hypothesis. Their simulations suggested that a ‘step’ at the base of the lithosphere could produce upwelling localised to the upper mantle, as was supported by seismic tomography. They concluded that edge-driven convection combined with shear-driven upwelling could produce the rates of upwelling calculated for the NVP over the area where volcanism has taken place. Building on this idea, Davies et al. (2015) proposed that the mantle hotspot considered responsible for a trail of Cenozoic volcanoes down the east Australian coast (the ‘Cosgrove Track’) could have been the initial trigger for volcanism in this particular convective cell. They estimated that the position of the east

Australian hotspot was approximately adjacent to the NVP immediately before the onset of volcanism, at 6.5-5 Ma, and that its entrainment in a convective cell might have provided the energy required for NVP initiation.

Although extensive work has been undertaken and numerous models suggested, the formation of a more detailed hypothesis to explain NVP genesis will benefit from the detailed mapping and classification of erupted products, along with precise dating work, such as is proposed for the current study.

2.5 NVP activity in the Melbourne Area

Despite their proximity to the metropolitan area, and relatively easy access, eruption centres and lava flows of the Melbourne area have received less scrutiny than those in more sparsely populated areas. Geomorphological studies by early workers noted the young appearance of some lava flows and their tendency to shift drainage channels to their margins (e.g., Hall, 1908). The geochemistry of lavas of the Melbourne area has been evaluated as part of province-wide and regional studies (e.g., Edwards, 1938; Bahat, 1967), and lava flows were mapped in rare Melbourne-focused studies (Hanks, 1955; Croker, 1984). Melbourne lava flows were sampled for K-Ar dating by McDougall et al. (1966), providing the first direct age constraints for any NVP products in the Melbourne area. The Melbourne area was divided into five $^{87}Sr/^{86}Sr$ zones by Price et al. (1988), which were assigned K-Ar ages by Gray and McDougall (2009; see **Table 2.2; Fig. 2.2**). Stewart (1975) and Croker (1984) built on the work of Hanks (1955) and assigned ages to each of the flows based on available K-Ar dating results. Heath (2014) reported the first high-precision $^{40}Ar/^{39}Ar$ ages for Melbourne basalt.

In some of the earliest work on the volcanic history of Melbourne, Hart (1894) discussed the formation of lava plains, filling ‘hollows’ in the Paleozoic basement. This study distinguished between ‘older’ and ‘newer’ volcanic rocks, noting the large number of ‘young’ eruption points to the north of Melbourne. It also highlighted the tendency for drainage channels to be filled by lava flows, and new channels to be formed at flow margins. Hall (1908) described the morphology of the lava plains and suggested that lava flows had often obstructed drainage channels and altered their courses.

Table 2.2: Initial $^{87}Sr/^{86}Sr$ zones of the Melbourne area (Gray and McDougall, 2009). The extent of each zone is displayed in **Fig. 2.2**.

Zone Number	$(^{87}Sr/^{86}Sr)_i$ Range	Mean Age (Ma)
1	0.70408–0.70427	0.94
2	0.70441–0.70452	0.99
3	0.70459–0.70467	0.92
4	0.70494–0.70511	2.31
5	0.70501–0.70542	2.66

All previous work on Melbourne area basalts has agreed on the presence of multiple compositionally distinct lava flows (Hart, 1894; Hanks, 1955; Stewart, 1975; Croker, 1984; Price et al., 1988). Studies of major element geochemistry (Edwards, 1938; Irving and Green, 1976; Croker, 1984; Price et al., 1997) have revealed a wide range of different rock types that essentially span the compositional range of the entire NVP (**Fig. 2.3**).

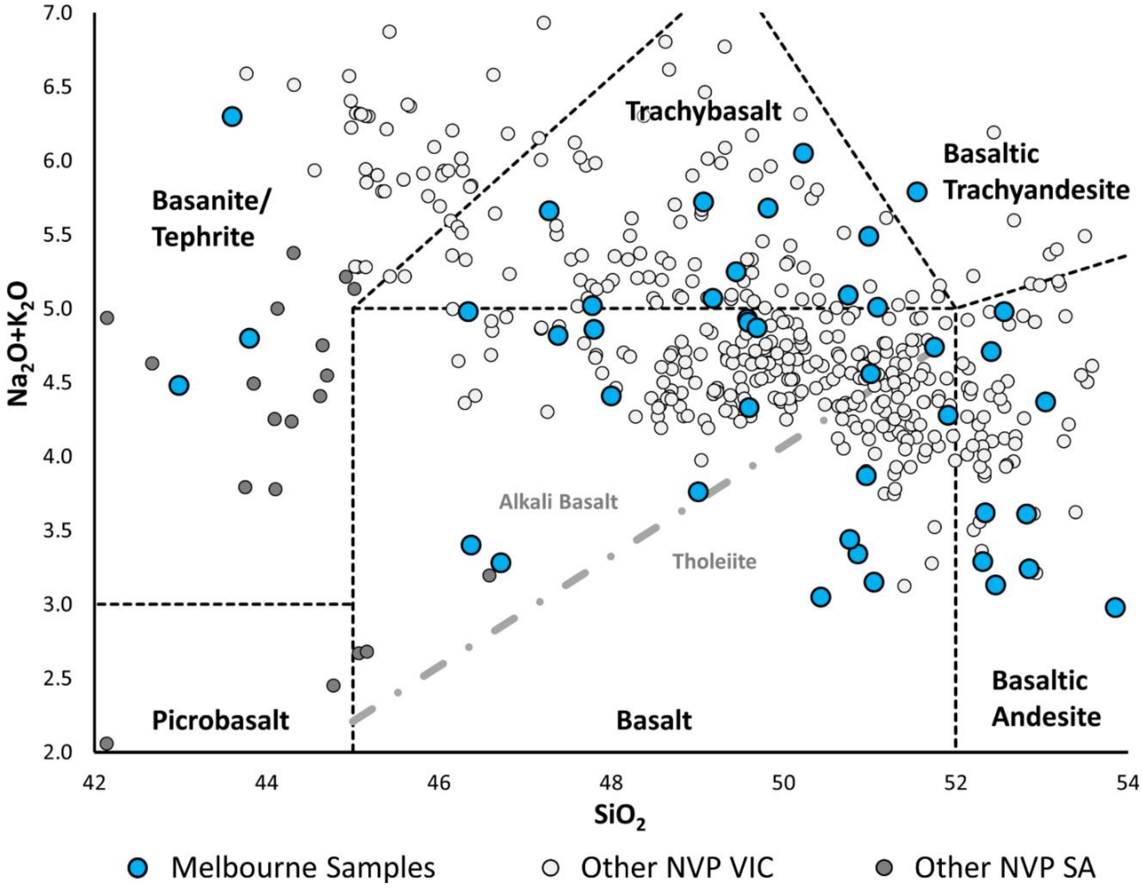

Figure 2.3: Total alkalis versus silica (TAS) diagram illustrating the range of Melbourne basalt major element chemistry based on previous literature (Edwards, 1938; Irving and Green, 1976; Croker, 1984; Price et al., 1997). The range of rock types is similar to that of the entire NVP (Frey and Green, 1974; Ellis, 1976; Irving and Green, 1976; Frey et al., 1978; McDonough et al., 1985; Price et al., 1997; Stone et al., 1997; Vogel and Keays, 1997; McBride et al., 2001; Foden et al., 2002; Demidjuk et al., 2007; data from Boyce et al., 2015; Oostingh et al., 2016).

The earliest account of the eruption history of the Melbourne area was given by Hanks (1955), who suggested that volcanism began in the Lower Pliocene (or earlier) and continued into the Upper Pleistocene. K-Ar work has subsequently provided an apparent age range of ~4.5 to 0.8 Ma for volcanism in the area (McDougall et al., 1966; Gray and

McDougall, 2009; Heath, 2014). The mapping of individual lava flows is made difficult by the fact that there may be several flows represented in any one location at different stratigraphic levels (Stewart, 1975; Croker, 1984). This has been further complicated by the destruction of natural outcrop as urban development has progressed. Previous flow mapping in the Melbourne area has relied either on geomorphology and borehole stratigraphy (Hanks, 1955; Stewart, 1975) or isotope systematics (Price et al., 1988; Price et al., 1997; Price et al., 2003; Gray and McDougall, 2009).

A number of NVP eruption centres located to the north of Melbourne have been suggested as sources of lava flows: Mount Fraser, Hayes Hill, Tulloch Hill, Mount Ridley, Aitken Hill, Crowes Hill, Ryans Hill and Stony Hill (**Fig. 2.4**; Hanks, 1955; Stewart, 1975; Croker, 1984; Hare et al., 2005). Croker (1984) attributed three separate flows outcropping along the Darebin and Merri Creeks, with K/Ar ages of ~4.5, 2.2, and 0.8 Ma, to Hayes Hill, a volcano located in Donnybrook (**Fig. 2.4**). Croker (1984) proposed that these three flows account for the majority of basalt in the east of Melbourne. Hare et al. (2005) suggested either Ryan’s Hill or Stony Hill as the source of basalt to the west of the Maribyrnong River, where a large number of K-Ar ages are in agreement, at ~2.6 Ma (**Fig. 2.5**). The area between Merri Creek and Deep Creek/Maribyrnong River has been purported to include a number of discreet and overlapping flows, erupted from Mt Fraser, Tulloch Hill, Aitken Hill, and multiple vents at each of Mount Ridley and Crowe Hill (Hanks, 1955; Stewart, 1975; Croker, 1984).

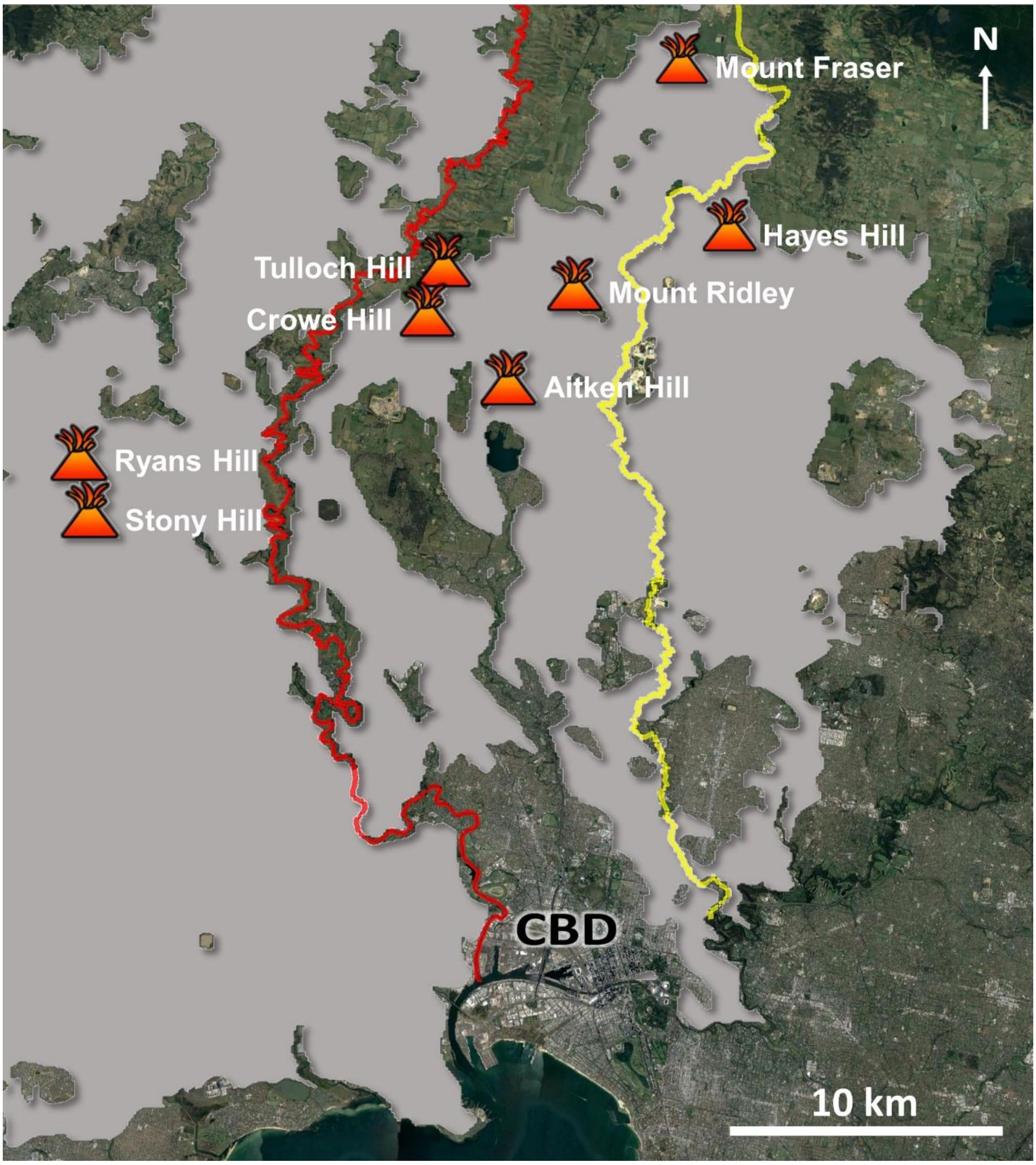

Figure 2.4: Eruption centres proposed as being the sources of Melbourne basalt, located to the north and northwest of Melbourne CBD. NVP lava flows are shown in grey. Merri Creek is highlighted in yellow and Maribyrnong River/Deep Creek in red.

Previous K-Ar and $^{40}Ar/^{39}Ar$ ages for the Melbourne area are shown in **Figure 2.5**. To the west, the majority of ages fall within the range 2.5-3.0 Ma, whereas in the east, most ages are between 0.8 and 1.0 Ma. In the central area, between Merri Creek and Maribyrnong River/Deep Creek, four ages are in the range 2.2-2.4 Ma; this area also includes the two oldest ages found for basalts in the Melbourne area (3.86 ± 0.07 Ma and 4.50 ± 0.30 Ma). ^{40}Ar/^{39}Ar ages (green) are typically about an order of magnitude more precise than K-Ar ages (blue). Indistinguishable ages at different locations are indicative either of single lava flows/flow packages sampled multiple times, or possibly peaks in volcanic activity at certain times where multiple eruptions occurred. In the absence of detailed flow mapping, it is not possible to evaluate which of these scenarios are more likely. A concise geochronological history of the NVP in the Melbourne area requires a multi-disciplinary approach that combines geomorphological and stratigraphic constraints, lava geochemistry and geochronology.

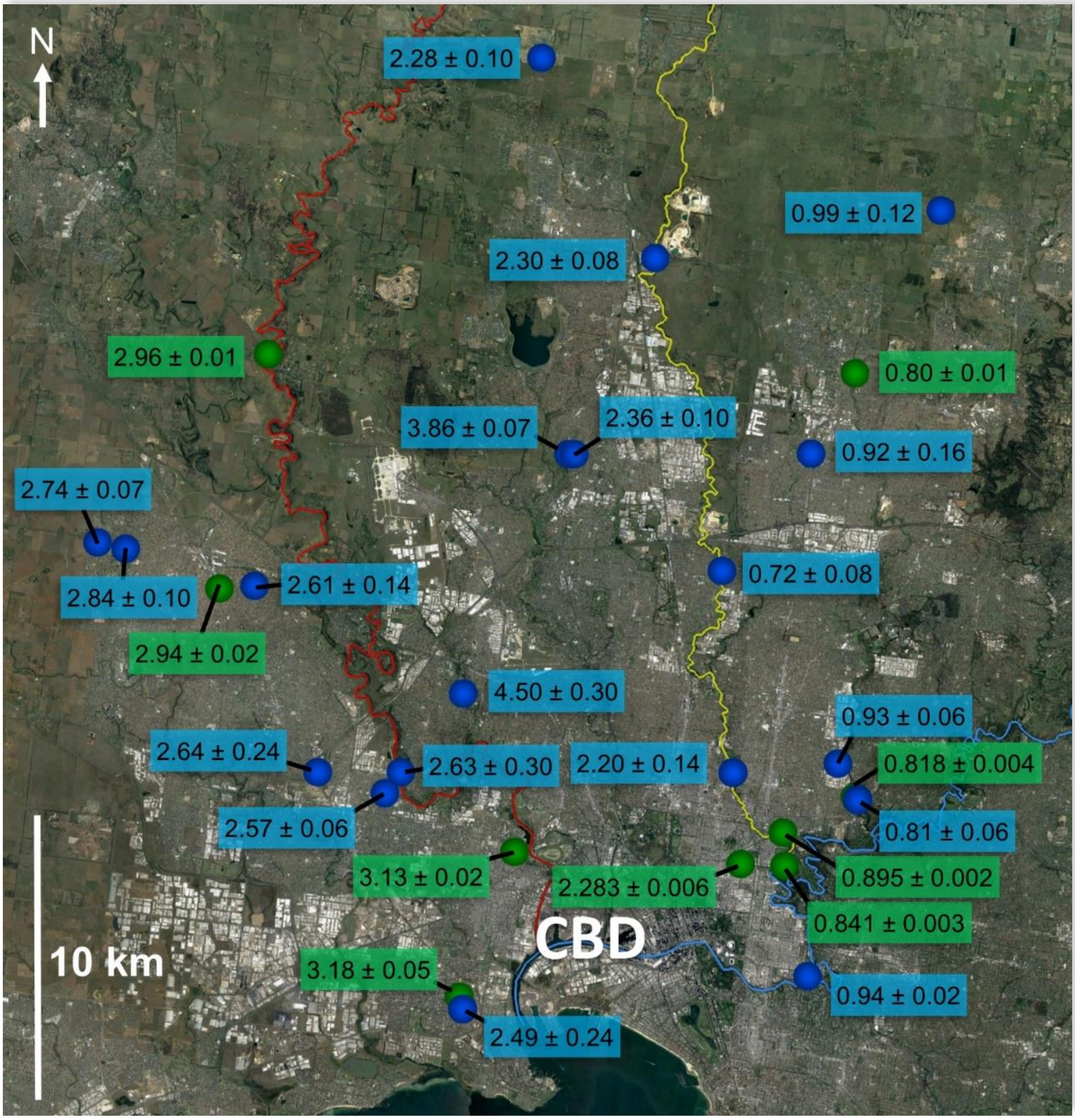

Figure 2.5: K-Ar (blue) and ^{40}Ar/^{39}Ar (green) ages from previous work within the Melbourne area of the NVP (McDougall et al., 1966; Gray and McDougall, 2009; Heath, 2014). Merri Creek is highlighted in yellow and Maribyrnong River/Deep Creek in red.

Chapter 3) Sample collection and preparation

3.1 Sample collection

Sampling sites across the Melbourne area were selected based on the availability of basaltic outcrop or borehole core samples (**Fig. 3.1**). Outcrop samples were primarily collected from road cuttings, natural cliffs and disused quarries (**Fig. 3.2**). Core samples were provided by the Victorian Geological Survey, GHD Australia and Golder Associates. The most important sample selection criteria were a low degree of visible weathering, minimal vesicularity, and coarsely crystalline texture (where possible). The freshest samples were favoured, as alteration is known to be detrimental to ^{40}Ar/^{39}Ar dating results (see section 4.1.1.4; Koppers et al., 2000; Baksi, 2007). Vesicles provide possible conduits for the flow of water through portions of a basalt flow, and vesicular regions may show higher degrees of alteration than surrounding non-vesicular regions. For this reason, samples were preferentially sourced from the centre of thick flow units, avoiding the vesicular regions commonly found at the base and top of basaltic flows (e.g., Walker, 1989). Additionally, the edges of vesicles are often glassy, and glass can be problematic for ^{40}Ar/^{39}Ar dating due to recoil issues (see **section 4.1.2.3.1**) or devitrification and argon loss. Coarser-grained samples were hence preferentially selected, to reduce the likelihood of large amounts of glass being present.

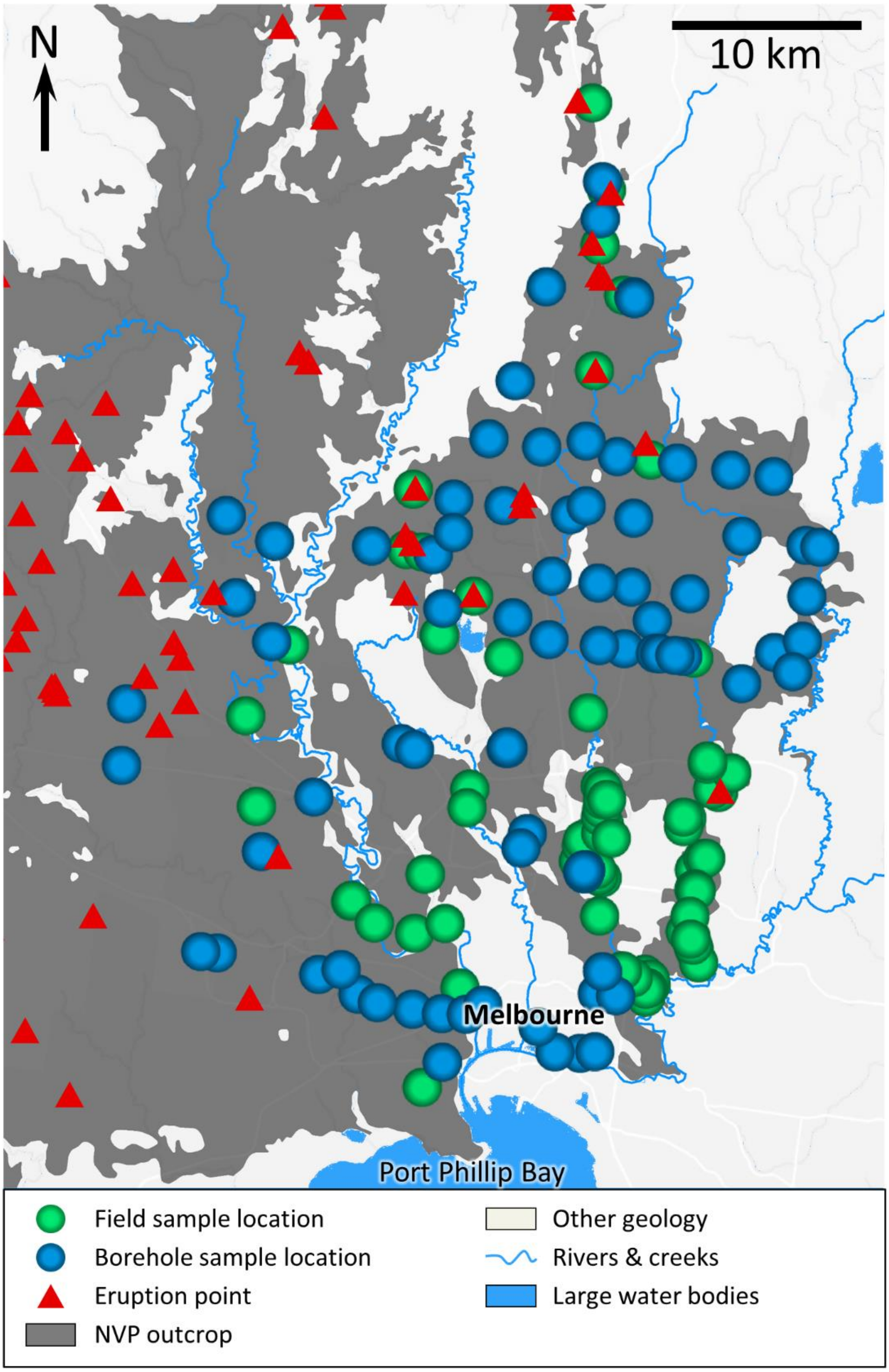

Figure 3.1: Sample locations across the Melbourne area, selected based on the availability of basalt outcrop or drill core.

In order to assign each of the lava flows to an individual eruption point, reference samples were collected from the eruption points themselves (**Fig. 3.3a**), or as close to the eruption point as possible (**Fig. 3.3b**). These samples were employed as archetypes for comparison with samples of uncertain origin.

Where drill core was available, samples were collected from multiple depths (up to 13 samples per borehole) to ensure that multiple lava flows were represented wherever possible, and to increase the likelihood of collecting samples suitable for ^{40}Ar/^{39}Ar geochronology. As with field samples, unaltered, massive basalt from the middle section of flows was targeted (**Fig. 3.4**). In total, 388 outcrop and borehole samples were collected from across the Melbourne area.

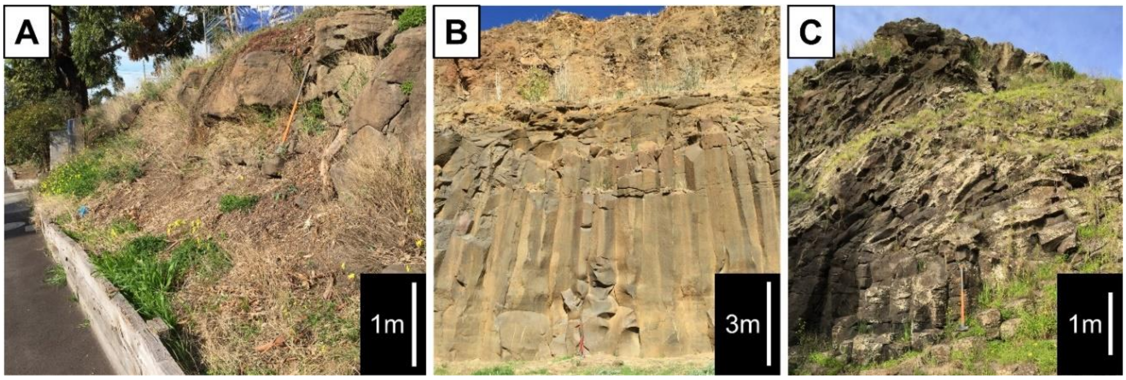

Figure 3.2: Field samples were collected from **a)** road cuttings, **b)** disused quarries and **c)** natural cliffs. Vesicular bands at the top and base of flows were avoided where possible.

Figure 3.3: a) Many samples were collected from eruption points, such as sample MH59 collected from Aitken Hill. **b)** Often, fresher and more easily collectible samples were sourced from the lava flow apron surrounding an eruption point, such as MH70, from near Mount Fraser (in background).

Figure 3.4: Borehole samples were preferentially selected from massive basalt in the middle sections of flows **(a)**, avoiding vesicular or altered sections **(b)** which were often at flow margins.

3.2 Sample preparation

3.2.1 Petrography and scanning electron microscopy

Petrographic thin sections were prepared from all collected samples (n = 388). An additional 285 sections from a 1970s basalt drilling program in the Melbourne area were provided by the Geological Survey of Victoria. A total of 15 polished sections were prepared for scanning electron microscopy (SEM) and energy dispersive X-ray spectrometry (EDS).

3.2.2 X-ray fluorescence (XRF) major element analysis

140 visibly unaltered samples were selected for major element analysis by XRF. Approximately 1 kg of each sample was fragmented using a jaw crusher, and fresh rock chips were selected for milling by tungsten-carbide or agate ring mill. Powders were combined with a mixed lithium metaborate/tetraborate flux and fused into glass beads.

3.2.3 Inductively coupled plasma mass spectrometry (ICP-MS)

A total of 27 samples were selected for trace element analysis by ICP-MS in order to cover the age range of Melbourne basalts and to allow distinction between particular flows with similar major element compositions (see section 7.2). Samples were fragmented using a jaw crusher, and rock chips with no obvious alteration were selected for milling using either a tungsten carbide or agate ring mill.

3.2.4 ^{40}Ar/^{39}Ar dating

35 unaltered, essentially holocrystalline groundmass samples and one unaltered plagioclase sample were selected for ^{40}Ar/^{39}Ar dating. To prepare groundmass samples,

basalt blocks were fragmented by jaw crusher, and the freshest fragments were selected for milling by disc mill. Milled material was sifted to a 150 – 250 μm size fraction and iron oxide-rich basaltic groundmass was concentrated by passing this material over a vertical magnet and retaining the magnetic fraction. This is affective because potassium (perhaps in anorthoclase or glass; Singer et al., 2004) and iron oxides (magnetite and/or ilmenite) are both concentrated in basaltic groundmass. Plagioclase crystals were removed from sample BA01 by hand, using an optical microscope. Although there was no visible alteration to potassium bearing phases, groundmass and plagioclase concentrates were treated in an ultrasonic bath with 5% HNO_3 (10 min), followed by 2% HF (2 min), deionised water (10 min), and acetone (3 min) in order to mitigate the effects of possible air contamination, secondary carbonate or glass. The cleaned concentrates (groundmass and plagioclase) were then hand-picked under a binocular microscope to remove remaining xenocrysts/phenocrysts, altered material and visible glass. For each sample, approximately 100 mg of purified material (approximately 25 mg of plagioclase sample BA01) was weighed into an aluminium packet and vacuum-sealed inside a quartz vial.

Chapter 4) Analytical Methods

4.1 Lava flow mapping

4.1.1 Petrography

Petrographic analysis has often been overlooked in flow mapping studies perhaps due to: (i) the perceived difficulty of resolving differences between similar fine-grained rocks; (ii) potential textural differences within a single flow that may occur due to varying rates of cooling and crystallisation within the flow package; and (iii) alteration obscuring original textures and mineralogy. In the NVP, previous workers have generally not employed detailed petrographic analysis in flow mapping studies, citing the above reasons and also the practical limitations to the number of thin sections required (e.g., Gray and McDougall, 2009). However, Heath (2014) identified that samples from distant locations of identical age and similar geochemistry in the Melbourne area commonly share petrographic features, such as phenocryst assemblage and grain size. This was taken as an indication that samples from individual flows might be differentiated based solely on diagnostic petrographic features, possibly providing an efficient means of mapping individual Melbourne area lava flows.

In the current study, over 650 petrographic thin sections were examined by transmitted light microscopy, performed on a Nikon LABOPHOT2-POL polarizing microscope. Plane and cross-polarised images were taken on a Leica DM750P polarizing microscope equipped with a Leica ICC50 W camera. A petrographic archetype was constructed for each flow based on phenocryst assemblage, modal mineral abundance and textures. As this archetype was better defined, each newly collected sample was assigned to a particular flow and a detailed map drawn (see **Chapter 6**).

4.1.2 Major element geochemistry

The presence of such a broad spectrum of rock types in the Melbourne area (**Fig. 2.3**) suggests that each lava flow might be identifiable based on major elements alone, since it is unlikely for a single lava flow to show a wide major-element composition. If each of the flows within the Melbourne area has unique geochemistry, it should be easier to differentiate between them, and easier for major element geochemistry to be utilised as a flow mapping tool.

4.1.2.1 Analytical methods for X-Ray Fluorescence spectrometry

Fused beads of 140 selected samples were analysed on a SPECTRO Xepos energy dispersive X-ray Fluorescence spectrometer at the University of Melbourne. Calibrations were constructed using a variety of internationally certified reference materials (AC-E, AGV-1, BCR-2, DNC-1, G2 and W2A). Analyses of secondary reference materials indicate measurement accuracy of better than 1–2% for most elements; the exceptions being P_2O_5 (up to 2%) and Na_2O (up to 4%).

4.1.3 Trace element geochemistry

The ideal geochemical tracer/s for mapping lava flows must be characteristic to all samples from a single flow, yet distinct for samples from different flows. Previous studies in other volcanic regions around the world have provided some promising insights into geochemical homogeneity within basaltic lava flows. In some cases, homogeneity has been revealed for whole-rock samples collected from several locations within the same flow (e.g., Sigmarsson et al., 1991). In other cases, significant differences in trace element geochemistry have been reported within a single flow over small distances (e.g., Lindstrom and Haskin, 1981). Particular immobile trace elements might prove to be the most robust geochemical tracers for individual lava flows, with vanadium (V) and zirconium (Zr) perhaps the most likely candidates (Maclennan et al., 2003; Boyce et al., 2015).

In a study of a 1783-1784 CE large basaltic eruption in southeast Iceland, Sigmarsson et al. (1991) focused on uranium (U) and thorium (Th) concentrations, and found that they differed by less than 7% over the 600 km^2 area of a single flow. Another flow in the northeast of Iceland was found to exhibit heterogeneity in almost every analysed element in a study by Maclennan et al. (2003). In that study, the trace element with the least variable concentration was shown to be V.

In a study of a series of basaltic eruptions from Mauna Loa, Hawaii, Rhodes (1983) found that, in most cases the differences in elemental abundances between flows were greater than the standard deviations of those abundances within flows. Rhodes (1983) found that it was possible to distinguish between flows in a single stratigraphic column based on geochemistry alone, and V and Zr were shown to have particularly low intra-flow variability in comparison to inter-flow variability. Some flows had far greater V and Zr variability than others, with standard deviations differing by more than an order of magnitude. Flows with more variable composition proved more difficult to distinguish (Rhodes, 1983).

In a study of basaltic andesites in southeast Brazil, a suite of less mobile elements and oxides were used to trace flows over distances of up to 50 km (Hartmann et al., 2013).

This study found that TiO_2, P_2O_5, Zr, Ta, Hf and Nb abundances could be used together to correlate individual flows in widely separated outcrops and boreholes (Hartmann et al., 2013). In Argentina, a long (~170 km) basaltic lava flow was found to show chemical homogeneity over smaller distances (~25 km) for most elements. However, samples from ≥50 km apart were chemically heterogeneous (Espanon et al., 2014).

In their study of Mount Rouse volcano, in the Western Plains sub-province of the NVP, Boyce et al. (2015) found that each generation of volcanic activity was distinguishable based on major and trace element geochemistry. In particular, Zr abundance was shown to have little variability within each batch of magma, whereas differences in Zr abundance between each batch of magma were significant (table 4.1).

Table 4.1: Zr abundances in samples from three different batches of magma from Mount Rouse. The standard deviation in each magma batch is much less than the difference in means between batches (adapted from Boyce et al., 2015).

Sample	MRV13	MRV16	MRV24a	R4G	R4AJ	R4AH	LK-L1-8	LK-M1-1	LK-L4-1
Batch	**A**	**A**	**A**	**B**	**B**	**B**	**C**	**C**	**C**
Zr (ppm)	138	124	120	228	244	252	356	393	393
	Mean = 127.3 ± 18.9 (2σ)			**Mean = 241.3 ± 24.4 (2σ)**			**Mean = 380.7 ± 42.7 (2σ)**		

In the Melbourne area, the wide range in major element concentrations (see **section 4.2.2**) eliminated the need for flow mapping by minor and trace element concentrations except in rare cases. Where samples of two flows were not separable based on either petrography or major element geochemistry, incompatible immobile trace elements provided a means of discerning between them (**see section 7.2**).

4.1.3.1 Analytical methods for Inductively coupled plasma mass spectrometry (ICP-MS)

Sample powders (100 mg) were digested using a ~1:3 HNO_3:HF solution in capped Teflon vials, heated to ~135°C overnight and then dried via hotplate evaporation. Dry powders were then refluxed twice in concentrated HNO_3 and dissolved in 3N HNO_3 overnight. Solutions were diluted with water, then an aliquant of each solution was removed and diluted with a 1.6% HNO_3 solution for a total dilution factor of ~5000. Analytical and drift-correction procedures followed those described in Eggins et al. (1997), with the exceptions that: 1) Tm, In and Bi were not used as internal standards as these are analytes; and 2) two digestions of USGS standard W-2 were used for instrument calibration.

Samples were analysed on an Agilent 7700x ICP-MS in the School of Earth Sciences, The University of Melbourne. The instrument was tuned to give Cerium oxide levels of < 1%. Four replicates of 100 scans per replicate were measured for each isotope. Dwell times were 10 milliseconds, except for Be, Nb, Zr, Mo, Cd, In, Sb, Hf, Ta, W, Tl, Bi, Th and U, for which dwell times were 30 milliseconds. Digests of recognised USGS basalt standard BHVO, and CRPG basalt standard BR were analysed as unknowns. The full ICP-MS trace element dataset is reported in **Appendix A.20.**

4.2 ^{40}Ar/^{39}Ar dating of basaltic rocks

4.2.1 The K-Ar decay scheme

K-Ar and ^{40}Ar/^{39}Ar dating rely on the natural decay of ^{40}K to ^{40}Ar, primarily by electron capture (λ(40Ke) + λ’(40Ke) = 0.581 × 10-10/yr; Steiger and Jäger, 1977). The dual decay scheme of ^{40}K (**Fig. 4.1**) involves the production of ^{40}Ca (89.2%) via electron emission, and ^{40}Ar by three different mechanisms. The majority of ^{40}Ar is produced by electron capture coupled with γ-ray emission. A very small amount of ^{40}Ar (0.16%) is produced by electron capture directly to the ground state, and an even smaller percentage (~0.001%) is produced by positron emission (β^+ decay; Beckinsale and Gale, 1969; McDougall and Harrison, 1999)

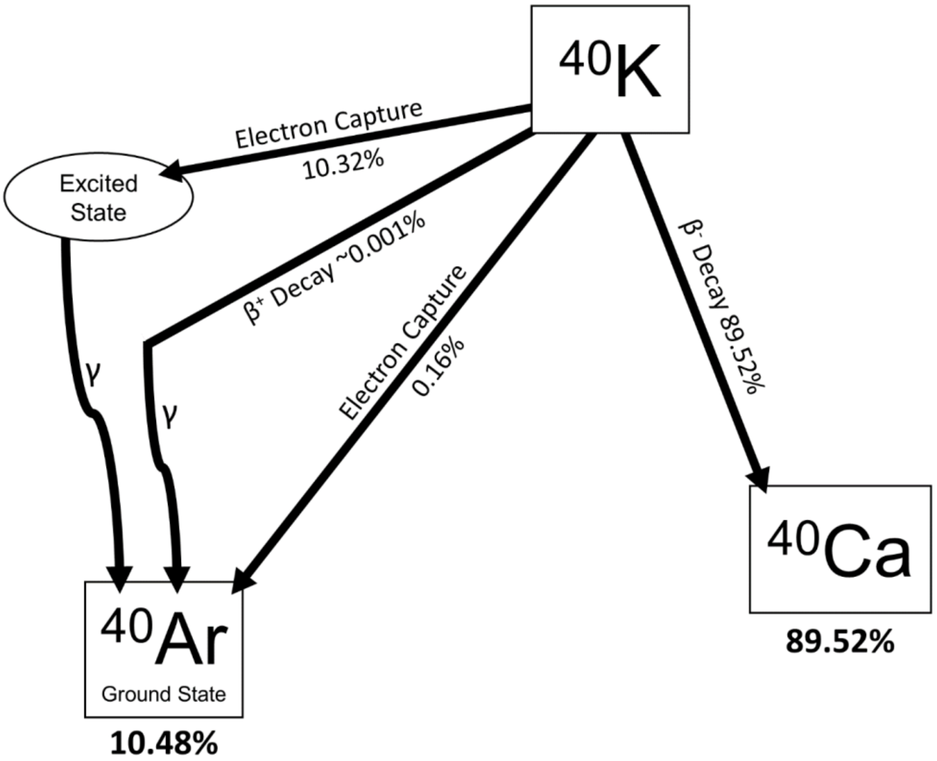

Figure 4.1: The dual decay of ^{40}K to ^{40}Ca and ^{40}Ar. Adapted from McDougall and Harrison (1999).

4.2.2 The K-Ar dating method

Although ^{40}Ca is the main product of ^{40}K decay, it is not commonly utilised in geochronology because calcium is a common constituent in most rocks and ^{40}Ca is the most common isotope of calcium (McDougall and Harrison, 1999). These factors together make the correction for D_0 (the number of daughter atoms at $t = 0$) unfeasible for most geological samples. Argon, however, is a noble gas, and hence is not present in the crystal structure of rock-forming minerals.

The K-Ar dating technique is based on the assumption that ^{40}Ar trapped within the crystal structure of a mineral is due to the radioactive decay of ^{40}K. With the formation of a melt, outgassing ideally causes all the ^{40}Ar to escape, essentially re-starting the timer. After crystallisation from the melt, and cooling below the closure temperature of rock-forming minerals (the temperature below which argon does not readily escape the crystal lattice), radiogenic ^{40}Ar becomes trapped in the crystal structure. The total amount of ^{40}Ar present will be proportional to the time since crystallisation and ^{40}K content, although in practise at least a small amount of non-radiogenic (atmospheric) ^{40}Ar is likely to have been trapped during crystallisation or introduced post-crystallisation (see **section 4.2.3**; McDougall and Harrison, 1999).

K is generally measured by flame photometry, with total K measured as a proxy for ^{40}K, since the ^{40}K/total K ratio is essentially constant in nature. ^{40}Ar is measured by noble gas mass spectrometry, and each isotope of Ar is measured individually (e.g., Lanphere, 2000). This means that multiple aliquots of each sample are required for a single age determination. Once ^{40}Ar and ^{40}K contents have been measured, a K-Ar age can be calculated, using the known decay rate of ^{40}K to ^{40}Ar (Steiger and Jäger, 1977), and applying a correction for trapped argon (conventionally assumed to be of modern atmospheric composition).

4.2.3 The correction for atmospheric argon

Although analyses are performed under vacuum, some proportion of atmospheric argon is present in most geological samples, so this must be accounted for by a correction that is applied in both K-Ar and $^{40}Ar/^{39}Ar$ dating. This correction utilises the fact that ^{36}Ar is not a (naturally) radiogenic isotope, so ^{36}Ar that is present (after the $(^{36}Ar/^{37}Ar)_{Ca}$ interference correction – see **section 4.2.5.3.2**) can be attributed to an external source – typically assumed to be the atmosphere. As the proportion of ^{40}Ar to ^{36}Ar present in the atmosphere is constant ($^{40}Ar/^{36}Ar = 298.56 \pm 0.62$; Lee et al., 2006), non-radiogenic ^{40}Ar can be deducted from the total ^{40}Ar to give the value for radiogenic ^{40}Ar ($^{40}Ar^*$) that is used in age calculations:

$$^{40}Ar^* = {}^{40}Ar_m - (^{36}Ar_c \times 298.56) \qquad \text{Equation 4.1}$$

where $^{40}Ar^*$ = Radiogenic ^{40}Ar, $^{40}Ar_m$ = Measured ^{40}Ar, and $^{36}Ar_c$ = Interference-corrected ^{36}Ar.

In $^{40}Ar/^{39}Ar$ step-heating experiments, a separate atmospheric correction is applied to each heating step.

4.2.4 Disadvantages of the K-Ar dating method

Historically, the K-Ar method was considered the primary radiogenic dating technique for a range of rock types, but shortfalls in the assumptions behind the method were apparent even in the earliest studies (e.g., Smits and Gentner, 1950). It is possible that samples contain reservoirs of argon that are neither of atmospheric composition nor radiogenically ingrown since eruption (e.g., Dalrymple and Moore, 1968; Lanphere and Dalrymple, 1976; Kelley, 2002). In such cases, K-Ar ages calculated assuming an atmospheric trapped argon composition will be erroneously old (e.g., Harrison, 1983). This additional ^{40}Ar is referred to as *extraneous* argon and may be present in fluid or melt inclusions (excess argon), or may be present in xenocrysts (inherited argon; e.g., Kelley, 2002). In previous studies, the presence of excess argon has been investigated using an inverse isochron diagram, by finding the 'initial' ^{40}Ar/^{36}Ar ratio ($[^{40}Ar/^{36}Ar]_i$; see **section 4.2.5.2.2**). Inherited argon may be present in xenoliths/xenocrysts that were not heated above their closure temperature (i.e. not completely outgassed) before crystallisation of the host-rock, or may be present in mineral inclusions within phenocrysts (e.g., Kelley, 2002; Phillips and Matchan, 2013). In this case, the ^{40}K from which the ^{40}Ar was produced would still be present within the rock, so inherited argon cannot be investigated by use of an inverse isochron diagram.

It is vital to K-Ar dating that any ^{40}Ar that is produced from ^{40}K is trapped in its position. If a rock is heated above the closure temperature of K-bearing minerals, or if alteration of K-bearing minerals occurs, ^{40}Ar may be able to escape the crystal structure (Foland et al., 1993). This is known as argon loss, and can lead to erroneously young K-Ar ages being calculated. In rocks that have never been buried at depth, the most common cause of argon loss is low-temperature alteration related to interaction between a rock and meteoric water or groundwater. Argon is commonly released in alteration reactions, and younger K-Ar ages are often found for altered rocks (Baksi, 2014).

Another issue with K-Ar dating is the fact that two separate aliquots of each sample must be analysed to obtain ^{40}K and ^{40}Ar values. If the K concentration of each aliquot is different, perhaps due to sample heterogeneity, calculated K-Ar ages will be erroneous.

4.2.5 ^{40}Ar/^{39}Ar dating

4.2.5.1 Theory behind the ^{40}Ar/^{39}Ar dating method

The ^{40}Ar/^{39}Ar dating method has been around for nearly half a century, and was designed as an improvement on the K-Ar method that was already widely used (Merrihue and Turner, 1966). The ^{40}Ar/^{39}Ar method is based on the fact that ^{39}K decays to ^{39}Ar at a predictable rate when bombarded by fast neutrons within a nuclear reactor. Since ^{39}Ar can only be produced in this way and does not occur naturally, the amount of ^{39}Ar present in a sample after irradiation can be used as a proxy for ^{39}K. As mentioned above, the ratio of ^{39}K to ^{40}K is essentially constant in nature, so the amount of ^{40}K in a sample can be calculated from the amount of measured ^{39}Ar after irradiation. The important ratio then becomes ^{40}Ar/^{39}Ar, which is utilised for age calculation via **equation 4.2**, after some corrections (Brereton, 1970; McDougall and Harrison, 1999):

$$t = \frac{1}{\lambda}\ln\left(1 + J\left(\frac{^{40}Ar^{*}}{^{39}Ar}\right)\right) \qquad \text{Equation 4.2}$$

where t = time, λ = the ^{40}K decay constant, and ^{40}Ar* = radiogenic argon.

The J-value is a measure of the intensity of radiation a sample has been subjected to, and includes calculation of the constant ratio of ^{39}K/^{40}K and branched decay of ^{40}K (McDougall and Harrison, 1999):

$$J = \frac{^{39}K}{^{40}K} \frac{\lambda}{\lambda_e + \lambda_{e\prime}} \Delta T \int ø(\varepsilon)\sigma(\varepsilon)\, d\varepsilon \qquad \text{Equation 4.3}$$

where λ_e and $\lambda_{e'}$ are the dual $^{40}K \rightarrow ^{40}Ar$ decay constants, ΔT is the duration of irradiation, $ø(\varepsilon)$ is the neutron flux density at energy ε and $\sigma(\varepsilon)$ is the neutron capture cross-section of ^{39}K for neutrons of energy ε.

4.2.5.2 Benefits of the $^{40}Ar/^{39}Ar$ dating method over the K-Ar dating technique

The most obvious benefit of the $^{40}Ar/^{39}Ar$ method is that the exact same aliquot can be used for measurement of both the proxy-parent isotope (^{39}Ar) and the daughter isotope (^{40}Ar), so problems of sample heterogeneity encountered by the K-Ar method are avoided. In addition, the $^{40}Ar/^{39}Ar$ method allows a sample to be progressively outgassed in a process known as ‘step-heating.’ This provides much more information about both the thermal history and argon composition of a sample than does a single age obtained by the K-Ar technique. It also allows isochron and inverse isochron diagrams to be constructed, so that the composition and distribution of trapped non-radiogenic argon can be assessed (inverse isochron diagrams are explained in **section 4.2.5.2.2**).

4.2.5.2.1 Step-heating spectra

Step-heating is accomplished by heating a sample (using a furnace or laser) over a number of steps, and releasing trapped argon incrementally (**Fig. 4.2**). $^{40}Ar^*/^{39}Ar$ ratios are measured for each heating step, and corrections are applied. By convention, an atmospheric trapped composition is assumed (e.g., Lee et al., 2006), and only analytical uncertainties are propagated. Argon in minerals with lower closure temperatures, or in less retentive sites within the crystal lattice, will be released in low temperature (low-T) steps. For rock samples, argon in high closure temperature minerals and from more retentive sites will be released in high temperature (High-T) steps. Since only some of the minerals within a rock may be affected by disturbance to argon isotope ratios, it is possible that only some heating steps are affected by any discordance that is present. These erroneous steps can be removed from age calculations, and the steps demonstrating constant ^{40}Ar*/^{39}Ar ratios (often the 'plateau'-forming steps – see below; **Fig 4.2a**) can be targeted. One common case is where low retention sites are affected by alteration, but the rest of the sample is fresh and unaltered (e.g., Baksi, 2014). Lower ^{40}Ar/^{39}Ar ratios would be expected in the lower temperature steps, and these steps could be excluded from the age calculation. In K-Ar dating, this would not be possible, and an erroneously young age might be derived (McDougall and Harrison, 1999).

4.2.5.2.1.1 Plateau ages

The most common method for calculating a ^{40}Ar/^{39}Ar cooling/crystallisation age from an age spectrum is by taking a weighted mean of consecutive ^{40}Ar*/^{39}Ar measurements that are within error of each other, propagating uncertainty in the J-value. This is known as a "plateau age" and although its definition varies somewhat between different studies, the following criteria are usually required for a statistical plateau (Fleck et al., 1977):

1) A minimum of three consecutive heating steps
2) All heating steps within two-sigma error of their mean
3) Includes at least 50% of the cumulative ^{39}Ar

Weighted mean ages comprising 30-50% of cumulative ^{39}Ar are sometimes reported in the literature, and commonly referred to as 'mini-plateaus' but are generally considered less robust (**Fig 4.2b**).

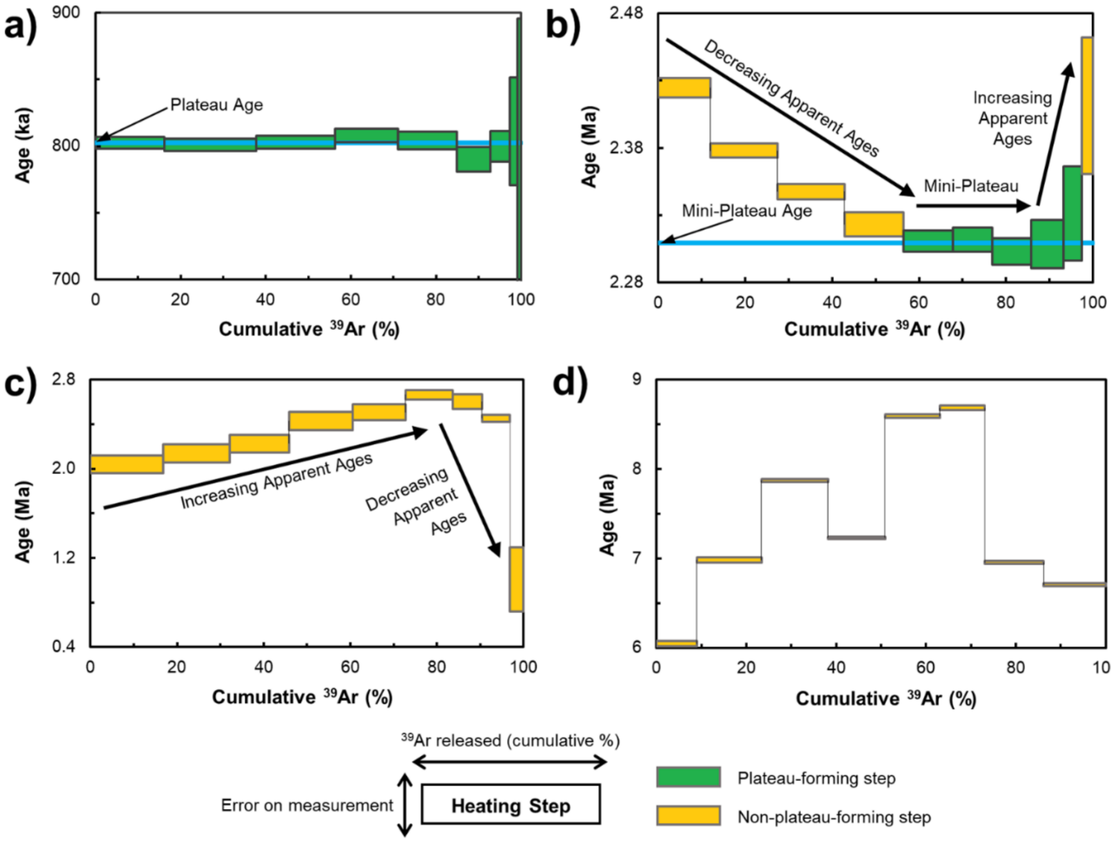

Figure 4.2: a) A step-heating spectrum showing very little discordance. All heating steps are within error of the plateau age. **b)** A decreasing step-heating spectrum with a mini-plateau containing less than 50% of the cumulative ^{39}Ar. Apparent ages increase in later heating steps, forming a 'saddle-shaped' spectrum. **c)** An increasing step-heating spectrum with decreasing apparent ages in later heating steps, forming a hump-shaped spectrum **d)** A completely discordant step-heating spectrum where apparent ages are scattered between 6 and 9 Ma with no obvious pattern.

4.2.5.2.1.2 Common types of age spectra

It is sometimes possible to produce a step heating spectrum that exhibits little or no disturbance to argon isotope ratios. In these cases, consecutive heating steps will be within error of each other, and there is no discernible pattern across the spectrum (**Fig. 4.2a**). Careful sample selection to avoid any glass or alteration can greatly improve the chances of achieving ideal results (McDougall and Harrison, 1999).

In the case of new-generation multi-collector mass spectrometers, such as the ARGUS VI, heating steps with apparent age differences as low as 0.1% are statistically distinguishable (Phillips et al., 2017). This makes it less likely that consecutive heating steps will form a plateau, but raises the possibility of distinguishing different causes of discordance. There are several types of discordant step-heating spectra that are often seen from young igneous rocks, each of which might prevent a plateau age being found, depending on the severity of discordance, and each type is considered in turn below.

Decreasing spectra

A common pattern of discordance in groundmass basalt samples, decreasing step-heating spectra are characterised by older ages in low-temperature (low-T) steps and younger ages in high-temperature (high-T) steps. In some cases, these spectra may flatten-out, and record a plateau section for the later heating steps. More commonly, apparent ages for later heating steps may begin to increase again after the initial decreasing pattern, forming a ‘saddle-shaped’ step heating spectrum (McDougall and Harrison, 1999; **Fig. 4.2b**).

Increasing spectra

Commonly observed for younger volcanic samples (<5 Ma), increasing step-heating spectra have younger apparent ages for early steps, increasing to older apparent ages for later steps. A plateau may be formed by mid- to high-T heating steps after the initial increase, or the trend may be reversed in later steps. A 'hump-shaped' heating spectrum is the result of increasing apparent ages for early heating steps and decreasing apparent ages in later steps (e.g., Hall, 2014; **Fig. 4.2c**)

Non-systematic discordance

Sometimes, step-heating spectra do not exhibit a simple pattern, and apparent ages may even be seemingly randomly scattered (e.g., **Fig. 4.2d**). Meaningful interpretation of such complex step-heating spectra is often not possible, as multiple factors likely contribute to the discordance. Non-systematic age spectra are rare in groundmass analyses provided that stringent sample selection criteria are adhered to (e.g., Baksi, 1974; Koppers et al., 2000; see **section 3.1**).

4.2.5.2.2 Inverse isochron diagrams

An important assumption of the ^{40}Ar/^{39}Ar and K-Ar methods is that the non-radiogenic trapped argon (see **section 4.2.3**) has the same isotopic composition as argon in the air (e.g., Lee et al., 2006; ^{40}Ar/^{36}Ar = 298.56 ± 0.62 [2σ]). If this assumption is valid the ^{36}Ar concentration can be used to calculate the amount of non-radiogenic ^{40}Ar that is present, and an accurate age might be calculated (McDougall and Harrison, 1999). Argon isotope ratio diagrams have routinely been employed to validate this assumption, and to decipher patterns of argon isotope release (Turner, 1971). The inverse isochron diagram plots

^{39}Ar/^{40}Ar against ^{36}Ar/^{40}Ar for each heating step, with associated errors forming an 'error ellipse' around each point (**Fig. 4.3**). The power of the inverse isochron is that the two main reservoirs of argon, radiogenic and non-radiogenic, are each represented, while graphical errors are minimised by making the most abundant isotope (^{40}Ar) the denominator of both variables (Dalrymple et al., 1988). Generally, a linear weighted least-squares regression is also calculated (York, 1968), taking each measurement and its uncertainty into account. Inverse isochron diagrams are at their most powerful where there are variable proportions of radiogenic and non-radiogenic argon released in each heating step causing a significant spread of data along the isochron, as is commonly the case in young basalt samples.

If a regression line is plotted for a series of heating steps containing various amounts of radiogenic and non-radiogenic argon, the x-intercept of this line should be the ^{39}Ar/^{40}Ar ratio of the purely radiogenic argon for a sample, which can be used to derive its (apparent) age (Turner, 1971). A sample that contains zero *radiogenic* argon will plot at x=0, since all ^{39}Ar is radiogenic (it is derived from reactor-induced neutron irradiation). The y-intercept of the regression line will therefore give the ^{36}Ar/^{40}Ar ratio of a sample's non-radiogenic trapped argon, assuming it is the same for each heating step. The inverse of this ratio is often reported, and is referred to as the ^{40}Ar/^{36}Ar initial ratio, commonly denoted (^{40}Ar/^{36}Ar)$_i$ (Merrihue and Turner, 1966; Dalrymple et al., 1988). This value will theoretically be equal to the measured air value of 298.56 ± 0.62 (Lee et al., 2006) in undisturbed samples.

Previous work has linked (^{40}Ar/^{36}Ar)$_i$ values greater than the atmospheric ratio to the presence of excess argon (e.g., Lanphere and Dalrymple, 1976; Phillips and Onstott, 1986), and $(^{40}Ar/^{36}Ar)_i$ lower than the atmospheric ratio have been linked to argon loss (Baksi, 2014) or a fractionated trapped component (e.g., Ozawa et al., 2006; Morgan et al., 2009). In some cases, non-atmospheric $(^{40}Ar/^{36}Ar)_i$ ratios from inverse isochrons have been interpreted as trapped argon compositions, and age spectra recalculated based on these ratios (Heizler and Harrison, 1988; Hodges et al., 2015; Oostingh et al., 2017). However, such an interpretation relies on the trapped composition being identical for each heating step, such that there is no discordance in inverse isochron space (**see chapter 5**).

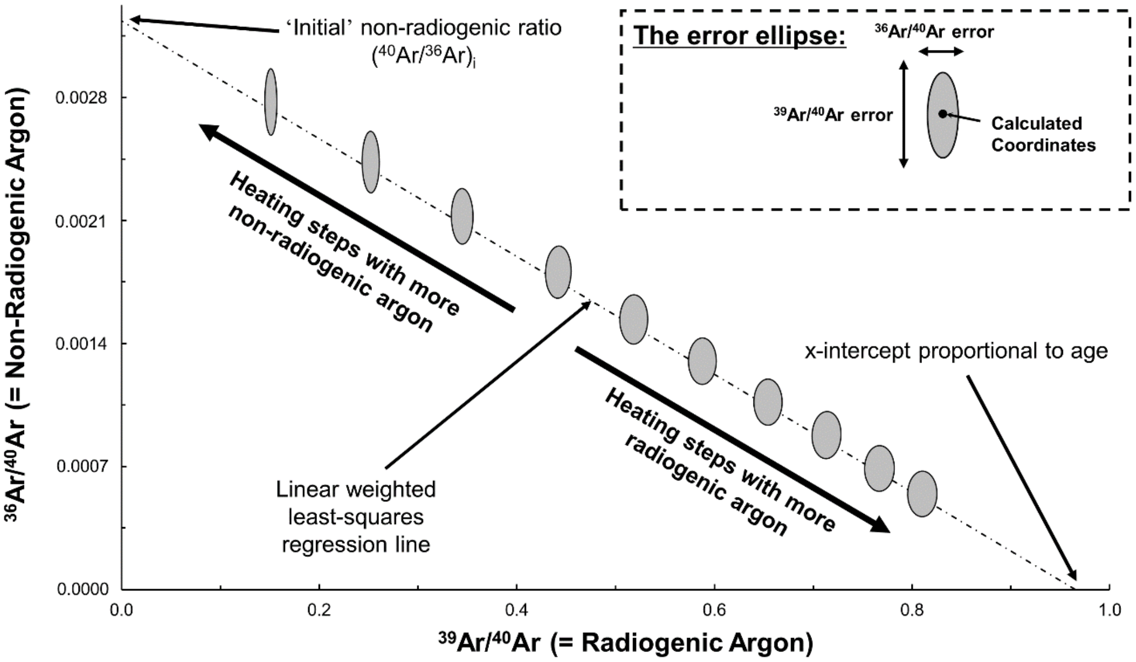

Figure 4.3: An inverse isochron diagram, with each heating step plotted as an error ellipse. An isochron age can be calculated from the $^{40}Ar/^{39}Ar$ value where the least-squares regression line crosses the x-intercept (Turner, 1971).

4.2.5.3 Complications of the $^{40}Ar/^{39}Ar$ dating method

As well as extraneous argon and argon loss, which impact both K-Ar and $^{40}Ar/^{39}Ar$ age determinations, there are several unique problems that must be overcome for $^{40}Ar/^{39}Ar$ dating to be successful. Reactor-induced ^{39}Ar and ^{37}Ar recoil can drastically alter step heating spectra (Turner and Cadogan, 1974; Onstott et al., 1995; Jourdan et al., 2007; Jourdan and Renne, 2014), but may be mitigated by employing stringent sample selection criteria, ideal irradiation times and Cd lining of irradiation cans. Neutron-induced interference reactions are unavoidable during irradiation but can be corrected for (Brereton, 1970). Mass-dependent fractionation might lead to over- or under-corrections for atmospheric ^{40}Ar (e.g., Trieloff et al., 2005).

4.2.5.3.1 ^{39}Ar and ^{37}Ar recoil

Necessary to the interpretation of ^{40}Ar/^{39}Ar step heating spectra is the assumption that all ^{39}Ar present in a sample after irradiation is in the same location as the parental ^{39}K atoms. Unfortunately, the energy released by the ^{39}K(n, p)^{39}Ar reaction is high enough that ^{39}Ar may be displaced by up to 0.4 μm (Onstott et al., 1995). This means that some ^{39}Ar may be released during a different heating step than the corresponding ^{40}Ar. In the worst cases, ^{39}Ar from the edges of mineral grains may be expelled from the system (into the atmosphere), and erroneously old ages will be found (Jourdan et al., 2007).

^{37}Ar is produced from ^{40}Ca during irradiation, and recoil of ^{37}Ar can also be problematic for ^{40}Ar/^{39}Ar dating because the amount of ^{37}Ar released by each heating step is used to correct for ^{36}Ar and ^{39}Ar that is also produced from calcium during irradiation (see **section 4.2.5.3.2**). This correction relies on any ^{37}Ar produced from ^{40}Ca remaining in the same location, and being released in the same heating step, as corresponding ^{36}Ar and ^{39}Ar (Jourdan and Renne, 2014).

Both ^{39}Ar and ^{37}Ar recoil loss/redistribution effects might be mitigated by avoiding very fine-grained or glassy samples. Recoil effects should decrease exponentially with increased grain size, as a lower proportion of the total ^{39}Ar and ^{37}Ar is ejected into adjacent phases or out of the system (Jourdan et al., 2007).

4.2.5.3.2 Interference reactions

During irradiation there are a number of other reactions that occur, leading to the production of argon isotopes. The impact of these interference reactions must be calculated and corrected for, before ^{40}Ar/^{39}Ar ages can be determined. The most important reactions are on calcium (^{40}Ca(n,α)^{36}Ar, ^{40}Ca(n,α)^{37}Ar and ^{42}Ca(n,α)^{39}Ar) and potassium (^{40}K(n,p)^{40}Ar), and correction factors are determined by irradiating pure calcium salts and potassium glass in the same nuclear reactor (Brereton, 1970; McDougall and Harrison, 1999).

4.2.5.3.3 Mass-dependent fractionation

Trieloff et al. (2005) showed that during step-heating of a sedimentary shungite sample, experimentally-induced mass-dependent fractionation caused a greater proportion of lighter Ar isotopes to be released in Low-T steps. They measured a ^{40}Ar/^{36}Ar range of 287.8 to >330 across a single step-heating experiment, and a range in ^{38}Ar/^{36}Ar values that were in line with an inverse square root ($m^{-1/2}$) mass dependency on the fractionation factor. Despite these findings, experimentally-induced mass-dependent fractionation has received very little scrutiny as a possible cause of discordance in ^{40}Ar/^{39}Ar data.

4.2.6 Applicability to this project

^{40}Ar/^{39}Ar dating has long been employed to extract absolute age data from basaltic rocks (e.g., Storey et al., 1995; Baksi and Archibald, 1997; Marzoli et al., 1999). The method is particularly suited to young (<5 Ma) basalts, such as those that are the focus of the current study, where the atmospheric argon component is more significant. This is because it allows for argon isotope ratios, and disturbance to those ratios, to be assessed over multiple heating steps. In the Melbourne area, the $^{40}Ar/^{39}Ar$ method has been successfully employed in a previous study to obtain new ages for groundmass basaltic material from 10 locations (Heath, 2014).

One aim of the current study is to evaluate causes of discordance in $^{40}Ar/^{39}Ar$ data from young basaltic samples. This issue has received little attention in previous studies, likely in part due to inferior analytical precision masking discordance. Performing $^{40}Ar/^{39}Ar$ analyses on multiple samples from individual eruption events enables direct comparison of concordant and discordant results of samples with known identical ages. This allows differences between these groups to be investigated, providing insight into the mechanisms behind common disturbances in argon isotope ratios. It is hoped that such insight will inform future workers on how discordance might be avoided and how data from samples exhibiting discordance should be treated in order to extract the most value.

4.2.7 $^{40}Ar/^{39}Ar$ analytical methods

Aluminium packets containing ~100 mg of groundmass for each sample were intercalated with neutron fluence monitors Alder Creek Rhyolite (ACR) Sanidine (UM#58; UM#70 and UM#71; 1.18144 ± 0.00068 Ma [2σ]; Phillips et al., 2017) or Fish Canyon Tuff (FCT) Sanidine (UM#77; 28.126 ± 0.019 Ma [2σ]; Phillips et al., 2017). Vials were irradiated at the CLICIT facility of the Oregon State University TRIGA (OSTR) reactor for 0.75 h (UM#58 and UM#70), 3 h (UM#71) and 20 h (UM#77). Following irradiation, aliquants (1 – 3 per sample) measuring ~30 – 70 mg were loaded into custom copper sample holders, covered with ZnS glass and placed in the sample chamber of a gas-handling system equipped with a Photon Machines Fusions 10.6 CO_2 laser and connected to a Thermo Fisher Scientific ARGUSVI mass spectrometer at The University of Melbourne. Details and configuration of the ARGUSVI system are discussed in Phillips and Matchan (2013) and Phillips et al. (2017).

Once under vacuum, the sample chamber and extraction line were baked overnight (≥12 h) at ~180°C. Following procedures previously described by Matchan and Phillips (2014), the bulk of atmospheric argon was removed from the samples via rastering of the 6 mm homogenised laser beam operated at 1 – 2% laser power. Groundmass step-heating experiments were then conducted using the 6 mm beam over a heating interval of 2.5 – 35% laser power (0.63 – 6.0 W), with a lasing time of ~1.5 – 3 min per heating step (two passes of the beam), depending on sample dimensions. Feldspar aliquant BA01-1 (see **chapter 6**) was step-heated using the 1 mm focused beam operating at 2 – 3% laser power (0.5 – 0.74W), and aliquants BA01-2 to BA01-6 were step-heated using the 0.15 mm focused beam operating at 0.1 – 1.5% laser power (<0.1 – 0.37 W). An alcohol-dry ice trap was used between the sample chamber and extraction line, and evolved gas was continually exposed to four SAES Zr-Al getters; three operating at room temperature and one at ~30 V (~400°C). In all cases, ^{36}Ar was measured on a Compact Discrete Dynode (CDD), and the remaining isotopes were measured on Faraday detectors. All Faraday detectors were fitted with 1×10^{12} Ω resistors during step heating experiments of irradiation can UM#58 samples (BH45B, MH01S, MH01N, MH02, MH04, MH05, MH07, MH09, MH10E, MH11, MH12). Following system upgrades, ^{39}Ar was measured on a Faraday equipped with a 1×10^{13} Ω resistor for UM#70 and UM#71 samples (BH47B, BH269, GRBH-01, KA7, KA13B, KA13L, KA13M, MH24, MH35, MH49, MH52,

MH56A, MH66, MH69, MH70, MH75C, MO43B, WO4, WW1A, YY3C, YY6). In the case of UM#77 samples (BA01, BB22, ME4J, MH68), ^{40}Ar, ^{39}Ar and ^{37}Ar were all measured on Faraday detectors with 1 x 10^{13} Ω resistors.

Correction factors for UM#58 samples were calculated based on measurements of K-glass and Ca-salts included in prolonged-irradiation package UM#60: $(^{36}\text{Ar}/^{37}\text{Ar})_{\text{Ca}}$ = (2.5713 ± 0.0023) x 10^{-4}; $(^{39}\text{Ar}/^{37}\text{Ar})_{\text{Ca}}$ = (6.6200 ± 0.0801) x 10^{-4}; $(^{40}\text{Ar}/^{39}\text{Ar})_{\text{K}}$ = (1.000 ± 0.050) x 10^{-10}; $(^{38}\text{Ar}/^{39}\text{Ar})_{\text{K}}$ = (1.2136 ± 0.0016) x 10^{-2}. Updated correction factors for K-glass and Ca-salts included in irradiation package UM#62 were applied to samples from cans UM#70, UM#71 and UM#77: $(^{36}\text{Ar}/^{37}\text{Ar})_{\text{Ca}}$ = (2.5782 ± 0.0018) x 10^{-4}; $(^{39}\text{Ar}/^{37}\text{Ar})_{\text{Ca}}$ = (6.5620 ± 0.0164) x 10^{-4}; $(^{40}\text{Ar}/^{39}\text{Ar})_{\text{K}}$ = (1.000 ± 0.050) x 10^{-10}; $(^{38}\text{Ar}/^{39}\text{Ar})_{\text{K}}$ = (1.2246 ± 0.0028) x 10^{-2} (see **Appendix A.21** for irradiation dates). All age calculations, age spectra and isochrons were generated using the ISOPLOT software package (Ludwig, 2012), and the decay constants of Steiger and Jäger (1977) were assumed. Unless otherwise stated, uncertainties in age determinations are quoted at the two-sigma level. J-values are reported with full ^{40}Ar/^{39}Ar results in **Appendices A.3 through A.14**.

4.3 Analytical methods for scanning electron microscopy

SEM petrography was undertaken at the University of Melbourne, using a Philips (FEI) XL30 environmental SEM equipped with an OXFORD INCA energy dispersive X-ray spectrometer (EDS). During the production of back-scattered electron (BSE) images, and elemental maps by EDS, a beam acceleration voltage of 15 kV was employed.

Chapter 5) An evidence-based approach to accurate interpretation of ^{40}Ar/^{39}Ar ages from basaltic rocks

M. Heath[a,]*, D. Phillips[a], E. Matchan[a]

[a] *School of Earth Sciences, The University of Melbourne, Parkville, VIC 3010, Australia*
*Corresponding author.
E-mail address: m.heath@student.unimelb.edu.au

Abstract

Since its inception in the late 1960s, the ^{40}Ar/^{39}Ar dating technique has been the premier method for determining the eruption ages of basaltic rocks, providing valuable insights into a plethora of terrestrial and planetary processes. Advances in multi-collector mass spectrometry and improved sample preparation procedures are enabling ever-improving analytical precision and clearer evaluation of the isotopic disturbances that affect many basaltic samples and cause discordant ^{40}Ar/^{39}Ar age spectra.

Here, we present ^{40}Ar/^{39}Ar step-heating data for multiple samples from two Quaternary basalt flows (0.8038 ± 0.0017 and 2.309 ± 0.009 Ma) of the intraplate Newer Volcanic Province, southeast Australia. A small proportion of these samples give concordant ^{40}Ar/^{39}Ar results, but most are variably discordant. The factors controlling these disturbances and implications for accurate age determination are examined and modelled in both step-heating spectra and inverse isochron space. We demonstrate that the proportion of radiogenic ^{40}Ar (^{40}Ar*) present in these samples strongly influences the nature of the discordance reflected in ^{40}Ar/^{39}Ar data. Mass-dependent fractionation appears to have a major influence on low-^{40}Ar* samples, whereas ^{39}Ar recoil

loss/redistribution effects are evident in samples with higher ^{40}Ar* proportions. The impact of mass fractionation is quantified via step-heating analyses of unirradiated basalt, whereby a ~4% difference in ^{38}Ar/^{36}Ar ratios is observed between low- and high-temperature heating steps.

On an inverse isochron plot (^{39}Ar/^{40}Ar vs ^{36}Ar/^{40}Ar), isotopic disturbance for groundmass samples primarily manifests as isochron rotation, leading to a negative correlation between (^{40}Ar/^{36}Ar)$_i$ values and associated ^{40}Ar/^{39}Ar ages. We propose a new framework for the interpretation of ^{40}Ar/^{39}Ar step-heating data for basaltic samples, through judicious evaluation of inverse isochron data, (^{40}Ar/^{36}Ar)$_i$ ratios and inverse isochron ages. Results from this study suggest that only samples exhibiting both flat ^{40}Ar/^{39}Ar age spectra and atmospheric (^{40}Ar/^{36}Ar)$_i$ ratios yield accurate eruption ages; in the case of more discordant age spectra, intermediate temperature steps with atmospheric (^{40}Ar/^{36}Ar)$_i$ ratios may provide the closest approximation of the eruption age.

5.1 Introduction

Precise and accurate ages for basaltic rocks are critical for constraining research questions ranging from global tectonics to magma petrogenesis, paleoclimatology and volcanic hazard assessment (e.g., Rampino and Stothers, 1988; Storey et al., 1995). ^{40}Ar/^{39}Ar geochronology remains the primary method for obtaining eruption ages of basaltic rocks (e.g., Hirano et al., 2008; Jourdan et al., 2014; Singer et al., 2014; Oostingh et al., 2017). However, accurate ^{40}Ar/^{39}Ar dating of basaltic rocks is often challenging, due to relatively low potassium contents and difficulties separating target potassic mineral phases. *Whole-rock* dating, as was commonly used in earlier K-Ar studies (e.g., McDougall et al., 1966), provides one approach to this problem, but is predicated on the assumption that all mineral phases crystallised contemporaneously (i.e. no xenocrysts, early phenocrysts or alteration). ^{40}Ar/^{39}Ar analysis of *groundmass* basaltic material is a refinement of the whole-rock technique, whereby relatively high-K aggregate grains are separated from inherited and altered phases (Koppers et al., 2000; Singer et al., 2004; Jicha et al., 2012). This approach has been employed in several recent high-precision ^{40}Ar/^{39}Ar studies on basaltic rocks (e.g., Matchan and Phillips, 2014; Oostingh et al., 2017). In some cases, ^{40}Ar/^{39}Ar studies have targeted plagioclase feldspar (e.g., Renne et al., 1990; Pringle et al., 1991). However, basaltic plagioclase typically contains <0.5 wt.% K_2O and is often fine-grained, making mineral separation time-consuming, particularly for Quaternary samples. The current study focuses exclusively on ^{40}Ar/^{39}Ar analyses of groundmass basaltic material; see Koppers et al. (2000) for a discussion of typical mineral phases outgassed during ^{40}Ar/^{39}Ar dating of basaltic groundmass.

Fresh, holocrystalline groundmass basaltic samples that have not experienced radiogenic ^{40}Ar (^{40}Ar*) loss, and are devoid of extraneous argon, sometimes produce relatively concordant step-heating age spectra (e.g., Singer et al., 2014). However, many basalts are non-ideal, possibly due to complex thermal histories, significant glass contents and/or alteration (e.g., Fleck et al., 1977; Foland et al., 1993; Koppers et al., 2000; Koppers et al., 2003; Baksi, 2007), and the interpretation of ^{40}Ar/^{39}Ar ages from discordant age spectra is often subjective and open to debate (e.g., Baksi, 2014). The order of magnitude improvement in analytical precision afforded by new multi-collector mass spectrometers (Matchan and Phillips, 2014), reveals more subtle disturbances of argon isotopic ratios, such that perfectly concordant step-heating spectra are rare.

When confronted with discordant $^{40}Ar/^{39}Ar$ age spectra, additional insight can be provided from *inverse isochron diagrams*, plotting $^{36}Ar/^{40}Ar$ versus $^{39}Ar/^{40}Ar$ ratios (Turner, 1971). In inverse isochron space, the $^{39}Ar/^{40}Ar$ intercept is equivalent to the $^{40}Ar^{*}/^{39}Ar$ ratio of the sample, and can be used to derive an apparent age. The $^{36}Ar/^{40}Ar$ intercept yields the 'initial' $^{40}Ar/^{36}Ar$ ratio [$(^{40}Ar/^{36}Ar)_i$], which is expected to approximate the atmospheric value of 298.56 ± 0.62 (2σ; Lee et al., 2006) in undisturbed basaltic groundmass samples. The primary use of isochron analysis in $^{40}Ar/^{39}Ar$ dating is to evaluate the assumption of an atmospheric composition for the *trapped* argon component (McDougall and Harrison, 1999). Previous work has attributed supra-atmospheric $(^{40}Ar/^{36}Ar)_i$ ratios to excess ^{40}Ar, and sub-atmospheric ratios to $^{40}Ar^{*}$ loss (e.g., Phillips and Onstott, 1986; Baksi, 2014). In some cases the $(^{40}Ar/^{36}Ar)_i$ ratio has also been used to re-calculate $^{40}Ar/^{39}Ar$ ages to improve the concordance of age spectra (e.g., Heizler and Harrison, 1988; Hodges et al., 2015; Oostingh et al., 2017). However, the validity of these interpretations and data treatment approaches have yet to be rigorously tested.

In this study, we compare apparent ages and $(^{40}Ar/^{36}Ar)_i$ ratios measured on multiple samples of groundmass material collected from two basaltic lava flows from the Newer Volcanic Province, southeast Australia. These samples produced variably disturbed age spectra and characteristic signatures in inverse isochron space that can be linked to mass fractionation and ^{39}Ar recoil loss/redistribution processes. We model the various types of isotopic disturbance expected for basaltic samples, and provide an evidence-based approach for the interpretation of $^{40}Ar/^{39}Ar$ age data from basaltic samples.

5.2 Sample locations

Samples were selected from two well preserved basaltic lava flows in the Melbourne area of southeast Australia (**Fig. 5.1a**). These flows form part of the intraplate Neogene–Quaternary Newer Volcanic Province (NVP), a predominantly basaltic lava field that covers approximately 23,000 km^2 of Victoria and South Australia (e.g., van den Hove et al., 2017b). Previous K-Ar (e.g., McDougall et al., 1966; Aziz-ur-Rahman and McDougall, 1972; McDougall and Gill, 1975; Gray and McDougall, 2009) and ^{40}Ar/^{39}Ar dating (e.g., Hare et al., 2005; Matchan and Phillips, 2011; Matchan and Phillips, 2014; Oostingh et al., 2017; Matchan et al., 2018), combined with cosmogenic dating studies (Stone et al., 1997; Gillen et al., 2010), thermoluminescence (Smith and Prescott, 1987) and ^{14}C (Gouramanis et al., 2010) work on the youngest eruption points (<100 ka), have constrained an age range of ~4.6 Ma to ~5 ka for the NVP.

The Melbourne area is located on the eastern margin of the NVP (**Fig. 5.1b**). A complex history of volcanism in this relatively confined area has been inferred from previous K-Ar work (McDougall et al., 1966; Gray and McDougall, 2009), spanning 4.6 to 0.8 Ma. Two large-volume lava flows in the Melbourne area with existing K-Ar age constraints were selected for this study, and are termed Flow A and Flow B. The lavas of Flow A travelled over 40 km, filling several tributaries and river channels to the north of Melbourne and extending southwards towards the current central business district (CBD) and Port Phillip Bay areas, forming a flow front up to 8 km wide (**Fig. 5.1b**). A total of 82 outcrop and borehole samples (0 – 57.6 m depth) were collected along Flow A, and the 11 freshest samples were selected for ^{40}Ar/^{39}Ar dating. The age of Flow A is constrained at 0.72 ± 0.08 Ma (2σ) to 0.99 ± 0.12 Ma (2σ) by K-Ar dating studies (McDougall et al., 1966; Gray and McDougall, 2009).

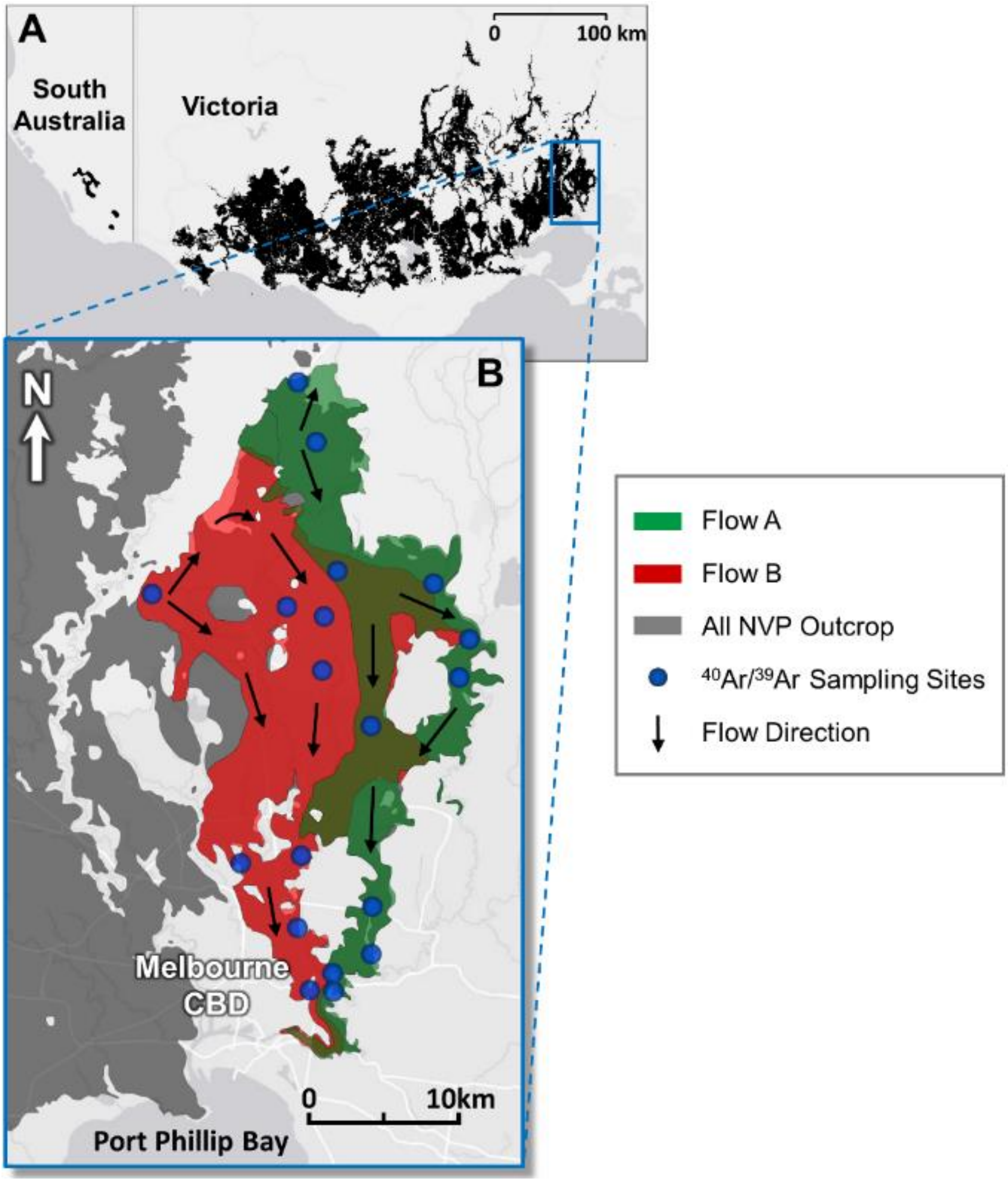

Figure 5.1: (a) Location of the Newer Volcanic Province in southeast Australia (shown in black). **(b)** Lava flows A and B in the Melbourne area. Flow directions are inferred from surface topography and borehole stratigraphy. Lighter colours are where flows A and B do not outcrop at surface.

Flow B travelled a distance of nearly 40 km, beginning in an elevated area in Melbourne's north-west and filling several river valleys, following their courses towards the current Melbourne CBD and Port Phillip Bay (**Fig. 5.1b**). A total of 132 outcrop and borehole samples (0 – 57.9 m depth) were collected along Flow B, with eight samples selected for $^{40}Ar/^{39}Ar$ dating. Previous K-Ar studies of Flow B samples suggest an age between 2.26 ± 0.14 Ma (2σ) and 2.36 ± 0.10 Ma (2σ; McDougall et al., 1966; Gray and McDougall, 2009).

5.3 Methods

5.3.1 Sample preparation

Following screening of samples in thin-section to evaluate their suitability for $^{40}Ar/^{39}Ar$ dating, groundmass separates were prepared by selecting rock fragments devoid of any visible alteration, and crushing these using a jaw crusher and ring mill. Samples were then sieved to 150-250μm and washed to remove fine particles. The groundmass material was concentrated by magnetic methods and purified via hand-picking under a binocular microscope to remove any glass, phenocrysts, xenocrysts or obviously altered fragments. Grains were treated with 5% HNO_3 at room temperature for 10 minutes in an ultrasonic bath to remove secondary carbonate, followed by 2% HF for 1 minute and deionised water for 10 minutes. Samples were weighed into foil packets and intercalated with packets of the neutron fluence monitor Alder Creek Rhyolite (ACR) Sanidine (1.18144 ± 0.00068 Ma [2σ]; Phillips et al., 2017) in a vacuum-sealed quartz glass vial. The vial was then irradiated in the CLICIT facility of the Oregon State University TRIGA reactor for either 45 minutes (irradiation cans UM#58 and UM#70) or 180 minutes (can UM#71).

5.3.2 ^{40}Ar/^{39}Ar analyses

Following irradiation, aliquants weighing ~30-70 mg were loaded into a copper sample holder and covered with a ZnS glass disc, before being placed into the sample chamber of a gas-handling system connected to a Thermo Fisher Scientific ARGUSVI mass spectrometer. Details of the ARGUSVI instrument are described in Phillips and Matchan (2013) and Phillips et al. (2017). After samples were loaded, the sample chamber and extraction line were baked at ~180°C for a minimum of 12 hours. Once an acceptable ultra-high vacuum level was reached, each aliquant was heated using a Photon Machines Fusions 10.6 CO_2 laser. As per Matchan and Phillips (2014), initial outgassing to remove loosely bound argon was achieved using four passes of the 6mm homogenised beam operated at 1% laser power (~0.25W), followed by six passes at 2% laser power (~0.49 W), and a further two passes at 1% laser power immediately before step-heating analyses. Aliquant MH70-3 was additionally outgassed with 6 passes at 3% laser power (0.74W), to test the effect of additional outgassing on low ^{40}Ar* yield samples. During the step-heating experiments, each aliquant was heated over a range of 2.5–35% laser power (~0.63 – 6.0W), with each step consisting of two passes of the beam. An alcohol-dry ice cold trap was deployed between the sample chamber and extraction line, and evolved gas was continually exposed to four NP10 SAES Zr-Al getters (4–5 minutes total gettering time), three operated at room temperature and one at ~30V (~400°C). ^{36}Ar was measured on a Compact Discrete Dynode (CDD) detector and the remaining argon isotopes were measured on Faraday detectors. All Faraday detectors were equipped with 1 x 10^{12} Ω resistors during analysis of samples included in irradiation can UM#58 (MH05, MH07, MH09, MH12 & B45B). The UM#70 & 71 samples (MH24, MH49, MH52, MH66, MH69, MH70, GRBH-01, KA7, KA13B, MO43B, WO4, YY3C & YY6) were analysed following system upgrades, with measurement of ^{39}Ar achieved using a Faraday detector equipped with a 1 x 10^{13} Ω resistor. In the case of the isotope mass fractionation step-heating experiment performed on unirradiated aliquants of MH70 (see section 3.3), both ^{38}Ar and ^{36}Ar were measured on the CDD detector via peak-hopping.

Reported argon isotope results are corrected for system blanks, mass discrimination, radioactive decay and reactor-induced interference reactions. Mass discrimination and detector bias were measured via an automated air pipette, assuming an atmospheric air ratio of 298.56 ± 0.62 (2σ; Lee et al., 2006). Line blanks were measured after every third or fourth analysis, and were typically < 0.5% of sample ^{40}Ar signals. Given the short sample irradiation durations, correction factors for the UM#58 samples were determined for K-glass and Ca-salts included in irradiation package UM#60 (OSTR CLICIT 44 hr irradiation): $(^{36}\mathrm{Ar}/^{37}\mathrm{Ar})_{\mathrm{Ca}} = (2.5713 \pm 0.0023) \times 10^{-4}$; $(^{39}\mathrm{Ar}/^{37}\mathrm{Ar})_{\mathrm{Ca}} = (6.620 \pm 0.080) \times 10^{-4}$; $(^{40}\mathrm{Ar}/^{39}\mathrm{Ar})_{\mathrm{K}} = (4.90 \pm 0.86) \times 10^{-4}$; $(^{38}\mathrm{Ar}/^{39}\mathrm{Ar})_{\mathrm{K}} = (1.2136 \pm 0.0016) \times 10^{-2}$. Updated correction factors determined for K-glass and Ca-salts included in irradiation package UM#62 (OSTR CLICIT 25 hr irradiation): $(^{36}\mathrm{Ar}/^{37}\mathrm{Ar})_{\mathrm{Ca}} = (2.5782 \pm 0.0018) \times 10^{-4}$; $(^{39}\mathrm{Ar}/^{37}\mathrm{Ar})_{\mathrm{Ca}} = (6.562 \pm 0.016) \times 10^{-4}$; $(^{38}\mathrm{Ar}/^{39}\mathrm{Ar})_{\mathrm{K}} = (1.2246 \pm 0.0028) \times 10^{-2}$ and irradiation package UM#80 (OSTR CLICIT 40 hr irradiation): $(^{40}\mathrm{Ar}/^{39}\mathrm{Ar})_{\mathrm{K}} = (3.89 \pm 0.21) \times 10^{-4}$ were applied to all other samples. Age spectra, weighted averages and inverse isochrons were calculated and plotted using the ISOPLOT software package (Ludwig, 2012). Age plateaus are defined as a minimum of three consecutive heating steps, each within 2σ error of the mean, and comprising 50% of the cumulative ^{39}Ar released (e.g., Fleck et al., 1977; McDougall and Harrison, 1999, and references therein).

5.3.3 XRF major element geochemistry

Powdered basalt samples were fused into glass beads using a mixed lithium metaborate/tetraborate flux. The samples were then analysed on a SPECTRO Xepos energy dispersive X-ray Fluorescence spectrometer at the University of Melbourne. Calibrations were constructed using a variety of internationally certified reference materials. Analyses of secondary reference materials indicate measurement accuracy of better than 1–2% for most elements; the exceptions being P_2O_5 (up to 2%) and Na_2O (up to 4%).

5.4 Results

5.4.1 Petrography and major element geochemistry

Flow A samples are essentially holocrystalline (<5% glass), with minimal alteration aside from iddingsite replacement of olivine (photomicrographs of Flow A samples are provided in **Appendix A.1**). Lavas at the base of the flow package are generally finer-grained and equigranular, with rare olivine phenocrysts (**Fig. 5.2a**), whereas olivine (up to 3mm) and plagioclase (up to 2mm) phenocrysts are common in more porphyritic lavas sampled from the upper part of the flow (**Fig. 5.2b**). Flow A samples can be classified geochemically as alkali to transitional basalts, with a general progression from alkalic to more tholeiitic compositions from the base to the top of the lava flow package (**Fig. 5.3**; the complete major element geochemical dataset is listed in **Appendix A.16)**. This unusual geochemical trend cannot be explained easily by fractionation or crustal contamination processes, raising the possibility that the lava package does not constitute a single eruption event. However, the lack of obvious inter-flow boundaries, sediments or paleosols, coupled with the gradational change from alkali to transitional compositions, indicate that this transition occurred over a very short period of time, likely reflecting tapping of successive magma batches during the same eruption cycle (e.g., McGee and Smith, 2016).

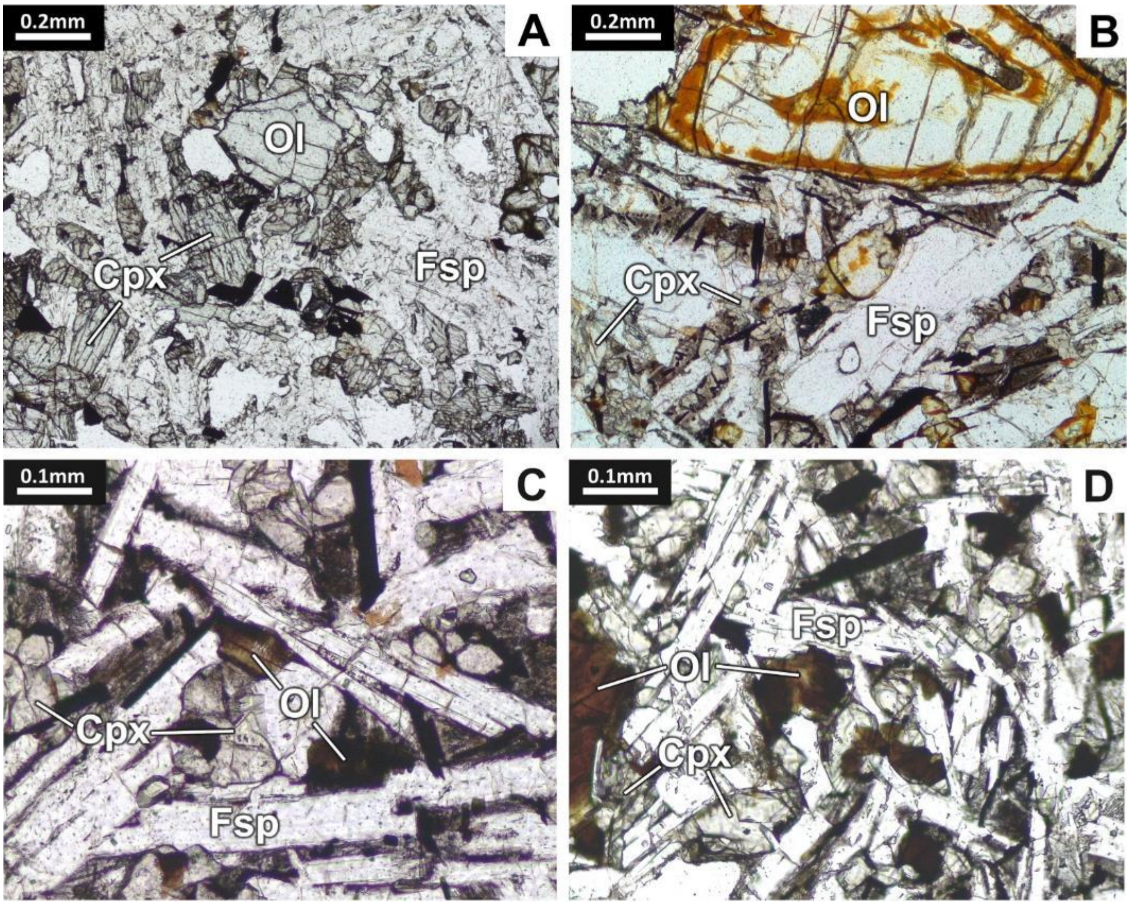

Figure. 5.2: Plane polarised images of: **(a)** Flow A sample YY3C, an alkali basalt collected from the lower part of the flow package; **(b)** Flow A sample MH70, a transitional basalt sample from the upper part of the flow package; **(c)** Flow B transitional basalt sample MH69 collected towards the top of the flow and; **(d)** Flow B sample MH52, also sampled near the top of the flow. Note the freshness of groundmass feldspar (Fsp) and clinopyroxene (Cpx), in all samples, and iddingsite alteration of olivine (Ol) in samples MH70, MH69 and MH52.

All Flow B samples are olivine-phyric, with clinopyroxene phenocrysts common in samples collected from the middle section of the flow. Samples from this section exhibit an ophitic texture, with common green-brown devitrified glass lining pore spaces. Samples from the base and upper parts of the flow are holocrystalline, with minor iddingsite alteration of olivine phenocrysts and fresh groundmass phases (**Figs. 5.2c&d;** photomicrographs of Flow B samples are provided in **Appendix A.1**). Lavas of Flow B show only minor, non-systematic variations in composition, and plot close to the boundary line between alkali basalt and tholeiite on a total alkali versus silica diagram (**Fig. 5.3**).

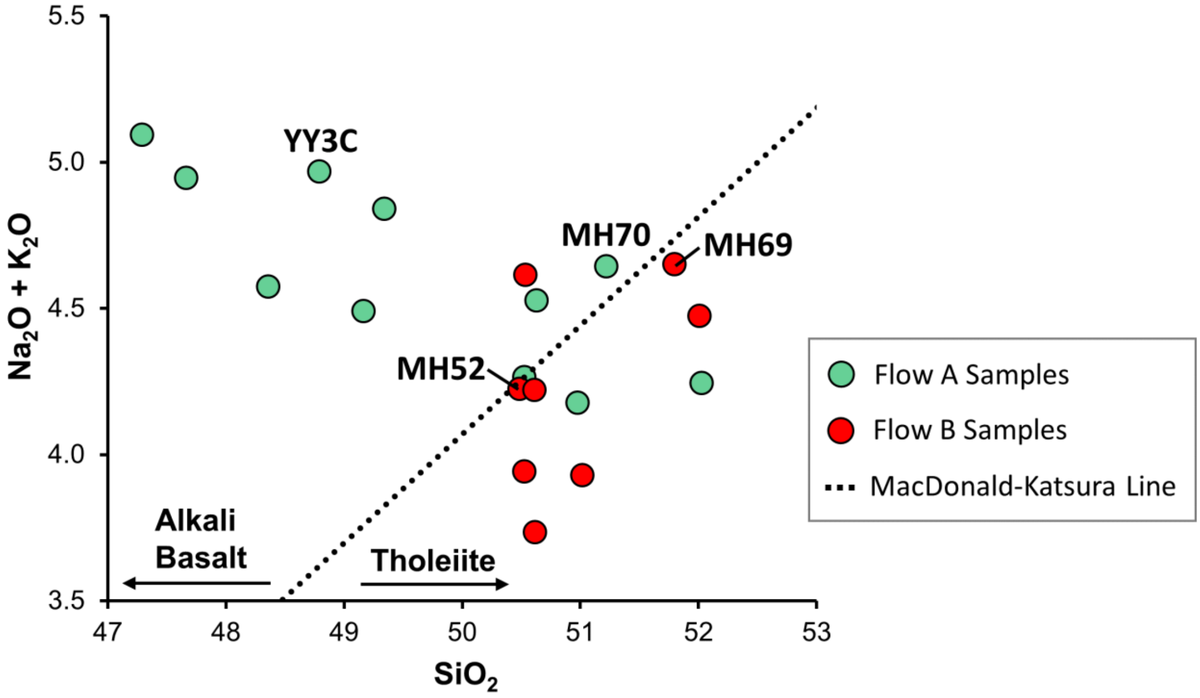

Figure 5.3: Total alkalis versus silica diagram for $^{40}Ar/^{39}Ar$ samples included in this study. The alkali basalt/tholeiite division is based on Macdonald and Katsura (1964). Note the transition of Flow A samples from alkali (base of flow) to tholeiitic basalt (top of flow), in the same lava package. XRF results are reported in **Appendix A.16**.

5.4.2 ^{40}Ar/^{39}Ar results

Unless otherwise stated, uncertainties in age determinations are quoted at the two-sigma level. The full ^{40}Ar/^{39}Ar dataset is reported in **Appendices A.3 and A.4**. Individual age spectra and inverse isochron diagrams for Flow A and Flow B samples are provided in **Appendix A.1**.

5.4.2.1 Flow A

Multiple aliquants of two samples from Flow A (WW1A, YY3C) exhibit ^{40}Ar/^{39}Ar age spectra with statistically significant plateau ages (see **Table 5.1**). The weighted mean ^{40}Ar*/^{39}Ar value for the plateau steps from all aliquants of WW1A equates to an age of 0.8089 ± 0.0021 Ma (95% confidence interval [CI]; MSWD = 2.5, p = 0.001), and a composite isochron of all plateau steps of this sample gives an atmospheric $(^{40}\mathrm{Ar}/^{36}\mathrm{Ar})_i$ value (296.8 ± 1.4 (95% CI; MSWD=2.4, p=0.002) and an age of 0.8137 ± 0.0039 Ma. Only two of the WW1A individual plateau ages are within two-sigma uncertainty (Table 1; **Appendix A.1**). The weighted mean ^{40}Ar*/^{39}Ar value of the highly concordant plateau-forming steps of three aliquants of YY3C gives an age of 0.8038 ± 0.0017 Ma (2σ; MSWD=1.7, p=0.036; **Table 5.1**), and an isochron including these steps indicates an atmospheric $(^{40}\mathrm{Ar}/^{36}\mathrm{Ar})_i$ value of 298.0 ± 1.3 (95% CI; MSWD=1.7, p=0.047); **Figs. 5.4a,b**) and an age of 0.8049 ± 0.0046 Ma.

Table 5.1. $^{40}Ar/^{39}Ar$ results for two concordant samples from Flow A

Sample	**Aliquant**	**Plateau Age[1] (Ma, ± 2σ)**	**% Total ^{39}Ar**	**MSWD**	**P**	**Combined Plateau Age[1] (Ma, ± 2σ)**	**MSWD**	**P**	**Combined Isochron Age[1] (Ma; ± 95% CI)**	**$(^{40}Ar/^{36}Ar)_i$ (± 95% CI)**	**MSWD**	**P**
WW1A	WW1A-1	0.8129 ± 0.0022	90.3	0.86	0.51	0.8089 ± 0.0021	2.5	0.001	0.8137 ± 0.0039	296.8 ± 1.4	2.4	0.002
	WW1A-2	0.8098 ± 0.0025	71.3	0.46	0.71							
	WW1A-3	0.8058 ± 0.0019	91.3	0.54	0.75							
YY3C	YY3C-1	0.8029 ± 0.0022	100	1.6	0.11	**0.8038 ± 0.0017**	1.7	0.036	**0.8049 ± 0.0046**	**298.0± 1.3**	1.7	0.047
	YY3C-2	0.8051 ± 0.0020	98.3	2.2	0.040							
	YY3C-3	0.8031 ± 0.0022	51.7	0.40	0.67							

[1] Ages calculated relative to an Alder Creek Rhyolite sanidine age of 1.1814 ± 0.006 (2σ; Phillips et al., 2017). The combined plateau age of YY3C is calculated from a weighted average of the $^{40}Ar^{*}/^{39}Ar$ values of all plateau steps, and indicates the eruption age of Flow A. Note that the combined isochron age for YY3C is indistinguishable from the combined plateau age. The corresponding $(^{40}Ar/^{36}Ar)_i$ value is within error of air (298.56 ± 0.62; Lee et al., 2006). Full $^{40}Ar/^{39}Ar$ results are reported in **Appendix A.3**.

Data from the remaining nine Flow A samples produced disturbed age spectra, and are highly scattered in inverse isochron space (e.g., aliquant MH70-2, **Figs. 5.4a,b; Table 2**). As illustrated in **Fig. 5.4b**, all nine discordant samples are characterised by rotated data arrays that yield sub-atmospheric (^{40}Ar/^{36}Ar)$_i$ ratios and older apparent ages (e.g., MH70-2: (^{40}Ar/^{36}Ar)$_i$ = 280.8 ± 0.4; t = 1.65 ± 0.25 Ma). Four of the nine discordant samples (MH09, MH24, MH66, and MH70) possess high ^{36}Ar contents (three to four times higher than in other Flow A samples) and correspondingly low ^{40}Ar* proportions (<10% of total ^{40}Ar), with data clustered near the ^{36}Ar/^{40}Ar axis in inverse isochron space (e.g., **Fig. 5.4b**). Overall, there is a correlation between older inverse isochron ages, low ^{40}Ar* yields, sub-atmospheric (^{40}Ar/^{36}Ar)$_i$ values and younger total-gas ages in the Flow A samples (**Fig. 5.4c**; **Table 5.2**; **Appendix A.1**).

5.4.2.2 Flow B

In contrast to Flow A, all samples from Flow B show at least minor discordance in their ^{40}Ar/^{39}Ar step-heating spectra (**Fig. 5.4d**; **Table 5.2**; **Appendix A.1**), complicating accurate age determination. However, concordant high-temperature (high-T) heating steps from three aliquants (KA7-1, KA13B-1 & MH69-1; **Table 5.3**) have elevated radiogenic yields (^{40}Ar* >30% of total ^{40}Ar), and atmospheric (^{40}Ar/^{36}Ar)$_i$ ratios. The weighted mean of the inverse isochron ages constrained for these high-T steps is 2.309 ± 0.009 Ma (2σ). As for Flow A, Flow B samples with severely disturbed age spectra are characterised by lower radiogenic ^{40}Ar yields (^{40}Ar* <25% of total ^{40}Ar), greater rotation of data arrays in inverse isochron space, and older apparent isochron ages (e.g., MH52-2; **Figs. 5.4e,f**).

Table 5.2. Summary of ^{40}Ar/^{39}Ar inverse isochron results for Flow A and B samples

Flow A

Sample	Lat.	Long.	Aliquant	^{40}Ar* Yield (%)	Inverse Isochron Age[1] (Ma, ± 95% CI)	(^{40}Ar/^{36}Ar)$_i$ (± 95% CI)	Total-Gas Age[1] (Ma, ±2σ)
MH66	-37.546	145.0082	MH66-1	1.7	1.29 ± 0.28	285.9 ± 5.1	0.362 ± 0.007
			MH66-2	0.7	1.45 ± 0.28	281.1 ± 5.6	0.156 ± 0.008
MH70	-37.470	144.9925	MH70-1	2.6	1.33 ± 0.25	288.4 ± 3.9	0.577 ± 0.071
			MH70-2	1.1	1.65 ± 0.25	280.8 ± 4.0	0.262 ± 0.072
			MH70-3	5.8	1.2 ± 1.4	292 ± 16	0.931 ± 0.049
MH24	-37.744	145.0343	MH24-1	5.5	0.988 ± 0.071	290.6 ± 2.7	0.672 ± 0.046
			MH24-2	4.4	1.02 ± 0.11	287.4 ± 4.7	0.547 ± 0.019
			MH24-3	5.3	1.03 ± 0.15	288.1 ± 6.6	0.611 ± 0.019
MH09	-	145.0333	MH09-1	7.3	0.90 ± 0.14	295.6 ± 5.3	0.796 ± 0.030
MO43B	-37.609	145.0993	MO43B-1	22.6	0.817 ± 0.032	296.3 ± 3.6	0.802 ± 0.015
			MO43B-2	23.4	0.774 ± 0.024	297.6 ± 2.8	0.767 ± 0.013
MH12	-37.772	145.0336	MH12-1	26.8	0.810 ± 0.016	298.9 ± 2.6	0.814 ± 0.014
			MH12-2	22.9	0.797 ± 0.017	300.8 ± 2.4	0.820 ± 0.014
WW1A	-37.435	144.9789	WW1A-1	30.2	0.8185 ± 0.0034	295.9 ± 1.2	0.801 ± 0.013
			WW1A-2	28.1	0.8152 ± 0.0032	296.11 ± 0.77	0.798 ± 0.010
			WW1A-3	30.6	0.8096 ± 0.0024	296.83 ± 0.66	0.799 ± 0.009
YY6	-37.587	145.1069	YY6-1	38.5	0.803 ± 0.013	296.7 ± 2.7	0.794 ± 0.009
			YY6-2	36.1	0.796 ± 0.016	297.5 ± 3.6	0.789 ± 0.008
MH05	-	145.0047	MH05-1	38.3	0.949 ± 0.091	284 ± 20	0.879 ± 0.016
YY3C	-37.554	145.0801	YY3C-1	43.6	0.8063 ± 0.0060	297.4 ± 1.8	0.802 ± 0.007
			YY3C-2	42.9	0.8111 ± 0.0080	296.3 ± 2.1	0.802 ± 0.006
			YY3C-3	40.3	0.7997 ± 0.0067	298.7 ± 1.6	0.800 ± 0.005
MH07	-	145.0053	MH07-1	43.9	0.795 ± 0.034	310 ± 10	0.836 ± 0.008

Flow B

Sample	Lat.	Long.	Aliquant	^{40}Ar* Yield (%)	Inverse Isochron Age[1] (Ma, ± 95% CI)	(^{40}Ar/^{36}Ar)$_i$ (± 95% CI)	Total-Gas Age[1] (Ma, ±2σ)
MH49	-	144.9785	MH49-1	13.0	2.85 ± 0.25	288.3 ± 6.0	2.29 ± 0.08
MH52	-37.714	144.9811	MH52-1	14.8	2.48 ± 0.13	293.5 ± 3.3	2.26 ±0 .05
			MH52-2	12.5	2.69 ± 0.16	284.9 ± 4.1	2.04 ± 0.05
			MH52-3	16.5	2.40 ± 0.21	296.2 ± 5.9	2.32 ± 0.02
GRBH01	-	144.9362	GRBH01-	19.6	2.409 ± 0.083	294.3 ± 4.0	2.28 ± 0.04
WO4	-	144.9969	WO4-1	24.7	2.370 ± 0.067	290.7 ± 4.2	2.18 ± 0.03
MH69	-37.560	144.8698	MH69-1	30.1	2.39 ± 0.10	294.8 ± 5.9	2.31 ± 0.03
			MH69-2	30.2	2.441 ± 0.076	290.3 ± 4.8	2.29 ± 0.02
KA7	-	144.9983	KA7-1	52.2	2.338 ± 0.059	298.0 ± 7.9	2.33 ± 0.01
KA13B	-37.568	144.9706	KA13B-1	60.6	2.350 ± 0.047	297.6 ± 8.0	2.33 ± 0.01
			KA13B-2	65.2	2.375 ± 0.074	293 ± 19	2.35 ± 0.01
BH45B	-37.794	144.9878	BH45B-1	72.8	2.153 ± 0.098	350 ± 27	2.30 ± 0.01
			BH45B-2	69.7	2.271 ± 0.090	296 ± 26	2.27 ± 0.01

[1]Ages calculated relative to an Alder Creek Rhyolite sanidine age of 1.1814 ± 0.006 (2σ; Phillips et al., 2017).

Samples described in detail in the text are highlighted in green (high ^{40}Ar* yield) and red (low ^{40}Ar* yield).

Apparent outliers highlighted in orange give (^{40}Ar/^{36}Ar)$_i$ values in excess of the atmospheric value (**Fig. 4**).

Full ^{40}Ar/^{39}Ar results are reported in **Appendices A.3 and A.4**.

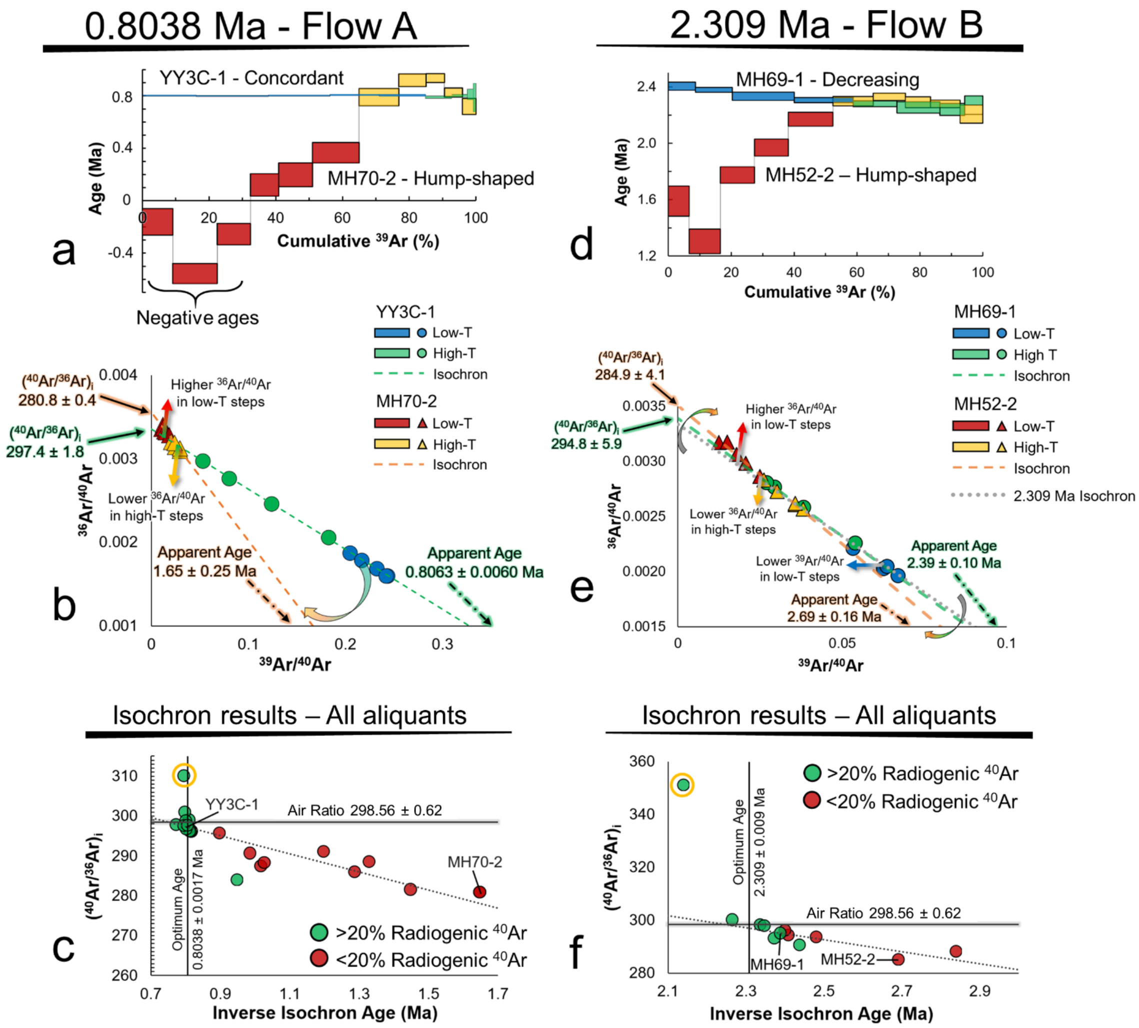

Figure 5.4: (**a**) Age spectra of typical concordant (YY3C-1) and discordant (MH70-2) aliquants from Flow A. Note the general staircase pattern and negative apparent ages in low-temperature steps of sample MH70-1, indicating mass fractionation. (**b**) Inverse isochron plot of YY3C-1 and MH70-2 Ar isotope data, showing clockwise rotation of the MH70-2 data array and corresponding old apparent age and sub-atmospheric (^{40}Ar/^{36}Ar)$_i$ value. The yellow and green apparent age arrows point to the x-axis at y = 0. **(c)** Inverse isochron apparent age and (^{40}Ar/^{36}Ar)$_i$ results for aliquants of flow A samples, showing a general correlation between older apparent ages and lower (^{40}Ar/^{36}Ar)$_i$ values, particularly for low-^{40}Ar* samples. The horizontal and vertical solid lines mark the

atmospheric $^{40}Ar/^{36}Ar$ composition (Lee et al., 2006) and the preferred eruption age of 0.8038 Ma, respectively; the dashed line indicates the correlation between older apparent ages and lower $(^{40}Ar/^{36}Ar)_i$ ratios. (**d**) Age spectrum for a more concordant aliquant (MH69-1; 30.1% $^{40}Ar^*$) from Flow B, plotted alongside a more discordant age spectrum (MH52-2; 12.5% $^{40}Ar^*$). (**e**) Inverse isochron diagram for samples MH69-1 and MH52-2 from Flow B; MH52-2 exhibits a sub-atmospheric $(^{40}Ar/^{36}Ar)_i$ value, and an apparent age that is older than the interpreted eruption age, indicating a clockwise rotation of the data array. The yellow and green apparent age arrows point to the x-axis at y = 0 (**f**) Inverse isochron apparent age and $(^{40}Ar/^{36}Ar)_i$ results plotted for all aliquants of Flow B samples. Also shown are horizontal and vertical solid lines marking the $^{40}Ar/^{36}Ar$ atmospheric composition (Lee et al., 2006) and the preferred eruption age of 2.309 Ma, respectively. Outliers circled in orange are highlighted in **Table 5.2**.

Table 5.3. Summary of preferred isochron ages and $(^{40}Ar/^{36}Ar)_i$ values for high $^{40}Ar^*$ samples from Flow B.

Sample	Aliquant	High % $^{40}Ar^*$ Steps	Preferred Isochron Age[1] (Ma, ± 95% CI)	Cumulative ^{39}Ar (%)	$(^{40}Ar/^{36}Ar)_i$ (± 95% CI)	MSWD	P
KA7	KA7-1	5 to 8	2.294 ± 0.080	44.82	299.8 ± 8.4	3.4	0.034
KA13B	KA13B-1	5 to 9	2.3090 ± 0.0097	40.94	298.8 ± 1.6	1.17	0.32
MH69	MH69-1	5 to 8	2.303 ± 0.043	41.27	297.1 ± 1.9	0.56	0.57

[1] Ages calculated relative to an Alder Creek Rhyolite sanidine age of 1.1814 ± 0.006 (2σ; Phillips et al., 2017). Full $^{40}Ar/^{39}Ar$ results are reported in **Appendix A.4**.

5.4.3 Results from step-heating study of unirradiated sample MH70 (Flow A)

To investigate the possibility of experimentally induced mass-fractionation, three aliquants of unirradiated groundmass material from sample MH70 were step-heated to monitor ^{38}Ar/^{36}Ar ratios (**Fig. 5.5**; **Appendix A.15**). All aliquants show a general increase in ^{38}Ar/^{36}Ar values with increasing laser power, from 0.182–0.187 to 0.188–0.192 over the first 90% of ^{38}Ar released, consistent with mass-dependent fractionation. A 4% difference in ^{38}Ar/^{36}Ar ratios (0.185–0.193) corresponds to a ca. 8% difference in ^{40}Ar/^{36}Ar ratios, assuming Rayleigh mass fractionation and an m$^{-½}$ dependence of the fractionation factor, equating to a range of ca. 286 – 310 in ^{40}Ar/^{36}Ar values, assuming fractionation from an atmospheric composition.

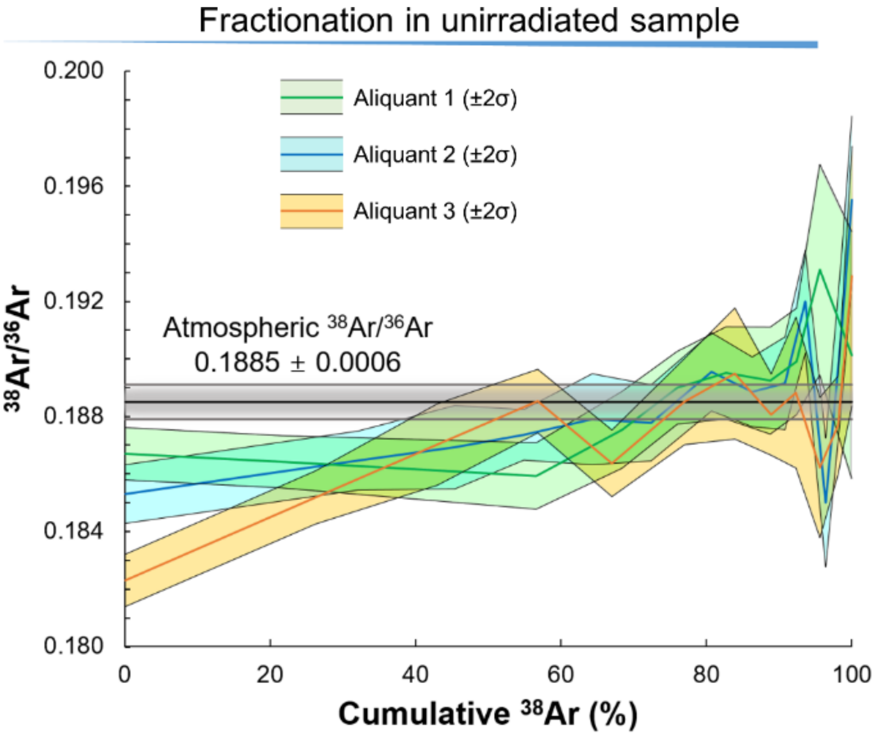

Figure 5.5: ^{38}Ar/^{36}Ar step-heating results of three unirradiated aliquants of sample MH70 from Flow A. The grey bar indicates the atmospheric ^{38}Ar/^{36}Ar ratio (0.1885 ± 0.0006 [2σ]; Lee et al. (2006)Lee et al. (2006)). Note the general increase in ^{38}Ar/^{36}Ar ratios with increasing temperature, consistent with mass-dependent fractionation.

5.5 Discussion

5.5.1 Timing of eruption events

5.5.1.1 Flow A

The two Flow A samples for which plateau ages can be calculated, WW1A and YY3C, give composite weighted mean ^{40}Ar*/^{39}Ar ages that are marginally distinct at the two-sigma level; 0.8089 ± 0.0021 Ma (WW1A) and 0.8038 ± 0.0017 Ma (YY3C). Sample WW1A, which yields the older, less statistically robust weighted mean ^{40}Ar*/^{39}Ar age, also yields an older composite inverse isochron age (0.8137 ± 0.0039 Ma for WW1A versus 0.8049 ± 0.0046 Ma for YY3C). As slightly older inverse isochron ages are observed to be associated with greater isotopic disturbance and rotation of data arrays in inverse isochron space, the YY3C age of 0.8038 ± 0.0017 Ma (the weighted mean ^{40}Ar*/^{39}Ar age of YY3C) is preferred as the eruption age for Flow A. This ^{40}Ar/^{39}Ar age is consistent with previous K-Ar studies (0.72 ± 0.08 to 0.99 ± 0.12 Ma [2σ]; McDougall et al., 1966; Gray and McDougall, 2009), but represents a twentyfold improvement in precision.

The lack of any consistent trend in total-gas ages for samples from different stratigraphic positions within the flow package (**Table 5.2**) is consistent with a negligible time gap between the initial alkali basalt magma pulse (MH07, MH12, MO43B & YY6), transitional magmatism (MH05, MH24, YY3C & WW1A) and final tholeiite pulse (MH09, MH66 & MH70). As only samples YY3C and WW1A provided reasonably robust eruption ages, the ^{40}Ar/^{39}Ar data alone do not exclude slight differences in age; however, the lack of erosional surfaces/paleosol development supports an insignificant time gap between alkalic and tholeiitic magmatism, such that all lavas in the Flow A package are regarded as equivalent in age.

5.5.1.2 Flow B

A weighted mean of the preferred isochron ages (excluding the more discordant steps) for three of the most concordant aliquants with the highest ^{40}Ar* contents (KA7-1, KA13B-1 & MH69-1) provides the best estimate for the eruption age of Flow B, at 2.309 ± 0.009 Ma (95% CI). These three isochron results exclude low-temperature (low-T) discordant heating steps (see **Appendix A.1**), and are preferred because they are characterised by atmospheric (^{40}Ar/^{36}Ar)$_i$ intercepts and indistinguishable ages (**Table 5.3**). This is in agreement with published K-Ar ages (2.18 ± 0.22 to 2.36 ± 0.10 Ma (2σ; McDougall et al., 1966; Gray and McDougall, 2009)).

5.5.2 Possible causes of discordant ^{40}Ar/^{39}Ar spectra

Argon isotopic data obtained from undisturbed basaltic samples should ideally yield flat age spectra (e.g., YY3C-1 in **Fig. 5.4a**). The disturbed age spectra from samples with higher ^{40}Ar* contents (>25% of total ^{40}Ar) from both Flow A and B generally decrease with increasing temperature, and exhibit anomalously old apparent ages in low-T steps, with ages becoming younger in later steps, sometimes approaching the eruption age (e.g., MH69-1; **Fig. 5.4d**). Total-gas ages for these samples are generally within error of the eruption age, but in some cases are either slightly older (e.g., MH05-1) or younger (e.g., B45-2; **Table 5.2**). ^{39}Ar recoil loss/redistribution, from high-K, early outgassing phases into low-K, late outgassing phases, with some ^{39}Ar lost from the system, might explain the decreasing pattern of step-heating spectra (e.g., Jourdan and Renne, 2014). Although there is no conclusive evidence for recoil being the dominant cause of disturbance in these samples, older apparent ages in low-T heating steps have commonly been attributed to ^{39}Ar recoil in basaltic samples (e.g., Koppers et al., 2000; Koppers et al., 2003) and it is difficult to explain the older apparent ages in low-T heating steps by any other mechanism. Extraneous argon contamination is a possibility, but it is unlikely that this process would only affect low-T steps. Note that ^{37}Ar recoil (e.g., Hall, 2014) is not considered to be significant, given the minor corrections required for ^{37}Ar$_{Ca}$ isotopic interferences.

Data from the handful of samples with low ^{40}Ar* contents (<25% of total ^{40}Ar), from both Flow A and Flow B, are invariably discordant, showing similar age spectra patterns. Data from all low-^{40}Ar* samples exhibit younger apparent ages in low-T heating steps and older apparent ages in high-T steps (e.g., MH70-2 & MH52-2; **Figs. 5.4a&d**). Importantly, in the case of the younger of the two flows (Flow A), some samples give *negative* apparent ages in low-T steps (e.g., MH70-2; **Fig. 5.4a**); in addition, for all low-^{40}Ar* samples, the oldest apparent ages are older than the interpreted eruption age (e.g., MH70-2 & MH52-2; **Figs. 5.4a&d; Appendix A.1**). The total-gas ages of samples with the lowest ^{40}Ar* levels (MH09, MH24, MH66, MH70 & MH52) are generally younger than the inferred eruption ages, suggesting either loss of ^{40}Ar and/or gain of ^{39}Ar or ^{36}Ar (**Table 5.2**; see discussion below).

The possible causes of the discordance in low-^{40}Ar* samples include ^{40}Ar* loss, complex ^{39}Ar recoil into low-retention phases, isobaric interferences and mass-dependent fractionation. The negative apparent ages in the low-T steps of some Flow A aliquants (e.g., MH70-2; **Fig. 5.4a**) cannot be caused by ^{40}Ar* loss or ^{39}Ar recoil loss/redistribution, as neither mechanism can generate ^{40}Ar*/^{39}Ar values less than zero. The most negative apparent age is -1.059 ± 0.167 Ma (2σ), calculated for heating step MH66-2a (**Appendix A.3**). Negative ages are most likely due to an overestimation of the ^{36}Ar content in low temperature steps, which would lead to underestimation of ^{40}Ar*. Elevated ^{36}Ar signals could be caused by isobaric interferences or mass-dependent fractionation processes. Assuming an eruption age of 0.804 Ma, the magnitude of the isobaric interference (e.g., from ^{36}Cl) required to generate an age of -1.059 Ma is 4.7% of the total mass 36 signal measured. However, there is little evidence of chlorine or hydrocarbon contamination in these samples. For example, signals at masses 37 and 39 in unirradiated aliquants of sample MH70 are essentially indistinguishable from analytical blanks (**Appendix A.15**). Furthermore, experiments on the high-resolution HELIX-MC *Plus*, reported in Phillips et al. (2017), showed undetectable contributions to mass 36 from chlorine or hydrocarbon compounds for analyses of MD-2 biotite (~3700ppm chlorine; Baksi et al., 1996). Therefore, it seems unlikely that isobaric interferences have had a material effect on the results reported here.

Mass-fractionation during crystallisation of a basaltic magma (e.g., Kaneoka, 1980) has been proposed as the cause for sub-atmospheric ^{40}Ar/^{36}Ar ratios observed in some lavas (e.g., Matsumoto and Kobayashi, 1995; Ozawa et al., 2006). While this could explain the anomalously young (and negative) ages found for low-T heating steps of low-^{40}Ar* yield samples, the anomalously old apparent ages found for later heating steps remain problematic.

Experimentally induced mass-dependent fractionation, whereby ^{36}Ar is released preferentially, resulting in sub-atmospheric ^{40}Ar/^{36}Ar compositions for low-T heating steps and younger (including negative) apparent ages (where an atmospheric trapped component is assumed) is an alternative explanation for the observed disturbance (e.g., Trieloff et al., 2005). This process is predicted to have a more significant impact on age spectra for samples with low ^{40}Ar* yields where calculation of the (^{40}Ar*/^{39}Ar) ratio is extremely sensitive to the correction for trapped argon. The argon isotopic measurements conducted on unirradiated sample MH70 (**Fig. 5.5; Appendix A.15**) demonstrate that mass-dependent isotopic fractionation can occur during step-heating of basaltic groundmass material. With this data in mind, we calculated the ^{40}Ar/^{36}Ar composition of non-radiogenic argon released for each heating step of sample MH70, assuming an eruption age of 0.804 Ma and an atmospheric trapped composition. Calculated ^{40}Ar/^{36}Ar values range from 286.0 (heating step MH70-2b) to 303.8 (heating step MH70-3c), with all heating steps falling within the range of values predicted from the ^{38}Ar/^{36}Ar step-heating experiments on the same sample (ca. 286 - 310).

While not excluding other possible causes of isotopic disturbances (e.g., ^{40}Ar* loss), the above calculations demonstrate that mass-fractionation alone could explain the argon isotopic disturbances in low-^{40}Ar* samples from Flow A. In contrast, samples with high ^{40}Ar* yields did not appear to be significantly affected by fractionation, which might suggest that the severity of fractionation depends on the microscopic architecture of individual samples. It is well known that constricted pathways for gas transport can lead to fractionation (e.g., Baksi and Farrar, 1973). If molecular flow is less constricted in samples with high ^{40}Ar* content, then fractionation might be less of a factor.

Petrographic thin sections of samples with variable ^{40}Ar* yields were re-examined to determine possible links between petrographic features and air contamination. Samples with low ^{40}Ar* yields might be expected to show more alteration features, or a microscopic architecture characterised by a high surface-to-volume ratio, resulting in increased adsorption of atmospheric argon and more constricted pathways for gas release upon heating. However, there is no clear textural distinction between samples with low and high ^{40}Ar* yields (e.g., MH52, **Fig. 5.2d**; MH69, **Fig. 5.2c**). Therefore, petrographic criteria alone do not appear effective at predicting whether basaltic samples are good candidates for groundmass ^{40}Ar/^{39}Ar dating (see **Appendix A.1** for petrographic images of samples).

5.5.3 Insights from inverse isochron diagrams

Argon isotopic data obtained from ‘undisturbed’ basaltic samples should ideally plot along a straight line in inverse isochron space. Because the impacts of common causes of disturbance are non-uniform across a step-heating experiment, the dominant effect in inverse isochron space is rotation of data arrays. Although it may not be possible to extract an acceptable eruption age from discordant data, careful examination of inverse isochrons can provide insight into the distribution of argon within a sample and the most likely type/s of disturbance, as well as placing some constraints on the timing of crystallisation.

For samples with high ^{40}Ar* proportions (>25% of total ^{40}Ar) that exhibit descending age spectra, ^{39}Ar/^{40}Ar values in low-T heating steps are slightly lower than predicted from the ideal isochron, and high-T heating steps tend to converge on the ideal isochron (e.g., MH69-1; **Fig 5.4e**). For samples with low ^{40}Ar* proportions (<25% of total ^{40}Ar), ^{36}Ar/^{40}Ar values for low-T heating steps are elevated compared to the ideal isochron, likely due to mass-dependent fractionation, whereas values for later heating steps are generally slightly lower than the ideal isochron (e.g., MH70-2 & MH52-2; **Figs. 5.4b&e**). Because the relative displacement of data from low-T and high-T steps is contrary for both high- and low-^{40}Ar* samples, the dominant effect is a clockwise rotation of data relative to the ideal isochron, leading to sub-atmospheric $(^{40}\text{Ar}/^{36}\text{Ar})_i$ values and isochron ages older than the true eruption ages (**Figs. 5.4c&f; Table 2**).

5.5.4 Modelling possible causes of argon isotopic disturbance

To further evaluate the possible effects of ^{39}Ar recoil, ^{40}Ar* loss and ^{40}Ar/^{36}Ar mass-dependent fractionation on ^{40}Ar/^{39}Ar step-heating data, we used a schematic model to illustrate the impact of these mechanisms on inverse isochrons and age spectra. The model is based on a 0.8 Ma lava flow with an atmospheric trapped ^{40}Ar/^{36}Ar composition, and no extraneous argon (**Figs. 5.6&7**). The modelling was used to evaluate the impact of ^{39}Ar recoil loss on samples with both high (**Figs. 5.6a,b**) and low (**Figs. 5.6a,c**) ^{40}Ar* proportions (40% and 10% respectively). ^{40}Ar* loss (**Fig. 5.7a**) and mass-dependent fractionation (**Fig. 5.7b**) were modelled for low-^{40}Ar* sample (10% ^{40}Ar*), as these mechanisms are likely to have a more significant impact on such samples. Lower ^{40}Ar* contents magnify the impact of ^{40}Ar/^{36}Ar fractionation, and are often linked with alteration, the major cause of ^{40}Ar* loss in basaltic rocks (e.g., Koppers et al., 2000; Baksi, 2007). ^{40}Ar* loss is presumed to have a greater effect on low-retention sites and early outgassing phases. Mass-dependent fractionation is modelled to induce a lower measured non-radiogenic $^{40}Ar/^{36}Ar$ ratio for low-T heating steps (where ^{36}Ar is preferentially outgassed), and a higher non-radiogenic $^{40}Ar/^{36}Ar$ ratio in high-T steps (due to elevated residual ^{40}Ar levels). For simplicity, modelling considers only fractionation between ^{40}Ar and ^{36}Ar, because the non-radiogenic trapped component appears to be the most affected.

5.5.4.1 Modelling results

^{39}Ar recoil modelling for a sample with a high proportion of $^{40}Ar^*$ results in a clockwise rotation of the inverse isochron array (**Fig. 5.6b**), producing erroneously old apparent ages and sub-atmospheric $(^{40}Ar/^{36}Ar)_i$ values. Conversely, rotation of the isochron is anti-clockwise for samples with low $^{40}Ar^*$ yields (**Fig. 5.6c**), producing erroneously young apparent ages and supra-atmospheric $(^{40}Ar/^{36}Ar)_i$ values. Modelling of $^{40}Ar^*$ loss predicts younger apparent ages for low-T heating steps, and a clockwise rotation of the inverse isochron array (**Fig. 5.7a**). Mass-dependent fractionation produces a similar result, but with higher apparent $^{40}Ar^*/^{39}Ar$ ratios in high-T steps (**Fig. 5.7b**). Mass fractionation modelling of samples with even lower $^{40}Ar^*$ contents (<10% of total ^{40}Ar) would produce negative apparent ages for low-T steps, similar to that observed in some Flow A samples.

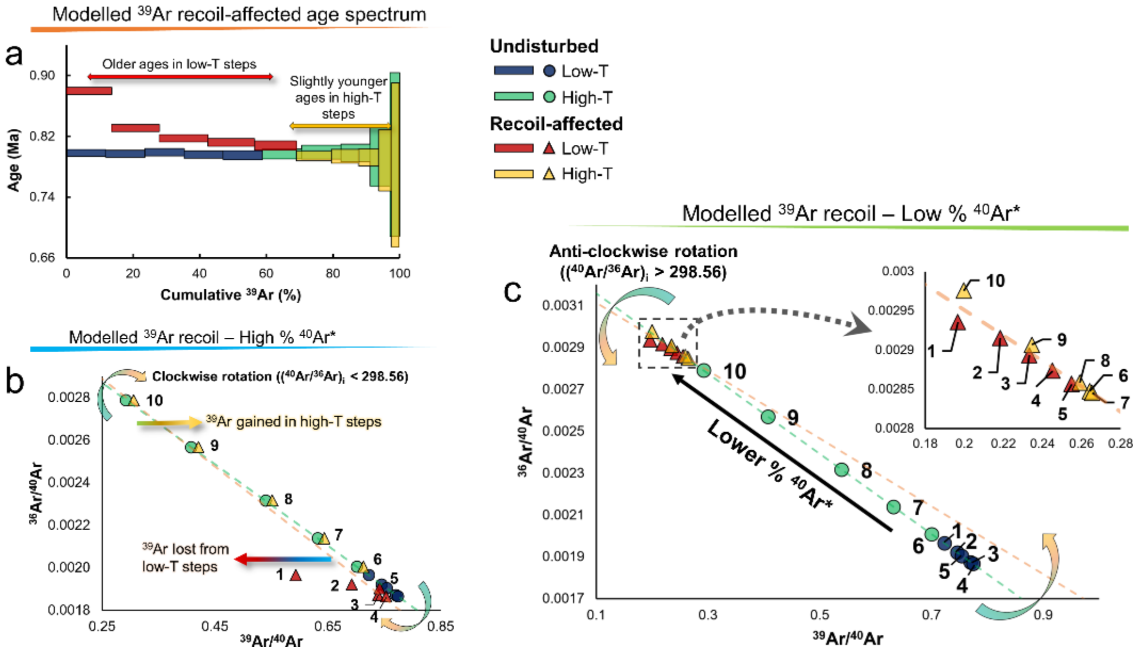

Figure 5.6: (**a**) Modelled step-heating spectrum for a ^{39}Ar recoil-affected sample (step heating spectra for both low- and high-^{40}Ar* recoil-affected samples are identical). **(b)** Inverse isochron diagram for a with high-^{40}Ar* sample (40% total ^{40}Ar*) plotted against a high-^{40}Ar* undisturbed sample (no ^{39}Ar recoil) for comparison. The results for the high-^{40}Ar* model match up well with those of high-^{40}Ar* aliquants of Flow B (see MH69-1 in **Fig. 5.4e**), with ^{39}Ar loss resulting in lower ^{39}Ar/^{40}Ar values in the low-T steps. (**c**) Inverse isochron diagram for a ^{39}Ar recoil-affected low-^{40}Ar* sample (10% total ^{40}Ar*) plotted against an undisturbed (no ^{39}Ar recoil) low-^{40}Ar* sample. Note the opposite rotation of the inverse isochrons for high-and low-^{40}Ar* content models. Step numbers are shown in bold.

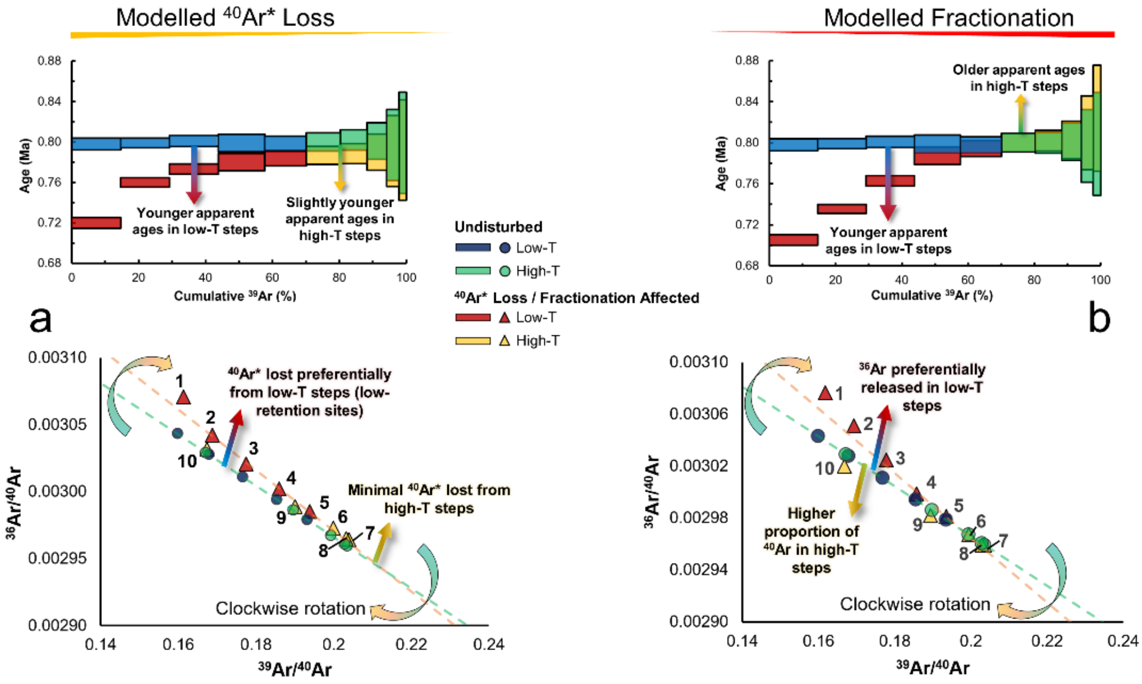

Figure 5.7: (a) Modelled ^{40}Ar* loss and (**b**) mass fractionation effects shown for a low-^{40}Ar* sample (10% total ^{40}Ar*) versus an undisturbed sample. The rotation of the inverse isochron is clockwise in both models, leading to sub- atmospheric (^{40}Ar/^{36}Ar)$_i$ ratios and anomalously old apparent ages. The fractionation model (**b**) gives results similar to the low-^{40}Ar* discordant samples from Flows A and B (e.g., MH70-2 & MH52-2 in **Fig. 5.4**). Step numbers are shown in bold.

Although all modelling was carried out assuming an atmospheric trapped argon composition, the resulting (^{40}Ar/^{36}Ar)$_i$ values were either below or above the atmospheric value, depending on both the mechanism of isotopic disturbance *and* the proportion of non-radiogenic argon. These results suggest that a non-atmospheric (^{40}Ar/^{36}Ar)$_i$ ratio could serve as an indicator of isotopic disturbance, with the degree of deviation from the atmospheric value reflecting the severity of discordance, and the direction of isochron rotation. It follows that the measured (^{40}Ar/^{36}Ar)$_i$ ratio will not provide an estimate of the true trapped non-radiogenic argon composition of basaltic samples; except in special cases – for example, where extraneous argon is shown to be present and no redistribution of argon has occurred. In all other cases, the intercepts of a discordant inverse isochron should be taken as artefacts of isochron rotation due to the heterogeneous redistribution of argon and fractionation. The negative relationship between $(^{40}Ar/^{36}Ar)_i$ values and isochron ages for samples of both flows in the current study (see **Figs. 5.4c,f**) supports this interpretation. The impact of this rotation on both $(^{40}Ar/^{36}Ar)_i$ ratios and apparent isochron ages is exemplified by the MH70-2 isochron (**Fig. 5.4b)**.

5.5.5 Causes of $^{40}Ar^*/^{39}Ar$ discordance for flows A and B

The above recoil modelling for a sample with high $^{40}Ar^*$ content (**Fig 5.6a&c)** gives results consistent with the type of discordance observed for samples with high radiogenic yield from both flows (e.g., MH69-1; **Fig. 5.4d&e**), suggesting that disturbance in these samples may be dominated by recoil redistribution of ^{39}Ar from high-K, low retention sites into low-K, high retention sites, with some ^{39}Ar lost to the atmosphere. This disturbance of isotopic ratios causes clockwise rotation of data-points in inverse isochron space, resulting in erroneously old apparent ages and sub-atmospheric $(^{40}Ar/^{36}Ar)_i$ values.

$^{38}Ar/^{36}Ar$ step-heating experiments on unirradiated samples (**Fig. 5.5**) and modelling results for low-$^{40}Ar^*$ samples (**Fig. 5.7b)** imply that experimentally induced mass-dependent fractionation is the dominant cause of data discordance for Flow A samples with extremely low proportions of $^{40}Ar^*$. Although we cannot rule out $^{40}Ar^*$ loss or ^{39}Ar recoil contributing to the discordance in these samples, neither mechanism can produce the negative ages associated with the low-T steps of some aliquants. As noted above, the 4% difference in $^{38}Ar/^{36}Ar$ ratios between low-T and high-T steps is consistent with a ca. 8% difference in $^{40}Ar/^{36}Ar$ ratios. This is in line with the apparent fractionation experienced by samples of Flow A with exceedingly low ^{40}Ar* contents (^{40}Ar/^{36}Ar = 286 - 303).

As the nature of discordance in the low-^{40}Ar* samples from both flows is similar, the disturbed Flow B data are also attributed largely to mass-dependent fractionation. Although Flow B samples lack negative ages, this is unsurprising, as these are older samples with higher ^{40}Ar* proportions (i.e. less sensitive to the atmospheric ^{40}Ar/^{36}Ar correction). As above, other causes for the discordance, such as ^{40}Ar* loss and recoil artefacts, cannot be entirely discounted.

5.5.6 Total-gas ages

Total-gas ages for samples with high ^{40}Ar* proportions from both lava flows are generally within error of eruption ages (**Table 5.2**). Notable exceptions are samples MH05 and MH07, which give total-gas ages of 0.879 ± 0.016 Ma and 0.839 ± 0.008 Ma respectively, considerably older than the eruption age of Flow A (0.8038 ± 0.0017 Ma). These older total-gas ages could be explained by ^{39}Ar recoil loss or extraneous ^{40}Ar; although it is not clear why only these particular samples were affected.

Erroneously young total-gas ages are associated with a minority of samples characterised by low ^{40}Ar* yields (<10%; see **Table 5.2**). Such low ^{40}Ar* yields would normally be grounds for discarding the age results from these samples; however it is instructive to examine the possible causes of the low total-gas ages. Some insight is provided by the different outgassing routines employed for sample MH70. With an extra heating step added to the pre-treatment procedure (6 traverses at 3% laser power), total-gas ages increased from 0.262 ± 0.072 Ma (2σ) to 0.931 ± 0.049 Ma (2σ); the former age being significantly younger, and the latter older, than the inferred eruption age of 0.8038 ± 0.0017 Ma. Possible causes for this discrepancy include ^{40}Ar* loss, and mass fractionation of ^{36}Ar either during pre-treatment procedures or at eruption/crystallisation.

^{40}Ar* loss is the more obvious candidate for low total-gas ages. However, some aliquants exhibit extremely low total-gas ages, requiring up to 80% loss of ^{40}Ar* (MH66-2: 156 ka; **Table 5.2**). Furthermore, low total-gas ages are not linked with visible alteration, but are more common in the younger of the two flows, where the non-radiogenic *trapped* argon component has a greater influence on age results. An alternative explanation is mass-fractionation during crystallisation affecting the trapped argon composition (e.g., Kaneoka, 1980). If atmospheric ^{36}Ar were preferentially incorporated into the samples at crystallisation, this would lead to an over-correction for atmospheric argon and anomalously young total-gas ages. It is not clear, however, why some samples would be affected by mass-fractionation during crystallisation while others were not.

A final possible explanation for these anomalously young total gas ages is that argon released prior to step-heating (e.g., during sample pre-treatment) was enriched in ^{40}Ar or depleted in ^{36}Ar due to experimentally induced complex mass fractionation. This behaviour is, however, at odds with that expected for mass fractionation, where low-T heating steps should preferentially release ^{36}Ar. In summary, the cause(s) of the low total-gas ages is not entirely clear and may be a combination of the above mechanisms. Samples with low ^{40}Ar* contents are most affected by such processes; as a consequence, age information from such samples should be treated with caution and it is vital that other age constraints (e.g., stratigraphy and paleomagnetism) are considered.

5.5.7 Interpretation of ^{40}Ar/^{39}Ar data for basaltic samples

Step-heating analyses of multiple samples from flows A and B demonstrate that accurate ^{40}Ar/^{39}Ar ages for basaltic material can be calculated for samples exhibiting flat, reproducible age spectra and atmospheric (^{40}Ar/^{36}Ar)$_i$ intercepts. Many of the samples that exhibit discordant age spectra also show apparently rotated inverse isochron data arrays that result in sub-atmospheric (^{40}Ar/^{36}Ar)$_i$ intercepts and erroneously old isochron ages. Although both the step-heating data and modelling work suggest that isochron ages are essentially meaningless for samples showing evidence of isotopic disturbance, it may still be possible to extract meaningful age constraints from discordant step-heating data.

The effects of fractionation, ^{40}Ar* loss and ^{39}Ar recoil may only impact low-T heating steps, with data from later steps converging on an undisturbed inverse isochron. As with the high-^{40}Ar* samples of Flow B (**Table 5.3**), it is necessary that the subset of higher temperature steps define a linear array in inverse isochron space (e.g., MH69-1 in **Fig 5.4e**), with an atmospheric (^{40}Ar/^{36}Ar)$_i$ value. If these two conditions are met, the apparent age given by this subset may be reliable. Depending on the spread of the data in inverse isochron space, step-heating of several aliquants and pooling of concordant data may be required to obtain a statistically robust regression model result.

Isochron ages for samples affected by ^{39}Ar recoil, ^{40}Ar* loss or fractionation should be interpreted as maximum ages if the (^{40}Ar/^{36}Ar)$_i$ value is sub-atmospheric, due to a clockwise rotation of the regression line (e.g., aliquant MH70-2 of Flow A; **Fig. 5.4b**). Conversely, if the (^{40}Ar/^{36}Ar)$_i$ value is supra-atmospheric, an inverse isochron will generally give a minimum age in basaltic groundmass samples. In many cases, it will not be possible to obtain a reliable minimum or maximum age from a single sample or aliquant, and multiple samples will be required. This is a particularly important consideration where analytical errors are large and initial ratios and isochron ages are poorly constrained. Given the severe isotopic disturbance observed for samples with low ^{40}Ar* yield, young basalt samples that are suitable for ^{40}Ar/^{39}Ar geochronology might be targeted by selecting those with the lowest ^{36}Ar contents. This could be assessed by collecting several samples from the same flow and outgassing a small quantity of unirradiated groundmass from each.

5.6 Conclusions

A sub-set of ^{40}Ar/^{39}Ar step-heating results from basaltic lava flows A and B, collected from the Melbourne area, exhibit relatively flat age spectra and atmospheric (^{40}Ar/^{36}Ar)$_i$ values, constraining eruption ages of 0.8038 ± 0.0017 and 2.309 ± 0.009 Ma (95% CI), respectively. The majority of samples from both flows yielded variably discordant ^{40}Ar/^{39}Ar results, and a correlation is observed between sub-atmospheric (^{40}Ar/^{36}Ar)$_i$ values and erroneously old apparent isochron ages. By measuring the increase in ^{38}Ar/^{36}Ar ratios during step-heating of unirradiated aliquants we have shown that mass-dependent fractionation can have a significant effect on the ^{40}Ar/^{39}Ar results of basaltic groundmass samples.

The dominant causes of the observed discordant ^{40}Ar/^{39}Ar results appear to be mass-dependent fractionation (low-^{40}Ar* samples) and ^{39}Ar recoil loss/redistribution (high-^{40}Ar* samples). We have demonstrated that the interpretation of (^{40}Ar/^{36}Ar)$_i$ values and inverse isochron ages for groundmass samples depends on the distribution of radiogenic *and* trapped argon in a given sample, and that a non-atmospheric (^{40}Ar/^{36}Ar)$_i$ ratio calculated from an inverse isochron diagram should not be regarded as the trapped argon composition. Based on the direction of isochron rotation, an inverse isochron age may be either a maximum or minimum estimate of the eruption age.

Results from this study suggest that a subset of concordant heating steps that generate a flat age spectrum and plot along an isochron with an atmospheric $(^{40}Ar/^{36}Ar)_i$ intercept are more likely to provide an accurate eruption age.

5.7 Addendum: The cause of low $^{40}Ar^*$ content in basaltic samples

$^{40}Ar/^{39}Ar$ analyses of both Flow A and Flow B basalt samples produced varied results. Samples showed a broad range of $^{40}Ar^*$ contents, including samples from the same flow, ranging from relatively high levels (e.g., YY6 = 36.9%) to extremely low $^{40}Ar^*$ contents (e.g., MH66 = 1.1%). It was noted in **section 5.5.2** that samples with lower $^{40}Ar^*$ contents generally produced more discordant age spectra and inverse isochron data, complicating the determination of an eruption age and rendering such samples undesirable as $^{40}Ar/^{39}Ar$ dating candidates. As mentioned in **section 5.5.2**, thin-section examination of both high- and low-$^{40}Ar^*$ samples, defined as >10% $^{40}Ar^*$ and <10% $^{40}Ar^*$, respectively, did not reveal any obvious difference between these two groups. As illustrated in **Fig. 5.8**, the volume of cryptocrystalline material in a sample was an unreliable indicator of $^{40}Ar^*$ content, and the same was generally true for glass and visible alteration phases, although glass contents were very low and alteration minor in all samples selected for $^{40}Ar/^{39}Ar$ analysis.

To investigate the cause of low ^{40}Ar* proportions further, back-scattered electron SEM images and x-ray elemental maps were generated for four samples of Flow A for which ^{40}Ar/^{39}Ar age data were available (YY6, MO43B, MH70 and MH66; **Fig. 5.9**). The aim of this study was to image the sub-microscopic architecture of both high- and low-^{40}Ar* samples, and assess whether there were any systematic differences between the two groups, with a focus on the distribution of potassium in each sample and the nature of K-bearing phases.

In each of these four samples, the dominant K-bearing phase was found to be anorthoclase, typically occurring in the groundmass as fine grains and interstitial pools, but ranging up to ca. 0.5 mm in MH70 (**Fig. 5.9c**). The major difference observed between high- and low-^{40}Ar* samples was that anorthoclase in the high-^{40}Ar* samples (YY6 & MO43B; **Figs. 5.9a & 5.9b)** was typically inclusion-free, whereas in the low-^{40}Ar* samples (MH70 & MH66; **Figs. 5.9c & 5.9d)** anorthoclase was generally inclusion-rich. Although the presence of inclusions in anorthoclase was not always a reliable indicator of low ^{40}Ar* content, as inclusions were sometimes present in anorthoclase in some high-^{40}Ar* samples, those with inclusion-free anorthoclase all had high-^{40}Ar* content. This suggests that inclusion-free anorthoclase could be utilised as a screening criterion for future ^{40}Ar/^{39}Ar work on basaltic groundmass samples, assuming that anorthoclase is present.

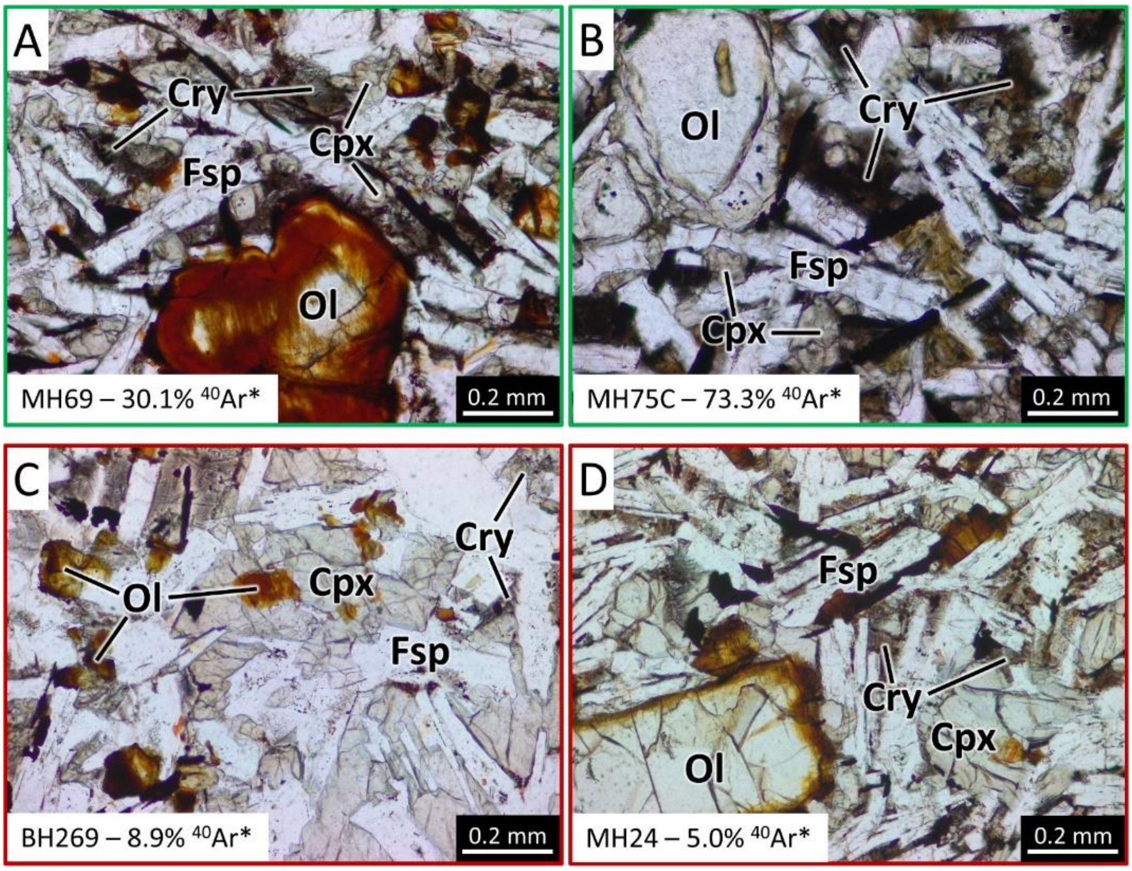

Figure 5.8: Samples MH69 **(a)** and MH75C **(b)** yielded relatively high $^{40}Ar^*$ contents, despite significant amounts of cryptocrystalline material (Cry) visible in thin section. Cryptocrystalline material in BH269 **(c)** and MH24 **(d)** was only minor, yet these samples yielded very low $^{40}Ar^*$ content, and discordant age spectra (see chapters 5 & 6).

The presence of mineral inclusions in K-bearing phases may constrict molecular pathways for argon release, leading to fractionation of argon isotopes. Constricted molecular flow is a well-established cause of fractionation in noble gas spectrometry (e.g., Baksi and Farrar, 1973), so this could explain why low-$^{40}Ar^*$ samples appear to be more affected by mass-dependent fractionation. Although SEM screening for inclusion-rich anorthoclase might be beneficial for $^{40}Ar/^{39}Ar$ dating, an alternative, and potentially more effective as screening tool may be analysis of ^{36}Ar-contents of weighed, unirradiated aliquants, as discussed in **section 5.5.7**. By this method, a small quantity of each ^{40}Ar/^{39}Ar dating candidate sample could be outgassed, with only the lowest ^{40}Ar*-content samples progressing to irradiation and subsequent step-heating analysis.

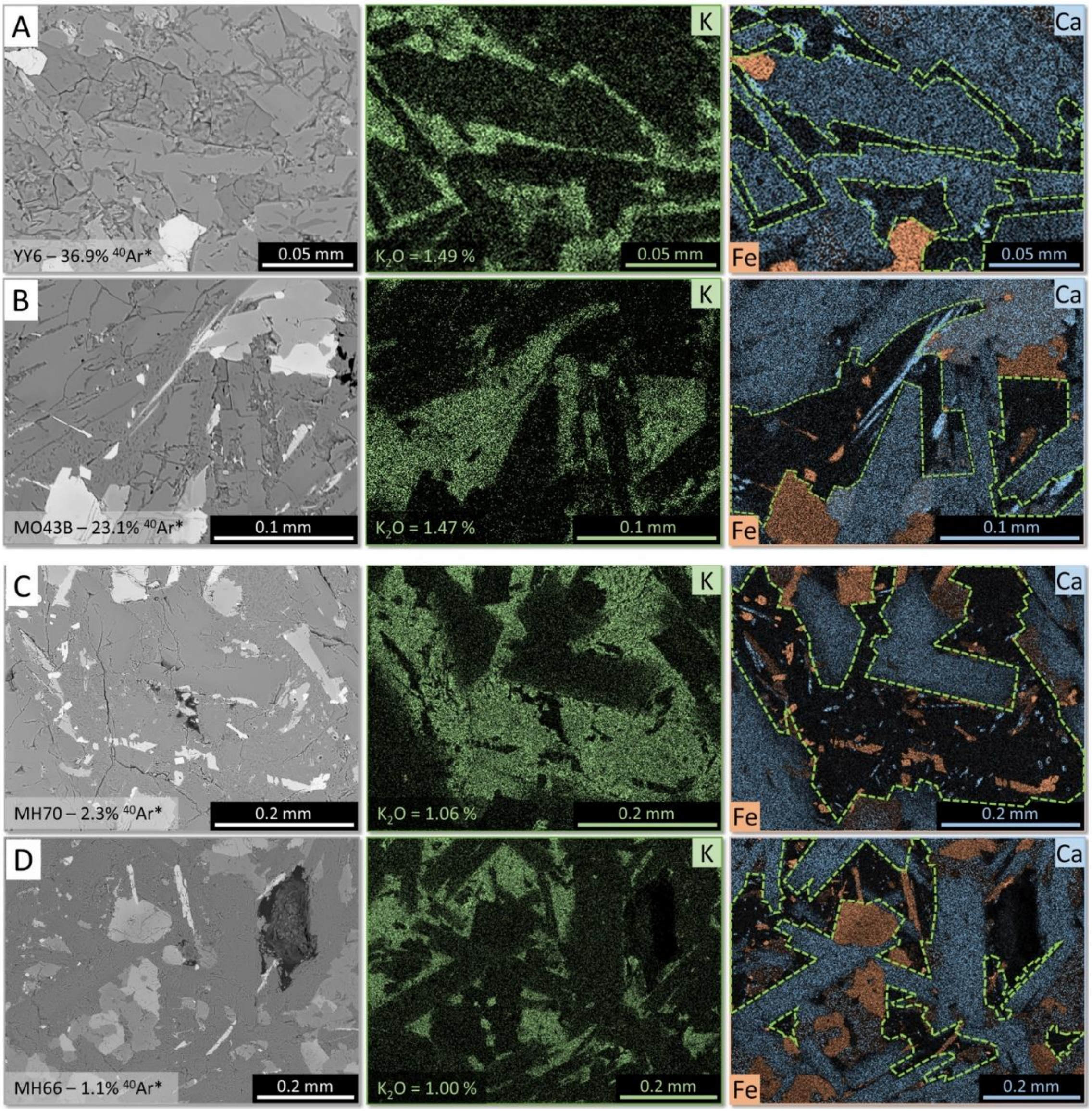

Figure 5.9: Back-scattered electron SEM images (left), K elemental maps (middle) and Ca-Fe composite elemental maps (right) of samples YY6 **(a)**, MO43B **(b)**, MH70 **(c)** and MH66 **(d)** from the Mount Fraser lava flow. Dashed lines in Ca-Fe elemental maps outline the locations of K-bearing phases.

Chapter 6) Basalt lava flows of the intraplate Newer Volcanic Province in south-east Australia (Melbourne region): $^{40}Ar/^{39}Ar$ geochronology reveals ~8 Ma of episodic activity.

M. Heath[a,*], D. Phillips[a], E. Matchan[a]

[a] *School of Earth Sciences, The University of Melbourne, Parkville, VIC 3010, Australia*
*Corresponding author.
E-mail address: m.heath@student.unimelb.edu.au

Abstract

Intraplate basaltic volcanism is one of the most common, yet poorly understood, types of volcanism. Intraplate continental basaltic volcanic provinces (ICBVPs) typically comprise tens to hundreds of usually monogenetic, small-volume eruption centres, often cumulatively producing significant volumes of mainly primitive basaltic magmas. A wide range of mechanisms have been invoked to account for ICBVP melt generation, ranging from deep mantle plumes to local tectonic perturbations of the lithospheric mantle. The key to understanding the cause(s) of intraplate volcanism is understanding the geochemical evolution of magmatism within a regional tectonic framework. Unfortunately, many ICBVPs contain complex arrays of overlying lava flows, with uncertain eruption sources and a lack of precise age constraints.

The Newer Volcanic Province (NVP) in south-eastern Australia is a young (Late Miocene to 5 ka), geochemically and volcanologically diverse ICBVP, comprising ≥416 volcanic centres covering an area of ~23,000 km^2. As with other ICBVPs, elucidating the underlying controls on magmatism has proved contentious, with recent studies favouring edge-driven convection, but divided as to the changing nature of volcanism. At the eastern boundary of the NVP, in the Melbourne area, previous work has indicated a complex network of lava flows representing almost the entire age and geochemical range of the NVP, making this an ideal microcosm for studying the evolution of the NVP.

In this study, a holistic approach to lava flow mapping is utilised to unravel the complex network, incorporating diagnostic petrography, geochemistry and precise ^{40}Ar/^{39}Ar geochronology. This work reveals seven major lava flows, here named the Tullamarine, Redstone Hill, Aitken Hill, Mount Kororoit, Fenton Hill, Tulloch Hill and Mount Fraser flows, along with eight smaller-volume flows, here named the Pretty Sally, Green Hill, Bald Hill, Mount Cooper, Mount Ridley, Crowe Hill, Springs Hill and Summerhill Road flows. ^{40}Ar/^{39}Ar ages for ten lava flows and eruption centres span an age range of 7.9–0.8 Ma. These new data reveal that alkalic, small-volume eruptions in the Melbourne area occurred exclusively between ~8 and 3.8 Ma. Post ~3.8 Ma, large-volume, tholeiitic eruptions dominated. A local progression from alkalic to tholeiitic volcanism is contrary to a province-wide progression from tholeiitic to alkalic volcanism observed by previous studies.

The earliest four eruptions (ca. 8 Ma) were aligned with the Cosgrove hotspot track and are probably unrelated to the broader NVP. The ages and geochemical variations of the younger flows are consistent with melt generation due to edge-driven convection. Magma composition might have been controlled by local perturbations within the convective cell, with tholeiitic magmas generated during high-degree melting in regions of more intense upwelling, and alkalic melts reflecting lower-degree melting and less-intense upwelling. The episodic nature of volcanism is likely due to restricted magma transport to the surface, which was only possible during brief periods of favourable tectonic conditions.

6.1 Introduction

Although intraplate basaltic volcanoes occur on every continent, the mechanisms responsible for their formation remain poorly understood. Despite the name, intraplate continental basaltic volcanic provinces (ICBVPs) are located in a variety of tectonic settings, but their formation is not directly linked to plate boundary processes. ICBVPs are typically composed of tens to hundreds of individual eruption centres, each contributing a small volume (~0.01 – 0.1 km^3 of dense rock equivalent) of erupted material, but cumulatively producing a similar volume to long-lived composite volcanoes (Németh, 2010). ICBVPs cover anywhere from 150 km^2 (Cima, USA) to 40 000 km^2 (Trans-Mexican Volcanic Belt) and volcanic flux rates wary widely (Valentine and Connor, 2015). ICBVPs are typically dominated by primitive magmas, attributed to fast ascent and simple plumbing systems (Smith & Nemeth 2017), although a range in composition from trachytic to andesitic (40-60% SiO_2; McGee and Smith, 2016) is common.

Melt generation of ICBVP magmas occurs in the mantle, with deep mantle plumes invoked to account for fields with high eruptive fluxes (e.g., Snake River Plain, USA; Kuntz et al., 1986; Hanan et al., 2008). However, there is growing evidence for tectonic controls on ICBVP volcanism, even in the highest-flux fields (Takada, 1994; Leeman et al., 2009; van den Hove et al., 2017b). A key to understanding the driving mechanisms behind intraplate volcanism is knowledge of the geochemical evolution of volcanism in ICBVPs through time. Here, progress has been hampered by a lack of precise age information and challenges in unravelling the often-complex array of overlying lava flows and identifying source eruption centres. The 4.6 Ma to ~5 ka Newer Volcanic Province (NVP) of southeast Australia (Gray and McDougall, 2009; Gouramanis et al., 2010), is a prime example of an ICBVP where geochronological constraints are relatively sparse, and few lava flows have been mapped or assigned to distinct eruption points.

In this study, we focus on the Melbourne area of the NVP (**Fig. 6.1**), which hosts a complex network of lava flows spanning a broad age range (~0.8 – 7.9 Ma). Its age and compositional range make it an ideal microcosm for the NVP, providing an opportunity for testing methods towards unravelling complex flow geometries in ICBVPs, involving a combination of petrography, geochemistry and high-precision ^{40}Ar/^{39}Ar geochronology. In turn, this information provides new insights into the evolution of magmatism in the Melbourne area, with implications for geodynamic models for NVP magmatism.

6.2. Geology of the Newer Volcanic Province (NVP)

The NVP covers an area of approximately 23,000 km^2, from the Melbourne area in Victoria to the eastern margin of South Australia (van den Hove et al., 2017b; **Fig 6.1**), and comprises over 416 eruption centres (Boyce, 2013). It has been sub-divided into three regions, referred to as the Central Highlands, Western Plains, and Mount Gambier sub-provinces (e.g., Hare and Cas, 2005; Boyce, 2013). Maars and volcanic complexes are common in the Western Plains and Mount Gambier sub-provinces, due to the presence of aquifers in the underlying Tertiary sediments (e.g., Joyce, 1975). In the Central Highlands, lava shields and scoria cones dominate, with lava flows filling narrow valleys etched into Palaeozoic basement rocks (e.g., Edwards, 1938).

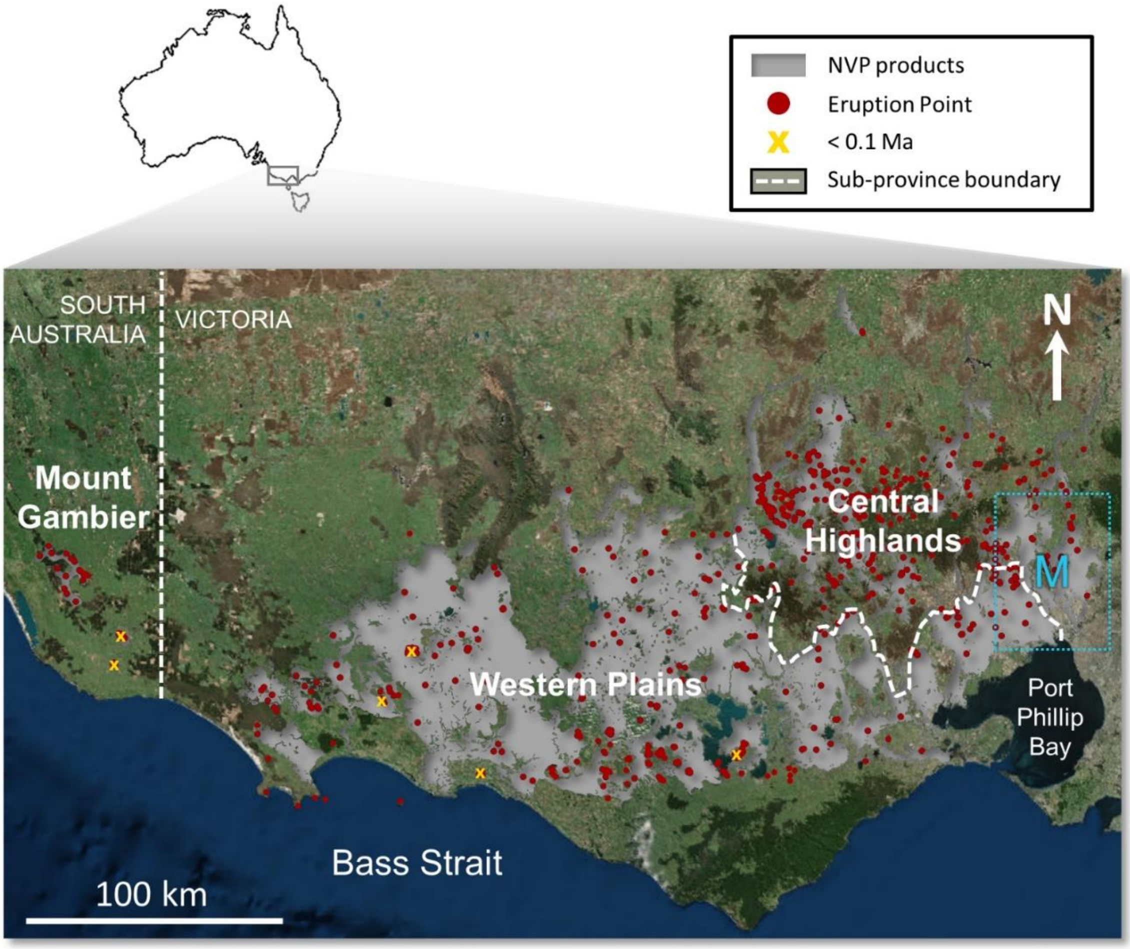

Figure 6.1: The extent of the NVP in Victoria and South Australia, divided into the Central Highlands, Western Plains and Mount Gambier sub-provinces. The dashed blue box outlines the Melbourne study area (M). Yellow crosses indicate eruption centres with published ages of less than 0.1 Ma (Smith and Prescott, 1987; Sherwood et al., 2004; Gillen et al., 2010; Gouramanis et al., 2010; Oostingh et al., 2017).

Although there is no simple age trend across the NVP, previous work has suggested that there may be some relationship between geographical location and age, as the youngest ages (<0.1 Ma) have been found for volcanoes in the south and west of the NVP (e.g., Gray and McDougall, 2009; **Fig. 6.1**). Eruptive products have, in some cases, been separated into a ‘plains series’ of large-volume tholeiitic eruptions, and a ‘cones series’, of smaller-volume, alkali-rich lavas. The cones series is inferred to be younger, and a link to a temporal evolution in magma generation has been proposed. However, the chemical distinction between the two series is often unclear, with younger transitional lavas being classified as cones series and older chemically identical lavas classified as plains series (e.g., Oostingh et al., 2016; Oostingh et al., 2017). Furthermore, studies of sub-surface lava flows have found alternating alkalic and tholeiitic compositions, without any evidence for a broad shift in composition over time (e.g., Hare et al., 2005).

Due to the small percentage of flows sampled, and generally surface-centric sampling of volcanic products, only a small proportion of the NVP has been mapped in detail (Hare et al., 2005; Boyce et al., 2014b; Matchan et al., 2016). The majority of previous K-Ar and ^{40}Ar/^{39}Ar studies have focused on the Western Plains sub-province (Price et al., 1997; Oostingh et al., 2017), but relatively few eruption points have been dated (ca. 30 out of >416 eruption centres). K-Ar dating studies have targeted the ‘plains’ basalts, and the majority of flows sampled in those studies are of unknown provenance (McDougall et al., 1966; Aziz-ur-Rahman and McDougall, 1972; McDougall and Gill, 1975; Gray and McDougall, 2009). Only recently has ^{40}Ar/^{39}Ar work produced age constraints for some individual eruption points (Matchan and Phillips, 2011; Ismail et al., 2013; Matchan and Phillips, 2014; Matchan et al., 2016; Oostingh et al., 2017; Matchan et al., 2018).

The cause of recent volcanism in south eastern Australia has been much debated, with early models involving crustal extension (e.g., Wellman and McDougall, 1974) and mantle plume-related melt generation (e.g., Sutherland, 1981). More recently, edge-driven convection has become the most commonly suggested cause of NVP activity (Demidjuk et al., 2007; Davies and Rawlinson, 2014; Davies et al., 2015; Oostingh et al., 2016; Cas et al., 2017; van den Hove et al., 2017b). This theory invokes a convective cell in the upper asthenospheric mantle caused by a steep gradient, or ‘edge’, at the base of the south eastern Australian lithosphere (**Fig. 6.2**). The rapid rate of Indo-Australian plate migration (60-70 mm/yr; DeMets et al., 2010) and local variations in lithospheric thickness support the formation of an edge-driven convective cell (e.g., Demidjuk et al., 2007; Davies and Rawlinson, 2014), and it has been proposed that entrainment of a mantle plume by the convective cell may have initiated volcanism (Davies et al., 2015). Tectonic controls on magma migration have been a focus of recent studies investigating the spatial alignment of NVP eruption points, clustering around major crustal structures (Lesti et al., 2008; van den Hove et al., 2017a) and the volume of eruptive products (Cas et al., 2017; van den Hove et al., 2017b). These studies found that a tectonic control on magmatism was supported by a tendency for NVP eruption points to be located along or near major faults (Lesti et al., 2008; van den Hove et al., 2017a), along with a newly quantified eruption volume for the NVP of 680 - 900 km^3, which places it within the range of other tectonically controlled ICBVPs worldwide (van den Hove et al., 2017b).

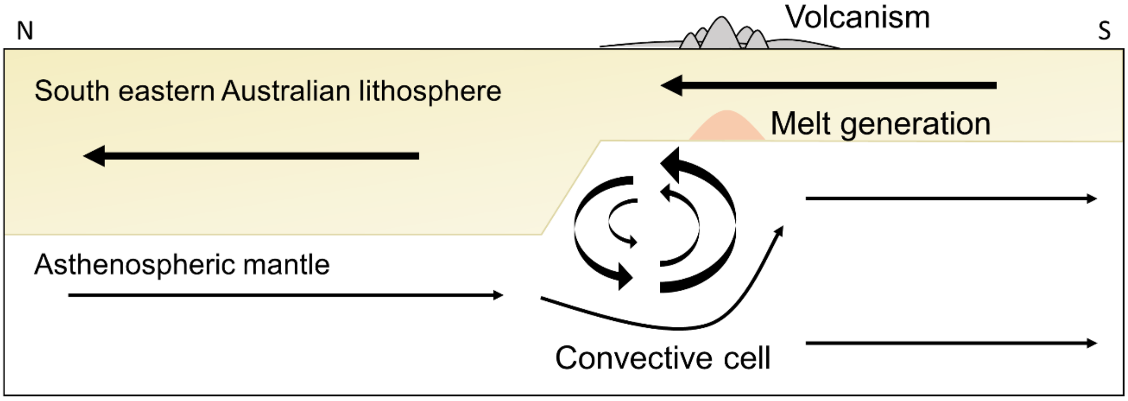

Figure 6.2: Schematic representation of the edge-driven convection model applied to south eastern Australia (adapted from Demidjuk et al., 2007).

6.2.1 NVP volcanism in the Melbourne area

Mapping of NVP products by surface features and geophysical methods has proven successful in some areas of the NVP (e.g., Boyce et al., 2014b; Blaikie et al., 2015), but is more challenging in a metropolitan setting. Due to difficulties in accessing outcrop, the volcanic landforms and eruptive products of the Melbourne area have received less scrutiny than those in less urbanised areas of the NVP. Early studies of the Melbourne area focused on modifications to drainage systems that occurred as a result of volcanism, noting that new drainage channels tended to be located along flow margins, at the contact with more easily dissected sediments or Paleozoic basement rocks (Hart, 1894; Hall, 1908). These studies refer to eruption points located to the north of Melbourne, but did not relate lava flows to specific eruption points. Ten eruption points located to the north of Melbourne (**Fig 6.3b**) were described by Hanks (1955), and their lava flows mapped via geomorphology and drill core stratigraphy. Hanks (1955) proposed relative ages for eleven eruption events (**Fig 6.3b**), along with likely drainage modifications. Based on geochemical studies, Price et al. (1988, 1997) divided the volcanic products of the Melbourne area into five strontium isotope ($^{87}Sr/^{86}Sr$) domains (**Fig. 6.3a**) and proposed a link between these domains and individual eruption events. Previous mapping work in the Melbourne area revealed complex lava flow geometries, generated by multiple separate eruption events. However, no studies, based either on geomorphology (e.g., Hanks, 1955), stratigraphic constraints (e.g., Stewart, 1975) or ($^{87}Sr/^{86}Sr)_i$ values (e.g., Price et al., 1988), have produced consistent lava flow maps.

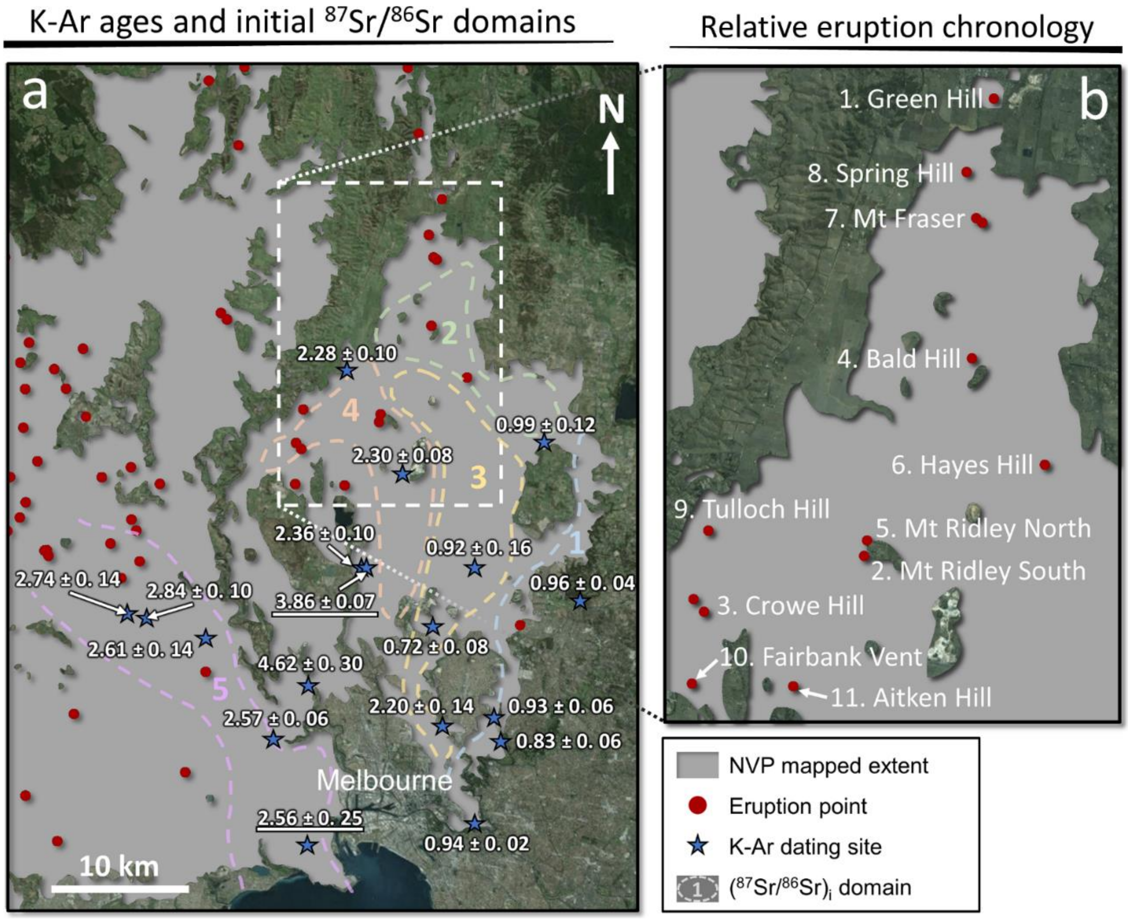

Figure 6.3: a) Initial $^{87}Sr/^{86}Sr$ domains and K-Ar ages (Ma) from previous work within the study area (McDougall et al., 1966; Price et al., 1988; errors are 2σ; Gray and McDougall, 2009). **b)** Relative eruption chronology (1 = oldest) of eruption points and vents to the north of Melbourne, as suggested by Hanks (1955).

Whole-rock basalt K-Ar ages ranging from ~0.72 to 4.62 Ma have been published for 18 locations in the Melbourne region (**Fig. 6.3a**), as part of an extensive geochronology campaign that began in the late 1960s (McDougall et al., 1966; Gray and McDougall, 2009). These ages were assigned to geographic locations only, rather than individual lava flows or eruption points (Gray and McDougall, 2009). Heath et al. (2018) published the first ^{40}Ar/^{39}Ar data for the Melbourne area, reporting ages for two distinct lava flows ('Flow A' and 'Flow B'); these flows were mapped in detail as part of the current study where they are referred to as the Mount Fraser and Tulloch Hill flows. Heath et al. (2018) reported an age for Flow A (Mount Fraser flow) of 0.8038 ± 0.0017 Ma, and assigned Flow B (Tulloch Hill flow) an age of 2.309 ± 0.009 Ma, in agreement with earlier K-Ar work. An anorthoclase megacryst erupted at Mount Kororoit, approximately 30 km north-west of Melbourne, was assigned an ^{40}Ar/^{39}Ar age of 3.74 ± 0.26 Ma (Ismail et al., 2013), but whether this should be interpreted as an eruption age remains unclear (e.g., Matchan et al., 2018).

6.3 Methods

6.3.1 Sample selection

A total of 388 basalt samples were collected from 162 locations across the Melbourne area for detailed lava flow-mapping (**Fig. 6.4**). Field locations were selected based on the availability of outcrop, with a focus on thick, massive basalt flows that lacked evident weathering. Sampling sites included disused quarries, road and river cuttings, and natural cliffs. Additional samples were obtained from drill core (up to ~80 m depth) drilled through NVP basalt as part of a 1960s Victorian Geological Survey project. Drill core samples were preferentially selected from the middle sections of thick lava packages.

Where possible, samples were collected from multiple depths within each borehole, allowing petrographic and geochemical data to be collected from multiple stratigraphic levels within each flow. Following thin-section inspection, the major element composition of 138 of the freshest samples was analysed via X-Ray Fluorescence (XRF), and 15 essentially holocrystalline, unaltered samples were selected for $^{40}Ar/^{39}Ar$ dating based on preliminary flow mapping results detailed below. In the case of sample BA01, groundmass material was deemed too altered for $^{40}Ar/^{39}Ar$ dating and late-stage plagioclase grains were instead selected.

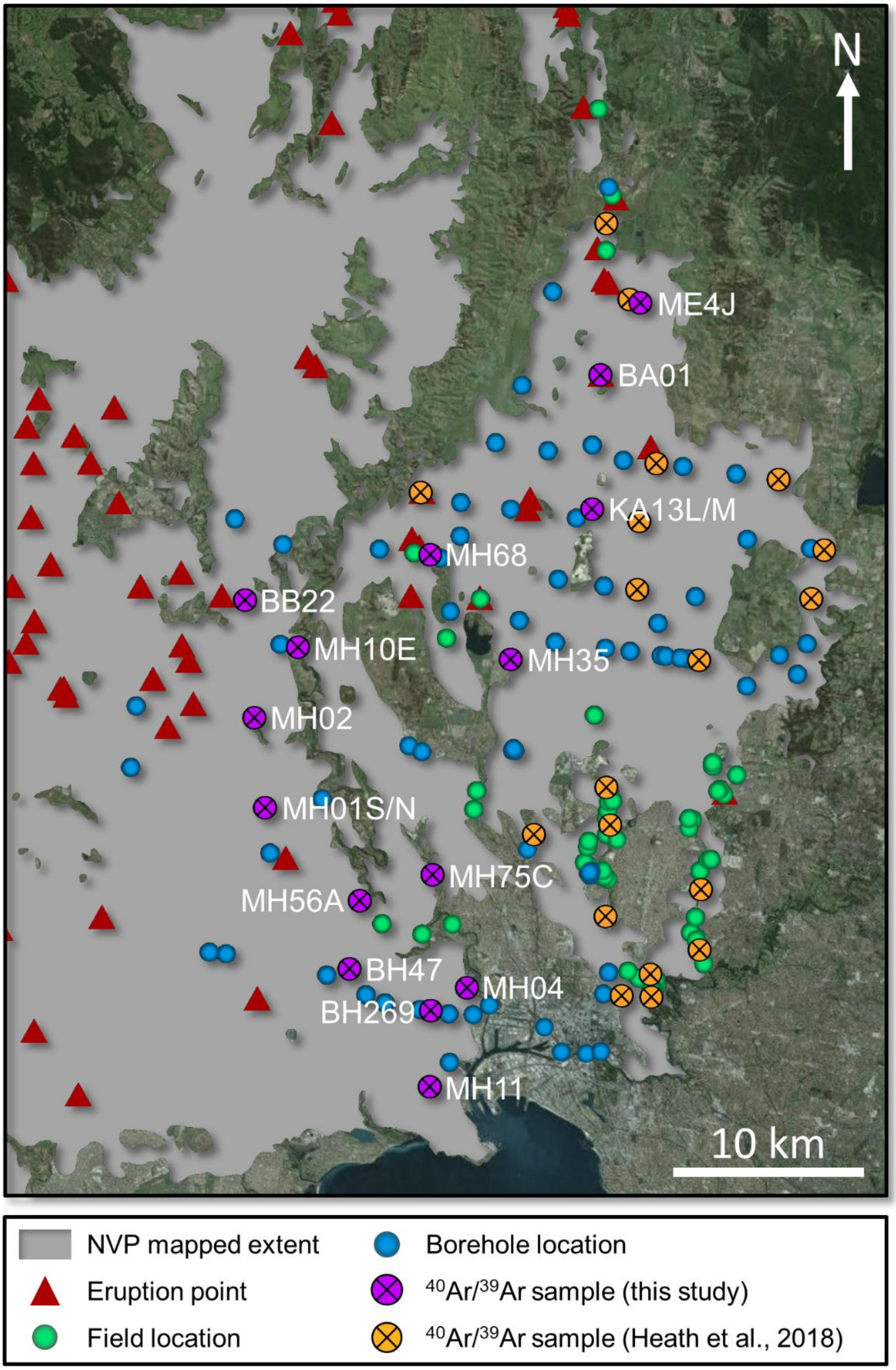

Figure 6.4: Field and borehole sample locations for the current study and Heath et al. (2018), with ^{40}Ar/^{39}Ar sample IDs displayed in white.

6.3.2 Sample preparation for $^{40}Ar/^{39}Ar$ geochronology and whole-rock geochemistry

After removal of visibly weathered material, samples were crushed, and a selection of fresh chips powdered using either a tungsten carbide or agate ring mill for XRF major element analysis. The remaining fresh chips were crushed with a disc mill and sieved to a 150 – 250 μm size fraction for $^{40}Ar/^{39}Ar$ geochronology. Plagioclase grains (0.5 – 5 mm) were selected from sample BA01 using a binocular microscope. For the remaining samples, groundmass material (150 – 250 μm) was concentrated via magnetic separation. Groundmass concentrates and BA01 plagioclase were treated in an ultrasonic bath with 5% HNO_3 (10 min), followed by 2% HF (2 min), deionised water (10 min), and acetone (3 min). The cleaned concentrates were then hand-picked under a binocular microscope to remove remaining xenocrysts/phenocrysts, altered material and visible glass.

6.3.3 $^{40}Ar/^{39}Ar$ analyses

For each sample, approximately 100 mg of groundmass (25 mg for plagioclase sample BA01) was weighed into aluminium packets and vacuum sealed in a quartz glass vial, intercalated with neutron fluence monitors Alder Creek Rhyolite (ACR) Sanidine (UM#58; UM#70 and UM#71; 1.18144 ± 0.00068 Ma [2σ]; Phillips et al., 2017) or Fish Canyon Tuff (FCT) Sanidine (UM#77; 28.126 ± 0.019 Ma [2σ]; Phillips et al., 2017). Vials were irradiated at the CLICIT facility of the Oregon State University TRIGA (OSTR) reactor for 0.75 h (UM#58 and UM#70), 3 h (UM#71) and 20 h (UM#77). Following irradiation, aliquants (1 – 3 per sample) measuring ~30 – 70 mg were loaded into custom copper sample holders, covered with ZnS glass and placed in the sample chamber of a gas-handling system equipped with a Photon Machines Fusions 10.6 CO_2

laser and connected to a Thermo Fisher Scientific ARGUSVI mass spectrometer at The University of Melbourne. Details and configuration of the ARGUSVI system are discussed in Phillips and Matchan (2013) and Phillips et al. (2017). Argon isotopic results have been corrected for system blanks, mass discrimination, radioactive decay and reactor-induced interference reactions. Detector bias and mass discrimination were measured via automated air pipette, assuming an atmospheric ^{40}Ar/^{36}Ar ratio of 298.56 ± 0.62 (2σ; Lee et al., 2006). Line blanks were measured every two to four analyses and were typically <0.5% of sample ^{40}Ar signals. ^{40}Ar/^{39}Ar analytical details are reported in **Appendix A.19**.

6.4 Results

6.4.1 Lava flow mapping

A multi-faceted approach was used for flow mapping, utilising field relationships, borehole stratigraphy, diagnostic petrographic features, geochemistry and ^{40}Ar/^{39}Ar geochronology. In rare cases, lava flow samples could be linked to specific eruption points based on field relationships alone (**Fig. 6.5a**). These samples were employed as archetypes for comparison against samples of uncertain origin. Samples of unknown origin (e.g., **Figs. 6.5b; c**) were then allocated to a particular flow/eruption centre based on petrography and major element geochemistry, predicated on consistent field relationships and stratigraphic considerations. ^{40}Ar/^{39}Ar dating results enabled assignment of some samples that were indistinguishable on the basis of petrography and geochemistry alone.

Figure 6.5: a) Small disused quarry, near the base of Mount Fraser (in background), which was the collection site for sample MH70. Other sample locations, such as **b)** MH75 and **c)** MH02, were further from any known eruption point, and their affinity with major flows was based on petrographic and geochemical parameters.

Samples were initially allocated to individual flows using a range of petrographic criteria, including phenocryst assemblages, grain size distributions, modal abundances, and, in some cases, diagnostic textural relationships (**Table 6.1**). However, there are a number of complications associated with the use of petrography in flow mapping studies. For example, textural differences occur within individual flows at different stratigraphic positions, likely due to differing cooling rates and flow dynamics. There are also differences in secondary phases and textures due to post-emplacement alteration. Where possible, these complications were circumvented by comparing samples from similar stratigraphic positions and avoiding samples with obvious weathering.

An illustration of the diagnostic use of petrography for lava flow mapping is the case of two samples from the lower part of the Mount Fraser lava flow (MO43B and YY6; **Figs. 6.6a; b**). These two samples exhibit highly similar features in thin section, including fine feldspar laths, ilmenite needles, blocky interstitial clinopyroxene and subhedral olivine microphenocrysts, thus allowing their assignment to the same flow. Similarly, in the west of the study area, samples from the Mount Kororoit flow could be allocated based solely on petrographic features, such as a characteristic ophitic texture (**Figs. 6.6c; d**) in the middle part of the lava flow. In both examples, diagnostic petrographic features could be traced for up to 40 km, allowing lava flow units to be mapped in detail.

A lava flow map for the Melbourne area was constructed initially using field relationships and petrography, and later augmented by geochemical and ^{40}Ar/^{39}Ar dating results (**Fig. 6.7)**. Borehole samples provided insight into the petrographic variations within individual flows and enabled some older flows to be more accurately mapped. In general, borehole sequences only record a single eruption event, with individual lava sheets and lobes separated by quenched surfaces; however, the deepest borehole, KA13 (78.6 m; **Fig. 6.4**), intersects three distinct flows (from oldest to youngest: the Mount Ridley Flow, the ‘Summerhill Road Flow’ (unknown provenance), and the Tulloch Hill Flow; **Fig. 6.7**). The most laterally extensive flows are the Tulloch Hill, Mount Kororoit, Mount Fraser and Tullamarine flows (**Fig. 6.7**). The Redstone Hill, Fenton Hill and Aitken Hill flows are intermediate in areal extent, and the Crowe Hill, Mount Ridley, Mount Cooper, Bald

Hill, Green Hill and Pretty Sally flows are confined to small areas near their respective eruption points (**Fig. 6.7**). It was difficult to determine the extent of the Springs Hill Flow as it is buried by the Mount Fraser Flow and was sampled in only one borehole.

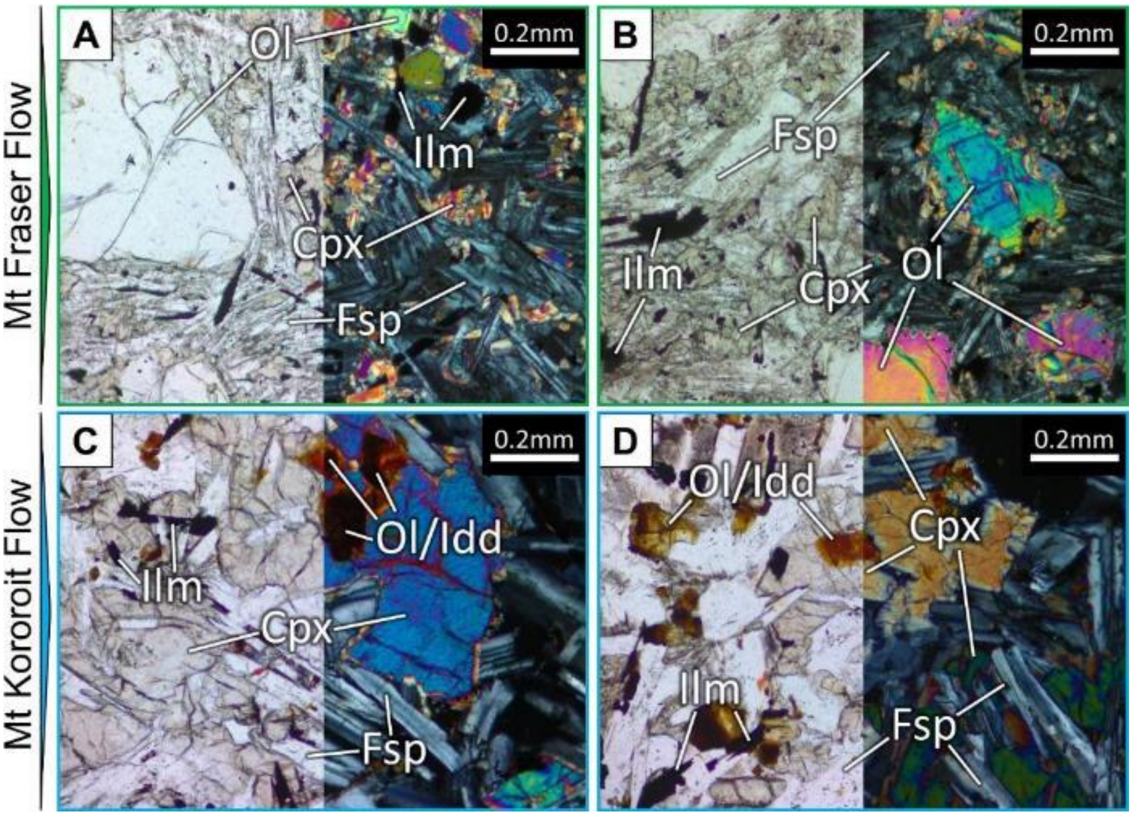

Figure 6.6: Plane-polarised (left) and cross-polarised (right) photomicrographs of samples from two flows with internally consistent petrographic features. Mount Fraser Flow samples **a)** MO43B and **b)** YY6 both display fine-grained groundmass feldspar (Fsp) and clinopyroxene (Cpx), with olivine (Ol) microphenocrysts and an intergranular texture. Mount Kororoit Flow samples **c)** BH269 and **d)** MH11, exhibit a diagnostic ophitic texture, with feldspar grains completely enclosed within large clinopyroxene grains.

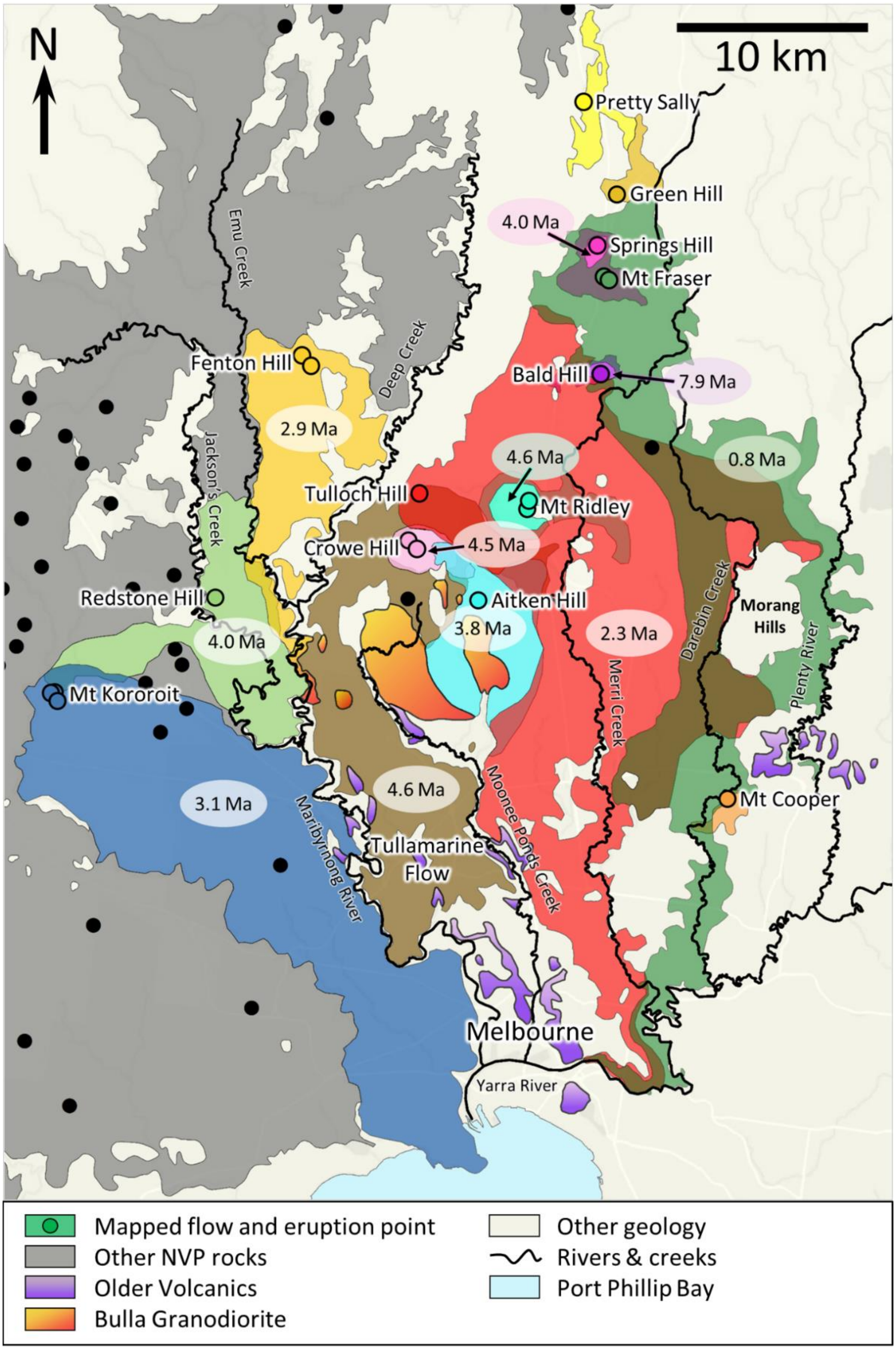

Figure 6.7: NVP lava flow map and ^{40}Ar/^{39}Ar geochronology of the Melbourne area. Drainage channels were commonly diverted to flow boundaries, leading to minimal overlap of different flows.

6.4.2 Major element geochemistry

Major element analysis was completed for 140 samples, with at least one sample selected from each flow (see **Table 6.1** for a summary of geochemical classifications of each flow). The full XRF major element dataset is reported in **Appendix A.18**.

On a total alkali versus silica (TAS) diagram (**Fig. 6.8a**), most samples from the Tulloch Hill, Mount Kororoit, Tullamarine, Fenton Hill, Summerhill Road and Springs Hill flows plot within the tholeiitic basalt field. As discussed briefly in Heath et al. (2018), samples of the Mount Fraser Flow units define a trend that crosses the division between alkali basalt and tholeiite, perpendicular to that expected for olivine (±clinopyroxene/plagioclase) fractionation (**Fig. 6.8a**), possibly indicative of magma mixing. Samples from the Aitken Hill and Redstone Hill flows plot near the trachybasalt-basaltic trachyandesite boundary, and samples from the Crowe Hill and Mount Ridley flows are located within or near the trachybasalt field. The Bald Hill Flow classifies as a basanite and the Green Hill, Pretty Sally and Mount Cooper flows plot near the alkali basalt-trachybasalt boundary. The larger volume flows (e.g., Tulloch Hill and Mount Kororoit flows) are generally high-silica and low-alkali basalts, whereas smaller volume flows (e.g., Crowe Hill and Mount Ridley flows) have higher alkali contents.

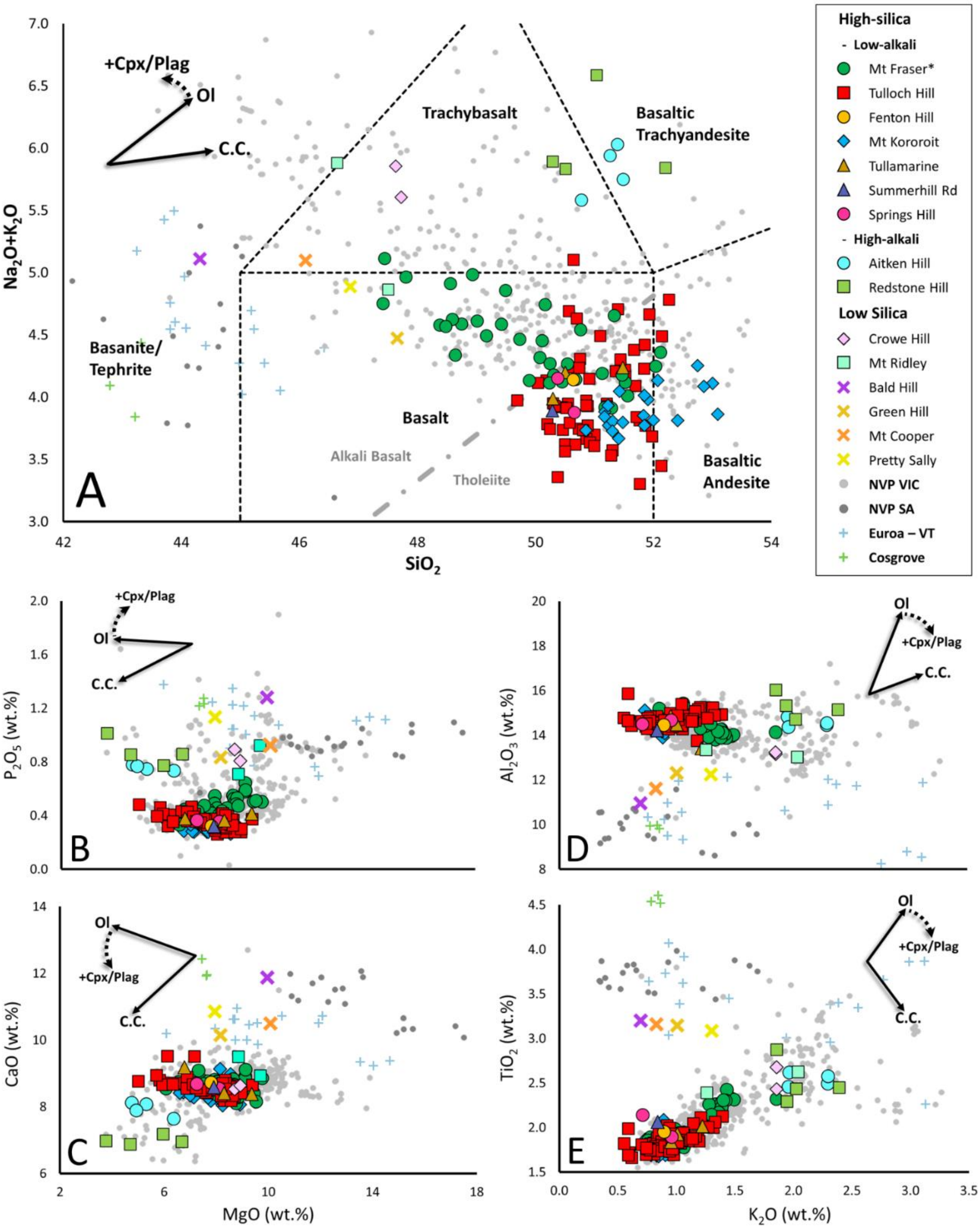

Figure 6.8: XRF major element geochemistry of samples from NVP lava flows in the Melbourne area. Black arrows show the trends expected from olivine (Ol) fractionation (forsterite component = 80%) and contamination by crustal rocks (C.C; bulk crust values from Rudnick and Gao, 2014). The dashed arrows

indicate the effect of clinopyroxene and plagioclase fractionation (+Cpx/Plag). The alkali basalt/tholeiite boundary is based on Macdonald and Katsura (1964). Published compositions for NVP samples are divided into those from Victoria (NVP VIC) and South Australia (Frey and Green, 1974; Ellis, 1976; Irving and Green, 1976; Frey et al., 1978; McDonough et al., 1985; Price et al., 1997; Stone et al., 1997; Vogel and Keays, 1997; McBride et al., 2001; Foden et al., 2002; Demidjuk et al., 2007; NVP SA; Boyce et al., 2015; Oostingh et al., 2016). Euroa - Violet Town (Euroa - VT) and Cosgrove Leucitite (Cosgrove) geochemical data is from Paul et al. (2005). *Mount Fraser Flow lava chemistry evolves from low- to high-silica with stratigraphic height.

Table 6.1: Diagnostic features of each flow and flow unit, listed in order of increasing age.

Flow(s)	Flow Unit	Defining Petrographic Features	Geochemical classification*
Mount Fraser	**A**	Intergranular texture, fine grained clinopyroxene	Trachybasalt to alkali basalt
	B	Coarse-grained clinopyroxene, (sub-trachytic texture)	Alkali basalt to transitional basalt
	C	Intergranular, porphyritic texture, olivine/plagioclase/clinopyroxene phenocrysts	Transitional basalt to tholeiite
Tulloch Hill	**A**	Intergranular texture	Transitional basalt to tholeiite
	B	Ophitic texture	
	C	Intergranular texture	
Fenton Hill		Ophitic texture, radial plagioclase, light brown devitrified glass, carbonate in pore spaces	Tholeiite
Mount Kororoit	**A**	Intergranular texture	Tholeiite to basaltic andesite
	B	Ophitic texture	
	C	Intergranular texture	
Aitken Hill		Clinopyroxene phenocrysts, porphyritic texture	Trachybasalt to basaltic trachyandesite
Summerhill Road		Sub-ophitic texture, carbonate in pore spaces	Tholeiite
Redstone Hill		Olivine, clinopyroxene and plagioclase phenocrysts, porphyritic and sometimes trachytic texture	Trachybasalt to basaltic trachyandesite
Springs Hill		Porphyritic texture, fine-grained groundmass	Tholeiite
Crowe Hill		Porphyritic texture, olivine and clinopyroxene phenocrysts, very fine-grained	Trachybasalt
Mount Ridley		Porphyritic texture, very fine grained	Trachybasalt to alkali basalt
Tullamarine		Porphyritic texture, large grain size	Tholeiite
Bald Hill, Pretty Sally, Green Hill and Mount Cooper		Porphyritic texture, interstitial feldspar with poikilitic clinopyroxene.	Basanite to alkali basalt

*Based on TAS classification diagram (**Fig. 6.8a**)

6.4.3 ^{40}Ar/^{39}Ar dating results

Of the 15 lava flows mapped in this study, 11 samples contained unaltered, essentially holocrystalline groundmass deemed suitable for ^{40}Ar/^{39}Ar analysis. Multiple samples from the Mount Kororoit (n = 6) and Redstone Hill (n = 2) lava flows were selected, and a single ^{40}Ar/^{39}Ar sample was selected from each of the Fenton Hill, Aitken Hill, Summerhill Road, Springs Hill, Crowe Hill, Mount Ridley, Tullamarine and Bald Hill flows. ^{40}Ar/^{39}Ar dating results for samples of the Tulloch Hill (n = 8) and Mount Fraser (n = 11) lava flows are reported in Heath et al. (2018). Age spectra, inverse isochrons and Ca/K spectra for individual aliquants are displayed in **Appendix A.2**. Complete ^{40}Ar/^{39}Ar datasets for each lava flow are reported in **Appendices A.5 – A.14**. 'Preferred' inverse isochrons and isochron ages were assigned on the basis of criteria outlined by Heath et al. (2018) and exclude data from discordant heating steps. Age plateaus are defined as three or more consecutive heating steps, each within 2σ error of the mean, and comprising a minimum 50% of the total ^{39}Ar released (e.g., Fleck et al., 1977; McDougall and Harrison, 1999, and references therein), or 30 – 50% of the total ^{39}Ar in the case of 'mini-plateaus'.

Springs Hill Flow

Three aliquants of sample ME4J from the Springs Hill Flow produced age spectra exhibiting statistically significant plateau ages (**Fig. 6.9a**). A weighted mean of the ^{40}Ar*/^{39}Ar values of all plateau-forming steps (n = 23) gives an age of 4.016 ± 0.013 Ma (MSWD = 1.2; p = 0.23). A composite inverse isochron for the same data gives an indistinguishable age of 4.029 ± 0.047 Ma (95% CI; MSWD = 1.2; p = 0.2) and an atmospheric (^{40}Ar/^{36}Ar)$_i$ intercept (298.1 ± 1.4). The three aliquants had a total combined radiogenic ^{40}Ar (^{40}Ar*) content of 24.3% (**Table 6.2**).

Bald Hill Flow

Six plagioclase grains from the Bald Hill lava flow were individually step-heated. Four grains produced concordant ages for the high-temperature (high-T) steps (**Fig. 6.9b**), yielding a weighted mean age of 7.931 ± 0.038 Ma (MSWD = 0.76; p = 0.65). A composite inverse isochron constructed from these steps gives an indistinguishable age of 7.962 ± 0.068 Ma (95% CI; MSWD = 0.72; p = 0.67) and an atmospheric $(^{40}Ar/^{36}Ar)_i$ value of 293.3 ± 9.7. The mean $^{40}Ar^*$ content for the four concordant aliquants was 79.9%. The remaining two grains produced discordant apparent ages of 5.5 – 371.3 Ma for individual heating steps.

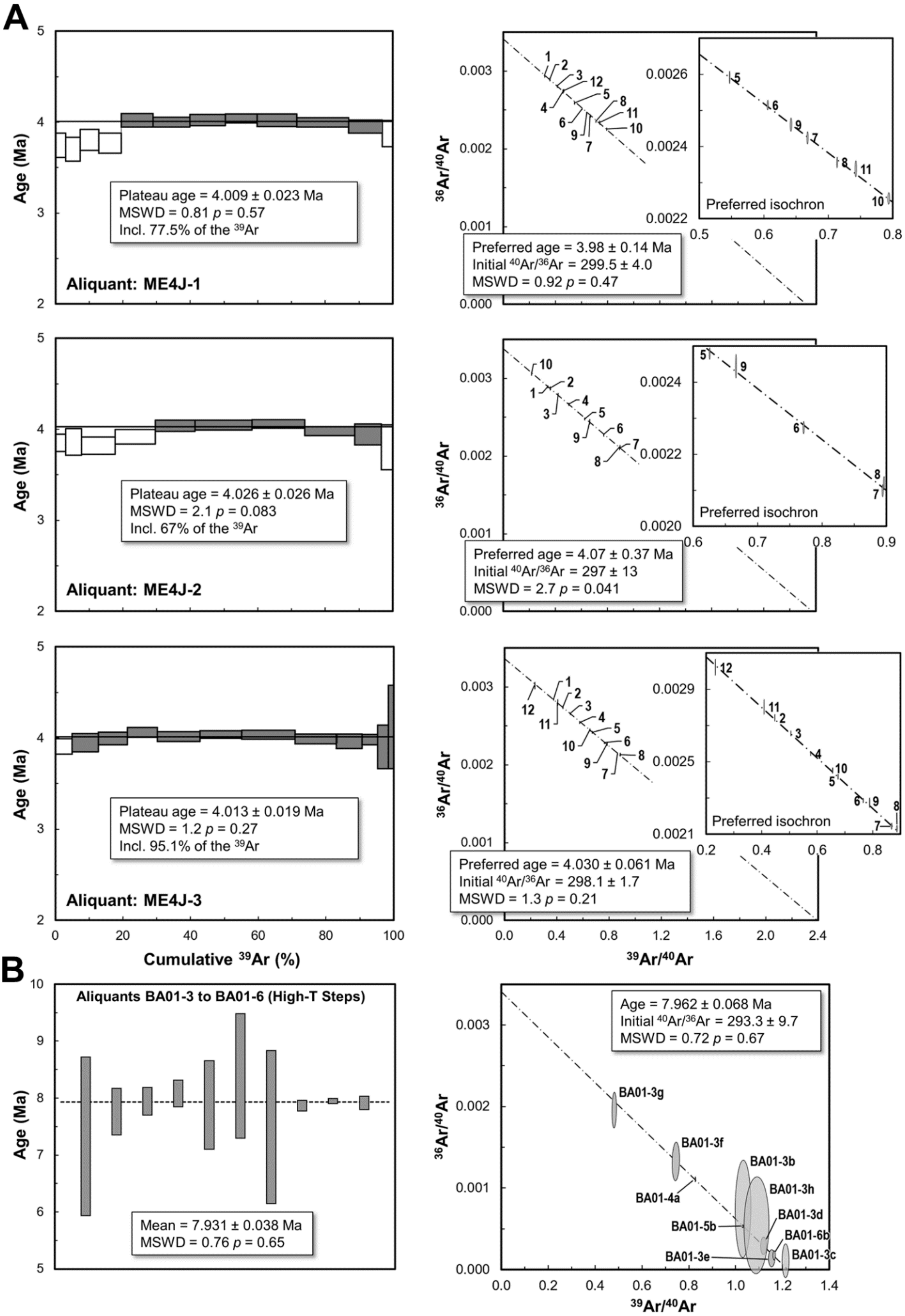
A
Age (Ma)
Plateau age = 4.009 ± 0.023 Ma
MSWD = 0.81 p = 0.57
Incl. 77.5% of the 39Ar
Aliquant: ME4J-1
36Ar/40Ar
Preferred age = 3.98 ± 0.14 Ma
Initial 40Ar/36Ar = 299.5 ± 4.0
MSWD = 0.92 p = 0.47
Preferred isochron
Plateau age = 4.026 ± 0.026 Ma
MSWD = 2.1 p = 0.083
Incl. 67% of the 39Ar
Aliquant: ME4J-2
Preferred age = 4.07 ± 0.37 Ma
Initial 40Ar/36Ar = 297 ± 13
MSWD = 2.7 p = 0.041
Preferred isochron
Plateau age = 4.013 ± 0.019 Ma
MSWD = 1.2 p = 0.27
Incl. 95.1% of the 39Ar
Aliquant: ME4J-3
Preferred age = 4.030 ± 0.061 Ma
Initial 40Ar/36Ar = 298.1 ± 1.7
MSWD = 1.3 p = 0.21
Preferred isochron
Cumulative 39Ar (%)
39Ar/40Ar
B
Aliquants BA01-3 to BA01-6 (High-T Steps)
Mean = 7.931 ± 0.038 Ma
MSWD = 0.76 p = 0.65
Age = 7.962 ± 0.068 Ma
Initial 40Ar/36Ar = 293.3 ± 9.7
MSWD = 0.72 p = 0.67
BA01-3g
BA01-3f
BA01-3b
BA01-4a
BA01-3h
BA01-3d
BA01-5b
BA01-6b
BA01-3e
BA01-3c

Figure 6.9: a) Age spectra (left) and inverse isochron diagrams (right) for groundmass aliquants of the Springs Hill flow. Plateau steps are shown in grey, and inverse isochron insets show the preferred isochrons including only these steps, with corresponding isochron ages. Step numbers are shown in bold. **b)** Weighted mean age calculated for high-temperature heating steps of single-grain aliquots of Bald Hill plagioclase sample BA01 (left), and the corresponding composite inverse isochron diagram (right), with step numbers labelled in bold.

Tullamarine Flow

Two groundmass aliquants of Tullamarine Flow sample MH75 were analysed, one of which (MH75C-2) yielded a plateau age of 4.5961 ± 0.0069 Ma (MSWD = 0.23; $p = 0.95$; **Fig. 6.10a**) with a ^{40}Ar* content of 72.2%. The corresponding inverse isochron for the plateau-forming steps gives an identical age of 4.595 ± 0.011 Ma (95% CI; MSWD = 0.27; $p = 0.9$) and an atmospheric (^{40}Ar/^{36}Ar)$_i$ value of 298.8 ± 1.4. Aliquant MH75C-1 yielded a more discordant age spectrum, with apparent ages decreasing from ca. 4.69 Ma to ca. 4.58 Ma with increasing temperature. A poorly fitted inverse isochron including all data (n = 18) gives an age of 4.653 ± 0.047 Ma (95% CI; MSWD = 40; $p < 0.001$), and a corresponding (^{40}Ar/^{36}Ar)$_i$ value of 294.1 ± 8.9.

Fenton Hill Flow

Two groundmass aliquants of Fenton Hill Flow sample MH10 were analysed. Aliquant MH10-1 produced an age spectrum that includes a mini-plateau segment in the high-T steps (**Fig. 6.10b**; n = 5; 42.9% cumulative ^{39}Ar) with an age of 2.943 ± 0.011 Ma (MSWD = 1.02; $p = 0.39$) and younger apparent ages for the low-temperature (low-T) steps. The total ^{40}Ar* content of MH10-1 was 69.6%. An inverse isochron constructed from the mini-plateau steps gives an indistinguishable age of 2.947 ± 0.040 Ma (95% CI; MSWD = 1.4; $p = 0.25$), with an atmospheric (^{40}Ar/^{36}Ar)$_i$ value of 297 ± 10. Aliquant MH10-2 yielded a discordant age spectrum with apparent ages generally decreasing from 3.29 ± 0.10 Ma (MH10-2a) to 3.073 ± 0.010 Ma (MH10-2l). An inverse isochron for this aliquant gives an apparent age of 3.081 ± 0.045 Ma (95% CI; MSWD = 21; $p < 0.001$) and a supra-atmospheric (^{40}Ar/^{36}Ar)$_i$ ratio of 304.5 ± 3.2.

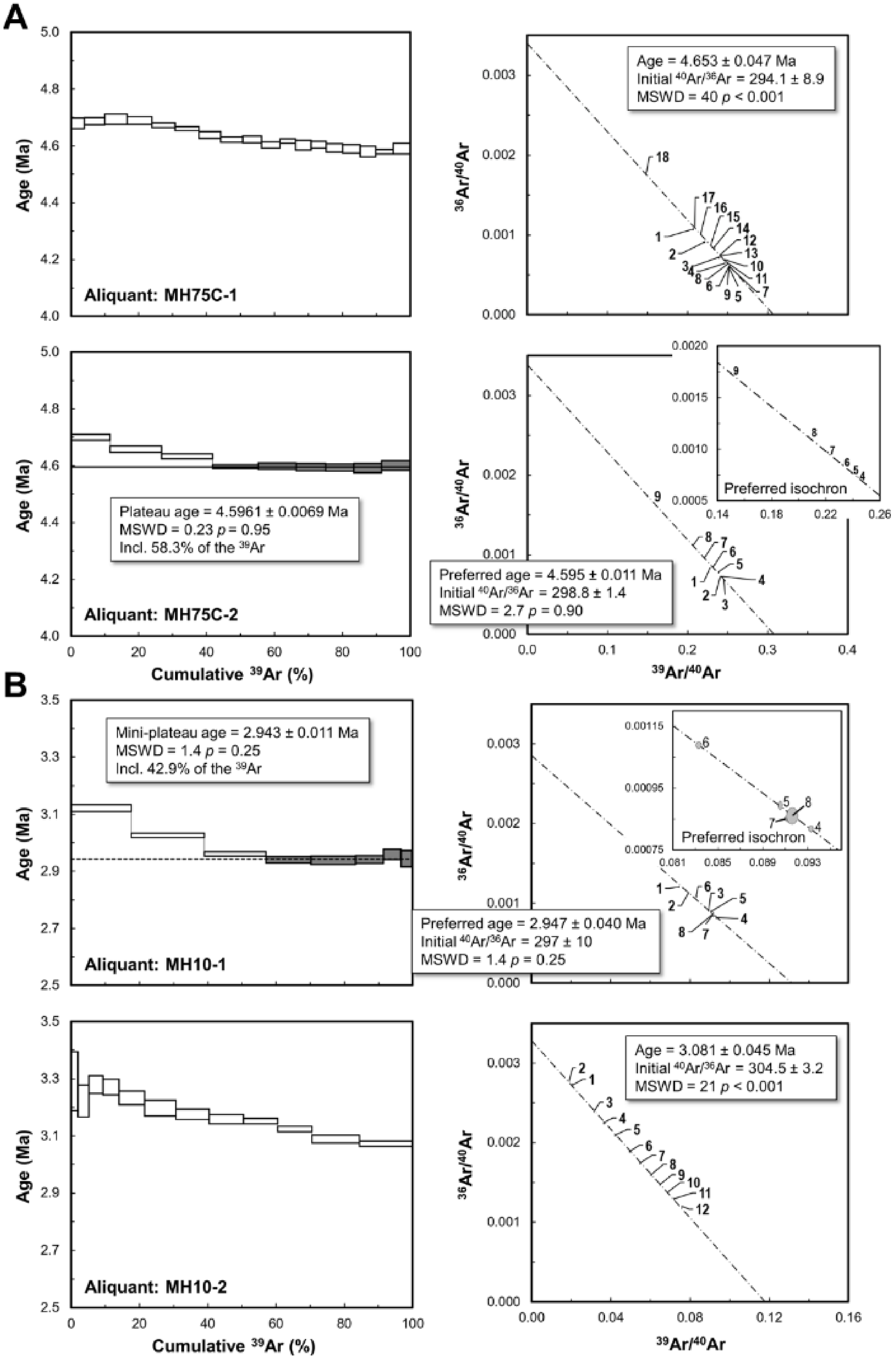
A
Aliquant: MH75C-1
Age = 4.653 ± 0.047 Ma
Initial ^{40}Ar/^{36}Ar = 294.1 ± 8.9
MSWD = 40 p < 0.001
Aliquant: MH75C-2
Plateau age = 4.5961 ± 0.0069 Ma
MSWD = 0.23 p = 0.95
Incl. 58.3% of the ^{39}Ar
Preferred age = 4.595 ± 0.011 Ma
Initial ^{40}Ar/^{36}Ar = 298.8 ± 1.4
MSWD = 2.7 p = 0.90
Preferred isochron
Age (Ma)
Cumulative ^{39}Ar (%)
^{36}Ar/^{40}Ar
^{39}Ar/^{40}Ar
B
Mini-plateau age = 2.943 ± 0.011 Ma
MSWD = 1.4 p = 0.25
Incl. 42.9% of the ^{39}Ar
Aliquant: MH10-1
Preferred age = 2.947 ± 0.040 Ma
Initial ^{40}Ar/^{36}Ar = 297 ± 10
MSWD = 1.4 p = 0.25
Preferred isochron
Aliquant: MH10-2
Age = 3.081 ± 0.045 Ma
Initial ^{40}Ar/^{36}Ar = 304.5 ± 3.2
MSWD = 21 p < 0.001
Age (Ma)
Cumulative ^{39}Ar (%)
^{36}Ar/^{40}Ar
^{39}Ar/^{40}Ar

Figure 6.10: Age spectra (left) and inverse isochron diagrams (right) for groundmass aliquants of the **a)** Tullamarine and **b)** Fenton Hill flows. Plateau and mini-plateau steps are shown in grey, and inverse isochron insets show the preferred isochrons including only these steps, with corresponding preferred isochron ages. Step numbers are shown in bold.

Redstone Hill Flow

A single groundmass aliquant was analysed from each of Redstone Hill Flow samples BB22 and MH02. The age spectrum for aliquant BB22-1 is hump-shaped, with apparent ages ranging from 3.27 ± 0.17 Ma to 4.059 ± 0.078 Ma, and a total $^{40}Ar^{*}$ content of 21.1%. A central mini-plateau representing 34.7% of the total ^{39}Ar has an age of 4.043 ± 0.022 Ma (MSWD = 0.91; $p = 0.45$) (**Fig. 6.11a**). An inverse isochron constructed from these intermediate steps gives an indistinguishable age of 4.041 ± 0.091 Ma (95% CI; MSWD = 1.2; $p = 0.3$) and an atmospheric $(^{40}Ar/^{36}Ar)_i$ intercept of 298.6 ± 3.1. Data from aliquant MH02-1 yield decreasing apparent ages with increasing laser power (6.258 ± 0.006 Ma to 5.797 ± 0.030 Ma), and show extreme discordance in inverse isochron space (**Appendix A.2**).

Mount Kororoit Flow

Age spectra for groundmass from all seven samples of the Mount Kororoit Flow (MH01S, MH01N, MH04, MH011, MH56A, BH47B, BH269) exhibit a general pattern of increasing apparent ages with increasing laser power (**e.g. Fig. 6.11b**), with values ranging from 1.997 ± 0.316 Ma (MH11-1a) to 3.286 ± 0.072 Ma (MH11-1s; **Appendix A.9**). Inverse isochrons for five aliquants (MH01S-1; MH01N-1; MH04-1; MH56A-1 &

BH47B-1) give (^{40}Ar/^{36}Ar)$_i$ intercepts within error of the atmospheric value. For these aliquants, which have a mean ^{40}Ar* content of 13.5%, a weighted mean inverse isochron age of 3.10 ± 0.12 Ma (MSWD = 0.4; p = 0.75) is calculated, excluding results from aliquant MH56A-1 (omitted due to contamination from a damaged cover glass). The other three aliquants (MH01N-2; MH11-1; BH269-1) give older inverse isochron ages (3.43 ± 0.12 to 3.50 ± 0.42 Ma [95% CI]) and were excluded from mean age calculations due to sub-atmospheric (^{40}Ar/^{36}Ar)$_i$ values (290.2 ± 1.6 to 293.1 ± 1.5) (see Heath et al. (2018).

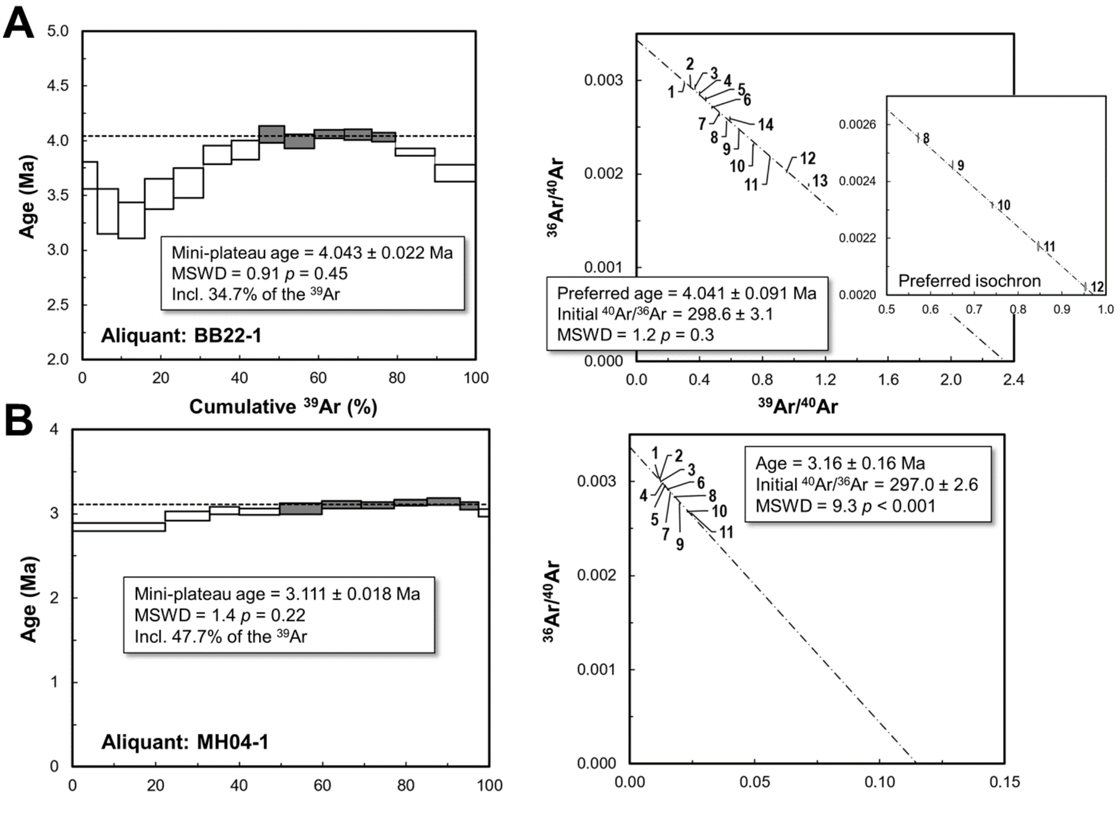

Figure 11: a) Age spectrum (left) and inverse isochron (right) of aliquant BB22-1 from the Redstone Hill flow. Mini-plateau steps are shown in grey, and the inverse isochron inset shows the preferred isochron including only these steps, with the corresponding preferred isochron age. **b)** The age spectrum (left) and inverse isochron (right) of aliquant MH04-1 are representative of results from the Mount Kororoit Flow. Mini-plateau steps are shown in grey.

Aitken Hill, Crowe Hill and Mount Ridley flows

All groundmass step-heating spectra for Aitken Hill, Crowe Hill and Mount Ridley flow samples are characterised by decreasing apparent ages with increasing temperature (**Fig. 6.12a-c**). Apparent ages for the Aitken Hill flow are between 4.009 ± 0.021 Ma (MH35-

1a) and 3.639 ± 0.064 Ma (MH35-1m; **Fig. 6.12a**). Total gas and inverse isochron ages for each aliquant are within error of the weighted mean total gas age of 3.8035 ± 0.0074 Ma (MSWD = 0.02; $p = 0.89$), with inverse isochrons exhibiting atmospheric ($^{40}Ar/^{36}Ar)_i$ intercepts, although with significant scatter (MSWD = 216 – 245). The two aliquants have a combined $^{40}Ar^*$ content of 78.2%.

Apparent ages the Crowe Hill Flow are between 4.615 ± 0.014 Ma (MH68-1a) and 4.127 ± 0.060 Ma (MH68-1a; **Fig. 6.12b**). Inverse isochrons of both aliquants exhibit significant scatter (MSWD = 160-167), and isochron ages are older than the weighted mean total-gas age of 4.4820 ± 0.0099 Ma (MSWD = 1.02; $p = 0.31$). The total $^{40}Ar^*$ from both aliquants was 76.2%.

The two aliquants of the Mount Ridley flow give apparent ages between 4.678 ± 0.006 Ma (KA13M-2a) and 4.429 ± 0.030 Ma (KA13M-1i; **Fig. 6.12c**), with a total $^{40}Ar^*$ content of 78.2%. Inverse isochron ages for each aliquant are 4.655 ± 0.061 Ma (95% CI; KA13M-1) and 4.709 ± 0.066 Ma (95% CI; KA13M-2), each with corresponding sub-atmospheric ($^{40}Ar/^{36}Ar)_i$ values (KA13M-1 = 288.6 ± 9.6; KA13M-2 = 276 ± 13) and exhibiting significant scatter (MSWD = 69 – 73). The combined weighted mean total-gas age is younger than both isochron ages, at 4.6065 ± 0.0067 Ma (MSWD = 2.2; $p = 0.14$).

Summerhill Road Flow

Age spectra of both aliquants of groundmass sample KA13L show increasing apparent ages with increasing laser power (**Fig. 6.12d**). The apparent age range for all heating steps is 3.223 ± 0.060 Ma (KA13L-1i) to 3.909 ± 0.018 Ma (KA13L-2g). Inverse isochron ages for each aliquant were 4.10 ± 0.11 Ma (KA13L-1; 95% CI; MSWD = 34; $p < 0.001$) and

4.065 ± 0.019 Ma (KA13L-2; 95% CI; MSWD = 0.89; $p = 0.5$), with corresponding sub-atmospheric $(^{40}\mathrm{Ar}/^{36}\mathrm{Ar})_i$ values of 265 ± 12 and 271.5 ± 2.0, respectively. A weighted mean of the total-gas ages for both aliquants is 3.82 ± 0.38 Ma (95% CI; MSWD = 21; $p < 0.001$), and total calculated $^{40}\mathrm{Ar}^*$ was 55.6%.

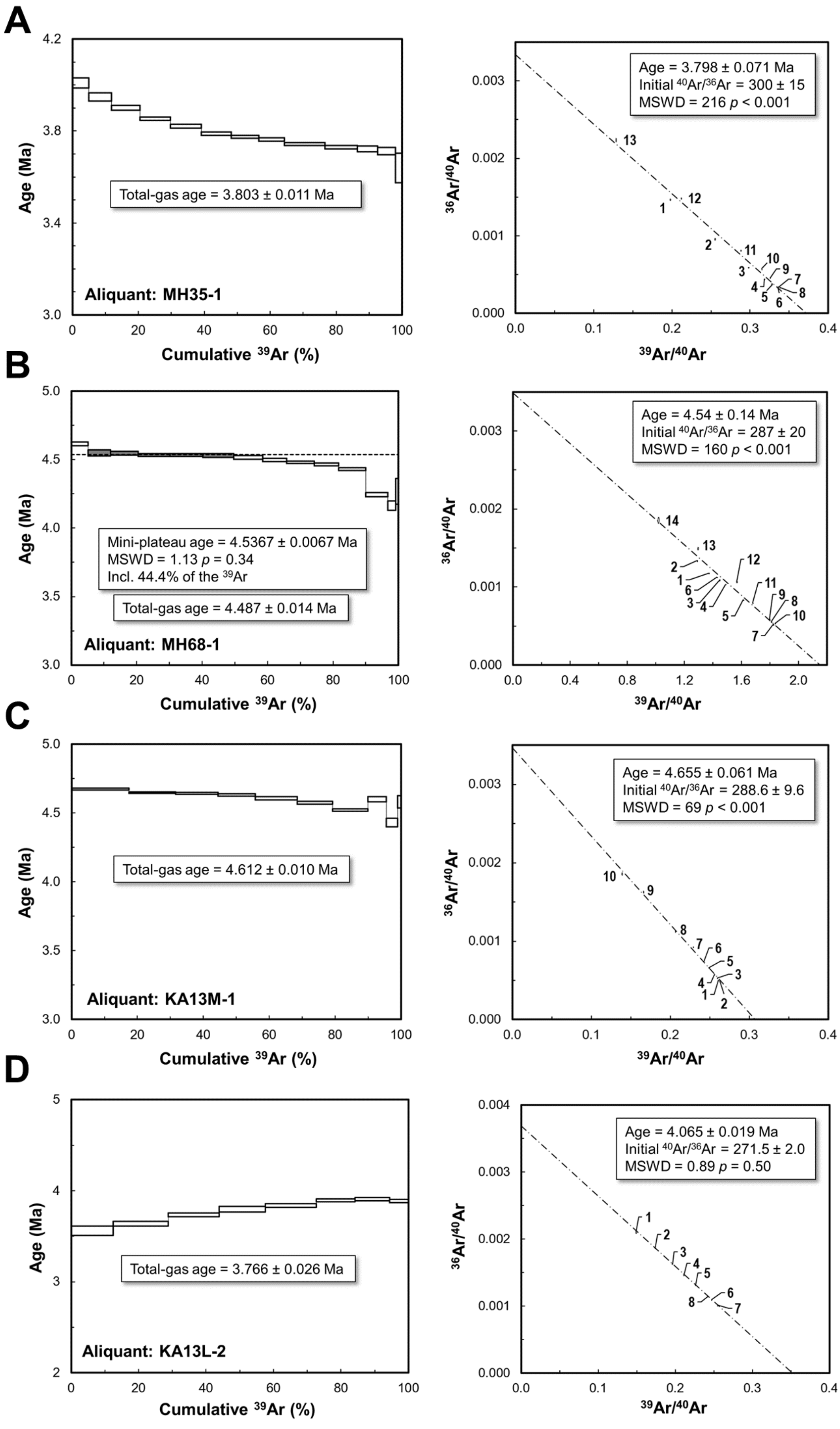
A
Age (Ma)
Cumulative ^{39}Ar (%)
Total-gas age = 3.803 ± 0.011 Ma
Aliquant: MH35-1
^{36}Ar/^{40}Ar
^{39}Ar/^{40}Ar
Age = 3.798 ± 0.071 Ma
Initial ^{40}Ar/^{36}Ar = 300 ± 15
MSWD = 216 p < 0.001
B
Mini-plateau age = 4.5367 ± 0.0067 Ma
MSWD = 1.13 p = 0.34
Incl. 44.4% of the ^{39}Ar
Total-gas age = 4.487 ± 0.014 Ma
Aliquant: MH68-1
Age = 4.54 ± 0.14 Ma
Initial ^{40}Ar/^{36}Ar = 287 ± 20
MSWD = 160 p < 0.001
C
Total-gas age = 4.612 ± 0.010 Ma
Aliquant: KA13M-1
Age = 4.655 ± 0.061 Ma
Initial ^{40}Ar/^{36}Ar = 288.6 ± 9.6
MSWD = 69 p < 0.001
D
Total-gas age = 3.766 ± 0.026 Ma
Aliquant: KA13L-2
Age = 4.065 ± 0.019 Ma
Initial ^{40}Ar/^{36}Ar = 271.5 ± 2.0
MSWD = 0.89 p = 0.50

Figure 6.12: Representative age spectra (left) and inverse isochron diagrams (right) for aliquants of the **a)** Aitken Hill, **b)** Crowe Hill, **c)** Mount Ridley, and **d)** Summerhill Road lava flows. Mini-plateau steps are shown in grey, and step numbers are shown in bold.

6.5 Discussion

6.5.1 Interpretation of ^{40}Ar/^{39}Ar results

The complex age spectra exhibited by many of the samples require cautious interpretation in order to constrain eruption ages (**Table 6.2**). Notably, several samples are characterised by isochrons with sub-atmospheric (^{40}Ar/^{36}Ar)$_i$ values. Heath et al. (2018) noted a correlation between erroneously old apparent isochron ages and sub-atmospheric (^{40}Ar/^{36}Ar)$_i$ values in basaltic groundmass samples. Heath et al. (2018) interpreted this relationship to be an artefact of isochron rotation, concluding that inverse isochron ages only give meaningful eruption ages where an atmospheric (^{40}Ar/^{36}Ar)$_i$ value is found; with rare exceptions. This study also showed that for age spectra exhibiting discordance, a good estimate of a sample's eruption age might be calculated by selecting a subset of heating steps that plot as a linear array in inverse isochron space and give an atmospheric (^{40}Ar/^{36}Ar)$_i$ intercept. If no such subset exists, it may not be possible to assign an eruption age to a given flow; however, a maximum or minimum age may be inferred from the inverse isochron, depending on whether the (^{40}Ar/^{36}Ar)$_i$ intercept is sub- or supra-atmospheric. Based on modelling results, new data, and qualitative observations made in previous studies, Heath et al. (2018) showed that a sub-atmospheric (^{40}Ar/^{36}Ar)$_i$ value is generally indicative of clockwise rotation of the isochron, with the corresponding apparent age systematically older than the eruption age. Conversely, a supra-atmospheric

(^{40}Ar/^{36}Ar)$_i$ value is indicative of anti-clockwise rotation, with the apparent isochron age being younger than the eruption age. It was also noted that robust application of this approach might require consistent data across multiple aliquants and/or samples.

Heath et al (2018) reported an eruption age of 0.8038 ± 0.0017 Ma (2σ) for the Mount Fraser Flow, calculated from the weighted mean of plateau-step ^{40}Ar*/^{39}Ar values from three aliquants of a single sample. The Tulloch Hill Flow was assigned an eruption age of 2.309 ± 0.009 Ma (2σ), calculated from the weighted mean of high-T inverse isochron ages (i.e. excluding low-T steps) for three aliquants from three different samples (Heath et al., 2018). While in both cases these data constrained atmospheric (^{40}Ar/^{36}Ar)$_i$ values and elevated ^{40}Ar* contents (>20% ^{40}Ar*), many other samples from the Mount Fraser and Tulloch Hill flows were characterised by very low ^{40}Ar* contents (as low as 0.7%), and produced age spectra with erroneously young (sometimes negative) apparent ages in low-T steps and erroneously old ages in high-T steps. Heath et al (2018) attributed this discordance to mass-dependent fractionation during step-heating analysis (e.g., Trieloff et al., 2005). Some samples with high-^{40}Ar* contents (>20% ^{40}Ar*) in the study of Heath et al (2018) yielded descending age spectra, attributed to recoil of ^{39}Ar, whereby ^{39}Ar is redistributed from high-K, early outgassing phases into low-K, later outgassing phases, with some ^{39}Ar lost to the atmosphere.

In the current study, groundmass samples from the Springs Hill and Tullamarine flows (ME4J and MH75) yielded atmospheric (^{40}Ar/^{36}Ar)$_i$ values and produced statistically significant plateau ages of 4.016 ± 0.013 Ma and 4.5961 ± 0.0069 Ma respectively, which are interpreted as eruption ages. Similarly, the Fenton Hill, Mount Kororoit, and Redstone Hill groundmass samples, together with high-T data for Bald Hill plagioclase, exhibit atmospheric ($^{40}Ar/^{36}Ar)_i$ values, and the preferred age results of 2.943 ± 0.011 Ma (mini-plateau age, Fenton Hill), 3.10 ± 0.12 Ma (inverse isochron weighted mean age, Mount Kororoit), 4.043 ± 0.022 Ma (mini-plateau age, Redstone Hill), and 7.931 ± 0.038 Ma (weighted mean high-T, Bald Hill) are interpreted as eruption ages.

Samples from the remaining four flows (Aitken Hill, Crowe Hill, Mount Ridley and Summerhill Road) produced highly discordant age spectra, complicating the assignment of eruption ages. Combined total-gas ages for aliquants of the Aitken Hill (3.8035 ± 0.0074 Ma), Crowe Hill (4.482 ± 0.010 Ma) and Mount Ridley (4.6065 ± 0.0067 Ma) flows are interpreted as maximum eruption ages given that patterns in age spectra and inverse isochron data are consistent with ^{39}Ar recoil loss/redistribution. The combined total-gas age for two aliquants of the Summerhill Road Flow (3.82 ± 0.38 Ma) is interpreted as a minimum age, as isochron results are consistent with the effects of mass-dependent fractionation (Heath et al., 2018).

Table 6.2: Preferred ^{40}Ar/^{39}Ar age constraints, radiogenic argon content and, where applicable, inferred dominant cause of isotopic disturbance in groundmass and plagioclase samples. Underlined ages are minimum or maximum eruption ages (see text).

Lava Flow	Age (Ma)	Error	Age Determination	Age type	^{40}Ar* (avg. %)[a]	Interpreted dominant cause of disturbance
Mount Fraser[b]	0.804	0.002	Plateau weighted mean (n=3)	Eruption age	42.2	N/A
Tulloch Hill[b]	2.309	0.009	Preferred isochron weighted mean (n=3)	Eruption age	47.6	^{39}Ar recoil
Fenton Hill	2.943	0.011	Mini-plateau (42.9% of cum. ^{39}Ar)	Eruption age	69.6	^{39}Ar recoil
Mount Kororoit	3.1	0.12	Isochron weighted mean (n=5)	Eruption age	13.5	Fractionation
Aitken Hill	3.804	0.007	Total gas weighted mean (n=2)	Maximum age	78.2	^{39}Ar recoil
Summerhill Road	3.82	0.38	Total gas weighted mean (n=2)	Minimum age	55.6	Fractionation
Redstone Hill	4.043	0.022	Mini-plateau (34.7% of cum. ^{39}Ar)	Eruption age	21.1	Fractionation
Springs Hill	4.016	0.013	Plateau weighted mean (n=3)	Eruption age	24.3	Fractionation
Crowe Hill	4.482	0.01	Total gas weighted mean (n=2)	Maximum age	76.2	^{39}Ar recoil
Tullamarine	4.596	0.007	Plateau age	Eruption age	72.2	^{39}Ar recoil
Mount Ridley	4.607	0.007	Total gas weighted mean (n=2)	Maximum age	78.2	^{39}Ar recoil
Bald Hill[c]	7.931	0.038	High-T step weighted mean (n=4)	Eruption Age	79.9	N/A

[a] Average of all aliquants included in age calculations, assuming an air ^{40}Ar/^{36}Ar ratio of 298.56 (Lee et al., 2006). [b] Data from Heath et al. (2018). [c] Plagioclase sample.

6.5.2 Lava flow map of the Melbourne area

As noted above, petrographic parameters proved to be effective for mapping many individual lava flows and flow units within the Melbourne area. The most useful petrographic features were phenocryst assemblages, modal mineral abundances, groundmass grain sizes, and diagnostic textures. Although differences in the positions of samples within individual flows and effects of post-emplacement history (e.g., weathering) introduced complications for classification, most samples were readily assigned to a particular flow based on petrographic features and field relationships alone. Major element geochemistry was effective at confirming differences between flows inferred from petrographic examination, but was generally not useful for distinguishing petrographically similar flows. The final lava flow map of the Melbourne area (**Fig. 6.7**) was constructed based on field relationships, stratigraphy, petrography, geochemistry, and ^{40}Ar/^{39}Ar age results (**Table 6.2**).

6.5.3 Eruption chronology and landscape evolution of the Melbourne area

>4.6 Ma: Pre-NVP volcanic activity

The oldest lava flows mapped as part of this study included a small-volume basanite flow originating from Bald Hill, a trachybasalt from Mount Cooper, and alkali basalts from Pretty Sally and Green Hill (**Fig. 6.7**). These lavas all have similar petrography and geochemistry, and are distinct from any other NVP lavas sampled in this study, having much higher CaO and TiO_2 and lower Al_2O_3 and SiO_2 contents (**Fig. 6.8**). The timing of these eruption events was probably ca. 7 – 8 Ma, based on unpublished K-Ar data from Mount Cooper (ca. 8 Ma; Schleiger, 1983) and the current ^{40}Ar/^{39}Ar age for Bald Hill (7.931 ± 0.038 Ma). It is notable that these ages are distinctly older than the generally accepted maximum age for the NVP (~4.6 Ma; Price et al., 2003; Gray and McDougall, 2009) – see discussion below. As no samples suitable for $^{40}Ar/^{39}Ar$ dating were recovered from the Pretty Sally or Green Hill lava flows, these volcanoes remain undated. However, given the similarities in lava petrography and geochemistry to the Bald Hill samples (**Fig. 6.8; Table 6.1**), and the advanced weathering of the flows, they are likely to be of a similar age to Bald Hill and Mount Cooper (~8 Ma).

4.6 – 3.8 Ma: The Beginning of NVP activity

Seven of the 15 flows mapped were erupted during an apparent peak in Melbourne area volcanism at 4.6 to 3.8 Ma. The first to erupt were the 4.596 ± 0.007 Ma, tholeiitic Tullamarine and the ≤4.607 ± 0.007 Ma trachybasalt to alkali basalt Mount Ridley flows. The source of the Tullamarine Flow could not be identified definitively, but may be buried near Crowe Hill where the flow reaches its highest elevation (~600 m.a.s.l.). Alternatively, the Tullamarine Flow may represent a separate batch of melt that was erupted from Mount Ridley. Mapping reveals that the Tullamarine Flow filled a valley located adjacent to the present-day Deep Creek and Maribyrnong River (**Fig. 6.7**), with a lava thickness of at least 25 m, and a flow-front reaching a maximum width of ~7 km. The 4.607 ± 0.0067 Ma flow from Mount Ridley (maximum age) was determined to be of relatively small volume, filling a narrow valley to the east. Although their ages are indistinguishable, the significant differences in geochemistry between these two lava flows (**Fig. 6.8**) precludes a common parental melt.

The small-volume trachybasaltic eruption at Crowe Hill occurred shortly after 4.482 Ma and aside from construction of the volcano itself, did not drastically alter drainage patterns. Following this eruption there was a ca. 440 ka period of apparent quiescence before two large-volume eruptions occurred at Redstone Hill (4.043 ± 0.022 Ma) and Springs Hill (4.016 ± 0.013 Ma). Flow mapping reveals that some lavas (trachybasalt – basaltic trachyandesite) from Redstone Hill flowed up to 10 km north and west of the eruption point in relatively thin sheets but the main lava mass flowed southwards, filling a deep drainage channel parallel to the current Deep Creek, that had itself likely formed marginal to the Tullamarine Flow (**Fig. 6.7**). This thick lava package terminated near the present-day Maribyrnong River, where its flow was probably obstructed, forming a near stationary body and the spectacular columnar basalt of the Organ Pipes (**Fig 6.5c**).

The tholeiitic Springs Hill Flow is only exposed at the eruption point itself, having been buried by the large-volume Mount Fraser Flow (**Fig. 6.7**). The stratigraphic relationship between the two flows was only directly observed in one borehole (ME4), but it is possible that the unidentified flow in borehole KA13 (Summerhill Road Flow), located ~13 km SSW of Springs Hill (**Fig. 6.4**), is part of the Springs Hill Flow. The minimum age of 3.82 ± 0.38 Ma for the tholeiitic Summerhill Road Flow (sample KA13L) is within error of the Springs Hill eruption age, and the major element compositions of the two flows are highly similar (**Fig. 6.8**). Sample KA13L is also petrographically similar to the dated Springs Hill sample (ME4J) and borehole KA13 is located down-drainage from the eruption point. If these samples belong to the same flow, the Springs Hill flow covers a much larger area than suggested by its mapped extent in **Fig. 6.7**, bringing it closer in volume to other eruptions of tholeiitic composition.

The trachybasaltic to basaltic trachyandesitic Aitken Hill eruption likely occurred shortly after 3.80 Ma (maximum eruption age), filling two tributaries of Moonee Ponds Creek or its precursor; one flowing approximately north-south through the Bulla Granodiorite, and another around its eastern margin (**Fig. 6.7**).

3.8 – 0.8 Ma: intermittent volcanic activity

Approximately 700 ka of apparent quiescence followed the eruption of Aitken Hill. At ca. 3.11 Ma Mount Kororoit erupted, with tholeiitic to basaltic andesitic lavas filling several drainage channels that flowed in a northwest-southeast direction parallel to the present-day Maribyrnong River (**Fig. 6.7**). This was followed by the eruption of Fenton Hill at 2.947 ± 0.040 Ma, where tholeiitic lavas filled the area between the present-day Deep and Emu creeks, flowing southwards before terminating at the eastern margin of the Redstone Hill Flow. Approximately 650 ka later, Tulloch Hill erupted at 2.309 ± 0.009 Ma, producing, based on its extent and the depth interval spanned in boreholes, the largest volume of lava for any single eruption within the Melbourne area. Tholeiitic to transitional lavas flowed to the east and north-east of Tulloch Hill following small paleochannels before being captured by the major north-south paleo drainage system and eventually entering the paleo-Yarra River.

Following the Tulloch Hill eruption, the Melbourne area experienced approximately 1.5 Ma of apparent volcanic quiescence. At 0.8038 ± 0.0017 Ma, the eruption of Mount Fraser began with an alkali basalt flow that followed the course of a paleochannel along the eastern margin of the Tulloch Hill flow and the Morang Hills before entering the Plenty River precursor and flowing south to the paleo-Yarra River where it terminated near the eastern margin of the current central business district of Melbourne, having travelled >40 km (**Fig 6.7**). Eruption continued with progressively more silica-rich lavas, eventually filling the channel to the east of the Morang Hills such that the final, tholeiitic lava unit was forced around the western margin, following a shallower channel eroded into the Tulloch Hill flow. This final flow unit apparently terminated upon meeting a precursor of the Merri Creek.

0.8 Ma to present: volcanic dormancy and modern drainage development

The Melbourne area has been dormant since the eruption at Mount Fraser, allowing the development of the current immature drainage system. Major drainage channels have predominantly formed along flow boundaries (**Fig 6.7**) (e.g., Skeats and James, 1937; Edwards, 1938; Ollier, 1985), thus generally following the orientation of the paleo-drainage network.

6.5.4 A comparison with previous mapping and geochronology

The extent of the Green Hill, Crowe Hill, Tulloch Hill and Aitken Hill lava flows mapped in this study are in agreement with the map of lava flows and vents to the north of Melbourne produced by Hanks (1955). The remaining flows mapped by Hanks (1955), however, could not be reconciled with petrographic, geochemical and stratigraphic evidence for samples collected in the current study. Likewise, the eruption chronology suggested by Hanks (1995) is inconsistent with the $^{40}Ar/^{39}Ar$ ages reported here (**Fig. 6.3b**). One of five $(^{87}Sr/^{86}Sr)_i$ domains within the Melbourne area (zone 5 in **Fig. 6.3a**; Price et al., 1988) correlates well with the Mount Kororoit flow. However, the remaining four domains either span several different flows (zones 3 and 4) or cover different parts of the same flow (zones 1 and 2). Thus, although $(^{87}Sr/^{86}Sr)_i$ domains provide insight into source characteristics, they do not appear to be an effective tool for flow mapping. This may be due to episodic tapping of the same or similar mantle source(s) by multiple eruption events, and in some cases (e.g., Mount Fraser; Heath et al., 2018), multiple mantle sources apparently tapped during a single eruption.

Individual flows were often emplaced in multiple separate layers, as quenched margins formed around individual lava tongues and sheets. Since the interfaces between these layers provided paths for ground and meteoric water flow, the effects of weathering are often more extreme in these areas, in some cases giving the appearance of a flow boundary. Interpretation of these intra-flow layers as flow boundaries has likely resulted in overestimation of the number of flows represented in boreholes from previous NVP studies, which may have hindered the interpretation of eruption chronology (Stewart, 1975; Cas et al., 2017; Oostingh et al., 2017).

6.5.5 Older eruption centres of the Melbourne area

The chemistries of the older (ca. 8–7 Ma) basanitic, trachybasaltic and alkali basalt eruption points (Pretty Sally, Green Hill, Bald Hill and Mount Cooper) are unlike other NVP products, with the exception of some lavas in the Mount Gambier sub-province in South Australia that have much higher CaO and TiO_2 and lower Al_2O_3 than any Victorian samples (**Fig. 6.8**; Irving and Green, 1976; McDonough et al., 1985; Foden et al., 2002). As mentioned above, the age constraints for Bald Hill and Mount Cooper are much older than the generally accepted initiation time of NVP volcanism, although the unpublished K-Ar age of Mount Cooper (ca. 8 Ma; Schleiger, 1983) must be treated with caution, leaving only the Bald Hill age of 7.931 ± 0.038 Ma from the current study as a robust age constraint. Leucitite samples collected from Cosgrove, ~135 km NNE of Bald Hill, possess geochemical affinities with these four flows (**Fig. 6.8**; Paul et al., 2005). The Cosgrove leucitites have been assigned an $^{40}Ar/^{39}Ar$ age of 8.9 ± 0.2 Ma (Cohen et al.,

2008) and interpreted as the surface expression of a long-lived mantle plume (the ‘Cosgrove Track’), inferred from age-progressive volcanism that matches well with reconstructed Australian plate movements (e.g., Davies et al., 2015). Although the Australian plate would be expected to cover the distance between Cosgrove and Bald Hill over approximately 2 myr, based on its current velocity (ca. 60-70 mm/yr; e.g., DeMets et al., 2010), the measured age difference of ca.1 myr between the Cosgrove leucitites and Bald Hill (and likely Mount Cooper, Pretty Sally and Green Hill) does not preclude them from being related to the same plume, given uncertainties in plume head velocities and the lateral extent of the melt region (Davies et al., 2015). Furthermore, the N-S alignment of the four Melbourne area volcanoes (Pretty Sally, Green Hill, Bald Hill and Mount Cooper; (**Fig. 6.7**) is consistent with plate motion reconstructions (e.g., Davies et al., 2015; Jones et al., 2017).

Lavas from the Euroa – Violet Town area (~140 km N-W of Melbourne) were the focus of a geochemical study by Paul et al. (2005). These basanites and alkali basalts also have higher CaO and lower Al_2O_3 than Victorian NVP products (**Fig. 6.8**), but their age is only constrained by a single K-Ar ‘minimum age’ of 6.82 Ma (Wellman, 1974). The Euroa – Violet Town area is positioned between Cosgrove and Melbourne, so it is possible that volcanic activity in this area was also an expression of the Cosgrove Track mantle plume. Robust age constraints on these lavas is required to confirm their affinity to the Cosgrove Track leucitites, or if unrelated, whether they should be considered part of the NVP or a separate volcanic province.

6.5.6 Volcanic evolution of the NVP

Recent studies on volcanism in south-eastern Australia have suggested a general progression from large-volume tholeiitic eruptions to smaller volume, more alkali-rich eruptions for the NVP (e.g., Price et al., 1997; Lesti et al., 2008; Gray and McDougall, 2009; Oostingh et al., 2016). However, this evolution is not observed in the Melbourne area, with the ^{40}Ar/^{39}Ar data indicating that alkalic eruptions occurred exclusively before 3.8 Ma. Since ~3.8 Ma, transitional to tholeiitic basalt magmatism has occurred, with the only exception being the initial pulse of alkali basalt magmatism at 0.804 Ma forming the basal unit of the Mount Fraser Flow. This raises the possibility that the apparent age difference between the ‘cones’ and ‘plains’ groupings commonly used in the literature is due to sampling bias and inconsistent use of the labels ‘cones’ and ‘plains’. In the current study, fresh samples were more difficult to locate in older, smaller-volume lavas, and these older eruption points were not recognised as such in any previous study. If this problem is common to the entire NVP, together with the relatively small number of borehole samples utilised in dating studies, may have resulted in an over-representation of age constraints for younger alkali basalts.

The volcanic record of the Melbourne area reflects multiple episodes of alkalic and tholeiitic melt generation since ca. 4.6 Ma. This is consistent with the effects of a long-lived edge-driven convective cell at the base of the south-east Australian lithosphere (Demidjuk et al., 2007; Davies and Rawlinson, 2014; Aivazpourporgou et al., 2015; Rawlinson et al., 2016), among other possibilities, but likely rules out earlier mantle plume models. Smaller-volume magmas of alkali basalt composition were generated by lower-degree melting, either of the same source as tholeiitic magmas, or a different source (e.g., pyroxenite rather than peridotite). Alkalic activity might therefore reflect mantle conditions less conducive to melt generation. In the edge-driven convection model, this might be accommodated by periods of less-intense convection. Tholeiitic magmas probably involve higher-degree melts, reflecting increased upwelling during periods of more intense convection. Alternating brief periods of activity and long periods of quiescence are the natural result of a tectonic control on magmatism (e.g., van den Hove et al., 2017b), where expression at the surface does not reflect a change in the melt generation regime, but is the result of lithospheric conditions that are favourable for magma transport. As south-eastern Australia has been under compression since before 4.6 Ma (Sandiford et al., 2004), such conditions were likely extremely rare.

If the four older volcanoes of this study (Pretty Sally, Green Hill, Bald Hill and Mount Cooper) are a southern expression of the Cosgrove Track, the 7.931 ± 0.038 Ma age of Bald Hill would suggest that its passage across the eastern boundary of the NVP occurred well before 4.6 Ma, which raises doubts about models requiring entrainment of the Cosgrove Track plume as a trigger for the initiation of NVP activity.

6.6 Conclusions

The diagnostic petrographic features of individual basalt flows, supported by geochemical, geomorphological and geochronological constraints, have allowed construction of a highly detailed lava flow map and volcanic history for the Melbourne area, improving understanding of how lava flows have influenced drainage patterns. Volcanic activity in this area is observed to span ~8 – 0.8 Ma. Classification of the oldest four volcanoes studied (Pretty Sally, Green Hill, Bald Hill and Mount Cooper) is problematic, as their products are geochemically distinct from the bulk of the NVP, and it is possible they are the result of volcanic activity unrelated to the NVP. These volcanoes show some geochemical affinity with leucitites further north in Victoria that have previously been attributed to the Cosgrove track. They are distributed in a N-S trending array, and existing age constraints for two of these centres (~8 Ma) are only slightly older than when the Cosgrove Track mantle plume might have been positioned beneath Melbourne.

The volcanic history of the Melbourne area records numerous tholeiitic to alkalic eruptions, often separated by long periods of intervening inactivity. Episodic, long-lived volcanism over a limited area is consistent with the edge-driven convection model. Expression at the surface is likely controlled by local tectonic conditions and is not a reflection of changes to the melting regime.

In contrast to apparent trends in other areas of the NVP, earliest NVP volcanism around Melbourne was dominated by small-volume trachybasalts, alkali basalts, and basanites. Since ~3.8 Ma, all eruptions within this area have been large-volume, and predominantly tholeiitic, with long periods (100s of ka to 1.5 Ma) of intervening quiescence. Although the volcanic evolution of the Melbourne area might not perfectly represent that of the wider NVP, it raises the possibility that the apparent geochemical evolution of the NVP from tholeiitic to alkalic proposed by some province-wide studies is an artefact of an unrepresentative sample-set.

Chapter 7) Trace element geochemistry of Melbourne basalts

7.1 Trace element geochemistry results

Samples from five lava flows were analysed for trace elements, selected to cover the age range and geochemical spectrum of the NVP in the Melbourne area (**Table 7.1**; **Appendix A.20**). Samples of the Mount Fraser Flow were separated into three units based on stratigraphy, petrography and major element geochemistry (denoted 'Mount Fraser A, B and C') in order to investigate the mechanism behind magma evolution during this complex eruption event (see **section 7.3**). Samples from Mt Fraser C were also compared with the upper petrographic unit of the Tulloch Hill Flow ('Tulloch Hill C'), as these two units were often difficult to separate, having similar petrographic features and major element geochemistry (see **section 7.2**).

Patterns generated from average rare earth element (REE) compositions of each flow and flow unit (**Fig. 7.1**) show a similarity to ocean island basalts, with greater enrichment of heavy rare earth elements (HREE) over light rare earth elements (LREE). This is in line with previous work on NVP products where variable melting of a garnet-bearing host has been invoked to explain this relationship (e.g., Frey and Green, 1974). Samples of the smallest volume flow (Mt Ridley) show the greatest enrichment in LREE and depleted HREE (La/Yb = 26.1), whereas those from the high-silica, high-alkali Aitken Hill flow have slightly less LREE enrichment and HREE depletion (La/Yb = 17.1). Samples from large volume flows (Mt Fraser, Tulloch Hill and Tullamarine) each show similar REE patterns, with the exception of two samples that are depleted in Ce. Samples from flow units Mt Fraser A, B, and C respectively show a trend of decreasing LREE enrichment.

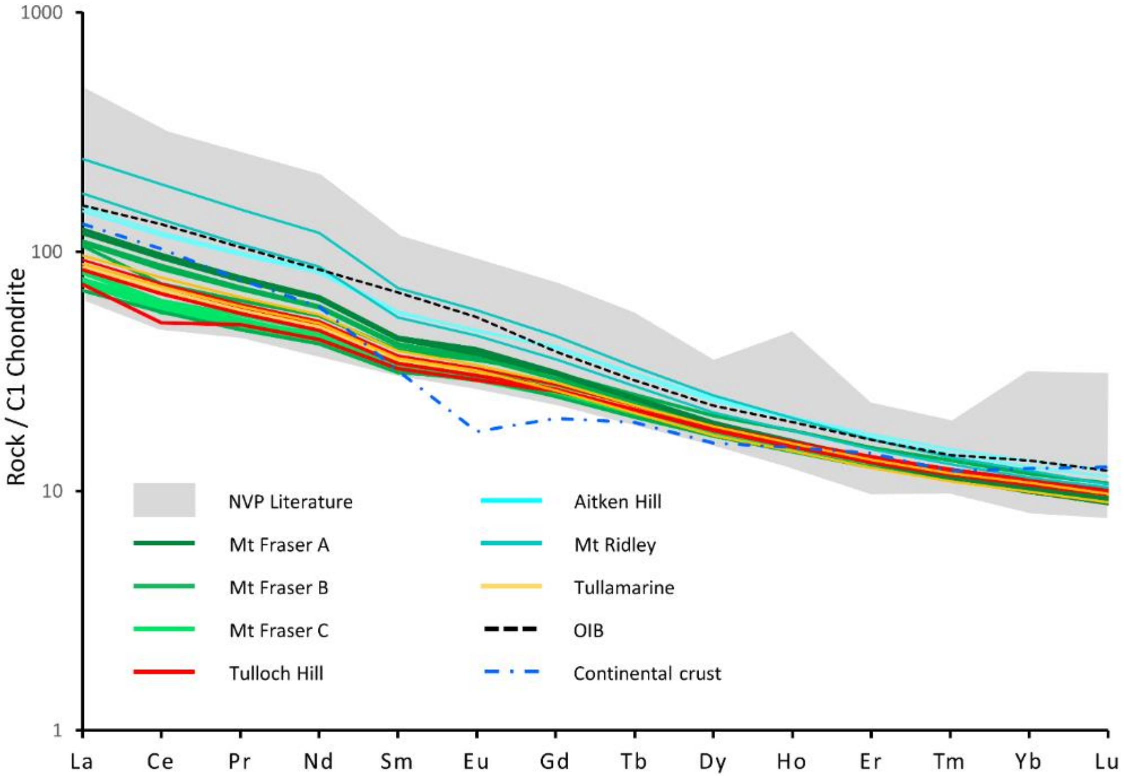

Figure 7.1: REE patterns of selected samples normalised to C1 chondrite (McDonough and Sun, 1995), with average ocean island basalt (OIB; Sun and McDonough, 1989) and continental crust (Rudnick and Gao, 2014) patterns for comparison (NVP Literature values from Frey and Green, 1974; Ellis, 1976; Irving and Green, 1976; Frey et al., 1978; McDonough et al., 1985; Price et al., 1997; Stone et al., 1997; Vogel and Keays, 1997; McBride et al., 2001; Foden et al., 2002; Demidjuk et al., 2007; Boyce et al., 2015; Oostingh et al., 2016).

Table 7.1 Average major and trace element abundance for selected lava flows of the Melbourne area.

Lava Flow:	**Mt Fraser A^b**	**$\pm 2\sigma^a$**	**Mt Fraser B^b**	**$\pm 2\sigma^a$**	**Mt Fraser C^b**	**$\pm 2\sigma^a$**	**Tulloch Hill**	**$\pm 2\sigma^a$**	**Aitken Hill**	**$\pm 2\sigma^a$**	**Tullamarine**	**$\pm 2\sigma^a$**	**Mt Ridley**	**$\pm 2\sigma^a$**
wt.% ↓														
Na_2O	3.21	*0.34*	3.40	*0.27*	3.19	*0.30*	3.06	*0.46*	3.68	*0.15*	3.14	*0.48*	3.70	*0.23*
MgO	8.96	*1.01*	7.89	*1.08*	7.51	*1.34*	7.73	*1.75*	5.54	*1.62*	7.51	*2.98*	9.24	*0.82*
Al_2O_3	13.99	*0.30*	14.53	*0.46*	14.68	*0.69*	14.62	*0.63*	14.52	*0.39*	14.33	*1.35*	13.12	*0.35*
SiO_2	48.34	*1.16*	49.91	*0.98*	51.27	*0.71*	50.94	*1.15*	50.89	*0.47*	50.72	*1.79*	46.89	*0.95*
P_2O_5	0.53	*0.06*	0.43	*0.08*	0.37	*0.07*	0.34	*0.09*	0.75	*0.04*	0.41	*0.08*	0.81	*0.21*
SO_3	0.02	*0.02*	0.02	*0.02*	0.02	*0.02*	0.02	*0.04*	0.01	*0.00*	0.03	*0.04*	0.02	*0.03*
K_2O	1.43	*0.29*	1.02	*0.39*	0.96	*0.17*	0.92	*0.39*	1.95	*0.02*	1.09	*0.21*	1.64	*0.78*
CaO	8.67	*0.52*	8.62	*0.46*	8.52	*0.22*	8.55	*0.42*	7.84	*0.44*	9.08	*1.81*	9.17	*0.58*
TiO_2	2.29	*0.10*	1.98	*0.21*	1.81	*0.13*	1.82	*0.20*	2.52	*0.17*	1.97	*0.18*	2.50	*0.23*
MnO	0.15	*0.01*	0.15	*0.02*	0.14	*0.01*	0.14	*0.02*	0.14	*0.01*	0.14	*0.01*	0.16	*0.00*
Fe_2O_3	12.20	*0.47*	11.85	*0.76*	11.32	*0.33*	11.64	*0.83*	11.68	*0.13*	11.29	*0.96*	12.36	*0.58*
ppm ↓														
V	180	*7*	165	*12*	157	*8*	170	*14*	155	*32*	165	*7*	198	*26*
Ni	189	*11*	190	*29*	159	*25*	157	*88*	146	*49*	210	*5*	261	*8*
Cu	45	*9*	44	*13*	44	*11*	47	*24*	42	*8*	42	*9*	57	*1*
Zn	115	*3*	114	*16*	110	*4*	112	*7*	129	*3*	108	*8*	122	*12*
Ga	18.5	*2.2*	19.6	*0.7*	19.2	*0.4*	19.9	*0.9*	22.4	*0.4*	18.8	*0.7*	20.4	*1.3*
Rb	29.9	*3.3*	24.4	*12.3*	23.2	*7.6*	25.2	*6.2*	46.3	*2.5*	26.9	*2.6*	38.4	*1.3*
Sr	681	*269*	504	*161*	407	*15*	440	*86*	562	*16*	481	*26*	842	*232*
Y	21.4	*0.4*	21.8	*3.8*	20.7	*1.3*	21.4	*1.0*	27.9	*0.9*	20.4	*1.6*	25.5	*3.0*
Zr	196	*1*	163	*41*	142	*6*	150	*21*	291	*24*	163	*13*	294	*95*

Table 7.1 (continued)

Nb	42	*1*	30	*14*	23	*2*	24	*7*	47	*0*	30	*2*	65	*18*
Mo	1.58	*0.31*	1.46	*0.31*	1.45	*0.22*	1.40	*0.44*	2.59	*0.09*	1.83	*0.63*	2.17	*0.12*
Cs	0.52	*0.14*	0.41	*0.23*	0.79	*0.32*	0.71	*0.41*	0.59	*0.30*	0.74	*0.00*	6.02	*10.21*
Ba	352	*19*	293	*96*	273	*99*	322	*74*	475	*8*	348	*12*	496	*95*
La	29.0	*0.9*	23.3	*8.2*	18.4	*1.6*	20.0	*2.7*	35.7	*1.3*	22.0	*1.8*	49.7	*16.4*
Ce	59	*2*	46	*15*	37	*3*	41	*9*	73	*2*	46	*4*	100	*34*
Pr	7.2	*0.2*	5.8	*1.8*	4.8	*0.3*	5.2	*0.6*	9.1	*0.2*	5.7	*0.5*	12.0	*4.0*
Nd	29	*1*	24	*7*	20	*1*	22	*2*	38	*1*	24	*2*	47	*15*
Sm	6.5	*0.1*	5.6	*1.2*	4.9	*0.3*	5.2	*0.4*	8.3	*0.1*	5.5	*0.4*	9.1	*2.6*
Eu	2.17	*0.08*	1.93	*0.30*	1.68	*0.10*	1.74	*0.12*	2.64	*0.02*	1.84	*0.10*	2.86	*0.70*
Tb	0.88	*0.02*	0.84	*0.13*	0.77	*0.05*	0.80	*0.02*	1.11	*0.02*	0.80	*0.06*	1.09	*0.20*
Dy	4.74	*0.08*	4.64	*0.63*	4.35	*0.26*	4.46	*0.13*	5.94	*0.15*	4.39	*0.38*	5.70	*0.92*
Ho	0.88	*0.02*	0.87	*0.13*	0.83	*0.05*	0.86	*0.03*	1.10	*0.02*	0.83	*0.06*	1.04	*0.12*
Er	2.13	*0.07*	2.18	*0.31*	2.11	*0.10*	2.18	*0.09*	2.72	*0.09*	2.08	*0.16*	2.51	*0.24*
Tm	0.28	*0.01*	0.30	*0.04*	0.29	*0.01*	0.30	*0.01*	0.36	*0.02*	0.28	*0.02*	0.33	*0.02*
Yb	1.62	*0.06*	1.70	*0.24*	1.71	*0.06*	1.77	*0.07*	2.09	*0.12*	1.68	*0.15*	1.90	*0.13*
Lu	0.22	*0.01*	0.24	*0.03*	0.24	*0.01*	0.25	*0.01*	0.29	*0.02*	0.23	*0.02*	0.26	*0.01*
Hf	4.50	*0.07*	3.89	*0.86*	3.49	*0.15*	3.70	*0.49*	6.60	*0.48*	3.94	*0.34*	6.48	*2.06*
Ta	2.51	*0.06*	1.90	*0.89*	1.37	*0.18*	1.55	*0.42*	3.50	*1.15*	2.32	*1.07*	4.06	*1.50*
Pb	2.48	*0.34*	2.51	*1.19*	2.70	*0.55*	3.15	*0.78*	3.79	*0.42*	3.05	*0.24*	4.39	*1.41*
Th	3.55	*0.13*	2.83	*1.10*	2.76	*0.53*	3.08	*0.79*	4.87	*0.04*	3.34	*0.24*	5.88	*1.77*
U	1.00	*0.10*	0.75	*0.33*	0.74	*0.16*	0.72	*0.16*	1.37	*0.03*	1.00	*0.02*	1.62	*0.66*

[a] Internal standard deviations in elemental abundance were calculated.

[b] Because the three flow units of the Mount Fraser flow had disparate geochemistry, they are listed separately.

7.2. Lava flow mapping by trace elements: the case of Mount Fraser vs Tulloch Hill

The two most problematic flow units to map in the study area were Mt Fraser C (the final eruptive unit from Mt Fraser) and Tulloch Hill C, which are located at similar stratigraphic positions and geographical locations (**see chapter 6**). It was not possible to confidently distinguish these samples based on either major element geochemistry or petrography (**Figs. 7.2a; b; c**). In practice, these two units could only be separated based on ^{40}Ar/^{39}Ar dating results and their position relative to other units (e.g., Tulloch Hill C was always located above Tulloch Hill B, and never above the Mount Fraser flow). However, since allocating individual samples in this way was extremely inefficient and often ambiguous, trace element concentrations were determined for seven samples from Mt Fraser C and five samples form Tulloch Hill C to investigate whether these flow units had any geochemical markers by which they could be separated. This exercise was also important for determining whether trace element geochemistry would be more effective than petrography and/or major element geochemistry as a flow mapping tool.

A spider diagram (**Fig. 7.2d**) illustrates the similarity between the incompatible element profiles of the two flow units. Although the patterns are similar, careful examination reveals specific incompatible element concentrations that are statistically distinguishable between the two units. Samples from Mt Fraser C have lower Zr and Ce concentrations, with no overlap between the two units at the 2σ-level. Concentrations of other incompatible elements (e.g., Nd & Hf) have only very minor overlap, and each flow unit plots as a separate cluster on bivariate diagrams (**Figs. 7.2e; f**). Accordingly, the flow identity of a given sample from either of these units could be confidently assigned on the basis Zr and Ce concentration Although its applicability to every such pair of flows in other locations cannot be inferred, incompatible element chemistry is likely to be a more effective flow mapping tool than either petrography or geochemistry.

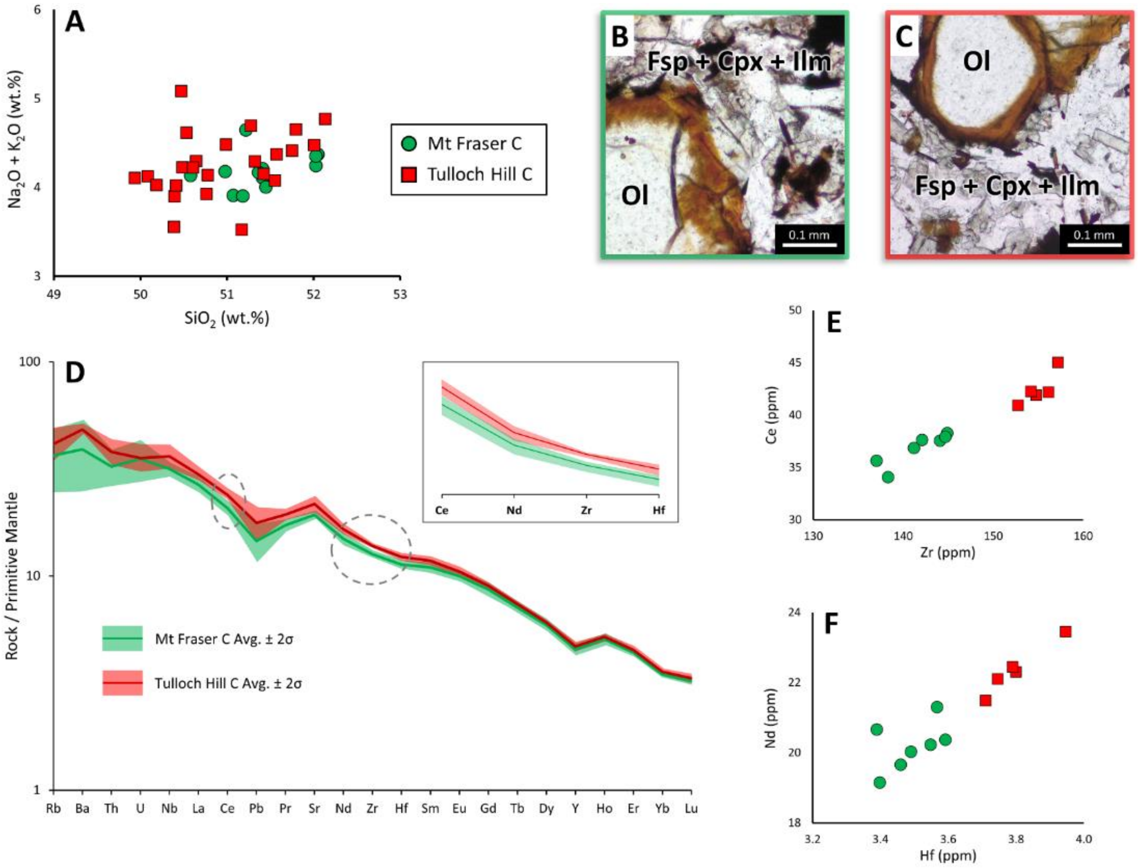

Figure 7.2: a) Total alkalis versus silica (TAS) diagram, showing the overlapping geochemistry of Mt Fraser C and Tulloch Hill C samples. Plane-polarised micrographs of Mt Fraser C (**b**) and Tulloch Hill C (**c**) samples show very similar features, with olivine phenocrysts (Ol) in a groundmass of fine-grained feldspar (Fsp), clinopyroxene (Cpx) and Ilmenite (Ilm). **d**) Primitive mantle-normalised spider diagram of Mt Fraser C and Tulloch Hill C average compositions shows overlap at the 2-sigma level for most elements, with Zr and Ce the only exceptions (Sun and McDonough, 1989). **e**) Mt Fraser C and Tulloch Hill C samples plot as separate clusters when Zr is plotted against Ce. **f**) Although Nd and Hf concentrations showed some overlap at the 2-sigma level, the two flow units plot as separate clusters in bivariate space.

7.3 Mount Fraser magma mixing

7.3.1 Background

In several cases throughout the Melbourne area, single flows were separated into multiple petrographic and/or geochemical units with no evidence for any time gap between these units (i.e. no paleosol horizons or erosional surfaces). For example, the middle petrographic units of the Mount Kororoit and Tulloch Hill flows were distinguished by an ophitic texture that was not present in under- or overlying flow units. In both cases, this petrographic difference was not matched by any difference in major element geochemistry. Both the Tulloch Hill and Mount Kororoit flows were large volume, allowing for the formation of lava channels and tubes, such that the ophitic texture characteristic of the central units (**Fig. 7.3a**) is likely due to slower cooling in comparison to the flow margins (**Fig. 7.3b**). Elsewhere in the study area, petrographically distinct sections of flows are commonly the result of differences in cooling rate or secondary textures resulting from alteration.

7.3.2 Mount Fraser flow units

As mentioned previously, in the case of the Mount Fraser Flow, three distinct flow units were identified based on *both* petrography and geochemistry. As discussed briefly in **chapters 5 and 6**, the eruption sequence began with an alkali basaltic magma pulse producing Mount Fraser A, the lower unit of the Mount Fraser Flow, which can be mapped for ca. 40 km from its source (**Figs. 7.4a; b**). A middle unit of transitional chemistry, Mount Fraser B, overlies the first along almost its entire length, and is also distinguished from Mount Fraser A by the presence of large clinopyroxene phenocrysts, an overall coarser grainsize and a sub-trachytic texture (**Fig. 7.4c**). The final flow unit, Mount Fraser C, outcrops at the surface between the eruption point and approximately three kilometres south-west of the Morang Hills (**Fig 7.4a**) where it terminates. This unit has a tholeiitic composition and is characterised by large olivine phenocrysts and fine-grained clinopyroxene (**Fig. 7.4d**) with occasional clinopyroxene and plagioclase phenocrysts.

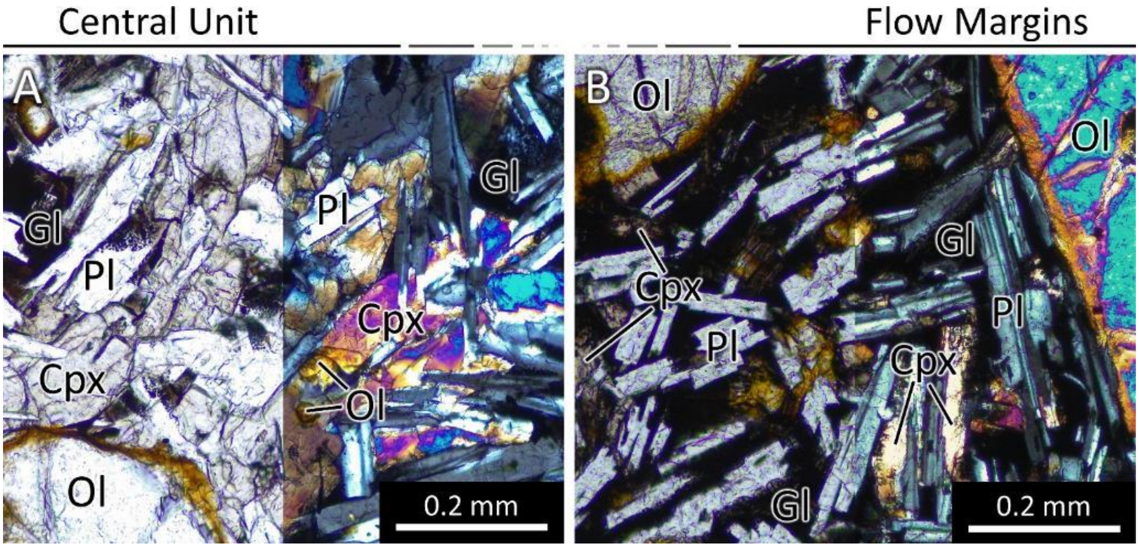

Figure 7.3: Plane-polarised (left) and cross-polarised (right) photomicrographs of typical samples from the central unit (**a**) and margins (**b**) of the Mount Kororoit Flow. Clinopyroxene (Cpx) is fine grained at the flow margins, but is coarse-grained in the central unit, where an ophitic texture is common. Ol = olivine; Pl = plagioclase; Gl = glass.

^{40}Ar/^{39}Ar ages are identical for all three flow units, and field observations (absence of paleosol horizons) also support emplacement over a short time period. As reported in **chapter 5**, multiple aliquants of two samples from the Mount Fraser Flow (WW1A, YY3C) exhibited age spectra with statistically significant plateaus. An age of 0.8038 ±

0.0017 Ma was calculated from a weighted average of ^{40}Ar*/^{39}Ar values for all plateau steps of sample YY3C (n = 19).

There is a gradational change in major element composition from Mount Fraser A through to C (**Fig. 7.5a**). However, this trend is inconsistent with magma evolution resulting from olivine ± clinopyroxene/plagioclase fractionation. On a MgO versus K_2O bivariate diagram (**Fig. 7.5b**), samples from Mount Fraser A and C form separate clusters with possible internal fractionation trends, and the Mount Fraser B samples plot either between these groups (e.g., WW1A) or within the Mount Fraser A or C clusters (e.g., YY3C, MH24 and MH32). The observed trends are consistent with those expected from lower crustal contamination (green arrows in **Figs. 7.5a and b**), however the degree of contamination that would be required to generate these signatures is unrealistically high, at >40% (**Fig 7.5**).

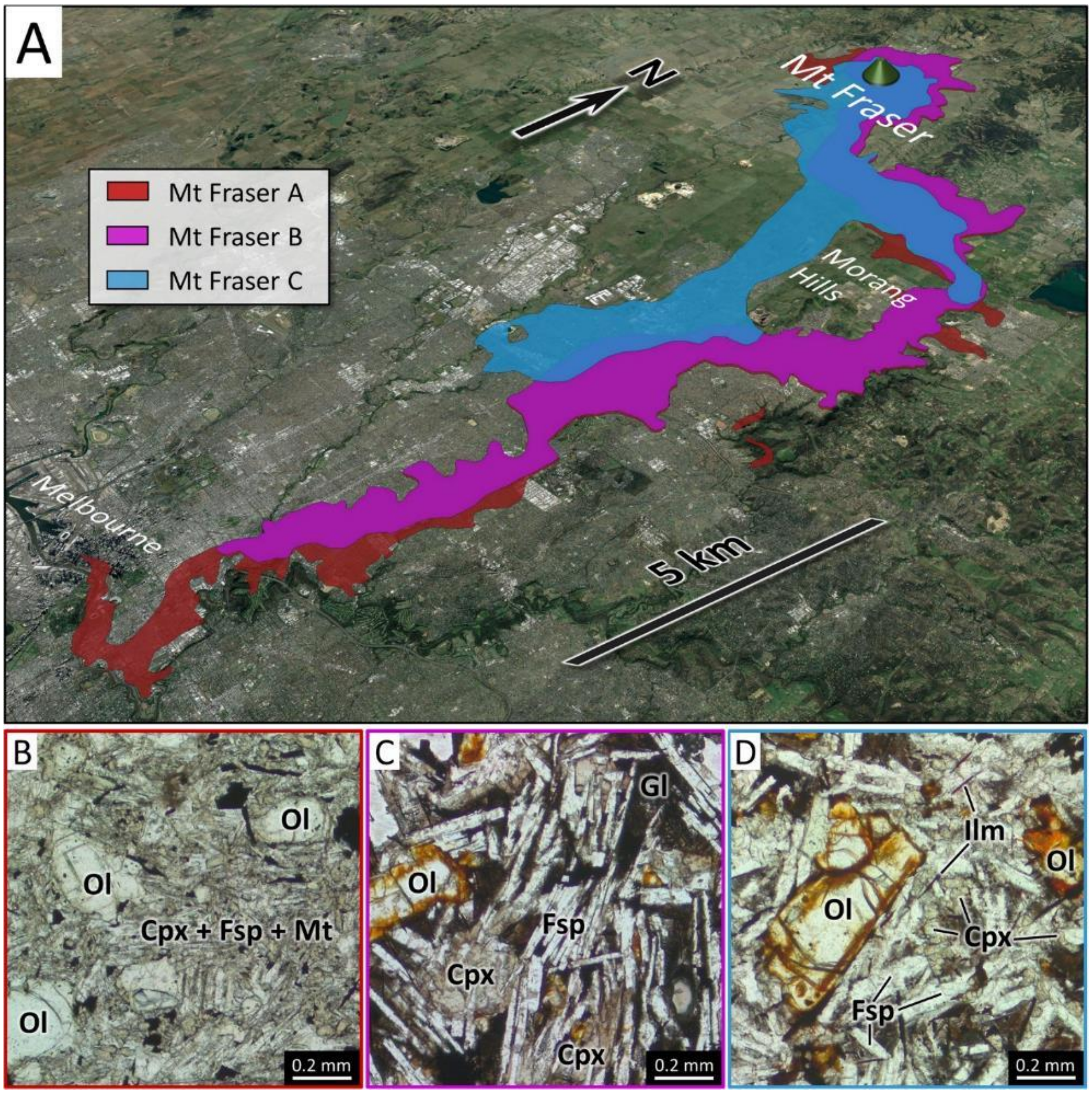

Figure 7.4: a) Non-vertical satellite image showing the areal extent of the three flow units erupted from Mount Fraser. **b)** Plane-polarised photomicrograph of a typical Mount Fraser A sample, with olivine (Ol) microphenocrysts in a fine-grained groundmass of clinopyroxene (Cpx), feldspar (Fsp) and magnetite (Mt). **c)** Plane-polarised photomicrograph of a typical Mount Fraser B sample, distinguished by having larger Cpx grains and a sub-trachytic texture **d)** Plane-polarised micrograph of a typical Mount Fraser C sample, with large Ol phenocrysts and fine-grained Cpx.

To investigate whether the change in lava composition could be explained by the mixing of two separate batches of magma, represented by Mount Fraser A and C, incompatible trace element concentrations were compared for Mount Fraser A, B and C. Data for Mount Fraser A and C form tight clusters and the relative position of each Mount Fraser B sample along the Mount Fraser A–Mount Fraser C magma mixing line is similar in all cases (**Fig 7.5c-e**). Mount Fraser B sample MH32 plots within the Mount Fraser C group, whereas samples YY3C and WW1A plot along the magma mixing line close to, but distinct from, the Mount Fraser A group. Sample YY3C, which has major element concentrations within the range of Mount Fraser A samples (**Figs. 7.5a; b**), is distinguished from Mount Fraser A by its incompatible trace element signature, which suggests a ~20% contribution from the Mount Fraser C component. Sample MH24 is displaced to higher HREE concentrations, plotting on the edge of or just outside of the 2σ-uncertainty envelope for Mount Fraser A and C samples (**Figs. 7.5c-e**.) The anomalous composition of MH24 could be explained by incipient alteration, as reported for other NVP basalt samples (Price et al., 1991), causing elevated REE concentrations but not affecting the less mobile HFSEs. This sample has a very low ^{40}Ar* content (^{40}Ar* = 5.0%; see **chapter 5**), which could reflect atmospheric argon contamination and/or ^{40}Ar* loss as a result of incipient alteration. However, sample MH66 from Mount Fraser C, which also had very a low ^{40}Ar* content (^{40}Ar* = 1.1% of total ^{40}Ar), did not have elevated HREE contents and plotted within the Mount Fraser C cluster in all bivariate diagrams (not labelled), indicating that incipient alteration might not be the only cause of low ^{40}Ar* content. When concentrations of immobile elements Nb and Zr are compared (**Fig. 6.5f**), sample MH24 can be seen to plot along the magma mixing line, indicating a ~90% contribution of the Mount Fraser C component.

It is possible that a third batch of magma, intermediate in chemistry, is responsible for the Mount Fraser B unit, but it is difficult to explain such a broad range of geochemistry from a single batch of melt. The progressive change in composition, as best illustrated in the TAS diagram (**Fig. 7.5a**), is also not consistent with three distinct batches of melt. Another possibility is that the change in chemistry is due to melting of a progressively shallower source, or an increasing degree of melting, with melt constantly or incrementally being transported to the surface. Such a process has been suggested for hotspot-type settings, as the underlying mantle becomes progressively hotter towards the centre of the plume (Wyllie, 1988), but this involves the generation of a far greater volume of melt than was erupted from Mount Fraser, and, as discussed previously, the NVP is unlikely to be hotspot related (e.g., van den Hove et al., 2017b).

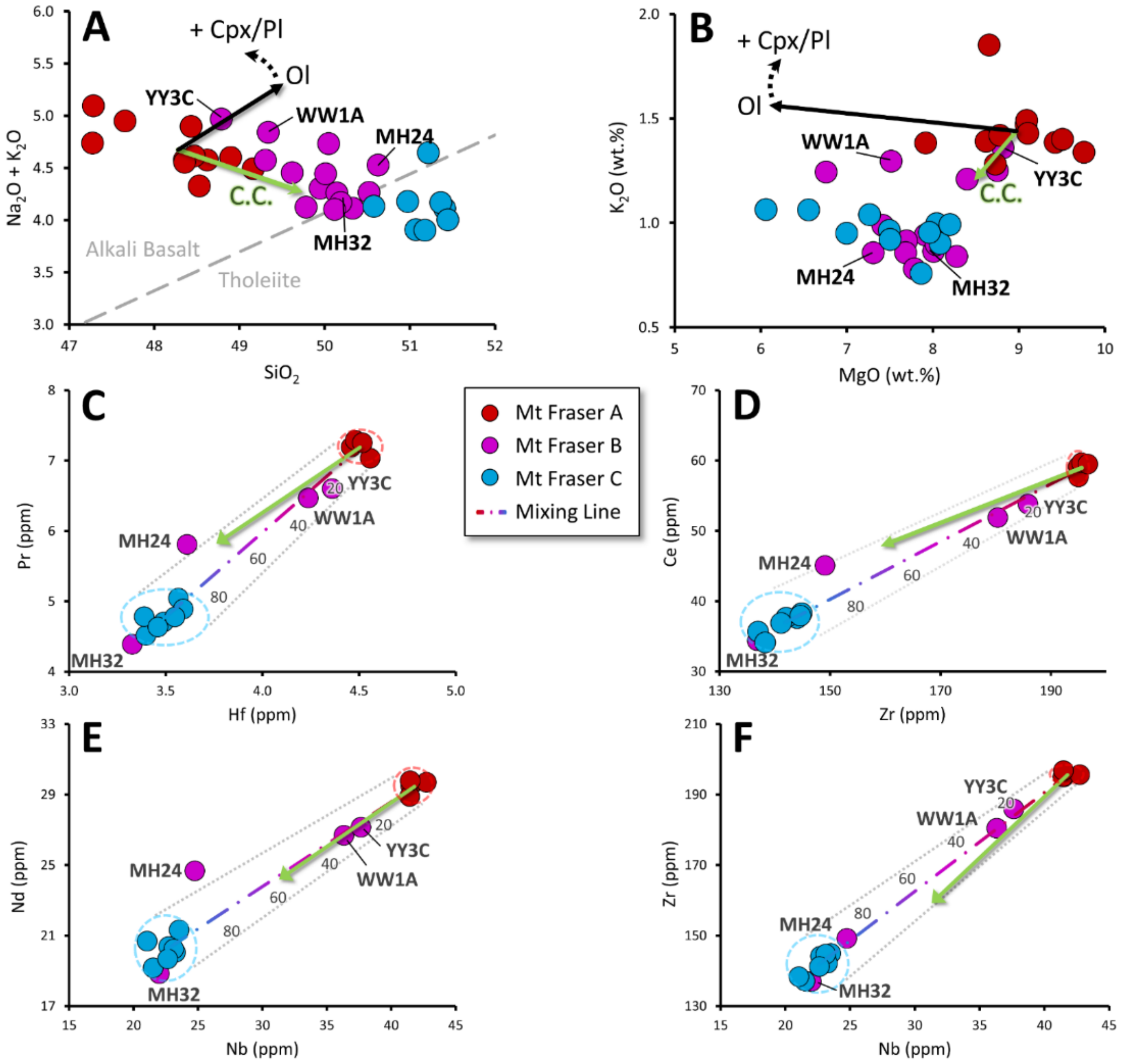

Figure 7.5: a) TAS diagram illustrating the geochemical trend from alkali basalt to tholeiite as the Mount Fraser eruption progressed. The black arrow shows the trend that would be expected from olivine (+ clinopyroxene/plagioclase) fractionation. **b**) The geochemical trend with the eruption of progressive flow units is not as evident when MgO is plotted against K_2O. **c-f**) Incompatible element bivariate plots show the trend expected from magma mixing of two components. Blue and red dashed circles show average (± 2σ) compositions of Mount Fraser units A and C, which were the compositions used as magma mixing end-members. The numbers next to the magma mixing line indicate the contribution

required from the Mount Fraser C component. The length of the green arrow in all figures indicates the expected effect of 40% lower crustal contamination (Rudnick and Gao, 2014). Contamination by a middle or upper crustal component does not match the observed geochemical trends.

The magma mixing hypothesis is supported by each of the Mount Fraser B samples plotting along the magma mixing line at a similar relative location in each of the HFSE vs. HREE bivariate plots, indicating a similar contribution from components Mount Fraser A and C. However, there is inconsistency between the contributions suggested by trace and major element concentrations, respectively. Sample MH32, for example, is lower in silica than any Mount Fraser C sample (**Fig. 7.5a**), indicating some contribution from the more silica-depleted Mount Fraser A component, but its trace element chemistry is indistinguishable from the Mount Fraser C group (**Figs. 7.5c-f**). Conversely, YY3C is only distinguishable from Mount Fraser A samples by its trace element composition. Despite these complications, I consider magma mixing the most likely cause of the progressive change in chemistry during the eruption at Mount Fraser, but note that it is likely not the only mechanism affecting magma composition. Recent work in other locations within the NVP has found that multiple compositionally distinct batches of melt have been erupted both consecutively and concurrently from single eruption centres (van Otterloo et al., 2014; Boyce et al., 2015), challenging the monogenetic paradigm for NVP volcanism. However, this is the first case where the change in composition is observed to be gradual and with an indication of mixing between different batches of magma.

Chapter 8) A preliminary multi-isochron model for constraining basalt ages from ‘disturbed’ ^{40}Ar/^{39}Ar results

8.1 Background

Discordance in ^{40}Ar/^{39}Ar data may be caused by ^{39}Ar or ^{37}Ar recoil, mass-dependent fractionation, argon loss or extraneous argon (excess or inherited). As demonstrated in **chapter 5**, inverse isochron diagrams can be employed to determine the possible causes of discordance and whether an apparent age should be interpreted as a maximum or minimum eruption age. Having an evidence-based framework by which to assess the validity of ^{40}Ar/^{39}Ar ages and extract meaningful age constraints from discordant age spectra is an important step, but the end goal of such work must be to transform seemingly undesirable, discordant datasets into a resource from which a sample’s actual age can be calculated. This chapter presents a new approach for extracting eruption ages from discordant data, here referred to as the ‘multi-isochron approach to ^{40}Ar/^{39}Ar dating’. Note that this approach was not adopted in chapters 5 or 6 as it is still under development.

8.2 The multi-isochron regression

One of the major conclusions from **chapter 5** was that rotation of an inverse isochron is almost ubiquitous in disturbed samples. As illustrated in **Fig. 8.1**, in the case of inverse isochron rotation, there is an inverse relationship between (^{40}Ar/^{36}Ar)$_i$ values and apparent isochron age. That is, as (^{40}Ar/^{36}Ar)$_i$ values become lower (more sub-atmospheric), the apparent isochron age increases (clockwise rotation). Conversely, as (^{40}Ar/^{36}Ar)$_i$ values become higher (more supra-atmospheric), apparent isochron ages decrease (anti-clockwise rotation). In both cases, discordance in inverse isochron space results in rotation of the isochron away from a sample's 'ideal' isochron (shown in green in **Fig. 8.1**). This ideal isochron is defined by an atmospheric $(^{40}Ar/^{36}Ar)_i$ value [298.56 ± 0.62 (2σ; Lee et al., 2006)] , and a $^{39}Ar/^{40}Ar$ intercept proportional to a sample's true age. Unfortunately, there is no way of knowing how much rotation has occurred from a discordant inverse isochron, so a sample's ideal isochron can only be found from an undisturbed sample (i.e. where the true age is constrained, e.g., YY3C in **chapter 5**).

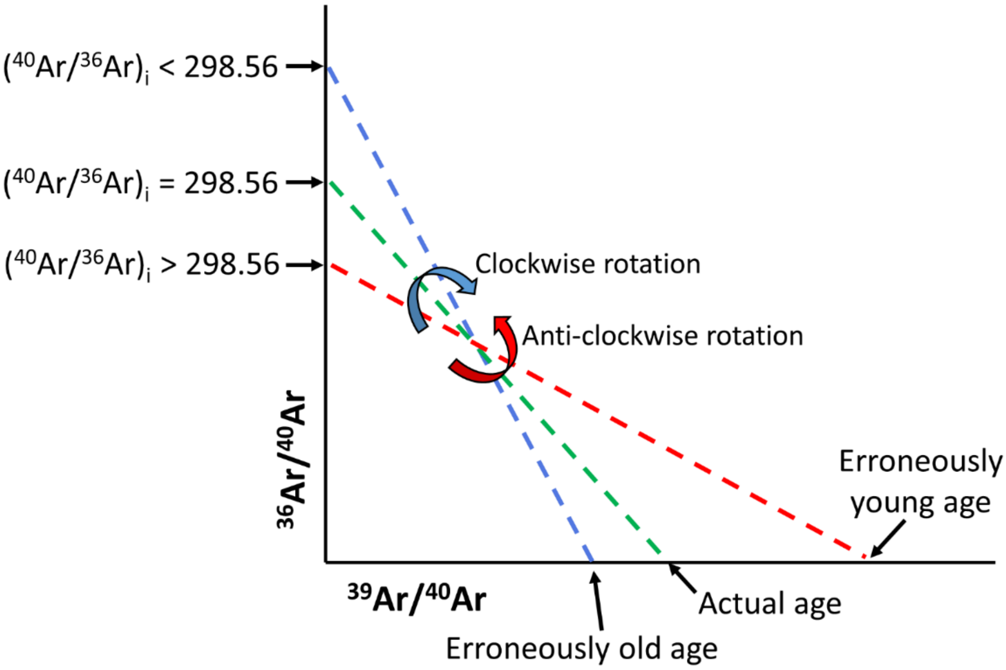

Figure 8.1: Schematic illustration of the effects of clockwise and anti-clockwise isochron rotation on $(^{40}Ar/^{36}Ar)_i$ values and apparent ages.

A demonstration of isochron rotation is provided by samples of the Mount Fraser Flow from **chapter 5** (age = 0.8038 ± 0.0017 Ma). In **Fig. 8.2**, $(^{40}Ar/^{36}Ar)_i$ values and apparent isochron ages of multiple aliquants from samples of the Mount Fraser Flow are plotted, illustrating the negative correlation between these two variables. Assuming that the atmospheric $^{40}Ar/^{36}Ar$ trapped composition defined by 'undisturbed' sample YY3C (**chapter 5**) is correct, and that the amount of rotation increases systematically with the degree of disturbance, the age of the ideal isochron should be able to be calculated using the formula for the regression line, as illustrated. This would involve assigning a y value of 298.56 (the atmospheric value) and solving for x (in the case of the Mount Fraser flow, this yields an x (age) value of 0.748 Ma). There are a number of issues, however, in using this method to find a sample's age. The first, evident from **Fig. 8.2,** is that there may be a large amount of scatter in isochron results from different samples/aliquants. This might be due to slightly different causes of discordance in each sample, such that the amount of rotation does not increase in a systematic way, and cannot be adequately represented by a single regression equation. The second obvious issue with this approach is the considerable time and cost involved in processing such a large number of aliquants and samples; each of the points plotted in **Fig. 8.2** is representative of at least ~12 hours of sample preparation and machine time. Fortunately, both of the above issues can be circumvented by plotting a multi-isochron regression from a single aliquant, using standard step-heating data.

A single step-heating experiment of a typical sample might include anywhere from four to forty heating steps, and an inverse isochron can be calculated for any group of three or more consecutive heating steps. Each aliquant does not, therefore, only have a single representative inverse isochron, but a number of alternative inverse isochrons, each with its own $({}^{40}Ar/{}^{36}Ar)_i$ value and apparent age (although there may naturally be some overlap). For example, a step-heating experiment with five steps can produce six inverse isochrons, and an experiment of 10 heating steps can produce 36. The total number of isochrons that can be calculated is expressed by the relationship:

$$((n-2)/2)*(1+(n-2)) \qquad \text{Equation 8.1}$$

where n is the number of heating steps.

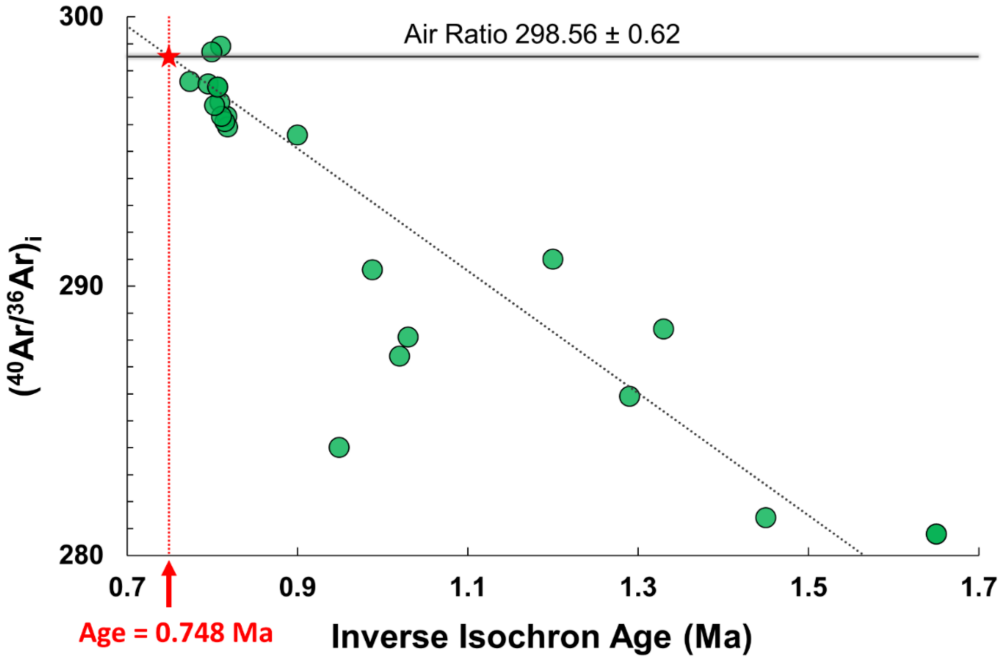

Figure 8.2: Inverse isochron results for aliquots of the Mount Fraser lava flow, showing a negative correlation between $(^{40}Ar/^{36}Ar)_i$ and inverse isochron age. The apparent age indicated by the regression is younger than the true eruption age of Mount Fraser (0.8038 ± 0.0017 Ma; see chapter 5).

As each of these inverse isochrons is from the same aliquant, their $(^{40}Ar/^{36}Ar)_i$ values and apparent ages are expected to increase or decrease in a systematic way, as the isochron is rotated further away from the ideal isochron. If the $(^{40}Ar/^{36}Ar)_i$ values and apparent ages of all possible isochrons are plotted and a regression line is fitted to this data, it should be possible to calculate the age of the ideal isochron by simply solving the regression equation for $(^{40}Ar/^{36}Ar)_i = 298.56$. **Fig. 8.3** presents an example of how a multi-isochron regression is generated, in this case using modelled data. Although the actual age of the sample is 0.8 Ma (input into the model), this is not evident from either the age spectrum (**Fig. 8.3a**) or inverse isochron diagram (**Fig. 8.3b**). Eight of the possible inverse isochrons are shown in **Fig. 8.3c**, and it is evident that as the ages of these isochrons approach the true age of 0.8 Ma, the $(^{40}Ar/^{36}Ar)_i$ values converge with the atmospheric value (298.56). When all possible isochron results are plotted (Age vs. ($^{40}Ar/^{36}Ar)_i$) and a regression fitted (**Fig. 8.3d)**, the age of the ideal isochron (0.8 Ma) can be calculated from the regression line solving for x = 298.56.

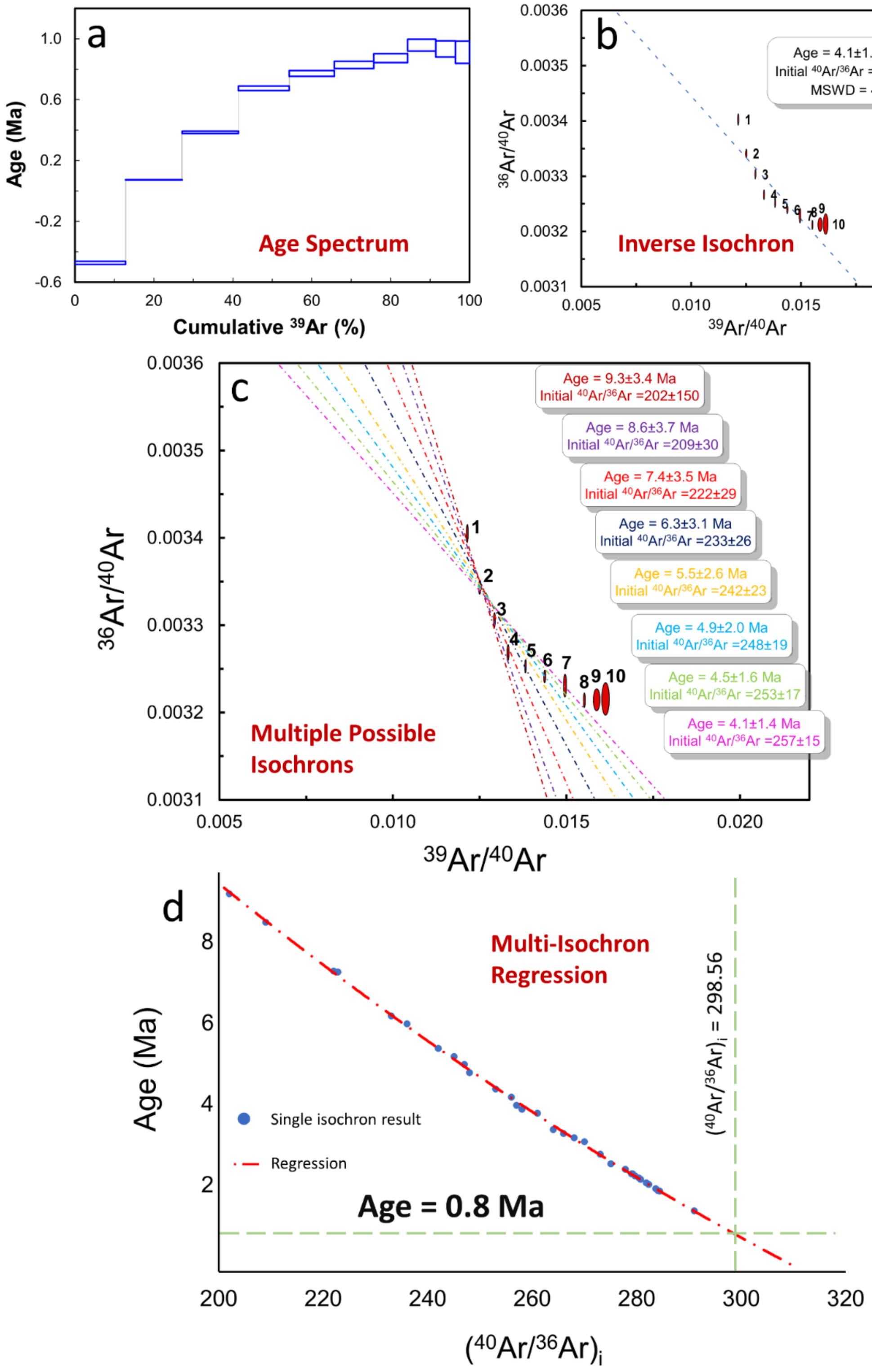

Figure 8.3: a) Modelled age spectrum for a 0.8 Ma sample that has been affected by mass-dependent fractionation. **b)** A modelled inverse isochron for the same sample, with erroneously old apparent age and sub-atmospheric (^{40}Ar/^{36}Ar)$_i$ value. **c)** Eight of the possible inverse isochrons plotted together in different colours, along with their calculated apparent ages and (^{40}Ar/^{36}Ar)$_i$ values which show an inverse relationship. **d)** Assuming a (^{40}Ar/^{36}Ar)$_i$ value of 298.56 for the ideal isochron, the multi-isochron regression gives an age of 0.8 Ma.

8.3 Preliminary results and discussion

Although the above example is a simplification of how a multi-isochron age would be calculated in an ideal situation, it is nonetheless a useful demonstration of the theory behind the method, showing that in principle it is possible extract an eruption age from discordant data. In **Fig. 8.4,** multi-isochron regressions are plotted for two aliquants from the current study in order to illustrate the method with actual mass spectrometer data. The age spectrum of MH70-1 (**Fig. 8.4a**) is characterised by increasing ages with increasing temperature, and there is little evidence to indicate the eruption age of the Mount Fraser Flow, from which it was sampled (0.8038 ± 0.0017 Ma – see **chapter 5**). Despite the extreme discordance evident from the age spectrum, coupled with the fact that it was outgassed over only nine heating steps, the basic multi-isochron regression (**Fig 8.4b**) gives an age of 0.793 Ma, almost within error of the eruption age. The saddle-shaped age spectrum of KA13B-1 (**Fig 8.4c**) includes a mini-plateau section with an age of 2.3101 ± 0.0056 Ma, within error of the calculated eruption age of Tulloch Hill (2.309 ± 0.009 Ma – see **chapter 5**). In this case, although the multi-isochron regression (**Fig 8.4d**) also gives an age within error of the eruption age, it does not improve on the age estimate of the mini-plateau. This rudimentary version of a multi-isochron regression indicates that the theory behind the method is sound, but the incorporation of error propagation and a true least-squares regression will hopefully make the regression far more powerful, with application even to samples showing minor discordance.

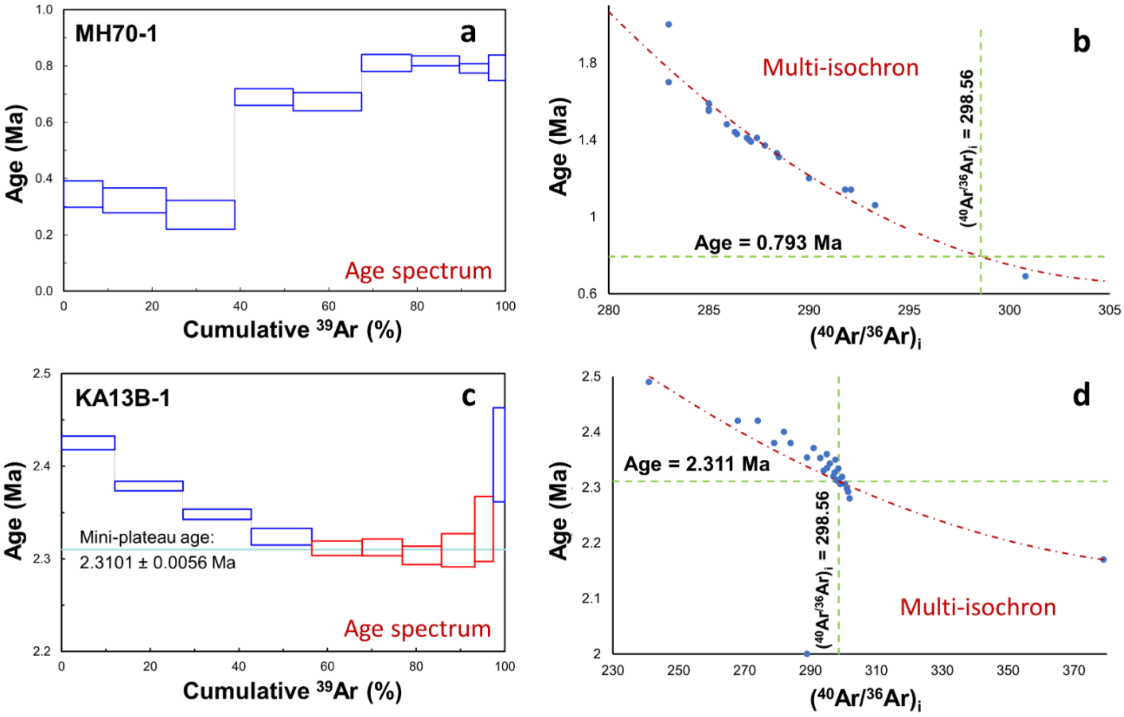

Figure 8.4: Age spectra and basic multi-isochron regressions for aliquants MH70-1 and KA13B-1, from the Mount Fraser and Tulloch Hill flows, respectively.

The following steps are proposed as a guide for determining a multi-isochron for a real sample:

1) Perform step-heating analyses over as many heating steps as possible (more steps = more isochrons).
2) Calculate inverse isochrons for each possible combination of ≥3 consecutive points, recording $^{36}Ar/^{40}Ar$ and $^{39}Ar/^{40}Ar$ intercepts of each isochron along with the associated errors.

3) Plot ^{40}Ar/^{36}Ar and ^{40}Ar/^{39}Ar intercept values of each possible isochron (as in **Fig. 8.3d**) including error ellipses, much like those of a single heating step on a standard inverse isochron (see **Fig. 3.3**).
4) Fit a weighted least-squares regression to the data, taking the uncertainty associated with each datum into account.
5) Solve regression equation for ^{40}Ar/^{36}Ar = 298.56 (^{36}Ar/^{40}Ar = 0.003349) to find the ^{40}Ar/^{39}Ar intercept of the ideal isochron [(^{40}Ar/^{39}Ar)$_i$].
6) Substitute the (^{40}Ar/^{39}Ar)$_i$ value into an amended age equation:

$$t = \frac{1}{\lambda}\ln\left(1 + J\left(\frac{^{40}Ar}{^{39}Ar}\right)_i\right) \qquad \text{Equation 8.2}$$

The results of future development and testing of this technique will determine whether it is a viable means of extracting a reportable and statistically valid eruption age. However, the method has the potential to significantly improve data treatment methods for young samples. Based on modelling results (**Fig 8.3**) and early testing on real data (**Fig. 8.4**), the multi-isochron approach is a considerable improvement over current data treatment methods for severely discordant basalt samples. Even for analyses with minor discordance, current practice often relies on human intervention for the selection of a subset of heating steps from which a preferred age is calculated (e.g., **section 5.5.1.2**), introducing an element of subjectivity and the possibility of human error. The multi-isochron technique could be employed to select the ideal isochron in a standardised (automated) way, without the need for subjective interpretation of the data.

Chapter 9) Conclusions

9.1 Addressing the aims of this study

1) To map the NVP lava flows of the Melbourne area based on geomorphology, petrography and geochemistry, and determine which of these characteristics are the most useful discriminators.

In the Melbourne area, geomorphology studies have been hindered by urban development, which has obscured the natural landscape and complicated the delineation of lava flows. This study illustrated the use of sample petrography and major and trace element geochemistry for distinguishing between individual lava flows in built-up areas such as this, paving the way for future work in similar areas. A total of 14 lava flows within the Melbourne area were mapped in detail, with 13 of these traced back to their eruption points. It was found that major element geochemistry alone was sometimes effective in separating individual flows, but was generally less useful than petrography as some flows were geochemically very similar. Trace element geochemistry was used for flow mapping purposes where petrography and major element geochemistry proved inconclusive in separating lava flows. In a study of two flow units (Mount Fraser C and Tulloch Hill C) that were inseparable based on either major element geochemistry or petrographic features, incompatible trace element concentrations were found to be extremely effective at separating samples into their respective units, as verified by $^{40}Ar/^{39}Ar$ dating. This was possible because such elements (e.g., Zr and Ce) showed only minor variability within flow units, compared to substantial disparities between units. Based on the results of this study, trace element geochemistry appears to be the most effective tool for separating samples from very similar basaltic lava flows, although in many cases petrographic analysis alone may be sufficient.

2) To constrain the ages and defining characteristics of each lava flow within the Melbourne area.

Geochemically, Melbourne lava flows have compositions ranging from silica-poor basanites, alkali basalts and trachybasalts to silica-rich basaltic andesites and trachyandesites; essentially spanning the compositional range of the entire NVP. The ages of these lava flows range from 7.931 ± 0.038 Ma (Bald Hill Flow) to 0.8038 ± 0.0016 Ma (Mount Fraser Flow), challenging the long-accepted age of 4.6 Ma for the onset of NVP activity. The oldest age either extends the range of the NVP, or is perhaps evidence of the mantle hot-spot that is purported to have triggered its initiation.

No evidence of a progression from tholeiitic to alkalic volcanism over time was observed, challenging assertions made in some previous province-wide studies. This suggests that, rather than a rapid shift from plume-assisted to stress-dependent volcanism as suggested by Oostingh et al. (2017) the mechanism behind volcanism has likely not changed since ~4.6 Ma. Such findings are consistent with modelling of a long-lived edge-driven convective cell at the base of the south-eastern Australian lithosphere (Demidjuk et al., 2007) generating partial melts that are erupted at the surface only during brief periods where favourable tectonic conditions make ascent through the crust possible (Davies et al., 2015; Cas et al., 2017; van den Hove et al., 2017b).

3) To investigate the common causes of disturbance in $^{40}Ar/^{39}Ar$ data from basaltic samples and determine how each of their effects can be recognised.

A step-heating model was created to assess the effects of discordance in basaltic samples. Modelling results indicated that mass-dependent fractionation would likely cause erroneously young ages to be found for low-temperature steps in basaltic samples, with erroneously old ages for higher-temperature steps. The effect of ^{39}Ar recoil was erroneously old ages for low-temperature steps, with ages for subsequent steps converging with the true eruption age. ^{40}Ar loss was found to cause erroneously young ages for low-temperature steps, increasing towards the true eruption age in later steps. The modelling work indicated that inverse isochron rotation, which has been largely overlooked in the literature, is almost ubiquitous in disturbed basaltic samples. The direction of isochron rotation and the distribution of data in inverse isochron space were shown to indicate the type of discordance affecting each sample. By combining the information gathered from age spectra and inverse isochrons, a dominant cause of disturbance was attributed to each of the samples analysed in this study.

Previous $^{40}Ar/^{39}Ar$ dating work on basaltic samples has focused predominantly on ^{40}Ar-loss as the most common cause of disturbance (e.g., Fleck et al., 1977; Foland et al., 1993; Koppers et al., 2000; Baksi, 2007; Baksi, 2014). In this study, however, there was no evidence for ^{40}Ar-loss in any of the >50 aliquants (36 samples) analysed. Rather, any disturbance to argon isotopes could be accounted for by either mass-dependent fractionation and/or ^{39}Ar recoil, with fractionation commonly impacting low-$^{40}Ar^*$ samples, and recoil being the dominant effect in high-$^{40}Ar^*$ samples.

4) To improve upon data treatment methods and the calculation of robust age constraints from disturbed $^{40}Ar/^{39}Ar$ data.

Via detailed inverse isochron analysis of a sample of known age it was shown that a sub-atmospheric $(^{40}Ar/^{36}Ar)_i$ intercept is paired with an erroneously old (or maximum) isochron age as a result of inverse isochron rotation. Conversely, supra-atmospheric $(^{40}Ar/^{36}Ar)_i$ intercepts were associated with erroneously young (or minimum) isochron ages. Samples apparently affected by mass-dependent fractionation were shown to give erroneously young total-gas ages, whereas apparently severely ^{39}Ar recoil-affected samples gave erroneously old total-gas ages. It was shown that it is possible to extract a meaningful estimate of an eruption age from discordant data in cases where an isochron with an atmospheric $(^{40}Ar/^{36}Ar)_i$ intercept can be constructed from a subset of heating steps.

Finally, the concept of a 'multi-isochron approach' for $^{40}Ar/^{39}Ar$ dating was proposed. This approach utilises the new knowledge around isochron rotation described above, and the assumption of an atmospheric $(^{40}Ar/^{39}Ar)_i$ intercept, to calculate an eruption age from discordant data. On modelled data, a multi-isochron regression generated an age far closer to the sample's true age than would be possible using current data treatment methods. With further testing, automated computation and targeted experimental design, the multi-isochron approach has the potential of significantly enhancing data treatment methods, particularly in young samples.

9.2 Recommendations for future work

A concise understanding of the mechanism(s) behind volcanism in south eastern Australia will rely on future geochronological and geochemical work on the entire suite of volcanic products, including those attributed to the NVP, and those that might fall outside accepted NVP timeframe/inferred compositional range. In the Melbourne area, the current study has produced robust age constraints for lava flows and eruption points younger than ~4.6 Ma, but it is left to future work to investigate the earlier volcanic history, and question the link between possible plume-related activity of the Cosgrove track and the initiation of NVP volcanism. Future work might focus on unravelling the geochronology of some of the older eruption points with less well-constrained ages (e.g., Pretty Sally, Green Hill and Mt Cooper) perhaps in conjunction with related volcanoes outside of the Melbourne area.

The techniques employed in the current study could be utilised for detailed lava flow mapping and geochronology studies in not only other areas of the NVP but also other intraplate volcanic provinces worldwide. In conjunction with petrogenetic and geodynamic studies, such analysis provides a solid foundation from which answers to some of the important questions around underlying causes and evolution of volcanism can be addressed.

Future $^{40}Ar/^{39}Ar$ dating studies of young basalts will see increasing instrumental precision and further refinement of techniques and constants. As precision increases, statistically acceptable plateau ages will become rarer, as will inverse isochron ages with atmospheric $(^{40}Ar/^{36}Ar)_i$ ratios, such that the assignment of robust eruption or crystallisation ages will be more difficult using conventional data treatment methods. It is speculated that the use of the multi-isochron approach will become progressively more viable as the precision of mass spectrometers and the precision and accuracy of the atmospheric ^{40}Ar/^{36}Ar ratio and other constants increase. Refinement of the multi-isochron dating method, including development of an automated program for generating a multi-isochron regression, must therefore be a focus of future work, with the potential of improving ^{40}Ar/^{39}Ar dating of young volcanic rocks.

References

Aivazpourporgou, S., Thiel, S., Hayman, P.C., Moresi, L.N. and Heinson, G., 2015. Decompression melting driving intraplate volcanism in Australia: Evidence from magnetotelluric sounding. Geophysical Research Letters, 42(2): 346-354.

Aziz-ur-Rahman and McDougall, I., 1972. Potassium-argon ages on the Newer Volcanics of Victoria. Proceedings of the Royal Society of Victoria, 85: 61.

Bahat, D., 1967. Some mineralogical, geochemical and petrological aspects of the Tertiary Alkaline Province in Victoria, *Unpublished PhD Thesis.* School of Earth Science, University of Melbourne.

Baker, H.F., 2008. ^{40}Ar/^{39}Ar dating of the Newer Volcanics: Reducing uncertainties in the sedimentary record of Victoria, *Unpublished Honours Thesis.* School of Earth Science, University of Melbourne.

Baksi, A. and Archibald, D.A., 1997. Mesozoic igneous activity in the Maranhao province, northern Brazil: ^{40}Ar/^{39}Ar evidence for separate episodes of basaltic magmatism. Earth and planetary science letters, 151(3-4): 139-153.

Baksi, A.K., 1974. Isotopic fractionation of a loosely held atmospheric argon component in the Picture Gorge Basalts. Earth and planetary science letters, 21(4): 431-438.

Baksi, A.K., 2007. A quantitative tool for detecting alteration in undisturbed rocks and minerals—I: Water, chemical weathering, and atmospheric argon. The Geological Society of America, 430: 285-303.

Baksi, A.K., 2014. ^{40}Ar/^{39}Ar ages of flood basalt provinces in Russia and China and their possible link to global faunal extinction events: A cautionary tale regarding alteration and loss of ^{40}Ar$*$. Journal of Asian Earth Sciences, 84: 118-130.

Baksi, A.K., Archibald, D. and Farrar, E., 1996. Intercalibration of ^{40}Ar/^{39}Ar dating standards. Chemical Geology, 129(3-4): 307-324.

Baksi, A.K. and Farrar, E., 1973. The orifice correction for K-Ar dating. Canadian Journal of Earth Sciences, 10: 1410-1414.

Beckinsale, R.D. and Gale, N.H., 1969. A reappraisal of the decay constants and branching ratio of 40K. Earth and planetary science letters, 6(4): 289-294.

Bishop, M.A., 2007. Point pattern analysis of eruption points for the Mount Gambier volcanic sub-province: a quantitative geographical approach to the understanding of volcano distribution. Area, 39(2): 230-241.

Blackburn, G., 1982. Further evidence on the age of tuff at Mount Gambier, South Australia. Transactions of the Royal Society of South Australia, 106: 163-167.

Blaikie, T., Ailleres, L., Betts, P. and Cas, R., 2014. A geophysical comparison of the diatremes of simple and complex maar volcanoes, Newer Volcanics Province, south-eastern Australia. Journal of Volcanology and Geothermal Research, 276: 64-81.

Blaikie, T., van Otterloo, J., Ailleres, L., Betts, P. and Cas, R., 2015. The erupted volumes of tephra from maar volcanoes and estimates of their VEI magnitude: examples from the late Cenozoic Newer Volcanics Province, south-eastern Australia. Journal of Volcanology and Geothermal Research, 301: 81-89.

Bowen, K.G., 1975. Potassium-argon dates: determinations carried out by the Geological Survey of Victoria. Mines Department, Victoria.

Boyce, J., 2013. The Newer Volcanics Province of southeastern Australia: a new classification scheme and distribution map for eruption centres. Australian Journal of Earth Sciences, 60(4): 449-462.

Boyce, J., Nicholls, I., Keays, R. and Hayman, P., 2014a. Victoria erupts: the Newer Volcanics Province of south-eastern Australia. Geology Today, 30(3): 105-109.

Boyce, J., Nicholls, I., Keays, R. and Hayman, P., 2015. Variation in parental magmas of Mt Rouse, a complex polymagmatic monogenetic volcano in the basaltic intraplate Newer Volcanics Province, southeast Australia. Contributions to mineralogy and petrology, 169(2): 11.

Boyce, J.A., Keays, R.R., Nicholls, I.A. and Hayman, P., 2014b. Eruption centres of the Hamilton area of the Newer Volcanics Province, Victoria, Australia: pinpointing volcanoes from a multifaceted approach to landform mapping. Australian Journal of Earth Sciences, 61(5): 735-754.

Brereton, N.R., 1970. Corrections for interfering isotopes in the ^{40}Ar/^{39}Ar dating method. Earth and Planetary Science Letters, 8: 427-433.

Cartwright, I., Weaver, T., Tweed, S., Ahearne, D., Cooper, M., Czapnik, K. and Tranter, J., 2002. Stable isotope geochemistry of cold CO2-bearing mineral spring waters, Daylesford, Victoria, Australia: sources of gas and water and links with waning volcanism. Chemical Geology, 185(1): 71-91.

Cas, R., van Otterloo, J., Blaikie, T. and van den Hove, J., 2017. The dynamics of a very large intra-plate continental basaltic volcanic province, the Newer Volcanics Province, SE Australia, and implications for other provinces. Geological Society, London, Special Publications, 446(1): 123-172.

Cayley, R., Webb, A. and Henley, K., 1995. Radiometric dating (K/Ar) on two samples of Newer Volcanic olivine basalt from the southwestern part of the Beaufort 1: 100 000 map sheet area. Geological Survey of Victoria unpublished report, 15.

Chang, C.-H., 2014. ^{40}Ar/^{39}Ar geochronology of Central Highlands basalts, Newer Volcanic Province, Victoria, *Unpublished Masters Thesis.* School of Earth Science, University of Melbourne.

Che, X., 2017. Constraints on the eruption history of Basalt in the Bacchus Marsh region of the Newer Volcanic Province, Victoria. Unpublished Masters Thesis Thesis, *Unpublished Masters Thesis.* School of Earth Science, University of Melbourne.

Chivas, A., Barnes, I., Evans, W., Lupton, J. and Stone, J., 1987. Liquid carbon dioxide of magmatic origin and its role in volcanic eruptions. Nature, 326(6113): 587-589.

Cohen, B., Knesel, K.M., Vasconcelos, P.M., Thiede, D.S. and Hergt, J., 2008. 40Ar/39Ar constraints on the timing and origin of Miocene leucitite volcanism in southeastern Australia. Australian Journal of Earth Sciences, 55(3): 407-418.

Croker, P.J., 1984. The report on the age and distribution of the Newer Volcanics to the north of Melbourne, *Unpublished Honours Thesis.* School of Earth Science, University of Melbourne.

Dalrymple, G.B., Lanphere, M. and Pringle, M., 1988. Correlation diagrams in ^{40}Ar/^{39}Ar dating: Is there a correct choice? Geophysical Research Letters, 15(6): 589-591.

Dalrymple, G.B. and Moore, J.G., 1968. Argon-40: excess in submarine pillow basalts from kilauea volcano, hawaii. Science, 161(3846): 1132-1135.

Davies, D.R. and Rawlinson, N., 2014. On the origin of recent intraplate volcanism in Australia. Geology, 42(12): 1031-1034.

Davies, D.R., Rawlinson, N., Iaffaldano, G. and Campbell, I.H., 2015. Lithospheric controls on magma composition along Earth's longest continental hotspot track. Nature, 525(7570): 511-514.

DeMets, C., Gordon, R. and Argus, D., 2010. Geologically current plate motions. Geophysical journal international, 181(1): 1-80.

Demidjuk, Z., Turner, S., Sandiford, M., George, R., Foden, J. and Etheridge, M., 2007. U-series isotope and geodynamic constraints on mantle melting processes beneath the Newer Volcanic Province in South Australia. Earth and planetary science letters, 261(3-4): 517-533.

Edwards, A.B., 1938. The Tertiary Volcanic Rocks of Central Victoria. The Quarterly journal of the Geological Society of London, 94(1-4): 243-320.

Edwards, J., 2004. Geology and geomorphology of the Lady Julia Percy Island volcano, a late Miocene submarine and subaerial volcano off the coast of Victoria, Australia. Proceedings of the Royal Society of Victoria, 116(1): 15.

Eggins, S.M., Woodhead, J.D., Kinsley, L.P.J., Mortimer, G.E., Sylvester, P., McCulloch, M.T., Hergt, J.M. and Handler, M.R., 1997. A simple method for the precise determination of $\geq$ 40 trace elements in geological samples by ICPMS using enriched isotope internal standardisation. Chemical Geology, 134(4): 311-326.

Elias, M., 1973. The geology and petrology of Mount Rouse, A volcano in the Destern District of Victoria, *Unpublished Honours Thesis.* School of Earth Science, University of Melbourne.

Ellis, D.J., 1976. High pressure cognate inclusions in the Newer Volcanics of Victoria. Contributions to Mineralogy and Petrology, 58(2): 149-180.

Espanon, V.R., Chivas, A.R., Phillips, D., Matchan, E.L. and Dosseto, A., 2014. Geochronological, morphometric and geochemical constraints on the Pampas Onduladas long basaltic flow (Payún Matrú Volcanic Field, Mendoza, Argentina). Journal of Volcanology and Geothermal Research, 289: 114-129.

Evans, J.A., 1980. Some volcanological aspects of the Camperdown area, Western District, Victoria, *Unpublished Honours Thesis.* School of Earth Science, University of Melbourne.

Ferguson, A.K., 1971. The geology and petrology of the Mount Porndon volcanic complex, *Unpublished Honours Thesis.* School of Earth Science, University of Melbourne.

Fleck, R.J., Sutter, J.F. and Elliot, D.H., 1977. Interpretation of discordant ^{40}Ar/^{39}Ar age-spectra of Mesozoic tholeiites from Antarctica. Geochimica et Cosmochimica Acta, 41: 15-32.

Foden, J., Song, S.H., Turner, S., Elburg, M., Smith, P.B., Van der Steldt, B. and Van Penglis, D., 2002. Geochemical evolution of lithospheric mantle beneath S.E. South Australia. Chemical Geology, 182(2): 663-695.

Foland, K.A., Fleming, T.H., Heimann, A. and Elliot, D.H., 1993. Potassium-argon dating of fine-grained basalts with massive Ar loss: Application of the ^{40}Ar/^{39}Ar technique to plagioclase and glass from the Kirkpatrick Basalt, Antarctica. Chemical Geology (Isotope Geoscience Section), 107: 173-190.

Ford, H., Fischer, K., Abt, D., Rychert, C. and Elkins Tanton, L., 2010. The lithosphere–asthenosphere boundary and cratonic lithospheric layering beneath Australia from Sp wave imaging. Earth and planetary science letters, 300(3-4): 299-310.

Frey, F. and Green, D., 1974. The mineralogy, geochemistry and origin of Iherzolite inclusions in Victorian basanites. Geochimica et cosmochimica acta, 38(7): 1023-1059.

Frey, F.A., Green, D.H. and Roy, S.D., 1978. Integrated Models of Basalt Petrogenesis: A Study of Quartz Tholeiites to Olivine Melilitites from South Eastern Australia Utilizing Geochemical and Experimental Petrological Data. Journal of Petrology, 19(3): 463-513.

Gawith, P.F., 1977. Geochemistry and petrography of the Tertiary volcanics from the Spring Hill - Tylden Area, central Victoria, *Unpublished Honours Thesis*, LaTrobe University.

Gill, E., 1981. Potassium/argon age of basalt in floor of Hopkins River, Allansford, SW Victoria, Australia. Victorian Naturalist, 98: 188-190.

Gillen, D., Honda, M., Chivas, A.R., Yatsevich, I., Patterson, D.B. and Carr, P.F., 2010. Cosmogenic ^{21}Ne exposure dating of young basaltic lava flows from the Newer Volcanic Province, western Victoria, Australia. Quaternary Geochronology, 5(1): 1-9.

Gouramanis, C., Wilkins, D. and De Deckker, P., 2010. 6000 years of environmental changes recorded in Blue Lake, South Australia, based on ostracod ecology and valve chemistry. Palaeogeography, Palaeoclimatology, Palaeoecology, 297(1): 223-237.

Graeber, F.M., Houseman, G.A. and Greenhalgh, S.A., 2002. Regional teleseismic tomography of the western Lachlan Orogen and the Newer Volcanic Province, southeast Australia. Geophysical Journal International, 149(2): 249-266.

Gray, C.M. and McDougall, I., 2009. K-Ar geochronology of basalt petrogenesis, Newer Volcanic Province, Victoria. Australian journal of earth sciences, 56(2): 245-258.

Hall, C., 2014. Direct measurement of recoil effects on ^{40}Ar/^{39}Ar standards. Special publication - Geological Society of London, 378(1): 53-62.

Hall, T.S., 1908. The Geology of the Melbourne District. Proceedings of the Victorian Institute of Engineers, 9: 151-153.

Hanan, Hanan, B., Shervais, J. and Vetter, S.K., 2008. Yellowstone plume–continental lithosphere interaction beneath the Snake River Plain. Geology, 36(1): 51.

Hanks, W., 1955. Newer Volcanic vents and lava fields between Wallan and Yuroke, Victoria. Proceedings of the Royal Society of Victoria, 67: 1-16.

Hare, A. and Cas, R., 2005. Volcanology and evolution of the Werribee Plains intraplate, basaltic lava flow-field, Newer Volcanics Province, southeast Australia. Australian Journal of Earth Sciences, 52(1): 59-78.

Hare, A.G., Cas, R.A.F., Musgrave, R. and Phillips, D., 2005. Magnetic and chemical stratigraphy for the Werribee Plains basaltic lava flow-field, Newer Volcanics Province, southeast Australia: implications for eruption frequency. Australian Journal of Earth Sciences, 52(1): 41-57.

Harrison, T.M., 1983. Some observations on the interpretation of 40Ar/39Ar age spectra. Chemical Geology, 41: 319-338.

Hart, T.S., 1894. The Volcanic Rocks of the Melbourne District. Victorian Naturalist, 11: 74-78.

Hartmann, L., Arena, K., Duarte, S. and Pertille, J., 2013. Long-distance lava correlation in the Paraná volcanic province along the Serra Geral cuesta, southeastern Brazil. International Journal of Earth Sciences, 102(6): 1655-1669.

Heath, M., 2014. High precision $^{40}Ar/^{39}Ar$ dating of selected basalt flows from the Newer Volcanic Province, Melbourne area, *Unpublished Masters Thesis.* School of Earth Science, University of Melbourne.

Heath, M., Phillips, D. and Matchan, E.L., 2018. An evidence-based approach to accurate interpretation of $^{40}Ar/^{39}Ar$ ages from basaltic rocks. Earth and Planetary Science Letters, 498: 65-76.

Heizler, M. and Harrison, T.M., 1988. Multiple trapped argon isotope components revealed by isochron analysis. Geochimica et Cosmochimica Acta, 52(5): 1295-1303.

Henley, K. and Webb, A., 1990. Radiometric dating on various granites and Newer Volcanics basalts. Geological Survey of Victoria Unpublished Report, 27.

Hirano, N., Koppers, A.A.P., Takahashi, A., Fujiwara, T. and Nakanishi, M., 2008. Seamounts, knolls and petit-spot monogenetic volcanoes on the subducting Pacific Plate. Basin Research, 20(4): 543-553.

Hodges, M.K.V., Turrin, B.D., Champion, D.E. and Swisher Iii, C.C., 2015. New argon-argon ($^{40}Ar/^{39}Ar$) radiometric age dates from selected subsurface basalt flows at the Idaho National Laboratory, Idaho. 2015-5028, Reston, VA.

Irving, A.J. and Green, D.H., 1976. Geochemistry and petrogenesis of the newer basalts of Victoria and South Australia. Journal of the Geological Society of Australia, 23(1): 45-66.

Ismail, R., 2010. $^{40}Ar/^{39}Ar$ dating of selected young volcanoes of the Newer Volcanic Province New ages on seven new locations, *Unpublished Honours Thesis.* School of Earth Science, University of Melbourne.

Ismail, R., Phillips, D. and Birch, W.D., 2013. $^{40}Ar/^{39}Ar$ dating of alkali feldspar megacrysts from selected young volcanoes of the Newer Volcanic Province, Victoria. Proceedings of the Royal Society of Victoria, 125(1/2): 59.

Jackson, M., Gibbons, F., Syers, J. and Mokma, D., 1972. Eolian influence on soils developed in a chronosequence of basalts of Victoria, Australia. Geoderma, 8(2-3): 147-163.

Jicha, B., Rhodes, J.M., Singer, B. and Garcia, M., 2012. $^{40}Ar/^{39}Ar$ geochronology of submarine Mauna Loa volcano, Hawaii. Journal of Geophysical Research, 117(B9).

Jones, I., Verdel, C., Crossingham, T. and Vasconcelos, P., 2017. Animated reconstructions of the Late Cretaceous to Cenozoic northward migration of Australia, and implications for the generation of east Australian mafic magmatism. Geosphere, 13(2): 460-481.

Jordan, S., Jowitt, S. and Cas, R., 2015. Origin of temporal-compositional variations during the eruption of Lake Purrumbete Maar, Newer Volcanics Province, southeastern Australia. Bulletin of Volcanology, 77(1): 883.

Jordan, S.C., 2013. Factors controlling the formation of a very large maar volcano and the fragmentation process in phreatomagmatic eruptions: Lake Purrumbete maar, southeastern Australia *Unpublished PhD Thesis.* School of Earth, Atmosphere and Environment, Monash University.

Jourdan, F., Mark, D. and Verati, C., 2014. Advances in $^{40}Ar/^{39}Ar$ dating: from archaeology to planetary sciences - introduction. Geological Society of London Special Publication, 378(1): 1-8.

Jourdan, F., Matzel, J. and Renne, P., 2007. ^{39}Ar and ^{37}Ar recoil loss during neutron irradiation of sanidine and plagioclase. Geochimica et Cosmochimica Acta, 71(11): 2791-2808.

Jourdan, F. and Renne, P., 2014. Neutron-induced ^{37}Ar recoil ejection in Ca-rich minerals and implications for ^{40}Ar/^{39}Ar dating. Geological Society of London Special Publication, 378(1): 33-52.

Joyce, B., 2004. The young volcanic regions of southeastern Australia: early studies, physical volcanology and eruption risk. Proceedings of the Royal Society of Victoria, 116(1): 1-13.

Joyce, E., 1975. Quaternary volcanism and tectonics in southeastern Australia. Bulletin of the Royal Society of New Zealand, 13: 169-176.

Joyce, E., 1999. A new regolith landform map of the western Victorian volcanic plains, Victoria, Australia, Regolith, pp. 117-126.

Joyce, E.B., 1983. Age relationships in the Newer Volcanic Province of southeastern Australia, Sixth Australian Geological Convention. Geological Society of Australia, Canberra.

Kaneoka, I., 1980. Rare gas isotopes and mass fractionation; An indicator of gas transport into or from a magma. Earth and Planetary Science Letters, 48: 284-292.

Kelley, S., 2002. Excess argon in K-Ar and Ar-Ar geochronology. Chemical geology, 188(1-2): 1-22.

King, S.D. and Anderson, D.L., 1998. Edge-driven convection. Earth and Planetary Science Letters, 160(3): 289-296.

Koppers, A.A.P., Staudigel, H. and Duncan, R., 2003. High-resolution ^{40}Ar/^{39}Ar dating of the oldest oceanic basement basalts in the western Pacific basin. Geochemistry, Geophysics, Geosystems: G3, 4(11).

Koppers, A.A.P., Staudigel, H. and Wijbrans, J., 2000. Dating crystalline groundmass separates of altered Cretaceous seamount basalts by the ^{40}Ar/^{39}Ar incremental heating technique. Chemical Geology, 166(1-2): 139-158.

Kuntz, M.A., Champion, D.E., Spiker, E.C. and Lefebvre, R.H., 1986. Contrasting magma types and steady-state, volume-predictable, basaltic volcanism along the Great Rift, Idaho. Geological Society of America Bulletin, 97(5): 579-594.

Lanphere, M., 2000. Comparison of conventional K-Ar and ^{40}Ar/^{39}Ar dating of young mafic volcanic rocks. Quaternary Research, 53(03): 294-301.

Lanphere, M. and Dalrymple, B.G., 1976. Identification of excess ^{40}Ar by the ^{40}Ar/^{39}Ar age spectrum technique. Earth and planetary science letters, 32(2): 141-148.

Lee, J.-Y., Marti, K., Severinghaus, J., Kawamura, K., Yoo, H.-S. and Kim, J., 2006. A redetermination of the isotopic abundances of atmospheric Ar. Geochimica et Cosmochimica Acta, 70(17): 4507-4512.

Leeman, W.P., Schutt, D.L. and Hughes, S.S., 2009. Thermal structure beneath the Snake River Plain: Implications for the Yellowstone hotspot. Journal of Volcanology and Geothermal Research, 188(1): 57-67.

Lesti, C., Giordano, G., Salvini, F. and Cas, R., 2008. Volcano tectonic setting of the intraplate, Pliocene-Holocene, Newer Volcanic Province (southeast Australia): Role of crustal fracture zones. Journal of Geophysical Research: Solid Earth, 113(B7).

Lindstrom, M.M. and Haskin, L.A., 1981. Compositional inhomogeneities in a single Icelandic tholeiite flow. Geochimica et Cosmochimica Acta, 45(1): 15-31.

Ludwig, K., 2012. User’s manual for Isoplot version 3.75–4.15: a geochronological toolkit for Microsoft. Excel Berkley Geochronological Center Special Publication(5).

Macdonald, G.A. and Katsura, T., 1964. Chemical composition of Hawaiian lavas. Journal of Petrology, 5(1): 82-133.

Maclennan, J., McKenzie, D., Hilton, F., Gronvöld, K. and Shimizu, N., 2003. Geochemical variability in a single flow from northern Iceland. Journal of Geophysical Research: Solid Earth, 108(B1).

Marzoli, A., Renne, P.R., Piccirillo, E.M., Ernesto, M., Bellieni, G. and De Min, A., 1999. Extensive 200-million-year-Old continental flood basalts of the central atlantic magmatic province. Science, 284(5414): 616-618.

Matchan, E. and Phillips, D., 2011. New ^{40}Ar/^{39}Ar ages for selected young (<1 Ma) basalt flows of the Newer Volcanic Province, southeastern Australia. Quaternary Geochronology, 6(3-4): 356-368.

Matchan, E. and Phillips, D., 2014. High precision multi-collector ^{40}Ar/^{39}Ar dating of young basalts: Mount Rouse volcano (SE Australia) revisited. Quaternary Geochronology, 22: 57-64.

Matchan, E.L., 2012. Calibration of the cosmogenic ^{21}Ne exposure dating technique for application to Quaternary volcanic chronology, *Unpublished PhD Thesis.* School of Earth Science, University of Melbourne.

Matchan, E.L., Joyce, E.B. and Phillips, D., 2016. A new ^{40}Ar/^{39}Ar eruption age for the Mount Widderin volcano, Newer Volcanic Province, Australia, with implications for eruption frequency in the region. Australian Journal of Earth Sciences, 63(2): 175-186.

Matchan, E.L., Phillips, D., Traine, E. and Zhu, D., 2018. ^{40}Ar/^{39}Ar ages of alkali feldspar xenocrysts constrain the timing of intraplate basaltic volcanism. Quaternary Geochronology, 47: 14-28.

Matsumoto, A. and Kobayashi, T., 1995. K/Ar age determination of late Quaternary volcanic rocks using the “mass fractionation correction procedure”: application to the Younger Ontake Volcano, central Japan. Chemical Geology, 125(1): 123-135.

McBride, J.S., Lambert, D.D., Nicholls, I.A. and Price, R.C., 2001. Osmium Isotopic Evidence for Crust?Mantle Interaction in the Genesis of Continental Intraplate Basalts from the Newer Volcanics Province, Southeastern Australia. Journal of Petrology, 42(6): 1197-1218.

McDonough, W.F., McCulloch, M.T. and Sun, S.S., 1985. Isotopic and geochemical systematics in Tertiary-Recent basalts from southeastern Australia and implications for the evolution of the sub-continental lithosphere. Geochimica et cosmochimica acta, 49(10): 2051-2067.

McDonough, W.F. and Sun, S.s., 1995. The composition of the Earth. Chemical Geology, 120(3): 223-253.

McDougall, I., Allsopp, H. and Chamalaun, F., 1966. Isotopic dating of the Newer Volcanics of Victoria, Australia, and geomagnetic polarity epochs. Journal of Geophysical Research, 71(24): 6107-6118.

McDougall, I. and Gill, E.D., 1975. Potassium-argon ages from the Quaternary succession in the Warrnambool-Port Fairy area, Victoria, Australia. Proceedings of the Royal Society of Victoria, 87(1/2): 175-178.

McDougall, I. and Harrison, T.M., 1999. Geochronology and Thermochronology by the ^{40}Ar/^{39}Ar Method. Oxford University Press, 269 pp.

McGee, L.E. and Smith, I.E., 2016. Interpreting chemical compositions of small scale basaltic systems: A review. Journal of Volcanology and Geothermal Research, 325: 45-60.

Merrihue, C. and Turner, G., 1966. Potassium-argon dating by activation with fast neutrons. Journal of Geophysical Research, 71(11): 2852-2857.

Mitchell, M.M., 1990. The geology and geochemistry of the Werribee Plain Newer Volcanics, Victoria, *Unpublished honours thesis,*LaTrobe University.

Morgan, L., Renne, P., Taylor, R.E. and WoldeGabriel, G., 2009. Archaeological age constraints from extrusion ages of obsidian: Examples from the Middle Awash, Ethiopia. Quaternary Geochronology, 4(3): 193-203.

Murphy, L.G., 1983. An investigation of the chemistry of groundmass from the Keilor Werribee Plains and the geology of the Bacchus Marsh area, *Unpublished Honours Thesis.* School of Earth Science, University of Melbourne.

Németh, K., 2010. Monogenetic volcanic fields: origin, sedimentary record, and relationship with polygenetic volcanism. Geological Society of America Special Papers, 470: 43-66.

Nosiara, M., 1981. Geology and geochemistry of Tower Hill, Western Victoria, *Unpublished Honours Thesis.* School of Earth Science, University of Melbourne.

O'Hanlon, E.M., 1975. A petrographic and geochemical study of the Devonian and Tertiary volcanics of the Macedon district, central Victoria, *Unpublished Honours Thesis,* LaTrobe University.

Ollier, C.D., 1985. Lava flows of Mount Rouse, western Victoria. Proceedings of the Royal Society of Victoria, 97(4): 167.

Onstott, T.C., Miller, M.L., Ewing, R.C., Arnold, G.W. and Walsh, D.S., 1995. Recoil refinements: Implications for the 40Ar/39Ar dating technique. Geochimica et Cosmochimica Acta, 59(9): 1821-1834.

Oostingh, K.F., Jourdan, F., Matchan, E.L. and Phillips, D., 2017. ^{40}Ar/^{39}Ar geochronology reveals rapid change from plume-assisted to stress-dependent volcanism in the Newer Volcanic Province, SE Australia. Geochemistry, Geophysics, Geosystems: G3, 18(3): 1065-1089.

Oostingh, K.F., Jourdan, F., Merle, R. and Chiaradia, M., 2016. Spatio-temporal Geochemical Evolution of the SE Australian Upper Mantle Deciphered from the Sr, Nd and Pb Isotope Compositions of Cenozoic Intraplate Volcanic Rocks. Journal of Petrology, 57(8): egw048.

Ozawa, A., Tagami, T. and Kamata, H., 2006. Argon isotopic composition of some Hawaiian historical lavas. Chemical Geology, 226(1-2): 66-72.

Paul, B., Hergt, J.M. and Woodhead, J.D., 2005. Mantle heterogeneity beneath the Cenozoic volcanic provinces of central Victoria inferred from trace-element and Sr, Nd, Pb and Hf isotope data. Australian Journal of Earth Sciences, 52(2): 243-260.

Phillips, D. and Matchan, E.L., 2013. Ultra-high precision ^{40}Ar/^{39}Ar ages for Fish Canyon Tuff and Alder Creek Rhyolite sanidine: New dating standards required? Geochimica et Cosmochimica Acta, 121: 229-239.

Phillips, D., Matchan, E.L., Honda, M. and Kuiper, K.F., 2017. Astronomical calibration of ^{40}Ar/^{39}Ar reference minerals using high-precision, multi-collector (ARGUSVI) mass spectrometry. Geochimica et Cosmochimica Acta, 196: 351-369.

Phillips, D. and Onstott, T.C., 1986. Application of ^{36}Ar/^{40}Ar versus ^{39}Ar/^{40}Ar correlation diagrams to the ^{40}Ar/^{39}Ar spectra of phlogopites from southern African kimberlites. Geophysical Research Letters, 13(7): 689-692.

Price, R., Gray, C., Nicholls, I. and Day, A., 1988. Cainozoic volcanic rocks. Geology of Victoria: 439-452.

Price, R.C., Gray, C.M. and Frey, F.A., 1997. Strontium isotopic and trace element heterogeneity in the plains basalts of the Newer Volcanic Province, Victoria, Australia. Geochimica et cosmochimica acta, 61(1): 171-192.

Price, R.C., Gray, C.M., Wilson, R.E., Frey, F.A. and Taylor, S.R., 1991. The effects of weathering on rare-earth element, Y and Ba abundances in Tertiary basalts from southeastern Australia. Chemical geology, 93(3-4): 245-265.

Price, R.C., Nicholls, I.A. and Gray, C.M., 2003. Cainozoic igneous activity. In: W.D. Birch (Editor), Geology of Victoria. Geological Society of Australia, Melbourne, pp. 361-375.

Pringle, M., Staudigel, H. and Gee, J., 1991. Jasper Seamount: Seven million years of volcanism. Geology, 19(4): 364.

Rampino, M.R. and Stothers, R.B., 1988. Flood basalt volcanism during the past 250 million years. Science, 241(4866): 663-668.

Rawlinson, N. and Fishwick, S., 2012. Seismic structure of the southeast Australian lithosphere from surface and body wave tomography. Tectonophysics, 572: 111-122.

Rawlinson, N., Pilia, S., Young, M., Salmon, M. and Yang, Y., 2016. Crust and upper mantle structure beneath southeast Australia from ambient noise and teleseismic tomography. Tectonophysics, 689: 143-156.

Renne, P.R., Ernesto, M., Pacca, I.G., Coe, R.S., Glen, J.M., Prévot, M. and Perrin, M., 1992. The Age of Paraná Flood Volcanism, Rifting of Gondwanaland, and the Jurassic-Cretaceous Boundary. Science, 258(5084): 975-979.

Renne, P.R., Onstott, T.C., D'Agrella-Filho, M.S., Pacca, I.G. and Teixeira, W., 1990. ^{40}Ar/^{39}Ar dating of 1.0–1.1 Ga magnetizations from the Saõ Francisco and Kalahari cratons: tectonic implications for Pan-African and Brasiliano mobile belts. Earth and Planetary Science Letters, 101(2): 349-366.

Rhodes, J., 1983. Homogeneity of lava flows: chemical data for historic Mauna Loan eruptions. Journal of Geophysical Research: Solid Earth, 88(S02).

Robertson, G.B., Prescott, J.R. and Hutton, J., 1996. Thermoluminescence dating of volcanic activity at Mount Gambier, South Australia. Transactions of the Royal Society of South Australia, 120(1): 7-12.

Rudnick, R.L. and Gao, S., 2014. 4.1 - Composition of the Continental Crust A2 - Holland, Heinrich D. In: K.K. Turekian (Editor), Treatise on Geochemistry (Second Edition). Elsevier, Oxford, pp. 1-51.

Sandiford, M., Wallace, M. and Coblentz, D., 2004. Origin of the in situ stress field in south-eastern Australia. Basin Research, 16(3): 325-338.

Schleiger, N.W., 1983. Geology of Mt. Cooper Bundoora, Unpublished Report.

Scutter, C., 1993. The volcanology and geomorphology of the Bullenmerri volcanic complex, Newer Volcanic Province, Western Victoria, *Unpublished Honours Thesis.* School of Earth Science, University of Melbourne.

Sherwood, J., Oyston, B. and Kershaw, A., 2004. The age and contemporary environments of Tower Volcano, Southwest Victoria, Australia. Proceedings of the Royal Society of Victoria, 116(1): 69-76.

Sigmarsson, O., Condomines, M., Grönvold, K. and Thordarson, T., 1991. Extreme magma homogeneity in the 1783–84 Lakagigar eruption: origin of a large volume of evolved basalt in Iceland. Geophysical Research Letters, 18(12): 2229-2232.

Singer, B., Ackert, R.P. and Guillou, H., 2004. ^{40}Ar/^{39}Ar and K-Ar chronology of Pleistocene glaciations in Patagonia. Geological Society of America Bulletin, 116(3): 434.

Singer, B., Jicha, B., Condon, D., Macho, A., Hoffman, K., Dierkhising, J., Brown, M., Feinberg, J. and Kidane, T., 2014. Precise ages of the Reunion event and Huckleberry Ridge excursion: Episodic clustering of geomagnetic instabilities and the dynamics of flow within the outer core. Earth and Planetary Science Letters, 405: 25-38.

Singleton, O.P., McDougall, I. and Mallett, C.W., 1976. The Pliocene-Pleistocene boundary in Southeastern Australia. Journal of the Geological Society of Australia, 23(3): 299-311.

Skeats, E.W. and James, A.V., 1937. Basaltic barriers and other surface features of the Newer Basalts of Western Victoria. Royal Society of Victoria.

Smith, B.W. and Prescott, J.R., 1987. Thermoluminescence dating of the eruption at Mt Schank, South Australia. Australian Journal of Earth Sciences, 34(3): 335-342.

Smits, F. and Gentner, W., 1950. Argonbestimmungen an kalium-mineralien I. Bestimmungen an tertiaren kalisalzen. Geochimica et Cosmochimica Acta, 1: 22-27.

Steiger, R.H. and Jäger, E., 1977. Subcommission on geochronology: Convention on the use of decay constants in geo- and cosmochronology. Earth and planetary science letters, 36(3): 359-362.

Stewart, G., 1975. The Newer Volcanics lava field north of Melbourne: Part 1. Gelogical Survey of Victoria *Unpublished Report* 1975/75.

Stewart, G., 1977. Geological logs of metropolitan basalt survey bores between the Western Highway and Sunbury. Gelogical Survey of Victoria *Unpublished Report* 1977/27.

Stone, J., Peterson, J.A., Fifield, L.K. and Cresswell, R.G., 1997. Cosmogenic chlorine-36 exposure ages for two basalt flows in the Newer Volcanics Province, western Victoria. Proceedings of the Royal Society of Victoria, 109: 121.

Storey, M., Mahoney, J.J., Saunders, A.D., Duncan, R.A., Kelley, S.P. and Coffin, M.F., 1995. Timing of Hot Spot-Related Volcanism and the Breakup of Madagascar and India. Science, 267(5199): 852-855.

Sun, S.-s. and McDonough, W.F., 1989. Chemical and isotopic systematics of oceanic basalts: implications for mantle composition and processes. Geological Society, London, Special Publications, 42(1): 313-345.

Sutalo, F. and Joyce, B., 2004. Long basaltic lava flows of the Mt. Rouse volcano in the Newer Volcanic Province of Southeastern Australia. Proceedings of the Royal Society of Victoria, 116(1): 37-49.

Sutherland, F., 1981. Migration in relation to possible tectonic and regional controls in eastern Australian volcanism. Journal of Volcanology and Geothermal Research, 9(2-3): 181-213.

Takada, A., 1994. The influence of regional stress and magmatic input on styles of monogenetic and polygenetic volcanism. Journal of Geophysical Research: Solid Earth, 99(B7): 13563-13573.

Traine, E., 2012. ^{40}Ar/^{39}Ar dating of selected late Quaternary volcanoes of the Newer Volcanics, Victoria: Trialling a new technique, *Unpublished Masters Thesis.* School of Earth Science, University of Melbourne.

Trieloff, M., Falter, M., Buikin, A., Korochantseva, E., Jessberger, E. and Altherr, R., 2005. Argon isotope fractionation induced by stepwise heating. Geochimica et Cosmochimica Acta, 69(5): 1253-1264.

Tunjc, J.A., 1988. The geology and geochemistry of the Mount Eccles volcanic complex, western Victoria *Unpublished Honours Thesis,* LaTrobe University.

Turner, G., 1971. ^{40}Ar-^{39}Ar ages from the lunar maria. Earth and Planetary Science Letters, 11(1-5): 169-191.

Turner, G. and Cadogan, P., 1974. Possible effects of ^{39}Ar recoil in ^{40}Ar-^{39}Ar dating, Lunar and Planetary Science Conference Proceedings, pp. 1601-1615.

Valentine, G.A. and Connor, C.B., 2015. Basaltic volcanic fields, The Encyclopedia of Volcanoes. Elsevier, pp. 423-439.

van den Hove, J., Grose, L., Betts, P.G., Ailleres, L., Van Otterloo, J. and Cas, R.A., 2017a. Spatial analysis of an intra-plate basaltic volcanic field in a compressional tectonic setting: South-eastern Australia. Journal of Volcanology and Geothermal Research, 335: 35-53.

van den Hove, J.C., Van Otterloo, J., Betts, P.G., Ailleres, L. and Cas, R.A., 2017b. Controls on volcanism at intraplate basaltic volcanic fields. Earth and Planetary Science Letters, 459: 36-47.

van Otterloo, J. and Cas, R.A., 2013. Reconstructing the eruption magnitude and energy budgets for the pre-historic eruption of the monogenetic ~ 5 ka Mt. Gambier Volcanic Complex, south-eastern Australia. Bulletin of Volcanology, 75(12): 769.

van Otterloo, J., Cas, R.A. and Sheard, M.J., 2013. Eruption processes and deposit characteristics at the monogenetic Mt. Gambier Volcanic Complex, SE Australia: implications for alternating magmatic and phreatomagmatic activity. Bulletin of Volcanology, 75(8): 737.

van Otterloo, J., Raveggi, M., Cas, R.A.F. and Maas, R., 2014. Polymagmatic Activity at the Monogenetic Mt Gambier Volcanic Complex in the Newer Volcanics Province, SE Australia: New Insights into the Occurrence of Intraplate Volcanic Activity in Australia. Journal of Petrology, 55(7): 1317-1351.

Vogel, D. and Keays, R., 1997. The petrogenesis and platinum-group element geochemistry of the Newer Volcanic Province, Victoria, Australia. Chemical geology, 136(3-4): 181-204.

Walker, G.P., 1989. Gravitational (density) controls on volcanism, magma chambers and intrusions. Australian Journal of Earth Sciences, 36(2): 149-165.

Wellman, P., 1974. Potassium-argon ages on the Cainozoic Volcanic rocks of Eastern Victoria, Australia. Journal of the Geological Society of Australia, 21(4): 359-376.

Wellman, P., 1983. Hotspot volcanism in Australia and New Zealand: Cainozoic and mid-Mesozoic. Tectonophysics, 96(3): 225-243.

Wellman, P. and McDougall, I., 1974. Cainozoic igneous activity in eastern Australia. Tectonophysics, 23(1-2): 49-65.

Wyllie, P., 1988. Solidus curves, mantle plumes, and magma generation beneath Hawaii. Journal of Geophysical Research, 93(B5): 4171-4181.

Yaxley, G.M., Green, D.H. and Kamenetsky, V., 1998. Carbonatite Metasomatism in the Southeastern Australian Lithosphere. Journal of Petrology, 39(11-12): 1917-1930.

Appendix A.1. Micrographs, age spectra, inverse isochrons and Ca/K plots of samples selected for ^{40}Ar/^{39}Ar dating from the Mount Fraser and Tulloch Hill flows (Flow A and Flow B respectively). Spectra, isochrons and Ca/K plots generated using the ISOPLOT software package (Ludwig, 2012). Box heights of age spectra and Ca/K plots are 2σ errors

A.1a. Mount Fraser Flow (Flow A)

Sample MH05

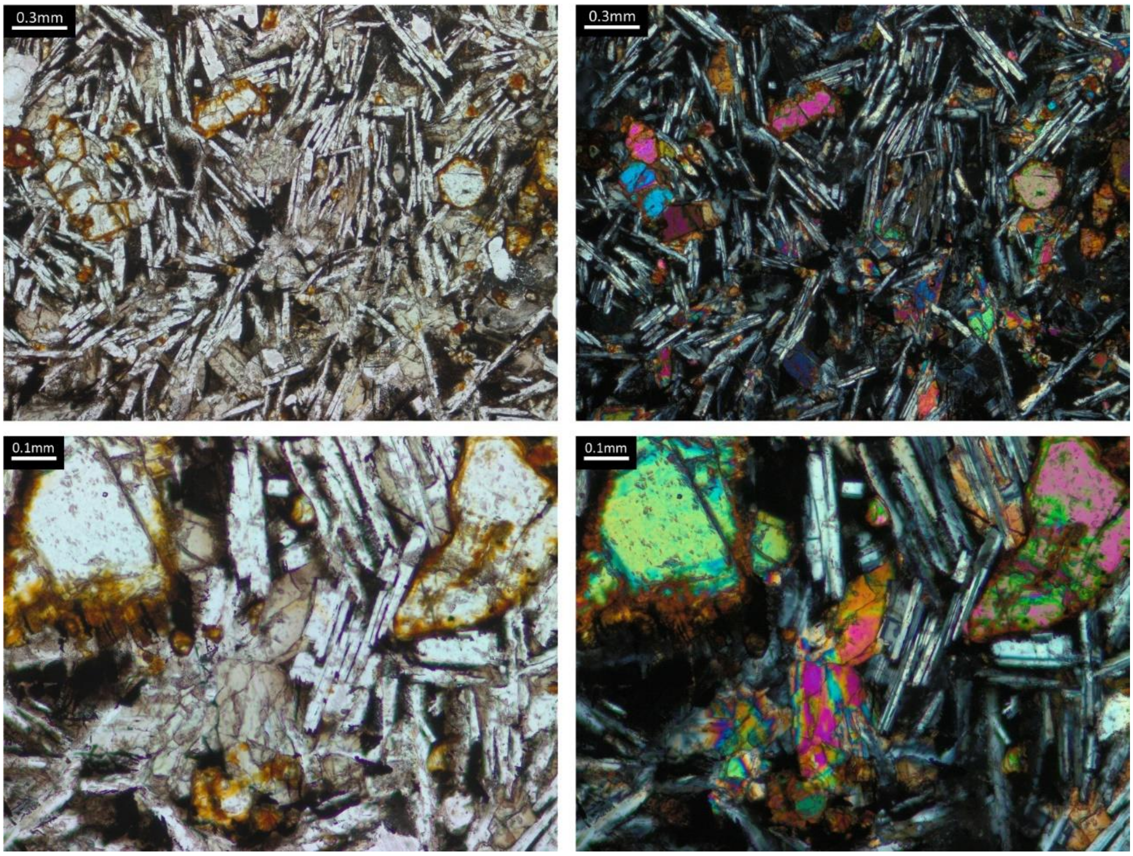

Figure A.1: Transmitted light photomicrographs of sample MH05.

MH05-1

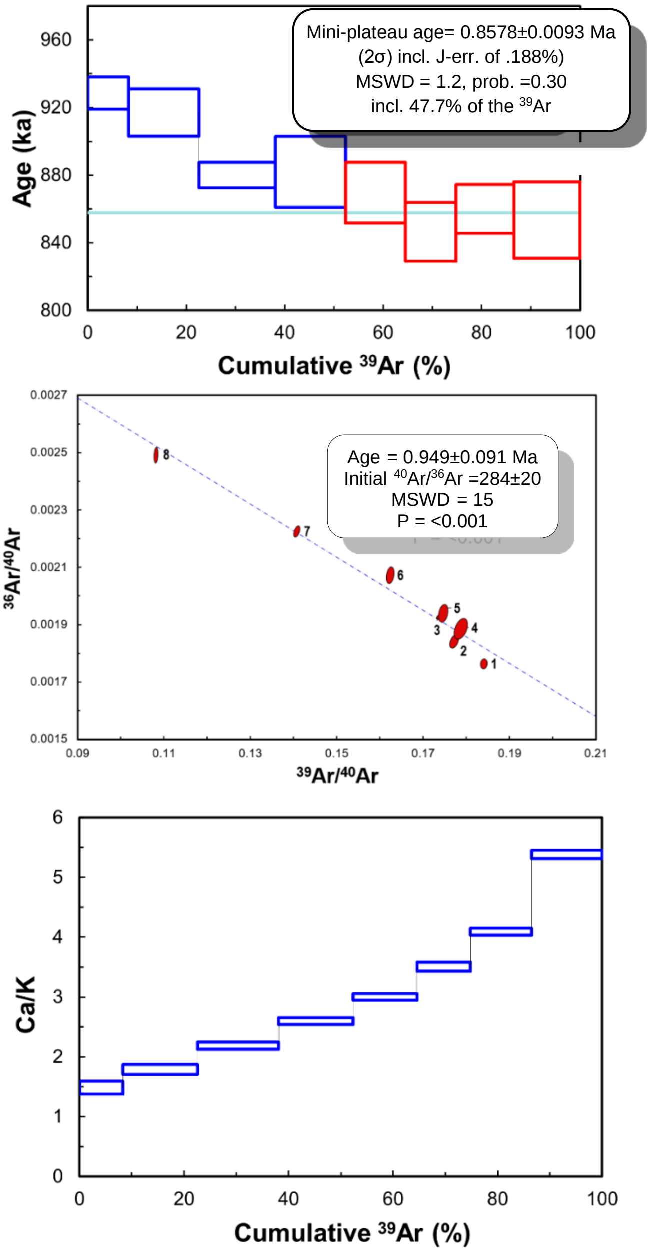

Figure A.2: ^{40}Ar/^{39}Ar age spectrum, inverse isochron and Ca/K plot of aliquant MH05-1.

Sample MH07

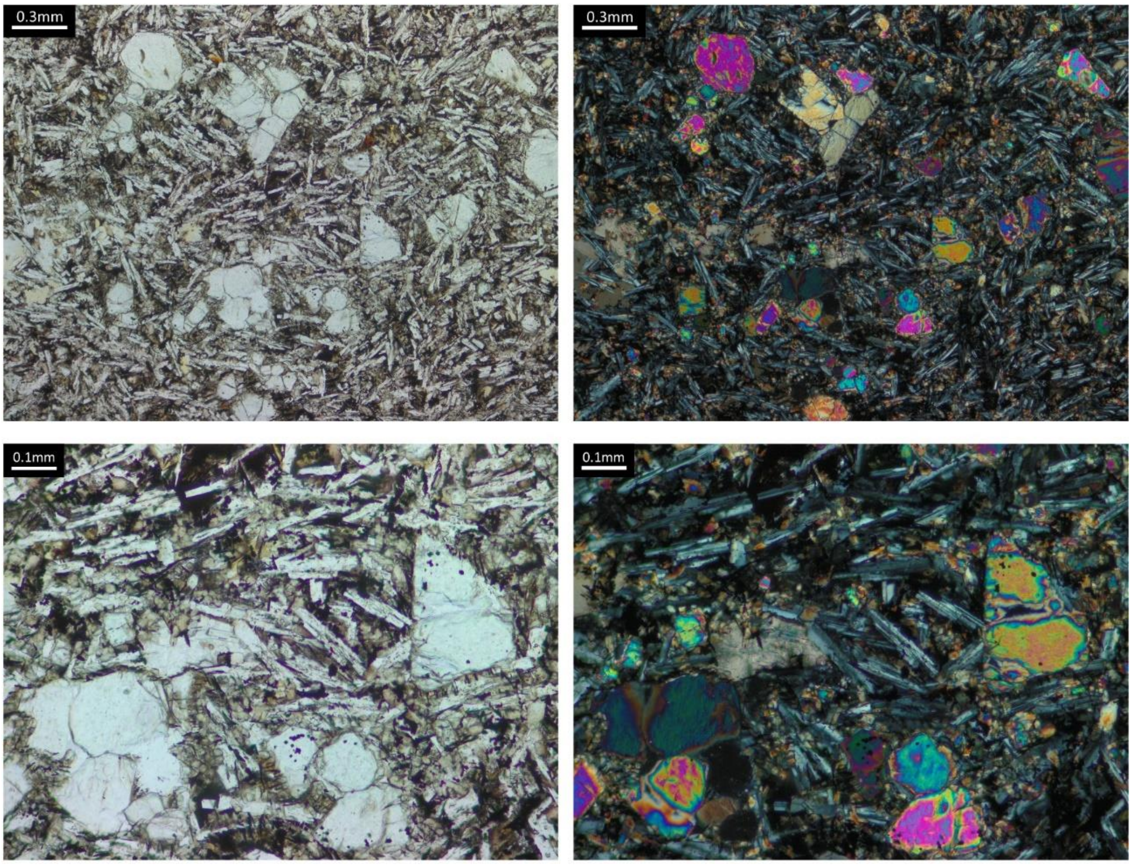

Figure A.3: Transmitted light photomicrographs of sample MH07.

MH07-1

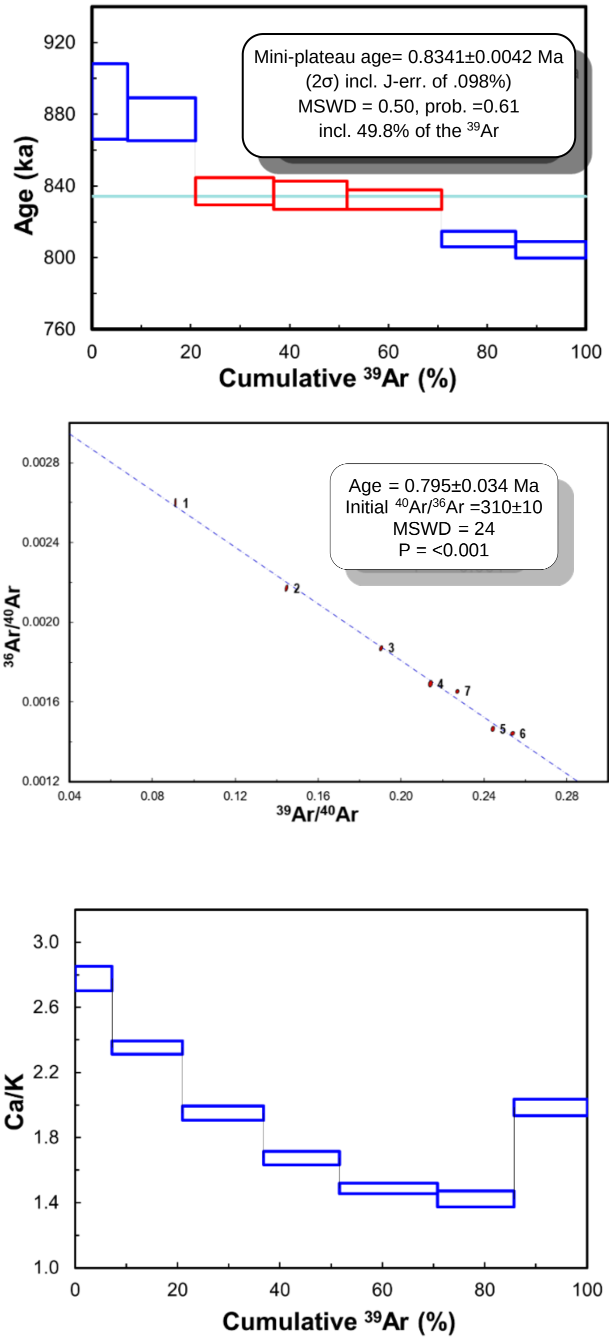

Figure A.4: ^{40}Ar/^{39}Ar age spectrum, inverse isochron and Ca/K plot of aliquant MH07-1.

Sample MH09

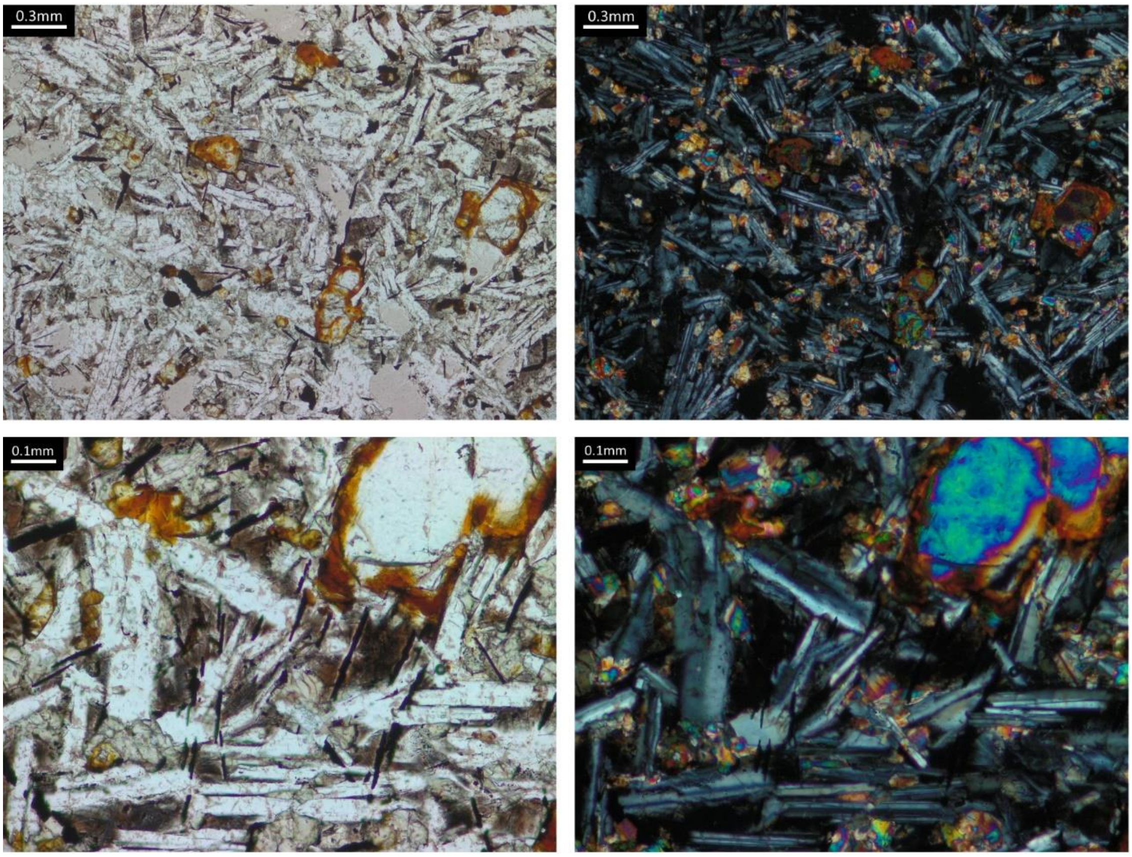

Figure A.5: Transmitted light photomicrographs of sample MH09.

MH09-1

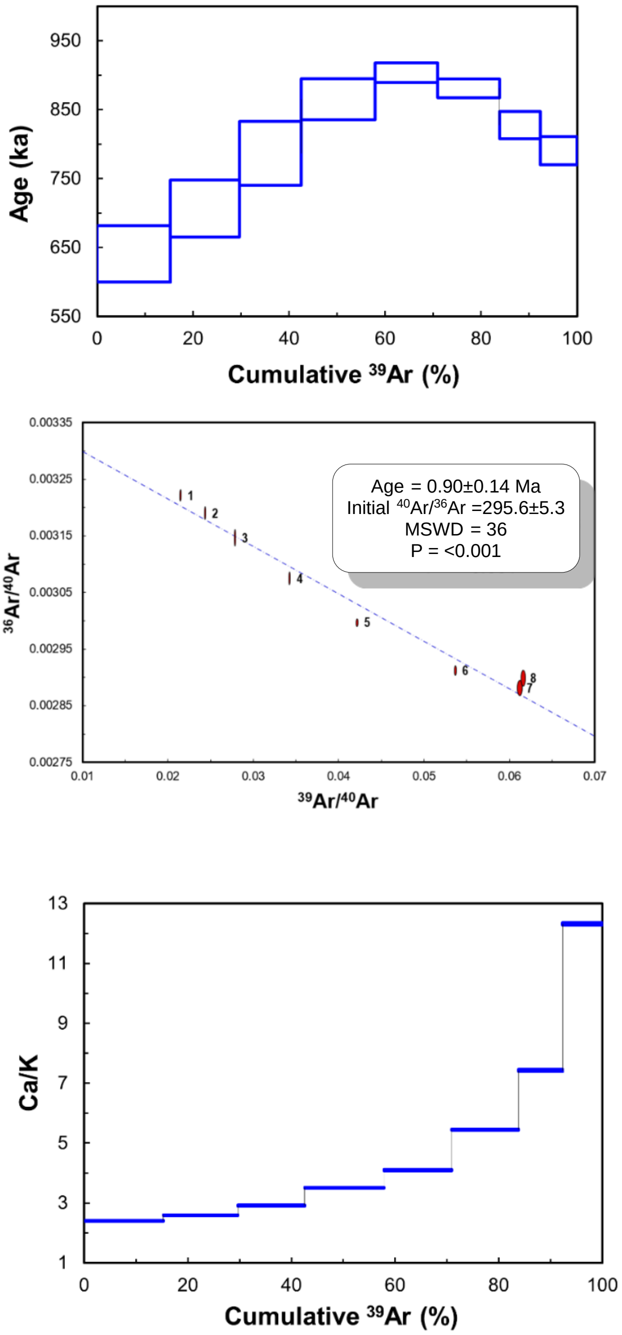

Figure A.6: ^{40}Ar/^{39}Ar age spectrum, inverse isochron and Ca/K plot of aliquant MH09-1.

Sample MH12

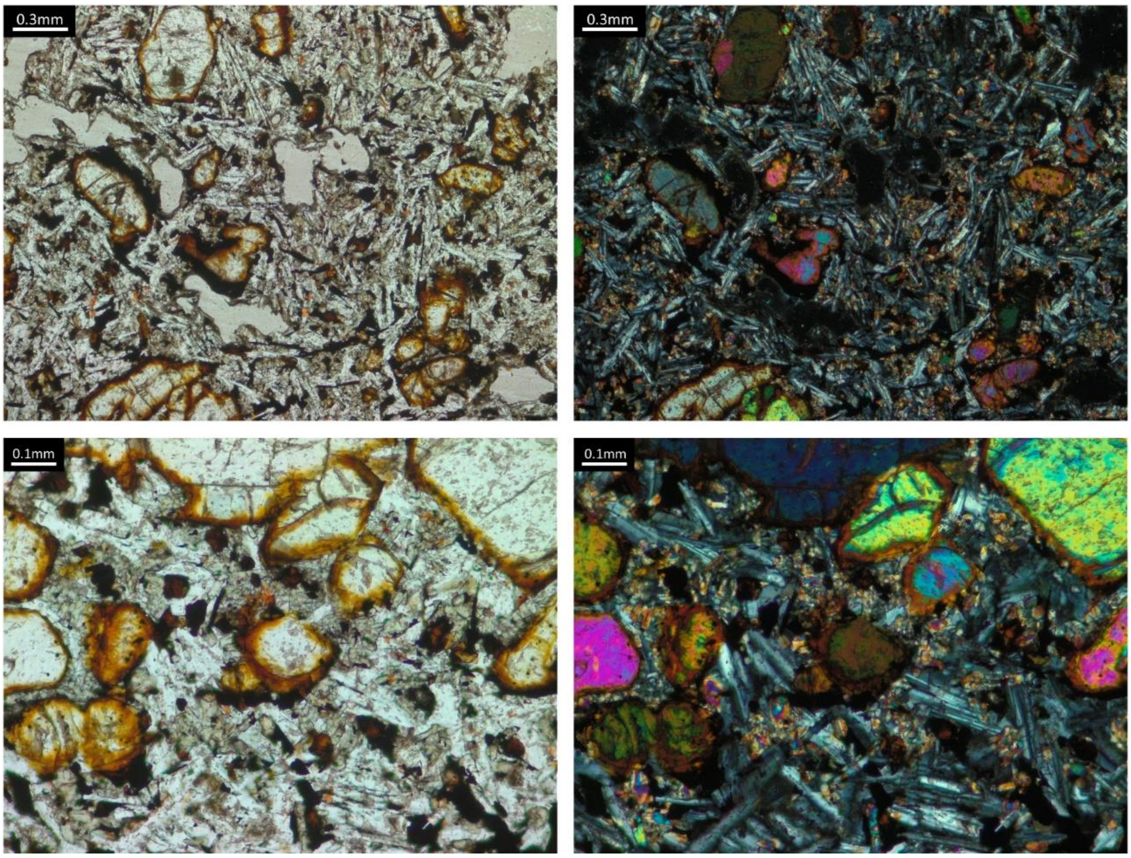

Figure A.7: Transmitted light photomicrographs of sample MH12.

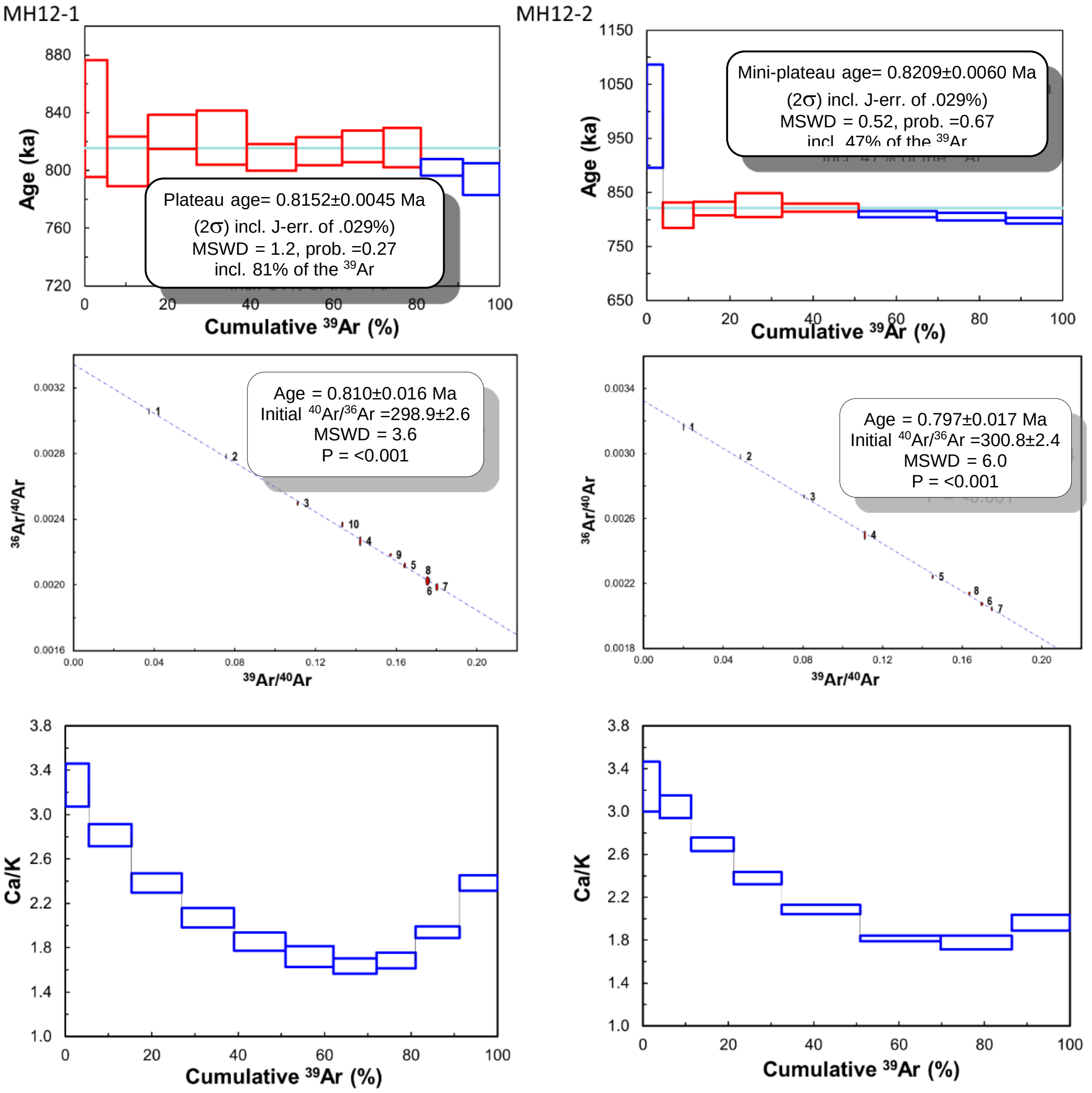

Figure A.8: ^{40}Ar/^{39}Ar age spectra, inverse isochrons and Ca/K plots of aliquants MH12-1 and MH12-2.

Sample MH24

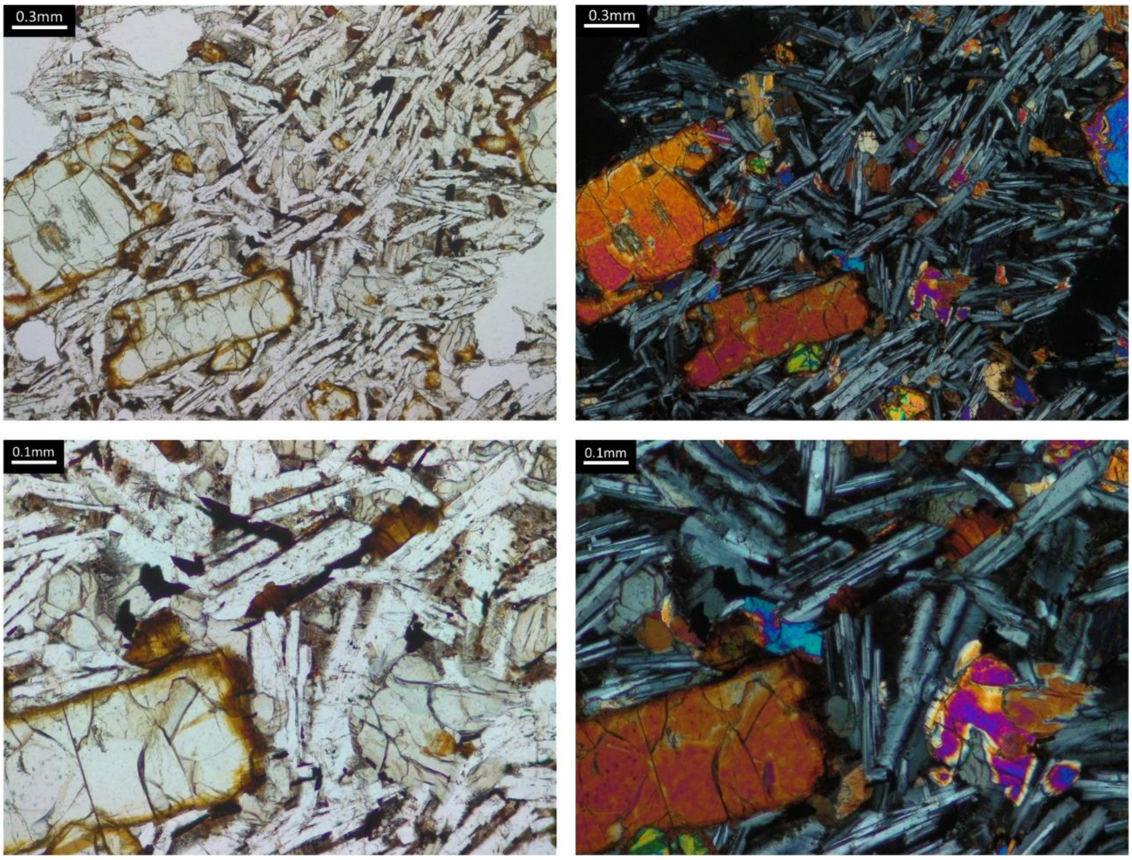

Figure A.9: Transmitted light photomicrographs of sample MH24.

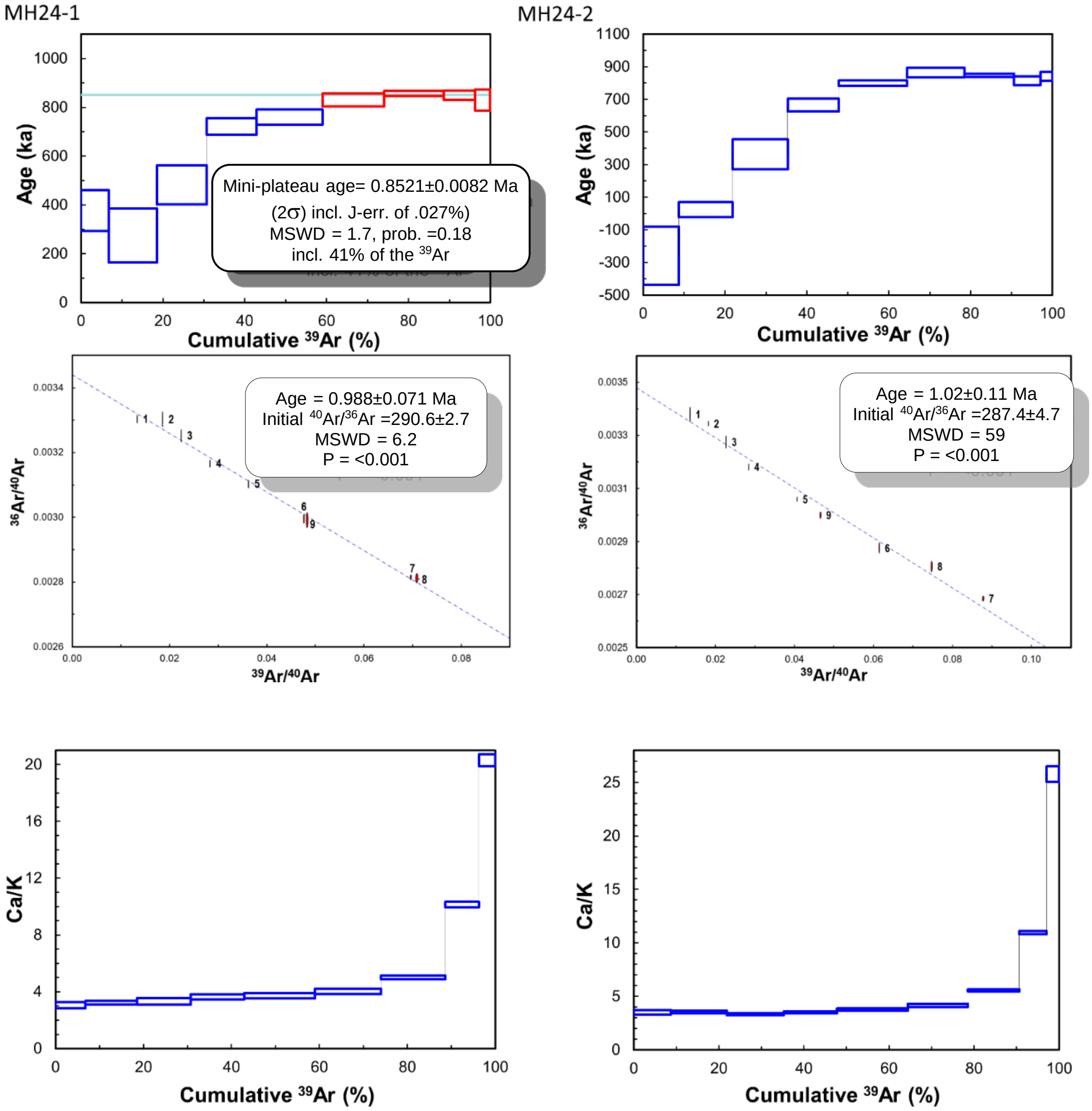

Figure A.10: ^{40}Ar/^{39}Ar age spectra, inverse isochrons and Ca/K plots of aliquants MH24-1 and MH24-2.

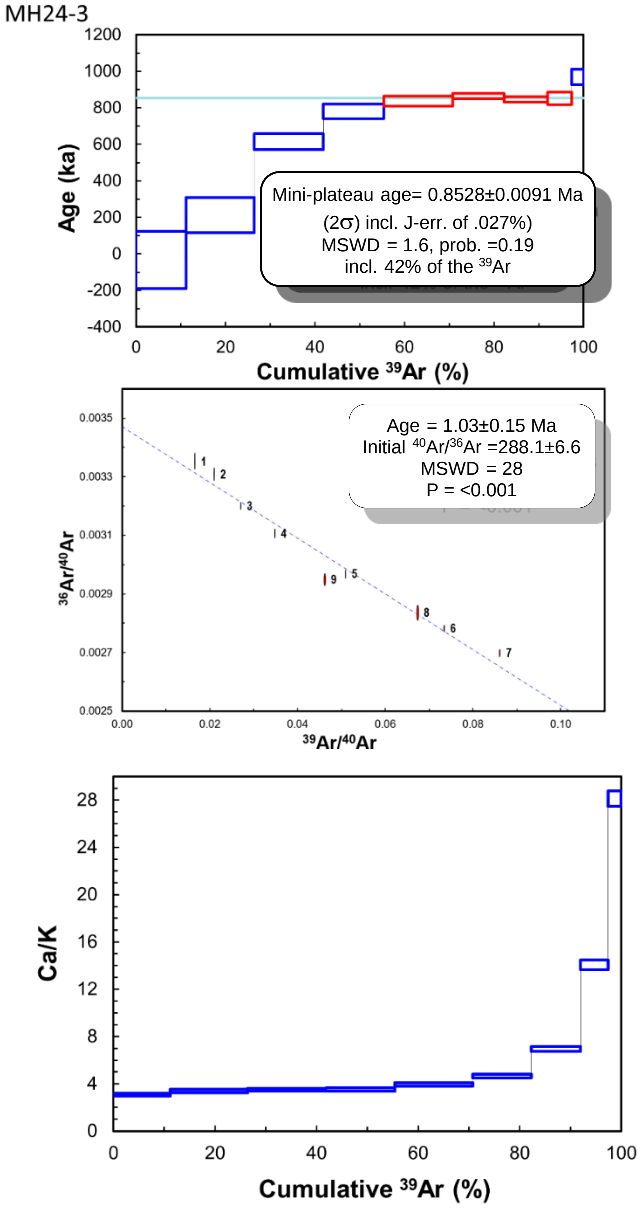

Mini-plateau age= 0.8528±0.0091 Ma
(2σ) incl. J-err. of .027%)
MSWD = 1.6, prob. =0.19
incl. 42% of the ^{39}Ar

Age = 1.03±0.15 Ma
Initial ^{40}Ar/^{36}Ar =288.1±6.6
MSWD = 28
P = <0.001

Figure A.11: ^{40}Ar/^{39}Ar age spectrum, inverse isochron and Ca/K plot of aliquant MH24-3.

Sample MH66

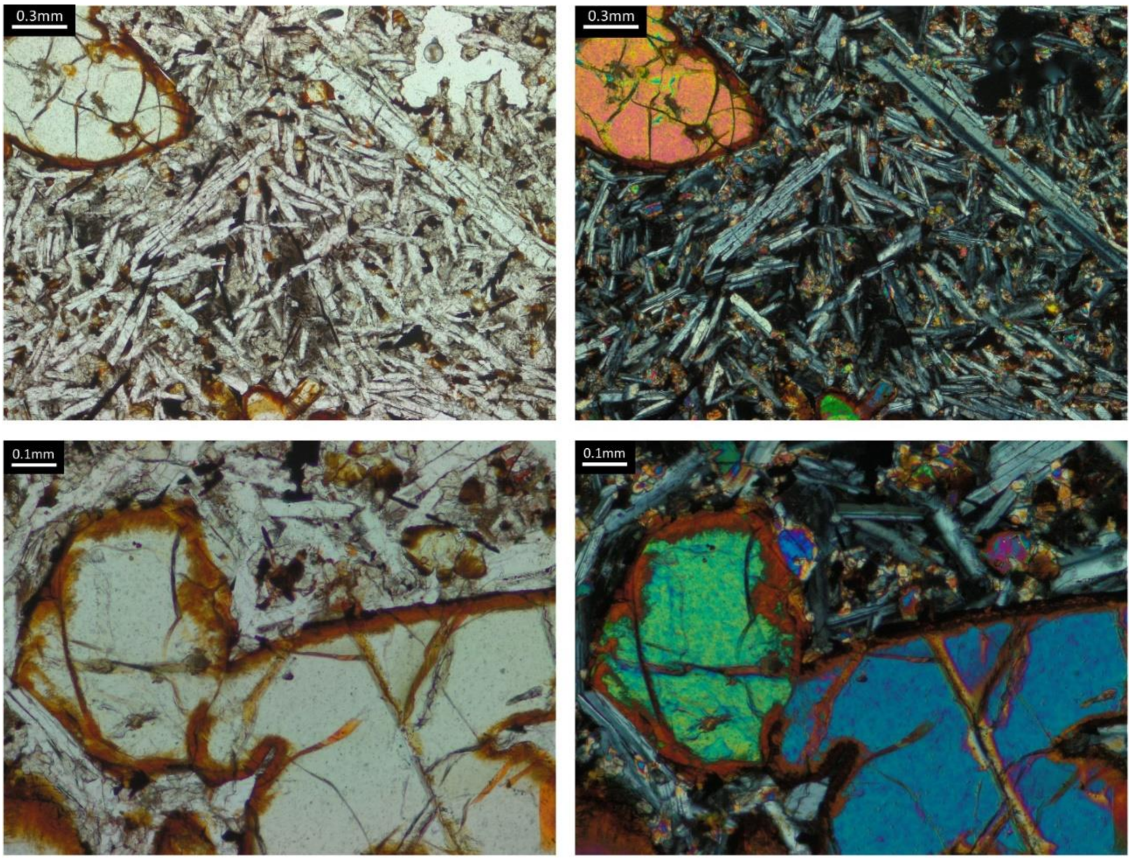

Figure A.12: Transmitted light photomicrographs of sample MH05.

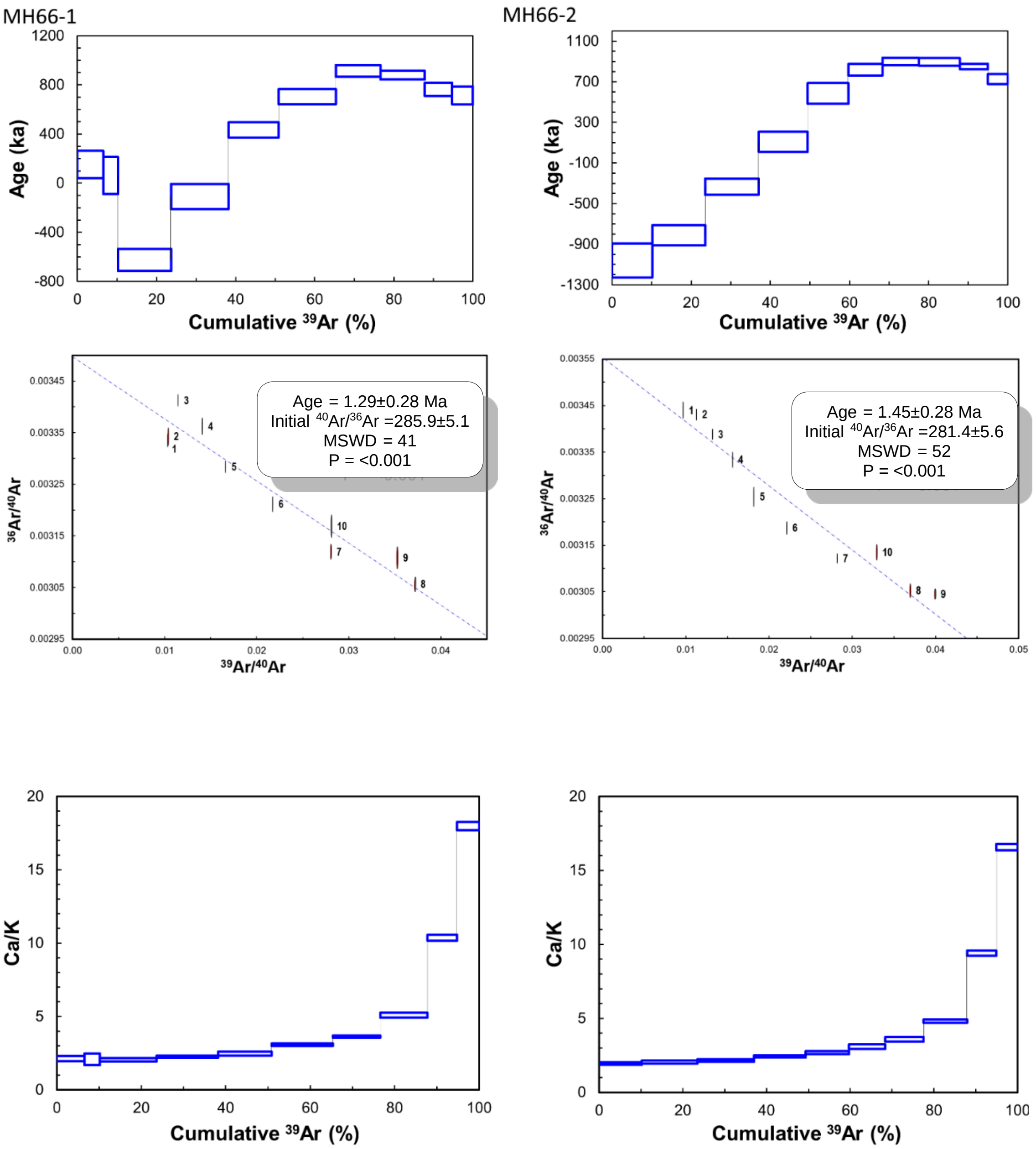

Figure A.13: ^{40}Ar/^{39}Ar age spectra, inverse isochrons and Ca/K plots of aliquants MH66-1 and MH66-2.

Sample MH70

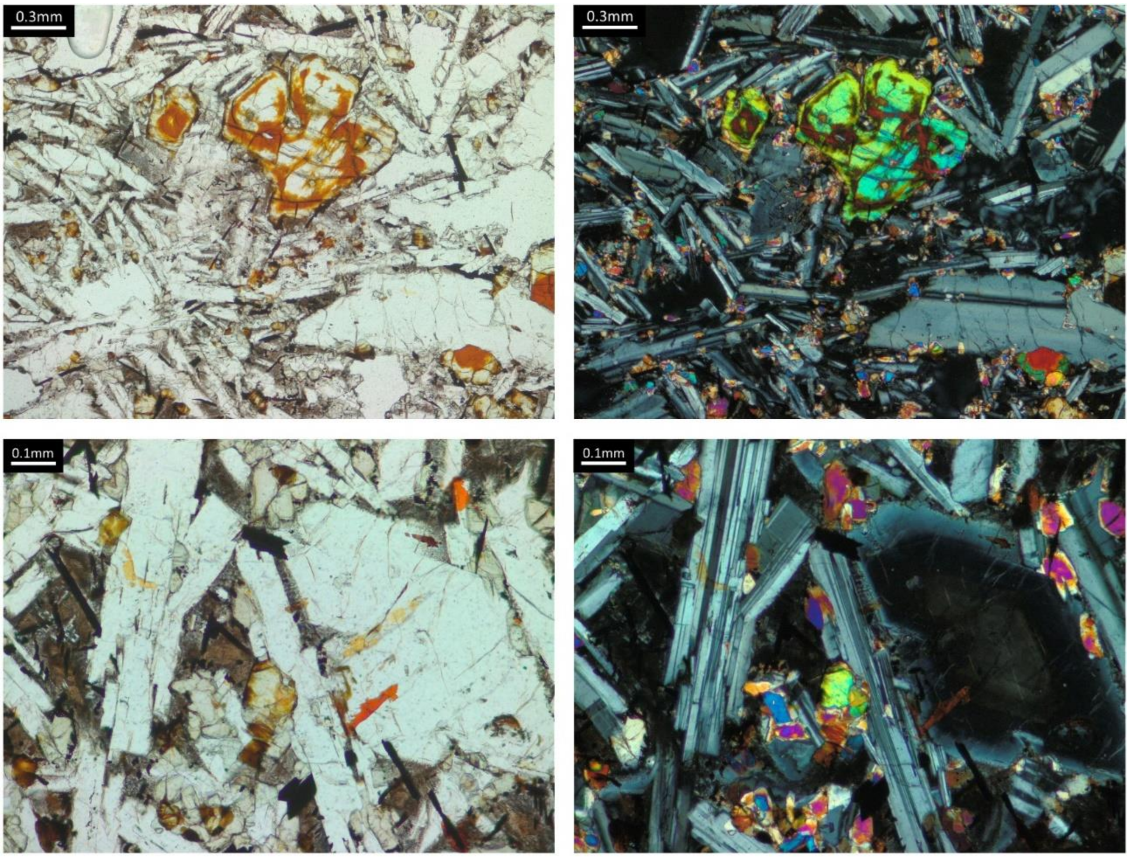

Figure A.14: Transmitted light photomicrographs of sample MH70.

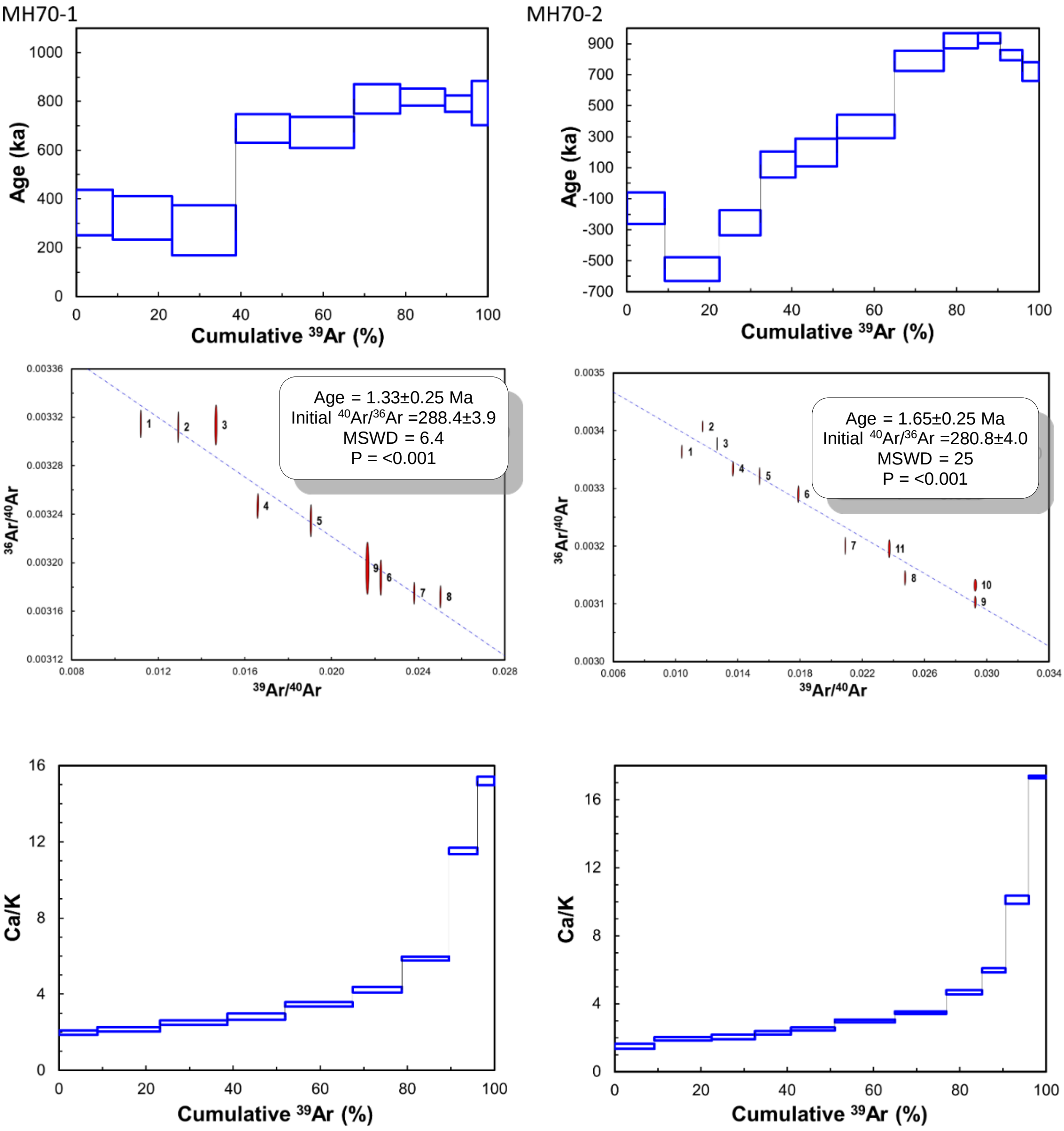

Figure A.15: ^{40}Ar/^{39}Ar age spectra, inverse isochrons and Ca/K plots of aliquants MH70-1 and MH70-2.

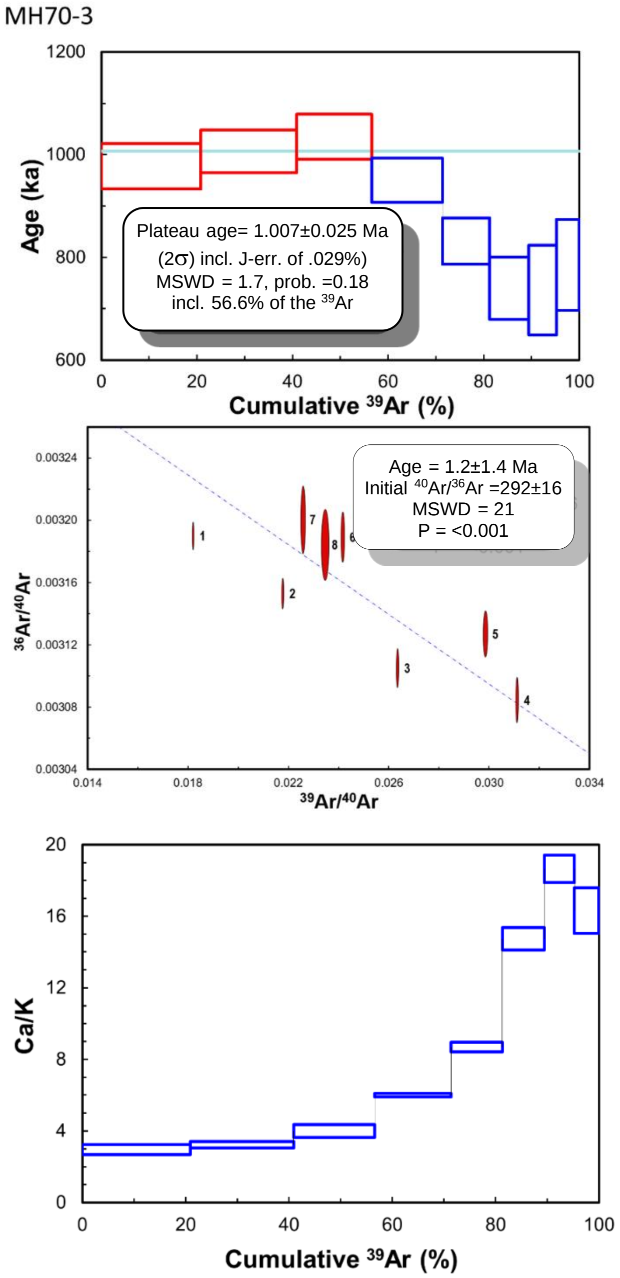

Figure A.16: ^{40}Ar/^{39}Ar age spectrum, inverse isochron and Ca/K plot of aliquant MH70-3.

Sample MO43B

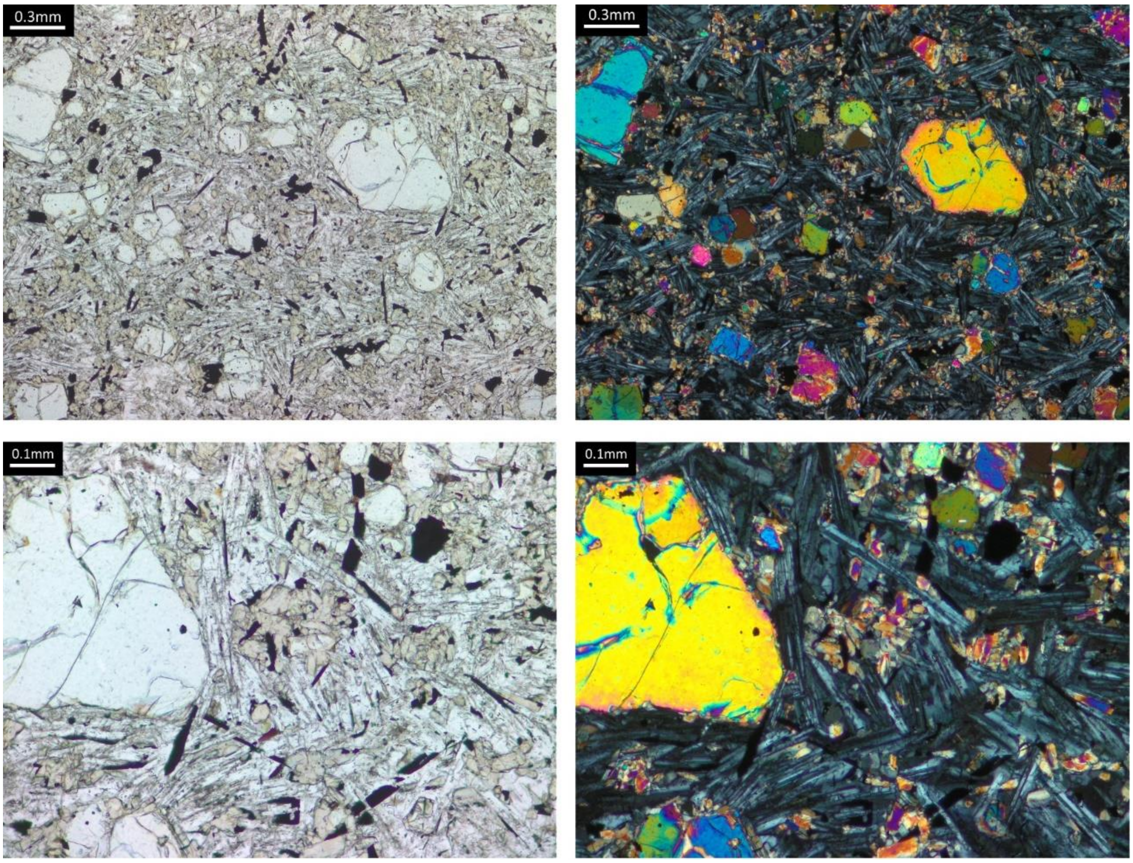

Figure A.17: Transmitted light photomicrographs of sample MO43B.

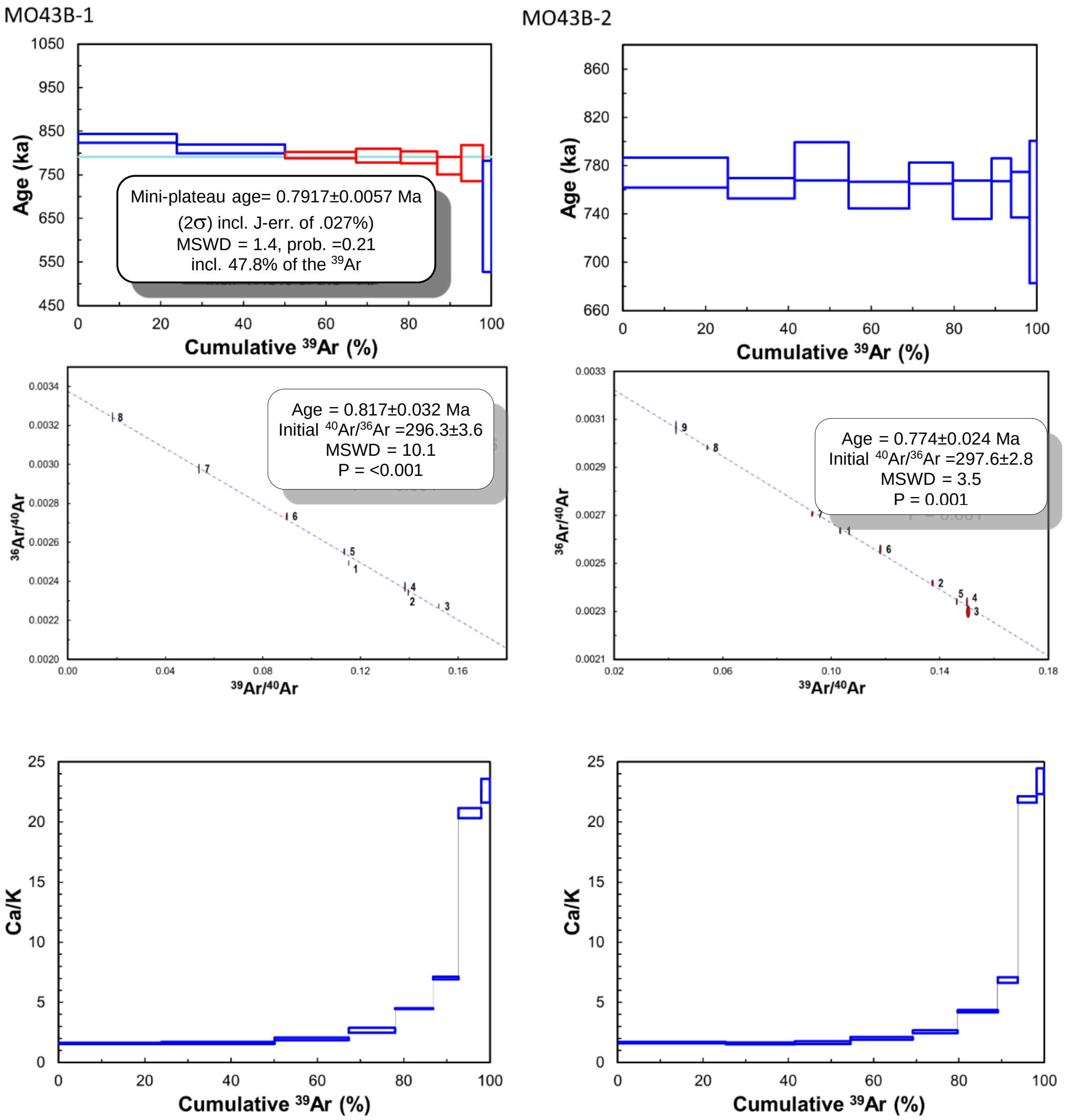

Figure A.18: $^{40}Ar/^{39}Ar$ age spectra, inverse isochrons and Ca/K plots of aliquants MO43B-1 and MO43B-2.

Sample WW1A

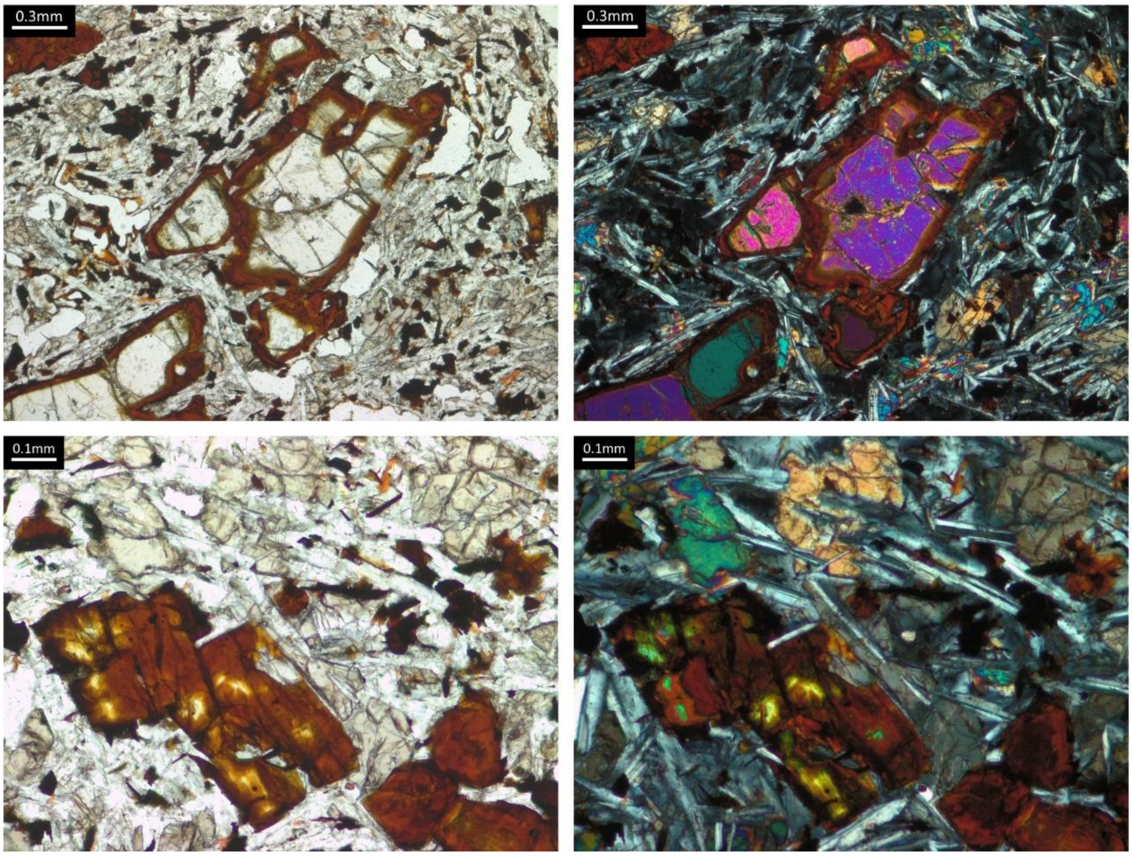

Figure A.19: Transmitted light photomicrographs of sample WW1A.

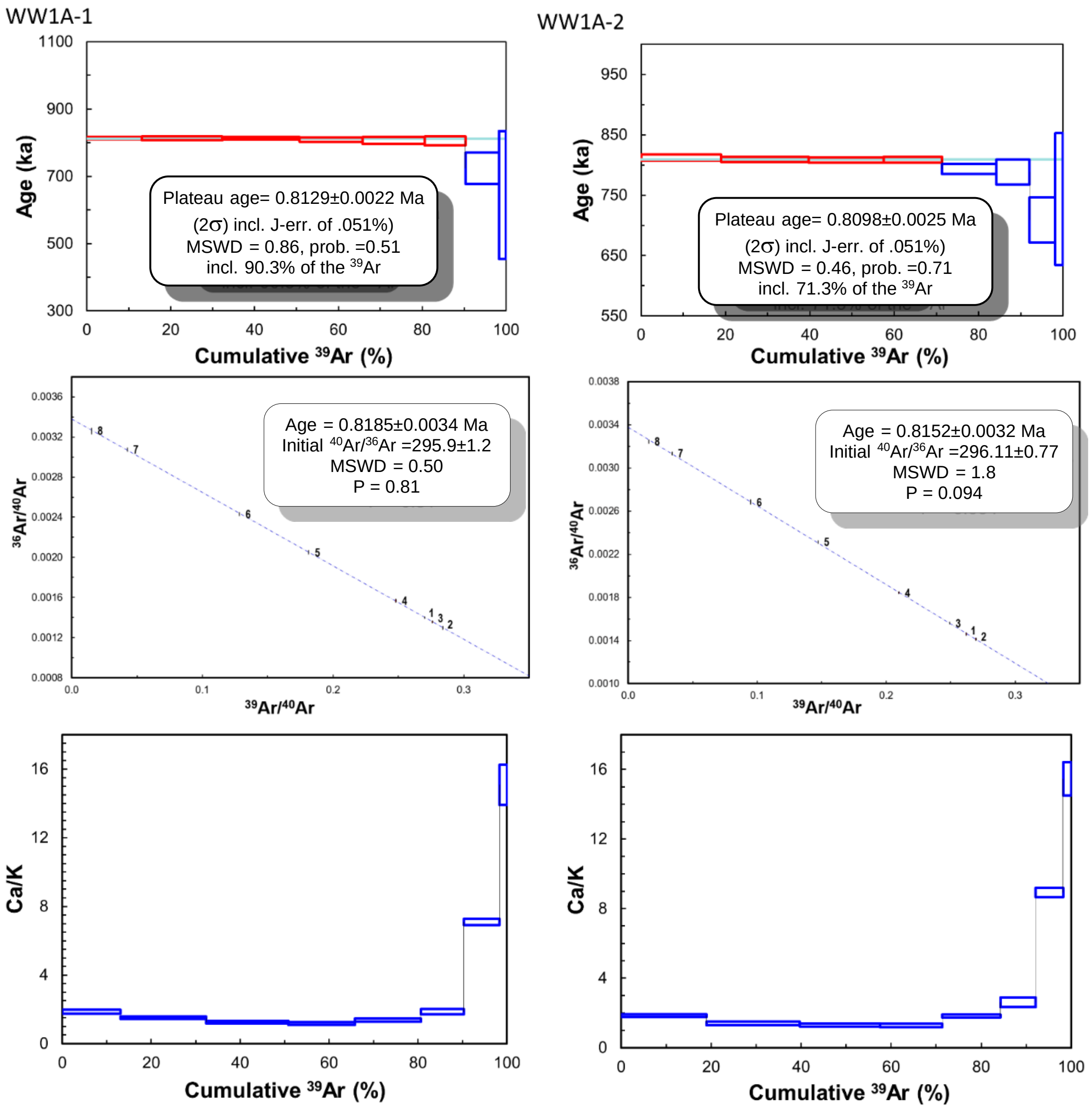

Figure A.20: ^{40}Ar/^{39}Ar age spectra, inverse isochrons and Ca/K plots of aliquants WW1A-1 and WW1A-2.

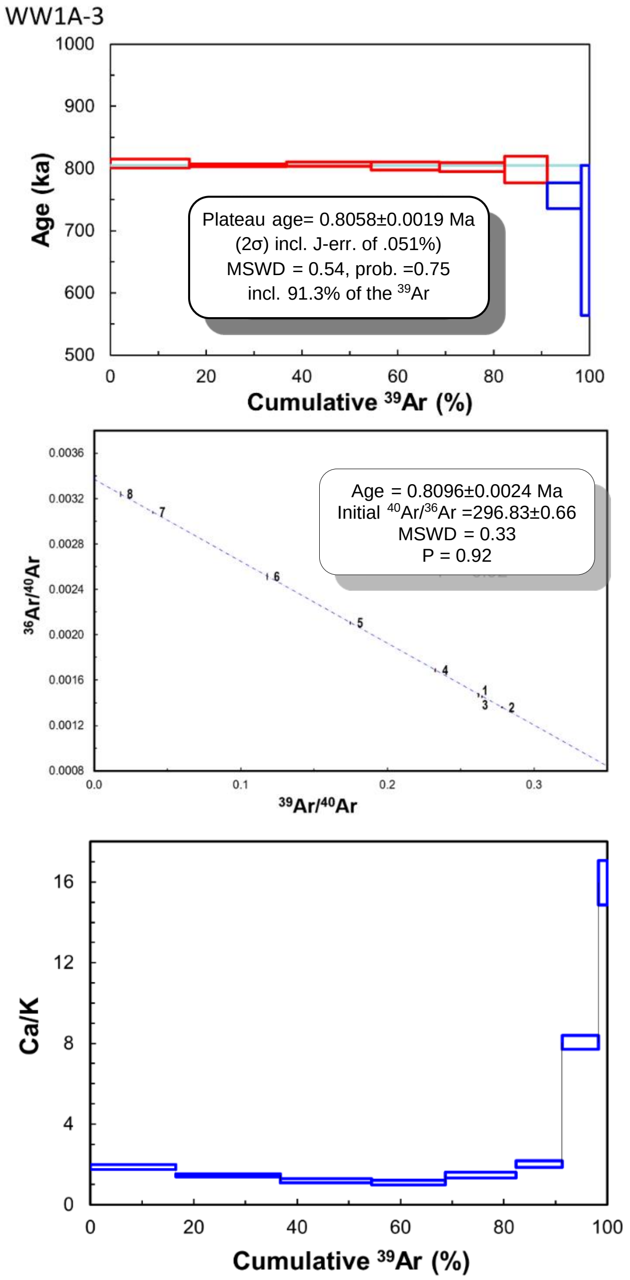

Figure A.21: ^{40}Ar/^{39}Ar age spectrum, inverse isochron and Ca/K plot of aliquant WW1A-3.

Sample YY3C

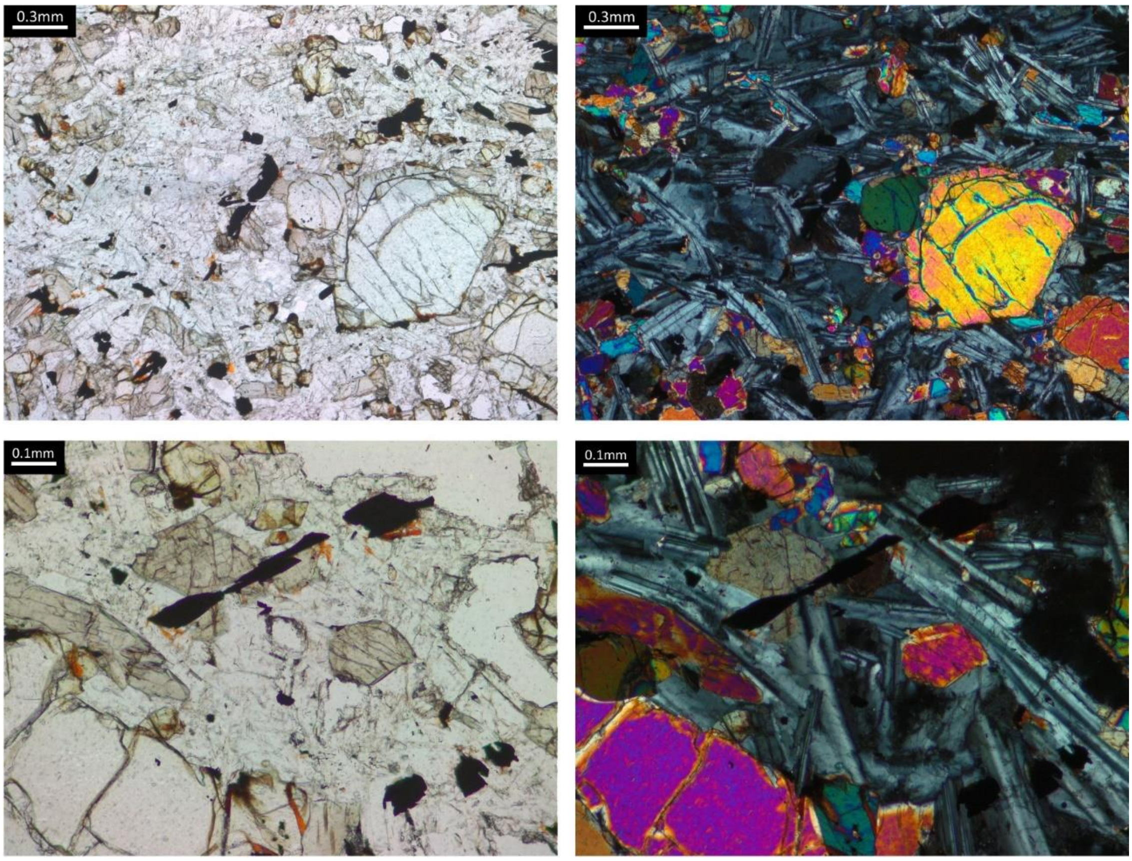

Figure A.22: Transmitted light photomicrographs of sample YY3C.

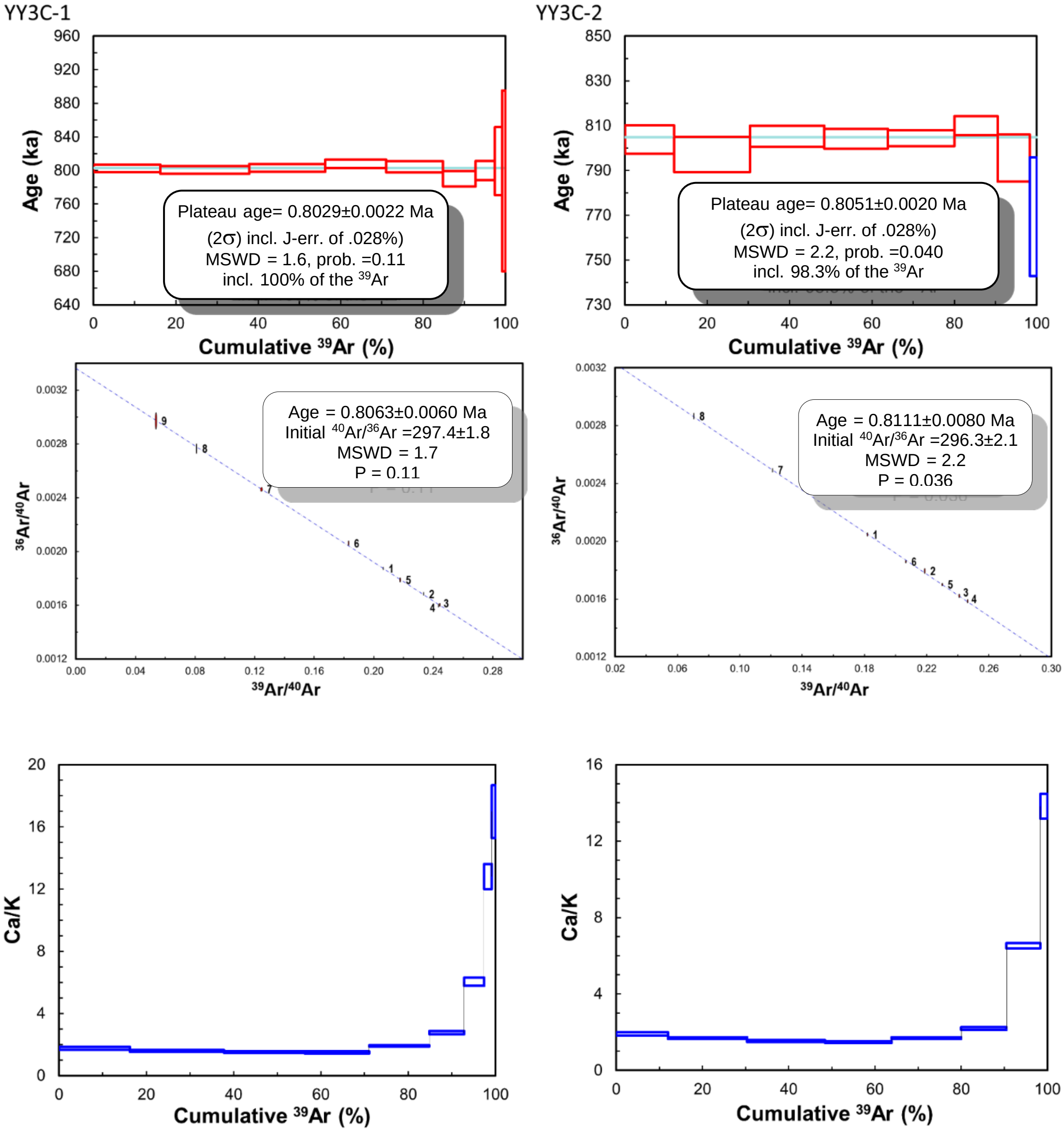

Figure A.23: ^{40}Ar/^{39}Ar age spectra, inverse isochrons and Ca/K plots of aliquants YY3C-1 and YY3C-2.

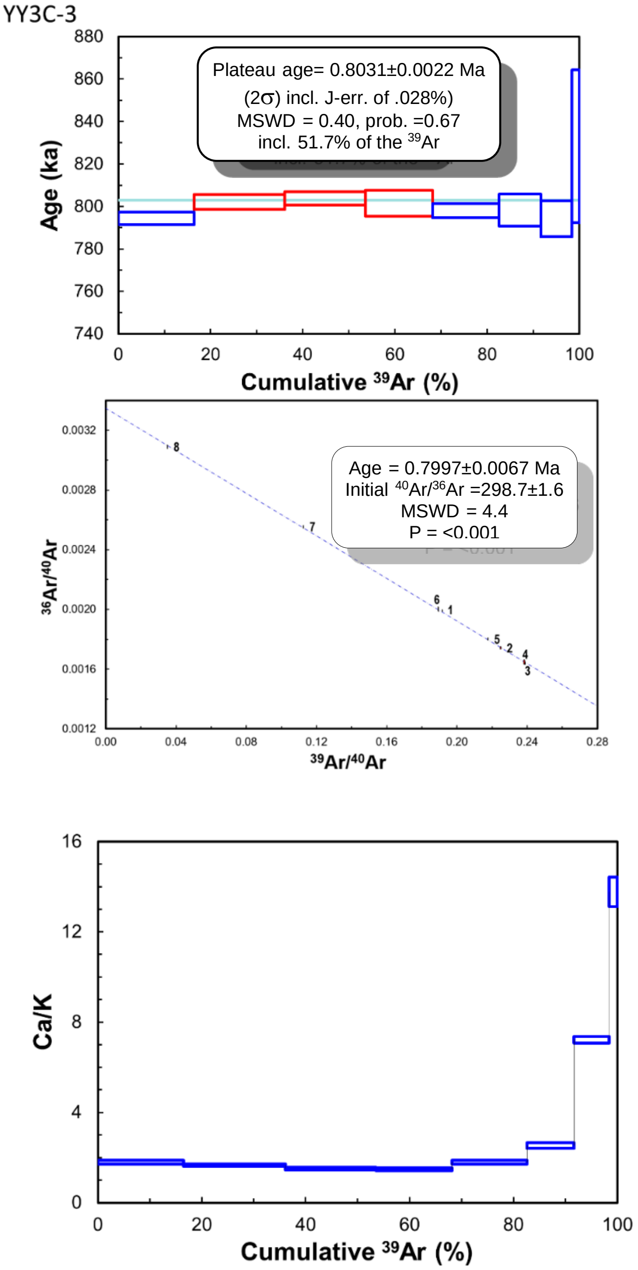

Figure A.24: ^{40}Ar/^{39}Ar age spectrum, inverse isochron and Ca/K plot of aliquant YY3C-3.

Sample YY6

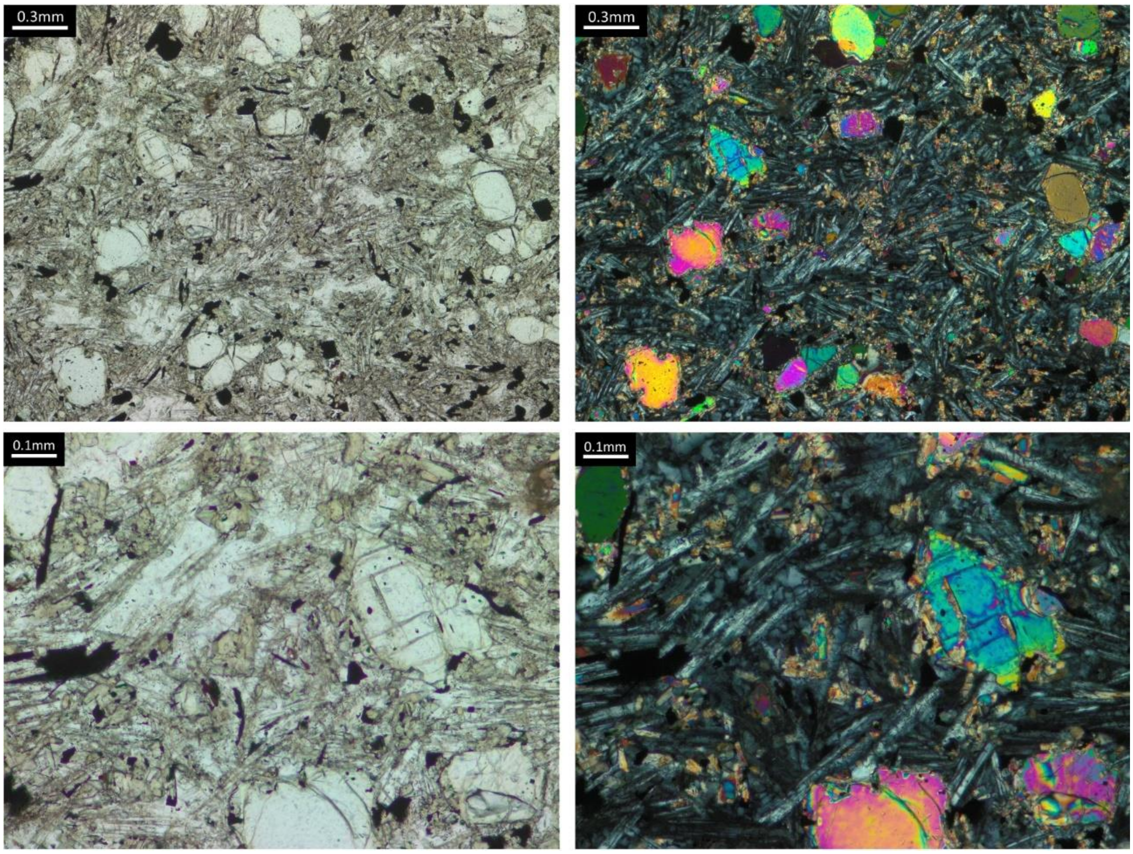

Figure A.25: Transmitted light photomicrographs of sample YY6.

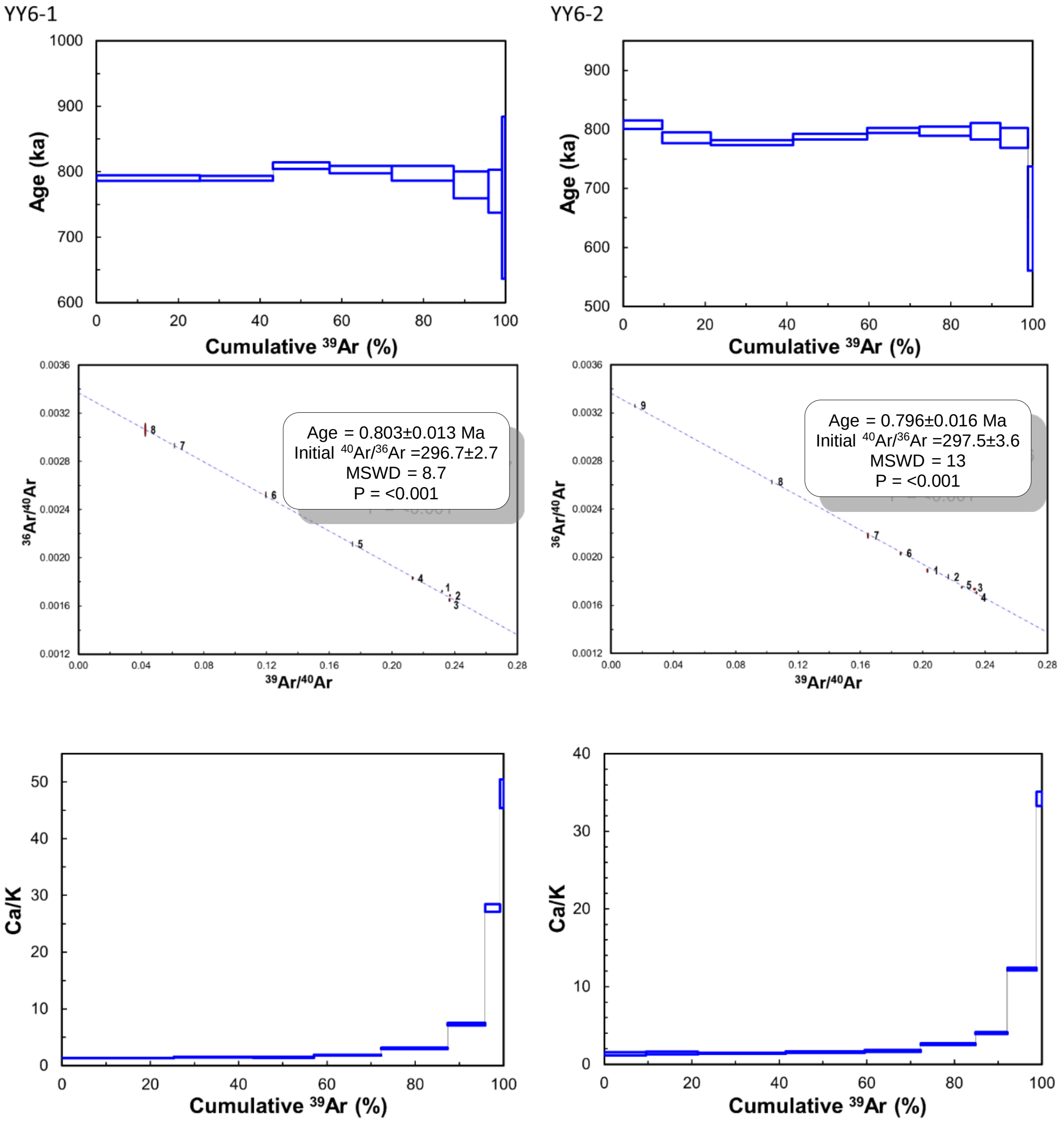

Figure A.26: ^{40}Ar/^{39}Ar age spectra, inverse isochrons and Ca/K plots of aliquants YY6-1 and YY6-2.

A.1b. Tulloch Hill Flow (Flow B)

Sample BH45B

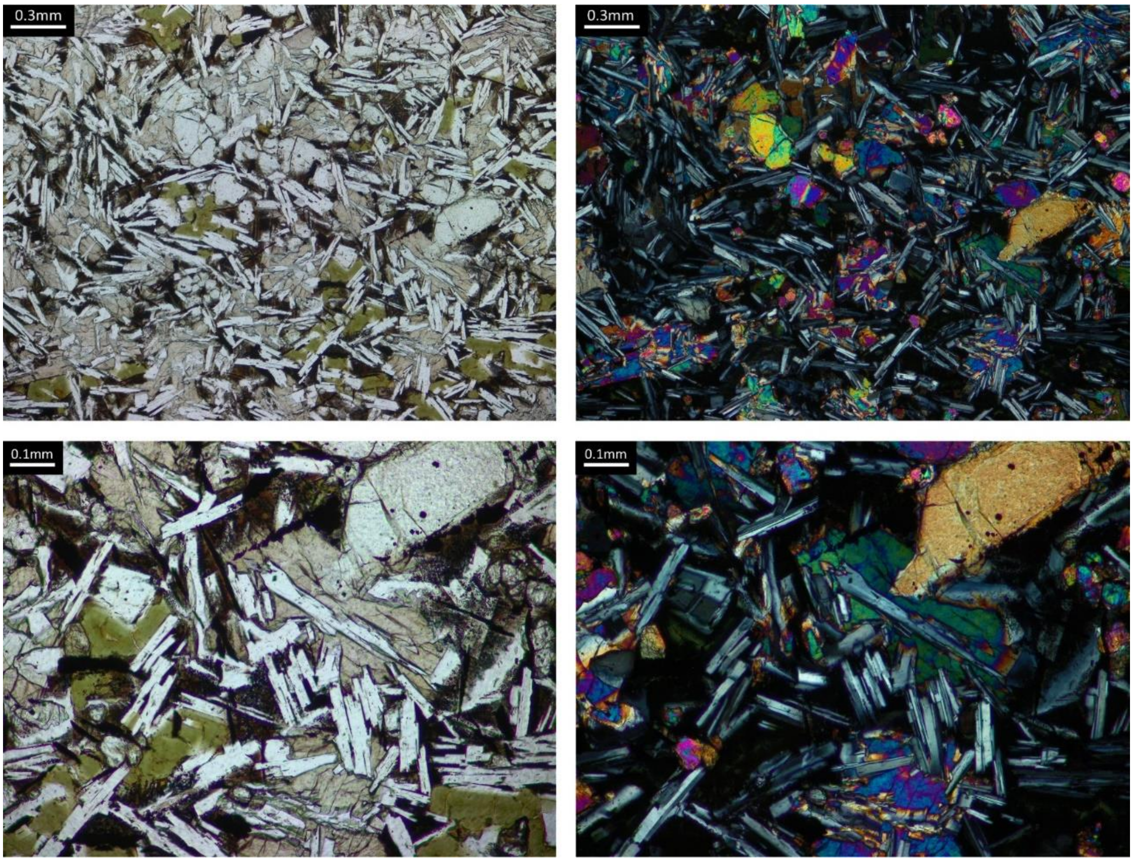

Figure A.27: Transmitted light photomicrographs of sample BH45B.

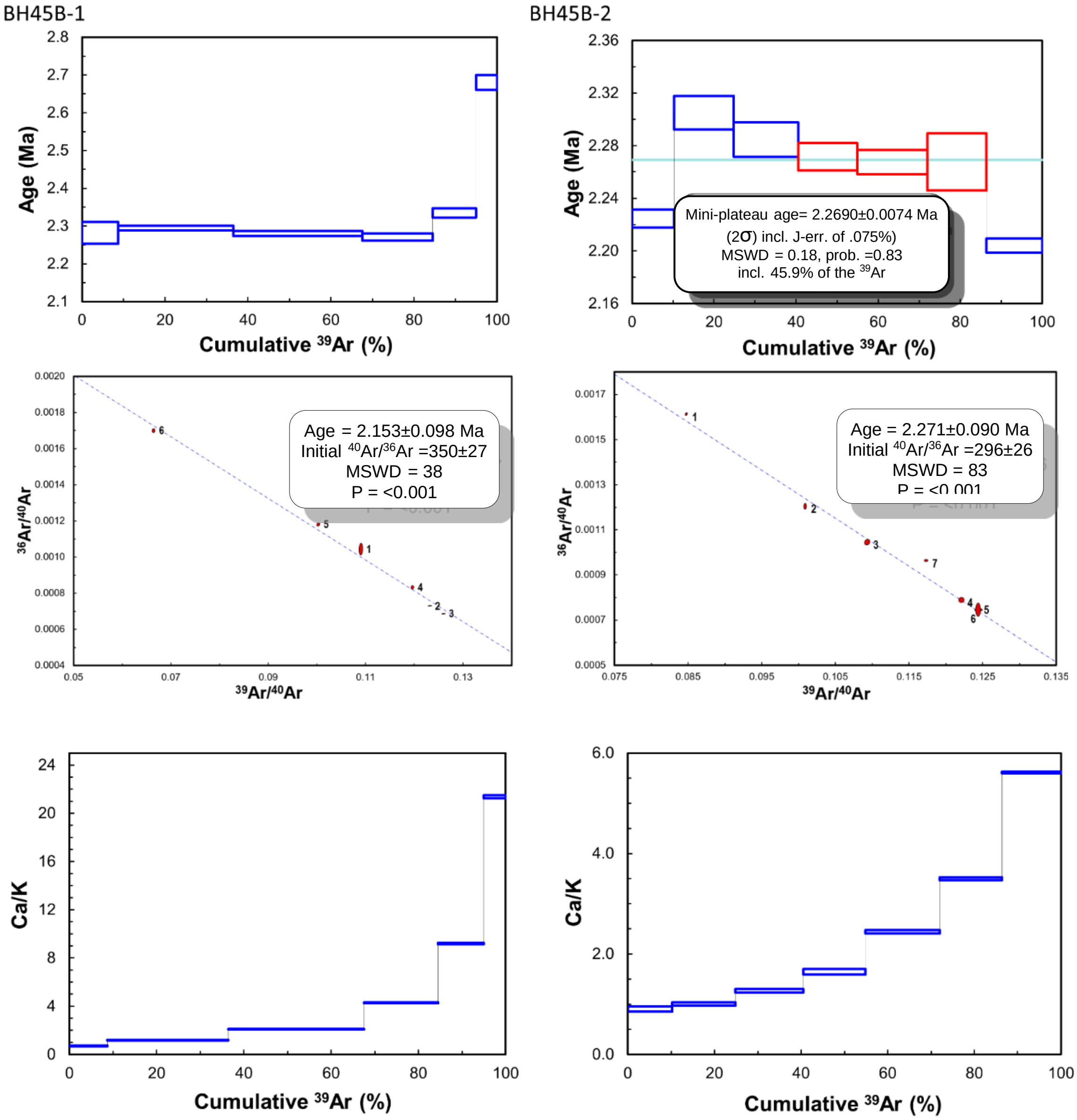

Figure A.28: ^{40}Ar/^{39}Ar age spectra, inverse isochrons and Ca/K plots of aliquants BH45B-1 and BH45B-2.

Sample GRBH-01

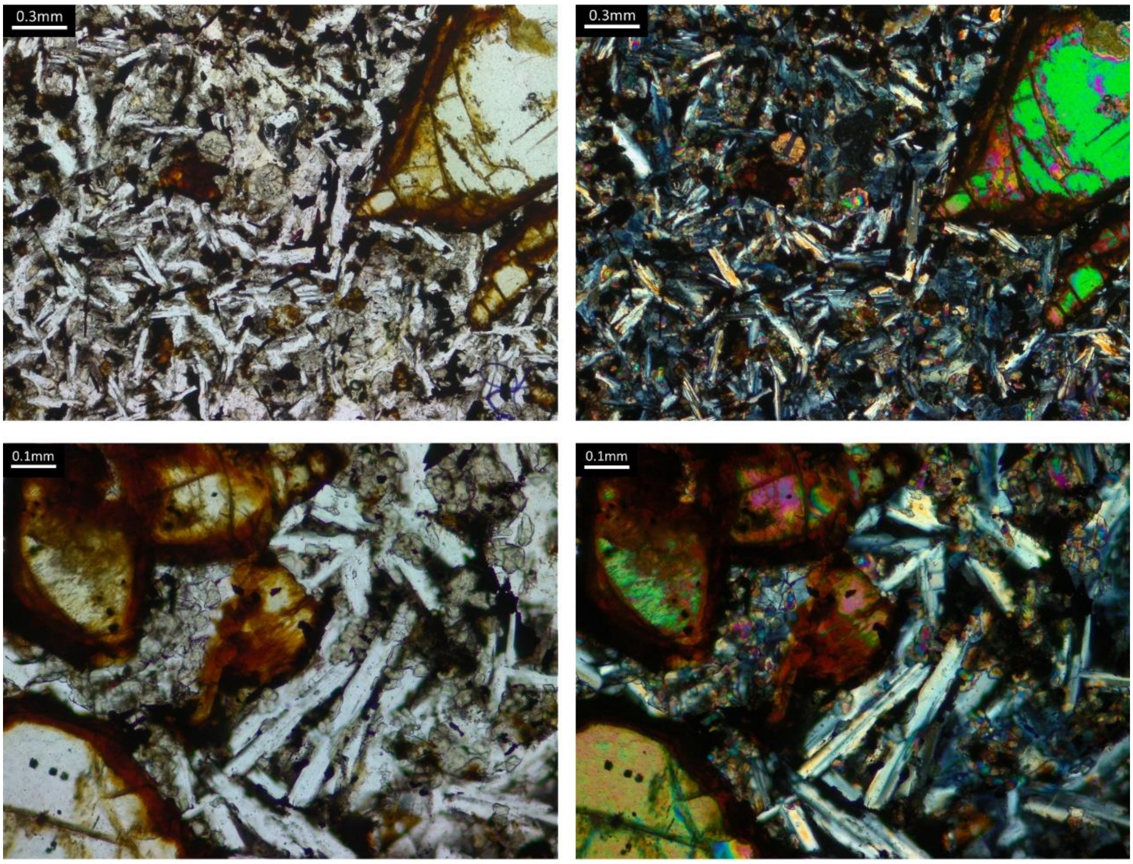

Figure A.29: Transmitted light photomicrographs of sample GRBH-01.

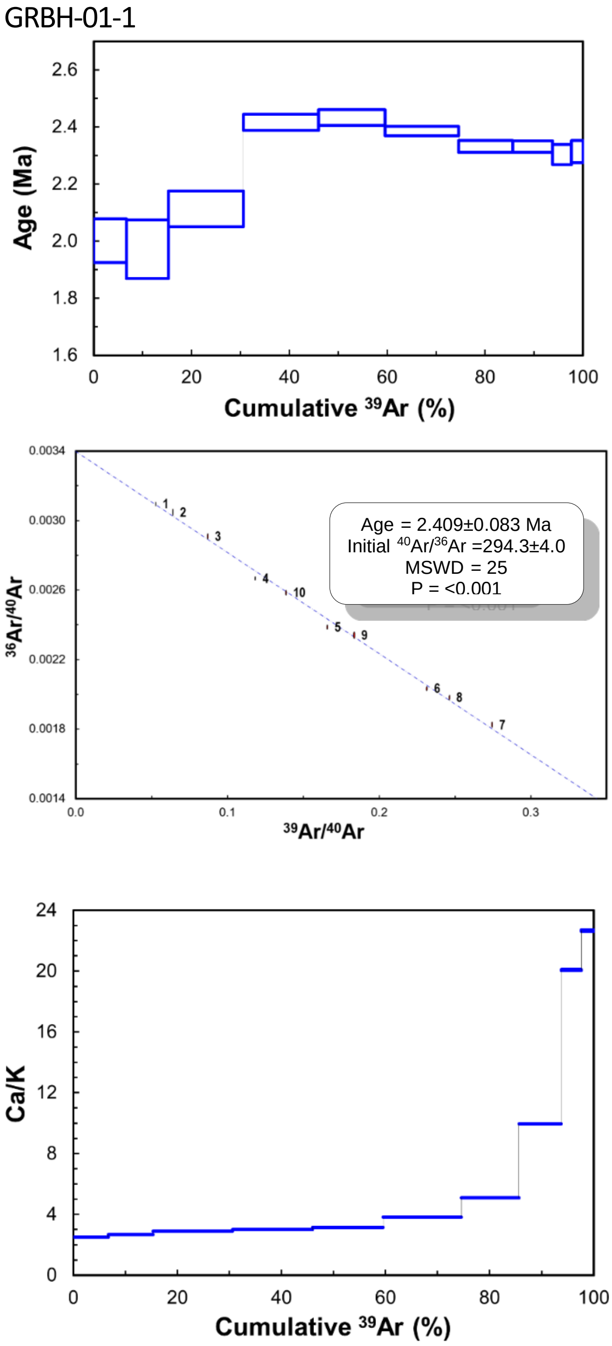

Age = 2.409±0.083 Ma
Initial $^{40}Ar/^{36}Ar$ =294.3±4.0
MSWD = 25
P = <0.001

Figure A.30: $^{40}Ar/^{39}Ar$ age spectrum, inverse isochron and Ca/K plot of aliquant GRBH-01-1.

Sample KA7

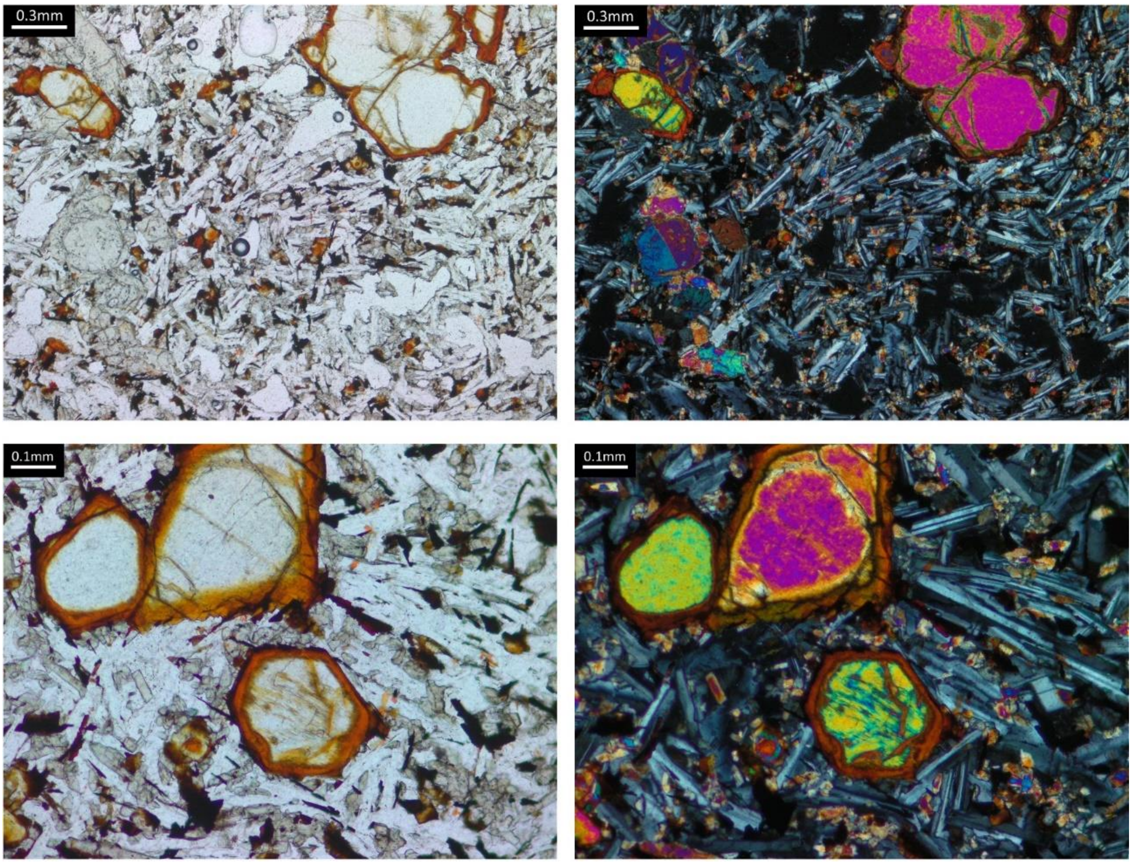

Figure A.31: Transmitted light photomicrographs of sample KA7.

KA7-1

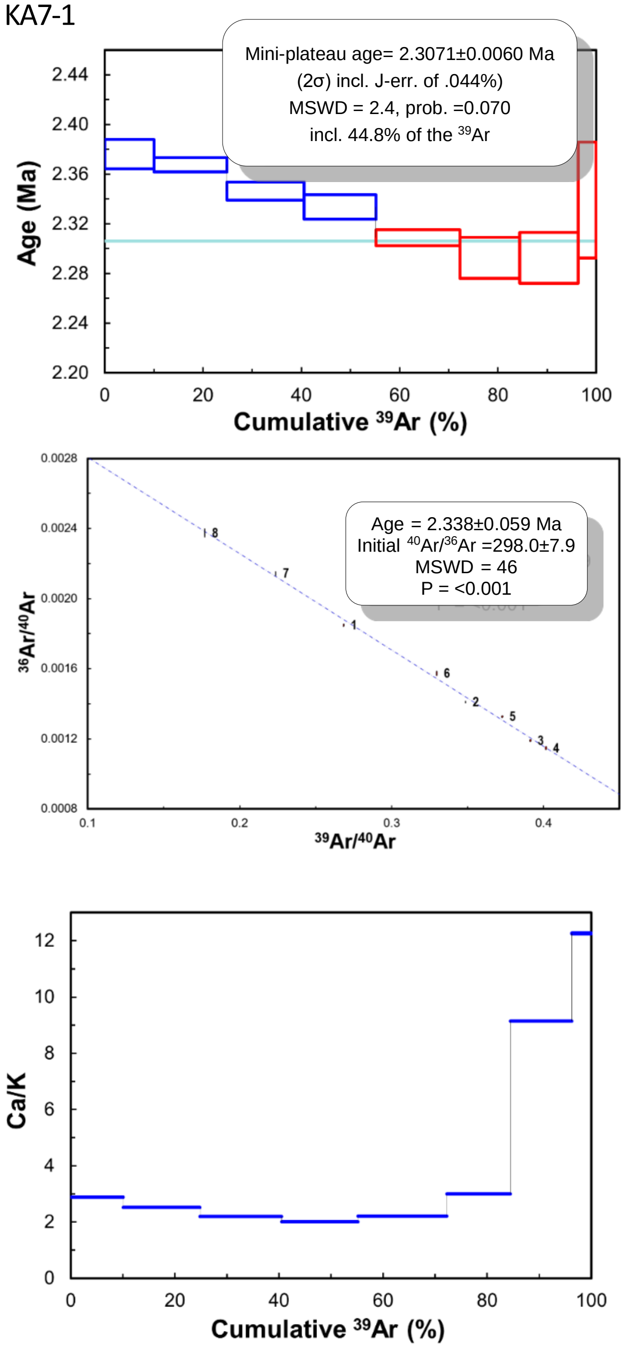

Figure A.32: ^{40}Ar/^{39}Ar age spectrum, inverse isochron and Ca/K plot of aliquant KA7-1.

Sample KA13B

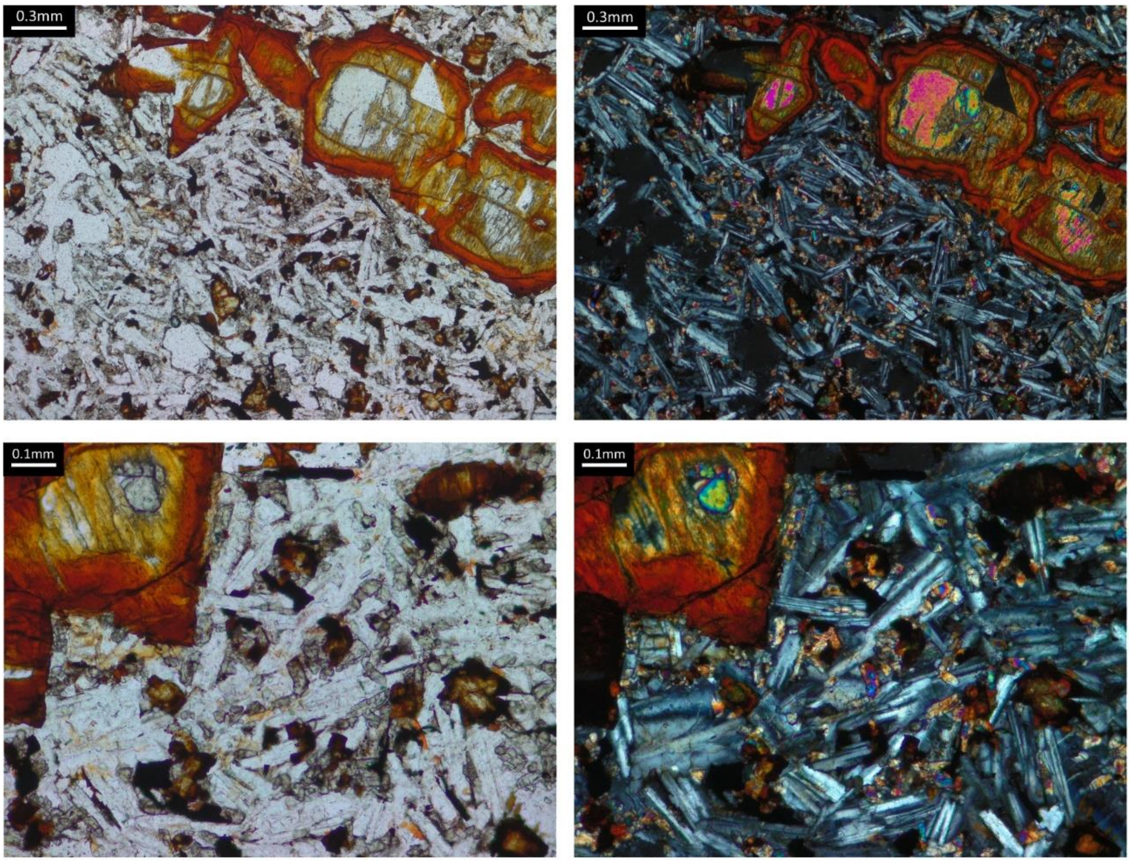

Figure A.33: Transmitted light photomicrographs of sample KA13B.

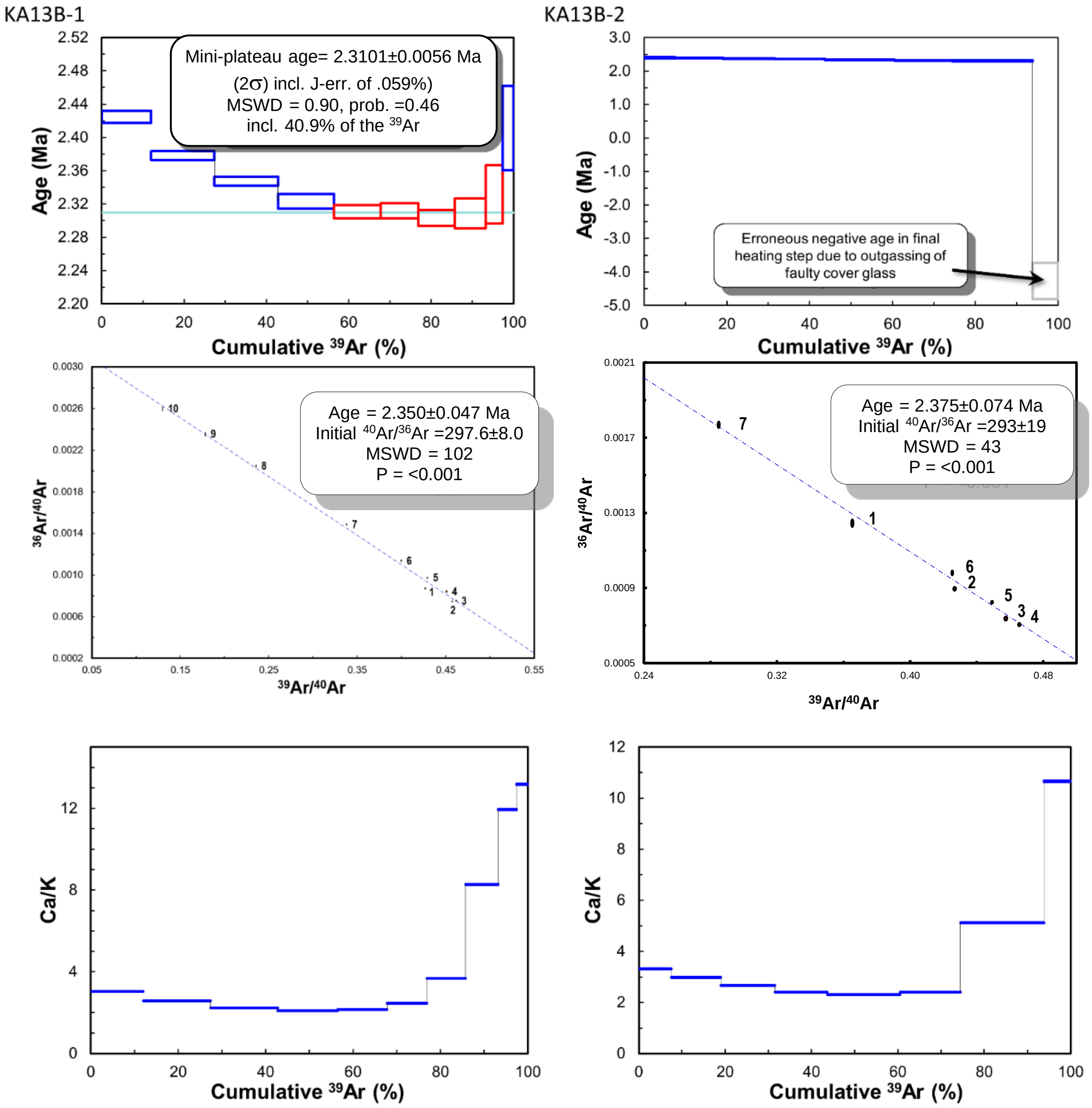

Figure A.34: ^{40}Ar/^{39}Ar age spectra, inverse isochrons and Ca/K plots of aliquants KA13B-1 and KA13B-2.

Sample MH49

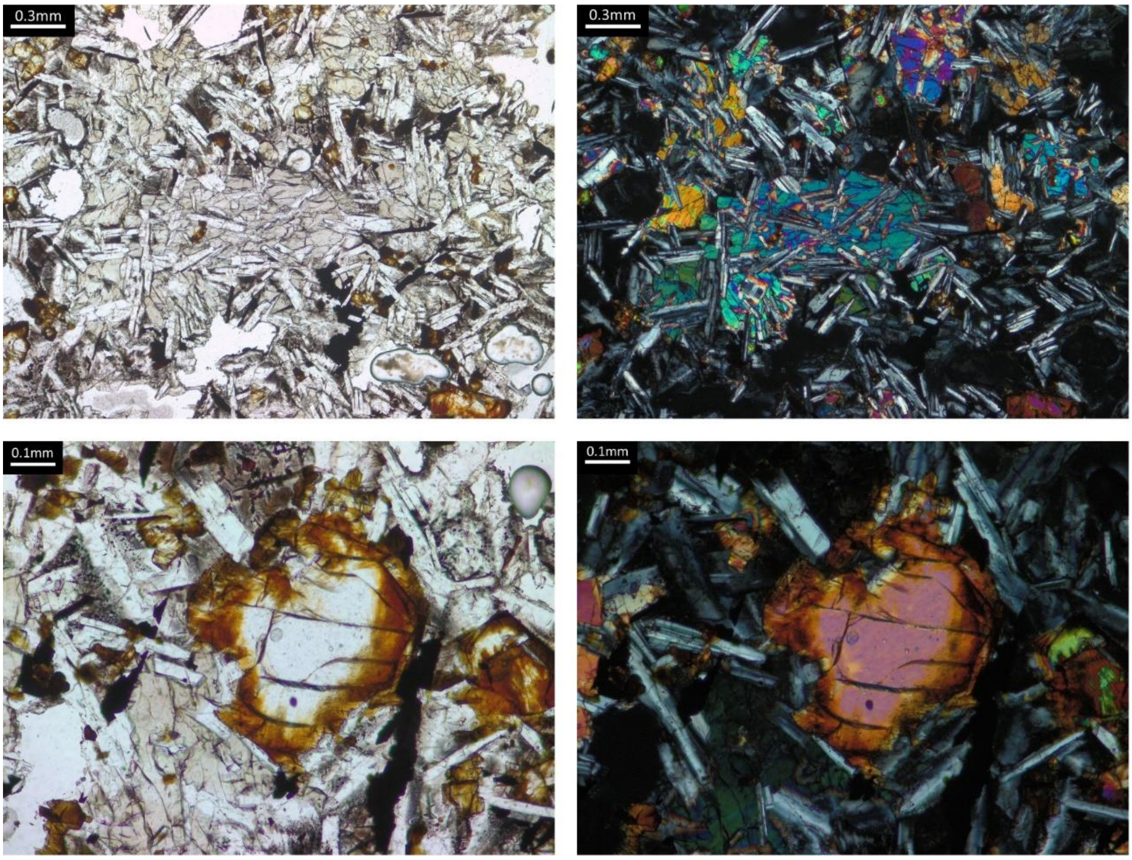

Figure A.35: Transmitted light photomicrographs of sample WW1A.

MH49-1

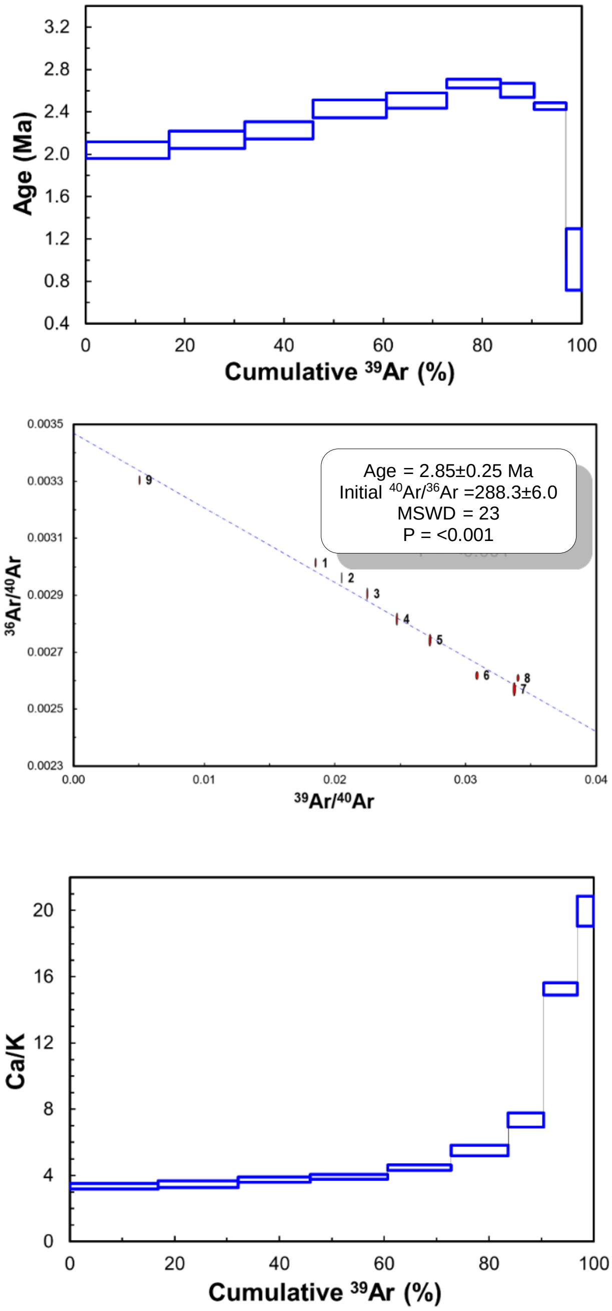

Figure A.36: ^{40}Ar/^{39}Ar age spectrum, inverse isochron and Ca/K plot of aliquant MH49-1.

Sample MH52

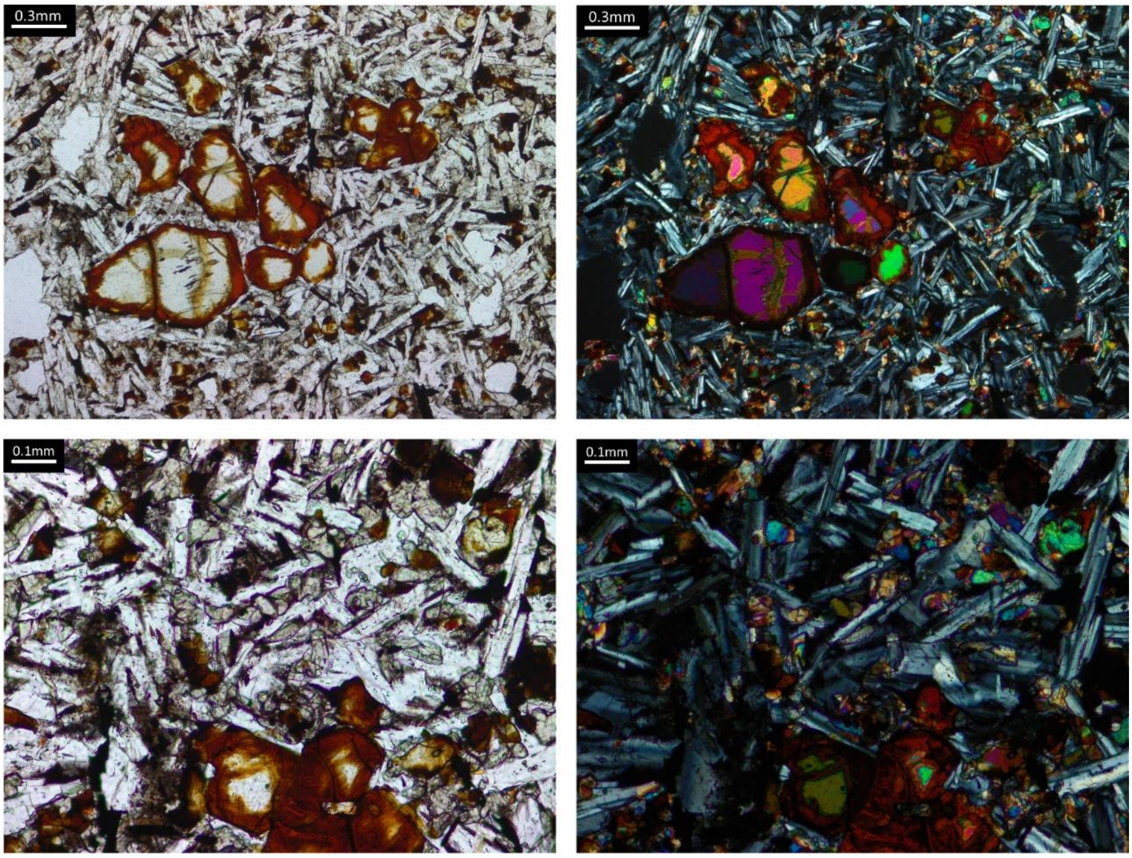

Figure A.37: Transmitted light photomicrographs of sample MH52.

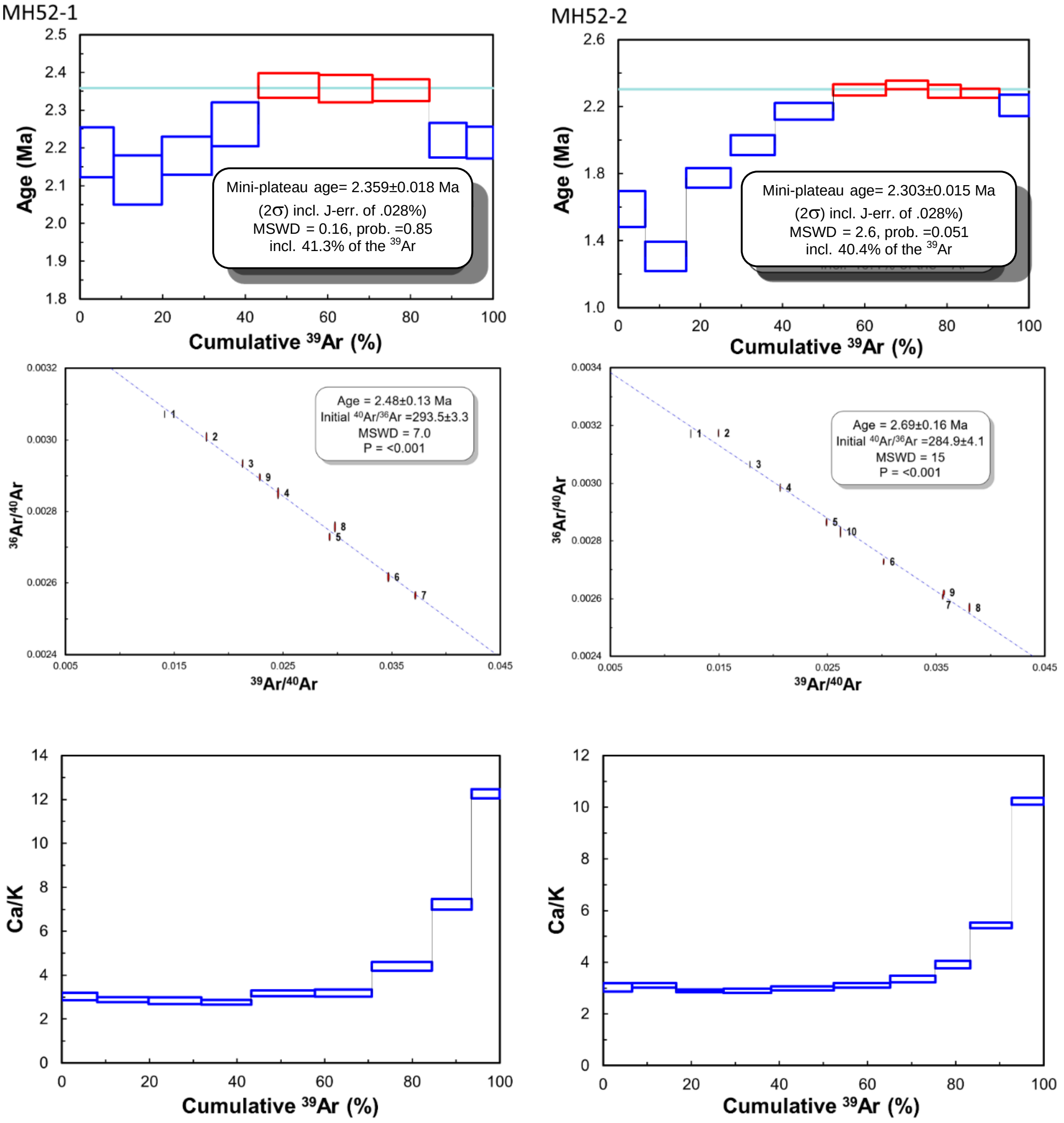

Figure A.38: ^{40}Ar/^{39}Ar age spectra, inverse isochrons and Ca/K plots of aliquants MH52-1 and MH52-2.

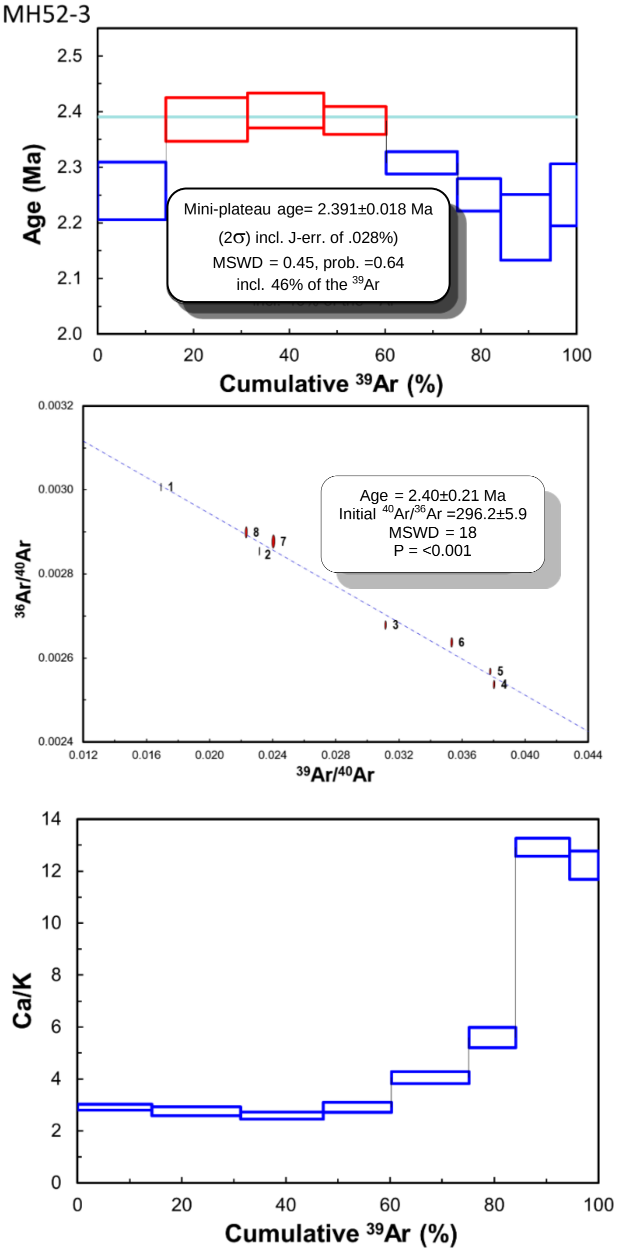

Figure A.39: ${}^{40}Ar/{}^{39}Ar$ age spectrum, inverse isochron and Ca/K plot of aliquant MH52-3.

Sample MH69

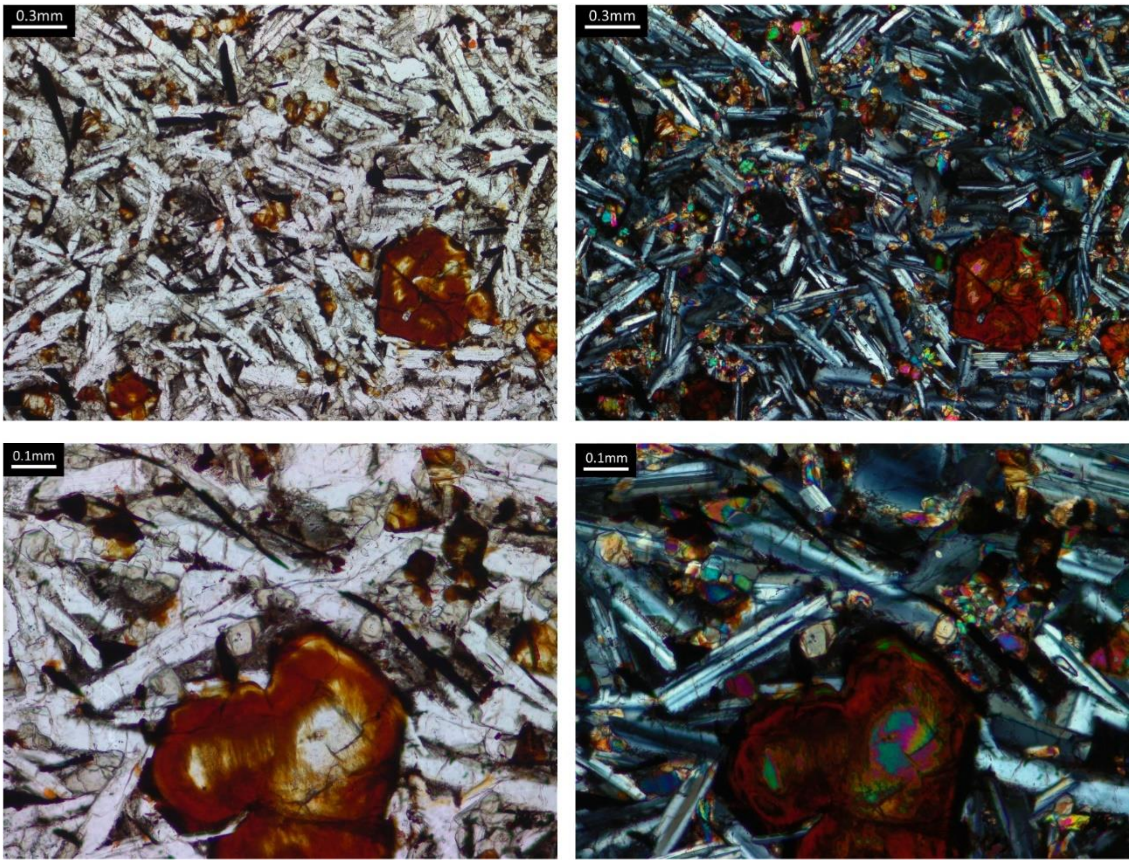

Figure A.40: Transmitted light photomicrographs of sample MH69.

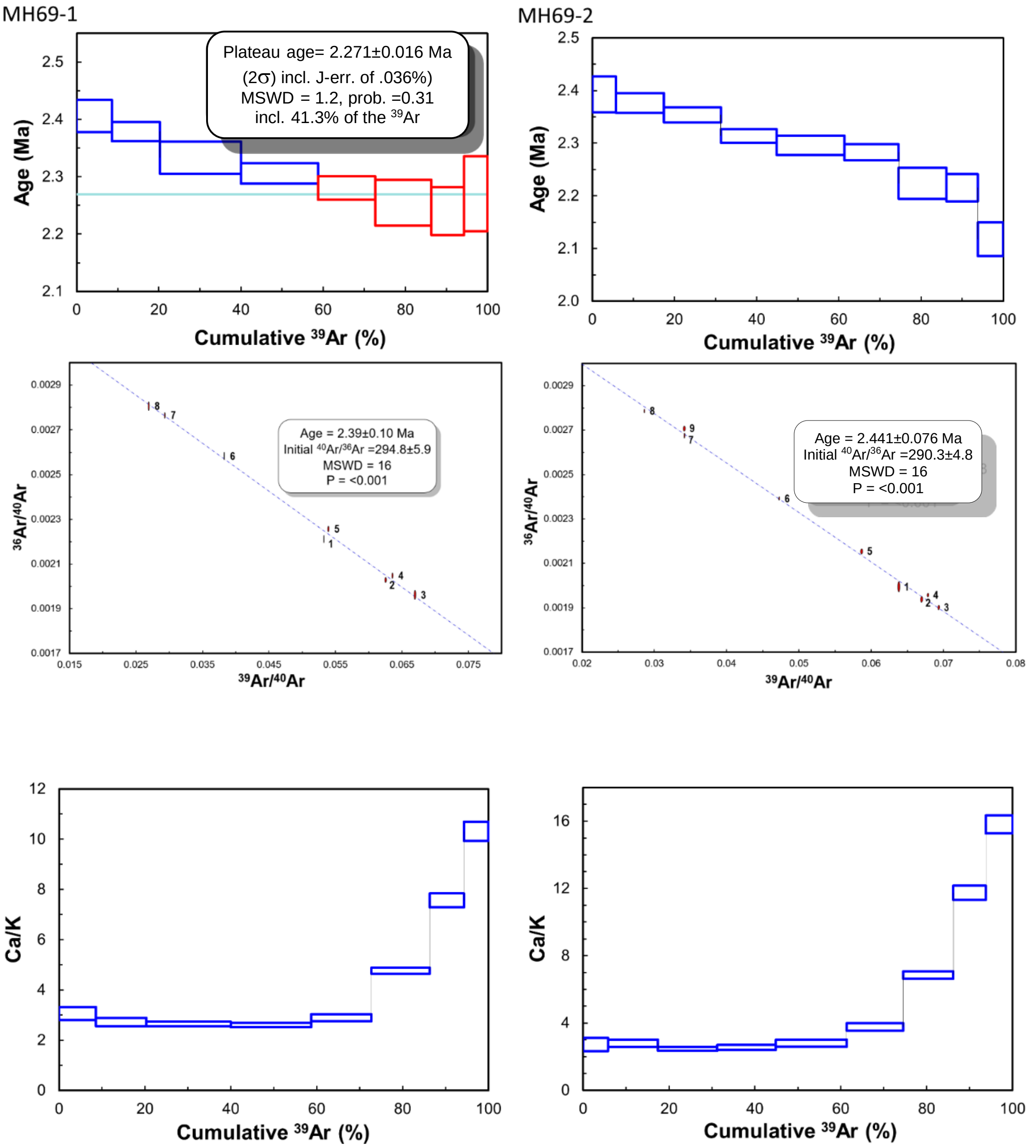

Figure A.41: ^{40}Ar/^{39}Ar age spectra, inverse isochrons and Ca/K plots of aliquants MH69-1 and MH69-2.

Sample WO4

Figure A.42: Transmitted light photomicrographs of sample WO4.

WO4-1

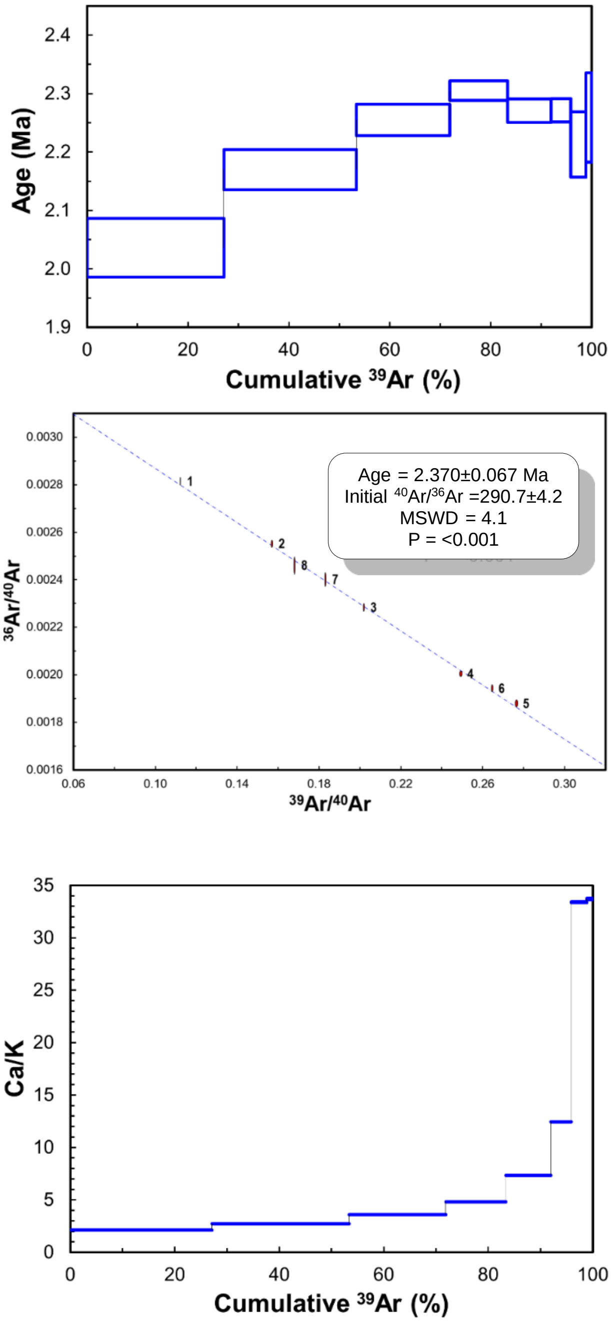

Figure A.43: ^{40}Ar/^{39}Ar age spectrum, inverse isochron and Ca/K plot of aliquant WO4-1.

Appendix A.2. Micrographs, age spectra, inverse isochrons and Ca/K plots of samples selected for $^{40}Ar/^{39}Ar$ dating from the Aitken Hill, Bald Hill, Crowe Hill, Fenton Hill, Mount Kororoit, Mount Ridley, Redstone Hill, Springs Hill, Summerhill Road and Tullamarine flows. Spectra, isochrons and Ca/K plots generated using the ISOPLOT software package (Ludwig, 2012). Box heights of age spectra and Ca/K plots are 2σ errors

A.2a. Aitken Hill Flow

Sample MH35

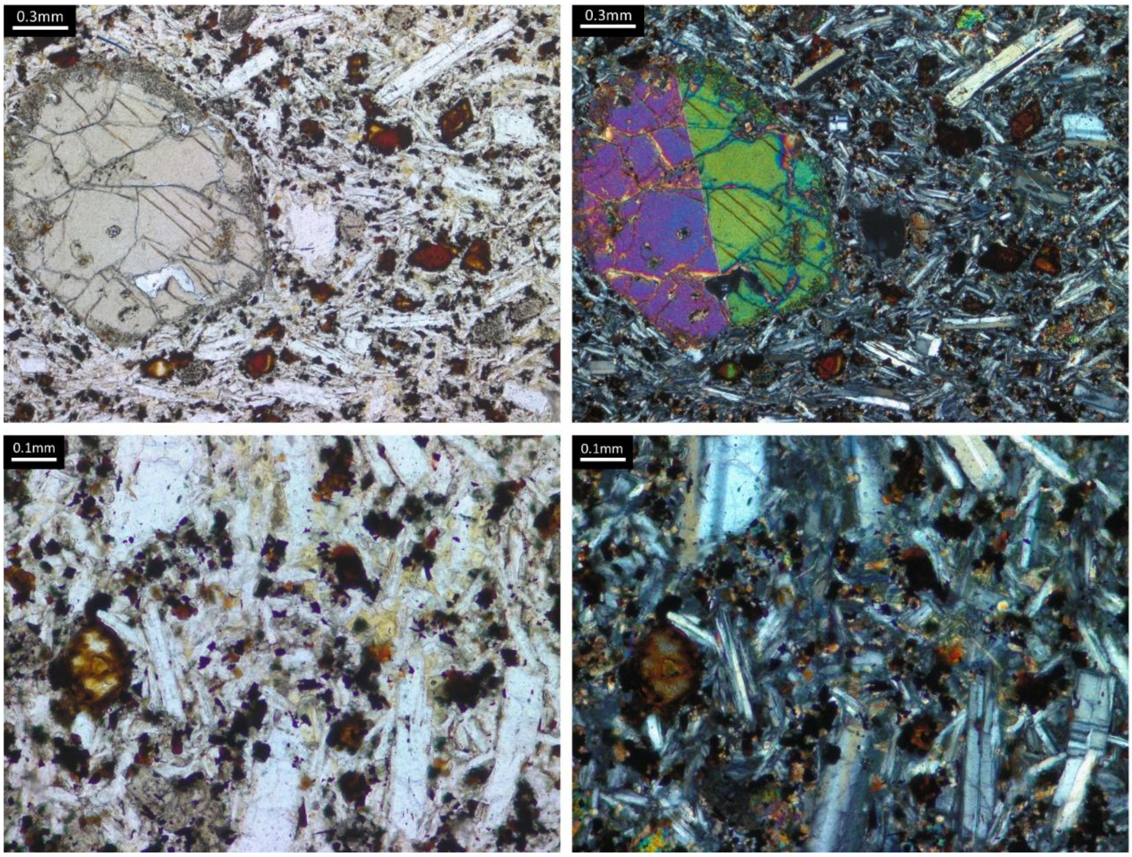

Figure A.44: Transmitted light photomicrographs of sample MH35.

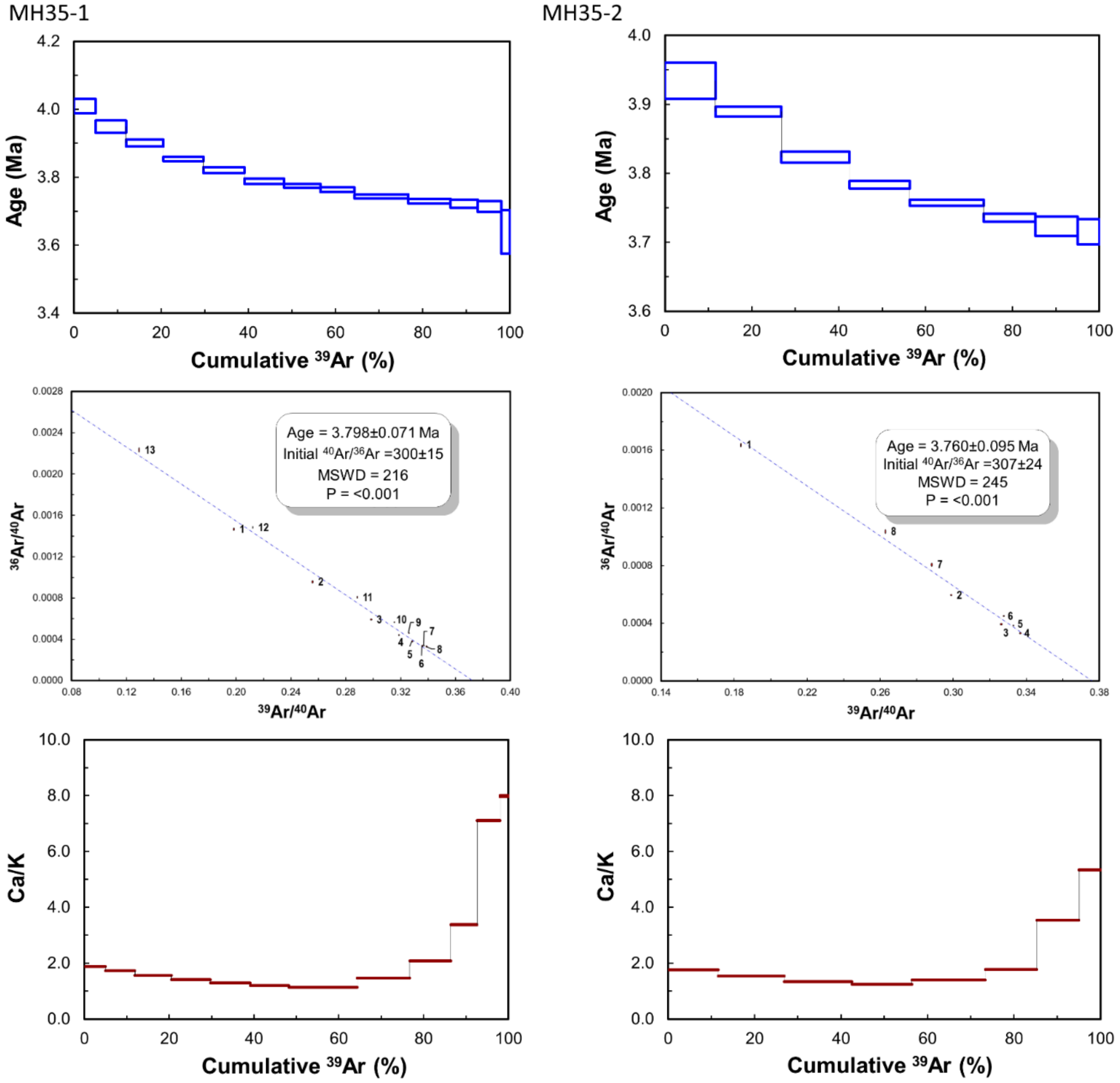

Figure A.45: $^{40}Ar/^{39}Ar$ age spectra, inverse isochrons and Ca/K plots of aliquants MH35-1 and MH35-2

A.2b. Bald Hill Flow

Sample BA01

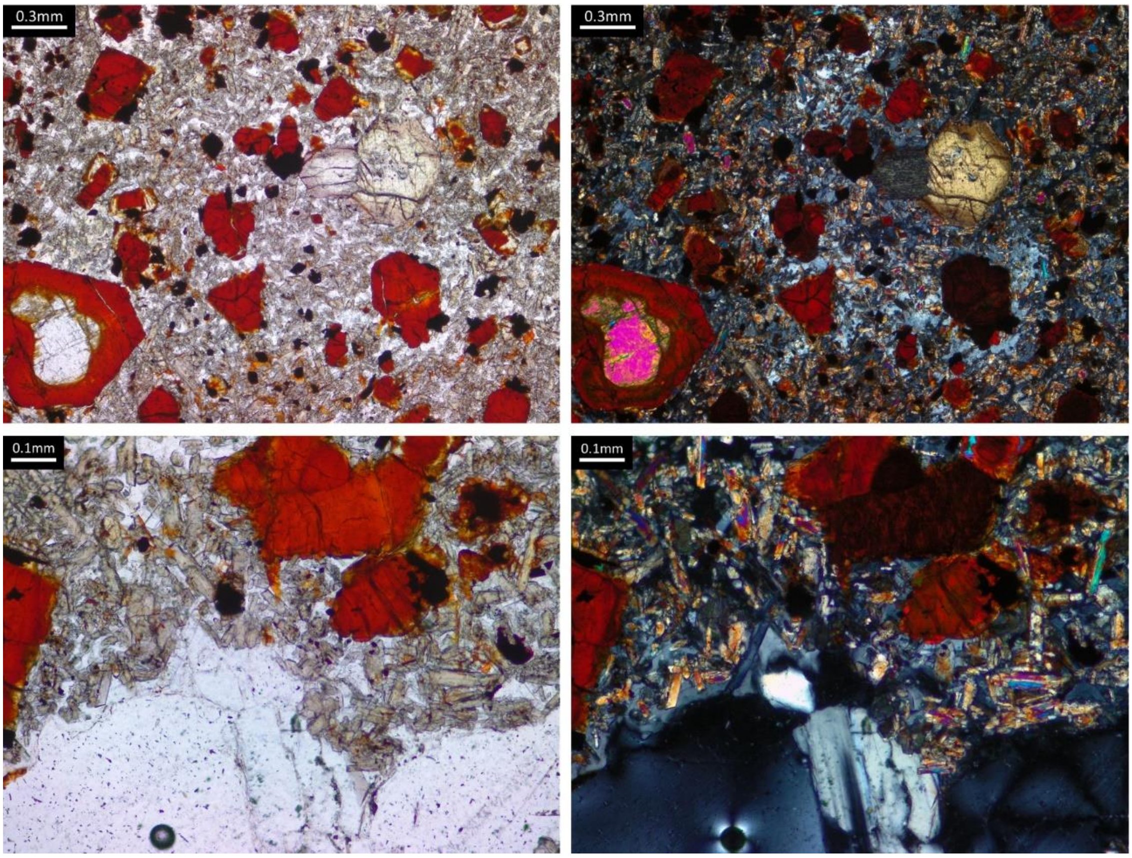

Figure A.46: Transmitted light photomicrographs of sample BA01.

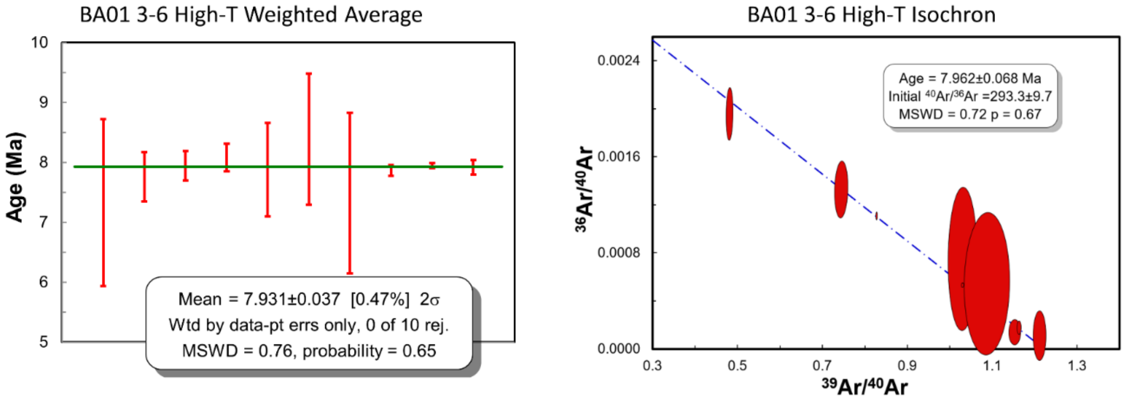

Figure A.47: High-T steps weighted average plot and high-T steps inverse isochron for aliquants BA01-3 to BA01-6 inclusive.

A.2c. Crowe Hill Flow

Sample MH68

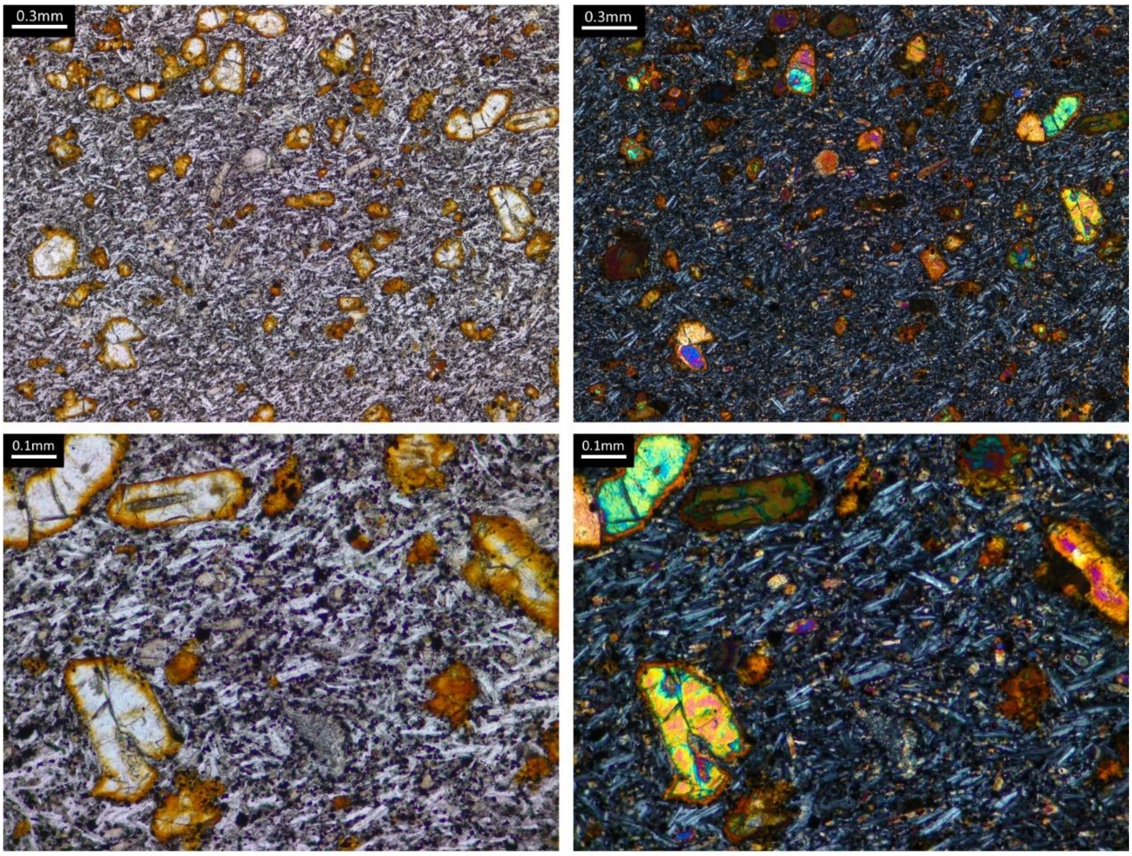

Figure A.48: Transmitted light photomicrographs of sample MH68.

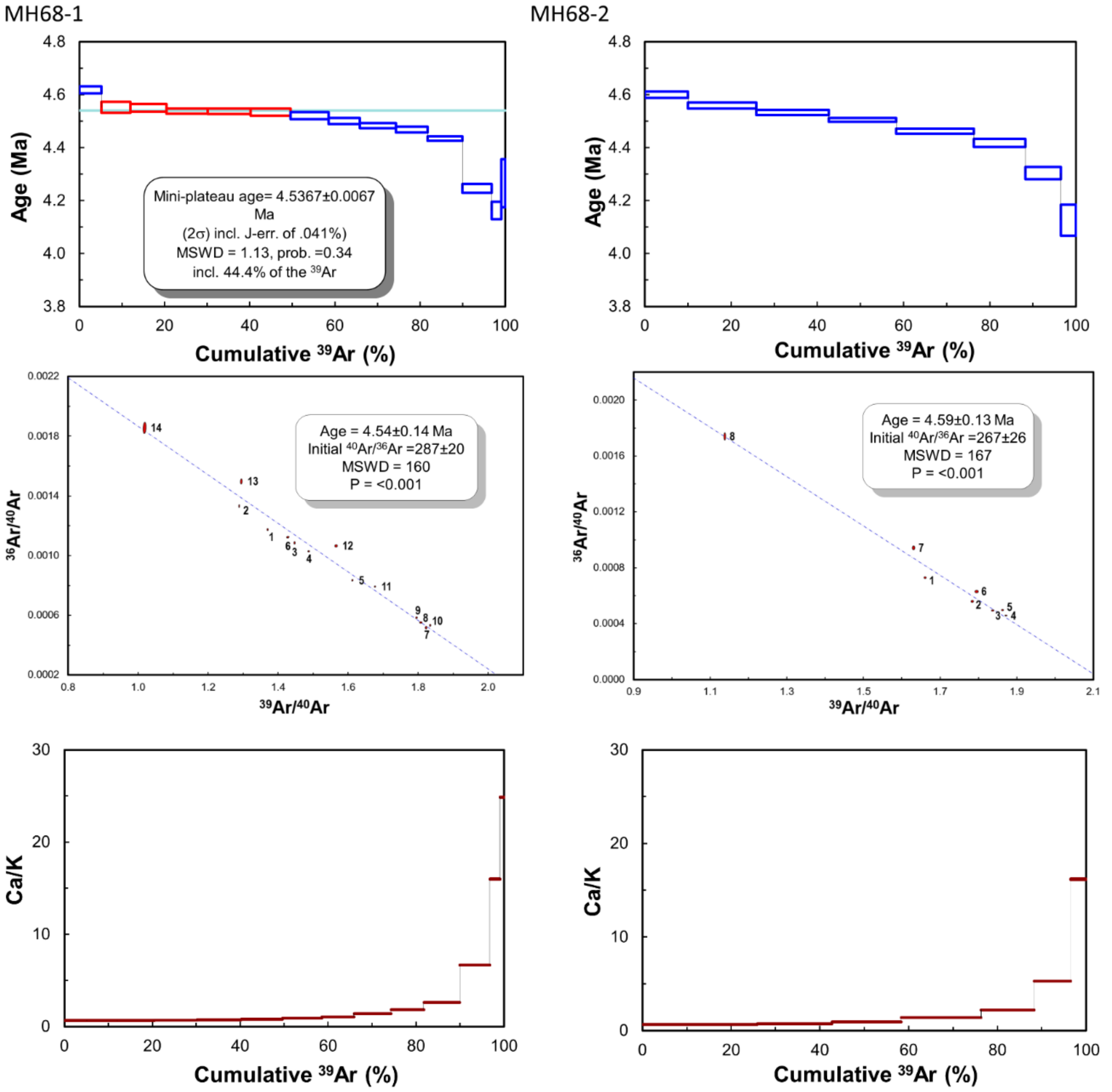

Figure A.49: ^{40}Ar/^{39}Ar age spectra, inverse isochrons and Ca/K plots of aliquants MH68-1 and MH68-2

A.2d. Fenton Hill Flow

Sample MH10

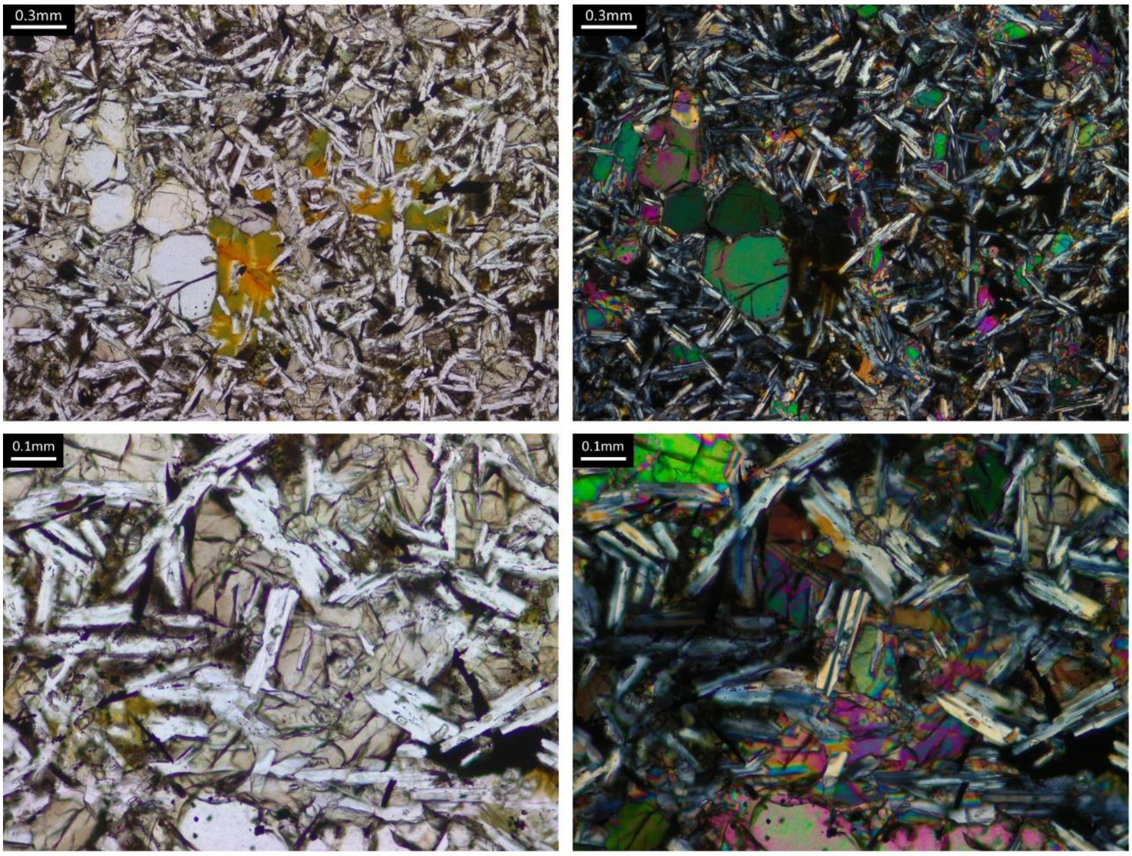

Figure A.50: Transmitted light photomicrographs of sample MH10.

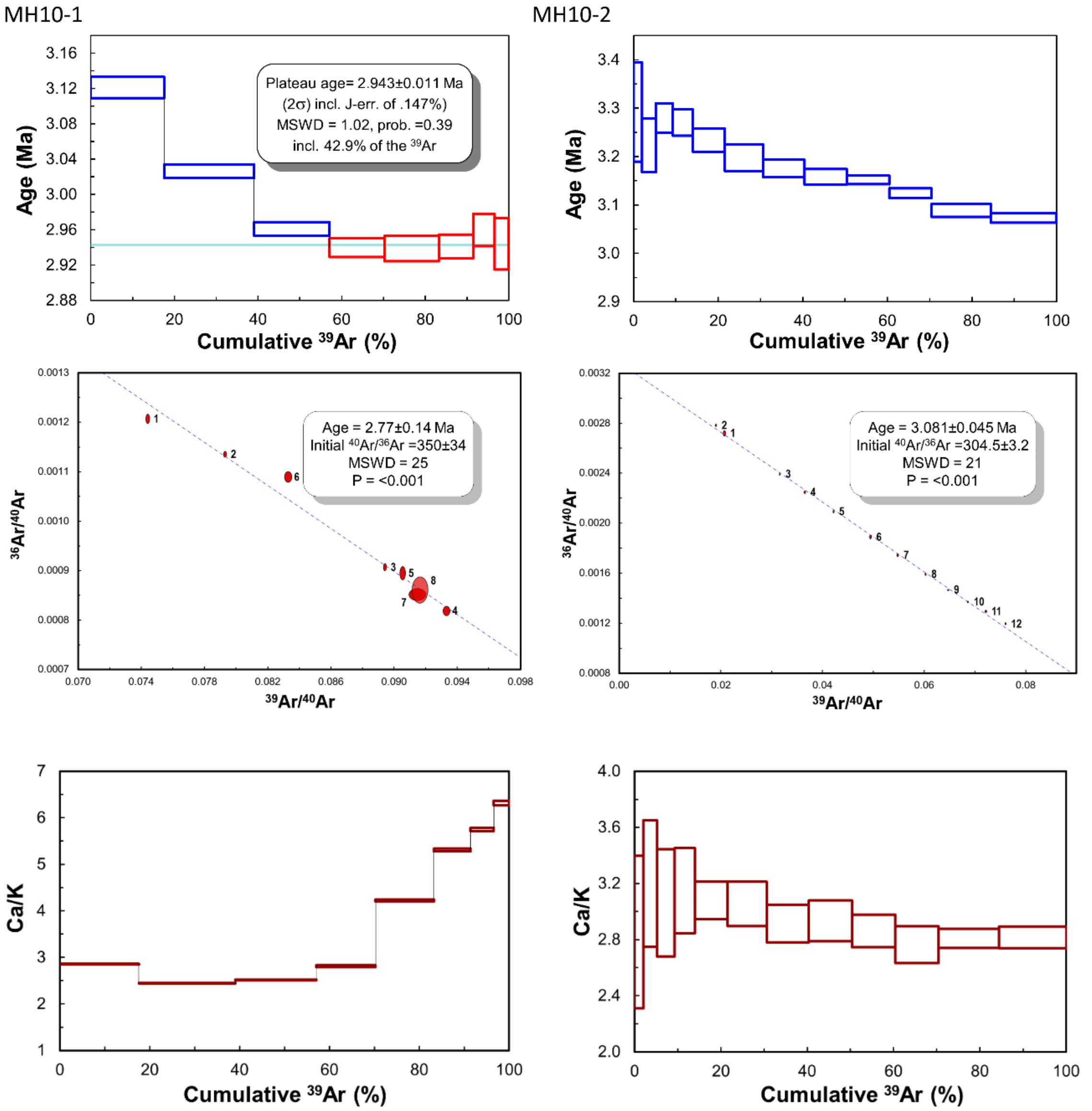

Figure A.51: ^{40}Ar/^{39}Ar age spectra, inverse isochrons and Ca/K plots of aliquants MH10-1 and MH10-2

A.2e. Mount Kororoit Flow

Sample BH47B

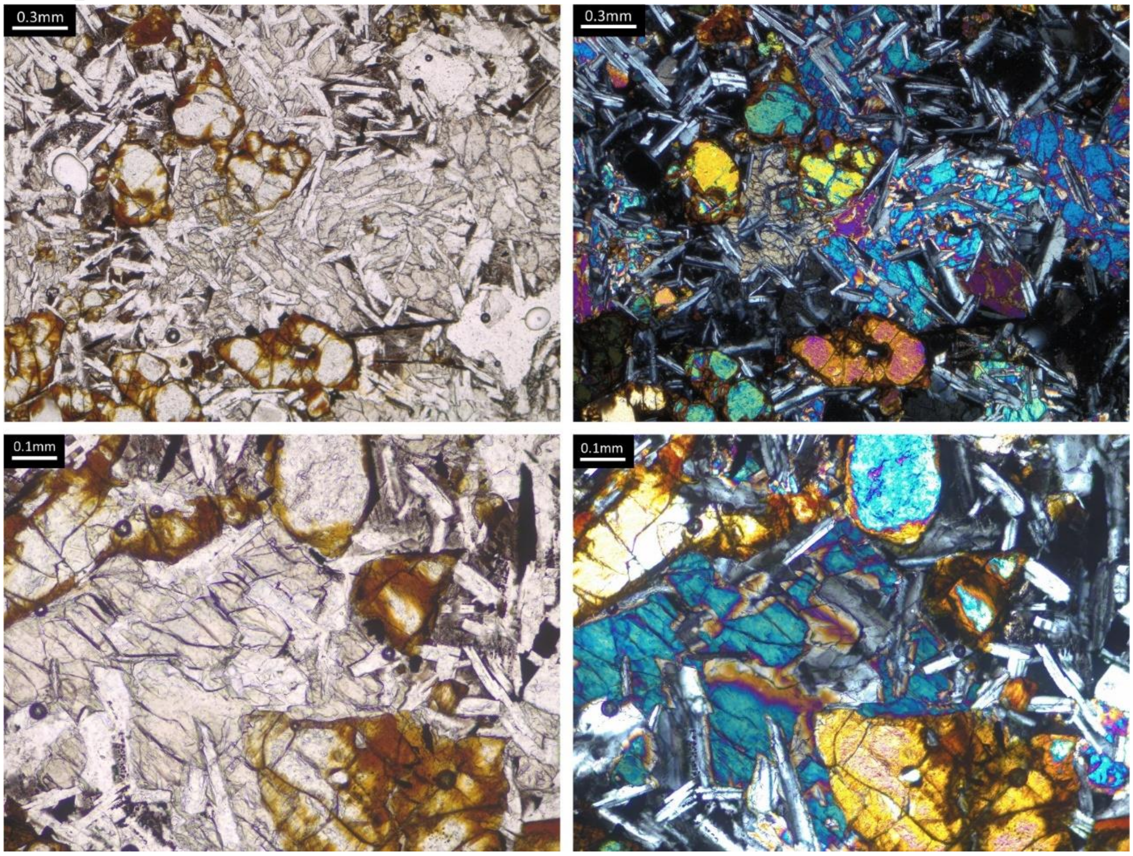

Figure A.52: Transmitted light photomicrographs of sample BH47B.

BH47B-1

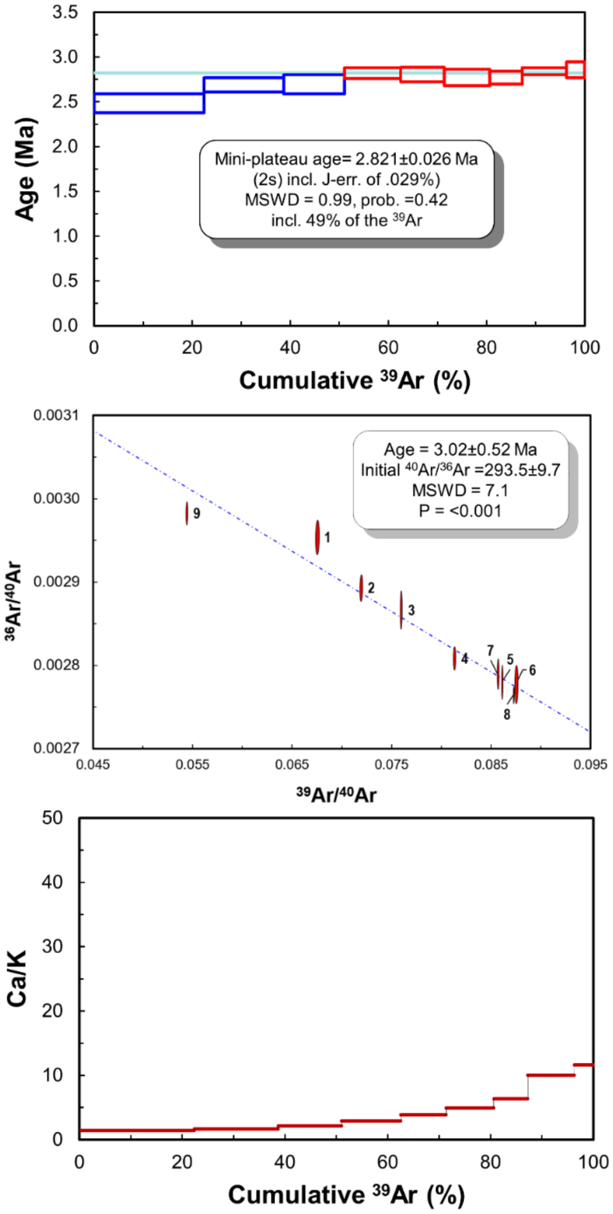

Figure A.53: ^{40}Ar/^{39}Ar age spectrum, inverse isochron and Ca/K plot of aliquant BH47B-1.

Sample BH269

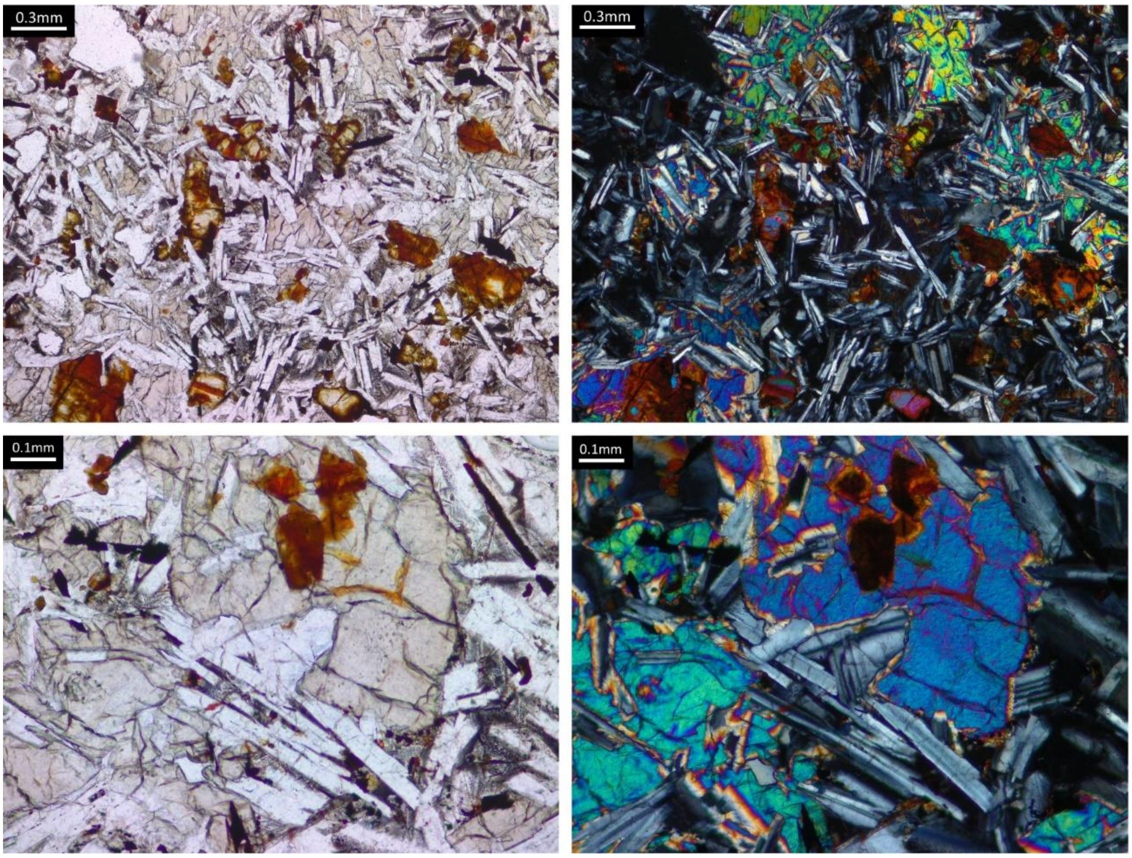

Figure A.54: Transmitted light photomicrographs of sample BH269.

BH269-1

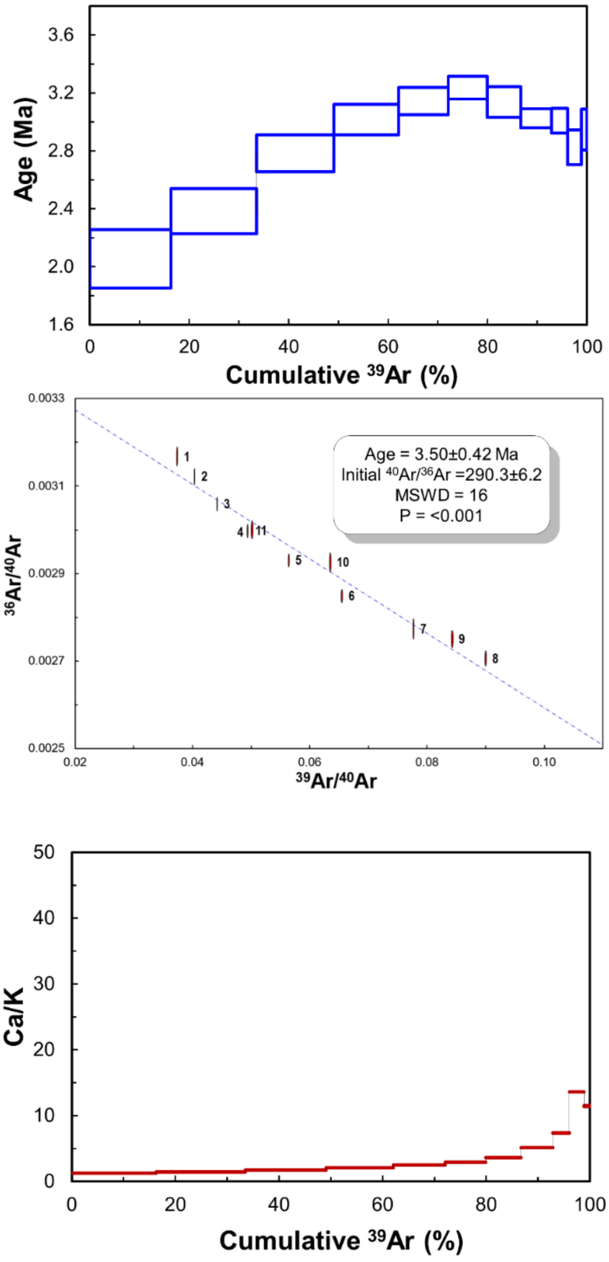

Figure A.55: ^{40}Ar/^{39}Ar age spectrum, inverse isochron and Ca/K plot of aliquant BH269-1.

Sample MH01N

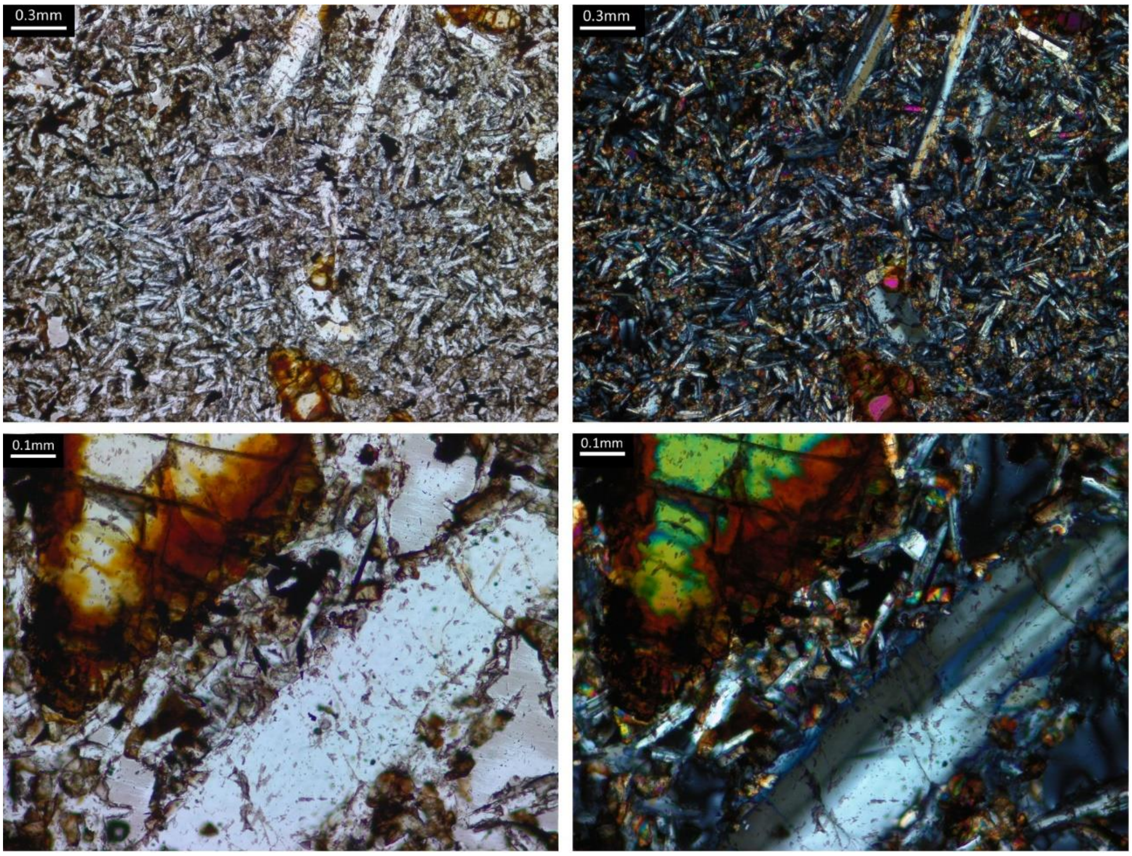

Figure A.56: Transmitted light photomicrographs of sample MH01N.

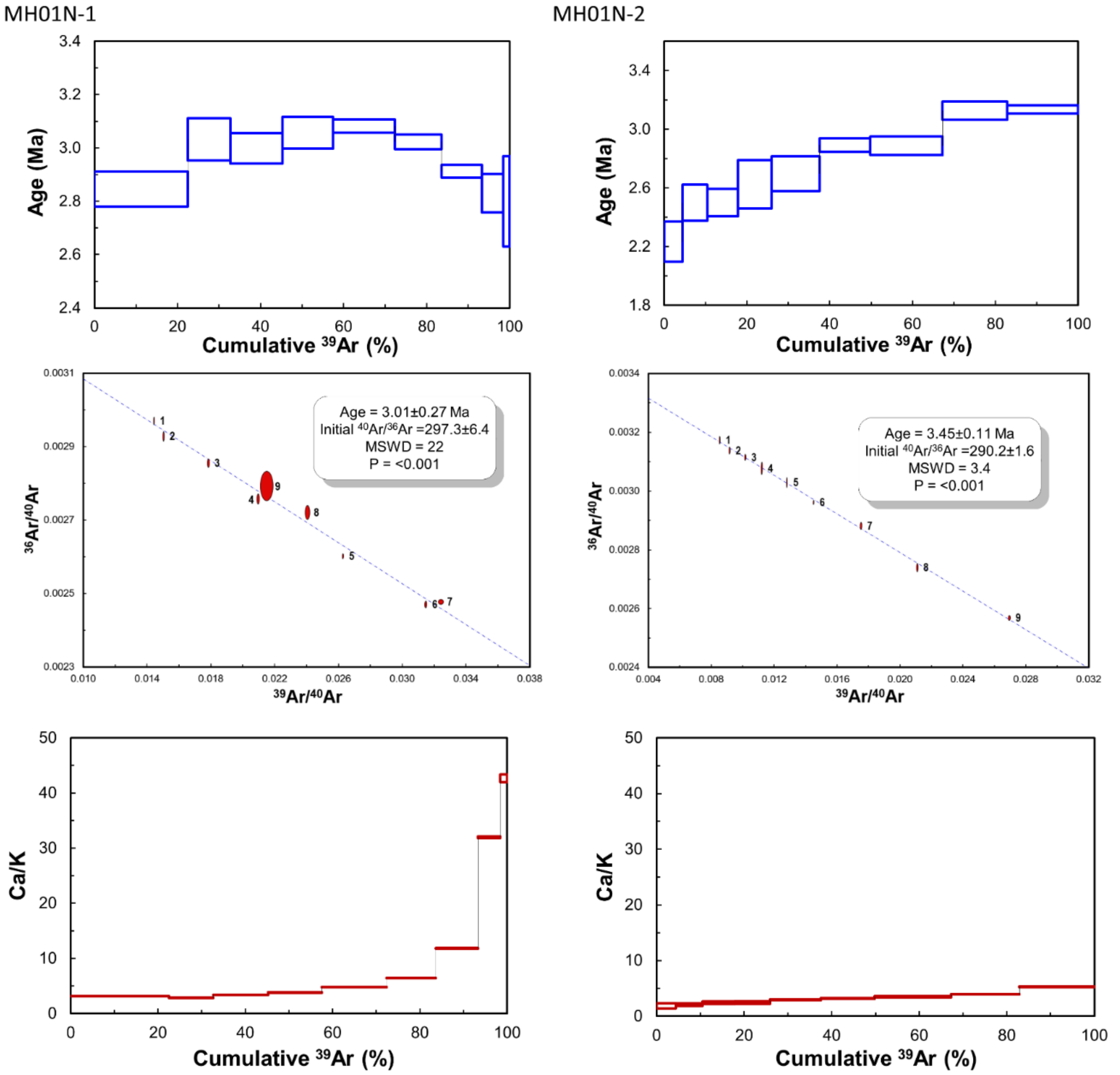

Figure A.57: ^{40}Ar/^{39}Ar age spectra, inverse isochrons and Ca/K plots of aliquants MH01N-1 and MH01N-2

Sample MH01S

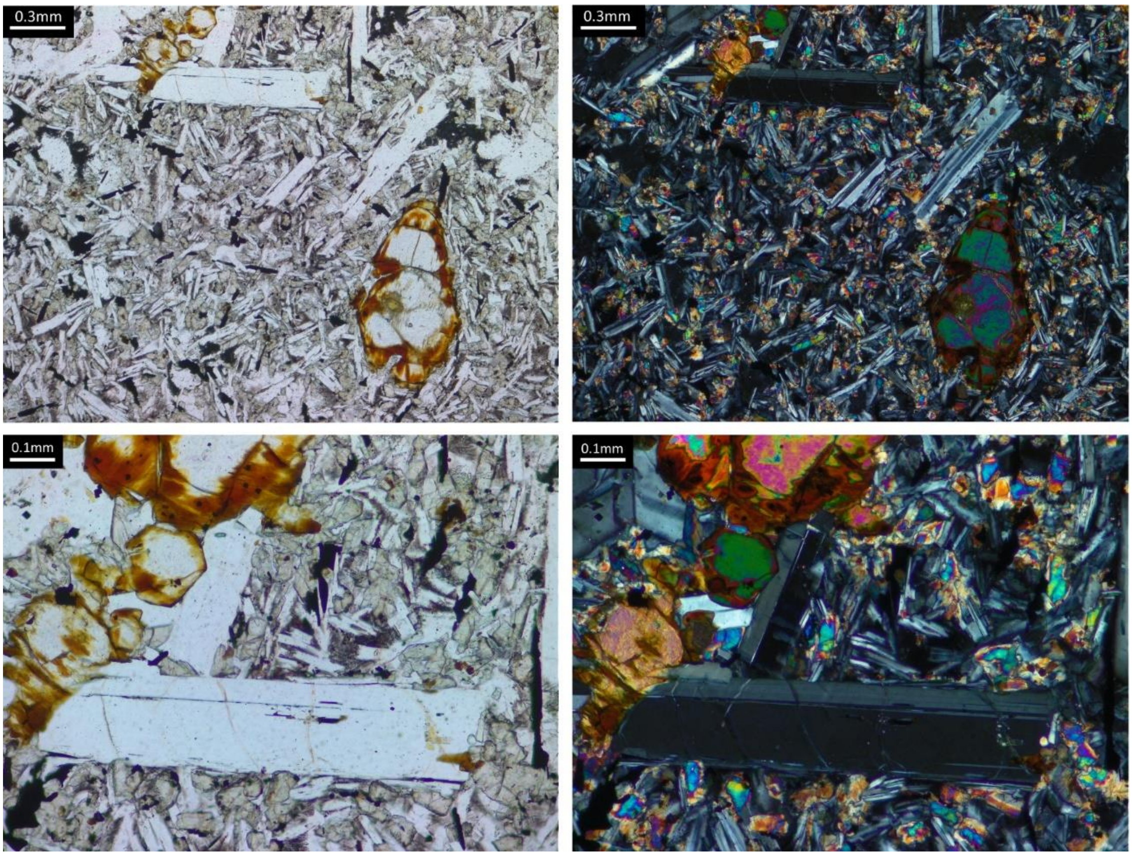

Figure A.58: Transmitted light photomicrographs of sample MH01S.

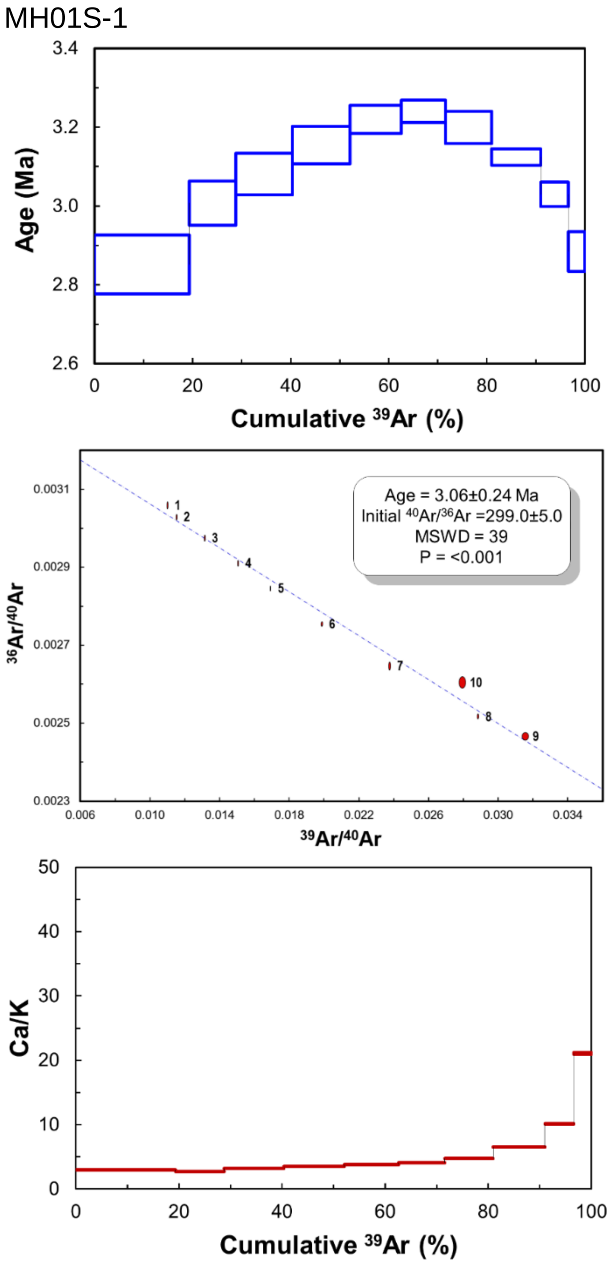

Figure A.59: ^{40}Ar/^{39}Ar age spectrum, inverse isochron and Ca/K plot of aliquant MH01S-1.

Sample MH04

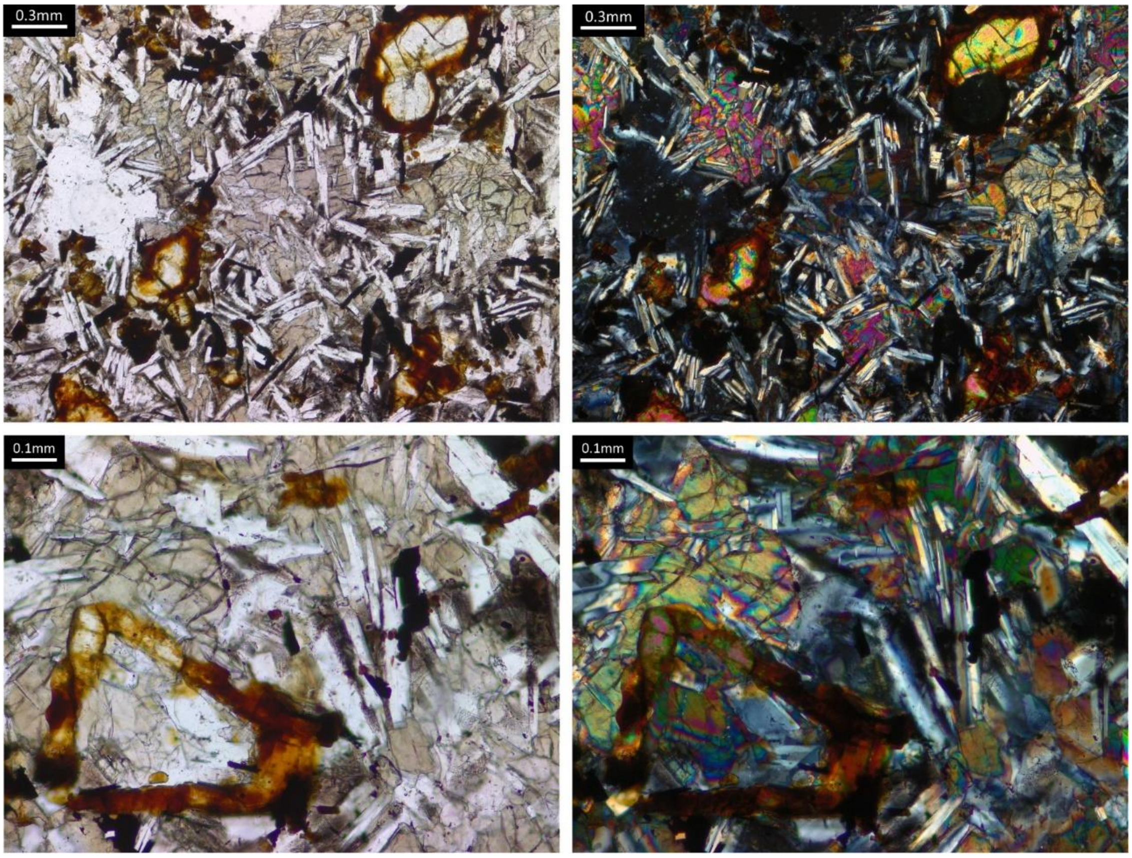

Figure A.60: Transmitted light photomicrographs of sample MH04.

MH04-1

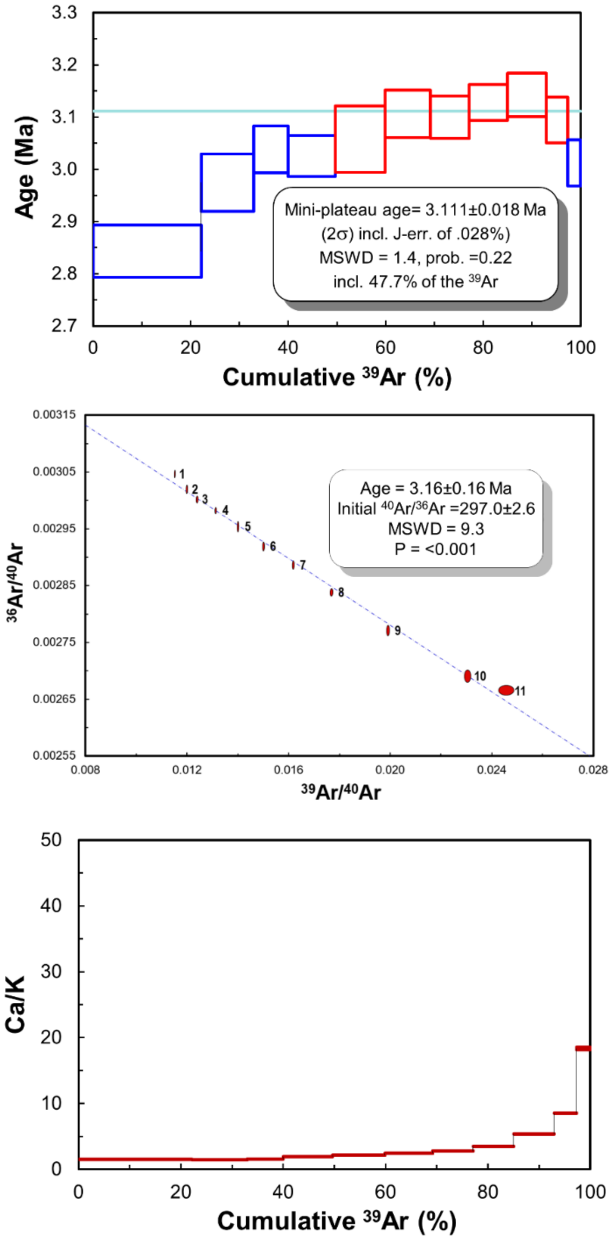

Figure A.61: ^{40}Ar/^{39}Ar age spectrum, inverse isochron and Ca/K plot of aliquant MH04-1.

Sample MH11

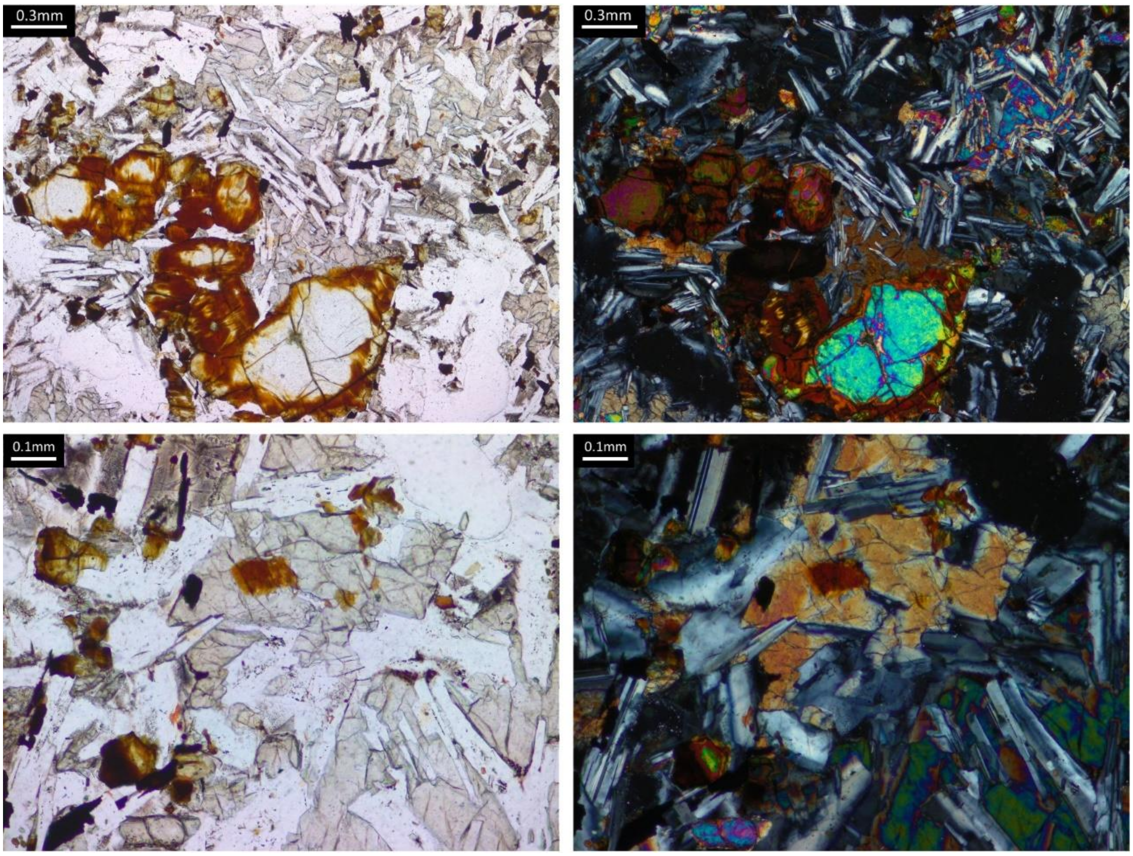

Figure A.62: Transmitted light photomicrographs of sample MH11.

MH11-1

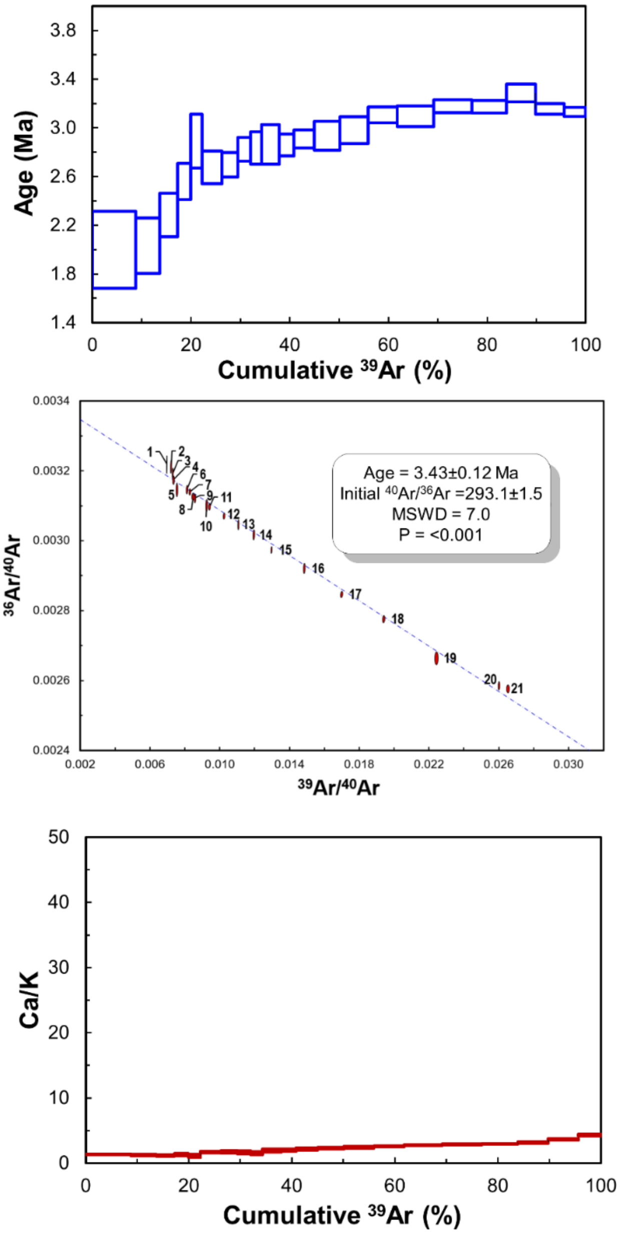

Figure A.63: ^{40}Ar/^{39}Ar age spectrum, inverse isochron and Ca/K plot of aliquant MH11-1.

Sample MH56A

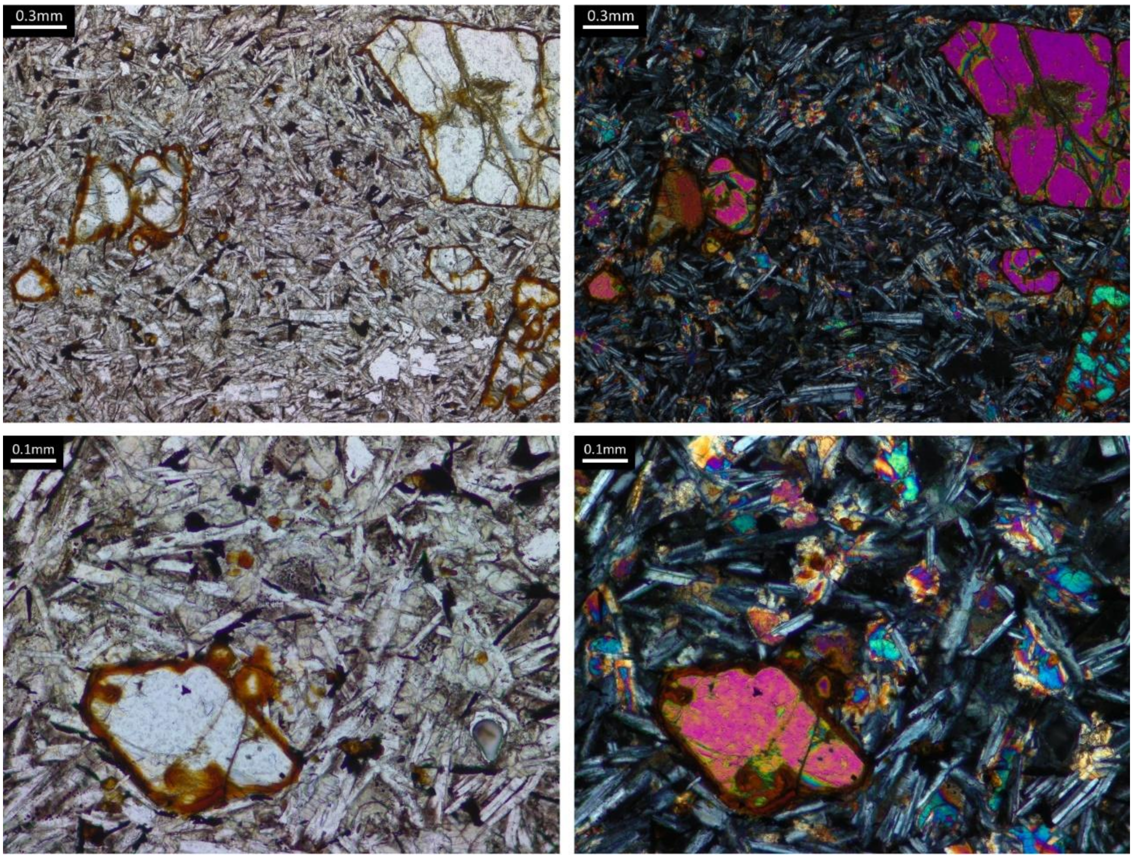

Figure A.64: Transmitted light photomicrographs of sample MH56A.

MH56A-1

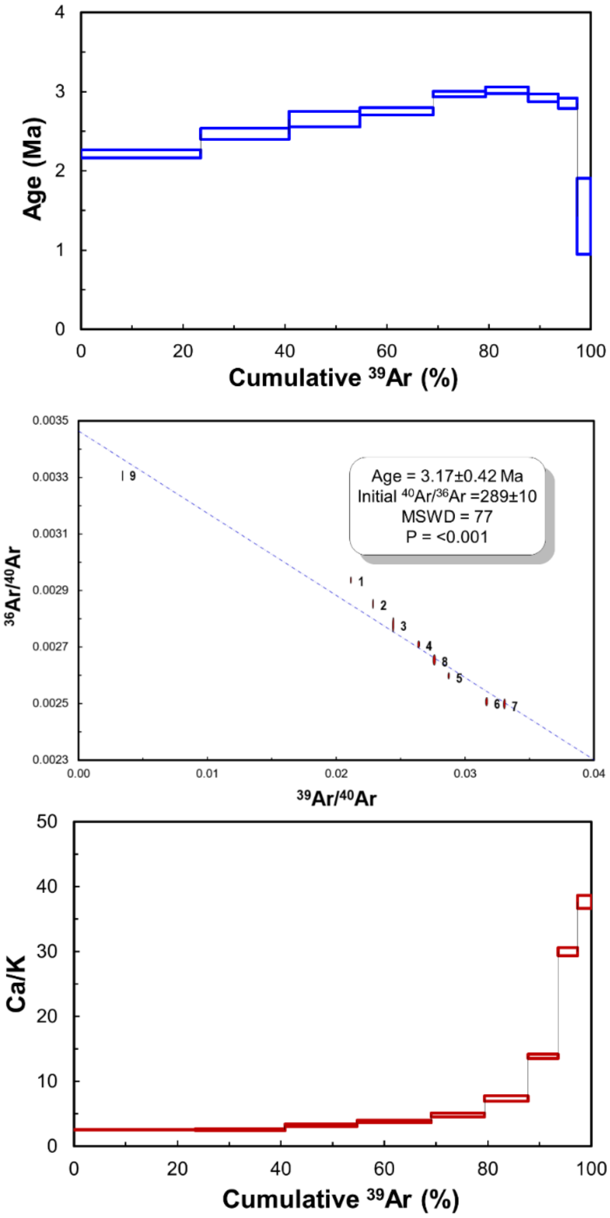

Figure A.65: ^{40}Ar/^{39}Ar age spectrum, inverse isochron and Ca/K plot of aliquant MH56A-1.

A.2f. Mount Ridley Flow

Sample KA13M

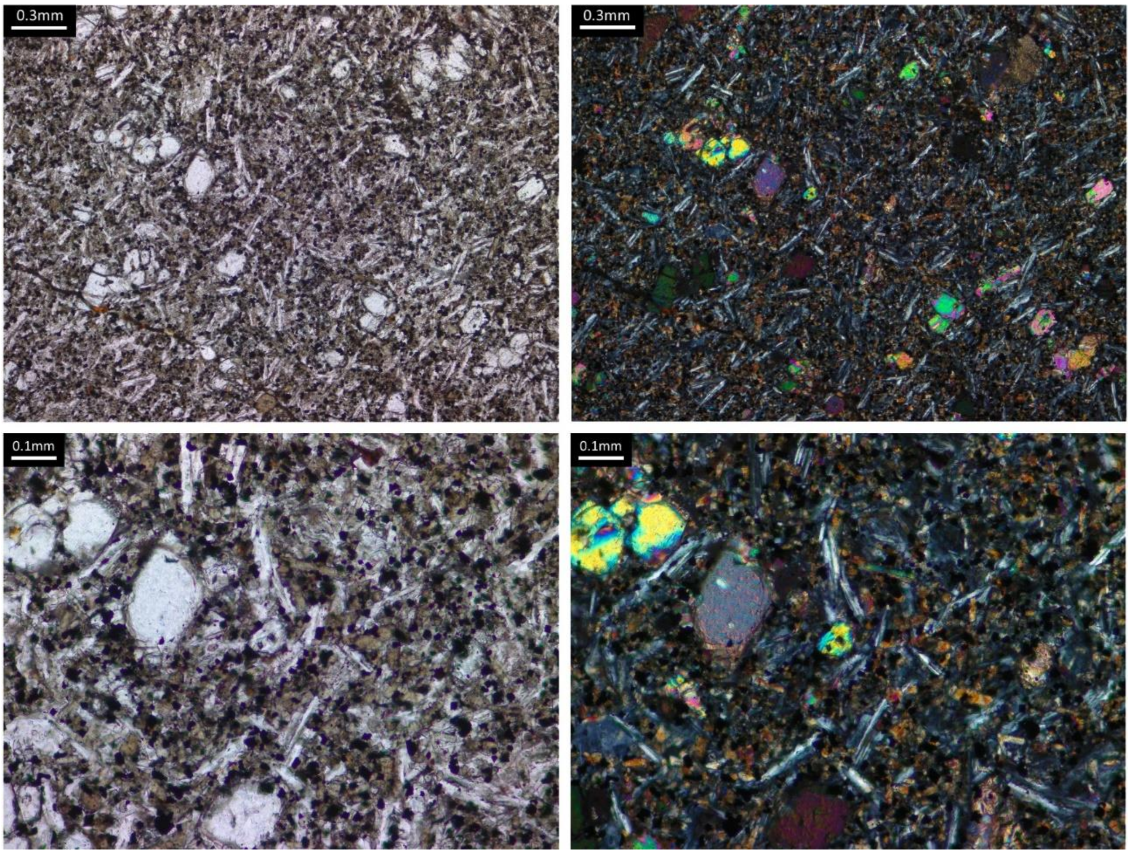

Figure A.66: Transmitted light photomicrographs of sample KA13M.

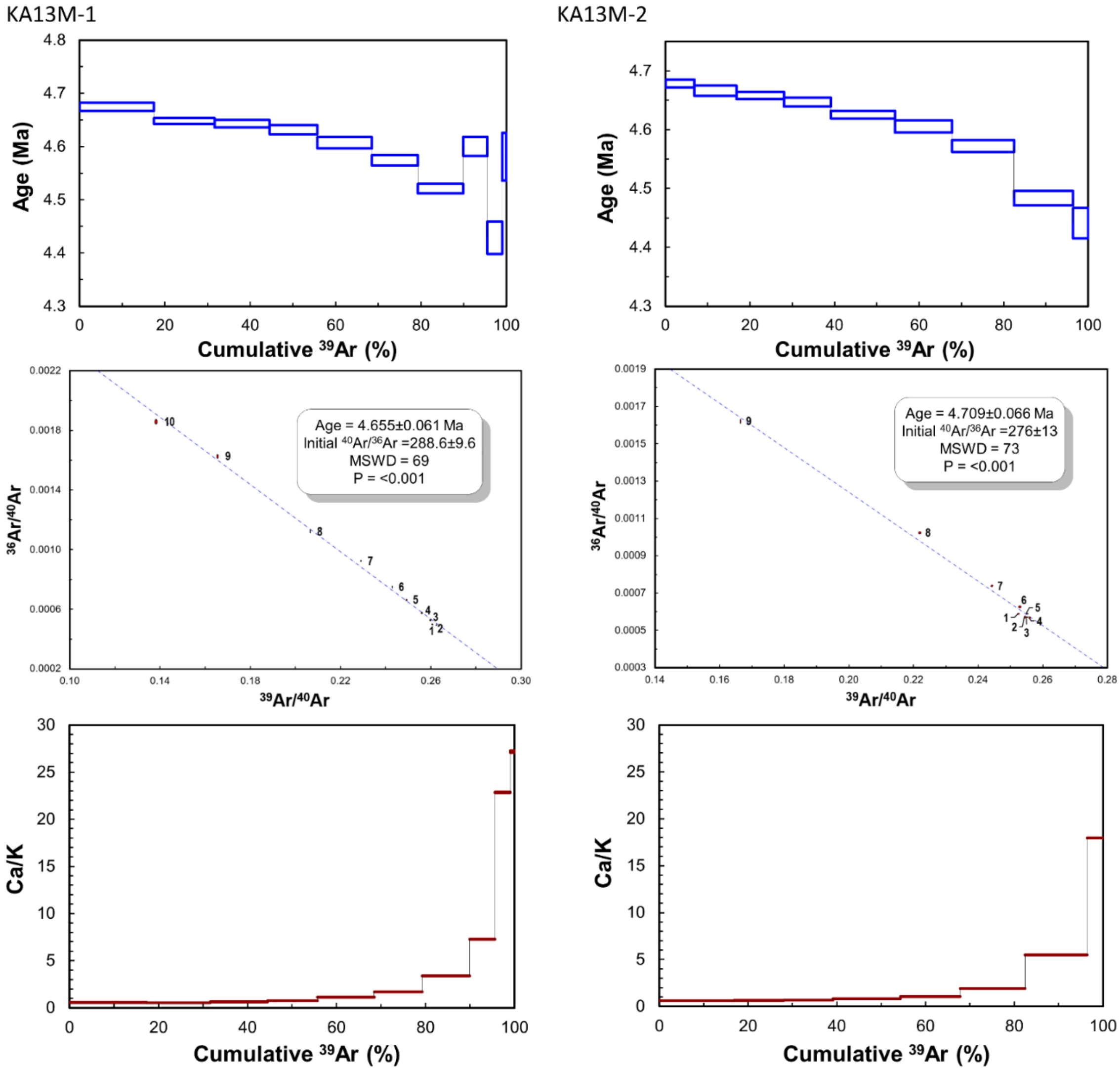

Figure A.67: ^{40}Ar/^{39}Ar age spectra, inverse isochrons and Ca/K plots of aliquants KA13M-1 and KA13M-2

A.2g. Redstone Hill Flow

Sample BB22

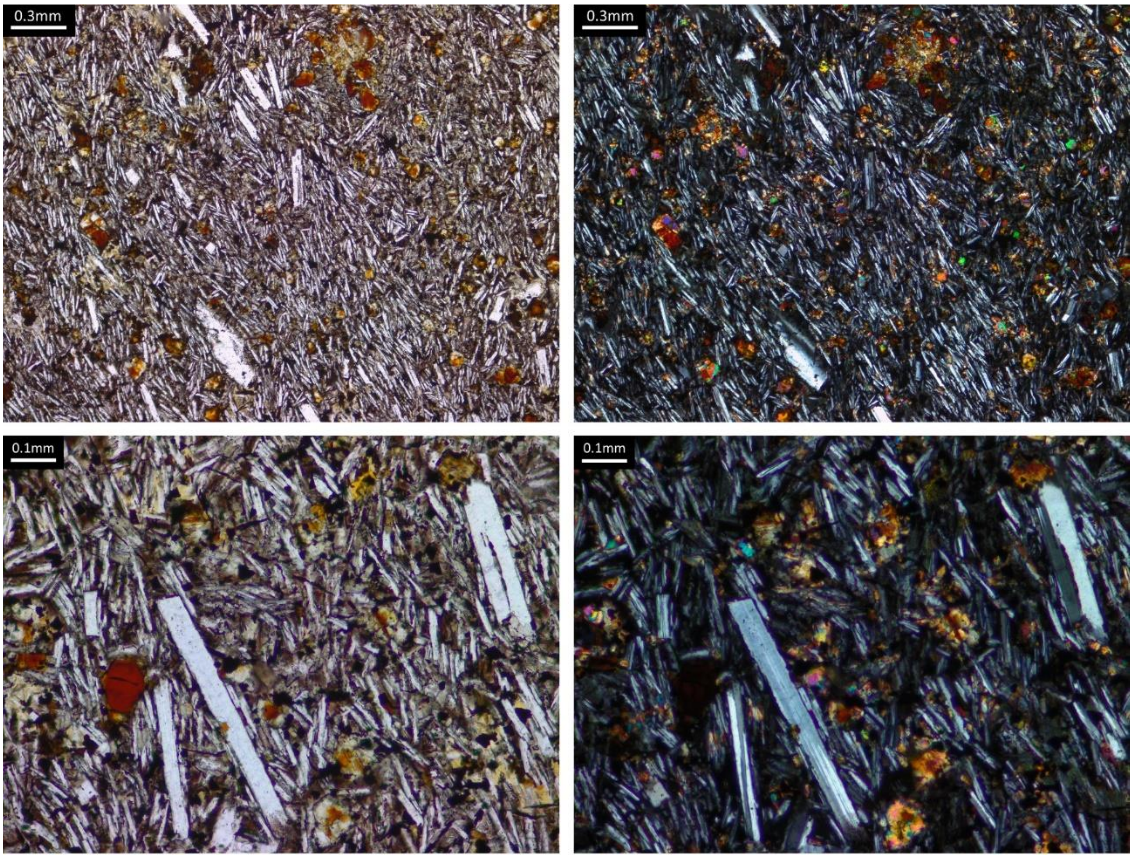

Figure A.68: Transmitted light photomicrographs of sample BB22.

BB22-1

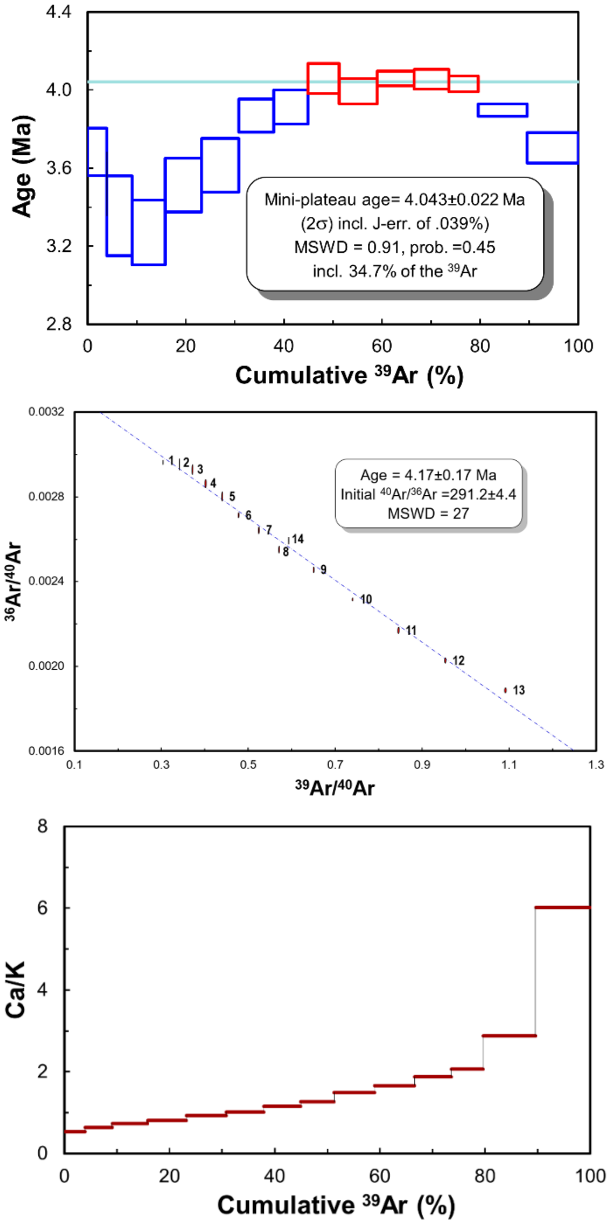

Figure A.69: ^{40}Ar/^{39}Ar age spectrum, inverse isochron and Ca/K plot of aliquant BB22-1.

Sample MH02

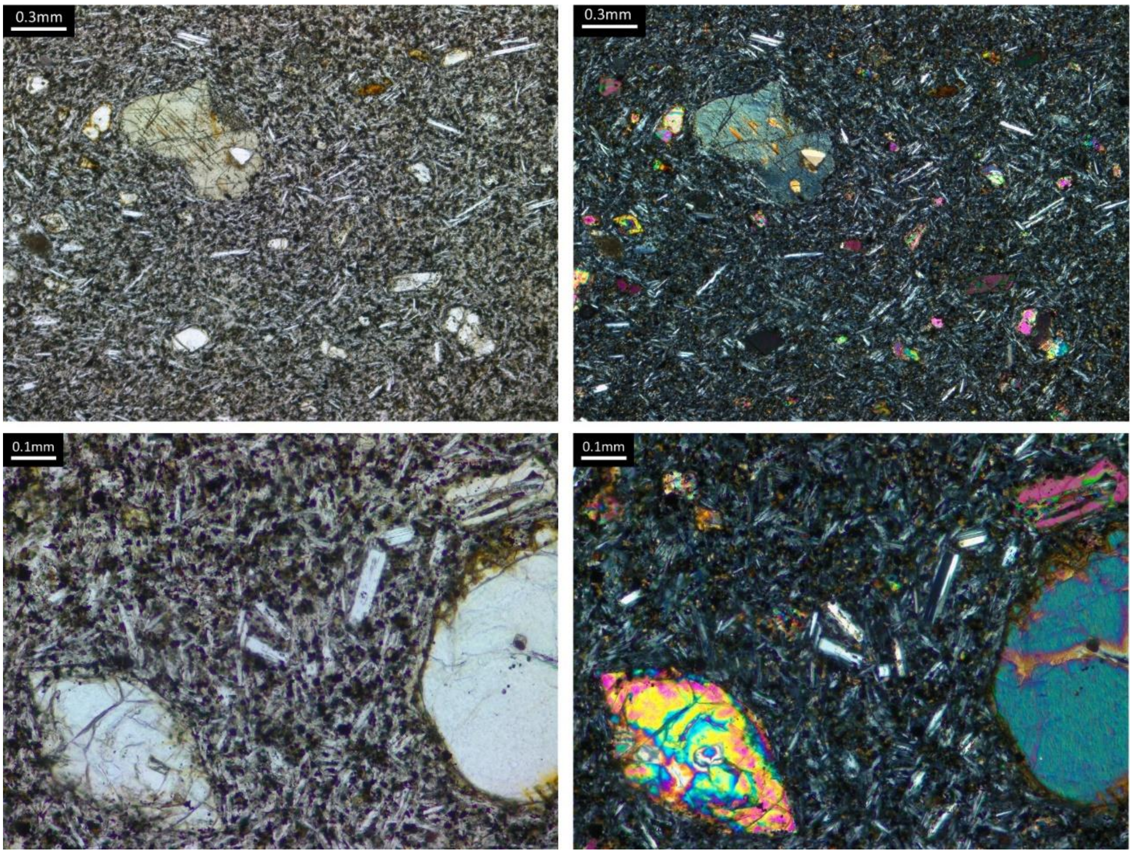

Figure A.70: Transmitted light photomicrographs of sample MH02.

MH02-1

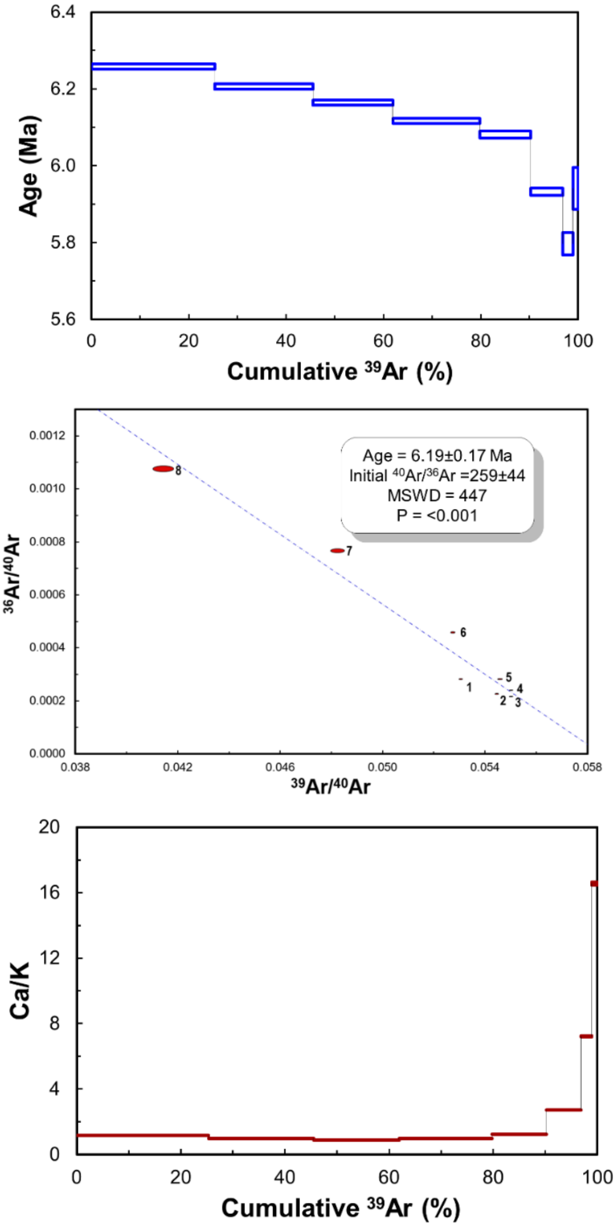

Figure A.71: ^{40}Ar/^{39}Ar age spectrum, inverse isochron and Ca/K plot of aliquant MH02-1.

A.2h. Springs Hill Flow

Sample ME4J

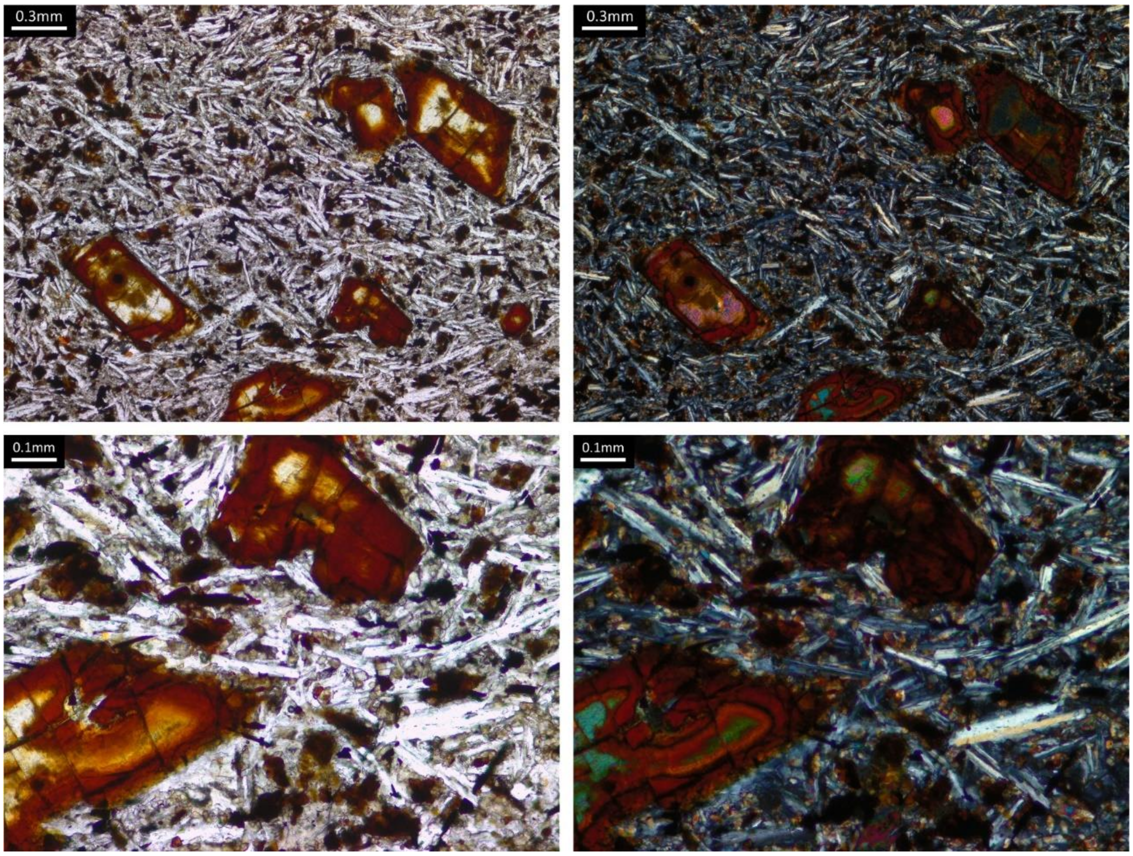

Figure A.72: Transmitted light photomicrographs of sample ME4J.

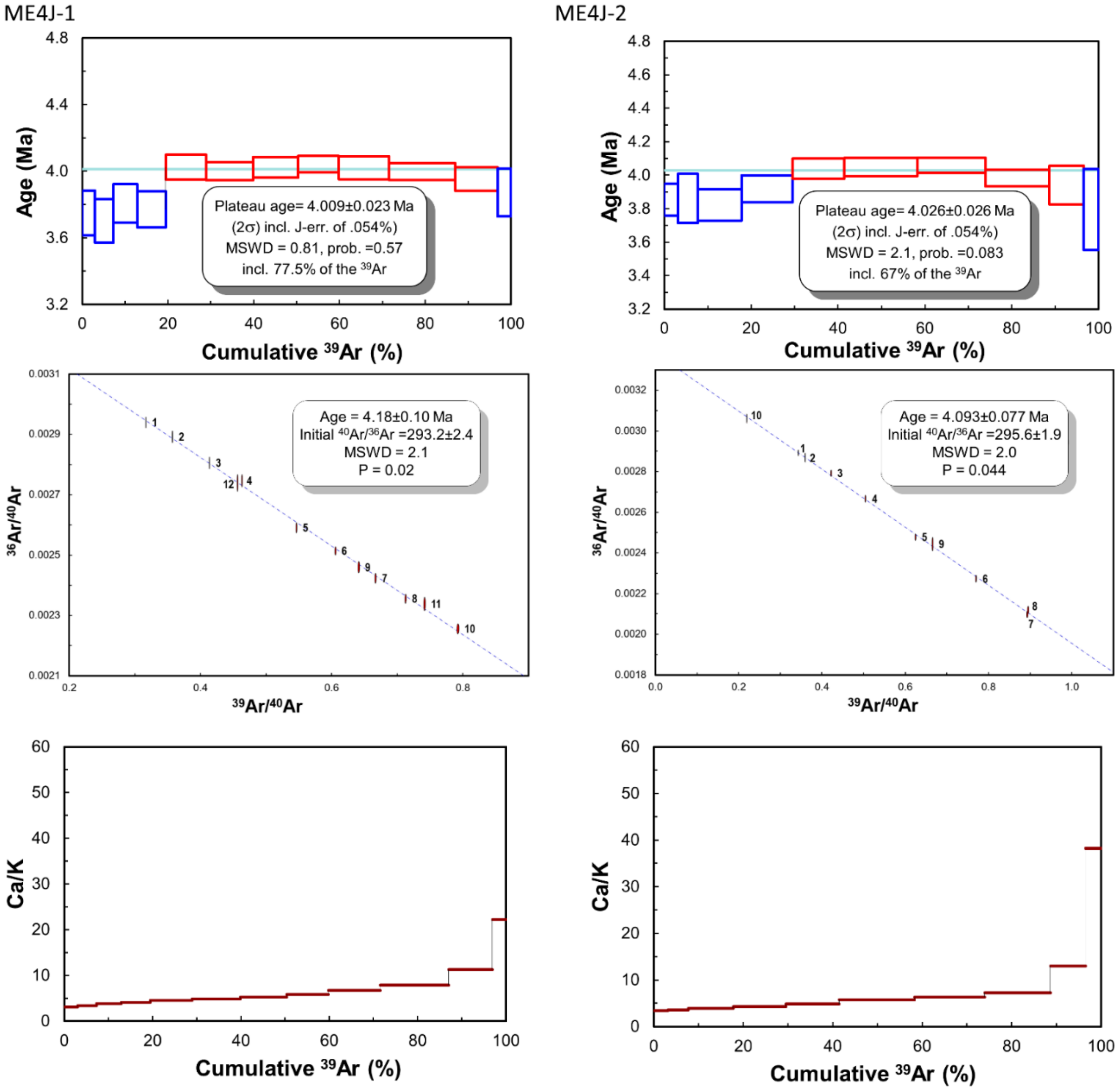

Figure A.73: ${}^{40}Ar/{}^{39}Ar$ age spectra, inverse isochrons and Ca/K plots of aliquants ME4J-1 and ME4J-2

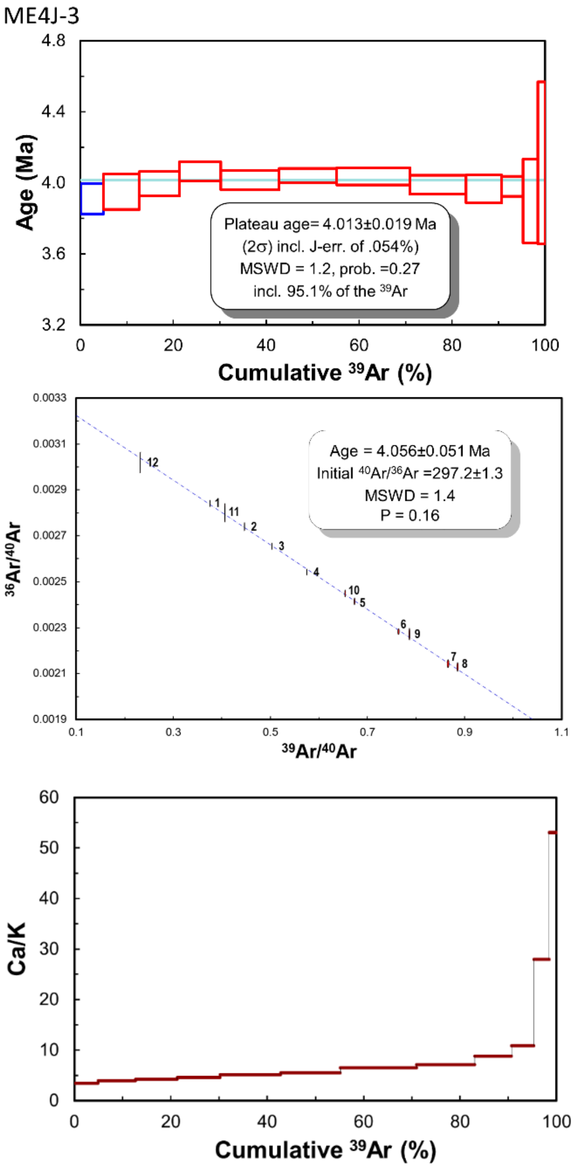

Figure A.74: ^{40}Ar/^{39}Ar age spectrum, inverse isochron and Ca/K plot of aliquant ME4J-3.

A.2i. Summerhill Rd Flow

Sample KA13L

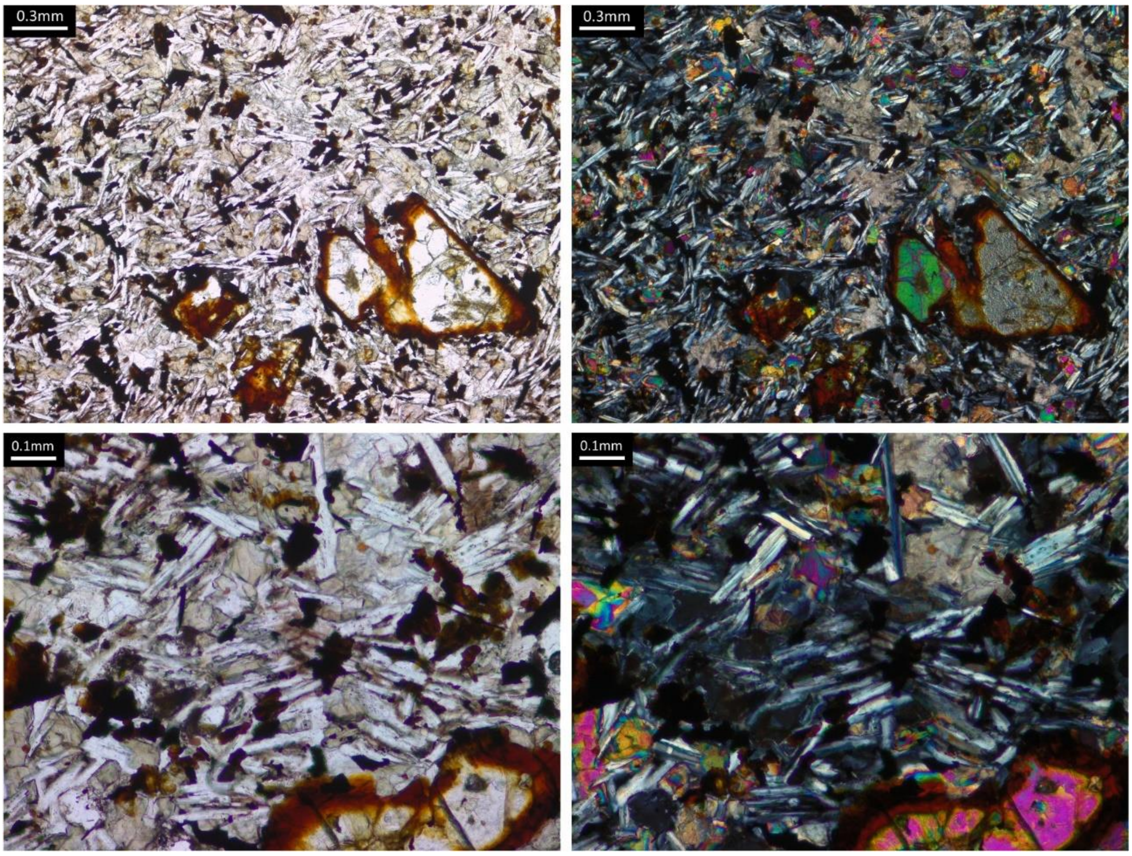

Figure A.75: Transmitted light photomicrographs of sample KA13L.

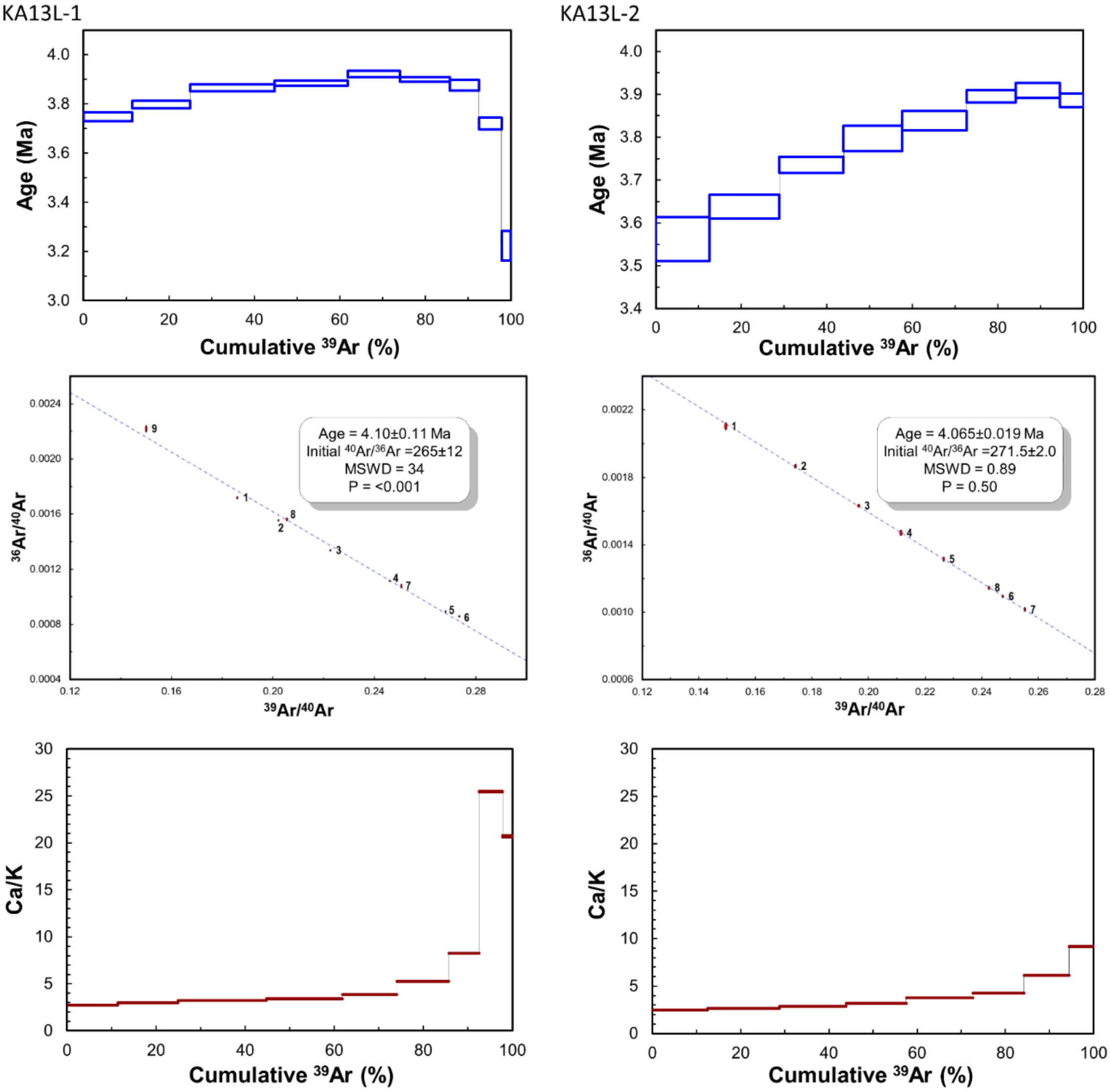

Figure A.76: ^{40}Ar/^{39}Ar age spectra, inverse isochrons and Ca/K plots of aliquants KA13L-1 and KA13L-2

A.2j. Tullamarine Flow

Sample MH75C

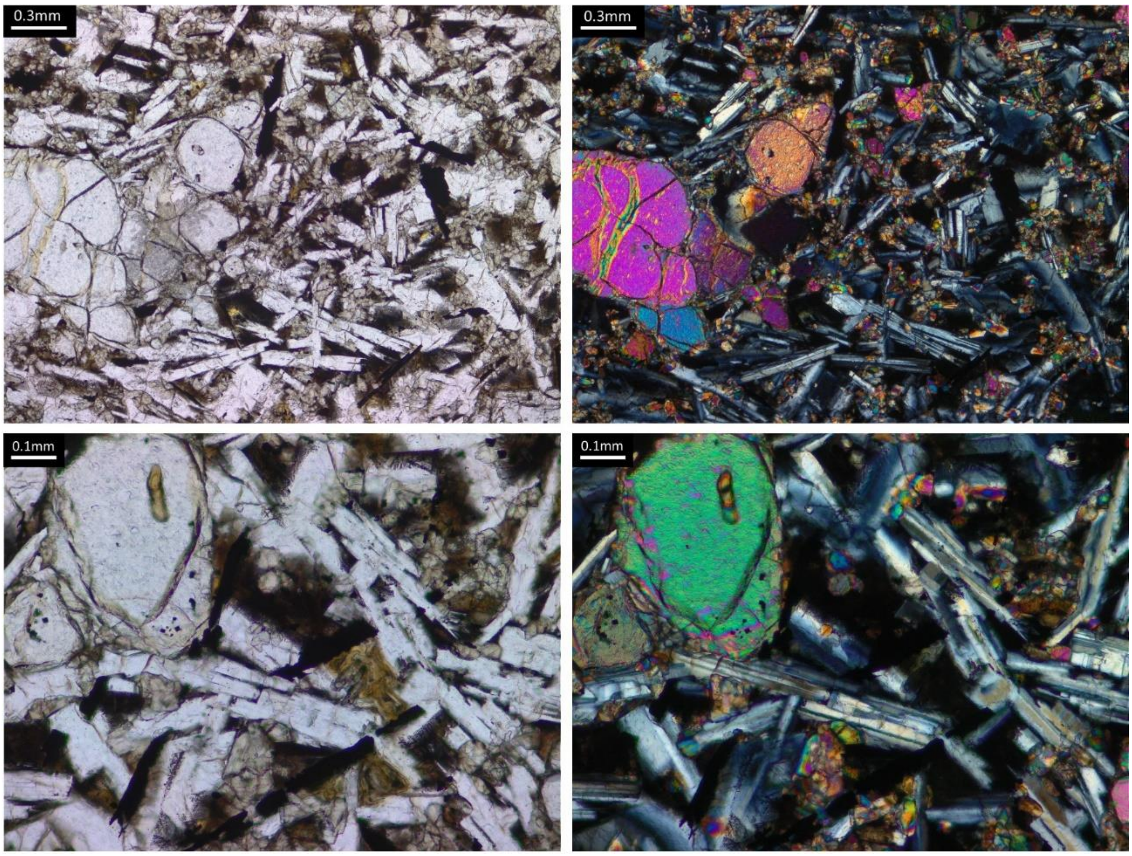

Figure A.77: Transmitted light photomicrographs of sample MH75C.

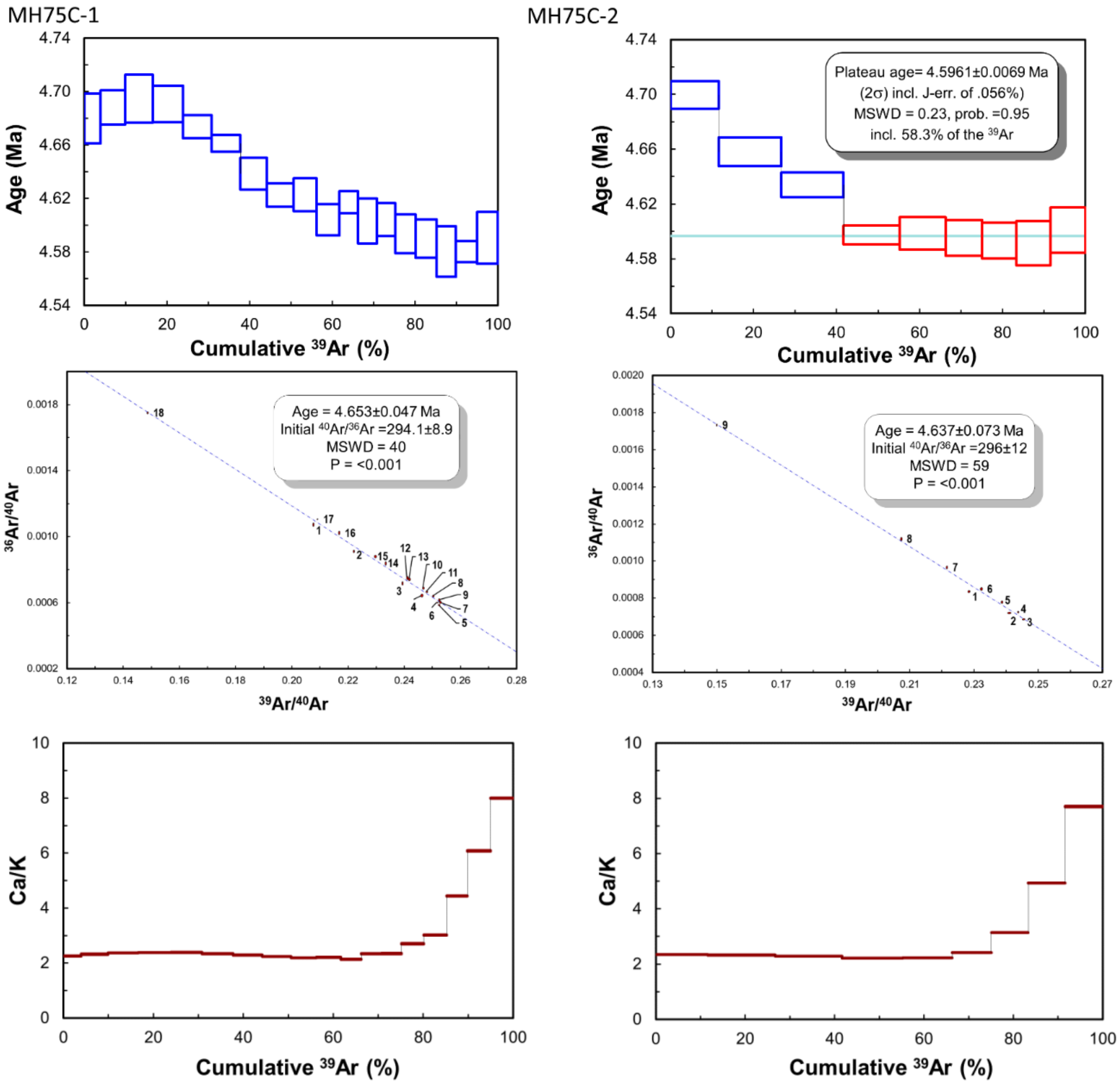

Figure A.78: ^{40}Ar/^{39}Ar age spectra, inverse isochrons and Ca/K plots of aliquants MH75C-1 and MH75C-2

Appendix A.3. ARGUSVI ^{40}Ar/^{39}Ar laser step-heating analytical results for Mount Fraser Flow (Flow A) samples

Table A.3a. ARGUSVI ^{40}Ar/^{39}Ar laser step-heating analytical results for sample MH05.[a,b,c,d,e]

Sample ID	Step No	Laser Power	^{40}Ar (fA)	±1σ	^{39}Ar (fA)[b]	±1σ	^{38}Ar (fA)	±1σ	^{37}Ar (fA)[b]	±1σ	^{36}Ar (fA)	±1σ	^{39}Ar (x10^{-14} mol)[d]	Ca/K	±1σ	%^{40}Ar*	^{40}Ar*/^{39}Ar	±1σ	Cum.% ^{39}Ar	Apparent Age (Ma)	±1σ	±1σ (%)
Aliquant: MH05-1		34.2 mg																				
MH05-1a[e]	1	3%	137.971	0.120	25.386	0.039	0.046	0.000	21.536	0.769	0.2434	0.0010	0.0901	1.485	0.053	47.33	2.57	0.01	8.30	0.928	0.005	0.5
MH05-1b[e]	2	4%	246.340	0.564	43.627	0.023	0.086	0.000	44.630	1.010	0.4538	0.0021	0.1549	1.790	0.041	44.99	2.54	0.02	22.57	0.917	0.007	0.8
MH05-1c[e]	3	5%	273.026	0.451	47.440	0.033	0.099	0.000	59.298	0.825	0.5270	0.0006	0.1684	2.187	0.030	42.36	2.44	0.01	38.09	0.880	0.004	0.4
MH05-1d[e]	4	6%	243.540	0.818	43.514	0.040	0.087	0.001	64.622	0.717	0.4596	0.0032	0.1545	2.599	0.029	43.66	2.44	0.03	52.32	0.882	0.010	1.2
MH05-1e[e]	5	7%	214.196	0.469	37.399	0.042	0.078	0.001	64.156	0.573	0.4156	0.0027	0.1328	3.002	0.027	42.06	2.41	0.02	64.55	0.869	0.009	1.0
MH05-1f[e]	6	8%	193.055	0.369	31.333	0.042	0.075	0.000	62.769	0.678	0.4005	0.0022	0.1112	3.506	0.038	38.06	2.35	0.02	74.80	0.846	0.009	1.0
MH05-1g	7	10%	254.855	0.479	35.856	0.027	0.107	0.000	83.871	0.585	0.5675	0.0018	0.1273	4.093	0.029	33.52	2.38	0.02	86.53	0.860	0.007	0.8
MH05-1h	8	14%	380.945	0.442	41.186	0.045	0.179	0.001	126.641	0.814	0.9498	0.0041	0.1462	5.381	0.035	25.56	2.36	0.03	100.00	0.853	0.011	1.3
																			Total gas age: 0.879 ± 0.016 Ma (2σ)			

[a] Data are corrected for mass spectrometer backgrounds, discrimination, radioactive decay and interference corrections. Errors are one sigma uncertainties and exclude uncertainties in the J-value (propagating this error only has an effect in the third decimal place)

[b] Interference corrections: $(^{36}Ar/^{37}Ar)_{Ca} = (2.5713 \pm 0.0023) \times 10^{-4}$; $(^{39}Ar/^{37}Ar)_{Ca} = (6.6200 \pm 0.0801) \times 10^{-4}$; $(^{40}Ar/^{39}Ar)_{K} = (4.9000 \pm 0.8575) \times 10^{-4}$; $(^{38}Ar/^{39}Ar)_{K} = (1.2136 \pm 0.0016) \times 10^{-2}$

[c] J-value is 0.0002000807 ± 0.0000003752 (0.188%;1σ), based on an age of 1.1814 ± 0.0006 Ma (2σ) for ACR sanidine (Phillips et al., 2017)

[d] Sensitivity = 3.55 x 10^{-17} mol/fA

[e] Heating steps where there was an indication of suppression of isotope signals, possibly due to hydrocarbon contamination. Affected cycles were removed from regression.

Table A.3b. ARGUSVI ^{40}Ar/^{39}Ar laser step-heating analytical results for sample MH07.[a,b,c,d,e]

Sample ID	Step No	Laser Power	^{40}Ar (fA)	±1σ	^{39}Ar (fA)[b]	±1σ	^{38}Ar (fA)	±1σ	^{37}Ar (fA)[b]	±1σ	^{36}Ar (fA)	±1σ	^{39}Ar ($\times 10^{-14}$ mol)[d]	Ca/K	±1σ	%^{40}Ar*	^{40}Ar*/^{39}Ar	±1σ	Cum.% ^{39}Ar	Apparent Age (Ma)	±1σ	±1σ (%)
Aliquant: MH07-1		35.4 mg																				
MH07-1a[e]	1	3%	410.309	0.406	37.357	0.041	0.201	0.001	59.278	0.790	1.0671	0.0034	0.1326	2.777	0.037	22.35	2.46	0.03	7.21	0.887	0.011	1.2
MH07-1b[e]	2	4%	492.609	0.828	71.257	0.068	0.202	0.001	95.800	0.799	1.0705	0.0027	0.2530	2.353	0.020	35.12	2.43	0.02	20.97	0.877	0.006	0.7
MH07-1c[e]	3	5%	431.263	0.591	82.070	0.035	0.152	0.000	91.461	1.016	0.8077	0.0021	0.2913	1.950	0.022	44.08	2.32	0.01	36.81	0.837	0.004	0.4
MH07-1d[e]	4	6%	358.682	0.463	76.749	0.095	0.115	0.000	73.436	0.886	0.6074	0.0022	0.2725	1.674	0.020	49.43	2.31	0.01	51.62	0.835	0.004	0.5
MH07-1e[e]	5	8%	406.355	0.411	99.172	0.079	0.112	0.000	84.341	0.916	0.5958	0.0020	0.3521	1.488	0.016	56.22	2.30	0.01	70.76	0.832	0.003	0.3
MH07-1f[e]	6	10%	305.645	0.309	77.534	0.095	0.083	0.000	63.038	1.049	0.4413	0.0010	0.2752	1.423	0.024	56.88	2.24	0.01	85.73	0.810	0.002	0.3
MH07-1g	7	14%	325.470	0.251	73.921	0.085	0.102	0.000	83.871	1.055	0.5390	0.0012	0.2624	1.986	0.025	50.55	2.23	0.01	100.00	0.804	0.002	0.3
																			Total gas age:	**0.836 ± 0.008 Ma (2σ)**		

[a] Data are corrected for mass spectrometer backgrounds, discrimination, radioactive decay and interference corrections. Errors are one sigma uncertainties and exclude uncertainties in the J-value (propagating this error only has an effect in the third decimal place)

[b] Interference corrections: $(^{36}Ar/^{37}Ar)_{Ca} = (2.5713 \pm 0.0023) \times 10^{-4}$; $(^{39}Ar/^{37}Ar)_{Ca} = (6.6200 \pm 0.0801) \times 10^{-4}$; $(^{40}Ar/^{39}Ar)_{K} = (4.9000 \pm 0.8575) \times 10^{-4}$; $(^{38}Ar/^{39}Ar)_{K} = (1.2136 \pm 0.0016) \times 10^{-2}$

[c] J-value is 0.0002002979 ± 0.0000001953 (0.098%;1σ), based on an age of 1.1814 ± 0.0006 Ma (2σ) for ACR sanidine (Phillips et al., 2017)

[d] Sensitivity = 3.55×10^{-17} mol/fA

[e] Heating steps where there was an indication of suppression of isotope signals, possibly due to hydrocarbon contamination. Affected cycles were removed from regression.

Table A.3c. ARGUSVI ^{40}Ar/^{39}Ar laser step-heating analytical results for sample MH09.[a,b,c,d]

Sample ID	**Step No**	**Laser Power**	**^{40}Ar (fA)**	**±1σ**	**^{39}Ar (fA)[b]**	**±1σ**	**^{38}Ar (fA)**	**±1σ**	**^{37}Ar (fA)[b]**	**±1σ**	**^{36}Ar (fA)**	**±1σ**	**^{39}Ar ($\times10^{-14}$ mol)[d]**	**Ca/K**	**±1σ**	**%^{40}Ar***	**^{40}Ar*/^{39}Ar**	**±1σ**	**Cum.% ^{39}Ar**	**Apparent Age (Ma)**	**±1σ**	**±1σ (%)**
Aliquant: MH09-1		33.4 mg																				
MH09-1a	1	3%	1857.250	0.780	39.855	0.030	1.128	0.001	54.868	0.153	5.9847	0.0071	0.1415	2.409	0.007	3.79	1.77	0.06	15.28	0.641	0.020	3.2
MH09-1b	2	3.5%	1542.726	0.571	37.534	0.035	0.928	0.001	55.716	0.134	4.9222	0.0069	0.1332	2.598	0.007	4.74	1.95	0.06	29.67	0.706	0.021	2.9
MH09-1c	3	4%	1207.849	0.399	33.597	0.037	0.717	0.001	56.000	0.197	3.8014	0.0070	0.1193	2.917	0.011	6.04	2.17	0.06	42.55	0.786	0.023	2.9
MH09-1d	4	5%	1168.155	0.386	39.991	0.027	0.677	0.001	80.199	0.181	3.5928	0.0053	0.1420	3.509	0.008	8.17	2.39	0.04	57.88	0.865	0.015	1.7
MH09-1e	5	6%	807.942	0.234	34.035	0.032	0.457	0.000	79.707	0.194	2.4219	0.0021	0.1208	4.098	0.011	10.50	2.49	0.02	70.93	0.903	0.007	0.8
MH09-1f	6	8%	628.947	0.151	33.729	0.033	0.345	0.000	105.070	0.122	1.8320	0.0020	0.1197	5.451	0.008	13.04	2.43	0.02	83.86	0.881	0.007	0.8
MH09-1g	7	10%	361.138	0.072	22.092	0.044	0.196	0.000	93.734	0.123	1.0406	0.0020	0.0784	7.425	0.018	13.97	2.28	0.03	92.33	0.828	0.010	1.2
MH09-1h	8	14%	324.618	0.039	19.996	0.033	0.177	0.000	140.807	0.099	0.9412	0.0018	0.0710	12.323	0.022	13.43	2.18	0.03	100.00	0.790	0.010	1.3
																			Total gas age:	**0.796 ± 0.030 Ma (2σ)**		

[a] Data are corrected for mass spectrometer backgrounds, discrimination, radioactive decay and interference corrections. Errors are one sigma uncertainties and exclude uncertainties in the J-value (propagating this error only has an effect in the third decimal place)

[b] Interference corrections: $(^{36}\text{Ar}/^{37}\text{Ar})_{\text{Ca}} = (2.5713 \pm 0.0023) \times 10^{-4}$; $(^{39}\text{Ar}/^{37}\text{Ar})_{\text{Ca}} = (6.6200 \pm 0.0801) \times 10^{-4}$; $(^{40}\text{Ar}/^{39}\text{Ar})_{\text{K}} = (4.9000 \pm 0.8575) \times 10^{-4}$; $(^{38}\text{Ar}/^{39}\text{Ar})_{\text{K}} = (1.2136 \pm 0.0016) \times 10^{-2}$

[c] J-value is 0.000200879 ± 0.0000000573 (0.029%;1σ), based on an age of 1.1814 ± 0.0006 Ma (2σ) for ACR sanidine (Phillips et al., 2017)

[d] Sensitivity = 3.55×10^{-17} mol/fA

Table A.3d. ARGUSVI ^{40}Ar/^{39}Ar laser step-heating analytical results for sample MH12.[a,b,c,d]

Sample ID	Step No	Laser Power	^{40}Ar (fA)	±1σ	^{39}Ar (fA)[b]	±1σ	^{38}Ar (fA)	±1σ	^{37}Ar (fA)[b]	±1σ	^{36}Ar (fA)	±1σ	^{39}Ar ($\times10^{-14}$ mol)[d]	Ca/K	±1σ	%^{40}Ar*	^{40}Ar*/^{39}Ar	±1σ	Cum.% ^{39}Ar	Apparent Age (Ma)	±1σ	±1σ (%)
Aliquant: MH12-1		30.8 mg																				
MH12-1a	1	3%	441.394	0.252	16.573	0.023	0.255	0.001	30.937	0.922	1.3502	0.0030	0.0588	3.267	0.097	8.67	2.31	0.06	5.45	0.836	0.020	2.4
MH12-1b	2	4%	396.161	0.095	29.972	0.014	0.208	0.000	48.230	0.857	1.1033	0.0024	0.1064	2.816	0.050	16.85	2.23	0.02	15.30	0.806	0.009	1.1
MH12-1c	3	5%	318.821	0.268	35.442	0.032	0.150	0.000	48.309	0.884	0.7968	0.0017	0.1258	2.385	0.044	25.39	2.28	0.02	26.95	0.827	0.006	0.7
MH12-1d	4	6%	259.581	0.203	36.868	0.024	0.111	0.001	43.629	0.909	0.5888	0.0031	0.1309	2.071	0.043	32.28	2.27	0.03	39.06	0.823	0.009	1.1
MH12-1e	5	7%	220.148	0.196	36.132	0.034	0.088	0.000	38.325	0.843	0.4669	0.0014	0.1283	1.856	0.041	36.68	2.23	0.01	50.94	0.809	0.005	0.6
MH12-1f	6	8%	191.921	0.161	33.782	0.025	0.073	0.000	33.235	0.911	0.3886	0.0014	0.1199	1.722	0.047	39.54	2.25	0.01	62.04	0.813	0.005	0.6
MH12-1g	7	9%	169.291	0.095	30.481	0.041	0.063	0.000	28.468	0.601	0.3367	0.0015	0.1082	1.634	0.035	40.61	2.26	0.02	72.06	0.816	0.005	0.7
MH12-1h	8	10%	155.670	0.101	27.303	0.043	0.059	0.000	26.295	0.556	0.3153	0.0017	0.0969	1.685	0.036	39.53	2.25	0.02	81.03	0.816	0.007	0.8
MH12-1i	9	12%	197.146	0.110	30.957	0.034	0.081	0.000	34.335	0.462	0.4306	0.0007	0.1099	1.941	0.026	34.79	2.22	0.01	91.21	0.802	0.003	0.4
MH12-1j	10	14%	200.810	0.117	26.754	0.029	0.090	0.000	36.467	0.538	0.4760	0.0013	0.0950	2.385	0.035	29.22	2.19	0.02	100.00	0.794	0.005	0.7
																			Total gas age:	0.814 ± 0.014 ka (2σ)		
Aliquant: MH12-2		45.8 mg																				
MH12-2a[e]	1	3%	812.069	0.130	16.216	0.022	0.485	0.001	29.952	1.080	2.5712	0.0072	0.0576	3.232	0.117	5.47	2.74	0.13	3.87	0.991	0.048	4.8
MH12-2b[e]	2	4%	638.672	0.492	31.070	0.030	0.359	0.001	54.070	0.947	1.9069	0.0030	0.1103	3.045	0.053	10.86	2.23	0.03	11.30	0.808	0.012	1.5
MH12-2c	3	5%	516.870	0.196	41.652	0.036	0.267	0.000	64.182	0.763	1.4151	0.0023	0.1479	2.697	0.032	18.26	2.27	0.02	21.25	0.820	0.006	0.8
MH12-2d	4	6%	422.981	0.233	46.996	0.039	0.199	0.001	63.894	0.769	1.0573	0.0047	0.1668	2.379	0.029	25.37	2.28	0.03	32.47	0.826	0.011	1.3
MH12-2e	5	8%	530.995	0.191	77.111	0.068	0.225	0.000	91.967	0.947	1.1921	0.0026	0.2737	2.087	0.022	32.97	2.27	0.01	50.89	0.822	0.004	0.5
MH12-2f	6	10%	465.422	0.210	79.073	0.093	0.182	0.000	82.044	0.578	0.9664	0.0019	0.2807	1.816	0.013	38.01	2.24	0.01	69.78	0.810	0.003	0.4
MH12-2g	7	12%	397.136	0.159	69.451	0.055	0.153	0.000	70.539	1.292	0.8127	0.0022	0.2466	1.777	0.033	38.90	2.22	0.01	86.37	0.805	0.004	0.4
MH12-2h	8	14%	348.763	0.080	57.040	0.057	0.141	0.000	64.008	1.198	0.7469	0.0013	0.2025	1.964	0.037	36.06	2.20	0.01	100.00	0.798	0.003	0.3
																			Total gas age:	0.820 ± 0.014 Ma (2σ)		

[a] Data are corrected for mass spectrometer backgrounds, discrimination, radioactive decay and interference corrections. Errors are one sigma uncertainties and exclude uncertainties in the J-value (propagating this error only has an effect in the third decimal place)

[b] Interference corrections: $(^{36}\mathrm{Ar}/^{37}\mathrm{Ar})_{\mathrm{Ca}} = (2.5713 \pm 0.0023) \times 10^{-4}$; $(^{39}\mathrm{Ar}/^{37}\mathrm{Ar})_{\mathrm{Ca}} = (6.6200 \pm 0.0801) \times 10^{-4}$; $(^{40}\mathrm{Ar}/^{39}\mathrm{Ar})_{\mathrm{K}} = (4.9000 \pm 0.8575) \times 10^{-4}$; $(^{38}\mathrm{Ar}/^{39}\mathrm{Ar})_{\mathrm{K}} = (1.2136 \pm 0.0016) \times 10^{-2}$

[c] J-value is 0.0002006698 ± 0.0000000587 (0.029%; 1σ), based on an age of 1.1814 ± 0.0006 Ma (2σ) for ACR sanidine (Phillips et al., 2017)

[d] Sensitivity = 3.55 x 10^{-17} mol/fA

[e] Heating steps where there was an indication of suppression of isotope signals, possibly due to hydrocarbon contamination. Affected cycles were removed from regression.

Table A.3e. ARGUSVI ^{40}Ar/^{39}Ar laser step-heating analytical results for sample MH24.[a,b,c,d]

Sample ID	Step No	Laser Power	^{40}Ar (fA)	±1σ	^{39}Ar (fA)[b]	±1σ	^{38}Ar (fA)	±1σ	^{37}Ar (fA)[b]	±1σ	^{36}Ar (fA)	±1σ	^{39}Ar ($\times 10^{-14}$ mol)[d]	Ca/K	±1σ	%^{40}Ar*	^{40}Ar*/^{39}Ar	±1σ	Cum.% ^{39}Ar	Apparent Age (Ma)	±1σ	±1σ (%)
Aliquant MH24-1		35.2 mg																				
MH24-1a	1	3%	1164.063	0.419	15.485	0.009	0.725	0.001	26.990	0.971	3.8468	0.0056	0.0550	3.050	0.110	1.34	1.00	0.11	6.78	0.377	0.042	11.1
MH24-1b	2	4%	1447.657	0.724	26.860	0.029	0.902	0.002	49.560	0.914	4.7830	0.0131	0.0954	3.229	0.060	1.36	0.73	0.15	18.55	0.274	0.056	20.3
MH24-1c	3	5%	1237.388	0.557	27.680	0.024	0.759	0.002	52.452	1.879	4.0253	0.0097	0.0983	3.316	0.119	2.88	1.29	0.11	30.67	0.482	0.040	8.3
MH24-1d	4	6%	985.094	0.355	27.892	0.013	0.588	0.001	58.036	1.464	3.1199	0.0040	0.0990	3.641	0.092	5.44	1.92	0.04	42.89	0.721	0.017	2.3
MH24-1e	5	8%	1015.173	0.305	36.743	0.021	0.594	0.001	78.159	1.951	3.1511	0.0050	0.1304	3.723	0.093	7.33	2.02	0.04	58.98	0.760	0.016	2.1
MH24-1f	6	10%	720.364	0.122	34.268	0.035	0.407	0.001	78.899	1.877	2.1589	0.0040	0.1216	4.029	0.096	10.52	2.21	0.03	73.99	0.830	0.013	1.6
MH24-1g	7	14%	478.875	0.235	33.327	0.020	0.254	0.000	95.451	1.279	1.3490	0.0012	0.1183	5.012	0.067	15.89	2.28	0.01	88.59	0.857	0.005	0.6
MH24-1h	8	20%	248.343	0.124	17.577	0.023	0.132	0.000	101.905	0.946	0.6986	0.0014	0.0624	10.146	0.095	16.01	2.26	0.03	96.29	0.849	0.009	1.1
MH24-1i	9	35%	175.687	0.047	8.472	0.013	0.099	0.000	98.240	1.034	0.5257	0.0016	0.0301	20.293	0.216	10.67	2.21	0.06	100.00	0.830	0.022	2.6
																			Total gas age:	0.672 ± 0.046 Ma (2σ)		
Aliquant MH24-2		36.3 mg																				
MH24-2a	1	3%	1759.724	0.774	23.688	0.012	1.121	0.004	47.597	1.347	5.9487	0.0187	0.0841	3.516	0.100	-0.93	-0.69	-0.24	8.73	-0.258	-0.089	34.6
MH24-2b	2	4%	1966.154	0.570	35.592	0.010	1.240	0.001	71.769	1.365	6.5777	0.0070	0.1264	3.529	0.067	0.12	0.07	0.06	21.85	0.025	0.023	93.3
MH24-2c	3	5%	1613.515	1.097	36.460	0.025	0.996	0.003	69.647	0.905	5.2860	0.0145	0.1294	3.343	0.043	2.19	0.97	0.12	35.28	0.364	0.046	12.7
MH24-2d	4	6%	1199.079	0.552	33.934	0.022	0.719	0.001	68.013	1.036	3.8148	0.0056	0.1205	3.507	0.053	5.01	1.77	0.05	47.79	0.665	0.019	2.9
MH24-2e	5	8%	1112.521	0.334	45.122	0.034	0.642	0.001	96.870	1.345	3.4044	0.0033	0.1602	3.757	0.052	8.64	2.13	0.02	64.42	0.799	0.009	1.1
MH24-2f	6	10%	623.798	0.181	38.280	0.022	0.338	0.001	91.314	1.599	1.7941	0.0051	0.1359	4.174	0.073	14.13	2.30	0.04	78.53	0.864	0.015	1.7
MH24-2g	7	14%	373.478	0.164	32.759	0.026	0.189	0.000	104.150	0.973	1.0031	0.0014	0.1163	5.564	0.052	19.81	2.26	0.01	90.60	0.848	0.005	0.6
MH24-2h	8	20%	234.209	0.115	17.486	0.015	0.124	0.000	109.544	0.760	0.6574	0.0020	0.0621	10.963	0.077	16.20	2.17	0.04	97.04	0.814	0.013	1.6
MH24-2i	9	35%	172.481	0.086	8.025	0.010	0.098	0.000	118.200	1.642	0.5175	0.0009	0.0285	25.777	0.359	10.43	2.24	0.04	100.00	0.841	0.013	1.6
																			Total gas age:	0.547 ± 0.019 Ma (2σ)		
Aliquant MH24-3		51.4 mg																				
MH24-3a	1	3%	2288.606	0.778	37.571	0.015	1.447	0.005	66.161	1.183	7.6768	0.0261	0.1334	3.082	0.055	-0.15	-0.09	-0.21	11.17	-0.034	-0.078	232.2
MH24-3b	2	4%	2450.946	1.618	51.185	0.029	1.529	0.004	98.870	1.970	8.1121	0.0213	0.1817	3.380	0.067	1.18	0.57	0.13	26.39	0.213	0.048	22.7
MH24-3c	3	5%	1931.233	1.101	51.972	0.022	1.166	0.002	104.217	1.525	6.1836	0.0094	0.1845	3.509	0.051	4.40	1.64	0.06	41.84	0.614	0.022	3.5
MH24-3d	4	6%	1313.712	0.512	45.567	0.021	0.770	0.002	91.184	1.820	4.0828	0.0080	0.1618	3.502	0.070	7.21	2.08	0.05	55.39	0.780	0.020	2.6
MH24-3e	5	8%	1017.497	0.265	51.715	0.027	0.570	0.001	116.721	1.959	3.0217	0.0062	0.1836	3.950	0.066	11.33	2.23	0.04	70.77	0.837	0.014	1.6
MH24-3f	6	10%	526.895	0.174	38.635	0.015	0.276	0.000	102.973	1.871	1.4668	0.0024	0.1372	4.664	0.085	16.89	2.30	0.02	82.26	0.864	0.007	0.8
MH24-3g	7	14%	379.917	0.106	32.689	0.018	0.193	0.000	129.675	1.883	1.0256	0.0020	0.1160	6.942	0.101	19.40	2.25	0.02	91.98	0.846	0.007	0.8
MH24-3h	8	20%	269.682	0.105	18.143	0.020	0.144	0.001	145.837	2.144	0.7652	0.0028	0.0644	14.067	0.207	15.29	2.27	0.05	97.37	0.853	0.017	2.0
MH24-3i	9	35%	191.790	0.084	8.842	0.017	0.107	0.000	142.042	1.632	0.5659	0.0016	0.0314	28.114	0.328	11.91	2.58	0.06	100.00	0.970	0.021	2.2
																			Total gas age:	0.611 ± 0.019 Ma (2σ)		

[a] Data are corrected for mass spectrometer backgrounds, discrimination, radioactive decay and interference corrections. Errors are one sigma uncertainties and exclude uncertainties in the J-value (propagating this error only has an effect in the third decimal place)

[b] Interference corrections: $(^{36}Ar/^{37}Ar)_{Ca} = (2.5798 \pm 0.0027) \times 10^{-4}$; $(^{39}Ar/^{37}Ar)_{Ca} = (6.5640 \pm 0.0135) \times 10^{-4}$; $(^{40}Ar/^{39}Ar)_{K} = (3.8900 \pm 0.2140) \times 10^{-4}$; $(^{38}Ar/^{39}Ar)_{K} = (1.1999 \pm 0.0004) \times 10^{-2}$

[c] J-value is 0.0002079768 ± 0.0000000562 (0.027%;1σ), based on an age of 1.1814 ± 0.0006 Ma (2σ) for ACR sanidine (Phillips et al., 2017)

[d] Sensitivity = 3.55×10^{-17} mol/fA

Table A.3f. ARGUSVI ^{40}Ar/^{39}Ar laser step-heating analytical results for sample MH66.[a,b,c,d]

Sample ID	Step No	Laser Power	^{40}Ar (fA)	±1σ	^{39}Ar (fA)[b]	±1σ	^{38}Ar (fA)	±1σ	^{37}Ar (fA)[b]	±1σ	^{36}Ar (fA)	±1σ	^{39}Ar (x10^{-14} mol)[d]	Ca/K	±1σ	%^{40}Ar*	^{40}Ar*/^{39}Ar	±1σ	Cum.% ^{39}Ar	Apparent Age (Ma)	±1σ	±1σ (%)
Aliquant: MH66-1		36.7 mg																				
MH66-1a	1	3%	1778.015	0.693	18.318	0.015	1.118	0.002	22.261	0.933	5.9306	0.0089	0.0650	2.127	0.089	0.41	0.40	0.15	6.52	0.151	0.056	37.1
MH66-1b	2	3%	1004.536	0.472	10.402	0.016	0.633	0.001	12.364	1.155	3.3587	0.0068	0.0369	2.080	0.194	0.18	0.17	0.20	10.22	0.064	0.075	117.7
MH66-1c	3	4%	3296.880	0.923	37.739	0.010	2.121	0.003	44.229	1.203	11.2535	0.0148	0.1340	2.051	0.056	-1.91	-1.67	-0.12	23.65	-0.625	-0.045	7.2
MH66-1d	4	5%	2898.751	0.928	40.811	0.021	1.838	0.003	52.850	0.870	9.7489	0.0184	0.1449	2.266	0.037	-0.41	-0.29	-0.14	38.17	-0.109	-0.051	46.8
MH66-1e	5	6%	2143.115	1.179	35.621	0.016	1.327	0.002	50.347	1.395	7.0398	0.0091	0.1265	2.474	0.069	1.93	1.16	0.08	50.85	0.435	0.031	7.2
MH66-1f	6	8%	1872.585	0.880	40.699	0.015	1.134	0.002	71.397	0.972	6.0158	0.0106	0.1445	3.070	0.042	4.09	1.88	0.08	65.33	0.704	0.030	4.3
MH66-1g	7	10%	1129.406	0.305	31.673	0.018	0.664	0.001	65.595	0.657	3.5237	0.0066	0.1124	3.624	0.036	6.85	2.44	0.06	76.60	0.915	0.024	2.6
MH66-1h	8	14%	844.277	0.439	31.386	0.015	0.487	0.001	91.460	1.520	2.5810	0.0047	0.1114	5.100	0.085	8.73	2.35	0.05	87.77	0.880	0.018	2.0
MH66-1i	9	20%	554.923	0.155	19.575	0.019	0.325	0.001	116.000	1.175	1.7250	0.0048	0.0695	10.371	0.106	7.19	2.04	0.07	94.74	0.764	0.027	3.6
MH66-1j	10	35%	526.317	0.121	14.783	0.011	0.314	0.001	151.894	1.177	1.6684	0.0048	0.0525	17.982	0.140	5.36	1.91	0.10	100.00	0.715	0.037	5.1
																			Total gas age:	0.362 ± 0.007 Ma (2σ)		
Aliquant: MH66-2		42.6 mg																				
MH66-2a	1	3%	3960.359	0.832	38.217	0.041	2.569	0.005	42.559	1.004	13.6265	0.0284	0.1357	1.949	0.046	-2.73	-2.83	-0.22	10.14	-1.059	-0.083	7.9
MH66-2b	2	4%	4477.950	0.940	50.417	0.035	2.896	0.004	59.299	1.451	15.3648	0.0219	0.1790	2.058	0.050	-2.44	-2.17	-0.13	23.52	-0.813	-0.049	6.1
MH66-2c	3	5%	3861.168	1.004	50.860	0.024	2.466	0.003	62.870	1.179	13.0842	0.0179	0.1806	2.163	0.041	-1.17	-0.89	-0.11	37.01	-0.333	-0.040	12.1
MH66-2d	4	6%	2998.240	1.349	46.720	0.025	1.884	0.004	64.898	1.044	9.9970	0.0197	0.1659	2.431	0.039	0.45	0.29	0.13	49.41	0.109	0.048	44.6
MH66-2e	5	7%	2134.026	0.875	38.781	0.021	1.309	0.003	59.485	1.194	6.9452	0.0174	0.1377	2.684	0.054	2.83	1.56	0.14	59.70	0.584	0.051	8.7
MH66-2f	6	8%	1474.878	0.531	32.612	0.016	0.886	0.002	57.543	1.399	4.7014	0.0081	0.1158	3.088	0.075	4.83	2.18	0.08	68.35	0.818	0.028	3.5
MH66-2g	7	10%	1227.783	0.307	34.613	0.012	0.723	0.001	70.846	1.559	3.8336	0.0052	0.1229	3.582	0.079	6.78	2.40	0.05	77.54	0.901	0.017	1.9
MH66-2h	8	14%	1059.714	0.434	39.145	0.032	0.610	0.001	107.837	1.316	3.2354	0.0062	0.1390	4.821	0.059	8.85	2.39	0.05	87.93	0.897	0.018	2.0
MH66-2i	9	20%	662.454	0.166	26.453	0.022	0.380	0.001	142.305	1.336	2.0175	0.0031	0.0939	9.414	0.089	9.07	2.27	0.04	94.94	0.851	0.013	1.6
MH66-2j	10	35%	578.832	0.174	19.052	0.013	0.342	0.001	180.487	1.175	1.8149	0.0040	0.0676	16.578	0.109	6.39	1.94	0.06	100.00	0.727	0.024	3.3
																			Total gas age:	0.156 ± 0.008 Ma (2σ)		

[a] Data are corrected for mass spectrometer backgrounds, discrimination, radioactive decay and interference corrections. Errors are one sigma uncertainties and exclude uncertainties in the J-value (propagating this error only has an effect in the third decimal place)

[b] Interference corrections: $(^{36}Ar/^{37}Ar)_{Ca}$ = (2.5798 ± 0.0027) x 10^{-4}; $(^{39}Ar/^{37}Ar)_{Ca}$ = (6.5640 ± 0.0135) x 10^{-4}; $(^{40}Ar/^{39}Ar)_{K}$ = (3.8900 ± 0.2140) x 10^{-4}; $(^{38}Ar/^{39}Ar)_{K}$ = (1.1999 ± 0.0004) x 10^{-2}

[c] J-value is 0.0002077283 ± 0.0000000558 (0.027%; 1σ), based on an age of 1.1814 ± 0.0006 Ma (2σ) for ACR sanidine (Phillips et al., 2017)

[d] Sensitivity = 3.55 x 10^{-17} mol/fA

Table A.3g. ARGUSVI ^{40}Ar/^{39}Ar laser step-heating analytical results for sample MH70.[a,b,c,d]

Sample ID	Step No	Laser Power	^{40}Ar (fA)	±1σ	^{39}Ar (fA)[b]	±1σ	^{38}Ar (fA)	±1σ	^{37}Ar (fA)[b]	±1σ	^{36}Ar (fA)	±1σ	^{39}Ar ($\times 10^{-14}$ mol)[d]	Ca/K	±1σ	%^{40}Ar*	^{40}Ar*/^{39}Ar	±1σ	Cum.% ^{39}Ar	Apparent Age (Ma)	±1σ	±1σ (%)
Aliquant: MH70-1		31.1 mg																				
MH70-1a	1	3%	1916.476	0.575	21.404	0.013	1.198	0.002	24.062	0.705	6.3530	0.0088	0.0760	1.967	0.058	1.03	0.92	0.12	8.86	0.345	0.047	13.6
MH70-1b	2	4%	2693.018	1.158	34.756	0.011	1.681	0.003	42.863	1.174	8.9198	0.0133	0.1234	2.158	0.059	1.11	0.86	0.12	23.24	0.322	0.044	13.8
MH70-1c	3	5%	2552.015	1.302	37.390	0.052	1.594	0.003	53.337	1.217	8.4570	0.0167	0.1327	2.496	0.057	1.06	0.72	0.14	38.71	0.271	0.051	19.0
MH70-1d	4	6%	1925.491	1.252	31.907	0.026	1.179	0.001	51.269	1.511	6.2523	0.0072	0.1133	2.812	0.083	3.05	1.84	0.08	51.92	0.690	0.029	4.2
MH70-1e	5	8%	1972.755	0.730	37.535	0.029	1.203	0.002	74.210	1.269	6.3815	0.0104	0.1332	3.460	0.059	3.42	1.80	0.09	67.45	0.673	0.032	4.7
MH70-1f	6	10%	1227.167	0.331	27.311	0.023	0.737	0.001	66.127	1.194	3.9121	0.0073	0.0970	4.237	0.077	4.82	2.17	0.08	78.75	0.811	0.030	3.7
MH70-1g	7	14%	1099.657	0.319	26.179	0.015	0.658	0.001	87.779	0.831	3.4915	0.0040	0.0929	5.868	0.056	5.21	2.19	0.05	89.58	0.818	0.018	2.2
MH70-1h	8	20%	632.311	0.196	15.818	0.005	0.378	0.000	104.122	0.739	2.0058	0.0023	0.0562	11.519	0.082	5.29	2.11	0.05	96.13	0.791	0.017	2.1
MH70-1i	9	35%	432.046	0.078	9.351	0.012	0.260	0.001	81.204	0.583	1.3807	0.0038	0.0332	15.197	0.111	4.59	2.12	0.12	100.00	0.793	0.046	5.8
																			Total gas age:	0.577 ± 0.071 Ma (2σ)		
Aliquant: MH70-2		36.9 mg																				
MH70-2a	1	3%	3154.685	1.861	32.827	0.031	2.001	0.003	28.031	1.377	10.6138	0.0135	0.1165	1.494	0.073	-0.45	-0.43	-0.14	9.18	-0.161	-0.051	31.3
MH70-2b	2	4%	4040.505	0.929	47.453	0.036	2.595	0.003	52.326	1.344	13.7688	0.0159	0.1685	1.930	0.050	-1.74	-1.48	-0.10	22.45	-0.555	-0.038	6.9
MH70-2c	3	4.5%	2820.382	1.326	35.725	0.023	1.796	0.002	41.546	1.374	9.5281	0.0121	0.1268	2.035	0.067	-0.86	-0.68	-0.11	32.45	-0.255	-0.040	15.9
MH70-2d	4	5%	2198.980	1.187	30.106	0.030	1.382	0.002	39.179	0.864	7.3328	0.0107	0.1069	2.277	0.050	0.44	0.32	0.11	40.87	0.120	0.042	35.2
MH70-2e	5	6%	2350.169	1.128	36.199	0.030	1.472	0.003	51.874	1.001	7.8076	0.0140	0.1285	2.508	0.048	0.81	0.53	0.12	50.99	0.198	0.045	22.6
MH70-2f	6	8%	2789.734	1.479	49.899	0.028	1.730	0.003	85.000	1.111	9.1802	0.0163	0.1771	2.981	0.039	1.75	0.98	0.10	64.95	0.367	0.038	10.4
MH70-2g	7	10%	2039.251	0.734	42.599	0.017	1.231	0.002	84.594	0.991	6.5287	0.0123	0.1512	3.475	0.041	4.41	2.11	0.09	76.86	0.791	0.033	4.2
MH70-2h	8	12%	1193.478	0.310	29.539	0.019	0.708	0.001	78.802	0.994	3.7542	0.0062	0.1049	4.668	0.059	6.09	2.46	0.06	85.12	0.920	0.024	2.6
MH70-2i	9	14%	665.068	0.186	19.449	0.017	0.389	0.001	66.211	0.746	2.0644	0.0028	0.0690	5.958	0.067	7.32	2.50	0.04	90.56	0.937	0.017	1.8
MH70-2j	10	20%	656.535	0.184	19.202	0.022	0.388	0.001	110.932	1.335	2.0570	0.0028	0.0682	10.110	0.122	6.46	2.21	0.04	95.93	0.826	0.017	2.0
MH70-2k	11	35%	612.786	0.239	14.537	0.012	0.369	0.001	143.991	0.271	1.9587	0.0038	0.0516	17.334	0.036	4.57	1.93	0.08	100.00	0.721	0.030	4.2
																			Total gas age:	0.262 ± 0.072 Ma (2σ)		
Aliquant: MH70-3		33.0 mg																				
MH70-3a	1	4%	1776.005	0.195	32.298	0.020	1.068	0.001	54.686	2.544	5.6658	0.0063	0.1147	2.963	0.138	4.75	2.61	0.06	20.86	0.978	0.022	2.2
MH70-3b	2	5%	1425.921	0.371	31.038	0.018	0.848	0.001	57.396	1.588	4.4962	0.0056	0.1102	3.236	0.090	5.86	2.69	0.06	40.90	1.007	0.021	2.1
MH70-3c	3	6%	922.762	0.286	24.301	0.018	0.540	0.001	55.529	2.530	2.8655	0.0047	0.0863	3.999	0.182	7.29	2.77	0.06	56.59	1.035	0.022	2.1
MH70-3d	4	8%	737.024	0.184	22.922	0.012	0.429	0.001	78.576	0.560	2.2735	0.0044	0.0814	5.999	0.043	7.90	2.54	0.06	71.39	0.950	0.022	2.3
MH70-3e	5	10%	513.424	0.149	15.322	0.020	0.303	0.001	76.005	1.189	1.6055	0.0031	0.0544	8.681	0.136	6.64	2.22	0.06	81.28	0.832	0.023	2.7
MH70-3f	6	14%	523.100	0.136	12.639	0.015	0.314	0.001	106.440	2.262	1.6683	0.0034	0.0449	14.738	0.314	4.78	1.98	0.08	89.45	0.740	0.030	4.1
MH70-3g	7	20%	398.308	0.123	8.990	0.014	0.240	0.001	95.775	1.964	1.2748	0.0035	0.0319	18.645	0.384	4.44	1.97	0.12	95.25	0.737	0.044	6.0
MH70-3h	8	35%	313.635	0.110	7.355	0.019	0.188	0.001	68.574	2.687	0.9988	0.0029	0.0261	16.315	0.641	4.92	2.10	0.12	100.00	0.786	0.044	5.6
																			Total gas age:	0.931 ± 0.049 Ma (2σ)		

[a] Data are corrected for mass spectrometer backgrounds, discrimination, radioactive decay and interference corrections. Errors are one sigma uncertainties and exclude uncertainties in the J-value (propagating this error only has an effect in the third decimal place)

[b] Interference corrections: $(^{36}\text{Ar}/^{37}\text{Ar})_{\text{Ca}} = (2.5798 \pm 0.0027) \times 10^{-4}$; $(^{39}\text{Ar}/^{37}\text{Ar})_{\text{Ca}} = (6.5640 \pm 0.0135) \times 10^{-4}$; $(^{40}\text{Ar}/^{39}\text{Ar})_{\text{K}} = (3.8900 \pm 0.2140) \times 10^{-4}$; $(^{38}\text{Ar}/^{39}\text{Ar})_{\text{K}} = (1.1999 \pm 0.0004) \times 10^{-2}$

[c] J-value is 0.0002074027 ± 0.0000000594 (0.029%;1σ), based on an age of 1.1814 ± 0.0006 Ma (2σ) for ACR sanidine (Phillips et al., 2017)

[d] Sensitivity = 3.55×10^{-17} mol/fA

Table A.3h. ARGUSVI ^{40}Ar/^{39}Ar laser step-heating analytical results for sample MO43B.[a,b,c,d]

Sample ID	Step No	Laser Power	^{40}Ar (fA)	±1σ	^{39}Ar (fA)[b]	±1σ	^{38}Ar (fA)	±1σ	^{37}Ar (fA)[b]	±1σ	^{36}Ar (fA)	±1σ	^{39}Ar (x10^{-14} mol)[d]	Ca/K	±1σ	%^{40}Ar*	^{40}Ar*/^{39}Ar	±1σ	Cum.% ^{39}Ar	Apparent Age (Ma)	±1σ	±1σ (%)
Aliquant: MO43B-1		40.8 mg																				
MO43B-1a	1	3%	699.168	0.112	80.475	0.020	0.329	0.001	73.186	1.120	1.7448	0.0037	0.2857	1.592	0.024	25.49	2.22	0.01	23.85	0.834	0.005	0.6
MO43B-1b	2	4%	634.423	0.152	88.515	0.028	0.280	0.001	82.350	2.164	1.4875	0.0041	0.3142	1.628	0.043	30.00	2.15	0.01	50.08	0.810	0.005	0.6
MO43B-1c	3	5%	381.547	0.095	58.021	0.007	0.164	0.000	65.180	2.026	0.8677	0.0019	0.2060	1.966	0.061	32.10	2.11	0.01	67.28	0.795	0.004	0.5
MO43B-1d	4	6%	262.070	0.050	36.200	0.015	0.117	0.000	55.177	2.180	0.6221	0.0026	0.1285	2.667	0.105	29.13	2.11	0.02	78.00	0.794	0.008	1.0
MO43B-1e	5	8%	263.169	0.042	29.789	0.016	0.127	0.000	76.190	0.371	0.6721	0.0017	0.1057	4.476	0.022	23.76	2.10	0.02	86.83	0.790	0.007	0.8
MO43B-1f	6	10%	221.572	0.091	19.868	0.015	0.114	0.000	79.769	0.620	0.6059	0.0017	0.0705	7.026	0.055	18.35	2.05	0.03	92.72	0.771	0.010	1.3
MO43B-1g	7	20%	326.686	0.124	17.536	0.011	0.183	0.001	207.941	2.117	0.9730	0.0032	0.0623	20.751	0.212	11.08	2.06	0.06	97.92	0.777	0.021	2.7
MO43B-1h	8	35%	388.668	0.097	7.026	0.011	0.238	0.001	90.780	1.974	1.2609	0.0040	0.0249	22.610	0.493	3.14	1.74	0.17	100.00	0.655	0.064	9.7
																			Total gas age:	0.802 ± 0.015 Ma (2σ)		
Aliquant: MO43B-2		66.9 mg																				
MO43B-2a	1	3%	1568.595	0.722	161.959	0.110	0.780	0.002	153.872	2.964	4.1378	0.0086	0.5750	1.663	0.032	21.24	2.06	0.02	25.33	0.775	0.006	0.8
MO43B-2b	2	3.5%	754.063	0.204	103.466	0.089	0.344	0.001	93.782	2.601	1.8248	0.0038	0.3673	1.586	0.044	27.75	2.02	0.01	41.51	0.761	0.004	0.6
MO43B-2c	3	4%	555.167	0.222	83.482	0.132	0.241	0.001	78.453	2.649	1.2774	0.0057	0.2964	1.645	0.056	31.30	2.08	0.02	54.56	0.784	0.008	1.0
MO43B-2d	4	5%	622.765	0.218	93.392	0.070	0.275	0.001	107.091	3.200	1.4580	0.0045	0.3315	2.007	0.060	30.10	2.01	0.01	69.16	0.756	0.006	0.7
MO43B-2e	5	6%	460.806	0.157	67.346	0.030	0.204	0.000	97.890	2.219	1.0796	0.0025	0.2391	2.544	0.058	30.05	2.06	0.01	79.70	0.774	0.004	0.6
MO43B-2f	6	8%	509.426	0.275	60.120	0.049	0.246	0.001	146.582	1.879	1.3042	0.0041	0.2134	4.267	0.055	23.57	2.00	0.02	89.10	0.752	0.008	1.0
MO43B-2g	7	10%	325.039	0.189	30.208	0.029	0.166	0.000	118.452	2.056	0.8799	0.0011	0.1072	6.862	0.119	19.18	2.06	0.01	93.82	0.777	0.005	0.6
MO43B-2h	8	20%	518.537	0.322	28.159	0.024	0.292	0.000	351.777	2.142	1.5473	0.0021	0.1000	21.862	0.134	10.91	2.01	0.03	98.22	0.756	0.009	1.2
MO43B-2i	9	35%	265.627	0.157	11.357	0.019	0.154	0.001	151.784	3.430	0.8147	0.0029	0.0403	23.388	0.530	8.43	1.97	0.08	100.00	0.742	0.029	4.0
																			Total gas age:	0.767 ± 0.013 Ma (2σ)		

[a] Data are corrected for mass spectrometer backgrounds, discrimination, radioactive decay and interference corrections. Errors are one sigma uncertainties and exclude uncertainties in the J-value (propagating this error only has an effect in the third decimal place)

[b] Interference corrections: $(^{36}Ar/^{37}Ar)_{Ca}$ = (2.5798 ± 0.0027) x 10^{-4}; $(^{39}Ar/^{37}Ar)_{Ca}$ = (6.5640 ± 0.0135) x 10^{-4}; $(^{40}Ar/^{39}Ar)_{K}$ = (3.8900 ± 0.2140) x 10^{-4}; $(^{38}Ar/^{39}Ar)_{K}$ = (1.1999 ± 0.0004) x 10^{-2}

[c] J-value is 0.0002087526 ± 0.0000000553 (0.027%;1σ), based on an age of 1.1814 ± 0.0006 Ma (2σ) for ACR sanidine (Phillips et al., 2017)

[d] Sensitivity = 3.55 x 10^{-17} mol/fA

Table A.3i. ARGUSVI ^{40}Ar/^{39}Ar laser step-heating analytical results for sample WW1A.[a,b,c,d]

Sample ID	Step No	Laser Power	^{40}Ar (fA)	±1σ	^{39}Ar (fA)[b]	±1σ	^{38}Ar (fA)	±1σ	^{37}Ar (fA)[b]	±1σ	^{36}Ar (fA)	±1σ	^{39}Ar (x10^{-14} mol)[d]	Ca/K	±1σ	%^{40}Ar*	^{40}Ar*/^{39}Ar	±1σ	Cum.% ^{39}Ar	Apparent Age (Ma)	±1σ	±1σ (%)
Aliquant: WW1A-1		41.2 mg																				
WW1A-1a	1	3%	221.004	0.046	59.644	0.022	0.058	0.000	63.618	2.052	0.3094	0.0009	0.2117	1.867	0.060	58.20	2.16	0.00	13.09	0.814	0.002	0.2
WW1A-1b	2	4%	309.077	0.049	87.761	0.018	0.076	0.000	76.229	1.729	0.4017	0.0023	0.3115	1.520	0.034	61.19	2.16	0.01	32.34	0.814	0.003	0.4
WW1A-1c	3	5%	304.632	0.055	84.050	0.028	0.078	0.000	60.478	1.779	0.4138	0.0013	0.2984	1.259	0.037	59.44	2.15	0.00	50.79	0.813	0.002	0.2
WW1A-1d	4	6%	276.447	0.061	68.528	0.022	0.082	0.000	46.162	1.673	0.4337	0.0020	0.2433	1.179	0.043	53.15	2.14	0.01	65.82	0.810	0.003	0.4
WW1A-1e	5	8%	372.109	0.123	67.419	0.016	0.144	0.001	52.940	1.797	0.7638	0.0030	0.2393	1.374	0.047	38.72	2.14	0.01	80.62	0.807	0.005	0.6
WW1A-1f	6	10%	343.912	0.086	44.073	0.007	0.158	0.000	46.939	1.924	0.8367	0.0026	0.1565	1.864	0.076	27.36	2.14	0.02	90.29	0.806	0.007	0.8
WW1A-1g	7	20%	866.745	0.364	36.625	0.015	0.503	0.001	148.549	1.818	2.6676	0.0075	0.1300	7.098	0.087	8.11	1.92	0.06	98.33	0.725	0.023	3.2
WW1A-1h	8	35%	507.841	0.132	7.629	0.013	0.312	0.001	65.734	2.531	1.6573	0.0064	0.0271	15.079	0.581	2.57	1.71	0.25	100.00	0.645	0.095	14.7
																			Total gas age:	0.801 ± 0.013 Ma (2σ)		
Aliquant: WW1A-2		39.5 mg																				
WW1A-2a	1	3%	298.451	0.087	78.136	0.026	0.082	0.000	82.111	1.894	0.4364	0.0018	0.2774	1.839	0.042	56.34	2.15	0.01	18.92	0.812	0.003	0.3
WW1A-2b	2	4%	318.452	0.092	85.780	0.032	0.085	0.000	68.393	2.593	0.4502	0.0016	0.3045	1.395	0.053	57.78	2.15	0.01	39.69	0.810	0.002	0.3
WW1A-2c	3	5%	296.020	0.056	73.695	0.018	0.087	0.000	54.960	2.002	0.4628	0.0014	0.2616	1.305	0.048	53.32	2.14	0.01	57.54	0.809	0.002	0.3
WW1A-2d	4	6%	271.836	0.049	57.001	0.033	0.094	0.000	41.716	1.626	0.5013	0.0012	0.2024	1.281	0.050	44.94	2.14	0.01	71.34	0.809	0.002	0.3
WW1A-2e	5	8%	362.844	0.087	53.309	0.025	0.158	0.000	55.568	1.305	0.8400	0.0019	0.1892	1.824	0.043	30.88	2.10	0.01	84.25	0.794	0.004	0.5
WW1A-2f	6	10%	340.911	0.130	32.312	0.031	0.173	0.001	48.272	2.589	0.9157	0.0029	0.1147	2.614	0.140	19.80	2.09	0.03	92.08	0.789	0.010	1.3
WW1A-2g	7	20%	749.268	0.142	25.298	0.014	0.443	0.001	129.039	1.968	2.3504	0.0042	0.0898	8.926	0.136	6.34	1.88	0.05	98.20	0.709	0.019	2.6
WW1A-2h	8	35%	474.204	0.213	7.426	0.015	0.290	0.001	65.600	2.036	1.5393	0.0035	0.0264	15.459	0.481	3.09	1.97	0.14	100.00	0.744	0.055	7.3
																			Total gas age:	0.798 ± 0.010 Ma (2σ)		
Aliquant: WW1A-3		38.0 mg																				
WW1A-3a	1	3%	248.123	0.067	65.020	0.033	0.069	0.000	69.569	2.196	0.3646	0.0019	0.2308	1.872	0.059	56.12	2.14	0.01	16.52	0.809	0.003	0.4
WW1A-3b	2	4%	286.321	0.112	79.577	0.050	0.074	0.000	66.503	1.591	0.3903	0.0006	0.2825	1.462	0.035	59.30	2.13	0.00	36.73	0.806	0.001	0.1
WW1A-3c	3	5%	263.900	0.079	69.744	0.029	0.072	0.000	47.485	2.046	0.3844	0.0010	0.2476	1.191	0.051	56.50	2.14	0.00	54.45	0.807	0.002	0.2
WW1A-3d	4	6%	240.679	0.094	55.965	0.029	0.077	0.000	35.140	1.786	0.4066	0.0015	0.1987	1.099	0.056	49.55	2.13	0.01	68.67	0.805	0.003	0.4
WW1A-3e	5	8%	308.518	0.096	53.819	0.030	0.123	0.000	45.249	2.283	0.6500	0.0016	0.1911	1.471	0.074	37.10	2.13	0.01	82.34	0.803	0.003	0.4
WW1A-3f	6	10%	298.682	0.078	35.164	0.015	0.142	0.001	40.723	1.616	0.7512	0.0033	0.1248	2.027	0.080	24.91	2.12	0.03	91.27	0.799	0.011	1.3
WW1A-3g	7	20%	693.721	0.229	27.518	0.027	0.403	0.000	126.521	2.687	2.1388	0.0025	0.0977	8.046	0.171	7.95	2.00	0.03	98.26	0.757	0.011	1.4
WW1A-3h	8	35%	388.790	0.117	6.838	0.010	0.238	0.001	62.376	2.135	1.2606	0.0036	0.0243	15.963	0.547	3.19	1.81	0.16	100.00	0.685	0.060	8.8
																			Total gas age:	0.799 ± 0.009 Ma (2σ)		

[a] Data are corrected for mass spectrometer backgrounds, discrimination, radioactive decay and interference corrections. Errors are one sigma uncertainties and exclude uncertainties in the J-value (propagating this error only has an effect in the third decimal place)

[b] Interference corrections: $(^{36}\mathrm{Ar}/^{37}\mathrm{Ar})_{Ca} = (2.5798 \pm 0.0027) \times 10^{-4}$; $(^{39}\mathrm{Ar}/^{37}\mathrm{Ar})_{Ca} = (6.5640 \pm 0.0135) \times 10^{-4}$; $(^{40}\mathrm{Ar}/^{39}\mathrm{Ar})_{K} = (3.8900 \pm 0.2140) \times 10^{-4}$; $(^{38}\mathrm{Ar}/^{39}\mathrm{Ar})_{K} = (1.1999 \pm 0.0004) \times 10^{-2}$

[c] J-value is 0.0002092906 ± 0.0000001057 (0.051%;1σ), based on an age of 1.1814 ± 0.0006 Ma (2σ) for ACR sanidine (Phillips et al., 2017)

[d] Sensitivity = 3.55 x 10^{-17} mol/fA

Table A.3j. ARGUSVI ^{40}Ar/^{39}Ar laser step-heating analytical results for sample YY3C.[a,b,c,d]

Sample ID	Step No	Laser Power	^{40}Ar (fA)	±1σ	^{39}Ar (fA)[b]	±1σ	^{38}Ar (fA)	±1σ	^{37}Ar (fA)[b]	±1σ	^{36}Ar (fA)	±1σ	^{39}Ar (x10^{-14} mol)[d]	Ca/K	±1σ	%^{40}Ar*	^{40}Ar*/^{39}Ar	±1σ	Cum.% ^{39}Ar	Apparent Age (Ma)	±1σ	±1σ (%)
Aliquant: YY3C-1		43.0 mg																				
YY3C-1a	1	3%	449.536	0.063	92.538	0.035	0.159	0.000	92.996	2.364	0.8432	0.0018	0.3285	1.759	0.045	43.99	2.14	0.01	16.20	0.803	0.002	0.3
YY3C-1b	2	4%	528.967	0.074	123.291	0.036	0.168	0.000	112.183	2.198	0.8910	0.0025	0.4377	1.592	0.031	49.70	2.13	0.01	37.78	0.801	0.002	0.3
YY3C-1c	3	5%	432.756	0.143	105.479	0.039	0.131	0.000	91.598	1.608	0.6940	0.0022	0.3745	1.520	0.027	52.12	2.14	0.01	56.25	0.803	0.002	0.3
YY3C-1d	4	6%	347.458	0.042	84.362	0.018	0.105	0.000	72.336	1.630	0.5558	0.0019	0.2995	1.501	0.034	52.24	2.15	0.01	71.02	0.808	0.003	0.3
YY3C-1e	5	8%	363.503	0.076	79.011	0.043	0.123	0.000	86.717	0.879	0.6507	0.0023	0.2805	1.921	0.020	46.55	2.14	0.01	84.85	0.804	0.003	0.4
YY3C-1f	6	10%	248.687	0.062	45.409	0.030	0.097	0.000	71.951	1.305	0.5129	0.0018	0.1612	2.773	0.050	38.42	2.10	0.01	92.80	0.790	0.005	0.6
YY3C-1g	7	14%	210.562	0.095	26.144	0.037	0.098	0.000	90.213	2.005	0.5187	0.0013	0.0928	6.039	0.135	26.45	2.13	0.02	97.38	0.800	0.006	0.7
YY3C-1h	8	20%	125.886	0.081	10.152	0.008	0.066	0.000	74.277	2.319	0.3482	0.0018	0.0360	12.804	0.400	17.42	2.16	0.05	99.15	0.811	0.020	2.5
YY3C-1i	9	35%	90.488	0.081	4.832	0.020	0.051	0.000	46.899	2.333	0.2691	0.0023	0.0172	16.985	0.848	11.20	2.10	0.14	100.00	0.788	0.054	6.8
																			Total gas age:	0.802 ± 0.007 Ma (2σ)		
Aliquant: YY3C-2		41.5 mg																				
YY3C-2a	1	3%	358.826	0.043	65.111	0.027	0.139	0.000	70.910	1.722	0.7350	0.0018	0.2311	1.906	0.046	38.85	2.14	0.01	12.01	0.804	0.003	0.4
YY3C-2b	2	4%	455.756	0.132	99.526	0.044	0.154	0.001	95.944	1.262	0.8189	0.0034	0.3533	1.687	0.022	46.35	2.12	0.01	30.36	0.797	0.004	0.5
YY3C-2c	3	5%	406.945	0.077	97.865	0.044	0.124	0.000	85.431	1.335	0.6601	0.0020	0.3474	1.528	0.024	51.57	2.14	0.01	48.40	0.805	0.002	0.3
YY3C-2d	4	6%	341.125	0.058	83.837	0.044	0.102	0.000	71.334	1.129	0.5411	0.0016	0.2976	1.489	0.024	52.63	2.14	0.01	63.86	0.804	0.002	0.3
YY3C-2e	5	8%	380.941	0.130	87.451	0.039	0.122	0.000	84.472	0.986	0.6484	0.0013	0.3105	1.690	0.020	49.18	2.14	0.00	79.98	0.805	0.002	0.2
YY3C-2f	6	10%	276.965	0.072	57.120	0.024	0.097	0.000	71.330	1.166	0.5149	0.0010	0.2028	2.185	0.036	44.49	2.16	0.01	90.51	0.810	0.002	0.3
YY3C-2g	7	20%	350.609	0.109	42.291	0.019	0.165	0.000	157.665	1.769	0.8742	0.0019	0.1501	6.524	0.073	25.55	2.12	0.01	98.31	0.796	0.005	0.7
YY3C-2h	8	35%	130.448	0.017	9.163	0.009	0.071	0.000	72.368	1.688	0.3740	0.0011	0.0325	13.821	0.323	14.39	2.05	0.04	100.00	0.770	0.013	1.7
																			Total gas age:	0.802 ± 0.006 Ma (2σ)		
Aliquant: YY3C-3		48.7 mg																				
YY3C-3a	1	3%	562.062	0.141	107.495	0.040	0.211	0.000	110.349	2.487	1.1209	0.0013	0.3816	1.796	0.040	40.45	2.12	0.00	16.44	0.795	0.002	0.2
YY3C-3b	2	4%	572.040	0.114	128.419	0.051	0.188	0.000	122.478	1.830	0.9972	0.0019	0.4559	1.669	0.025	47.95	2.14	0.00	36.09	0.802	0.002	0.2
YY3C-3c	3	5%	478.567	0.129	114.076	0.027	0.148	0.000	97.835	1.968	0.7849	0.0015	0.4050	1.501	0.030	51.03	2.14	0.00	53.53	0.804	0.002	0.2
YY3C-3d	4	6%	401.091	0.132	95.420	0.041	0.125	0.000	80.784	1.967	0.6612	0.0025	0.3387	1.482	0.036	50.78	2.13	0.01	68.13	0.802	0.003	0.4
YY3C-3e	5	8%	436.119	0.127	94.740	0.018	0.148	0.000	97.011	2.279	0.7863	0.0013	0.3363	1.792	0.042	46.16	2.13	0.00	82.62	0.798	0.002	0.2
YY3C-3f	6	10%	312.785	0.047	59.108	0.027	0.118	0.000	85.456	2.003	0.6268	0.0020	0.2098	2.530	0.059	40.17	2.13	0.01	91.66	0.798	0.004	0.5
YY3C-3g	7	20%	394.049	0.134	44.207	0.016	0.190	0.000	182.415	1.810	1.0066	0.0016	0.1569	7.221	0.072	23.73	2.12	0.01	98.43	0.795	0.004	0.5
YY3C-3h	8	35%	295.789	0.092	10.295	0.015	0.172	0.000	81.036	1.929	0.9146	0.0016	0.0365	13.775	0.328	7.68	2.21	0.05	100.00	0.829	0.018	2.2
																			Total gas age:	0.800 ± 0.005 Ma (2σ)		

[a] Data are corrected for mass spectrometer backgrounds, discrimination, radioactive decay and interference corrections. Errors are one sigma uncertainties and exclude uncertainties in the J-value (propagating this error only has an effect in the third decimal place)

[b] Interference corrections: $(^{36}\mathrm{Ar}/^{37}\mathrm{Ar})_{\mathrm{Ca}}$ = (2.5798 ± 0.0027) x 10^{-4}; $(^{39}\mathrm{Ar}/^{37}\mathrm{Ar})_{\mathrm{Ca}}$ = (6.5640 ± 0.0135) x 10^{-4}; $(^{40}\mathrm{Ar}/^{39}\mathrm{Ar})_{\mathrm{K}}$ = (3.8900 ± 0.2140) x 10^{-4}; $(^{38}\mathrm{Ar}/^{39}\mathrm{Ar})_{\mathrm{K}}$ = (1.1999 ± 0.0004) x 10^{-2}

[c] J-value is 0.0002082306 ± 0.0000000583 (0.028%;1σ), based on an age of 1.1814 ± 0.0006 Ma (2σ) for ACR sanidine (Phillips et al., 2017)

[d] Sensitivity = 3.55 x 10^{-17} mol/fA

Table A.3k. ARGUSVI ^{40}Ar/^{39}Ar laser step-heating analytical results for sample YY6.[a,b,c,d]

Sample ID	Step No	Laser Power	^{40}Ar (fA)	±1σ	^{39}Ar (fA)[b]	±1σ	^{38}Ar (fA)	±1σ	^{37}Ar (fA)[b]	±1σ	^{36}Ar (fA)	±1σ	^{39}Ar (x10^{-14} mol)[d]	Ca/K	±1σ	%^{40}Ar*	^{40}Ar*/^{39}Ar	±1σ	Cum.% ^{39}Ar	Apparent Age (Ma)	±1σ	±1σ (%)
Aliquant: YY6-1		39.7 mg																				
YY6-1a	1	3%	365.690	0.059	84.664	0.058	0.119	0.000	63.865	1.304	0.6306	0.0016	0.3006	1.320	0.027	48.52	2.10	0.01	25.32	0.790	0.002	0.3
YY6-1b	2	3.5%	252.793	0.063	59.817	0.047	0.080	0.000	50.412	1.338	0.4270	0.0009	0.2124	1.475	0.039	49.57	2.09	0.00	43.21	0.790	0.002	0.2
YY6-1c	3	4%	195.773	0.090	46.275	0.022	0.061	0.000	38.701	1.511	0.3232	0.0010	0.1643	1.464	0.057	50.71	2.15	0.01	57.06	0.809	0.003	0.3
YY6-1d	4	5%	239.030	0.105	50.854	0.022	0.083	0.000	53.088	1.285	0.4378	0.0011	0.1805	1.827	0.044	45.31	2.13	0.01	72.27	0.803	0.003	0.3
YY6-1e	5	7%	289.247	0.093	50.426	0.024	0.115	0.000	87.562	1.629	0.6116	0.0025	0.1790	3.039	0.057	36.86	2.11	0.01	87.35	0.798	0.006	0.7
YY6-1f	6	10%	237.977	0.095	28.374	0.026	0.113	0.000	117.979	1.798	0.6005	0.0025	0.1007	7.276	0.111	24.66	2.07	0.03	95.84	0.780	0.010	1.3
YY6-1g	7	20%	184.329	0.063	11.231	0.009	0.102	0.000	178.346	2.199	0.5405	0.0016	0.0399	27.789	0.343	12.45	2.04	0.04	99.19	0.771	0.016	2.1
YY6-1h	8	35%	63.880	0.022	2.694	0.011	0.037	0.000	73.762	1.922	0.1958	0.0015	0.0096	47.923	1.264	8.50	2.02	0.16	100.00	0.761	0.062	8.1
																			Total gas age:	0.794 ± 0.009 Ma (2σ)		
Aliquant: YY6-2		56.9 mg																				
YY6-2a	1	2.5%	277.186	0.105	56.281	0.037	0.099	0.000	43.119	3.134	0.5245	0.0018	0.1998	1.341	0.097	43.50	2.14	0.01	9.53	0.808	0.004	0.4
YY6-2b	2	3%	323.056	0.103	69.868	0.028	0.112	0.001	57.319	3.591	0.5944	0.0028	0.2480	1.436	0.090	45.06	2.08	0.01	21.37	0.786	0.005	0.6
YY6-2c	3	4%	508.508	0.097	118.606	0.197	0.167	0.000	96.506	1.979	0.8842	0.0017	0.4211	1.424	0.029	48.08	2.06	0.01	41.46	0.778	0.002	0.3
YY6-2d	4	5%	454.231	0.095	106.510	0.093	0.146	0.000	96.198	2.780	0.7762	0.0021	0.3781	1.581	0.046	48.98	2.09	0.01	59.50	0.788	0.002	0.3
YY6-2e	5	6%	335.332	0.211	75.480	0.050	0.111	0.000	74.313	2.813	0.5881	0.0012	0.2680	1.723	0.065	47.64	2.12	0.01	72.29	0.798	0.002	0.3
YY6-2f	6	8%	398.286	0.231	74.020	0.033	0.153	0.000	108.557	2.760	0.8101	0.0024	0.2628	2.567	0.065	39.27	2.11	0.01	84.83	0.797	0.004	0.5
YY6-2g	7	10%	259.874	0.125	42.845	0.035	0.107	0.000	97.860	1.578	0.5671	0.0026	0.1521	3.997	0.065	34.84	2.11	0.02	92.09	0.797	0.007	0.9
YY6-2h	8	20%	381.466	0.164	39.388	0.025	0.189	0.001	275.811	1.776	1.0028	0.0029	0.1398	12.254	0.079	21.51	2.08	0.02	98.76	0.786	0.008	1.1
YY6-2i	9	35%	481.490	0.270	7.318	0.010	0.296	0.001	142.866	1.870	1.5705	0.0027	0.0260	34.163	0.450	2.62	1.72	0.12	100.00	0.650	0.044	6.8
																			Total gas age:	0.789 ± 0.008 Ma (2σ)		

[a] Data are corrected for mass spectrometer backgrounds, discrimination, radioactive decay and interference corrections. Errors are one sigma uncertainties and exclude uncertainties in the J-value (propagating this error only has an effect in the third decimal place)

[b] Interference corrections: $(^{36}Ar/^{37}Ar)_{Ca} = (2.5798 \pm 0.0027) \times 10^{-4}$; $(^{39}Ar/^{37}Ar)_{Ca} = (6.5640 \pm 0.0135) \times 10^{-4}$; $(^{40}Ar/^{39}Ar)_{K} = (3.8900 \pm 0.2140) \times 10^{-4}$; $(^{38}Ar/^{39}Ar)_{K} = (1.1999 \pm 0.0004) \times 10^{-2}$

[c] J-value is 0.0002091058 ± 0.0000000502 (0.024%;1σ), based on an age of 1.1814 ± 0.0006 Ma (2σ) for ACR sanidine (Phillips et al., 2017)

[d] Sensitivity = 3.55 x 10^{-17} mol/fA

Table A.3k. Mount Fraser Flow (Flow A) age calculation

Sample: YY3C

Step ID:	$^{40}Ar^*/^{39}Ar_K$	±1σ
YY3C-1a	2.137	0.006
YY3C-1b	2.133	0.006
YY3C-1c	2.138	0.006
YY3C-1d	2.152	0.007
YY3C-1e	2.142	0.009
YY3C-1f	2.104	0.012
YY3C-1g	2.131	0.015
YY3C-1h	2.160	0.054
YY3C-1i	2.098	0.143
YY3C-2a	2.141	0.008
YY3C-2b	2.123	0.010
YY3C-2c	2.144	0.006
YY3C-2d	2.142	0.006
YY3C-2e	2.142	0.005
YY3C-2f	2.157	0.006
YY3C-2g	2.119	0.014
YY3C-3b	2.136	0.005
YY3C-3c	2.141	0.004
YY3C-3d	2.135	0.008

		±95% CI	±1σ
Weighted Avg:	2.1402	0.0043	0.00215
λ:	5.543E-10		
J:	0.0002082		5.83E-08

$t = 1/\lambda \ln (1 + J\,(^{40}Ar^*/^{39}Ar_K))$

Age (Ma): 0.8038 ± 0.0017 (2σ)

Appendix A.4. ARGUSVI ^{40}Ar/^{39}Ar laser step-heating analytical results for Tulloch Hill Flow (Flow B) samples

Table A.4a. ARGUSVI ^{40}Ar/^{39}Ar laser step-heating analytical results for sample BH45B.[a,b,c,d,e]

Sample ID	Step No	Laser Power	^{40}Ar (fA)	±1σ	^{39}Ar (fA)[b]	±1σ	^{38}Ar (fA)	±1σ	^{37}Ar (fA)[b]	±1σ	^{36}Ar (fA)	±1σ	^{39}Ar ($\times10^{-14}$ mol)[d]	Ca/K	±1σ	%^{40}Ar*	^{40}Ar*/^{39}Ar	±1σ	Cum.% ^{39}Ar	Apparent Age (Ma)	±1σ	±1σ (%)
Aliquant: BH45B-1		30.1 mg																				
BH45B-1a[e]	1	2.5%	310.665	0.435	33.837	0.021	0.061	0.001	13.810	0.408	0.3247	0.0042	0.1201	0.714	0.021	68.79	6.32	0.04	8.72	2.282	0.014	0.6
BH45B-1b[e]	2	4%	873.531	0.533	107.492	0.115	0.120	0.000	73.535	0.588	0.6386	0.0007	0.3816	1.197	0.010	78.17	6.35	0.01	36.43	2.295	0.003	0.1
BH45B-1c[e]	3	6%	959.767	0.691	120.825	0.129	0.124	0.000	145.658	0.517	0.6600	0.0007	0.4289	2.110	0.008	79.46	6.31	0.01	67.57	2.280	0.003	0.1
BH45B-1d[e]	4	8%	550.230	0.396	65.744	0.047	0.087	0.000	160.480	0.740	0.4589	0.0024	0.2334	4.272	0.020	75.10	6.29	0.01	84.52	2.270	0.005	0.2
BH45B-1e[e]	5	12%	403.962	0.432	40.456	0.036	0.090	0.000	212.534	0.771	0.4773	0.0016	0.1436	9.194	0.034	64.72	6.46	0.02	94.95	2.334	0.006	0.3
BH45B-1f	6	20%	295.616	0.124	19.612	0.039	0.095	0.000	239.396	0.519	0.5028	0.0014	0.0696	21.362	0.063	49.22	7.42	0.03	100.00	2.680	0.010	0.4
																			Total gas age:	2.30 ± 0.01 Ma (2σ)		
Aliquant: BH45B-2		42.5 mg																				
BH45B-2a[e]	1	3%	711.539	0.363	60.287	0.027	0.215	0.000	31.116	0.863	1.1397	0.0014	0.2140	0.903	0.025	52.17	6.16	0.01	10.23	2.225	0.003	0.2
BH45B-2b[e]	2	4%	851.406	0.239	85.893	0.065	0.192	0.001	49.173	0.830	1.0160	0.0048	0.3049	1.002	0.017	64.37	6.38	0.02	24.81	2.305	0.006	0.3
BH45B-2c[e]	3	5%	845.658	0.956	92.445	0.080	0.165	0.001	66.828	0.919	0.8743	0.0043	0.3282	1.265	0.017	69.13	6.32	0.02	40.50	2.284	0.007	0.3
BH45B-2d[e]	4	6%	692.102	0.374	84.510	0.090	0.101	0.001	79.528	1.241	0.5382	0.0034	0.3000	1.647	0.026	76.78	6.29	0.01	54.84	2.271	0.005	0.2
BH45B-2e[e]	5	8%	812.646	0.406	101.119	0.158	0.112	0.000	141.113	0.923	0.5960	0.0023	0.3590	2.442	0.016	78.10	6.28	0.01	72.01	2.267	0.005	0.2
BH45B-2f[e]	6	10%	681.486	0.116	84.761	0.091	0.094	0.002	169.348	0.740	0.5004	0.0083	0.3009	3.496	0.016	78.07	6.28	0.03	86.39	2.268	0.011	0.5
BH45B-2g[e]	7	14%	683.240	0.164	80.169	0.067	0.123	0.000	257.029	0.316	0.6502	0.0014	0.2846	5.611	0.008	71.58	6.10	0.01	100.00	2.204	0.003	0.1
																			Total gas age:	2.27 ± 0.01 Ma (2σ)		

[a] Data are corrected for mass spectrometer backgrounds, discrimination, radioactive decay and interference corrections. Errors are one sigma uncertainties and exclude uncertainties in the J-value (propagating this error only has an effect in the third decimal place)

[b] Interference corrections: $(^{36}Ar/^{37}Ar)_{Ca} = (2.5713 \pm 0.0023) \times 10^{-4}$; $(^{39}Ar/^{37}Ar)_{Ca} = (6.6200 \pm 0.0801) \times 10^{-4}$; $(^{40}Ar/^{39}Ar)_{K} = (4.9000 \pm 0.8575) \times 10^{-4}$; $(^{38}Ar/^{39}Ar)_{K} = (1.2136 \pm 0.0016) \times 10^{-2}$

[c] J-value is 0.0002003522 ± 0.0000001503 (0.075%;1σ), based on an age of 1.1814 ± 0.0006 Ma (2σ) for ACR sanidine (Phillips et al., 2017)

[d] Sensitivity = 3.55×10^{-17} mol/fA

[e] Heating steps where there was an indication of suppression of isotope signals, possibly due to hydrocarbon contamination. Affected cycles were removed from regression.

Table A.4b. ARGUSVI ^{40}Ar/^{39}Ar laser step-heating analytical results for sample GRBH-01.[a,b,c,d]

Sample ID	Step No	Laser Power	^{40}Ar (fA)	±1σ	^{39}Ar (fA)[b]	±1σ	^{38}Ar (fA)	±1σ	^{37}Ar (fA)[b]	±1σ	^{36}Ar (fA)	±1σ	^{39}Ar ($\times 10^{-14}$ mol)[d]	Ca/K	±1σ	%^{40}Ar*	^{40}Ar*/^{39}Ar	±1σ	Cum.% ^{39}Ar	Apparent Age (Ma)	±1σ	±1σ (%)
Aliquant: GRBH-01-1		44.6 mg																				
GRBH-01-1a	1	2.5%	1378.809	0.593	72.440	0.053	0.805	0.001	103.501	0.161	4.2730	0.0063	0.2572	2.500	0.004	7.47	1.42	0.03	6.69	2.002	0.038	1.9
GRBH-01-1b	2	3%	1456.732	0.626	93.121	0.066	0.837	0.002	142.383	0.266	4.4421	0.0112	0.3306	2.676	0.005	8.96	1.40	0.04	15.30	1.972	0.052	2.6
GRBH-01-1c	3	4%	1903.447	1.047	165.475	0.167	1.045	0.002	273.987	0.677	5.5428	0.0118	0.5874	2.898	0.008	13.06	1.50	0.02	30.59	2.114	0.031	1.5
GRBH-01-1d	4	5%	1408.780	0.507	166.746	0.068	0.709	0.001	285.692	0.174	3.7593	0.0055	0.5919	2.998	0.002	20.33	1.72	0.01	45.99	2.417	0.015	0.6
GRBH-01-1e	5	6%	886.016	0.337	146.966	0.081	0.399	0.001	265.475	0.231	2.1163	0.0047	0.5217	3.161	0.003	28.69	1.73	0.01	59.57	2.433	0.014	0.6
GRBH-01-1f	6	8%	702.432	0.288	162.574	0.091	0.269	0.001	355.606	0.199	1.4293	0.0030	0.5771	3.828	0.003	39.25	1.70	0.01	74.59	2.386	0.008	0.3
GRBH-01-1g	7	10%	435.809	0.122	119.616	0.054	0.150	0.001	348.391	0.185	0.7956	0.0030	0.4246	5.097	0.004	45.49	1.66	0.01	85.65	2.332	0.011	0.5
GRBH-01-1h	8	14%	357.014	0.189	87.885	0.022	0.133	0.000	499.934	0.185	0.7079	0.0020	0.3120	9.955	0.004	40.79	1.66	0.01	93.77	2.332	0.010	0.4
GRBH-01-1i	9	20%	228.341	0.055	41.924	0.039	0.101	0.000	480.874	0.322	0.5349	0.0017	0.1488	20.073	0.023	30.06	1.64	0.01	97.64	2.304	0.018	0.8
GRBH-01-1j	10	35%	184.446	0.061	25.556	0.029	0.090	0.000	330.987	0.149	0.4770	0.0012	0.0907	22.665	0.028	22.79	1.64	0.01	100.00	2.314	0.020	0.8
																			Total gas age:	2.28 ± 0.04 Ma (2σ)		

[a] Data are corrected for mass spectrometer backgrounds, discrimination, radioactive decay and interference corrections. Errors are one sigma uncertainties and exclude uncertainties in the J-value (propagating this error only has an effect in the third decimal place)

[b] Interference corrections: $(^{36}Ar/^{37}Ar)_{Ca} = (2.5798 \pm 0.0027) \times 10^{-4}$; $(^{39}Ar/^{37}Ar)_{Ca} = (6.5640 \pm 0.0135) \times 10^{-4}$; $(^{40}Ar/^{39}Ar)_{K} = (3.8900 \pm 0.2140) \times 10^{-4}$; $(^{38}Ar/^{39}Ar)_{K} = (1.1999 \pm 0.0004) \times 10^{-2}$

[c] J-value is 0.0007804341 ± 0.000000439 (0.056%; 1σ), based on an age of 1.1814 ± 0.0006 Ma (2σ) for ACR sanidine (Phillips et al., 2017)

[d] Sensitivity = 3.55×10^{-17} mol/fA

Table A.4c. ARGUSVI ^{40}Ar/^{39}Ar laser step-heating analytical results for sample KA7.[a,b,c,d]

Sample ID	Step No	Laser Power	^{40}Ar (fA)	±1σ	^{39}Ar (fA)[b]	±1σ	^{38}Ar (fA)	±1σ	^{37}Ar (fA)[b]	±1σ	^{36}Ar (fA)	±1σ	^{39}Ar (x10^{-14} mol)[d]	Ca/K	±1σ	%^{40}Ar*	^{40}Ar*/^{39}Ar	±1σ	Cum.% ^{39}Ar	Apparent Age (Ma)	±1σ	±1σ (%)
Aliquant: KA7-1		41.1 mg																				
KA7-1a	1	0.03	494.176	0.173	132.663	0.056	0.172	0.000	218.882	0.309	0.9151	0.0017	0.4710	2.887	0.004	44.71	1.67	0.00	10.03	2.377	0.006	0.249
KA7-1b	2	0.04	561.746	0.079	195.826	0.045	0.149	0.000	282.223	0.409	0.7930	0.0013	0.6952	2.522	0.004	57.85	1.66	0.00	24.85	2.369	0.003	0.123
KA7-1c	3	0.05	529.702	0.201	207.295	0.083	0.119	0.000	260.839	0.258	0.6322	0.0016	0.7359	2.202	0.002	64.36	1.64	0.00	40.53	2.347	0.004	0.154
KA7-1d	4	0.06	482.435	0.130	193.706	0.054	0.105	0.000	223.158	0.245	0.5546	0.0022	0.6877	2.016	0.002	65.67	1.64	0.00	55.18	2.335	0.005	0.210
KA7-1e	5	0.08	604.709	0.175	225.437	0.068	0.151	0.000	284.740	0.105	0.8034	0.0015	0.8003	2.210	0.001	60.32	1.62	0.00	72.23	2.310	0.003	0.138
KA7-1f	6	0.1	490.520	0.152	161.689	0.079	0.146	0.001	277.746	0.144	0.7726	0.0031	0.5740	3.006	0.002	52.97	1.61	0.01	84.46	2.294	0.008	0.361
KA7-1g	7	0.2	698.121	0.175	156.159	0.027	0.282	0.001	815.697	0.408	1.4977	0.0037	0.5544	9.141	0.005	35.95	1.61	0.01	96.27	2.294	0.010	0.446
KA7-1h	8	0.35	278.512	0.059	49.317	0.020	0.125	0.001	345.710	0.218	0.6620	0.0027	0.1751	12.267	0.009	29.04	1.64	0.02	100.00	2.340	0.023	0.998
																			Total gas age:	2.33 ± 0.01 Ma (2σ)		

[a] Data are corrected for mass spectrometer backgrounds, discrimination, radioactive decay and interference corrections. Errors are one sigma uncertainties and exclude uncertainties in the J-value (propagating this error only has an effect in the third decimal place)

[b] Interference corrections: $(^{36}Ar/^{37}Ar)_{Ca}$ = (2.5798 ± 0.0027) x 10^{-4}; $(^{39}Ar/^{37}Ar)_{Ca}$ = (6.5640 ± 0.0135) x 10^{-4}; $(^{40}Ar/^{39}Ar)_K$ = (3.8900 ± 0.2140) x 10^{-4}; $(^{38}Ar/^{39}Ar)_K$ = (1.1999 ± 0.0004) x 10^{-2}

[c] J-value is 0.0007916025 ± 0.0000003493 (0.044%;1σ), based on an age of 1.1814 ± 0.0006 Ma (2σ) for ACR sanidine (Phillips et al., 2017)

[d] Sensitivity = 3.55 x 10^{-17} mol/fA

Table A.4d. ARGUSVI ^{40}Ar/^{39}Ar laser step-heating analytical results for sample KA13B.[a,b,c,d,e]

Sample ID	Step No	Laser Power	^{40}Ar (fA)	±1σ	^{39}Ar (fA)[b]	±1σ	^{38}Ar (fA)	±1σ	^{37}Ar (fA)[b]	±1σ	^{36}Ar (fA)	±1σ	^{39}Ar ($\times 10^{-14}$ mol)[d]	Ca/K	±1σ	%^{40}Ar*	^{40}Ar*/^{39}Ar	±1σ	Cum.% ^{39}Ar	Apparent Age (Ma)	±1σ	±1σ (%)
Aliquant: KA13B-1		44.1 mg																				
KA13B-1a	1	3%	358.449	0.079	152.727	0.073	0.059	0.000	265.620	0.157	0.3134	0.0012	0.5422	3.044	0.002	73.89	1.73	0.00	12.00	2.425	0.004	0.2
KA13B-1b	2	4%	429.347	0.146	196.013	0.067	0.061	0.000	288.530	0.242	0.3212	0.0011	0.6958	2.576	0.002	77.65	1.70	0.00	27.40	2.379	0.003	0.1
KA13B-1c	3	5%	425.245	0.170	196.090	0.090	0.061	0.000	250.032	0.225	0.3214	0.0011	0.6961	2.231	0.002	77.42	1.68	0.00	42.80	2.348	0.003	0.1
KA13B-1d	4	6%	386.197	0.155	173.883	0.090	0.061	0.000	207.642	0.156	0.3257	0.0017	0.6173	2.090	0.002	74.81	1.66	0.00	56.46	2.324	0.004	0.2
KA13B-1e	5	7%	336.996	0.125	144.485	0.042	0.062	0.000	178.167	0.278	0.3288	0.0013	0.5129	2.158	0.003	70.86	1.65	0.00	67.81	2.311	0.004	0.2
KA13B-1f	6	8%	289.834	0.064	115.648	0.060	0.062	0.000	162.254	0.243	0.3302	0.0012	0.4105	2.455	0.004	65.97	1.65	0.00	76.90	2.312	0.004	0.2
KA13B-1g	7	10%	332.889	0.070	112.309	0.013	0.093	0.000	235.800	0.151	0.4952	0.0013	0.3987	3.674	0.002	55.58	1.65	0.00	85.72	2.304	0.005	0.2
KA13B-1h	8	14%	407.401	0.073	95.655	0.044	0.157	0.000	452.436	0.258	0.8354	0.0020	0.3396	8.277	0.006	38.77	1.65	0.01	93.24	2.309	0.009	0.4
KA13B-1i	9	20%	298.689	0.051	53.054	0.031	0.133	0.000	361.904	0.282	0.7040	0.0022	0.1883	11.937	0.012	29.62	1.67	0.01	97.40	2.332	0.018	0.8
KA13B-1j	10	35%	255.529	0.095	33.046	0.022	0.125	0.000	248.840	0.082	0.6649	0.0020	0.1173	13.178	0.010	22.31	1.73	0.02	100.00	2.412	0.025	1.1
																			Total gas age:	2.34 ± 0.01 Ma (2σ)		
Aliquant: KA13B-2		42.7 mg																				
KA13B-2a	1	3%	256.234	0.074	92.755	0.058	0.061	0.000	175.806	0.378	0.3261	0.0020	0.3293	3.317	0.007	61.99	1.71	0.01	7.56	2.395	0.009	0.4
KA13B-2b	2	4%	333.049	0.130	140.424	0.086	0.059	0.000	239.554	0.302	0.3115	0.0013	0.4985	2.985	0.004	72.07	1.71	0.00	19.01	2.390	0.004	0.2
KA13B-2c	3	5%	339.615	0.160	153.320	0.086	0.050	0.000	233.198	0.208	0.2657	0.0014	0.5443	2.662	0.003	76.63	1.70	0.00	31.51	2.374	0.004	0.2
KA13B-2d	4	6%	324.225	0.149	148.922	0.058	0.046	0.000	204.874	0.287	0.2436	0.0010	0.5287	2.407	0.003	77.55	1.69	0.00	43.65	2.361	0.003	0.1
KA13B-2e	5	8%	466.215	0.210	206.735	0.043	0.076	0.000	272.490	0.371	0.4038	0.0013	0.7339	2.307	0.003	74.13	1.67	0.00	60.50	2.338	0.003	0.1
KA13B-2f	6	10%	407.748	0.135	171.359	0.051	0.078	0.000	235.748	0.302	0.4148	0.0020	0.6083	2.408	0.003	69.62	1.66	0.00	74.47	2.317	0.005	0.2
KA13B-2g	7	20%	836.335	0.410	237.598	0.157	0.280	0.001	694.640	0.493	1.4875	0.0055	0.8435	5.116	0.005	46.89	1.65	0.01	93.83	2.308	0.010	0.4
KA13B-2h[e]	8	35%	8237.816	4.366	75.641	0.036	5.347	0.009	460.492	0.456	28.3635	0.0469	0.2685	10.654	0.012	-2.80	-3.05	-0.19	100.00	-4.267	-0.272	6.4
																			Total gas age:	2.35 ± 0.01 Ma (2σ)		

[a] Data are corrected for mass spectrometer backgrounds, discrimination, radioactive decay and interference corrections. Errors are one sigma uncertainties and exclude uncertainties in the J-value (propagating this error only has an effect in the third decimal place)

[b] Interference corrections: $(^{36}Ar/^{37}Ar)_{Ca} = (2.5798 \pm 0.0027) \times 10^{-4}$; $(^{39}Ar/^{37}Ar)_{Ca} = (6.5640 \pm 0.0135) \times 10^{-4}$; $(^{40}Ar/^{39}Ar)_{K} = (3.8900 \pm 0.2140) \times 10^{-4}$; $(^{38}Ar/^{39}Ar)_{K} = (1.1999 \pm 0.0004) \times 10^{-2}$

[c] J-value is 0.000775597 ± 0.0000004557 (0.059%;1σ), based on an age of 1.1814 ± 0.0006 Ma (2σ) for ACR sanidine (Phillips et al., 2017)

[d] Sensitivity = 3.55×10^{-17} mol/fA

[e] Excess non-radiogenic Ar from faulty cover glass outgassed in heating step KA13B-2h (gray cells)

Table A.4e. ARGUSVI $^{40}Ar/^{39}Ar$ laser step-heating analytical results for sample MH49.[a,b,c,d]

Sample ID	Step No	Laser Power	^{40}Ar (fA)	±1σ	^{39}Ar (fA)[b]	±1σ	^{38}Ar (fA)	±1σ	^{37}Ar (fA)[b]	±1σ	^{36}Ar (fA)	±1σ	^{39}Ar ($\times 10^{-14}$ mol)[d]	Ca/K	±1σ	%$^{40}Ar^*$	$^{40}Ar^*/^{39}Ar$	±1σ	Cum.% ^{39}Ar	Apparent Age (Ma)	±1σ	±1σ (%)
Aliquant: MH49-1		40.4 mg																				
MH49-1a	1	0.03	1977.070	0.534	36.499	0.026	1.124	0.002	69.748	1.716	5.9608	0.0126	0.1296	3.344	0.082	9.99	5.41	0.10	16.84	2.041	0.039	1.9
MH49-1b	2	0.035	1615.871	0.339	33.058	0.011	0.902	0.002	65.658	1.912	4.7850	0.0120	0.1174	3.476	0.101	11.59	5.66	0.11	32.10	2.137	0.041	1.9
MH49-1c	3	0.04	1329.185	0.385	29.799	0.015	0.728	0.002	63.756	1.340	3.8628	0.0105	0.1058	3.744	0.079	13.23	5.90	0.11	45.85	2.227	0.040	1.8
MH49-1d	4	0.05	1295.514	0.790	31.987	0.016	0.688	0.002	71.556	1.353	3.6491	0.0115	0.1136	3.915	0.074	15.90	6.44	0.11	60.61	2.430	0.042	1.7
MH49-1e	5	0.06	968.569	0.707	26.368	0.023	0.501	0.002	67.439	1.175	2.6568	0.0080	0.0936	4.476	0.078	18.11	6.65	0.09	72.78	2.509	0.036	1.4
MH49-1f	6	0.08	764.272	0.245	23.553	0.026	0.377	0.001	74.140	2.103	2.0019	0.0043	0.0836	5.509	0.156	21.79	7.07	0.06	83.65	2.668	0.021	0.8
MH49-1g	7	0.1	435.938	0.122	14.671	0.015	0.211	0.001	61.568	1.824	1.1208	0.0042	0.0521	7.344	0.218	23.24	6.91	0.09	90.42	2.605	0.033	1.3
MH49-1h	8	0.2	410.444	0.127	13.931	0.011	0.202	0.000	121.454	1.491	1.0712	0.0019	0.0495	15.257	0.188	22.08	6.51	0.04	96.85	2.454	0.016	0.6
MH49-1i	9	0.35	1367.511	0.438	6.830	0.022	0.852	0.002	77.941	1.755	4.5193	0.0087	0.0242	19.971	0.454	1.33	2.67	0.38	100.00	1.007	0.145	14.4
																			Total gas age:	2.29 ± 0.08 Ma (2σ)		

[a] Data are corrected for mass spectrometer backgrounds, discrimination, radioactive decay and interference corrections. Errors are one sigma uncertainties and exclude uncertainties in the J-value (propagating this error only has an effect in the third decimal place)

[b] Interference corrections: $(^{36}Ar/^{37}Ar)_{Ca} = (2.5798 \pm 0.0027) \times 10^{-4}$; $(^{39}Ar/^{37}Ar)_{Ca} = (6.5640 \pm 0.0135) \times 10^{-4}$; $(^{40}Ar/^{39}Ar)_{K} = (3.8900 \pm 0.2140) \times 10^{-4}$; $(^{38}Ar/^{39}Ar)_{K} = (1.1999 \pm 0.0004) \times 10^{-2}$

[c] J-value is 0.0002092594 ± 0.0000001242 (0.059%;1σ), based on an age of 1.1814 ± 0.0006 Ma (2σ) for ACR sanidine (Phillips et al., 2017)

[d] Sensitivity = 3.55×10^{-17} mol/fA

Table A.4f. ARGUSVI ^{40}Ar/^{39}Ar laser step-heating analytical results for sample MH52.[a,b,c,d]

Sample ID	Step No	Laser Power	^{40}Ar (fA)	±1σ	^{39}Ar (fA)[b]	±1σ	^{38}Ar (fA)	±1σ	^{37}Ar (fA)[b]	±1σ	^{36}Ar (fA)	±1σ	^{39}Ar ($\times 10^{-14}$ mol)[d]	Ca/K	±1σ	%^{40}Ar*	^{40}Ar*/^{39}Ar	±1σ	Cum.% ^{39}Ar	Apparent Age (Ma)	±1σ	±1σ (%)
Aliquant: MH52-1		35.8 mg																				
MH52-1a	1	3%	1384.910	0.499	19.558	0.013	0.802	0.001	33.782	0.969	4.2555	0.0056	0.0694	3.023	0.087	8.26	5.85	0.09	8.12	2.189	0.033	1.5
MH52-1b	2	4%	1563.923	0.594	28.094	0.028	0.887	0.001	46.317	0.907	4.7062	0.0079	0.0997	2.885	0.057	10.16	5.65	0.09	19.79	2.116	0.033	1.5
MH52-1c	3	5%	1371.475	0.699	29.169	0.015	0.759	0.001	47.263	1.287	4.0245	0.0062	0.1036	2.836	0.077	12.39	5.83	0.07	31.91	2.180	0.025	1.2
MH52-1d	4	6%	1106.730	0.299	27.176	0.020	0.595	0.001	42.941	0.860	3.1565	0.0070	0.0965	2.765	0.055	14.85	6.05	0.08	43.20	2.263	0.029	1.3
MH52-1e	5	8%	1197.828	0.228	35.093	0.031	0.616	0.001	63.634	1.308	3.2688	0.0050	0.1246	3.173	0.065	18.52	6.32	0.04	57.78	2.366	0.016	0.7
MH52-1f	6	10%	903.154	0.226	31.342	0.028	0.446	0.001	57.074	1.411	2.3637	0.0050	0.1113	3.187	0.079	21.86	6.30	0.05	70.80	2.357	0.018	0.8
MH52-1g	7	14%	889.034	0.400	33.058	0.024	0.430	0.001	83.321	1.835	2.2812	0.0040	0.1174	4.411	0.097	23.39	6.29	0.04	84.53	2.354	0.014	0.6
MH52-1h	8	20%	729.177	0.204	21.710	0.013	0.379	0.001	89.635	1.497	2.0108	0.0044	0.0771	7.225	0.121	17.67	5.93	0.06	93.55	2.221	0.023	1.0
MH52-1i	9	35%	679.432	0.149	15.535	0.017	0.371	0.001	108.897	0.910	1.9677	0.0029	0.0552	12.267	0.103	13.53	5.92	0.06	100.00	2.215	0.021	0.9
																			Total gas age:	2.26 ± 0.05 Ma (2σ)		
Aliquant: MH52-2		44.0 mg																				
MH52-2a	1	3%	1959.781	1.078	24.284	0.010	1.172	0.002	42.126	1.098	6.2186	0.0110	0.0862	3.036	0.079	5.26	4.25	0.14	6.57	1.590	0.053	3.3
MH52-2b	2	4%	2462.250	0.517	36.811	0.020	1.474	0.003	65.451	0.966	7.8170	0.0143	0.1307	3.112	0.046	5.21	3.49	0.12	16.54	1.306	0.044	3.3
MH52-2c	3	5%	2240.579	0.605	40.005	0.018	1.295	0.002	66.257	0.513	6.8692	0.0102	0.1420	2.898	0.022	8.47	4.74	0.08	27.37	1.775	0.029	1.6
MH52-2d	4	6%	1923.440	1.096	39.678	0.027	1.082	0.002	65.707	0.976	5.7426	0.0099	0.1409	2.898	0.043	10.86	5.27	0.08	38.11	1.971	0.030	1.5
MH52-2e	5	8%	2113.738	0.909	52.628	0.037	1.142	0.002	89.929	1.130	6.0566	0.0113	0.1868	2.990	0.038	14.45	5.80	0.07	52.35	2.172	0.025	1.1
MH52-2f	6	10%	1567.198	0.831	47.282	0.028	0.806	0.001	84.063	1.311	4.2762	0.0065	0.1678	3.111	0.049	18.54	6.14	0.04	65.15	2.299	0.017	0.7
MH52-2g	7	12%	1062.771	0.276	37.837	0.015	0.522	0.001	72.519	1.413	2.7707	0.0042	0.1343	3.354	0.065	22.16	6.23	0.03	75.39	2.330	0.013	0.5
MH52-2h	8	14%	771.881	0.270	29.382	0.014	0.374	0.001	65.662	1.242	1.9826	0.0049	0.1043	3.911	0.074	23.31	6.12	0.05	83.35	2.292	0.019	0.8
MH52-2i	9	20%	975.802	0.459	34.826	0.020	0.482	0.001	108.172	1.109	2.5577	0.0039	0.1236	5.436	0.056	21.74	6.09	0.04	92.77	2.280	0.013	0.6
MH52-2j	10	35%	1019.945	0.255	26.701	0.017	0.545	0.001	156.056	0.972	2.8886	0.0077	0.0948	10.228	0.064	15.44	5.90	0.09	100.00	2.208	0.032	1.5
																			Total gas age:	2.04 ± 0.05 Ma (2σ)		
Aliquant: MH52-3		43.1 mg																				
MH52-3a	1	3%	2461.981	0.739	41.642	0.013	1.396	0.002	69.277	1.329	7.4044	0.0093	0.1478	2.911	0.056	10.21	6.04	0.07	14.24	2.258	0.026	1.1
MH52-3b	2	4%	2155.425	0.647	49.924	0.015	1.160	0.002	78.491	2.513	6.1529	0.0085	0.1772	2.751	0.088	14.77	6.38	0.05	31.30	2.387	0.020	0.8
MH52-3c	3	5%	1493.262	0.523	46.525	0.028	0.754	0.001	68.810	1.780	4.0008	0.0063	0.1652	2.588	0.067	20.01	6.42	0.04	47.21	2.403	0.016	0.7
MH52-3d	4	6%	1003.086	0.331	38.156	0.014	0.480	0.001	63.448	2.148	2.5453	0.0041	0.1355	2.910	0.099	24.24	6.37	0.03	60.25	2.385	0.012	0.5
MH52-3e	5	8%	1151.879	0.323	43.531	0.018	0.557	0.001	100.855	2.827	2.9573	0.0037	0.1545	4.054	0.114	23.35	6.18	0.03	75.14	2.312	0.010	0.4
MH52-3f	6	10%	744.150	0.253	26.294	0.017	0.370	0.001	84.005	2.910	1.9618	0.0033	0.0933	5.591	0.194	21.29	6.03	0.04	84.12	2.255	0.014	0.6
MH52-3g	7	20%	1259.982	0.731	30.296	0.040	0.683	0.001	223.608	2.999	3.6240	0.0075	0.1076	12.916	0.174	14.13	5.87	0.08	94.48	2.199	0.029	1.3
MH52-3h	8	35%	723.189	0.376	16.140	0.020	0.395	0.001	112.702	2.520	2.0961	0.0037	0.0573	12.220	0.274	13.46	6.03	0.07	100.00	2.258	0.027	1.2
																			Total gas age:	2.32 ± 0.02 Ma (2σ)		

[a] Data are corrected for mass spectrometer backgrounds, discrimination, radioactive decay and interference corrections. Errors are one sigma uncertainties and exclude uncertainties in the J-value (propagating this error only has an effect in the third decimal place)

[b] Interference corrections: $(^{36}Ar/^{37}Ar)_{Ca} = (2.5798 \pm 0.0027) \times 10^{-4}$; $(^{39}Ar/^{37}Ar)_{Ca} = (6.5640 \pm 0.0135) \times 10^{-4}$; $(^{40}Ar/^{39}Ar)_{K} = (3.8900 \pm 0.2140) \times 10^{-4}$; $(^{38}Ar/^{39}Ar)_{K} = (1.1999 \pm 0.0004) \times 10^{-2}$

[c] J-value is 0.0002075654 ± 0.0000000576 (0.028%;1σ), based on an age of 1.1814 ± 0.0006 Ma (2σ) for ACR sanidine (Phillips et al., 2017)

[d] Sensitivity = 3.55×10^{-17} mol/fA

Table A.4g. ARGUSVI $^{40}Ar/^{39}Ar$ laser step-heating analytical results for sample MH69.[a,b,c,d]

Sample ID	Step No	Laser Power	^{40}Ar (fA)	±1σ	^{39}Ar (fA)[b]	±1σ	^{38}Ar (fA)	±1σ	^{37}Ar (fA)[b]	±1σ	^{36}Ar (fA)	±1σ	^{39}Ar ($\times 10^{-14}$ mol)[d]	Ca/K	±1σ	$\%^{40}Ar^*$	$^{40}Ar^*/^{39}Ar$	±1σ	Cum.% ^{39}Ar	Apparent Age (Ma)	±1σ	±1σ (%)
Aliquant: MH69-1		40.9 mg																				
MH69-1a	1	3%	534.282	0.107	28.442	0.010	0.223	0.001	49.755	2.133	1.1821	0.0035	0.1010	3.061	0.131	33.94	6.38	0.04	8.58	2.407	0.014	0.6
MH69-1b	2	4%	622.282	0.143	38.917	0.026	0.238	0.001	60.489	1.809	1.2625	0.0028	0.1382	2.720	0.081	39.43	6.30	0.02	20.31	2.380	0.008	0.3
MH69-1c	3	6%	975.620	0.478	65.317	0.035	0.361	0.002	98.736	1.648	1.9150	0.0080	0.2319	2.645	0.044	41.40	6.18	0.04	40.00	2.334	0.014	0.6
MH69-1d	4	8%	977.205	0.303	62.117	0.020	0.377	0.001	92.524	1.479	2.0016	0.0048	0.2205	2.607	0.042	38.84	6.11	0.02	58.73	2.307	0.009	0.4
MH69-1e	5	10%	859.707	0.335	46.355	0.021	0.366	0.001	76.653	1.929	1.9412	0.0040	0.1646	2.894	0.073	32.59	6.04	0.03	72.71	2.281	0.010	0.4
MH69-1f	6	14%	1181.502	0.378	45.194	0.019	0.575	0.001	123.027	1.566	3.0528	0.0079	0.1604	4.764	0.061	22.86	5.98	0.05	86.34	2.256	0.020	0.9
MH69-1g	7	20%	898.580	0.198	26.349	0.015	0.469	0.001	113.873	2.090	2.4857	0.0049	0.0935	7.563	0.139	17.41	5.94	0.06	94.28	2.241	0.021	0.9
MH69-1h	8	35%	705.434	0.141	18.972	0.011	0.373	0.001	111.802	2.062	1.9804	0.0055	0.0674	10.313	0.190	16.18	6.02	0.09	100.00	2.271	0.033	1.4
																			Total gas age:	2.31 ± 0.03 Ma (2σ)		
Aliquant: MH69-2		40.8 mg																				
MH69-2a	1	3%	281.965	0.079	17.971	0.013	0.106	0.001	28.046	2.042	0.5631	0.0027	0.0638	2.731	0.199	40.38	6.34	0.04	5.75	2.391	0.017	0.7
MH69-2b	2	4%	546.612	0.186	36.563	0.026	0.200	0.001	58.358	2.242	1.0603	0.0029	0.1298	2.793	0.107	42.09	6.29	0.02	17.44	2.375	0.009	0.4
MH69-2c	3	5%	623.932	0.275	43.202	0.021	0.224	0.000	60.664	1.307	1.1879	0.0025	0.1534	2.457	0.053	43.16	6.23	0.02	31.26	2.353	0.007	0.3
MH69-2d	4	6%	628.680	0.251	42.592	0.026	0.232	0.000	62.153	1.772	1.2318	0.0021	0.1512	2.554	0.073	41.50	6.13	0.02	44.89	2.312	0.006	0.3
MH69-2e	5	8%	877.996	0.360	51.459	0.044	0.357	0.001	82.265	3.048	1.8933	0.0038	0.1827	2.798	0.104	35.62	6.08	0.02	61.35	2.294	0.009	0.4
MH69-2f	6	10%	874.292	0.358	41.271	0.013	0.395	0.000	89.018	2.631	2.0936	0.0023	0.1465	3.775	0.112	28.51	6.04	0.02	74.55	2.280	0.007	0.3
MH69-2g	7	14%	1066.971	0.448	36.382	0.013	0.539	0.001	142.558	2.261	2.8576	0.0043	0.1292	6.857	0.109	20.04	5.88	0.04	86.19	2.219	0.014	0.6
MH69-2h	8	20%	831.913	0.141	23.749	0.015	0.438	0.000	159.332	2.905	2.3211	0.0024	0.0843	11.741	0.214	16.70	5.85	0.03	93.78	2.208	0.012	0.5
MH69-2i	9	35%	570.320	0.245	19.432	0.030	0.291	0.000	175.477	2.952	1.5462	0.0024	0.0690	15.803	0.267	19.06	5.59	0.04	100.00	2.112	0.015	0.7
																			Total gas age:	2.29 ± 0.02 Ma (2σ)		

[a] Data are corrected for mass spectrometer backgrounds, discrimination, radioactive decay and interference corrections. Errors are one sigma uncertainties and exclude uncertainties in the J-value (propagating this error only has an effect in the third decimal place)

[b] Interference corrections: $(^{36}Ar/^{37}Ar)_{Ca} = (2.5798 \pm 0.0027) \times 10^{-4}$; $(^{39}Ar/^{37}Ar)_{Ca} = (6.5640 \pm 0.0135) \times 10^{-4}$; $(^{40}Ar/^{39}Ar)_K = (3.8900 \pm 0.2140) \times 10^{-4}$; $(^{38}Ar/^{39}Ar)_K = (1.1999 \pm 0.0004) \times 10^{-2}$

[c] J-value is 0.0002093754 ± 0.0000000754 (0.036%;1σ), based on an age of 1.1814 ± 0.0006 Ma (2σ) for ACR sanidine (Phillips et al., 2017)

[d] Sensitivity = 3.55×10^{-17} mol/fA

Table A.4h. ARGUSVI ^{40}Ar/^{39}Ar laser step-heating analytical results for sample WO4.[a,b,c,d]

Sample ID	Step No	Laser Power	^{40}Ar (fA)	±1σ	^{39}Ar (fA)[b]	±1σ	^{38}Ar (fA)	±1σ	^{37}Ar (fA)[b]	±1σ	^{36}Ar (fA)	±1σ	^{39}Ar (x10^{-14} mol)[d]	Ca/K	±1σ	%^{40}Ar*	^{40}Ar*/^{39}Ar	±1σ	Cum.% ^{39}Ar	Apparent Age (Ma)	±1σ	±1σ (%)
Aliquant: WO4-1		42.3 mg																				
WO4-1a	1	3%	2630.995	1.342	294.556	0.136	1.396	0.003	359.523	0.536	7.4074	0.0167	1.0457	2.136	0.003	15.94	1.42	0.02	27.13	2.037	0.025	1.2
WO4-1b	2	4%	1818.904	0.819	285.007	0.151	0.875	0.002	445.693	0.847	4.6436	0.0111	1.0118	2.737	0.005	23.78	1.52	0.01	53.38	2.171	0.017	0.8
WO4-1c	3	5%	996.979	0.359	200.956	0.107	0.429	0.001	411.367	0.794	2.2778	0.0061	0.7134	3.582	0.007	31.79	1.58	0.01	71.88	2.256	0.013	0.6
WO4-1d	4	6%	501.493	0.085	124.826	0.104	0.190	0.000	343.623	0.457	1.0057	0.0024	0.4431	4.817	0.008	40.12	1.61	0.01	83.38	2.306	0.009	0.4
WO4-1e	5	8%	339.437	0.122	93.732	0.063	0.120	0.000	392.461	0.385	0.6382	0.0021	0.3327	7.327	0.009	43.86	1.59	0.01	92.01	2.272	0.010	0.4
WO4-1f	6	10%	158.817	0.049	41.963	0.018	0.058	0.000	298.971	0.230	0.3086	0.0010	0.1490	12.468	0.011	41.98	1.59	0.01	95.88	2.273	0.010	0.4
WO4-1g	7	20%	177.573	0.041	32.466	0.021	0.080	0.000	619.714	0.341	0.4264	0.0021	0.1153	33.404	0.028	28.31	1.55	0.02	98.87	2.215	0.028	1.3
WO4-1h	8	35%	73.373	0.026	12.308	0.008	0.034	0.000	237.073	0.244	0.1806	0.0011	0.0437	33.707	0.041	26.52	1.58	0.03	100.00	2.262	0.038	1.7
																			Total gas age:	2.18 ± 0.03 Ma (2σ)		

[a] Data are corrected for mass spectrometer backgrounds, discrimination, radioactive decay and interference corrections. Errors are one sigma uncertainties and exclude uncertainties in the J-value (propagating this error only has an effect in the third decimal place)

[b] Interference corrections: $(^{36}Ar/^{37}Ar)_{Ca} = (2.5798 \pm 0.0027) \times 10^{-4}$; $(^{39}Ar/^{37}Ar)_{Ca} = (6.5640 \pm 0.0135) \times 10^{-4}$; $(^{40}Ar/^{39}Ar)_K = (3.8900 \pm 0.2140) \times 10^{-4}$; $(^{38}Ar/^{39}Ar)_K = (1.1999 \pm 0.0004) \times 10^{-2}$

[c] J-value is 0.0007934385 ± 0.0000005376 (0.068%;1σ), based on an age of 1.1814 ± 0.0006 Ma (2σ) for ACR sanidine (Phillips et al., 2017)

[d] Sensitivity = 3.55 x 10^{-17} mol/fA

Table A.4i. Tulloch Hill Flow (Flow B) age calculation

Sample	Aliquant	Age (Ma)	± 95% CI
KA7	KA7-1	2.294	0.08
KA13B	KA13B-1	2.309	0.01
MH69	MH69-1	2.303	0.04

Preferred Eruption Age: 2.309 ± 0.009 Ma (2σ)

Appendix A.5. ARGUSVI ^{40}Ar/^{39}Ar laser step-heating analytical results for Aitken Hill Flow samples

Table A.5a. ARGUSVI ^{40}Ar/^{39}Ar laser step-heating analytical results for sample MH35.[a,b,c,d]

Sample ID	Step No	Laser Power	^{40}Ar (fA)	±1σ	^{39}Ar (fA)[b]	±1σ	^{38}Ar (fA)	±1σ	^{37}Ar (fA)[b]	±1σ	^{36}Ar (fA)	±1σ	^{39}Ar (x10^{-14} mol)[d]	Ca/K	±1σ	%^{40}Ar*	^{40}Ar*/^{39}Ar	±1σ	Cum.% ^{39}Ar	Apparent Age (Ma)	±1σ	±1σ (%)
Aliquant: MH35-1					J-Value = 0.0007842344 ± 0.0000003528 (0.045%;1σ)																	
MH35-1a	1	0.025	481.12	0.26	95.292	0.065	0.13310	0.00040	102.76	0.16	0.7061	0.0021	0.3383	1.8871	0.0032	56.18	2.8367	0.0075	4.98	4.009	0.011	0.265
MH35-1b	2	0.03	519.02	0.26	132.580	0.081	0.09381	0.00048	131.26	0.15	0.4977	0.0025	0.4707	1.7326	0.0022	71.36	2.7940	0.0063	11.90	3.9487	0.0088	0.224
MH35-1c	3	0.035	552.25	0.26	164.65	0.13	0.06178	0.00026	147.17	0.16	0.3278	0.0014	0.5845	1.5641	0.0021	82.27	2.7597	0.0037	20.50	3.9002	0.0052	0.132
MH35-1d	4	0.04	550.67	0.22	175.368	0.054	0.04578	0.00020	141.41	0.23	0.2429	0.0011	0.6226	1.4111	0.0023	86.82	2.7266	0.0024	29.66	3.8535	0.0033	0.086
MH35-1e	5	0.045	550.36	0.25	180.609	0.089	0.03923	0.00027	133.29	0.19	0.2081	0.0014	0.6412	1.2915	0.0020	88.70	2.7032	0.0030	39.09	3.8205	0.0043	0.112
MH35-1f	6	0.05	518.764	0.062	174.121	0.080	0.03290	0.00027	119.15	0.10	0.1746	0.0014	0.6181	1.1975	0.0012	89.94	2.6800	0.0028	48.19	3.7878	0.0040	0.104
MH35-1g	7	0.055	473.09	0.10	159.271	0.040	0.03014	0.00020	103.57	0.15	0.1599	0.0010	0.5654	1.1379	0.0017	89.90	2.6706	0.0022	56.51	3.7745	0.0031	0.081
MH35-1h	8	0.06	442.28	0.12	149.735	0.055	0.02754	0.00020	97.45	0.15	0.1461	0.0011	0.5316	1.1390	0.0019	90.12	2.6624	0.0025	64.33	3.7629	0.0035	0.092
MH35-1i	9	0.08	725.34	0.19	236.294	0.090	0.06282	0.00028	198.77	0.15	0.3333	0.0015	0.8388	1.4721	0.0012	86.27	2.6485	0.0023	76.67	3.7433	0.0032	0.086
MH35-1j	10	0.1	592.03	0.18	186.532	0.063	0.06305	0.00025	222.12	0.24	0.3345	0.0013	0.6622	2.0838	0.0023	83.12	2.6385	0.0025	86.41	3.7291	0.0036	0.096
MH35-1k	11	0.12	412.047	0.091	118.671	0.023	0.06285	0.00032	229.16	0.32	0.3334	0.0017	0.4213	3.3793	0.0048	75.83	2.6334	0.0044	92.61	3.7219	0.0062	0.166
MH35-1l	12	0.2	492.23	0.11	104.231	0.031	0.13788	0.00035	423.09	0.11	0.7315	0.0019	0.3700	7.1035	0.0028	55.63	2.6273	0.0055	98.05	3.7133	0.0078	0.211
MH35-1m	13	0.35	289.37	0.06	37.299	0.040	0.12206	0.00053	170.15	0.23	0.6476	0.0028	0.1324	7.983	0.014	33.19	2.575	0.023	100.00	3.639	0.032	0.885
																			Total gas age: 3.803 ± 0.011 Ma (2σ)			
Aliquant: MH35-2					J-Value = 0.0007842344 ± 0.0000003528 (0.045%;1σ)																	
MH35-2a	1	0.03	1418.25	0.60	260.19	0.11	0.43816	0.0015	262.08	0.18	2.3245	0.0078	0.9237	1.7627	0.0014	51.06	2.7835	0.0093	11.60	3.934	0.013	0.334
MH35-2b	2	0.04	1143.67	0.38	341.50	0.14	0.12879	0.00042	299.82	0.55	0.6832	0.0022	1.2123	1.5364	0.0029	82.15	2.7516	0.0025	26.83	3.8889	0.0035	0.090
MH35-2c	3	0.05	1076.22	0.51	350.91	0.19	0.08018	0.00041	269.88	0.32	0.4254	0.0021	1.2457	1.3459	0.0017	88.19	2.7051	0.0027	42.47	3.8231	0.0039	0.102
MH35-2d	4	0.06	926.01	0.26	311.55	0.12	0.05813	0.00028	221.48	0.29	0.3084	0.0015	1.1060	1.2441	0.0017	90.05	2.6767	0.0019	56.36	3.7831	0.0027	0.072
MH35-2e	5	0.08	1143.60	0.31	380.51	0.14	0.08341	0.00024	304.34	0.29	0.4425	0.0013	1.3508	1.3997	0.0014	88.44	2.6582	0.0016	73.33	3.7570	0.0023	0.061
MH35-2f	6	0.1	815.63	0.22	267.02	0.13	0.06942	0.00022	272.29	0.24	0.3683	0.0012	0.9479	1.7845	0.0018	86.51	2.6428	0.0020	85.23	3.7352	0.0028	0.075
MH35-2g	7	0.14	761.58	0.15	219.34	0.10	0.11607	0.00066	443.90	0.24	0.6158	0.0035	0.7786	3.5417	0.0025	75.85	2.6340	0.0050	95.01	3.7228	0.0070	0.189
MH35-2h	8	0.18	425.85	0.12	111.823	0.040	0.08331	0.00045	341.08	0.37	0.4420	0.0024	0.3970	5.3378	0.0061	69.01	2.6282	0.0065	100.00	3.7145	0.0092	0.247
																			Total gas age: 3.804 ± 0.010 Ma (2σ)			

[a] Data are corrected for mass spectrometer backgrounds, discrimination, radioactive decay and interference corrections. Errors are one sigma uncertainties and exclude uncertainties in the J-value (propagating this error only has an effect in the third decimal place)

[b] Interference corrections: $(^{36}\mathrm{Ar}/^{37}\mathrm{Ar})_{\mathrm{Ca}} = (2.5798 \pm 0.0027) \times 10^{-4}$; $(^{39}\mathrm{Ar}/^{37}\mathrm{Ar})_{\mathrm{Ca}} = (6.5640 \pm 0.0135) \times 10^{-4}$; $(^{40}\mathrm{Ar}/^{39}\mathrm{Ar})_{\mathrm{K}} = (3.8900 \pm 0.2140) \times 10^{-4}$; $(^{38}\mathrm{Ar}/^{39}\mathrm{Ar})_{\mathrm{K}} = (1.1999 \pm 0.0004) \times 10^{-2}$

[c] J-value is 0.0007842344 ± 0.0000003528 (0.045%;1σ), based on an age of 1.1814 ± 0.0006 Ma (2σ) for ACR sanidine (Phillips et al., 2017)

[d] Sensitivity = 3.55×10^{-17} mol/fA

Table A.5b. Aitken Hill Flow Age Calculation

Aliquant	Total Gas Age
MH35-1	3.803 ± 0.011 Ma
MH35-2	3.804 ± 0.010 Ma
Weighted Avg Age:	3.8035 ± 0.0074 Ma

Appendix A.6. ARGUSVI ^{40}Ar/^{39}Ar laser step-heating analytical results for Bald Hill Flow samples

Table A.6a. ARGUSVI ^{40}Ar/^{39}Ar laser step-heating analytical results for sample BA01.[a,b,c,d]

Sample ID	Step No	Laser Power	^{40}Ar (fA)	±1σ	^{39}Ar (fA)[b]	±1σ	^{38}Ar (fA)	±1σ	^{37}Ar (fA)[b]	±1σ	^{36}Ar (fA)	±1σ	^{39}Ar (x10^{-14} mol)[d]	Ca/K	±1σ	%^{40}Ar*	^{40}Ar*/^{39}Ar	±1σ	Cum.% ^{39}Ar	Apparent Age (Ma)	±1σ	±1σ (%)	Included in age calc? y/n
Aliquant: BA01-1					J-Value = 0.0054040012 ± 0.0000024885 (0.046%;1σ)																		
Mineral: Anorthoclase 1 grain																							
BA01-1a	1	3.0%	5121.652	0.00	117.97	0.19	0.0838	0.0022	35.793	0.079	0.444	0.012	0.4188	0.5309	0.0015	97.41	42.289	0.075	84.80	371.31	0.60	0.16026154	n
BA01-1b	2	2.0%	1258.56	0.39	4.08	0.015	0.7735	0.0010	0.832	0.086	4.10	0.0052	0.0145	0.357	0.037	2.66	8.20	0.39	87.73	78.2	3.7	4.67970262	n
BA01-1c	3	3.0%	3380.8	1.0	17.07	0.012	2.0920	0.0019	2.760	0.084	11.098	0.010	0.0606	0.2829	0.0086	1.99	3.95	0.19	100.00	38.1	1.8	4.71669927	n
																			Total gas age: 325.5 ± 1.7 Ma (2σ)				
Aliquant: BA01-2					J-Value = 0.0054040012 ± 0.0000024885 (0.046%;1σ)																		
Mineral: Anorthoclase 1 grain																							
BA01-2a	1	0.1%	2.387	0.082	0.007	0.011	0.001402	0.000040	0.006	0.013	0.00744	0.00021	0.0000	1.6	4.3	6.98	25	44	0.05	225	376	167.245975	n
BA01-2b	2	0.3%	93.672	0.077	9.201	0.018	0.05346	0.00011	6.313	0.074	0.28363	0.00057	0.033	1.201	0.014	9.60	0.977	0.020	70.44	9.50	0.20	2.09178056	n
BA01-2c	3	0.5%	6.940	0.043	1.255	0.012	0.003658	0.000056	0.863	0.066	0.01940	0.00030	0.0045	1.203	0.093	16.53	0.914	0.079	80.04	8.89	0.76	8.60244054	n
BA01-2d	4	0.9%	3.635	0.062	0.724	0.011	0.002037	0.000051	0.479	0.077	0.01081	0.00027	0.0026	1.16	0.19	11.25	0.57	0.14	85.58	5.5	1.4	25.001947	n
BA01-2e	5	1.5%	14.582	0.056	1.885	0.016	0.00810	0.00010	1.204	0.075	0.04295	0.00053	0.0067	1.118	0.070	12.05	0.933	0.090	100.00	9.07	0.87	9.61946692	n
																			Total gas age: 9.3 ± 1.3 Ma (2σ)				
Aliquant: BA01-3					J-Value = 0.0054040012 ± 0.0000024885 (0.046%;1σ)																		
Mineral: Anorthoclase 1 grain																							
BA01-3a	1	0.1%	0.178	0.045	0.019	0.014	0.000226	0.000081	0.028	0.048	0.00120	0.00043	0.0001	2.5	4.7	-100.87	-9.3	-9.7	0.05	-93	-99	107.001749	n
BA01-3b	2	0.2%	2.793	0.036	2.878	0.010	0.00039	0.00013	13.498	0.088	0.00209	0.00068	0.0102	8.206	0.061	77.58	0.753	0.072	7.55	7.33	0.70	9.51000784	y
BA01-3c	3	0.3%	8.119	0.040	9.839	0.011	0.00017	0.00013	52.403	0.085	0.00090	0.00068	0.0349	9.321	0.019	96.65	0.798	0.021	33.20	7.76	0.21	2.64390597	y
BA01-3d	4	0.4%	8.697	0.036	9.718	0.019	0.000480	0.000073	71.908	0.050	0.00255	0.00039	0.0345	12.949	0.027	91.21	0.817	0.013	58.54	7.94	0.12	1.54044685	y
BA01-3e	5	0.5%	6.990	0.033	8.059	0.014	0.000186	0.000057	68.379	0.064	0.00099	0.00030	0.0286	14.848	0.029	95.75	0.831	0.012	79.54	8.08	0.12	1.43622205	y
BA01-3f	6	0.7%	4.894	0.039	3.6435	0.0083	0.001227	0.000089	29.76	0.11	0.00651	0.00047	0.0129	14.296	0.060	60.28	0.810	0.040	89.04	7.88	0.39	4.95130304	y
BA01-3g	7	1.0%	5.310	0.030	2.556	0.012	0.001961	0.000089	21.923	0.096	0.01040	0.00047	0.0091	15.011	0.094	41.50	0.862	0.056	95.70	8.39	0.55	6.53152313	y
BA01-3h	8	1.5%	1.515	0.029	1.648	0.008	0.000155	0.000069	14.02	0.10	0.00082	0.00037	0.0058	14.89	0.13	83.72	0.770	0.069	100.00	7.49	0.67	8.95096953	y
																			Total gas age: 7.84 ± 0.62 Ma (2σ)				
Aliquant: BA01-4					J-Value = 0.0054040012 ± 0.0000024885 (0.046%;1σ)																		
Mineral: Anorthoclase 1 grain																							
BA01-4a	1	1.5%	45.736	0.029	37.840	0.021	0.00956	0.00011	61.00	0.11	0.05072	0.00058	0.1343	2.8213	0.0053	66.87	0.8085	0.0047	100.00	7.865	0.046	0.57861734	y
																			Total gas age: 7.865 ± 0.092 Ma (2σ)				
Aliquant: BA01-5					J-Value = 0.0054040012 ± 0.0000024885 (0.046%;1σ)																		
Mineral: Anorthoclase 1 grain																							
BA01-5a	1	0.3%	12.32	0.13	2.301	0.017	0.006368	0.000079	3.768	0.032	0.03378	0.00042	0.0082	2.866	0.032	18.13	0.971	0.079	1.80	9.44	0.77	8.11445676	n
BA01-5b	2	1.5%	121.87	0.13	125.508	0.026	0.01222	0.00016	256.630	0.085	0.06484	0.00086	0.4456	3.5783	0.0014	84.08	0.8168	0.0023	100.00	7.946	0.022	0.28195304	y
																			Total gas age: 7.973 ± 0.072 Ma (2σ)				
Aliquant: BA01-6					J-Value = 0.0054040012 ± 0.0000024885 (0.046%;1σ)																		
Mineral: Anorthoclase 1 grain																							
BA01-6a	1	0.3%	10.562	0.063	13.046	0.019	0.000189	0.000092	29.229	0.047	0.00100	0.00049	0.0463	3.9206	0.0086	97.13	0.787	0.012	20.29	7.65	0.12	1.55852002	n
BA01-6b	2	1.5%	44.067	0.077	51.265	0.015	0.00148	0.00019	283.68	0.20	0.0079	0.0010	0.1820	9.6837	0.0075	94.63	0.8139	0.0061	100.00	7.917	0.059	0.74816068	y
																			Total gas age: 7.86 ± 0.14 Ma (2σ)				

[a] Data are corrected for mass spectrometer backgrounds, discrimination, radioactive decay and interference corrections. Errors are one sigma uncertainties and exclude uncertainties in the J-value (propagating this error only has an effect in the third decimal place)

[b] Interference corrections: $(^{36}Ar/^{37}Ar)_{Ca}$ = (2.5798 ± 0.0027) x 10^{-4}; $(^{39}Ar/^{37}Ar)_{Ca}$ = (6.5640 ± 0.0135) x 10^{-4}; $(^{40}Ar/^{39}Ar)_{K}$ = (3.8900 ± 0.2140) x 10^{-4}; $(^{38}Ar/^{39}Ar)_{K}$ = (1.1999 ± 0.0004) x 10^{-2}

[c] J-value is 0.0054040012 ± 0.0000024885 (0.046%; 1σ), based on an age of 28.126 ± 0.019 Ma (2σ) for FC sanidine (Phillips et al., 2017)

[d] Sensitivity = 3.55 x 10^{-17} mol/fA

Table A.6b. Bald Hill Flow Age Calculation

Sample: BA01

Step ID:	$^{40}Ar^{*}/^{39}Ar_K$	±1σ
BA01-3b	0.753	0.072
BA01-3c	0.798	0.021
BA01-3d	0.817	0.013
BA01-3e	0.831	0.012
BA01-3f	0.810	0.040
BA01-3g	0.862	0.056
BA01-3h	0.770	0.069
BA01-4a	0.809	0.005
BA01-5b	0.817	0.002
BA01-6b	0.814	0.006

		±1σ	±1σ (%)
Weighted Avg:	0.8153	0.0019	0.233043
λ:	5.543E-10		
J:	0.005404	2.4885E-06	0.046049

$t = 1/\lambda \ln (1 + J (^{40}Ar^{*}/^{39}Ar_K))$

			±1σ (%)	±1σ (Ma)	±2σ (Ma)
Age (Ma):	7.9311	±	0.2370	0.0188	0.0376

Appendix A.7. ARGUSVI ^{40}Ar/^{39}Ar laser step-heating analytical results for Crowe Hill Flow samples

Table A.7a. ARGUSVI ^{40}Ar/^{39}Ar laser step-heating analytical results for sample MH68.[a,b,c,d]

Sample ID	Step No	Laser Power	^{40}Ar (fA)	±1σ	^{39}Ar (fA)[b]	±1σ	^{38}Ar (fA)	±1σ	^{37}Ar (fA)[b]	±1σ	^{36}Ar (fA)	±1σ	^{39}Ar (x10^{-14} mol)[d]	Ca/K	±1σ	%^{40}Ar*	^{40}Ar*/^{39}Ar	±1σ	Cum.% ^{39}Ar	Apparent Age (Ma)	±1σ	±1σ (%)
Aliquant: MH68-1							J-Value = 0.005413217 ± 0.0000022248 (0.041%;1σ)															
MH68-1a	1	2.5%	408.294	0.087	559.76	0.24	0.09057	0.00022	213.35	0.17	0.4805	0.0012	1.9872	0.66701	0.00060	64.83	0.47314	0.00068	5.17	4.6147	0.0067	0.14
MH68-1b	2	3.0%	571.43	0.20	736.82	0.25	0.14382	0.00047	272.22	0.27	0.7630	0.0025	2.6157	0.64655	0.00068	60.11	0.4664	0.0011	11.98	4.549	0.010	0.23
MH68-1c	3	3.5%	633.55	0.19	917.14	0.50	0.13005	0.00040	345.43	0.22	0.6899	0.0021	3.2559	0.65911	0.00055	67.45	0.46620	0.00076	20.46	4.5471	0.0074	0.16
MH68-1d	4	4.0%	703.82	0.14	1047.71	0.72	0.13682	0.00025	408.35	0.50	0.7258	0.0014	3.7194	0.6821	0.0010	69.17	0.46493	0.00052	30.14	4.5347	0.0051	0.11
MH68-1e	5	4.5%	674.06	0.24	1087.77	0.37	0.10632	0.00031	458.02	0.25	0.5640	0.0016	3.8616	0.73686	0.00047	74.97	0.46487	0.00053	40.19	4.5341	0.0051	0.11
MH68-1f	6	5.0%	713.78	0.40	1019.83	0.86	0.15155	0.00027	470.48	0.50	0.8040	0.0015	3.6204	0.8073	0.0011	66.33	0.46453	0.00070	49.62	4.5308	0.0068	0.15
MH68-1g	7	5.5%	529.01	0.26	964.91	0.23	0.05183	0.00039	504.57	0.42	0.2750	0.0020	3.4254	0.91511	0.00079	84.42	0.46317	0.00070	58.54	4.5176	0.0068	0.15
MH68-1h	8	6.0%	438.96	0.22	794.35	0.55	0.04590	0.00019	486.62	0.43	0.2435	0.0010	2.8199	1.0720	0.0012	83.38	0.46110	0.00057	65.88	4.4974	0.0055	0.12
MH68-1i	9	7.0%	509.45	0.26	915.19	0.19	0.05624	0.00022	747.11	0.68	0.2984	0.0012	3.2489	1.4286	0.0013	82.46	0.45932	0.00049	74.34	4.4801	0.0048	0.11
MH68-1j	10	8.0%	438.05	0.18	804.14	0.17	0.04415	0.00025	846.62	0.50	0.2342	0.0013	2.8547	1.8425	0.0012	83.98	0.45779	0.00055	81.77	4.4652	0.0053	0.12
MH68-1k	11	10.0%	527.73	0.21	885.70	0.21	0.07914	0.00022	1320.4	1.1	0.4198	0.0012	3.1442	2.6088	0.0023	76.20	0.45432	0.00047	89.95	4.4314	0.0046	0.10
MH68-1l	12	14.0%	472.47	0.21	740.13	0.57	0.09497	0.00035	2827.6	2.5	0.5038	0.0019	2.6275	6.6859	0.0078	68.12	0.43512	0.00087	96.79	4.2443	0.0085	0.20
MH68-1m	13	20.0%	192.90	0.14	249.89	0.16	0.05445	0.00026	2282.7	1.5	0.2889	0.0014	0.8871	15.986	0.015	55.26	0.4268	0.0018	99.10	4.163	0.017	0.41
MH68-1n	14	35.0%	95.43	0.15	97.235	0.034	0.03339	0.00028	1381.83	0.59	0.1771	0.0015	0.3452	24.870	0.014	44.57	0.4376	0.0048	100.00	4.268	0.046	1.1
																			Total gas age: 4.487 ± 0.014 Ma (2σ)			
Aliquant: MH68-2							J-Value = 0.005413217 ± 0.0000022248 (0.041%;1σ)															
MH68-2a	1	3.0%	681.77	0.17	1130.62	0.80	0.09401	0.00034	432.2	1.0	0.4987	0.0018	4.0137	0.6690	0.0016	78.11	0.47131	0.00060	10.01	4.5969	0.0059	0.13
MH68-2b	2	4.0%	1003.67	0.47	1788.27	0.93	0.10627	0.00056	671.5	1.8	0.5638	0.0030	6.3484	0.6571	0.0018	83.17	0.46713	0.00061	25.83	4.5561	0.0060	0.13
MH68-2c	3	5.0%	1038.31	0.47	1905.1	1.3	0.09696	0.00037	823.0	1.7	0.5144	0.0020	6.7630	0.7560	0.0016	85.15	0.46441	0.00051	42.70	4.5296	0.0050	0.11
MH68-2d	4	6.0%	943.90	0.36	1764.58	0.99	0.08173	0.00023	955.8	1.7	0.4336	0.0012	6.2643	0.9479	0.0018	86.22	0.46155	0.00039	58.31	4.5019	0.0038	0.08
MH68-2e	5	8.0%	1091.37	0.44	2031.1	1.0	0.10276	0.00049	1637.6	2.4	0.5451	0.0026	7.2106	1.4109	0.0022	85.03	0.45719	0.00049	76.29	4.4593	0.0048	0.11
MH68-2f	6	10.0%	753.97	0.37	1351.6	1.3	0.08983	0.00052	1718.1	1.9	0.4766	0.0027	4.7980	2.2247	0.0032	81.07	0.45258	0.00079	88.25	4.4144	0.0077	0.17
MH68-2g	7	14.0%	570.19	0.16	928.48	0.78	0.10148	0.00065	2811.2	2.8	0.5384	0.0035	3.2961	5.2985	0.0069	71.76	0.4410	0.0012	96.47	4.302	0.012	0.27
MH68-2h	8	35.0%	351.19	0.11	398.51	0.36	0.11529	0.00076	3683.2	3.2	0.6116	0.0040	1.4147	16.174	0.020	47.98	0.4231	0.0031	100.00	4.127	0.030	0.72
																			Total gas age: 4.477 ± 0.014 Ma (2σ)			

[a] Data are corrected for mass spectrometer backgrounds, discrimination, radioactive decay and interference corrections. Errors are one sigma uncertainties and exclude uncertainties in the J-value (propagating this error only has an effect in the third decimal place)

[b] Interference corrections: $(^{36}Ar/^{37}Ar)_{Ca}$ = (2.5798 ± 0.0027) x 10^{-4}; $(^{39}Ar/^{37}Ar)_{Ca}$ = (6.5640 ± 0.0135) x 10^{-4}; $(^{40}Ar/^{39}Ar)_{K}$ = (3.8900 ± 0.2140) x 10^{-4}; $(^{38}Ar/^{39}Ar)_{K}$ = (1.1999 ± 0.0004) x 10^{-2}

[c] J-value is 0.005413217 ± 0.0000022248 (0.041%; 1σ), based on an age of 28.126 ± 0.019 Ma (2σ) for FC sanidine (Phillips et al., 2017)

[d] Sensitivity = 3.55 x 10^{-17} mol/fA

Table A.7b. Crowe Hill Flow Age Calculation

Aliquant	Total Gas Age
MH68-1	4.487 ± 0.014 Ma
MH68-2	4.477 ± 0.014 Ma
Weighted Avg Age:	4.482 ± 0.010 Ma

Appendix A.8. ARGUSVI ^{40}Ar/^{39}Ar laser step-heating analytical results for Fenton Hill Flow samples

Table A.8a. ARGUSVI ^{40}Ar/^{39}Ar laser step-heating analytical results for sample MH10.[a,b,c,d,e]

Sample ID	Step No	Laser Power	^{40}Ar (fA)	±1σ	^{39}Ar (fA)[b]	±1σ	^{38}Ar (fA)	±1σ	^{37}Ar (fA)[b]	±1σ	^{36}Ar (fA)	±1σ	^{39}Ar ($\times 10^{-14}$ mol)[d]	Ca/K	±1σ	%^{40}Ar*	^{40}Ar*/^{39}Ar	±1σ	Cum.% ^{39}Ar	Apparent Age (Ma)	±1σ	±1σ (%)
Aliquant: MH10-1					J-Value = 0.0002014205 ± 0.0000002954 (0.147%;1σ)																	
MH10-1a	1	0.03	732.86	0.14	54.519	0.034	0.16681	0.00054	88.795	0.088	0.8849	0.0028	0.1935	2.8502	0.0033	63.95	8.596	0.017	17.58	3.1210	0.0061	0.19
MH10-1b	2	0.04	840.19	0.18	66.610	0.030	0.17997	0.00039	92.99	0.12	0.9547	0.0021	0.2365	2.4432	0.0034	66.07	8.334	0.010	39.05	3.0260	0.0038	0.13
MH10-1c	3	0.05	625.84	0.16	55.947	0.020	0.10708	0.00035	80.50	0.11	0.5681	0.0019	0.1986	2.5179	0.0034	72.90	8.155	0.011	57.09	2.9608	0.0039	0.13
MH10-1d	4	0.06	437.318	0.083	40.798	0.038	0.06755	0.00033	65.56	0.22	0.3583	0.0017	0.1448	2.812	0.010	75.53	8.097	0.015	70.24	2.9398	0.0054	0.18
MH10-1e	5	0.08	444.41	0.14	40.230	0.029	0.07502	0.00047	97.06	0.22	0.3980	0.0025	0.1428	4.222	0.010	73.26	8.093	0.020	83.22	2.9384	0.0072	0.24
MH10-1f	6	0.1	305.092	0.055	25.409	0.030	0.06268	0.00025	77.08	0.20	0.3325	0.0014	0.0902	5.309	0.015	67.46	8.100	0.019	91.41	2.9410	0.0067	0.23
MH10-1g	7	0.12	174.794	0.051	15.986	0.038	0.02808	0.00016	52.50	0.11	0.14898	0.00087	0.0568	5.747	0.018	74.55	8.152	0.025	96.56	2.9597	0.0092	0.31
MH10-1h	8	0.14	116.402	0.099	10.664	0.023	0.01890	0.00024	38.51	0.13	0.1003	0.0013	0.0379	6.320	0.025	74.28	8.109	0.040	100.00	2.944	0.015	0.50
																			Total gas age: 2.995 ± 0.012 Ma (2σ)			
Aliquant: MH10-2					J-Value = 0.0002014205 ± 0.0000002954 (0.147%;1σ)																	
MH10-2a	1	0.025	310.417	0.065	6.403	0.032	0.15933	0.00054	10.4	1.0	0.8453	0.0029	0.0227	2.85	0.27	18.70	9.07	0.14	2.01	3.292	0.051	1.56
MH10-2b	2	0.03	541.598	0.065	10.251	0.024	0.28450	0.00048	18.7	1.3	1.5093	0.0025	0.0364	3.20	0.23	16.80	8.877	0.077	5.22	3.223	0.028	0.86
MH10-2c	3	0.035	407.97	0.21	12.857	0.012	0.18426	0.00031	22.5	1.4	0.9775	0.0016	0.0456	3.06	0.19	28.47	9.033	0.042	9.26	3.279	0.015	0.46
MH10-2d	4	0.04	414.417	0.091	15.087	0.032	0.17585	0.00031	27.1	1.3	0.9329	0.0016	0.0536	3.15	0.15	32.79	9.008	0.038	13.99	3.270	0.014	0.42
MH10-2e	5	0.05	574.29	0.18	24.146	0.028	0.22679	0.00046	42.49	0.91	1.2032	0.0025	0.0857	3.079	0.066	37.45	8.907	0.033	21.57	3.234	0.012	0.37
MH10-2f	6	0.06	585.166	0.082	28.889	0.037	0.20881	0.00065	50.4	1.3	1.1077	0.0035	0.1026	3.055	0.078	43.48	8.808	0.038	30.63	3.198	0.014	0.43
MH10-2g	7	0.07	567.32	0.12	31.048	0.035	0.18674	0.00044	51.7	1.2	0.9906	0.0024	0.1102	2.914	0.067	47.86	8.746	0.025	40.37	3.1754	0.0091	0.29
MH10-2h	8	0.08	530.43	0.12	31.946	0.026	0.15944	0.00041	53.6	1.3	0.8458	0.0022	0.1134	2.934	0.073	52.39	8.699	0.022	50.39	3.1582	0.0080	0.25
MH10-2i	9	0.09	496.414	0.055	32.101	0.029	0.13747	0.00019	52.5	1.1	0.7293	0.0010	0.1140	2.862	0.058	56.14	8.681	0.013	60.46	3.1519	0.0045	0.14
MH10-2j	10	0.1	465.30	0.11	31.894	0.020	0.12049	0.00024	50.4	1.2	0.6392	0.0013	0.1132	2.765	0.065	58.98	8.605	0.013	70.46	3.1243	0.0049	0.16
MH10-2k	11	0.12	617.236	0.068	44.464	0.039	0.15086	0.00048	71.34	0.85	0.8003	0.0025	0.1578	2.808	0.034	61.29	8.508	0.019	84.41	3.0889	0.0068	0.22
MH10-2l	12	0.14	654.623	0.085	49.686	0.035	0.14778	0.00037	79.9	1.1	0.7840	0.0020	0.1764	2.815	0.039	64.24	8.464	0.013	100.00	3.0731	0.0048	0.16
																			Total gas age: 3.157 ± 0.019 Ma (2σ)			

[a] Data are corrected for mass spectrometer backgrounds, discrimination, radioactive decay and interference corrections. Errors are one sigma uncertainties and exclude uncertainties in the J-value (propagating this error only has an effect in the third decimal place)

[b] Interference corrections: $(^{36}\mathrm{Ar}/^{37}\mathrm{Ar})_{Ca} = (2.5713 \pm 0.0023) \times 10^{-4}$; $(^{39}\mathrm{Ar}/^{37}\mathrm{Ar})_{Ca} = (6.6200 \pm 0.0801) \times 10^{-4}$; $(^{40}\mathrm{Ar}/^{39}\mathrm{Ar})_{K} = (4.9000 \pm 0.8575) \times 10^{-4}$; $(^{38}\mathrm{Ar}/^{39}\mathrm{Ar})_{K} = (1.2136 \pm 0.0016) \times 10^{-2}$

[c] J-value is 0.0002014205 ± 0.0000002954 (0.147%;1σ), based on an age of 1.1814 ± 0.0006 Ma (2σ) for ACR sanidine (Phillips et al., 2017)

[d] Sensitivity = 3.55×10^{-17} mol/fA

[e] Heating steps where there was an indication of suppression of isotope signals, possibly due to hydrocarbon contamination. Affected cycles were removed from regression.

Appendix A.9. ARGUSVI ^{40}Ar/^{39}Ar laser step-heating analytical results for Mount Kororoit Flow samples

Table A.9a. ARGUSVI ^{40}Ar/^{39}Ar laser step-heating analytical results for sample MH01S.[a,b,c,d,e]

Sample ID	Step No	Laser Power	^{40}Ar (fA)	±1σ	^{39}Ar (fA)[b]	±1σ	^{38}Ar (fA)	±1σ	^{37}Ar (fA)[b]	±1σ	^{36}Ar (fA)	±1σ	^{39}Ar (x10^{-14} mol)[d]	Ca/K	±1σ	%^{40}Ar*	^{40}Ar*/^{39}Ar	±1σ	Cum.% ^{39}Ar	Apparent Age (Ma)	±1σ	±1σ (%)
Aliquot: MH01S-1					J-Value = 0.0002013266 ± 0.0000000961 (0.048%;1σ)																	
MH01S-1a	1	3.0%	4404.1	1.5	48.411	0.039	2.5404	0.0030	82.06	0.21	13.477	0.016	0.1719	2.9664	0.0079	8.64	7.86	0.10	19.34	2.852	0.037	1.3
MH01S-1b	2	3.0%	2052.15	0.66	23.632	0.025	1.1720	0.0011	36.96	0.15	6.2176	0.0057	0.0839	2.737	0.011	9.54	8.287	0.078	28.77	3.007	0.028	0.94
MH01S-1c	3	3.5%	2209.53	0.73	29.025	0.022	1.2395	0.0012	53.06	0.22	6.5754	0.0066	0.1030	3.199	0.013	11.15	8.489	0.072	40.37	3.081	0.026	0.85
MH01S-1d	4	4.0%	1951.57	0.57	29.366	0.024	1.0710	0.0012	58.96	0.13	5.6816	0.0061	0.1043	3.5138	0.0084	13.08	8.693	0.066	52.10	3.155	0.024	0.76
MH01S-1e	5	4.5%	1552.76	0.45	26.277	0.015	0.83318	0.00076	56.94	0.20	4.4200	0.0040	0.0933	3.792	0.013	15.01	8.871	0.049	62.59	3.219	0.018	0.55
MH01S-1f	6	5.0%	1130.31	0.36	22.455	0.017	0.58704	0.00050	52.26	0.23	3.1143	0.0027	0.0797	4.072	0.018	17.74	8.929	0.039	71.56	3.240	0.014	0.44
MH01S-1g	7	6.0%	989.40	0.30	23.521	0.025	0.49376	0.00080	63.83	0.20	2.6194	0.0042	0.0835	4.749	0.016	20.96	8.815	0.056	80.95	3.199	0.020	0.64
MH01S-1h	8	8.0%	872.07	0.16	25.156	0.015	0.41387	0.00043	93.61	0.21	2.1956	0.0023	0.0893	6.512	0.015	24.83	8.609	0.028	91.00	3.124	0.010	0.33
MH01S-1i	9	10.0%	443.99	0.11	14.016	0.035	0.20645	0.00032	80.96	0.16	1.0952	0.0017	0.0498	10.109	0.032	26.35	8.348	0.043	96.60	3.030	0.015	0.51
MH01S-1j	10	14.0%	304.771	0.061	8.518	0.024	0.14968	0.00035	102.67	0.22	0.7940	0.0019	0.0302	21.094	0.075	22.21	7.948	0.070	100.00	2.884	0.025	0.87
																			Total gas age: 3.073 ± 0.047 Ma (2σ)			

[a] Data are corrected for mass spectrometer backgrounds, discrimination, radioactive decay and interference corrections. Errors are one sigma uncertainties and exclude uncertainties in the J-value (propagating this error only has an effect in the third decimal place)

[b] Interference corrections: $(^{36}Ar/^{37}Ar)_{Ca} = (2.5713 \pm 0.0023) \times 10^{-4}$; $(^{39}Ar/^{37}Ar)_{Ca} = (6.6200 \pm 0.0801) \times 10^{-4}$; $(^{40}Ar/^{39}Ar)_{K} = (4.9000 \pm 0.8575) \times 10^{-4}$; $(^{38}Ar/^{39}Ar)_{K} = (1.2136 \pm 0.0016) \times 10^{-2}$

[c] J-value is 0.0002013266 ± 0.0000000961 (0.048%;1σ), based on an age of 1.1814 ± 0.0006 Ma (2σ) for ACR sanidine (Phillips et al., 2017)

[d] Sensitivity = 3.55 x 10^{-17} mol/fA

[e] Heating steps where there was an indication of suppression of isotope signals, possibly due to hydrocarbon contamination. Affected cycles were removed from regression.

Table A.9b. ARGUSVI ^{40}Ar/^{39}Ar laser step-heating analytical results for sample MH01N.[a,b,c,d,e]

Sample ID	Step No	Laser Power	^{40}Ar (fA)	±1σ	^{39}Ar (fA)[b]	±1σ	^{38}Ar (fA)	±1σ	^{37}Ar (fA)[b]	±1σ	^{36}Ar (fA)	±1σ	^{39}Ar (x10^{-14} mol)[d]	Ca/K	±1σ	%^{40}Ar*	^{40}Ar*/^{39}Ar	±1σ	Cum.% ^{39}Ar	Apparent Age (Ma)	±1σ	±1σ (%)
Aliquot: MH01N-1					J-Value = 0.0002013545 ± 0.0000001379 (0.069%;1σ)																	
MH01N-1a	1	3.0%	2984.23	0.98	43.045	0.028	1.6711	0.0024	77.24	0.17	8.865	0.013	0.1528	3.1400	0.0072	11.31	7.840	0.090	22.51	2.846	0.033	1.2
MH01N-1b	2	3.0%	1297.02	0.43	19.494	0.019	0.7161	0.0013	31.89	0.10	3.7988	0.0070	0.0692	2.863	0.010	12.56	8.35	0.11	32.70	3.032	0.040	1.3
MH01N-1c	3	3.5%	1342.98	0.38	23.958	0.040	0.7230	0.0012	46.21	0.18	3.8353	0.0062	0.0851	3.376	0.014	14.74	8.261	0.080	45.23	2.998	0.029	1.0
MH01N-1d	4	4.0%	1119.86	0.37	23.482	0.038	0.5821	0.0012	51.27	0.28	3.0879	0.0062	0.0834	3.821	0.022	17.68	8.429	0.081	57.51	3.059	0.029	1.0
MH01N-1e	5	5.0%	1080.56	0.36	28.393	0.018	0.52990	0.00057	77.39	0.24	2.8111	0.0030	0.1008	4.770	0.015	22.33	8.497	0.035	72.36	3.084	0.013	0.41
MH01N-1f	6	6.0%	683.43	0.23	21.516	0.019	0.31825	0.00047	79.10	0.23	1.6883	0.0025	0.0764	6.434	0.019	26.24	8.336	0.037	83.61	3.026	0.013	0.45
MH01N-1g	7	8.0%	572.82	0.11	18.559	0.033	0.26755	0.00032	125.48	0.25	1.4194	0.0017	0.0659	11.832	0.032	26.02	8.032	0.031	93.32	2.915	0.011	0.39
MH01N-1h	8	12.0%	406.77	0.13	9.790	0.024	0.20864	0.00060	178.87	0.19	1.1068	0.0032	0.0348	31.973	0.085	18.76	7.80	0.10	98.44	2.830	0.036	1.3
MH01N-1i	9	14.0%	138.842	0.079	2.986	0.023	0.07312	0.00043	72.86	0.15	0.3879	0.0023	0.0106	42.70	0.34	16.59	7.71	0.23	100.00	2.800	0.085	3.0
																			Total gas age: 2.971 ± 0.053 Ma (2σ)			
Aliquot: MH01N-2					J-Value = 0.0002013545 ± 0.0000001379 (0.069%;1σ)																	
MH01N-2a	1	2.5%	1105.41	0.42	9.421	0.014	0.6613	0.0011	10.0	1.3	3.5083	0.0058	0.0334	1.86	0.24	5.24	6.15	0.19	4.38	2.234	0.068	3.1
MH01N-2b	2	3.0%	1421.25	0.87	13.019	0.030	0.8407	0.0013	15.29	0.92	4.4602	0.0067	0.0462	2.05	0.12	6.31	6.88	0.17	10.44	2.499	0.061	2.5
MH01N-2c	3	3.5%	1569.55	0.66	15.938	0.023	0.9217	0.0012	21.7	1.1	4.8894	0.0064	0.0566	2.38	0.12	6.99	6.89	0.13	17.85	2.500	0.046	1.9
MH01N-2e	4	4.0%	1551.1	1.5	17.380	0.025	0.8999	0.0023	24.6	1.2	4.774	0.012	0.0617	2.48	0.12	8.10	7.23	0.23	25.93	2.625	0.082	3.1
MH01N-2f	5	5.0%	1944.05	0.95	24.920	0.013	1.1105	0.0025	42.15	0.68	5.891	0.013	0.0885	2.960	0.047	9.52	7.43	0.16	37.52	2.697	0.060	2.2
MH01N-2g	6	6.0%	1823.09	0.73	26.442	0.019	1.01798	0.00091	48.32	0.73	5.4005	0.0048	0.0939	3.198	0.048	11.56	7.969	0.061	49.82	2.893	0.022	0.77
MH01N-2h	7	8.0%	2142.1	1.0	37.535	0.051	1.1640	0.0020	74.9	1.2	6.175	0.010	0.1332	3.494	0.056	13.94	7.954	0.088	67.28	2.887	0.032	1.1
MH01N-2i	8	10.0%	1590.47	0.46	33.552	0.032	0.8216	0.0018	75.76	0.52	4.3589	0.0095	0.1191	3.951	0.028	18.18	8.616	0.086	82.88	3.127	0.031	1.0
MH01N-2j	9	14.0%	1365.08	0.42	36.811	0.041	0.66108	0.00084	111.77	0.91	3.5071	0.0044	0.1307	5.314	0.044	23.30	8.639	0.039	100.00	3.135	0.014	0.45
																			Total gas age: 2.844 ± 0.079 Ma (2σ)			

[a] Data are corrected for mass spectrometer backgrounds, discrimination, radioactive decay and interference corrections. Errors are one sigma uncertainties and exclude uncertainties in the J-value (propagating this error only has an effect in the third decimal place)

[b] Interference corrections: $(^{36}Ar/^{37}Ar)_{Ca}$ = (2.5713 ± 0.0023) x 10^{-4}; $(^{39}Ar/^{37}Ar)_{Ca}$ = (6.6200 ± 0.0801) x 10^{-4}; $(^{40}Ar/^{39}Ar)_{K}$ = (4.9000 ± 0.8575) x 10^{-4}; $(^{38}Ar/^{39}Ar)_{K}$ = (1.2136 ± 0.0016) x 10^{-2}

[c] J-value is 0.0002013545 ± 0.0000001379 (0.069%;1σ), based on an age of 1.1814 ± 0.0006 Ma (2σ) for ACR sanidine (Phillips et al., 2017)

[d] Sensitivity = 3.55 x 10^{-17} mol/fA

[e] Heating steps where there was an indication of suppression of isotope signals, possibly due to hydrocarbon contamination. Affected cycles were removed from regression.

Table A.9c. ARGUSVI ^{40}Ar/^{39}Ar laser step-heating analytical results for sample MH04.[a,b,c,d,e]

Sample ID	Step No	Laser Power	^{40}Ar (fA)	±1σ	^{39}Ar (fA)[b]	±1σ	^{38}Ar (fA)	±1σ	^{37}Ar (fA)[b]	±1σ	^{36}Ar (fA)	±1σ	^{39}Ar (x10^{-14} mol)[d]	Ca/K	±1σ	%^{40}Ar*	^{40}Ar*/^{39}Ar	±1σ	Cum.% ^{39}Ar	Apparent Age (Ma)	±1σ	±1σ (%)
Aliquot: MH04-1					J-Value = 0.0002010887 ± 0.0000000558 (0.028%;1σ)																	
MH04-1a	1	3.0%	5513.5	2.1	63.426	0.042	3.1670	0.0024	56.15	0.18	16.801	0.013	0.2252	1.5493	0.0050	9.02	7.842	0.070	22.17	2.843	0.025	0.89
MH04-1b	2	3.0%	2573.34	0.85	30.812	0.022	1.4651	0.0014	25.87	0.20	7.7723	0.0073	0.1094	1.470	0.012	9.83	8.206	0.076	32.94	2.974	0.028	0.93
MH04-1c	3	3.0%	1633.16	0.56	20.199	0.025	0.92422	0.00070	17.87	0.14	4.9030	0.0037	0.0717	1.548	0.012	10.37	8.382	0.062	40.01	3.038	0.022	0.74
MH04-1d	4	3.5%	2100.79	0.63	27.542	0.030	1.18122	0.00084	29.79	0.20	6.2664	0.0044	0.0978	1.893	0.013	10.94	8.346	0.054	49.63	3.025	0.020	0.65
MH04-1e	5	4.0%	2090.62	0.65	29.241	0.021	1.1642	0.0016	36.23	0.15	6.1762	0.0083	0.1038	2.1683	0.0093	11.80	8.435	0.088	59.86	3.057	0.032	1.0
MH04-1f	6	4.5%	1783.20	0.48	26.723	0.028	0.9813	0.0010	37.18	0.18	5.2056	0.0053	0.0949	2.435	0.012	12.84	8.570	0.063	69.20	3.106	0.023	0.73
MH04-1g	7	5.0%	1400.90	0.45	22.637	0.024	0.76226	0.00074	35.85	0.25	4.0438	0.0039	0.0804	2.771	0.020	13.82	8.551	0.056	77.11	3.099	0.020	0.66
MH04-1h	8	6.0%	1279.78	0.44	22.614	0.029	0.68481	0.00059	44.88	0.19	3.6329	0.0031	0.0803	3.473	0.016	15.25	8.629	0.047	85.02	3.128	0.017	0.55
MH04-1i	9	8.0%	1140.13	0.32	22.690	0.026	0.59565	0.00079	69.56	0.23	3.1599	0.0042	0.0805	5.365	0.019	17.25	8.669	0.057	92.95	3.142	0.021	0.66
MH04-1j	10	10.0%	545.51	0.15	12.558	0.028	0.27673	0.00045	61.16	0.10	1.4681	0.0024	0.0446	8.523	0.023	19.65	8.537	0.061	97.34	3.094	0.022	0.71
MH04-1k	11	14.0%	310.101	0.084	7.613	0.039	0.15585	0.00020	79.79	0.17	0.8268	0.0011	0.0270	18.340	0.102	20.40	8.309	0.061	100.00	3.012	0.022	0.74
																			Total gas age: 3.017 ± 0.047 Ma (2σ)			

[a] Data are corrected for mass spectrometer backgrounds, discrimination, radioactive decay and interference corrections. Errors are one sigma uncertainties and exclude uncertainties in the J-value (propagating this error only has an effect in the third decimal place)

[b] Interference corrections: $(^{36}Ar/^{37}Ar)_{Ca}$ = (2.5713 ± 0.0023) x 10^{-4}; $(^{39}Ar/^{37}Ar)_{Ca}$ = (6.6200 ± 0.0801) x 10^{-4}; $(^{40}Ar/^{39}Ar)_{K}$ = (4.9000 ± 0.8575) x 10^{-4}; $(^{38}Ar/^{39}Ar)_{K}$ = (1.2136 ± 0.0016) x 10^{-2}

[c] J-value is 0.0002010887 ± 0.0000000558 (0.028%;1σ), based on an age of 1.1814 ± 0.0006 Ma (2σ) for ACR sanidine (Phillips et al., 2017)

[d] Sensitivity = 3.55 x 10^{-17} mol/fA

[e] Heating steps where there was an indication of suppression of isotope signals, possibly due to hydrocarbon contamination. Affected cycles were removed from regression.

Table A.9d. ARGUSVI ^{40}Ar/^{39}Ar laser step-heating analytical results for sample MH11.[a,b,c,d,e]

Sample ID	Step No	Laser Power	^{40}Ar (fA)	±1σ	^{39}Ar (fA)[b]	±1σ	^{38}Ar (fA)	±1σ	^{37}Ar (fA)[b]	±1σ	^{36}Ar (fA)	±1σ	^{39}Ar (x10^{-14} mol)[d]	Ca/K	±1σ	%^{40}Ar*	^{40}Ar*/^{39}Ar	±1σ	Cum.% ^{39}Ar	Apparent Age (Ma)	±1σ	±1σ (%)
Aliquot: MH11-1					J-Value = 0.0002001349 ± 0.0000003302 (0.165%;1σ)																	
MH11-1a	1	3.0%	5882.2	9.5	41.022	0.026	3.571	0.010	32.01	0.56	18.942	0.051	0.1456	1.366	0.024	3.86	5.53	0.44	8.77	2.00	0.16	7.9
MH11-1b	2	3.0%	3181.0	3.6	22.962	0.033	1.9267	0.0040	16.15	0.61	10.221	0.021	0.0815	1.231	0.046	4.07	5.63	0.32	13.67	2.03	0.11	5.6
MH11-1c	3	3.0%	2263.8	2.1	16.548	0.035	1.3632	0.0022	11.13	0.56	7.232	0.012	0.0587	1.177	0.059	4.63	6.33	0.25	17.21	2.284	0.090	3.9
MH11-1d	4	3.0%	1742.8	1.0	12.839	0.030	1.0428	0.0015	9.60	0.61	5.5322	0.0081	0.0456	1.309	0.083	5.23	7.10	0.20	19.95	2.560	0.074	2.9
MH11-1e	5	3.0%	1421.56	0.80	10.741	0.036	0.8432	0.0020	6.91	0.71	4.473	0.011	0.0381	1.13	0.12	6.06	8.01	0.31	22.25	2.89	0.11	3.8
MH11-1f	6	3.5%	2319.0	1.8	18.879	0.035	1.3758	0.0019	18.33	0.76	7.299	0.010	0.0670	1.699	0.071	6.04	7.41	0.19	26.28	2.675	0.067	2.5
MH11-1g	7	3.5%	1782.4	1.1	14.804	0.030	1.0555	0.0011	14.69	0.92	5.5994	0.0057	0.0526	1.74	0.11	6.21	7.47	0.14	29.44	2.697	0.050	1.8
MH11-1h	8	3.5%	1451.02	0.70	12.292	0.037	0.8554	0.0009	11.65	0.87	4.5378	0.0050	0.0436	1.66	0.12	6.63	7.83	0.14	32.07	2.824	0.049	1.7
MH11-1i	9	3.5%	1208.98	0.22	10.393	0.023	0.7118	0.0012	9.06	0.68	3.7759	0.0064	0.0369	1.53	0.11	6.75	7.86	0.19	34.29	2.834	0.067	2.4
MH11-1j	10	4.0%	1824.7	1.0	16.909	0.031	1.0673	0.0023	18.7	1.2	5.662	0.012	0.0600	1.94	0.12	7.36	7.94	0.23	37.90	2.864	0.082	2.8
MH11-1k	11	4.0%	1447.14	0.71	13.649	0.025	0.8453	0.0010	15.52	0.77	4.4846	0.0051	0.0485	1.989	0.099	7.48	7.93	0.12	40.82	2.860	0.045	1.6
MH11-1l	12	4.5%	1900.3	1.1	19.488	0.032	1.1006	0.0010	24.35	0.97	5.8388	0.0055	0.0692	2.186	0.087	8.27	8.06	0.10	44.98	2.908	0.037	1.3
MH11-1m	13	5.0%	2183.8	1.4	24.182	0.031	1.2545	0.0024	31.52	0.87	6.655	0.013	0.0858	2.281	0.063	9.01	8.14	0.17	50.15	2.935	0.060	2.0
MH11-1n	14	5.5%	2254.8	1.6	26.964	0.032	1.2829	0.0024	37.50	0.95	6.806	0.012	0.0957	2.434	0.062	9.88	8.26	0.15	55.91	2.981	0.055	1.8
MH11-1o	15	6.0%	2120.9	1.4	27.532	0.027	1.1894	0.0013	40.75	0.46	6.3100	0.0068	0.0977	2.590	0.029	11.18	8.609	0.090	61.79	3.106	0.032	1.0
MH11-1p	16	7.0%	2333.2	1.8	34.663	0.043	1.2853	0.0023	54.18	0.60	6.819	0.012	0.1231	2.735	0.030	12.75	8.58	0.12	69.20	3.096	0.043	1.4
MH11-1q	17	8.0%	2116.1	1.6	35.971	0.045	1.1360	0.0013	58.82	0.52	6.0265	0.0067	0.1277	2.862	0.026	14.97	8.808	0.071	76.89	3.177	0.026	0.81
MH11-1r	18	9.0%	1693.6	1.1	32.885	0.036	0.8867	0.0013	55.49	0.39	4.7039	0.0068	0.1167	2.953	0.021	17.08	8.794	0.070	83.91	3.172	0.025	0.80
MH11-1s	19	10.0%	1223.93	0.48	27.451	0.048	0.6149	0.0017	49.86	0.79	3.2619	0.0090	0.0975	3.178	0.051	20.43	9.11	0.10	89.78	3.286	0.036	1.1
MH11-1t	20	12.0%	1053.10	0.40	27.408	0.015	0.5135	0.0010	56.78	0.88	2.7239	0.0053	0.0973	3.625	0.056	22.78	8.751	0.060	95.63	3.157	0.022	0.68
MH11-1u	21	14.0%	770.11	0.14	20.434	0.023	0.3742	0.0006	50.56	0.93	1.9851	0.0034	0.0725	4.330	0.080	23.04	8.683	0.052	100.00	3.132	0.019	0.59

Total gas age: 2.85 ± 0.12 Ma (2σ)

[a] Data are corrected for mass spectrometer backgrounds, discrimination, radioactive decay and interference corrections. Errors are one sigma uncertainties and exclude uncertainties in the J-value (propagating this error only has an effect in the third decimal place)

[b] Interference corrections: $(^{36}Ar/^{37}Ar)_{Ca}$ = (2.5713 ± 0.0023) x 10^{-4}; $(^{39}Ar/^{37}Ar)_{Ca}$ = (6.6200 ± 0.0801) x 10^{-4}; $(^{40}Ar/^{39}Ar)_K$ = (4.9000 ± 0.8575) x 10^{-4}; $(^{38}Ar/^{39}Ar)_K$ = (1.2136 ± 0.0016) x 10^{-2}

[c] J-value is 0.0002001349 ± 0.0000003302 (0.165%;1σ), based on an age of 1.1814 ± 0.0006 Ma (2σ) for ACR sanidine (Phillips et al., 2017)

[d] Sensitivity = 3.55 x 10^{-17} mol/fA

[e] Heating steps where there was an indication of suppression of isotope signals, possibly due to hydrocarbon contamination. Affected cycles were removed from regression.

Table A.9e. ARGUSVI ^{40}Ar/^{39}Ar laser step-heating analytical results for sample MH56A.[a,b,c,d,e]

Sample ID	Step No	Laser Power	^{40}Ar (fA)	±1σ	^{39}Ar (fA)[b]	±1σ	^{38}Ar (fA)	±1σ	^{37}Ar (fA)[b]	±1σ	^{36}Ar (fA)	±1σ	^{39}Ar (x10^{-14} mol)[d]	Ca/K	±1σ	%^{40}Ar*	^{40}Ar*/^{39}Ar	±1σ	Cum.% ^{39}Ar	Apparent Age (Ma)	±1σ	±1σ (%)
Aliquot: MH56A-1					J-Value = 0.0002092906 ± 0.0000001126 (0.054%;1σ)																	
MH56A-1a	1	3.0%	2603.80	0.68	55.047	0.028	1.4397	0.0023	81.26	0.84	7.638	0.012	0.1954	2.583	0.027	12.42	5.876	0.067	23.48	2.217	0.025	1.1
MH56A-1b	2	3.5%	1770.64	0.97	40.488	0.031	0.9507	0.0023	59.6	1.7	5.043	0.012	0.1437	2.577	0.073	14.96	6.542	0.094	40.76	2.468	0.036	1.4
MH56A-1c	3	4.0%	1340.0	1.1	32.729	0.022	0.7007	0.0026	60.7	1.7	3.717	0.014	0.1162	3.246	0.093	17.18	7.03	0.13	54.72	2.653	0.049	1.8
MH56A-1d	4	5.0%	1274.05	0.52	33.628	0.040	0.6494	0.0012	73.9	1.9	3.4452	0.0066	0.1194	3.84	0.10	19.27	7.299	0.061	69.06	2.754	0.023	0.84
MH56A-1e	5	6.0%	841.27	0.30	24.182	0.016	0.41091	0.00070	66.7	2.0	2.1799	0.0037	0.0858	4.83	0.14	22.64	7.875	0.048	79.38	2.971	0.018	0.61
MH56A-1f	6	8.0%	618.51	0.28	19.601	0.018	0.29145	0.00069	82.4	2.3	1.5461	0.0036	0.0696	7.35	0.21	25.37	8.005	0.058	87.74	3.020	0.022	0.72
MH56A-1g	7	12.0%	416.31	0.24	13.765	0.009	0.19549	0.00056	109.0	1.3	1.0371	0.0030	0.0489	13.86	0.16	25.62	7.750	0.067	93.61	2.924	0.025	0.86
MH56A-1h	8	20.0%	317.51	0.14	8.771	0.013	0.15854	0.00045	150.3	1.5	0.8410	0.0024	0.0311	29.99	0.30	20.91	7.571	0.084	97.35	2.856	0.032	1.1
MH56A-1i[e]	9	35.0%	1815.77	0.74	6.202	0.021	1.1316	0.0024	133.5	1.7	6.003	0.013	0.0220	37.66	0.51	1.29	3.78	0.64	100.00	1.43	0.24	17
																			Total gas age: 2.619 ± 0.059 Ma (2σ)			

[a] Data are corrected for mass spectrometer backgrounds, discrimination, radioactive decay and interference corrections. Errors are one sigma uncertainties and exclude uncertainties in the J-value (propagating this error only has an effect in the third decimal place)

[b] Interference corrections: $(^{36}Ar/^{37}Ar)_{Ca} = (2.5798 \pm 0.0027) \times 10^{-4}$; $(^{39}Ar/^{37}Ar)_{Ca} = (6.5640 \pm 0.0135) \times 10^{-4}$; $(^{40}Ar/^{39}Ar)_{K} = (3.8900 \pm 0.2140) \times 10^{-4}$; $(^{38}Ar/^{39}Ar)_{K} = (1.1999 \pm 0.0004) \times 10^{-2}$

[c] J-value is 0.0002092906 ± 0.0000001126 (0.054%;1σ), based on an age of 1.1814 ± 0.0006 Ma (2σ) for ACR sanidine (Phillips et al., 2017)

[d] Sensitivity = 3.55 x 10^{-17} mol/fA

[e] Heating steps where faulty cover glass was outgassed, introducing air contamination

Table A.9f. ARGUSVI ^{40}Ar/^{39}Ar laser step-heating analytical results for sample BH269.[a,b,c,d,e]

Sample ID	Step No	Laser Power	^{40}Ar (fA)	±1σ	^{39}Ar (fA)[b]	±1σ	^{38}Ar (fA)	±1σ	^{37}Ar (fA)[b]	±1σ	^{36}Ar (fA)	±1σ	^{39}Ar (x10^{-14} mol)[d]	Ca/K	±1σ	%^{40}Ar*	^{40}Ar*/^{39}Ar	±1σ	Cum.% ^{39}Ar	Apparent Age (Ma)	±1σ	±1σ (%)
Aliquot: BH269-1					J-Value = 0.0007859562 ± 0.0000002894 (0.037%;1σ)																	
BH269-1a	1	2.5%	4646.8	2.4	173.33	0.11	2.7752	0.0076	126.31	0.28	14.722	0.040	0.6153	1.2752	0.0029	5.41	1.450	0.071	16.26	2.05	0.10	4.9
BH269-1b	2	3.0%	4559.0	2.1	183.60	0.10	2.6834	0.0062	155.12	0.20	14.236	0.033	0.6518	1.4785	0.0021	6.77	1.682	0.055	33.49	2.383	0.078	3.3
BH269-1c	3	3.5%	3762.66	0.87	166.001	0.025	2.1698	0.0047	166.79	0.24	11.511	0.025	0.5893	1.7583	0.0025	8.66	1.964	0.045	49.06	2.782	0.064	2.3
BH269-1d	4	4.0%	2809.39	0.87	138.538	0.050	1.5876	0.0032	165.01	0.23	8.422	0.017	0.4918	2.0843	0.0031	10.50	2.128	0.037	62.06	3.015	0.053	1.8
BH269-1e	5	4.5%	1891.96	0.68	106.544	0.038	1.0453	0.0022	151.96	0.33	5.545	0.012	0.3782	2.4960	0.0055	12.49	2.219	0.033	72.06	3.143	0.047	1.5
BH269-1f	6	5.0%	1278.58	0.32	83.596	0.044	0.6867	0.0015	141.26	0.18	3.6428	0.0078	0.2968	2.9572	0.0040	14.94	2.285	0.028	79.90	3.236	0.040	1.2
BH269-1g	7	6.0%	933.02	0.28	72.417	0.030	0.4878	0.0017	152.26	0.19	2.5879	0.0090	0.2571	3.6796	0.0048	17.19	2.214	0.037	86.70	3.137	0.053	1.7
BH269-1h	8	8.0%	732.40	0.24	65.835	0.038	0.37365	0.00094	193.86	0.29	1.9822	0.0050	0.2337	5.1531	0.0083	19.19	2.135	0.023	92.87	3.025	0.032	1.1
BH269-1i	9	10.0%	401.10	0.11	33.766	0.031	0.20798	0.00063	142.12	0.29	1.1033	0.0033	0.1199	7.365	0.017	17.87	2.123	0.030	96.04	3.008	0.042	1.4
BH269-1j	10	20.0%	473.81	0.17	30.028	0.021	0.26136	0.00079	233.40	0.31	1.3865	0.0042	0.1066	13.602	0.021	12.63	1.993	0.042	98.86	2.824	0.060	2.1
BH269-1k	11	35.0%	242.73	0.11	12.153	0.014	0.13729	0.00038	79.59	0.24	0.7283	0.0020	0.0431	11.460	0.038	10.41	2.080	0.050	100.00	2.946	0.071	2.4
																			Total gas age: 2.75 ± 0.13 Ma (2σ)			

[a] Data are corrected for mass spectrometer backgrounds, discrimination, radioactive decay and interference corrections. Errors are one sigma uncertainties and exclude uncertainties in the J-value (propagating this error only has an effect in the third decimal place)

[b] Interference corrections: $(^{36}Ar/^{37}Ar)_{Ca}$ = (2.5798 ± 0.0027) x 10^{-4}; $(^{39}Ar/^{37}Ar)_{Ca}$ = (6.5640 ± 0.0135) x 10^{-4}; $(^{40}Ar/^{39}Ar)_{K}$ = (3.8900 ± 0.2140) x 10^{-4}; $(^{38}Ar/^{39}Ar)_{K}$ = (1.1999 ± 0.0004) x 10^{-2}

[c] J-value is 0.0007859562 ± 0.0000002894 (0.037%;1σ), based on an age of 1.1814 ± 0.0006 Ma (2σ) for ACR sanidine (Phillips et al., 2017)

[d] Sensitivity = 3.55 x 10^{-17} mol/fA

[e] Heating steps where there was an indication of suppression of isotope signals, possibly due to hydrocarbon contamination. Affected cycles were removed from regression.

Table A.9g. ARGUSVI ^{40}Ar/^{39}Ar laser step-heating analytical results for sample BH47B.[a,b,c,d,e]

Sample ID	Step No	Laser Power	^{40}Ar (fA)	±1σ	^{39}Ar (fA)[b]	±1σ	^{38}Ar (fA)	±1σ	^{37}Ar (fA)[b]	±1σ	^{36}Ar (fA)	±1σ	^{39}Ar ($\times 10^{-14}$ mol)[d]	Ca/K	±1σ	%^{40}Ar*	^{40}Ar*/^{39}Ar	±1σ	Cum.% ^{39}Ar	Apparent Age (Ma)	±1σ	±1σ (%)
Aliquot: BH47B-1					J-Value = 0.0007876857 ± 0.0000002257 (0.029%;1σ)																	
BH47B-1a	1	3.0%	3667.4	2.1	247.55	0.23	2.0421	0.0057	204.43	0.37	10.834	0.030	0.8788	1.4452	0.0029	11.81	1.749	0.038	22.38	2.484	0.053	2.1
BH47B-1b	2	3.5%	2503.5	1.3	180.01	0.10	1.3654	0.0030	171.80	0.42	7.243	0.016	0.6390	1.6701	0.0042	13.62	1.894	0.027	38.65	2.689	0.039	1.4
BH47B-1c	3	4.0%	1800.15	0.72	136.693	0.052	0.9728	0.0032	166.93	0.46	5.161	0.017	0.4853	2.1371	0.0059	14.41	1.898	0.037	51.01	2.695	0.053	2.0
BH47B-1d	4	5.0%	1566.32	0.44	127.321	0.069	0.8292	0.0017	215.57	0.28	4.3992	0.0090	0.4520	2.9630	0.0042	16.15	1.986	0.021	62.51	2.821	0.030	1.1
BH47B-1e	5	6.0%	1135.95	0.32	97.806	0.024	0.5953	0.0018	215.52	0.43	3.1579	0.0094	0.3472	3.8562	0.0078	17.00	1.975	0.029	71.36	2.804	0.041	1.5
BH47B-1f	6	8.0%	1168.91	0.54	102.299	0.072	0.6120	0.0021	290.64	0.18	3.247	0.011	0.3632	4.9720	0.0047	17.08	1.951	0.032	80.60	2.771	0.046	1.7
BH47B-1g	7	10.0%	859.73	0.17	73.641	0.029	0.4521	0.0012	267.92	0.14	2.3984	0.0064	0.2614	6.3669	0.0041	16.71	1.951	0.026	87.26	2.770	0.037	1.3
BH47B-1h	8	20.0%	1143.70	0.14	99.772	0.015	0.59603	0.00089	571.22	0.38	3.1620	0.0047	0.3542	10.0193	0.0069	17.46	2.001	0.014	96.28	2.842	0.020	0.71
BH47B-1i	9	35.0%	757.22	0.27	41.174	0.026	0.42576	0.00080	273.52	0.25	2.2587	0.0043	0.1462	11.625	0.013	10.94	2.013	0.032	100.00	2.858	0.045	1.6
																			Total gas age: 2.702 ± 0.084 Ma (2σ)			

[a] Data are corrected for mass spectrometer backgrounds, discrimination, radioactive decay and interference corrections. Errors are one sigma uncertainties and exclude uncertainties in the J-value (propagating this error only has an effect in the third decimal place)

[b] Interference corrections: $(^{36}\mathrm{Ar}/^{37}\mathrm{Ar})_{Ca} = (2.5798 \pm 0.0027) \times 10^{-4}$; $(^{39}\mathrm{Ar}/^{37}\mathrm{Ar})_{Ca} = (6.5640 \pm 0.0135) \times 10^{-4}$; $(^{40}\mathrm{Ar}/^{39}\mathrm{Ar})_{K} = (3.8900 \pm 0.2140) \times 10^{-4}$; $(^{38}\mathrm{Ar}/^{39}\mathrm{Ar})_{K} = (1.1999 \pm 0.0004) \times 10^{-2}$

[c] J-value is 0.0007876857 ± 0.0000002257 (0.029%;1σ), based on an age of 1.1814 ± 0.0006 Ma (2σ) for ACR sanidine (Phillips et al., 2017)

[d] Sensitivity = 3.55×10^{-17} mol/fA

[e] Heating steps where there was an indication of suppression of isotope signals, possibly due to hydrocarbon contamination. Affected cycles were removed from regression.

Table A.9h. Mt Kororoit age calculation

Aliquant	Isochron Age (Ma)	±2σ
MH01S-1	3.06	0.24
MH01N-1	3.01	0.27
MH04-1	3.16	0.16
BH47B-1	3.02	0.52
Wtd Avg. Age (Ma):	**3.10**	**0.12**

Appendix A.10. ARGUSVI $^{40}Ar/^{39}Ar$ laser step-heating analytical results for Mount Ridley Flow samples

Table A.10a. ARGUSVI $^{40}Ar/^{39}Ar$ laser step-heating analytical results for sample KA13M.[a,b,c,d]

Sample ID	Step No	Laser Power	^{40}Ar (fA)	±1σ	^{39}Ar (fA)[b]	±1σ	^{38}Ar (fA)	±1σ	^{37}Ar (fA)[b]	±1σ	^{36}Ar (fA)	±1σ	^{39}Ar ($x10^{-14}$ mol)[d]	Ca/K	±1σ	$\%^{40}Ar^*$	$^{40}Ar^*/^{39}Ar$	±1σ	Cum.% ^{39}Ar	Apparent Age (Ma)	±1σ
Aliquant: KA13M-1					J-Value = 0.0007948441 ± 0.0000005843 (0.074%;1σ)																
KA13M-1a	1	0.025	981.83	0.27	255.938	0.097	0.09247	0.00032	84.69	0.17	0.4906	0.0017	0.9086	0.5790	0.0012	85.07	3.2640	0.0026	17.41	4.6743	0.0037
KA13M-1b	2	0.03	796.20	0.20	209.002	0.059	0.07447	0.00019	66.75	0.24	0.3951	0.0010	0.7420	0.5589	0.0020	85.18	3.2452	0.0020	31.62	4.6475	0.0028
KA13M-1c	3	0.035	730.26	0.22	189.722	0.059	0.07276	0.00021	69.11	0.20	0.3860	0.0011	0.6735	0.6374	0.0018	84.21	3.2417	0.0024	44.52	4.6425	0.0034
KA13M-1d	4	0.04	642.99	0.23	164.664	0.069	0.06975	0.00023	72.49	0.21	0.3700	0.0012	0.5846	0.7704	0.0023	82.81	3.2339	0.0029	55.72	4.6313	0.0042
KA13M-1e	5	0.05	752.65	0.24	187.64	0.10	0.09410	0.00035	123.25	0.25	0.4992	0.0018	0.6661	1.1495	0.0024	80.19	3.2168	0.0036	68.48	4.6068	0.0052
KA13M-1f	6	0.06	652.848	0.085	158.665	0.041	0.09228	0.00034	156.24	0.24	0.4895	0.0018	0.5633	1.7232	0.0027	77.60	3.1935	0.0035	79.27	4.5735	0.0050
KA13M-1g	7	0.08	682.00	0.25	156.348	0.050	0.11900	0.00025	304.26	0.25	0.6313	0.0013	0.5550	3.4056	0.0030	72.36	3.1566	0.0031	89.90	4.5207	0.0045
KA13M-1h	8	0.1	401.387	0.048	83.035	0.022	0.08503	0.00033	345.93	0.21	0.4511	0.0017	0.2948	7.2906	0.0048	66.44	3.2120	0.0064	95.55	4.6000	0.0091
KA13M-1i	9	0.2	307.756	0.043	51.153	0.041	0.09443	0.00033	667.79	0.37	0.5009	0.0018	0.1816	22.846	0.022	51.40	3.093	0.011	99.03	4.429	0.015
KA13M-1j	10	0.35	102.520	0.039	14.255	0.026	0.03594	0.00013	221.36	0.21	0.19064	0.00068	0.0506	27.174	0.055	44.48	3.199	0.016	100.00	4.581	0.022
																			Total gas age: 4.612 ± 0.010 Ma (2σ)		
Aliquant: KA13M-2					J-Value = 0.0007948441 ± 0.0000005843 (0.074%;1σ)																
KA13M-2a	1	0.025	760.23	0.27	191.762	0.073	0.08451	0.00016	66.71	0.27	0.44831	0.00087	0.6808	0.6088	0.0024	82.39	3.2665	0.0023	6.89	4.6779	0.0033
KA13M-2b	2	0.03	1084.89	0.26	275.943	0.075	0.11740	0.00048	96.26	0.32	0.6228	0.0026	0.9796	0.6105	0.0020	82.85	3.2577	0.0030	16.81	4.6654	0.0044
KA13M-2c	3	0.035	1227.60	0.39	312.99	0.11	0.13241	0.00027	113.28	0.30	0.7025	0.0015	1.1111	0.6334	0.0017	82.91	3.2521	0.0022	28.06	4.6574	0.0032
KA13M-2d	4	0.04	1200.31	0.32	307.00	0.12	0.12894	0.00041	118.95	0.21	0.6841	0.0022	1.0898	0.6781	0.0012	82.98	3.2446	0.0027	39.09	4.6466	0.0038
KA13M-2e	5	0.05	1662.10	0.52	423.78	0.19	0.18525	0.00033	200.08	0.39	0.9828	0.0018	1.5044	0.8262	0.0017	82.34	3.2297	0.0023	54.32	4.6253	0.0032
KA13M-2f	6	0.06	1484.11	0.49	375.14	0.21	0.17541	0.00066	230.79	0.33	0.9306	0.0035	1.3317	1.0766	0.0017	81.27	3.2155	0.0036	67.80	4.6051	0.0051
KA13M-2g	7	0.08	1667.16	0.82	406.92	0.17	0.23248	0.00072	443.82	0.58	1.2333	0.0038	1.4445	1.9087	0.0026	77.91	3.1922	0.0037	82.43	4.5717	0.0053
KA13M-2h	8	0.14	1757.37	0.58	389.68	0.26	0.33940	0.00082	1225.6	1.6	1.8005	0.0044	1.3834	5.5041	0.0079	69.41	3.1303	0.0042	96.43	4.4832	0.0060
KA13M-2i	9	0.35	596.65	0.13	99.214	0.022	0.18247	0.00056	1017.42	0.54	0.9680	0.0030	0.3522	17.946	0.010	51.56	3.1008	0.0091	100.00	4.441	0.013
																			Total gas age: 4.602 ± 0.009 Ma (2σ)		

[a] Data are corrected for mass spectrometer backgrounds, discrimination, radioactive decay and interference corrections. Errors are one sigma uncertainties and exclude uncertainties in the J-value (propagating this error only has an effect in the third decimal place)

[b] Interference corrections: $(^{36}Ar/^{37}Ar)_{Ca} = (2.5798 \pm 0.0027) \times 10^{-4}$; $(^{39}Ar/^{37}Ar)_{Ca} = (6.5640 \pm 0.0135) \times 10^{-4}$; $(^{40}Ar/^{39}Ar)_{K} = (3.8900 \pm 0.2140) \times 10^{-4}$; $(^{38}Ar/^{39}Ar)_{K} = (1.1999 \pm 0.0004) \times 10^{-2}$

[c] J-value is 0.0007948441 ± 0.0000005843 (0.074%;1σ), based on an age of 1.1814 ± 0.0006 Ma (2σ) for ACR sanidine (Phillips et al., 2017)

[d] Sensitivity = 3.55×10^{-17} mol/fA

Table A.10b. Mount Ridley Flow age calculation

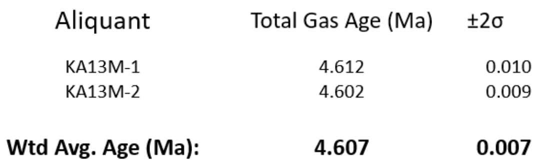

Aliquant	Total Gas Age (Ma)	±2σ
KA13M-1	4.612	0.010
KA13M-2	4.602	0.009
Wtd Avg. Age (Ma):	**4.607**	**0.007**

Appendix A.11. ARGUSVI ^{40}Ar/^{39}Ar laser step-heating analytical results for Redstone Hill Flow samples

Table A.11a. ARGUSVI ^{40}Ar/^{39}Ar laser step-heating analytical results for sample MH02.[a,b,c,d]

Sample ID	Step No	Laser Power	^{40}Ar (fA)	±1σ	^{39}Ar (fA)[b]	±1σ	^{38}Ar (fA)	±1σ	^{37}Ar (fA)[b]	±1σ	^{36}Ar (fA)	±1σ	^{39}Ar (x10^{-14} mol)[d]	Ca/K	±1σ	%^{40}Ar*	^{40}Ar*/^{39}Ar	±1σ	Cum.% ^{39}Ar	Apparent Age (Ma)	±1σ	±1σ (%)
Aliquot: MH02-1					J-Value = 0.0002013823 ± 0.0000001797 (0.089%;1σ)																	
MH02-1a	1	0.03	2865.74	0.92	152.052	0.052	0.15289	0.00040	102.28	0.17	0.8111	0.0021	0.5398	1.1772	0.0020	91.55	17.2545	0.0094	25.34	6.2579	0.0034	0.054
MH02-1b	2	0.035	2222.01	0.64	121.042	0.050	0.09520	0.00037	68.42	0.15	0.5050	0.0020	0.4297	0.9892	0.0022	93.21	17.112	0.010	45.51	6.2061	0.0036	0.059
MH02-1c	3	0.04	1790.99	0.54	98.554	0.037	0.07331	0.00014	50.90	0.13	0.38889	0.00074	0.3499	0.9038	0.0024	93.51	16.9945	0.0087	61.94	6.1637	0.0032	0.051
MH02-1d	4	0.05	1948.37	0.51	107.223	0.046	0.08844	0.00015	61.018	0.099	0.46915	0.00078	0.3806	0.9959	0.0017	92.81	16.8648	0.0089	79.81	6.1168	0.0032	0.053
MH02-1e	5	0.06	1146.21	0.38	62.578	0.037	0.06125	0.00020	44.96	0.13	0.3249	0.0011	0.2222	1.2574	0.0037	91.53	16.766	0.013	90.24	6.0811	0.0046	0.075
MH02-1f	6	0.08	750.59	0.15	39.599	0.025	0.06502	0.00017	62.00	0.15	0.34494	0.00089	0.1406	2.7401	0.0067	86.28	16.354	0.013	96.84	5.9318	0.0047	0.080
MH02-1g	7	0.1	260.607	0.073	12.572	0.028	0.03768	0.00015	51.93	0.19	0.19989	0.00078	0.0446	7.228	0.031	77.10	15.982	0.040	98.93	5.797	0.015	0.25
MH02-1h	8	0.14	154.296	0.077	6.393	0.026	0.03131	0.00013	60.48	0.21	0.16608	0.00069	0.0227	16.556	0.088	67.86	16.380	0.075	100.00	5.941	0.027	0.46
																			Total gas age: 6.154 ± 0.008 Ma (2σ)			

[a] Data are corrected for mass spectrometer backgrounds, discrimination, radioactive decay and interference corrections. Errors are one sigma uncertainties and exclude uncertainties in the J-value (propagating this error only has an effect in the third decimal place)

[b] Interference corrections: $(^{36}Ar/^{37}Ar)_{Ca}$ = (2.5713 ± 0.0023) x 10^{-4}; $(^{39}Ar/^{37}Ar)_{Ca}$ = (6.6200 ± 0.0801) x 10^{-4}; $(^{40}Ar/^{39}Ar)_{K}$ = (4.9000 ± 0.8575) x 10^{-4}; $(^{38}Ar/^{39}Ar)_{K}$ = (1.2136 ± 0.0016) x 10^{-2}

[c] J-value is 0.0002013823 ± 0.0000001797 (0.089%;1σ), based on an age of 1.1814 ± 0.0006 Ma (2σ) for ACR sanidine (Phillips et al., 2017)

[d] Sensitivity = 3.55 x 10^{-17} mol/fA

[e] Heating steps where there was an indication of suppression of isotope signals, possibly due to hydrocarbon contamination. Affected cycles were removed from regression.

Table A.11b. ARGUSVI ^{40}Ar/^{39}Ar laser step-heating analytical results for sample BH22.[a,b,c,d]

Sample ID	Step No	Laser Power	^{40}Ar (fA)	±1σ	^{39}Ar (fA)[b]	±1σ	^{38}Ar (fA)	±1σ	^{37}Ar (fA)[b]	±1σ	^{36}Ar (fA)	±1σ	^{39}Ar (x10^{-14} mol)[d]	Ca/K	±1σ	%^{40}Ar*	^{40}Ar*/^{39}Ar	±1σ	Cum.% ^{39}Ar	Apparent Age (Ma)	±1σ	±1σ (%)
Aliquot: BB22-1					J-Value = 0.0054163893 ± 0.0000021341 (0.039%;1σ)																	
BB22-1a	1	0.025	1313.26	0.42	398.56	0.13	0.7342	0.0016	123.43	0.14	3.8949	0.0082	1.4149	0.54197	0.00066	11.45	0.3773	0.0063	3.91	3.683	0.061	1.7
BB22-1b	2	0.03	1548.42	0.64	529.15	0.33	0.8628	0.0035	193.88	0.63	4.577	0.018	1.8785	0.6412	0.0021	11.75	0.344	0.010	9.09	3.36	0.10	3.0
BB22-1c	3	0.035	1840.6	1.8	684.66	0.84	1.0173	0.0035	288.67	0.69	5.397	0.018	2.4305	0.7378	0.0020	12.46	0.3350	0.0085	15.81	3.271	0.083	2.5
BB22-1d	4	0.04	1877.9	1.3	754.3	1.4	1.0143	0.0032	349.83	0.98	5.381	0.017	2.6779	0.8116	0.0027	14.45	0.3598	0.0071	23.20	3.513	0.069	2.0
BB22-1e	5	0.045	1764.1	1.2	775.64	0.77	0.9325	0.0034	412.7	1.1	4.947	0.018	2.7535	0.9312	0.0027	16.28	0.3703	0.0070	30.81	3.615	0.069	1.9
BB22-1f	6	0.05	1522.7	1.1	726.77	0.69	0.7795	0.0019	423.63	0.75	4.135	0.010	2.5800	1.0201	0.0021	18.91	0.3964	0.0044	37.93	3.869	0.043	1.1
BB22-1g	7	0.055	1360.81	0.60	713.80	0.42	0.6785	0.0020	473.65	0.85	3.599	0.010	2.5340	1.1612	0.0022	21.03	0.4009	0.0045	44.93	3.913	0.043	1.1
BB22-1h	8	0.06	1137.60	0.47	649.66	0.31	0.5477	0.0016	469.72	0.56	2.9054	0.0085	2.3063	1.2653	0.0016	23.74	0.4158	0.0040	51.30	4.059	0.039	0.96
BB22-1i	9	0.07	1209.10	0.41	786.28	0.31	0.5602	0.0016	670.81	0.76	2.9719	0.0086	2.7913	1.4930	0.0018	26.61	0.4093	0.0033	59.00	3.995	0.032	0.81
BB22-1j	10	0.08	1046.02	0.30	774.73	0.27	0.45701	0.00094	738.49	0.54	2.4244	0.0050	2.7503	1.6681	0.0014	30.79	0.4159	0.0020	66.60	4.059	0.019	0.47
BB22-1k	11	0.09	844.38	0.48	713.96	0.30	0.3458	0.0011	765.21	0.70	1.8346	0.0060	2.5346	1.8756	0.0019	35.12	0.4155	0.0026	73.60	4.055	0.025	0.63
BB22-1l	12	0.1	643.94	0.28	613.99	0.37	0.24645	0.00077	726.26	0.55	1.3074	0.0041	2.1796	2.0700	0.0020	39.37	0.4130	0.0021	79.62	4.032	0.020	0.50
BB22-1m	13	0.14	933.36	0.43	1019.74	0.74	0.3322	0.0010	1677.3	1.4	1.7625	0.0054	3.6201	2.8784	0.0032	43.60	0.3993	0.0017	89.61	3.897	0.016	0.42
BB22-1n	14	0.35	1786.74	0.66	1059.47	0.35	0.8742	0.0026	3643.4	3.6	4.638	0.014	3.7611	6.0181	0.0063	22.50	0.3795	0.0040	100.00	3.705	0.039	1.1
																			Total gas age: 3.797 ± 0.089 Ma (2σ)			

[a] Data are corrected for mass spectrometer backgrounds, discrimination, radioactive decay and interference corrections. Errors are one sigma uncertainties and exclude uncertainties in the J-value (propagating this error only has an effect in the third decimal place)

[b] Interference corrections: $(^{36}Ar/^{37}Ar)_{Ca}$ = (2.5798 ± 0.0027) x 10^{-4}; $(^{39}Ar/^{37}Ar)_{Ca}$ = (6.5640 ± 0.0135) x 10^{-4}; $(^{40}Ar/^{39}Ar)_{K}$ = (3.8900 ± 0.2140) x 10^{-4}; $(^{38}Ar/^{39}Ar)_{K}$ = (1.1999 ± 0.0004) x 10^{-2}

[c] J-value is 0.0054163893 ± 0.0000021341 (0.039%;1σ), based on an age of 28.1260 ± 0.0093 Ma (1σ) for FC sanidine (Phillips et al., 2017)

[d] Sensitivity = 3.55 x 10^{-17} mol/fA

[e] Heating steps where there was an indication of suppression of isotope signals, possibly due to hydrocarbon contamination. Affected cycles were removed from regression.

Appendix A.12. ARGUSVI ^{40}Ar/^{39}Ar laser step-heating analytical results for Springs Hill Flow samples

Table A.12a. ARGUSVI ^{40}Ar/^{39}Ar laser step-heating analytical results for sample ME4J.[a,b,c,d]

Sample ID	Step No	Laser Power	^{40}Ar (fA)	±1σ	^{39}Ar (fA)[b]	±1σ	^{38}Ar (fA)	±1σ	^{37}Ar (fA)[b]	±1σ	^{36}Ar (fA)	±1σ	^{39}Ar (x10^{-14} mol)[d]	Ca/K	±1σ	%^{40}Ar*	^{40}Ar*/^{39}Ar	±1σ	Cum.% ^{39}Ar	Apparent Age (Ma)	±1σ	±1σ (%)
Aliquot: ME4J-1					J-Value = 0.0053888774 ± 0.0000029213 (0.054%;1σ)																	
ME4J-1a	1	2.5%	449.89	0.14	142.475	0.047	0.24935	0.00062	256.09	0.31	1.3228	0.0033	0.5058	3.1455	0.0039	12.21	0.3857	0.0070	3.00	3.746	0.068	1.8
ME4J-1b	2	3.0%	567.73	0.12	202.88	0.13	0.30964	0.00086	392.65	0.62	1.6427	0.0046	0.7202	3.3868	0.0058	13.61	0.3810	0.0067	7.28	3.700	0.065	1.8
ME4J-1c	3	3.5%	642.49	0.31	265.840	0.085	0.33989	0.00098	580.77	0.84	1.8032	0.0052	0.9437	3.8232	0.0057	16.21	0.3917	0.0059	12.89	3.804	0.058	1.5
ME4J-1d	4	4.0%	672.11	0.20	311.35	0.12	0.3481	0.0011	738.93	0.98	1.8466	0.0058	1.1053	4.1533	0.0058	17.97	0.3880	0.0056	19.45	3.768	0.054	1.4
ME4J-1e	5	5.0%	823.09	0.24	449.80	0.18	0.4021	0.0011	1172.34	0.45	2.1330	0.0058	1.5968	4.5611	0.0025	22.63	0.4141	0.0039	28.94	4.021	0.037	0.93
ME4J-1f	6	6.0%	852.66	0.34	516.43	0.27	0.40413	0.00088	1437.85	0.72	2.1439	0.0047	1.8333	4.8724	0.0035	24.92	0.4116	0.0028	39.83	3.997	0.027	0.68
ME4J-1g	7	7.0%	749.48	0.30	500.10	0.19	0.34245	0.00098	1505.79	0.90	1.8167	0.0052	1.7753	5.2693	0.0037	27.62	0.4141	0.0032	50.37	4.021	0.031	0.76
ME4J-1h	8	8.0%	627.58	0.26	447.50	0.17	0.27868	0.00070	1495.7	1.2	1.4784	0.0037	1.5886	5.8491	0.0051	29.66	0.4161	0.0026	59.81	4.040	0.025	0.62
ME4J-1i	9	10.0%	869.72	0.40	558.00	0.34	0.4033	0.0012	2153.6	1.5	2.1396	0.0066	1.9809	6.7542	0.0061	26.55	0.4139	0.0036	71.58	4.019	0.035	0.87
ME4J-1j	10	14.0%	923.52	0.48	732.37	0.47	0.3928	0.0011	3306.7	2.6	2.0836	0.0061	2.5999	7.9013	0.0080	32.63	0.4116	0.0026	87.02	3.997	0.025	0.63
ME4J-1k	11	20.0%	632.25	0.27	469.14	0.31	0.2786	0.0011	3024.6	2.3	1.4781	0.0057	1.6655	11.282	0.011	30.19	0.4070	0.0037	96.91	3.953	0.036	0.91
ME4J-1l	12	35.0%	320.90	0.12	146.505	0.092	0.16570	0.00069	1856.3	1.6	0.8790	0.0036	0.5201	22.173	0.024	18.21	0.3990	0.0075	100.00	3.875	0.072	1.9
																			Total gas			
																				age: 3.954 ± 0.075 Ma (2σ)		
Aliquot: ME4J-2					J-Value = 0.0053888774 ± 0.0000029213 (0.054%;1σ)																	
ME4J-2a	1	2.5%	313.639	0.075	107.595	0.027	0.17109	0.00033	213.70	0.15	0.9076	0.0018	0.3820	3.4758	0.0026	13.60	0.3965	0.0049	3.09	3.850	0.048	1.2
ME4J-2b	2	3.0%	449.08	0.14	161.437	0.019	0.24303	0.00076	329.12	0.22	1.2893	0.0041	0.5731	3.5677	0.0024	14.28	0.3974	0.0075	7.73	3.859	0.073	1.9
ME4J-2c	3	4.0%	827.86	0.21	349.32	0.26	0.4360	0.0011	782.39	0.72	2.3127	0.0056	1.2401	3.9195	0.0046	16.59	0.3932	0.0048	17.76	3.819	0.047	1.2
ME4J-2d	4	5.0%	813.78	0.42	410.93	0.33	0.4092	0.0010	1004.08	0.81	2.1706	0.0055	1.4588	4.2760	0.0049	20.36	0.4033	0.0042	29.56	3.916	0.040	1.0
ME4J-2e	5	6.0%	662.79	0.25	414.17	0.15	0.30976	0.00080	1151.12	0.84	1.6433	0.0042	1.4703	4.8638	0.0039	25.97	0.4157	0.0031	41.45	4.037	0.030	0.75
ME4J-2f	6	8.0%	761.74	0.35	587.11	0.21	0.3265	0.0010	1933.3	1.6	1.7319	0.0054	2.0842	5.7627	0.0051	32.11	0.4167	0.0028	58.31	4.047	0.027	0.67
ME4J-2g	7	10.0%	609.23	0.26	544.35	0.17	0.24102	0.00079	1970.0	1.7	1.2786	0.0042	1.9324	6.3334	0.0057	37.33	0.4179	0.0024	73.95	4.058	0.023	0.56
ME4J-2h	8	14.0%	573.49	0.24	513.61	0.16	0.22917	0.00081	2127.3	1.5	1.2157	0.0043	1.8233	7.2482	0.0056	36.70	0.4099	0.0026	88.70	3.980	0.025	0.62
ME4J-2i	9	20.0%	411.94	0.18	274.382	0.080	0.1898	0.0010	2041.0	1.4	1.0068	0.0055	0.9741	13.018	0.010	27.02	0.4058	0.0060	96.58	3.941	0.058	1.5
ME4J-2j	10	35.0%	542.53	0.24	119.188	0.053	0.31307	0.00093	2605.4	2.1	1.6609	0.0050	0.4231	38.254	0.035	8.60	0.391	0.013	100.00	3.80	0.12	3.2
																			Total gas			
																				age: 3.968 ± 0.077 Ma (2σ)		
Aliquot: ME4J-3					J-Value = 0.0053888774 ± 0.0000029213 (0.054%;1σ)																	
ME4J-3a	1	2.5%	447.77	0.13	168.349	0.052	0.23994	0.00046	337.53	0.17	1.2729	0.0025	0.5976	3.5086	0.0020	15.13	0.4024	0.0044	4.93	3.908	0.043	1.1
ME4J-3b	2	3.0%	593.75	0.14	264.93	0.11	0.30688	0.00085	601.258	0.078	1.6280	0.0045	0.9405	3.9715	0.0017	18.14	0.4065	0.0051	12.69	3.948	0.050	1.3
ME4J-3c	3	3.5%	584.91	0.20	294.35	0.09	0.29288	0.00065	713.31	0.27	1.5538	0.0034	1.0449	4.2409	0.0021	20.69	0.4111	0.0035	21.31	3.993	0.034	0.86
ME4J-3d	4	4.0%	526.85	0.18	302.93	0.12	0.25266	0.00052	797.27	0.57	1.3404	0.0028	1.0754	4.6058	0.0037	24.04	0.4181	0.0028	30.18	4.061	0.027	0.67
ME4J-3e	5	5.0%	639.22	0.29	430.39	0.26	0.29127	0.00074	1272.781	1.171	1.5452	0.0039	1.5279	5.1752	0.0057	27.82	0.4133	0.0028	42.79	4.014	0.027	0.68
ME4J-3f	6	6.0%	551.93	0.20	421.81	0.29	0.23773	0.00054	1335.6	1.1	1.2611	0.0028	1.4974	5.5410	0.0059	31.77	0.4158	0.0021	55.14	4.038	0.020	0.50
ME4J-3g	7	8.0%	622.45	0.26	539.18	0.36	0.25158	0.00083	2013.8	1.2	1.3346	0.0044	1.9141	6.5362	0.0058	35.97	0.4154	0.0025	70.94	4.034	0.024	0.60
ME4J-3h	8	10.0%	466.77	0.19	413.44	0.22	0.18751	0.00070	1698.0	1.2	0.9948	0.0037	1.4677	7.1872	0.0064	36.36	0.4106	0.0027	83.04	3.988	0.027	0.67
ME4J-3i	9	12.0%	330.10	0.11	259.71	0.13	0.14146	0.00066	1317.64	0.41	0.7505	0.0035	0.9220	8.8785	0.0053	32.11	0.4083	0.0041	90.65	3.965	0.039	0.99
ME4J-3j	10	14.0%	241.103	0.094	157.836	0.084	0.11138	0.00028	983.99	0.67	0.5909	0.0015	0.5603	10.9100	0.0094	26.82	0.4098	0.0029	95.27	3.980	0.028	0.71
ME4J-3k	11	20.0%	267.629	0.064	108.789	0.042	0.14138	0.00084	1739.6	1.1	0.7500	0.0044	0.3862	27.984	0.021	16.33	0.402	0.012	98.46	3.90	0.12	3.0
ME4J-3l	12	35.0%	226.816	0.064	52.553	0.018	0.12912	0.00078	1593.62	0.80	0.6850	0.0041	0.1866	53.067	0.032	9.83	0.424	0.024	100.00	4.12	0.23	5.5
																			Total gas			
																				age: 4.002 ± 0.072 Ma (2σ)		

[a] Data are corrected for mass spectrometer backgrounds, discrimination, radioactive decay and interference corrections. Errors are one sigma uncertainties and exclude uncertainties in the J-value (propagating this error only has an effect in the third decimal place)

[b] Interference corrections: $(^{36}Ar/^{37}Ar)_{Ca} = (2.5798 \pm 0.0027) \times 10^{-4}$; $(^{39}Ar/^{37}Ar)_{Ca} = (6.5640 \pm 0.0135) \times 10^{-4}$; $(^{40}Ar/^{39}Ar)_K = (3.8900 \pm 0.2140) \times 10^{-4}$; $(^{38}Ar/^{39}Ar)_K = (1.1999 \pm 0.0004) \times 10^{-2}$

[c] J-value is 0.0053888774 ± 0.0000029213 (0.054%; 1σ), based on an age of 28.126 ± 0.019 Ma (2σ) for FC sanidine (Phillips et al., 2017)

[d] Sensitivity = 3.55 x 10^{-17} mol/fA

Table A.12b. Springs Hill age calculation

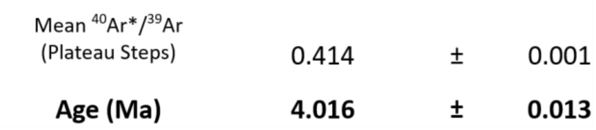

Mean ^{40}Ar*/^{39}Ar (Plateau Steps)	0.414	±	0.001
Age (Ma)	**4.016**	**±**	**0.013**

Appendix A.13. ARGUSVI ^{40}Ar/^{39}Ar laser step-heating analytical results for Summerhill Road Flow samples

Table A.13a. ARGUSVI ^{40}Ar/^{39}Ar laser step-heating analytical results for sample KA13L.[a,b,c,d]

Sample ID	Step No	Laser Power	^{40}Ar (fA)	±1σ	^{39}Ar (fA)[b]	±1σ	^{38}Ar (fA)	±1σ	^{37}Ar (fA)[b]	±1σ	^{36}Ar (fA)	±1σ	^{39}Ar (x10^{-14} mol)[d]	Ca/K	±1σ	%^{40}Ar*	^{40}Ar*/^{39}Ar	±1σ	Cum.% ^{39}Ar	Apparent Age (Ma)	±1σ	±1σ (%)
Aliquant: KA13L-1					J-Value = 0.0007946151 ± 0.0000005841 (0.074%;1σ)																	
KA13L-1a	1	0.025	428.34	0.18	79.608	0.031	0.13891	0.00028	123.93	0.25	0.7369	0.0015	0.2826	2.7244	0.0057	48.63	2.6169	0.0061	11.41	3.7475	0.0087	0.233
KA13L-1b	2	0.03	467.38	0.16	94.394	0.025	0.13708	0.00029	161.40	0.29	0.7272	0.0015	0.3351	2.9923	0.0054	53.54	2.6513	0.0051	24.93	3.7967	0.0073	0.193
KA13L-1c	3	0.04	620.79	0.24	138.087	0.048	0.15668	0.00038	255.88	0.17	0.8312	0.0020	0.4902	3.2428	0.0025	60.02	2.6986	0.0048	44.72	3.8644	0.0069	0.177
KA13L-1d	4	0.05	485.23	0.15	119.257	0.035	0.10215	0.00024	232.69	0.27	0.5419	0.0013	0.4234	3.4145	0.0041	66.65	2.7122	0.0035	61.81	3.8838	0.0050	0.128
KA13L-1e	5	0.06	319.030	0.093	85.435	0.022	0.05371	0.00022	188.59	0.26	0.2849	0.0012	0.3033	3.8630	0.0054	73.33	2.7384	0.0043	74.05	3.9214	0.0061	0.157
KA13L-1f	6	0.08	298.633	0.090	81.594	0.028	0.04828	0.00015	245.17	0.17	0.25615	0.00081	0.2897	5.2583	0.0041	74.38	2.7227	0.0033	85.74	3.8989	0.0047	0.121
KA13L-1g	7	0.1	189.765	0.082	47.532	0.007	0.03859	0.00022	224.07	0.21	0.2047	0.0012	0.1687	8.2497	0.0079	67.78	2.7064	0.0076	92.56	3.876	0.011	0.281
KA13L-1h	8	0.2	178.344	0.059	36.615	0.027	0.05254	0.00019	532.83	0.35	0.2787	0.0010	0.1300	25.466	0.025	53.33	2.5980	0.0084	97.80	3.721	0.012	0.324
KA13L-1i	9	0.35	102.367	0.042	15.336	0.015	0.04284	0.00020	181.35	0.43	0.2273	0.0011	0.0544	20.694	0.052	33.71	2.250	0.021	100.00	3.223	0.030	0.937
																			Total gas age:	**3.835 ± 0.015 Ma (2σ)**		
Aliquant: KA13L-2					J-Value = 0.0007946151 ± 0.0000005841 (0.074%;1σ)																	
KA13L-2a	1	0.03	1032.21	0.47	154.16	0.18	0.4096	0.0017	219.87	0.42	2.1731	0.0089	0.5473	2.4960	0.0056	37.14	2.487	0.018	12.50	3.562	0.025	0.714
KA13L-2b	2	0.04	1159.21	0.53	201.68	0.14	0.4084	0.0012	307.41	0.60	2.1668	0.0062	0.7160	2.6674	0.0055	44.19	2.5401	0.0097	28.85	3.638	0.014	0.381
KA13L-2c	3	0.05	945.91	0.33	185.75	0.15	0.29133	0.00071	305.83	0.50	1.5455	0.0038	0.6594	2.8813	0.0053	51.21	2.6082	0.0067	43.90	3.735	0.010	0.255
KA13L-2d	4	0.06	797.84	0.30	168.56	0.13	0.2216	0.0011	307.16	0.55	1.1754	0.0057	0.5984	3.1888	0.0062	56.01	2.651	0.010	57.57	3.797	0.015	0.394
KA13L-2e	5	0.08	821.89	0.25	186.033	0.086	0.20413	0.00089	401.90	0.90	1.0829	0.0047	0.6604	3.7807	0.0086	60.66	2.6801	0.0078	72.65	3.838	0.011	0.292
KA13L-2f	6	0.1	575.95	0.16	142.434	0.063	0.11903	0.00043	345.92	0.62	0.6315	0.0023	0.5056	4.2501	0.0078	67.26	2.7200	0.0051	84.20	3.8950	0.0073	0.187
KA13L-2g	7	0.14	496.13	0.15	126.514	0.046	0.09520	0.00048	442.57	0.38	0.5050	0.0026	0.4491	6.1218	0.0057	69.60	2.7298	0.0062	94.45	3.9091	0.0089	0.228
KA13L-2h	8	0.18	282.299	0.099	68.414	0.029	0.06101	0.00023	358.57	0.41	0.3237	0.0012	0.2429	9.172	0.011	65.76	2.7139	0.0056	100.00	3.8863	0.0079	0.204
																			Total gas age:	**3.766 ± 0.026 Ma (2σ)**		

[a] Data are corrected for mass spectrometer backgrounds, discrimination, radioactive decay and interference corrections. Errors are one sigma uncertainties and exclude uncertainties in the J-value (propagating this error only has an effect in the third decimal place)

[b] Interference corrections: $(^{36}Ar/^{37}Ar)_{Ca} = (2.5798 \pm 0.0027) \times 10^{-4}$; $(^{39}Ar/^{37}Ar)_{Ca} = (6.5640 \pm 0.0135) \times 10^{-4}$; $(^{40}Ar/^{39}Ar)_{K} = (3.8900 \pm 0.2140) \times 10^{-4}$; $(^{38}Ar/^{39}Ar)_{K} = (1.1999 \pm 0.0004) \times 10^{-2}$

[c] J-value is 0.0007946151 ± 0.0000005841 (0.074%;1σ), based on an age of 1.1814 ± 0.0006 Ma (2σ) for ACR sanidine (Phillips et al., 2017)

[d] Sensitivity = 3.55 x 10^{-17} mol/fA

Table A.13b. Summerhill Road Flow age calculation

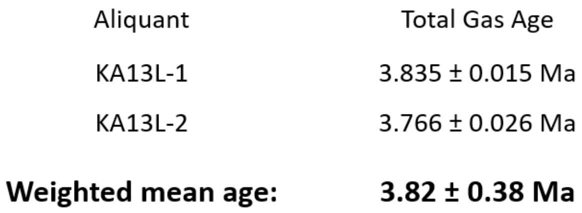

Aliquant	Total Gas Age
KA13L-1	3.835 ± 0.015 Ma
KA13L-2	3.766 ± 0.026 Ma
Weighted mean age:	**3.82 ± 0.38 Ma**

Appendix A.14. ARGUSVI ^{40}Ar/^{39}Ar laser step-heating analytical results for Tullamarine Flow samples

Table A.14a. ARGUSVI ^{40}Ar/^{39}Ar laser step-heating analytical results for sample MH75C.[a,b,c,d]

Sample ID	Step No	Laser Power	^{40}Ar (fA)	±1σ	^{39}Ar (fA)[b]	±1σ	^{38}Ar (fA)	±1σ	^{37}Ar (fA)[b]	±1σ	^{36}Ar (fA)	±1σ	^{39}Ar (x10^{-14} mol)[d]	Ca/K	±1σ	%^{40}Ar*	^{40}Ar*/^{39}Ar	±1σ	Cum.% ^{39}Ar	Apparent Age (Ma)	±1σ	±1σ (%)
Aliquant: MH75C-1					J-Value = 0.0007933329 ± 0.000000443 (0.056%;1σ)																	
MH75C-1a	1	2.5%	294.52	0.10	61.109	0.026	0.05964	0.00024	78.70	0.30	0.3164	0.0013	0.2169	2.2536	0.0085	67.92	3.2738	0.0065	3.94	4.6795	0.0093	0.20
MH75C-1b	2	3.0%	417.17	0.12	92.565	0.040	0.07173	0.00024	122.70	0.34	0.3805	0.0012	0.3286	2.3196	0.0066	72.76	3.2794	0.0045	9.92	4.6876	0.0064	0.14
MH75C-1c	3	3.5%	431.33	0.11	103.154	0.029	0.05844	0.00040	139.90	0.14	0.3100	0.0021	0.3662	2.3734	0.0025	78.53	3.2842	0.0063	16.58	4.6943	0.0090	0.19
MH75C-1d	4	4.0%	457.99	0.24	112.725	0.046	0.05562	0.00029	153.44	0.19	0.2951	0.0015	0.4002	2.3821	0.0031	80.76	3.2814	0.0048	23.86	4.6903	0.0068	0.15
MH75C-1e	5	4.5%	425.68	0.14	107.394	0.057	0.04708	0.00014	146.45	0.35	0.24976	0.00076	0.3813	2.3864	0.0058	82.47	3.2694	0.0030	30.79	4.6732	0.0043	0.092
MH75C-1f	6	5.0%	428.86	0.14	107.888	0.033	0.04867	0.00010	144.40	0.32	0.25818	0.00054	0.3830	2.3423	0.0053	82.02	3.2606	0.0022	37.75	4.6607	0.0032	0.068
MH75C-1g	7	5.5%	393.840	0.079	99.533	0.059	0.04475	0.00023	130.31	0.19	0.2374	0.0012	0.3533	2.2910	0.0036	81.99	3.2448	0.0042	44.18	4.6380	0.0060	0.13
MH75C-1h	8	6.0%	397.23	0.11	99.381	0.039	0.04791	0.00016	127.06	0.27	0.25419	0.00086	0.3528	2.2374	0.0048	80.89	3.2334	0.0031	50.59	4.6219	0.0044	0.095
MH75C-1i	9	6.5%	344.48	0.12	86.896	0.035	0.04008	0.00021	108.55	0.19	0.2126	0.0011	0.3085	2.1860	0.0039	81.56	3.2338	0.0043	56.20	4.6223	0.0061	0.13
MH75C-1j	10	7.0%	344.716	0.097	85.021	0.029	0.04477	0.00020	107.30	0.24	0.2375	0.0011	0.3018	2.2085	0.0050	79.42	3.2205	0.0041	61.69	4.6034	0.0058	0.13
MH75C-1k	11	7.5%	283.056	0.074	70.169	0.025	0.03562	0.00011	85.47	0.27	0.18898	0.00056	0.2491	2.1315	0.0068	80.06	3.2298	0.0029	66.22	4.6168	0.0041	0.088
MH75C-1l	12	8.0%	290.56	0.12	70.003	0.017	0.04113	0.00025	93.58	0.28	0.2182	0.0013	0.2485	2.3393	0.0071	77.57	3.2200	0.0059	70.74	4.6027	0.0084	0.18
MH75C-1m	13	9.0%	285.41	0.11	68.972	0.043	0.03995	0.00015	92.45	0.40	0.21193	0.00082	0.2448	2.346	0.010	77.82	3.2207	0.0043	75.19	4.6038	0.0062	0.13
MH75C-1n	14	10.0%	326.683	0.085	76.193	0.021	0.05168	0.00024	117.49	0.42	0.2741	0.0013	0.2705	2.699	0.010	74.94	3.2133	0.0051	80.11	4.5932	0.0073	0.16
MH75C-1o	15	12.0%	344.674	0.083	79.117	0.041	0.05723	0.00023	136.37	0.29	0.3036	0.0012	0.2809	3.0164	0.0066	73.69	3.2108	0.0050	85.22	4.5896	0.0072	0.16
MH75C-1p	16	14.0%	329.33	0.11	71.356	0.026	0.06358	0.00029	181.11	0.20	0.3373	0.0015	0.2533	4.4417	0.0051	69.41	3.2040	0.0066	89.83	4.5798	0.0095	0.21
MH75C-1q	17	20.0%	383.066	0.046	80.057	0.027	0.07991	0.00012	278.17	0.29	0.42392	0.00066	0.2842	6.0807	0.0067	66.95	3.2040	0.0028	94.99	4.5798	0.0039	0.086
MH75C-1r	18	35.0%	522.17	0.17	77.552	0.027	0.17244	0.00031	354.53	0.25	0.9148	0.0016	0.2753	8.0001	0.0063	47.69	3.2113	0.0068	100.00	4.590	0.010	0.21
																			Total gas age:	4.633 ± 0.013 Ma (2σ)		
Aliquant: MH75C-2					J-Value = 0.0007933329 ± 0.000000443 (0.056%;1σ)																	
MH75C-2a	1	3.0%	1164.91	0.47	265.892	0.090	0.18357	0.00048	356.74	0.74	0.9738	0.0025	0.9439	2.3479	0.0049	75.03	3.2876	0.0035	11.59	4.6993	0.0050	0.11
MH75C-2b	2	4.0%	1436.72	0.63	346.02	0.26	0.19522	0.00046	460.91	0.94	1.0356	0.0025	1.2284	2.3310	0.0051	78.47	3.2585	0.0037	26.68	4.6577	0.0053	0.11
MH75C-2c	3	5.0%	1403.86	0.77	344.34	0.17	0.18162	0.00034	449.14	0.74	0.9635	0.0018	1.2224	2.2826	0.0039	79.50	3.2415	0.0032	41.70	4.6334	0.0045	0.098
MH75C-2d	4	6.0%	1273.51	0.15	310.157	0.096	0.17431	0.00042	393.31	0.53	0.9247	0.0022	1.1011	2.2191	0.0031	78.31	3.2159	0.0024	55.22	4.5968	0.0035	0.075
MH75C-2e	5	7.0%	1064.42	0.27	253.979	0.097	0.15622	0.00061	323.81	0.27	0.8287	0.0032	0.9016	2.2312	0.0021	76.75	3.2168	0.0041	66.30	4.5981	0.0059	0.13
MH75C-2f	6	8.0%	867.39	0.29	201.381	0.083	0.13894	0.00053	277.86	0.26	0.7371	0.0028	0.7149	2.4146	0.0025	74.62	3.2145	0.0046	75.08	4.5948	0.0065	0.14
MH75C-2g	7	10.0%	853.83	0.25	189.048	0.062	0.15557	0.00051	339.65	0.24	0.8253	0.0027	0.6711	3.1441	0.0024	71.13	3.2131	0.0046	83.32	4.5928	0.0065	0.14
MH75C-2h	8	14.0%	910.84	0.36	188.713	0.055	0.19239	0.00063	531.75	0.25	1.0206	0.0033	0.6699	4.9311	0.0027	66.54	3.2119	0.0057	91.55	4.5911	0.0081	0.18
MH75C-2i	9	35.0%	1293.55	0.40	193.790	0.031	0.42290	0.00066	853.10	0.67	2.2435	0.0035	0.6880	7.7038	0.0062	48.22	3.2186	0.0058	100.00	4.6007	0.0083	0.18
																			Total gas age:	4.623 ± 0.011 Ma (2σ)		

[a] Data are corrected for mass spectrometer backgrounds, discrimination, radioactive decay and interference corrections. Errors are one sigma uncertainties and exclude uncertainties in the J-value (propagating this error only has an effect in the third decimal place)

[b] Interference corrections: $(^{36}Ar/^{37}Ar)_{Ca}$ = (2.5798 ± 0.0027) x 10^{-4}; $(^{39}Ar/^{37}Ar)_{Ca}$ = (6.5640 ± 0.0135) x 10^{-4}; $(^{40}Ar/^{39}Ar)_{K}$ = (3.8900 ± 0.2140) x 10^{-4}; $(^{38}Ar/^{39}Ar)_{K}$ = (1.1999 ± 0.0004) x 10^{-2}

[c] J-value is 0.0007933329 ± 0.000000443 (0.056%;1σ), based on an age of 1.1814 ± 0.0006 Ma (2σ) for ACR sanidine (Phillips et al., 2017)

[d] Sensitivity = 3.55 x 10^{-17} mol/fA

Appendix A.15. ARGUSVI ^{40}Ar/^{39}Ar laser step-heating analytical results for unirradiated sample MH70.

Table A.15a. ARGUSVI ^{40}Ar/^{39}Ar laser step-heating analytical results for unirradiated sample MH70.[a,b]

			Original Data										Discrimination-Corrected									
Step ID	Step#	Laser Power	^{40}Ar (fA)	%Error (1σ)	^{39}Ar (fA)	%Error (1σ)	^{38}Ar (fA)	%Error (1σ)	^{37}Ar (fA)	%Error (1σ)	^{36}Ar (fA)	%Error (1σ)	^{40}Ar (fA)	%Error (1σ)	^{38}Ar (fA)	%Error (1σ)	^{36}Ar (fA)	%Error (1σ)	Cum. % ^{38}Ar	^{38}Ar/^{36}Ar	%Error (1σ)
Aliquot: MH70-1																					
MH70-1a	1	3%	3021.391	0.086	0.115482	17.216	1.828686	0.099	0.018998	59.33	9.554313	0.065	3021.391	0.086	1.853531	0.220034	9.942612	0.104644	21.4	0.1864	0.2436
MH70-1b	2	4%	5025.815	0.095	0.104158	10.375	3.00271	0.129	0.006979	170.227	15.73011	0.185	5025.815	0.095	3.043505	0.235063	16.3694	0.202362	56.6	0.1859	0.3102
MH70-1c	3	4.5%	1700.061	0.084	0.013146	69.467	1.008466	0.267	-0.00678	-137.732	5.237791	0.101	1700.061	0.084	1.022167	0.331516	5.450661	0.130101	68.4	0.1875	0.3561
MH70-1d	4	5%	1099.492	0.083	0.022112	54.174	0.651669	0.155	0.001994	493.796	3.35845	0.207	1099.492	0.083	0.660523	0.250278	3.494942	0.222653	76.0	0.1890	0.3350
MH70-1e	5	6%	964.9663	0.086	0.019667	105.307	0.567196	0.316	-0.00638	-199.929	2.915154	0.183	964.9663	0.086	0.574902	0.372115	3.033629	0.200535	82.7	0.1895	0.4227
MH70-1f	6	8%	894.9286	0.085	0.042907	33.313	0.519988	0.403	0.006832	85.683	2.676287	0.184	894.9286	0.085	0.527053	0.448356	2.785055	0.201448	88.8	0.1892	0.4915
MH70-1g	7	10%	527.4984	0.085	0.069345	31.881	0.304577	0.413	-0.00415	-242.496	1.562134	0.148	527.4984	0.085	0.308715	0.457365	1.625621	0.169202	92.4	0.1899	0.4877
MH70-1h	8	14%	462.7047	0.076	0.03181	26.391	0.274908	0.923	-0.00892	-104.438	1.386669	0.046	462.7047	0.076	0.278643	0.943686	1.443025	0.094029	95.6	0.1931	0.9484
MH70-1i	9	35%	627.3744	0.087	0.034906	53.224	0.377949	1.097	0.012919	53.734	1.936227	0.158	627.3744	0.087	0.383084	1.114461	2.014918	0.178015	100.0	0.1901	1.1286
Aliquot: MH70-2																					
MH70-2a	1	2.5%	4741.237	0.103	0.132789	9.184	2.871748	0.204	0.003682	214.029	15.00071	0.165	4741.237	0.103	2.910764	0.204	15.61036	0.184256	32.1	0.1865	0.2749
MH70-2b	2	2.75%	1973.738	0.107	0.111622	7.823	1.187135	0.318	0.013651	97.391	6.185707	0.206	1973.738	0.107	1.203264	0.318	6.437102	0.221724	45.4	0.1869	0.3877
MH70-2c	3	3%	1414.661	0.101	0.10052	8.677	0.847821	0.173	0.025064	65.54	4.407515	0.135	1414.661	0.101	0.85934	0.173	4.586642	0.157957	54.9	0.1874	0.2343
MH70-2d	4	3.5%	1421.238	0.103	0.037175	34.144	0.844312	0.397	0.009423	154.128	4.376601	0.112	1421.238	0.103	0.855783	0.397	4.554471	0.138814	64.3	0.1879	0.4206
MH70-2e	5	4%	1218.955	0.105	0.036604	24.618	0.720525	0.251	0.009645	151.042	3.73747	0.232	1218.955	0.105	0.730314	0.251	3.889365	0.246068	72.4	0.1878	0.3515
MH70-2f	6	5%	1266.505	0.111	0.077285	20.344	0.747016	0.303	0.006931	210.345	3.83862	0.174	1266.505	0.111	0.757165	0.303	3.994626	0.192357	80.7	0.1895	0.3589
MH70-2g	7	6%	864.0586	0.085	0.035145	39.09	0.499351	0.226	0.014026	57.783	2.575404	0.212	864.0586	0.085	0.506135	0.226	2.680072	0.227309	86.3	0.1889	0.3205
MH70-2h	8	8%	704.4867	0.082	0.047721	24.505	0.404245	0.389	0.007699	127.417	2.081634	0.152	704.4867	0.082	0.409737	0.389	2.166234	0.172712	90.8	0.1891	0.4256
MH70-2i	9	10%	428.7141	0.082	0.066832	19.559	0.25082	0.43	0.004974	159.957	1.27247	0.162	428.7141	0.082	0.254228	0.43	1.324185	0.181575	93.6	0.1920	0.4668
MH70-2j	10	14%	438.249	0.085	0.011675	77.173	0.25357	0.577	0.010844	139.383	1.335006	0.162	438.249	0.085	0.257015	0.577	1.389262	0.181575	96.4	0.1850	0.6049
MH70-2k	11	20%	324.52	0.075	0.052435	42.879	0.195883	0.648	0.018849	88.308	0.998839	0.207	324.52	0.075	0.198544	0.648	1.039433	0.222653	98.6	0.1910	0.6852
MH70-2l	12	35%	197.5284	0.068	0.052472	24.874	0.12192	0.706	0.037376	38.935	0.607343	0.219	197.5284	0.068	0.123576	0.706	0.632026	0.233851	100.0	0.1955	0.7437
Aliquot: MH70-3																					
MH70-3a	1	2.5%	4001.43	0.122	0.091276	20.38	2.407197	0.169	0.022401	61.294	12.66151	0.164	4001.43	0.122	2.439902	0.169	13.17609	0.183361	26.2	0.1852	0.2494
MH70-3b	2	3%	2571.76	0.164	0.15881	9.968	1.55068	0.269	0.018484	79.827	8.075878	0.253	2571.76	0.164	1.571748	0.269	8.404092	0.265959	43.0	0.1870	0.3783
MH70-3c	3	3.5%	2103.428	0.163	0.177215	11.918	1.264362	0.152	0.031954	43.064	6.532089	0.236	2103.428	0.163	1.28154	0.152	6.797561	0.249843	56.8	0.1885	0.2924
MH70-3d	4	4%	1598.764	0.127	0.015611	88.666	0.93867	0.207	-0.0019	-840.102	4.905764	0.216	1598.764	0.127	0.951423	0.207	5.10514	0.231044	67.0	0.1864	0.3102
MH70-3e	5	5%	1557.973	0.136	0.039767	48.733	0.916477	0.277	0.008835	157.899	4.735186	0.273	1557.973	0.136	0.928928	0.277	4.92763	0.285052	77.0	0.1885	0.3975
MH70-3f	6	6%	1088.946	0.131	0.033312	35.33	0.635798	0.561	0.001324	984.993	3.268153	0.199	1088.946	0.131	0.644436	0.561	3.400975	0.215236	83.9	0.1895	0.6009
MH70-3g	7	8%	810.6714	0.08	0.017844	54.025	0.464106	0.339	0.010657	86.156	2.403714	0.14	810.6714	0.08	0.470411	0.339	2.501404	0.162251	88.9	0.1881	0.3758
MH70-3h	8	10%	528.9444	0.088	0.012583	96.838	0.307476	0.642	0.006636	165.017	1.586079	0.248	528.9444	0.088	0.311653	0.642	1.650539	0.261208	92.3	0.1888	0.6931
MH70-3i	9	14%	522.9243	0.084	0.022176	43.643	0.306201	0.63	0.006528	145.135	1.601545	0.157	522.9243	0.084	0.310361	0.63	1.666634	0.177128	95.6	0.1862	0.6544
MH70-3j	10	20%	396.1529	0.068	0.023257	63.645	0.233648	0.403	0.010779	78.606	1.212515	0.195	396.1529	0.068	0.236822	0.403	1.261793	0.211543	98.1	0.1877	0.4551
MH70-3k	11	35%	283.2538	0.081	0.041257	39.674	0.172193	1.146	0.01908	52.293	0.869562	0.216	283.2538	0.081	0.174532	1.146	0.904902	0.231044	100.0	0.1929	1.1691

[a] Data are corrected for mass spectrometer backgrounds and discrimination. Errors are one sigma uncertainties.

[b] Sensitivity = 3.55 x 10^{-17} mol/fA

Appendix A.16. Major element X-Ray Fluorescence (XRF) results for Chapter 5 ^{40}Ar/^{39}Ar samples

Table A.16a. Major element XRF results for Flow A and Flow B ^{40}Ar/^{39}Ar samples

	Sample			XRF results normalised to 100% sum concentration										
Flow	Sample	Latitude	Longditude	Na2O (%)	MgO (%)	Al2O3 (%)	SiO2 (%)	P2O5 (%)	SO3 (%)	K2O (%)	CaO (%)	TiO2 (%)	MnO (%)	Fe2O3 (%)
A	M043B	-37.60974	145.09926	3.62	9.09	13.90	47.29	0.58	0.02	1.47	8.88	2.31	0.16	12.37
	MH007	-37.794712	145.005337	3.24	9.76	13.79	48.36	0.50	0.05	1.34	8.84	2.26	0.16	11.70
	YY6 100'	-37.58706	145.10686	3.46	9.09	13.97	47.66	0.64	0.02	1.49	8.83	2.31	0.16	12.08
	MH012	-37.772822	145.033633	3.21	8.73	13.91	49.17	0.50	0.01	1.28	8.65	2.26	0.16	12.12
	MH-24	-37.744786	145.034344	3.67	7.31	15.15	50.63	0.36	0.02	0.86	9.05	1.95	0.12	10.62
	MH005	-37.784129	145.00472	3.41	7.69	14.52	50.53	0.38	0.04	0.86	8.75	1.93	0.15	11.75
	YY3C	-37.55428	145.08007	3.61	8.82	14.13	48.79	0.47	0.01	1.36	8.25	2.16	0.15	11.97
	MH-66-1	-37.546739	145.008221	3.18	8.05	14.45	50.98	0.35	0.02	1.00	8.52	1.77	0.14	11.26
	MH009	-37.638239	145.033312	3.29	7.00	14.36	52.03	0.41	0.03	0.95	8.57	1.84	0.14	11.37
	MH-70	-37.470439	144.992475	3.58	6.56	15.39	51.22	0.33	0.01	1.06	8.72	1.77	0.14	11.00
	WW1A	-37.43505	144.97888	3.54	7.52	14.47	49.34	0.47	0.01	1.30	8.49	2.14	0.15	12.27
B	MH-52	-37.714826	144.981138	3.17	7.57	14.56	50.49	0.36	0.03	1.06	8.40	1.93	0.15	12.04
	MH-60A	-37.697396	144.978845	3.16	7.43	14.67	50.61	0.35	0.02	1.06	8.46	1.93	0.15	11.90
	MH-69	-37.560257	144.869803	3.46	6.21	15.11	51.80	0.40	0.02	1.19	8.68	1.84	0.14	10.90
	KA7 46'	-37.57363	144.99826	3.35	6.86	14.71	50.53	0.42	0.01	1.27	8.84	1.99	0.15	11.54
	GRBH-01	-37.719253	144.936219	3.43	5.70	15.34	52.01	0.39	0.02	1.05	8.91	1.93	0.12	10.86
	MH-49	-37.757234	144.97849	3.14	8.02	14.59	50.62	0.26	0.01	0.60	8.62	1.71	0.14	12.07
	BH045B	-37.794108	144.987782	3.11	8.35	14.36	50.53	0.27	0.06	0.84	8.79	1.81	0.15	11.74
	WO4 163'	-37.60548	144.99692	2.90	8.33	14.40	51.02	0.36	0.02	1.03	8.35	1.82	0.14	11.28

Appendix A.17. Chapter 5 Modelling Details

A.17a. Modelling approach

The simple models used in this study were designed to illustrate the effects of several common causes of argon isotopic ratio disturbance on young groundmass basalt samples. The results generated from the models do not specifically quantify the effects of disturbance, but rather are intended to assist in the interpretation of common patterns of discordance observed in $^{40}Ar/^{39}Ar$ age spectra and inverse isochron plots.

A.17b. Input variables for original (undisturbed) isochrons and age spectra:

Age: 0.8 Ma

J-value: 0.000775

$^{40}Ar*/^{39}Ar$ intercept: 0.572

The proportions of $^{40}Ar*$, ^{39}Ar and ^{36}Ar assigned to each heating step are listed in **Table A.17a**.

Table A.17a: Fraction of $^{40}Ar*$, ^{39}Ar and ^{36}Ar released in each step:

Step #	**1**	**2**	**3**	**4**	**5**	**6**	**7**	**8**	**9**	**10**
$^{40}Ar*$ (Fraction of total)	0.14	0.13	0.13	0.12	0.11	0.10	0.09	0.07	0.06	0.05
^{36}Ar (Fraction of total)	0.13	0.12	0.12	0.11	0.10	0.10	0.09	0.08	0.08	0.07
^{39}Ar (Fraction of total)	0.15	0.15	0.15	0.14	0.12	0.10	0.08	0.06	0.04	0.02
$^{39}Ar/^{40}Ar*$ ratio	0.57	0.57	0.57	0.57	0.57	0.57	0.57	0.57	0.57	0.57

The predicted amount of total ^{40}Ar that would be measured in each step ($^{40}Ar_{(measured)}$) was calculated using Equation **A.1**:

$$^{40}Ar_{(measured)} = {}^{40}Ar* + {}^{36}Ar \times 298.56 \quad \textbf{(A.1)}$$

A.17c. Input variables for the ^{39}Ar recoil model:

^{39}Ar recoil is assumed to cause both loss and redistribution of ^{39}Ar from the sample. ^{39}Ar recoil loss is considered to affect early outgassing lattice sites. The total ^{39}Ar recoil loss in Figure 6a and 6b is 2.7%. The maximum ^{39}Ar lost from any step was ~11% from step 1. ^{39}Ar recoil is also assumed to redistribute some ^{39}Ar from early outgassing phases into late outgassing phases. The maximum increase in ^{39}Ar for figures 6a and 6b was 0.7%, for step 10.

Table A.17b. ^{39}Ar recoil effect on each heating step:

Step #	**1**	**2**	**3**	**4**	**5**	**6**	**7**	**8**	**9**	**10**
^{39}Ar Original (Fraction of total)	0.146	0.146	0.146	0.139	0.124	0.102	0.080	0.058	0.036	0.022
^{39}Ar New (Fraction of total)	0.134	0.144	0.146	0.140	0.126	0.106	0.083	0.060	0.038	0.023
^{39}Ar/^{40}Ar* ratio	0.64	0.60	0.59	0.58	0.58	0.57	0.57	0.57	0.57	0.57

A.17d. Input variables for the low-^{40}Ar* sample models

The 'low % ^{40}Ar* models' were generated by increasing the amount of ^{36}Ar, particularly in early heating steps, by multiplying the ^{36}Ar by the following factors (**Table A.17c**):

Table A.17c. ^{36}Ar multipliers for each heating step in low-^{40}Ar* models.

Step #	**1**	**2**	**3**	**4**	**5**	**6**	**7**	**8**	**9**	**10**
^{36}Ar Multiplier	9	9	9	8.6	7.8	6.6	5.4	4.2	3	2.2

The total ^{40}Ar was then calculated for each step, using Equation **A.2**, where $^{36}\mathrm{Ar}_{\mathrm{New}}$ is a product of the original ^{36}Ar content of each step and the ^{36}Ar multiplier for that step:

$$^{40}\mathrm{Ar}_{\mathrm{Measured}} = {}^{40}\mathrm{Ar}^* + {}^{36}\mathrm{Ar}_{\mathrm{New}} \times 298.5 \quad \textbf{(A.2)}$$

A.17e. Input variables for the ^{40}Ar* loss model:

^{40}Ar* loss is assumed to remove ^{40}Ar* preferentially from early steps. This was modelled by decreasing the fraction of ^{40}Ar* in each step using the factors in **Table A.17d**.

Table A.17d. Fraction of original ^{40}Ar* remaining after ^{40}Ar* loss from each heating step.

Step #	**1**	**2**	**3**	**4**	**5**	**6**	**7**	**8**	**9**	**10**
^{40}Ar*$_{\text{(fraction of original)}}$	0.90	0.95	0.97	0.98	0.98	0.98	0.99	0.99	0.99	0.99
^{39}Ar/^{40}Ar* ratio	0.51	0.54	0.55	0.56	0.56	0.56	0.56	0.56	0.57	0.57

The expected $^{40}\mathrm{Ar}_{\mathrm{(Measured)}}$ after ^{40}Ar* loss was calculated using Equation **A.3**:

$$^{40}\mathrm{Ar}_{\mathrm{Measured}} = {}^{40}\mathrm{Ar}^* \text{ x } {}^{40}\mathrm{Ar}^*_{\text{(fraction of original)}} + {}^{36}\mathrm{Ar}_{\mathrm{New}} \times 298.5 \quad \textbf{(A.3)}$$

A.17f. Input variables for the fractionation model:

Fractionation is assumed to cause the preferential release of ^{36}Ar in early heating steps, leading to an excess of ^{40}Ar in later heating steps. This process was modelled by varying the ^{40}Ar/^{36}Ar value used to calculate the measured ^{40}Ar for each step (**Table A.17e**).

Table A.17e. ^{40}Ar/^{36}Ar values used to calculate the total ^{40}Ar for each heating step.

Step #	**1**	**2**	**3**	**4**	**5**	**6**	**7**	**8**	**9**	**10**
$(^{40}\mathrm{Ar}/^{36}\mathrm{Ar})_{(\text{non-rad})}$	296.0	296.3	296.7	297.0	297.3	297.7	298.0	298.3	298.7	299.0
^{39}Ar/^{40}Ar* ratio	0.51	0.52	0.53	0.54	0.55	0.56	0.56	0.57	0.57	0.58

The expected $^{40}\mathrm{Ar}_{(\text{Measured})}$ after fractionation was calculated using Equation **A.4**:

$$^{40}\mathrm{Ar}_{\text{Measured}} = {}^{40}\mathrm{Ar}^{*} + {}^{36}\mathrm{Ar}_{\text{New}} \times ({}^{40}\mathrm{Ar}/{}^{36}\mathrm{Ar})_{(\text{non-rad})} \quad \textbf{(A.4)}$$

Appendix A.18. Major element X-Ray Fluorescence (XRF) results

Table A.18a. Major element XRF results for Mount Fraser Flow samples[a]

Sample ID	Flow	Na_2O	MgO	Al_2O_3	SiO_2	P_2O_5	K_2O	CaO	TiO_2	Fe_2O_3	Mg#	$Na_2O + K_2O$
M043B	Mt Fraser Flow	3.62	9.09	13.90	47.29	0.58	1.47	8.88	2.31	12.37	63.11	5.09
MH07	Mt Fraser Flow	3.24	9.76	13.79	48.36	0.50	1.34	8.84	2.26	11.70	66.01	4.58
YY6 100'	Mt Fraser Flow	3.46	9.09	13.97	47.66	0.64	1.49	8.83	2.31	12.08	63.67	4.95
BH173 3.58m	Mt Fraser Flow	3.36	8.50	14.00	48.11	0.51	1.34	9.42	2.23	12.11	62.05	4.70
ME4I	Mt Fraser Flow	3.31	9.11	13.83	47.28	0.59	1.43	9.08	2.42	12.51	62.90	4.74
MH20C	Mt Fraser Flow	3.19	8.62	14.22	48.62	0.55	1.39	8.80	2.26	11.95	62.70	4.57
MH20H	Mt Fraser Flow	3.04	8.66	14.09	48.43	0.52	1.85	8.64	2.31	12.03	62.64	4.90
MH12	Mt Fraser Flow	3.21	8.73	13.91	49.17	0.50	1.28	8.65	2.26	12.12	62.65	4.49
BABH-01	Mt Fraser Flow	3.22	7.92	14.22	48.90	0.55	1.38	8.79	2.27	12.37	59.85	4.60
ME2 29'6"	Mt Fraser Flow	3.19	8.78	14.01	48.47	0.53	1.42	8.53	2.30	12.36	62.33	4.61
MO46A	Mt Fraser Flow	3.17	9.42	13.85	48.36	0.50	1.38	8.37	2.22	12.31	64.08	4.55
WW1B	Mt Fraser Flow	2.93	9.51	14.07	48.53	0.51	1.40	8.13	2.30	12.24	64.41	4.33
MH15	Mt Fraser Flow	3.36	7.91	14.51	49.95	0.49	0.94	8.67	1.92	11.83	60.91	4.31
MH17A	Mt Fraser Flow	3.25	8.01	14.53	50.33	0.45	0.86	8.73	1.81	11.63	61.62	4.11
MH22	Mt Fraser Flow	3.35	7.70	14.42	50.15	0.44	0.91	8.68	2.00	12.02	59.86	4.26
MH29	Mt Fraser Flow	3.46	7.42	14.62	50.01	0.42	0.99	8.79	1.98	11.96	59.10	4.44
MH-24	Mt Fraser Flow	3.67	7.31	15.15	50.63	0.36	0.86	9.05	1.95	10.62	61.59	4.53
MH05	Mt Fraser Flow	3.41	7.69	14.52	50.53	0.38	0.86	8.75	1.93	11.75	60.38	4.26
MH32	Mt Fraser Flow	3.27	8.04	14.54	50.19	0.36	0.90	8.72	1.81	11.78	61.39	4.17
MH36A	Mt Fraser Flow	3.28	8.28	14.48	49.78	0.42	0.84	8.69	1.89	11.96	61.71	4.12
MH37A	Mt Fraser Flow	3.32	7.79	14.65	50.12	0.42	0.78	8.69	1.89	11.96	60.26	4.10
KA10 87'6"	Mt Fraser Flow	3.20	8.75	14.37	49.62	0.48	1.25	8.08	2.09	11.78	63.38	4.45
MO47A	Mt Fraser Flow	3.49	6.76	14.75	50.05	0.44	1.24	8.62	2.05	12.22	56.32	4.73
MO47C	Mt Fraser Flow	3.36	8.40	14.27	49.31	0.45	1.21	8.43	2.06	12.11	61.77	4.57
YY3C	Mt Fraser Flow	3.61	8.82	14.13	48.79	0.47	1.36	8.25	2.16	11.97	63.18	4.97
WW1A	Mt Fraser Flow	3.54	7.52	14.47	49.34	0.47	1.30	8.49	2.14	12.27	58.80	4.84
MH66	Mt Fraser Flow	3.18	8.05	14.45	50.98	0.35	1.00	8.52	1.77	11.26	62.47	4.18
WO1 23'	Mt Fraser Flow	3.01	8.09	14.33	51.07	0.40	0.90	8.46	1.80	11.58	61.94	3.91
MH09	Mt Fraser Flow	3.29	7.00	14.36	52.03	0.41	0.95	8.57	1.84	11.37	58.92	4.24
KA10 16'6"	Mt Fraser Flow	3.19	7.51	14.63	51.41	0.37	0.92	8.66	1.73	11.22	60.91	4.11
YY2 19'	Mt Fraser Flow	3.13	7.27	14.68	51.37	0.43	1.04	8.58	1.79	11.37	59.82	4.17
YY3A	Mt Fraser Flow	3.05	7.96	14.41	51.45	0.35	0.95	8.35	1.75	11.37	62.00	4.00
YY6 8'	Mt Fraser Flow	3.14	7.87	14.58	51.18	0.33	0.76	8.49	1.85	11.44	61.56	3.90
MH-70	Mt Fraser Flow	3.58	6.56	15.39	51.22	0.33	1.06	8.72	1.77	11.00	58.14	4.64
ME4A	Mt Fraser Flow	3.29	6.06	15.29	52.03	0.38	1.06	8.52	1.94	11.11	55.97	4.35
ME4F	Mt Fraser Flow	3.14	8.20	14.61	50.58	0.43	0.99	8.35	1.91	11.43	62.56	4.13

[a] Normalised to 100% sum concentration

Table A.18b. Major element XRF results for Tulloch Hill Flow samples[a]

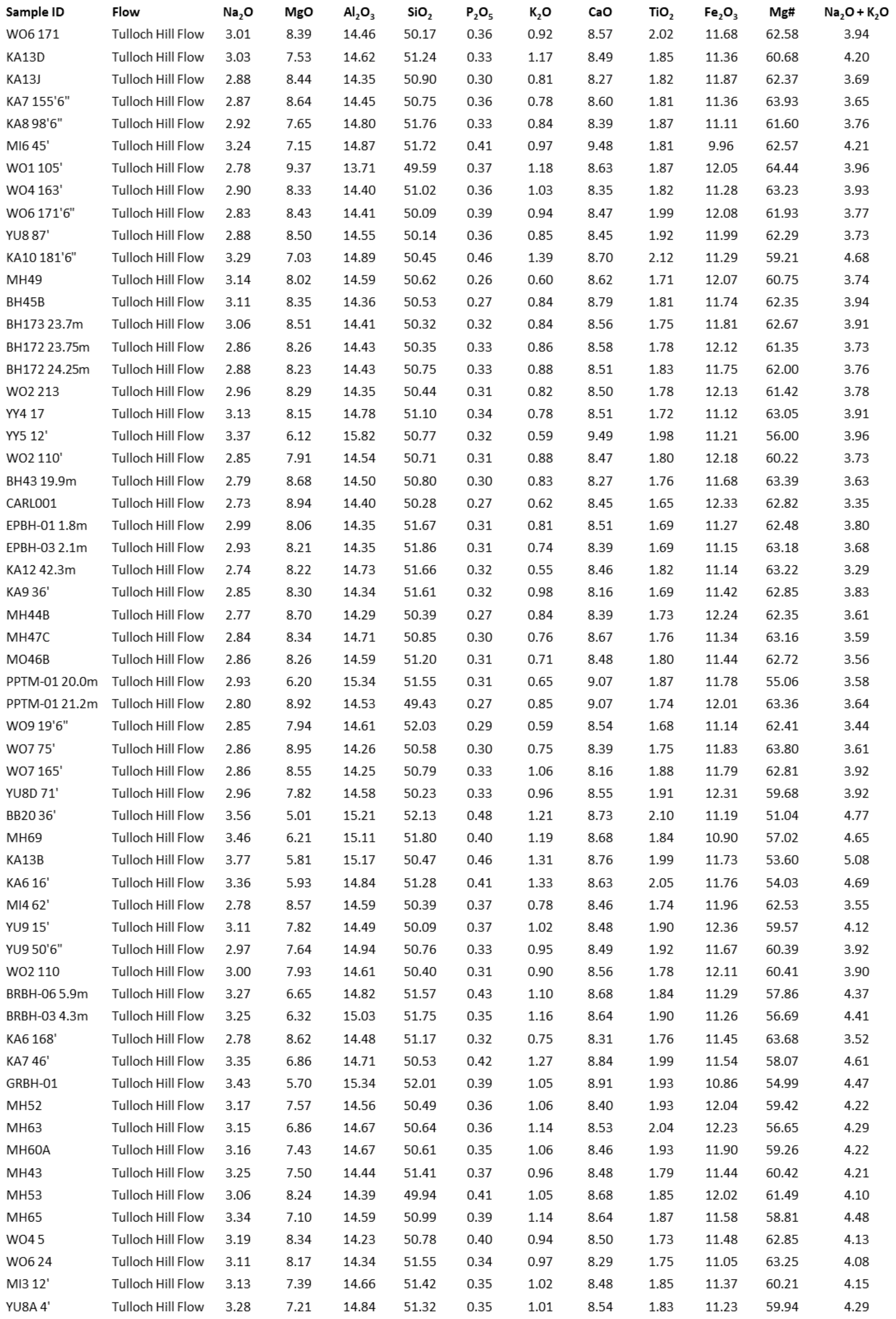

Sample ID	Flow	Na_2O	MgO	Al_2O_3	SiO_2	P_2O_5	K_2O	CaO	TiO_2	Fe_2O_3	Mg#	$Na_2O + K_2O$
WO6 171	Tulloch Hill Flow	3.01	8.39	14.46	50.17	0.36	0.92	8.57	2.02	11.68	62.58	3.94
KA13D	Tulloch Hill Flow	3.03	7.53	14.62	51.24	0.33	1.17	8.49	1.85	11.36	60.68	4.20
KA13J	Tulloch Hill Flow	2.88	8.44	14.35	50.90	0.30	0.81	8.27	1.82	11.87	62.37	3.69
KA7 155'6"	Tulloch Hill Flow	2.87	8.64	14.45	50.75	0.36	0.78	8.60	1.81	11.36	63.93	3.65
KA8 98'6"	Tulloch Hill Flow	2.92	7.65	14.80	51.76	0.33	0.84	8.39	1.87	11.11	61.60	3.76
MI6 45'	Tulloch Hill Flow	3.24	7.15	14.87	51.72	0.41	0.97	9.48	1.81	9.96	62.57	4.21
WO1 105'	Tulloch Hill Flow	2.78	9.37	13.71	49.59	0.37	1.18	8.63	1.87	12.05	64.44	3.96
WO4 163'	Tulloch Hill Flow	2.90	8.33	14.40	51.02	0.36	1.03	8.35	1.82	11.28	63.23	3.93
WO6 171'6"	Tulloch Hill Flow	2.83	8.43	14.41	50.09	0.39	0.94	8.47	1.99	12.08	61.93	3.77
YU8 87'	Tulloch Hill Flow	2.88	8.50	14.55	50.14	0.36	0.85	8.45	1.92	11.99	62.29	3.73
KA10 181'6"	Tulloch Hill Flow	3.29	7.03	14.89	50.45	0.46	1.39	8.70	2.12	11.29	59.21	4.68
MH49	Tulloch Hill Flow	3.14	8.02	14.59	50.62	0.26	0.60	8.62	1.71	12.07	60.75	3.74
BH45B	Tulloch Hill Flow	3.11	8.35	14.36	50.53	0.27	0.84	8.79	1.81	11.74	62.35	3.94
BH173 23.7m	Tulloch Hill Flow	3.06	8.51	14.41	50.32	0.32	0.84	8.56	1.75	11.81	62.67	3.91
BH172 23.75m	Tulloch Hill Flow	2.86	8.26	14.43	50.35	0.33	0.86	8.58	1.78	12.12	61.35	3.73
BH172 24.25m	Tulloch Hill Flow	2.88	8.23	14.43	50.75	0.33	0.88	8.51	1.83	11.75	62.00	3.76
WO2 213	Tulloch Hill Flow	2.96	8.29	14.35	50.44	0.31	0.82	8.50	1.78	12.13	61.42	3.78
YY4 17	Tulloch Hill Flow	3.13	8.15	14.78	51.10	0.34	0.78	8.51	1.72	11.12	63.05	3.91
YY5 12'	Tulloch Hill Flow	3.37	6.12	15.82	50.77	0.32	0.59	9.49	1.98	11.21	56.00	3.96
WO2 110'	Tulloch Hill Flow	2.85	7.91	14.54	50.71	0.31	0.88	8.47	1.80	12.18	60.22	3.73
BH43 19.9m	Tulloch Hill Flow	2.79	8.68	14.50	50.80	0.30	0.83	8.27	1.76	11.68	63.39	3.63
CARL001	Tulloch Hill Flow	2.73	8.94	14.40	50.28	0.27	0.62	8.45	1.65	12.33	62.82	3.35
EPBH-01 1.8m	Tulloch Hill Flow	2.99	8.06	14.35	51.67	0.31	0.81	8.51	1.69	11.27	62.48	3.80
EPBH-03 2.1m	Tulloch Hill Flow	2.93	8.21	14.35	51.86	0.31	0.74	8.39	1.69	11.15	63.18	3.68
KA12 42.3m	Tulloch Hill Flow	2.74	8.22	14.73	51.66	0.32	0.55	8.46	1.82	11.14	63.22	3.29
KA9 36'	Tulloch Hill Flow	2.85	8.30	14.34	51.61	0.32	0.98	8.16	1.69	11.42	62.85	3.83
MH44B	Tulloch Hill Flow	2.77	8.70	14.29	50.39	0.27	0.84	8.39	1.73	12.24	62.35	3.61
MH47C	Tulloch Hill Flow	2.84	8.34	14.71	50.85	0.30	0.76	8.67	1.76	11.34	63.16	3.59
MO46B	Tulloch Hill Flow	2.86	8.26	14.59	51.20	0.31	0.71	8.48	1.80	11.44	62.72	3.56
PPTM-01 20.0m	Tulloch Hill Flow	2.93	6.20	15.34	51.55	0.31	0.65	9.07	1.87	11.78	55.06	3.58
PPTM-01 21.2m	Tulloch Hill Flow	2.80	8.92	14.53	49.43	0.27	0.85	9.07	1.74	12.01	63.36	3.64
WO9 19'6"	Tulloch Hill Flow	2.85	7.94	14.61	52.03	0.29	0.59	8.54	1.68	11.14	62.41	3.44
WO7 75'	Tulloch Hill Flow	2.86	8.95	14.26	50.58	0.30	0.75	8.39	1.75	11.83	63.80	3.61
WO7 165'	Tulloch Hill Flow	2.86	8.55	14.25	50.79	0.33	1.06	8.16	1.88	11.79	62.81	3.92
YU8D 71'	Tulloch Hill Flow	2.96	7.82	14.58	50.23	0.33	0.96	8.55	1.91	12.31	59.68	3.92
BB20 36'	Tulloch Hill Flow	3.56	5.01	15.21	52.13	0.48	1.21	8.73	2.10	11.19	51.04	4.77
MH69	Tulloch Hill Flow	3.46	6.21	15.11	51.80	0.40	1.19	8.68	1.84	10.90	57.02	4.65
KA13B	Tulloch Hill Flow	3.77	5.81	15.17	50.47	0.46	1.31	8.76	1.99	11.73	53.60	5.08
KA6 16'	Tulloch Hill Flow	3.36	5.93	14.84	51.28	0.41	1.33	8.63	2.05	11.76	54.03	4.69
MI4 62'	Tulloch Hill Flow	2.78	8.57	14.59	50.39	0.37	0.78	8.46	1.74	11.96	62.53	3.55
YU9 15'	Tulloch Hill Flow	3.11	7.82	14.49	50.09	0.37	1.02	8.48	1.90	12.36	59.57	4.12
YU9 50'6"	Tulloch Hill Flow	2.97	7.64	14.94	50.76	0.33	0.95	8.49	1.92	11.67	60.39	3.92
WO2 110	Tulloch Hill Flow	3.00	7.93	14.61	50.40	0.31	0.90	8.56	1.78	12.11	60.41	3.90
BRBH-06 5.9m	Tulloch Hill Flow	3.27	6.65	14.82	51.57	0.43	1.10	8.68	1.84	11.29	57.86	4.37
BRBH-03 4.3m	Tulloch Hill Flow	3.25	6.32	15.03	51.75	0.35	1.16	8.64	1.90	11.26	56.69	4.41
KA6 168'	Tulloch Hill Flow	2.78	8.62	14.48	51.17	0.32	0.75	8.31	1.76	11.45	63.68	3.52
KA7 46'	Tulloch Hill Flow	3.35	6.86	14.71	50.53	0.42	1.27	8.84	1.99	11.54	58.07	4.61
GRBH-01	Tulloch Hill Flow	3.43	5.70	15.34	52.01	0.39	1.05	8.91	1.93	10.86	54.99	4.47
MH52	Tulloch Hill Flow	3.17	7.57	14.56	50.49	0.36	1.06	8.40	1.93	12.04	59.42	4.22
MH63	Tulloch Hill Flow	3.15	6.86	14.67	50.64	0.36	1.14	8.53	2.04	12.23	56.65	4.29
MH60A	Tulloch Hill Flow	3.16	7.43	14.67	50.61	0.35	1.06	8.46	1.93	11.90	59.26	4.22
MH43	Tulloch Hill Flow	3.25	7.50	14.44	51.41	0.37	0.96	8.48	1.79	11.44	60.42	4.21
MH53	Tulloch Hill Flow	3.06	8.24	14.39	49.94	0.41	1.05	8.68	1.85	12.02	61.49	4.10
MH65	Tulloch Hill Flow	3.34	7.10	14.59	50.99	0.39	1.14	8.64	1.87	11.58	58.81	4.48
WO4 5	Tulloch Hill Flow	3.19	8.34	14.23	50.78	0.40	0.94	8.50	1.73	11.48	62.85	4.13
WO6 24	Tulloch Hill Flow	3.11	8.17	14.34	51.55	0.34	0.97	8.29	1.75	11.05	63.25	4.08
MI3 12'	Tulloch Hill Flow	3.13	7.39	14.66	51.42	0.35	1.02	8.48	1.85	11.37	60.21	4.15
YU8A 4'	Tulloch Hill Flow	3.28	7.21	14.84	51.32	0.35	1.01	8.54	1.83	11.23	59.94	4.29

[a] Normalised to 100% sum concentration

Table A.18c. Major element XRF results for all other flows[a]

Sample ID	Flow	Na_2O	MgO	Al_2O_3	SiO_2	P_2O_5	K_2O	CaO	TiO_2	Fe_2O_3	Mg#	$Na_2O + K_2O$
MH10E	Fenton Hill Flow	3.24	7.80	14.44	50.62	0.32	0.90	8.71	1.95	11.80	60.63	4.14
MH04	Mt Kororoit Flow	2.99	8.14	13.89	51.17	0.29	0.89	9.13	1.78	11.55	62.16	3.88
MH11	Mt Kororoit Flow	3.10	8.05	14.17	51.90	0.27	0.88	8.21	1.72	11.53	61.93	3.98
BH47B	Mt Kororoit Flow	3.06	7.78	14.45	51.72	0.30	0.94	8.16	1.76	11.44	61.28	4.00
BH46 11.2m	Mt Kororoit Flow	3.16	7.62	14.42	51.32	0.28	0.88	8.35	1.76	11.87	59.94	4.04
BH 267 11.4m	Mt Kororoit Flow	2.96	8.07	14.32	51.07	0.30	0.87	8.62	1.72	11.70	61.63	3.83
BH1432 9.7m	Mt Kororoit Flow	2.93	7.92	14.27	51.13	0.32	0.83	8.55	1.69	12.00	60.59	3.77
BH15010 10.5m	Mt Kororoit Flow	2.88	8.31	14.25	51.31	0.29	0.78	8.21	1.69	11.94	61.86	3.66
BH15128 7.0m	Mt Kororoit Flow	3.07	6.72	15.08	52.28	0.28	0.73	8.41	1.86	11.20	58.30	3.80
BH206 15.3m	Mt Kororoit Flow	2.83	8.89	14.09	50.74	0.30	0.90	8.05	1.81	12.03	63.27	3.73
BH259 7.9m	Mt Kororoit Flow	2.89	8.24	14.28	51.20	0.31	0.91	8.12	1.77	11.92	61.68	3.80
BH269 12.2m	Mt Kororoit Flow	2.98	7.96	14.25	51.08	0.29	0.95	8.57	1.78	11.70	61.32	3.92
MH01N	Mt Kororoit Flow	3.25	7.13	14.68	52.99	0.28	0.86	8.27	1.74	10.63	60.97	4.11
MH01S	Mt Kororoit Flow	3.20	7.07	14.56	52.84	0.28	0.88	8.43	1.75	10.81	60.39	4.09
MA40A 28'6"	Mt Kororoit Flow	2.99	6.99	14.87	52.98	0.33	0.87	8.32	1.70	10.63	60.49	3.85
MA41 17'	Mt Kororoit Flow	3.35	6.58	14.77	52.62	0.42	0.89	8.39	2.08	10.52	59.31	4.24
MH56A	Mt Kororoit Flow	3.30	7.67	14.60	51.95	0.28	0.82	8.25	1.70	11.07	61.74	4.12
MH76	Mt Kororoit Flow	2.87	8.59	14.31	51.36	0.28	0.92	8.33	1.73	11.24	64.01	3.79
BH01 7.0m	Mt Kororoit Flow	2.81	8.53	14.06	51.19	0.26	0.90	8.96	1.69	11.22	63.91	3.72
BH259 1.3m	Mt Kororoit Flow	3.05	8.22	14.21	51.71	0.30	0.79	8.02	1.74	11.59	62.31	3.84
WD-BH-160 4.9m	Mt Kororoit Flow	2.93	8.12	14.32	51.73	0.28	0.83	8.20	1.68	11.54	62.13	3.76
BH1333 41.5m	Mt Kororoit Flow	2.96	7.81	14.62	51.87	0.36	0.85	8.69	1.67	10.80	62.74	3.80
MH34	Aitken Hill Flow	3.63	5.31	14.41	51.13	0.74	2.29	8.05	2.49	11.52	51.77	5.92
MH35	Aitken Hill Flow	3.76	4.73	14.72	51.13	0.77	1.95	8.06	2.44	11.61	48.70	5.71
MH59C	Aitken Hill Flow	3.61	6.36	14.33	50.66	0.73	1.96	7.62	2.61	11.75	55.76	5.57
YU5 9'	Aitken Hill Flow	3.72	4.93	14.50	51.26	0.77	2.29	7.87	2.57	11.69	49.55	6.01
MH02	Redstone Hill Flow	4.19	5.97	15.14	51.03	0.77	2.39	7.18	2.44	10.72	56.47	6.58
BB22 109'	Redstone Hill Flow	3.88	4.69	15.28	52.08	0.85	1.94	6.85	2.28	11.75	48.20	5.83
BB23D	Redstone Hill Flow	3.79	6.68	14.67	50.38	0.85	2.02	6.93	2.43	11.85	56.76	5.81
BB23A	Redstone Hill Flow	4.02	3.77	15.97	50.15	1.01	1.85	6.95	2.87	13.00	40.32	5.87
ME4J	Springs Hill Flow	3.15	7.24	14.44	50.49	0.36	0.71	8.65	2.13	12.34	57.73	3.86
MH71	Springs Hill Flow	3.18	8.10	14.64	50.28	0.35	0.96	8.53	1.89	11.73	61.68	4.14
KA13L	Summerhill Rd Flow	3.04	7.88	14.18	50.14	0.32	0.84	8.56	2.05	12.55	59.38	3.88
MH68	Crowe Hill Flow	3.98	8.66	13.10	47.42	0.89	1.85	8.48	2.67	12.34	62.05	5.83
MH67	Crowe Hill Flow	3.74	8.89	13.20	47.56	0.81	1.85	8.61	2.42	12.43	62.49	5.59
KA13M	Mt Ridley Flow	3.82	9.65	12.95	46.41	0.92	2.03	8.89	2.61	12.07	65.06	5.85
MI5 114'	Mt Ridley Flow	3.59	8.83	13.30	47.36	0.71	1.26	9.46	2.38	12.65	61.93	4.85
MH75C	Tullamarine Flow	2.96	9.30	13.33	50.18	0.41	1.21	8.32	2.00	11.50	65.33	4.17
YU6 5'	Tullamarine Flow	3.28	6.77	14.82	51.37	0.38	0.95	9.16	1.83	11.08	58.71	4.23
MI4 142'	Tullamarine Flow	2.97	8.29	14.46	50.19	0.36	1.01	8.39	1.92	12.07	61.53	3.98
MH73	Pretty Sally Flow	3.57	7.91	12.19	46.67	1.13	1.30	10.81	3.07	12.77	59.07	4.87
MH72	Green Hill Flow	3.45	8.14	12.26	47.49	0.83	1.00	10.11	3.13	13.08	59.16	4.46
BA01	Bald Hill Flow	4.40	9.92	10.91	44.12	1.28	0.69	11.82	3.19	13.04	63.91	5.09
MH18B	Mt Cooper Flow	4.25	10.04	11.56	45.93	0.92	0.83	10.45	3.15	12.33	65.48	5.08

[a]Normalised to 100% sum concentration

Appendix A.19. $^{40}Ar/^{39}Ar$ analytical details for Chapter 6

Once under vacuum, the sample chamber and extraction line were baked overnight (≥12 h) at ~180°C . Following procedures previously described by Matchan and Phillips (2014), the bulk of atmospheric argon was removed from the samples via rastering of the 6 mm homogenised laser beam operated at 1 – 2% laser power. Groundmass step-heating experiments were then conducted using the 6 mm beam over a heating interval of 2.5 – 35% laser power (0.63 – 6.0 W), with a lasing time of ~1.5 – 3 min per heating step (two passes of the beam), depending on sample dimensions. Feldspar aliquant BA01-1 was step-heated using the 1 mm focused beam operating at 2 – 3% laser power (0.5 – 0.74W), and aliquants BA01-2 to BA01-6 were step-heated using the 0.15 mm focused beam operating at 0.1 – 1.5% laser power (<0.1 – 0.37W). An alcohol-dry ice trap was used between the sample chamber and extraction line, and evolved gas was continually exposed to four SAES Zr-Al getters; three operating at room temperature and one at ~30V (~400°C). In all cases, ^{36}Ar was measured on a Compact Discrete Dynode (CDD), and the remaining isotopes were measured on Faraday detectors. All Faraday detectors were fitted with 1×10^{12} Ω resistors during step heating experiments of irradiation can UM#58 samples (MH01S, MH01N, MH02, MH04, MH10, MH11). Following system upgrades, ^{39}Ar was measured on a Faraday equipped with a 1×10^{13} Ω resistor for UM#70 and UM#71 samples (BH47B, BH269, KA13L, KA13M, MH35, MH56, MH75C). In the case of UM#77 samples (BB22, ME4J, BA01, MH68), ^{40}Ar, ^{39}Ar and ^{37}Ar were all measured on Faraday detectors with 1×10^{13} Ω resistors.

Correction factors for UM#58 samples were calculated based on measurements of K-glass and Ca-salts included in prolonged-irradiation package UM#60: $(^{36}Ar/^{37}Ar)_{Ca} = (2.5713 \pm 0.0023) \times 10^{-4}$; $(^{39}Ar/^{37}Ar)_{Ca} = (6.6200 \pm 0.0801) \times 10^{-4}$; $(^{40}Ar/^{39}Ar)_{K} = (1.000 \pm 0.050) \times 10^{-10}$; $(^{38}Ar/^{39}Ar)_{K} = (1.2136 \pm 0.0016) \times 10^{-2}$. Updated correction factors for K-glass and Ca-salts included in irradiation package UM#62 were applied to samples from cans UM#70, UM#71 and UM#77: $(^{36}Ar/^{37}Ar)_{Ca} = (2.5782 \pm 0.0018) \times 10^{-4}$; $(^{39}Ar/^{37}Ar)_{Ca} = (6.5620 \pm 0.0164) \times 10^{-4}$; $(^{40}Ar/^{39}Ar)_{K} = (1.000 \pm 0.050) \times 10^{-10}$; $(^{38}Ar/^{39}Ar)_{K} = (1.2246 \pm 0.0028) \times 10^{-2}$. All age calculations, age spectra and isochrons were generated using the ISOPLOT software package (Ludwig, 2012), and the decay constants of Steiger and Jäger (1977) were assumed.

Appendix A.20. ICP-MS trace element concentrations of selected samples

Table A.20a. ICP-MS trace element concentrations of selected samples

Flow Unit	Mt Fraser C							Mt Fraser B				Mt Fraser A				Tulloch Hill A					Tulloch Hill B	Aitken Hill		Tullamarine		Mt Ridley	
Sample ID	KA10 16'6"	MH43	MH66	WO1 23'	YY2 19'	YY3A	YY6 8'	MH24	MH32	WW1A	YY3C	ME2 29'6"	ME4I	M043B	YY6 100'	KA7 46'	MH52	MH60A	MH69	MI3 12'	MH49	MH35	MH59C	MH57	MH75C	KA13M	MI5 114'
Li	8.97	7.05	9.07	7.03	9.29	8.17	6.46	5.81	7.44	8.66	7.91	8.48	7.36	7.88	7.62	9.76	8.59	8.54	10.89	9.21	7.17	9.68	10.17	4.89	7.95	9.50	8.29
Be	1.15	1.18	1.28	1.20	1.16	1.22	1.15	1.22	1.09	1.40	1.44	1.51	1.52	1.38	1.55	1.42	1.29	1.28	1.38	1.33	1.04	1.93	2.00	1.24	1.32	2.40	1.80
Sc	20.4	20.6	20.4	19.9	20.8	20.5	20.9	21.6	21.0	20.6	19.7	20.6	20.3	20.6	20.4	21.9	21.4	21.4	20.9	21.0	21.6	16.8	18.2	20.2	20.6	19.0	22.3
V	150	158	163	155	158	159	154	161	158	174	167	183	183	178	175	183	164	168	172	171	163	139	170	168	162	185	211
Cr	260	250	297	261	252	272	268	294	286	336	296	301	256	271	270	295	303	299	284	301	309	172	218	350	330	348	347
Ni	147	151	164	166	138	173	172	175	179	210	197	199	186	186	186	131	207	198	86	131	187	121	170	212	207	265	257
Cu	48.1	49.3	32.5	41.0	43.8	43.6	48.8	44.2	50.5	47.1	32.8	38.0	47.3	49.1	47.6	62.0	53.4	46.4	23.8	45.3	51.9	38.2	46.3	38.0	46.8	56.3	57.6
Zn	109	112	105	110	110	110	110	101	112	120	122	117	116	115	113	112	118	114	107	109	110	128	130	105	112	127	116
Ga	19.1	19.5	19.1	18.9	19.4	19.2	19.3	20.1	19.3	19.8	19.2	20.2	18.5	17.9	17.2	20.4	19.6	19.8	20.4	20.0	19.1	22.7	22.2	18.4	19.1	21.0	19.7
As	0.41	0.58	0.60	0.45	0.57	0.53	0.50	0.44	0.45	0.91	0.43	0.58	0.58	0.67	0.84	0.50	0.48	0.63	0.55	0.49	0.48	1.09	1.02	0.58	0.53	14.81	0.76
Rb	23.9	24.7	25.3	16.1	27.2	26.2	18.8	17.1	19.7	29.3	31.6	32.0	27.7	31.0	29.0	24.6	25.8	24.4	30.6	26.0	19.9	45.0	47.5	25.6	28.2	39.1	37.8
Sr	404	407	407	414	408	416	392	443	414	545	615	571	911	628	613	492	438	447	465	446	352	554	569	494	468	958	726
Y	20.3	21.0	20.4	19.9	20.3	20.7	22.1	24.9	19.8	21.1	21.3	21.6	21.4	21.6	21.1	21.7	20.6	20.9	21.5	22.0	21.8	27.4	28.3	19.7	21.2	27.0	24.1
Zr	137	145	144	142	141	145	138	149	137	180	186	195	196	197	195	157	155	156	154	153	127	303	279	157	170	341	246
Nb	21.5	23.1	22.7	23.3	22.7	23.5	21.1	24.8	22.0	36.3	37.7	41.4	42.7	41.5	41.5	28.9	24.5	24.7	25.8	25.3	17.5	47.2	46.8	29.0	31.1	73.6	55.7
Mo	1.41	1.59	1.43	1.28	1.54	1.54	1.33	1.39	1.44	1.31	1.72	1.68	1.77	1.42	1.43	1.64	1.37	1.23	1.61	1.54	1.03	2.63	2.54	1.52	2.15	2.11	2.23
Cd	0.06	0.06	0.06	0.05	0.05	0.05	0.06	0.05	0.06	0.08	0.08	0.07	0.09	0.12	0.11	0.08	0.09	0.08	0.11	0.06	0.07	0.14	0.12	0.05	0.07	0.12	0.10
In	0.06	0.07	0.06	0.06	0.06	0.06	0.07	0.07	0.07	0.06	0.07	0.07	0.08	0.08	0.07	0.07	0.07	0.07	0.07	0.07	0.07	0.08	0.08	0.06	0.07	0.09	0.08
Sn	1.65	1.74	1.72	1.68	1.69	1.74	1.67	1.71	1.58	1.81	1.94	2.07	1.98	1.94	1.95	1.79	1.82	1.89	1.99	1.92	1.65	2.79	2.84	1.74	1.90	2.75	2.24
Sb	0.04	0.04	0.04	0.04	0.04	0.04	0.04	0.03	0.03	0.05	0.04	0.04	0.04	0.04	0.05	0.03	0.04	0.04	0.05	0.04	0.03	0.06	0.06	0.04	0.04	0.10	0.05
Cs	0.83	0.84	0.86	0.53	0.97	0.92	0.56	0.42	0.53	0.22	0.48	0.48	0.52	0.63	0.45	0.32	0.72	0.67	0.98	0.85	0.69	0.44	0.74	0.74	0.73	11.12	0.91
Ba	240	253	389	265	255	276	232	265	230	347	332	368	342	351	348	349	323	343	335	338	241	471	479	342	354	543	448
La	17.2	18.2	19.2	18.1	17.8	19.7	18.4	25.1	16.3	25.7	26.3	28.2	29.4	29.2	29.2	21.9	20.1	20.1	20.4	19.9	17.3	35.1	36.4	21.1	22.9	57.9	41.5
Ce	35.6	37.9	37.6	37.6	36.9	38.3	34.1	45.1	34.3	51.9	53.8	57.6	59.7	59.5	59.1	45.0	41.9	42.2	42.3	40.9	30.9	71.7	73.7	43.9	47.8	117.3	83.7
Pr	4.51	4.78	4.89	4.70	4.63	5.04	4.78	5.81	4.39	6.47	6.60	7.03	7.29	7.25	7.19	5.62	5.33	5.32	5.27	5.13	4.60	9.03	9.22	5.50	5.99	13.97	9.98
Nd	19.2	20.2	20.4	20.0	19.7	21.3	20.7	24.7	18.8	26.7	27.1	28.9	29.7	29.8	29.5	23.5	22.5	22.3	22.1	21.5	19.7	37.4	38.3	23.0	25.0	54.8	39.5
Sm	4.69	4.96	4.80	4.76	4.79	5.05	5.08	5.76	4.64	5.98	6.10	6.38	6.51	6.53	6.39	5.44	5.25	5.23	5.20	5.06	4.81	8.23	8.32	5.31	5.71	10.43	7.87
Eu	1.63	1.69	1.64	1.64	1.67	1.72	1.78	1.98	1.67	2.03	2.04	2.11	2.21	2.18	2.16	1.83	1.77	1.77	1.74	1.71	1.64	2.65	2.63	1.79	1.89	3.21	2.51
Gd	4.98	5.20	5.07	5.00	5.02	5.29	5.54	6.21	4.95	5.85	5.90	6.12	6.27	6.21	6.13	5.54	5.35	5.32	5.33	5.31	5.21	7.87	7.99	5.24	5.66	8.85	7.07
Tb	0.75	0.78	0.76	0.74	0.76	0.80	0.81	0.91	0.74	0.84	0.85	0.87	0.89	0.89	0.87	0.82	0.79	0.79	0.80	0.79	0.79	1.10	1.12	0.77	0.82	1.19	0.99
Dy	4.25	4.39	4.28	4.18	4.30	4.42	4.61	5.08	4.18	4.63	4.67	4.75	4.77	4.77	4.67	4.60	4.44	4.41	4.43	4.43	4.46	5.86	6.01	4.20	4.58	6.17	5.24
Ho	0.81	0.85	0.82	0.81	0.82	0.83	0.88	0.98	0.80	0.86	0.86	0.89	0.88	0.88	0.86	0.88	0.84	0.84	0.85	0.85	0.87	1.09	1.11	0.80	0.86	1.10	0.98
Er	2.07	2.14	2.10	2.05	2.08	2.13	2.20	2.44	2.01	2.12	2.15	2.17	2.11	2.16	2.09	2.24	2.13	2.11	2.19	2.16	2.22	2.67	2.76	2.00	2.16	2.63	2.39
Tm	0.29	0.30	0.29	0.28	0.29	0.29	0.30	0.33	0.28	0.29	0.29	0.29	0.28	0.29	0.28	0.31	0.29	0.29	0.30	0.30	0.30	0.35	0.37	0.27	0.29	0.34	0.32
Yb	1.69	1.73	1.71	1.68	1.69	1.71	1.77	1.90	1.60	1.64	1.64	1.66	1.60	1.64	1.59	1.79	1.73	1.71	1.79	1.79	1.79	2.04	2.15	1.60	1.75	1.96	1.84
Lu	0.24	0.24	0.24	0.23	0.24	0.24	0.25	0.27	0.23	0.23	0.23	0.23	0.22	0.23	0.22	0.25	0.24	0.24	0.25	0.25	0.25	0.28	0.30	0.22	0.24	0.26	0.25
Hf	3.40	3.55	3.59	3.49	3.46	3.57	3.39	3.61	3.33	4.24	4.36	4.56	4.48	4.52	4.46	3.95	3.79	3.80	3.75	3.71	3.18	6.84	6.36	3.77	4.11	7.51	5.45
Ta	1.28	1.37	1.54	1.40	1.34	1.41	1.25	1.54	1.39	2.29	2.39	2.50	2.50	2.56	2.49	1.85	1.58	1.56	1.64	1.54	1.15	4.08	2.93	1.78	2.85	4.81	3.30
Tl	0.06	0.08	0.07	0.08	0.07	0.09	0.05	0.03	0.05	0.04	0.03	0.01	0.03	0.05	0.04	0.03	0.05	0.04	0.15	0.08	0.07	0.07	0.07	0.08	0.08	0.05	0.03
Pb	2.61	2.72	3.11	2.77	2.69	2.85	2.13	2.08	1.89	3.42	2.64	2.68	2.22	2.57	2.46	3.08	2.88	3.24	3.73	3.45	2.52	3.59	4.00	2.93	3.17	5.09	3.68
Bi	0.01	0.01	0.01	0.01	0.01	0.01	0.02	0.00	0.00	0.00	0.01	0.01	0.01	0.01	0.01	0.01	0.01	0.01	0.01	0.01	0.01	0.03	0.01	0.00	0.01	0.02	0.01
Th	2.63	2.81	3.07	2.88	2.75	2.96	2.20	2.41	2.18	3.31	3.44	3.60	3.44	3.60	3.56	3.42	2.96	2.99	3.50	3.28	2.31	4.88	4.85	3.22	3.46	6.77	5.00
U	0.69	0.85	0.77	0.77	0.75	0.78	0.57	0.57	0.61	0.90	0.94	0.95	0.96	1.07	1.03	0.68	0.73	0.72	0.84	0.77	0.57	1.36	1.38	1.01	0.99	1.95	1.29

Appendix A.21. Irradiation Dates

Table A.21a. Irradiation dates for samples, K-glass and Ca salts

Date	Can#	Material
20/02/2014	58	Basalt Groundmass Samples
9/04/2014	60	K-Glass and Ca Salts
4/06/2015	62	K-Glass and Ca Salts
21/03/2016	70	Basalt Groundmass Samples
4/08/2016	71	Basalt Groundmass Samples
13/07/2017	77	Basalt Groundmass and Feldspar Samples